DISS. ETH NO. 24146

SOURCE LOCALIZATION OF ACOUSTIC EMISSIONS USING MULTI-SEGMENT PATHS BASED ON A HETEROGENEOUS VELOCITY MODEL IN STRUCTURAL CONCRETE

A thesis submitted to attain the degree of

DOCTOR OF SCIENCES of ETH ZURICH
(Dr. sc. ETH Zurich)

presented by

STEPHAN GOLLOB

Diplom-Ingenieur, Technical University of Vienna

born 12th April 1986

citizen of Austria

accepted on the recommendation of

Prof. Thomas Vogel (ETH Zurich, Examiner)
Prof. Dr. Thomas Schumacher (Portland State University, Co-examiner)

2017

Abstract

In recent years, the preservation of existing structures has attained equal significance as the construction of new ones, and structural health assessment of existing structures is becoming ever more relevant. Hence, the employment and advancement of innovative ultrasonic testing methods such as acoustic emission (AE) analysis seem like logical steps. Acoustic emissions are caused by the release of strain energy due to deterioration processes or internal friction. The released energy causes the excitation of elastic waves radiating away from the source, which are recorded at the surface of the structure. Acoustic emissions are a passive phenomenon mostly associated with a destruction process. In structural engineering, concrete cracking and reinforcement rupture can be detected by analyzing AE events that occur during loading and unloading of a structure. Further progress of AE analysis, and in particular successful AE source localization, depends on how the wave propagation behavior is modeled and taken into account.

Air-filled cracks represent impenetrable barriers for elastic wave propagation in solids; waves have to bypass the crack. Nevertheless, waves can travel to every part of the specimen that can be reached without passing through air. The most common source location estimation methods assume straight wave propagation paths and a global wave velocity. Both assumptions are inaccurate for cracked reinforced concrete. If a wave bypasses a crack, it is not possible for the wave travel path to be straight. Moreover, the different constituents of reinforced concrete have different wave velocities, which also affects the wave travel paths.

Numerical modeling of elastic wave propagation has become a valuable tool if combined with physical tests. Models that can take into account the complex structure of concrete have been developed in recent years. Complex velocity models allow a realistic consideration of the influences of heterogeneous materials on the wave propagation path. Since computer capacity and processor speed are steadily increasing, the physical relation between acoustic emissions and elastic wave propagation can be treated numerically.

In order to develop a source localization algorithm, numerical wave propagation combined with fundamental wave propagation equations were used to investigate and visualize the wave propagation behavior in heterogeneous materials in general, and concrete and reinforced concrete in particular. A new source location estimation method, called *FastWay*, has been developed from the obtained findings, which uses multi-linear wave propagation paths and a heterogeneous velocity model. *FastWay* was evaluated using numerical simulations, a small-scale experiment, and a large-scale experiment.

Kurzfassung

Heutzutage ist der Erhalt von bestehenden Tragwerken von gleicher Bedeutung wie die Erstellung neuer Strukturen. Aus diesem Grund wird auch die Zustandserfassung bestehender Tragwerke immer wichtiger. Es ist daher ein logischer Schritt, innovative Untersuchungsmethoden wie die Schallemissionsanalyse anzuwenden und auch weiterzuentwickeln. Schallemissionen treten bei der plötzlichen Freisetzung von Energie durch strukturelle Veränderungen wie z.B. Bruchprozessen auf. Die freigesetzte Energie breitet sich in Form von elastischen Wellen aus, die sich von der Quelle wegbewegen. Die von ihnen verursachten Teilchenbewegungen, also Verformungen, können von Sensoren aufgezeichnet werden. Schallemissionen sind daher ein passives Phänomen, welches meist im Zusammenhang mit zerstörenden Prozessen auftritt. Im Bauingenieurwesen kann die Schallemissionsanalyse dazu benützt werden, Prozesse wie das Reissen von Beton oder das Brechen von Bewehrung zu lokalisieren. Die Weiterentwicklung der Schallemissionsanalyse und insbesondere der Lokalisierungsgenauigkeit hängt stark von der Art der Berücksichtigung und Modellierung der Wellenausbreitung ab.

Die Luft in Rissen stellt ein undurchdringliches Hindernis für die elastische Wellenausbreitung in Festkörpern dar. Nichtsdestotrotz kann eine elastische Welle jeden Punkt in einem Versuchskörper erreichen, sofern eine feste Verbindung zwischen diesem und der Schallquelle besteht. Allerdings setzen alle gebräuchlichen Lokalisierungsmethoden einen geraden Wellenausbreitungspfad und eine konstante Wellenausbreitungsgeschwindigkeit voraus. Diese beiden Annahmen sind jedoch im Falle von gerissenem Stahlbeton nicht korrekt. Der Wellenpfad kann nicht gerade sein, wenn die Welle am Weg von der Quelle zum Sensor einen Riss umgehen muss. Weiters ist die Annahme einer globalen Geschwindigkeit im Falle von Stahlbeton, einer Kombination aus unterschiedlichen Materialien, eine grobe Vereinfachung. Die unterschiedlichen Wellenausbreitungsgeschwindigkeiten in den verschiedenen Materialien beeinflussen auch die Wellenfront.

Aufgrund der kontinuierlichen Steigerung der Rechengeschwindigkeit und Prozessorleistung von Computern ist es möglich, die Ausbreitung der von Schallemissionen verursachten elastischen Wellen numerisch abzuschätzen. Wenn ein heterogenes Geschwindigkeitsmodell als Grundlage für eine solche Wellenausbreitungssimulation dient, ist es möglich, auf diese Art und Weise den Einfluss von heterogenen Bestandteilen in einem Versuchskörper auf die Wellenausbreitung zu simulieren, zu untersuchen und zu visualisieren. Numerische Modelle von Beton und Stahlbeton stehen hierfür zu Verfügung. Daher sind numerische Wellenausbreitungssimulationen in Kombination mit physikalischen Tests gut dazu geeignet, verschiedene Einflüsse auf die Wellenausbreitung zu erkennen und zu verifizieren.

Die Wellenausbreitung in heterogenen Materialien allgemein und in Stahlbeton im Besonderen wurde mit Hilfe solcher Wellenausbreitungssimulationen in Kombination mit den grundlegenden Wellenausbreitungsgleichungen untersucht. Die Erkenntnisse dienten als Grundlage für die Entwicklung einer neuen Lokalisierungsmethode, welche auf multilinearen Wellenpfaden basiert und ein heterogenes Geschwindigkeitsmodell als Input verarbeitet. Diese

neue Methode, genannt *FastWay*, wurde anschliessend mit Hilfe einer Vielzahl von Simulationen sowie je einem kleinmassstäbigen und einem grossmassstäbigen Experiment evaluiert.

Acknowledgments

First and foremost, I would like to express my sincere gratitude and appreciation to my supervisor Prof. Thomas Vogel, who gave me the opportunity of pursuing my doctoral studies in his research group. The freedom of developing my research focus over time, which led to a number of interesting digressions, made this dissertation possible in the first place. His kind support enabled me to participate in several conferences all over the world, leading to a greatly facilitated exchange of ideas and knowledge. Further, I would like to thank my co-supervisor, Prof. Dr. Thomas Schumacher, for his support, guidance, and availability throughout this dissertation. The financial support by the Swiss National Science Foundation is gratefully acknowledged.

In addition, I would like to thank Thomas Schumacher for his supervision and for providing manpower during my research visit at the Portland State University. I also would like to extend my thanks to the whole iSTAR laboratory team, especially Prof. Dr. Peter Dusicka and Thomas Bennett for their help with the laboratory equipment, preparation of my test setup, and the experimental procedure. Dr. Lassaad Mhamdi was of great help during my research stay at the Portland State University regarding the design of the experiments and the experimental procedure, as well as the analysis of the data gained from the tests. Ali Hafiz provided great support during the preparation of the test setup and the entire experimental program. I would also like to thank his wife, who provided us with delicious food even during our work-filled weekends. A special thanks to Eric Pannese and Neil Hoult from Queens University for helping us with the digital image correlation.

My arrival in Zurich was facilitated greatly by Renate Amatore, who took care of all the housing and administrative issues, enabling me to concentrate on my research from the first day on, and ensuring that I felt welcome from the start. I would also like to express my gratitude to Lucia Keller for taking care of the administration of the group.

Sincere thanks to all my colleagues at the Institute of Structural Engineering for the excellent time together. I would like to acknowledge my current and former research group colleagues, Yasmin Lemcherreq, Salma Mozaffari Kojidi, Christina Röthlin, Gosia Felux, Christian Spathelf, Gabriel-Martin Elekes, Fernando Ortiz Quintana, Dr. Holger Diederich, Dr. René Ringli, Dr. Borja Herraiz Gomez, Prof. Dr. Stephan Fricker, Dr. Thomas Wolf, Dr. Georg Kocur, Dr. Patrick Fehlmann, and Dr. Kristian Schellenberg for creating a pleasant work environment and for their assistance and support in my daily work. Borja, Holger, Christian, and René were particularly helpful during the early stage of my research at ETH. Dr. Georg Kocur introduced me to numerical wave propagation simulations and was of great help during the development of my scientific articles. My present colleagues did a great job relieving me during the final phase of my dissertation.

I would further like to thank my friends in Zurich, Vienna, and Portland. They ensured that I enjoyed my free time and provided a welcome distraction from research. I owe special thanks to Laura and Borja, my former neighbors and flatmates. They made sure that I had friends and acquaintances in Zurich from the beginning.

Special thanks to my family, who always supported and accompanied me on my path leading up to this moment. I also owe an enormous debt of gratitude to my wife, Meryem, who supported me first during my application to ETH and moving from Vienna to Zurich, then by joining me in Switzerland and encouraging me to visit Portland for three months, and finally by accepting that I spent many nights in the office. Thank you for all your love and patience.

Contents

Chapter 1

Introduction

In recent years, the preservation of existing structures has attained equal significance as the construction of new ones, and the structural health assessment of existing structures is becoming ever more relevant. Hence, the employment and advancement of innovative ultrasonic testing methods such as acoustic emission analysis (AE analysis) seem like logical steps. Acoustic emissions are caused by the release of strain energy due to deterioration processes or internal friction. The released energy causes the excitation of elastic waves radiating away from the source [41]. The emitted waves (small transient displacements) are recorded at the surface of the structure, generally by piezoelectric sensors, and converted into electrical signals. The gained information is of practical interest for the monitoring and assessment of structures. The publication of Kaiser's dissertation [26] is often quoted as the beginning of AE analysis. Kaiser concentrated on homogeneous materials, with the focus on steel. Acoustic emissions are a passive phenomenon mostly associated with a destruction process [23]. In structural engineering, concrete cracking and reinforcement rupture [9–11, 40] can be detected by analyzing AE events that occur during loading and unloading of a structure. These events can be analyzed either qualitatively or quantitatively. Qualitative (or signal-based) AE analysis methods make use of basic parameters of recorded signals and aim at identifying the load history and stage of degradation of the material. In quantitative (or parameter-based) AE analysis methods, all characteristics of an acoustic emission source are analyzed. Therefore, the wave propagation between source and sensors needs to be considered. In previous studies in the field of geophysics, significant results were achieved with respect to the determination of arrival times of the primary waves (picking) [36], source localization of acoustic emission events, and crack kinematics (moment-tensor analysis) [2]. For AE analysis of concrete, further progress, and in particular successful source localization depends on how wave propagation is modeled in concrete and how other components of structural concrete elements such as reinforcement, post-tensioning tendons, or inserts are taken into account with respect to the applied velocity models.

Numerical modeling of elastic wave propagation has become a valuable tool in combination with physical tests. Models have been developed that can take into account the complex structure of concrete. Complex velocity models allow a realistic consideration of the influences of heterogeneous materials on wave propagation and are capable of taking into account reinforcement bars or similar items, such as prestressing steel or cladding tubes. Complex velocity models of the specimen can be used to approximate the wave propagation path. Due to the continuous increases in computer capacity and processor speed, the physical relationship between acoustic emissions and elastic wave propagation can be expressed numerically. For example, solutions of elastodynamic equations can be calculated extremely rapidly and visualized very realistically [45]. Parallel processing and high-speed computer clusters permit the simulation

of complex elastic wave propagation in different geometries and with variable material models. Some promising simplifications have been introduced in the modeling of concrete that make it possible to take heterogeneous material properties into account.

Numerical wave propagation simulations are well suited to be used for investigations of various influences on the wave propagation behavior. They can be used to visualize and quantify how heterogeneity affects wave propagation. To do so, a numerical model of the specimen is needed. In order to create a realistic numerical model of the specimen, both the inner structure of the specimen and the relevant material properties such as the density and wave propagation velocity have to be known. Obtaining this information can be a complex task. One possible way of obtaining information about the inner structure is to X-ray the specimen; however, this is generally only possible for small specimens. Acoustic tomography is another option for determining the inner structure of a specimen for AE analysis. However, two facts limit the successful application of acoustic tomography. First, a large number of sensors and an even larger number of sources are needed in order to obtain an accurate high-resolution numerical model of the specimen. Thus, it is only possible to analyze a small (part of a) specimen. Secondly, straight wave propagation paths are assumed in acoustic tomography, whereas the fastest wave may not propagate along a straight path (see Chapter 2). However, introducing non-straight wave propagation paths in acoustic tomography would lead to too many unknowns in the iterative calculation of the wave propagation velocity of each voxel comprising the numerical model of the specimen. Even though acoustic tomography cannot be used to obtain an accurate high-resolution velocity model of the specimen, it can be used to identify damaged areas [3, 4] or to obtain a 2D tomogram of a section in order to locate reinforcements or tendons [38].

In order to develop a source localization algorithm, numerical wave propagation combined with fundamental wave propagation equations was used to investigate and visualize the wave propagation behavior in heterogeneous materials in general, and concrete and reinforced concrete in particular (see Chapters 2 and 5). Based on the findings of this investigation, a new source location estimation method called *FastWay* has been developed (see Section 3.4). Numerical models based on construction plans can be used as input for more sophisticated source location estimation methods for reinforced concrete elements (see Chapter 3). However, anything known even if not shown in construction plans, such as honeycombing and especially cracks, should also be included in the numerical models. The specimen should be inspected at least visually and the gained information included in the numerical model. Several existing types of numerical models that are needed as input for this method have been evaluated, edited, and extended (see Chapter 4). Finally, the *FastWay* method was evaluated with numerical simulations (see Chapter 5), a small-scale experiment (see Chapter 6), and a large-scale experiment (see Chapter 7).

This research project was funded by the Swiss National Science Foundation SNF (grant number 200021_153371).

Chapter 2

Elastic Wave Propagation

As mentioned in the previous chapter, acoustic emissions are caused by a sudden internal release of strain energy, for example due to material fracture. The released energy manifests as elastic waves [1] radiating away from the source [23, 41]. Sensors (primarily piezo-electrical sensors) record the (surface) displacement caused by these elastic waves. The recorded signals can subsequently be used as input for various analyses (for example for source localization; see Chapter 3). The wave propagation path is of particular interest for most of the possible AE analysis applications. Wave propagation in general and estimating the fastest wave propagation path in particular are an integral component of this dissertation. Passages of this chapter have been published in [16, 17].

2.1 Elastic Wave Propagation in Homogeneous Media

2.1.1 Elastic wave propagation in infinite homogeneous media

Elastic waves in an isotropic homogeneous infinite space propagate along a straight path. The spherical wave front propagates away from its source, as illustrated in Fig. 2.1. In an infinite solid, pressure waves (p-waves) and shear waves (s-waves) occur, whereas in ideal liquids or gases, shear waves do not occur. P-waves and s-waves are called body waves [50] and they propagate independently with their characteristic wave velocities c_p and c_s, respectively. According to Sutilov [55], their wave velocities

$$c_p{}^2 = \frac{E(1-\nu_0)}{\rho(1+\nu_0)(1-2\nu_0)} \tag{2.1}$$

and

$$c_s{}^2 = \frac{E}{2\rho(1+\nu_0)} \tag{2.2}$$

are functions of the Young's modulus E and the dynamic Poisson's ratio ν_0. The ratio of the two body-wave velocities of a particular material

$$\frac{c_s}{c_p} = \sqrt{\frac{1-2\nu_0}{2-2\nu_0}} \tag{2.3}$$

depends solely on its Poisson's ratio. Eq. (2.3) illustrates that a p-wave propagates faster than an s-wave in the same material, with the exception of auxetic materials with $\nu_0 < 0$ [53].

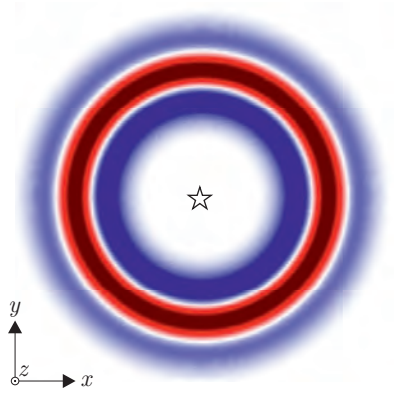

Fig. 2.1: Illustration of the wave propagation within an isotropic homogeneous infinite space. The location of an explosive Ricker-type source is marked with ☆.

2.1.2 Elastic wave propagation in finite homogeneous media

If the incident wave propagates through a solid homogeneous material towards a free boundary and interacts with the surface, the wave is split into a reflected and a refracted wave at the boundary. One of these two waves is a p-wave, the other an sv-wave (see Fig. 2.3 (a) and (b)). Shear waves (s-waves) can be either sh-waves or sv-waves. An sv-wave is an s-wave with "vertically"* polarized particles. The particles move in the plane of observation and normal to the direction of wave propagation. An incident sv-wave is reflected and refracted at the free boundary (see Fig. 2.3 (b)). An sh-wave is an s-wave with horizontally polarized particles. The particle motion is perpendicular to the plane of observation and normal to the direction of wave propagation [59]. An sh-wave interacting with a boundary is not refracted but reflected exclusively as an sh-wave. An incident p-wave (P_0) is reflected as a p-wave (P_1) at a free boundary and refracted as an sv-wave (SV_1), as illustrated in Fig. 2.3 (a). P-waves and sv-waves are coupled by their interaction with the boundary. Snellius formulated a relationship between the angle of incidence Θ_0 and the refraction and reflection angles as well as the corresponding phase velocities c_0, c_p and c_s [5]:

$$\frac{\sin \Theta_i}{\sin \Theta_j} = \frac{c_i}{c_j}. \tag{2.4}$$

Transforming the equation that Θ_S is formulated as a function of Θ_P, c_p, and c_s yields

$$\Theta_S = \arcsin\left(\frac{c_s}{c_p} \sin \Theta_P\right) < \Theta_P. \tag{2.5}$$

If the incident wave is a p-wave (P_0) with the incident angle Θ_0, the angle of the reflected p-wave (P_1) is defined as $\Theta_P = \Theta_0$, as the ratio of the velocities $c_p/c_p = 1$ (see Eqs. (2.4) and (2.5)). Because $c_s/c_p < 1$ (excluding auxetics), the refraction angle Θ_S of the sv-wave (SV_1) is smaller than the incident angle of the p-wave (P_0), as illustrated in Fig. 2.3 (a). On the other hand, if the incident wave is an sv-wave (SV_0) with the incident angle Θ_0, the angle of the reflected sv-wave (SV_1) is defined as $\Theta_{SV} = \Theta_0$, as the ratio of the velocities $c_s/c_s = 1$. Because $c_s/c_p < 1$ (excluding auxetics), the refraction angle Θ_P of the p-wave (P_1) is larger than the incident angle of the sv-wave (SV_0), as illustrated in Fig. 2.3 (b), with the limitation $0 \leq \sin(\Theta_P) \leq 1$. This

*The term "vertical" originates from the field of seismology. The waves of an earthquake are considered to propagate parallel to the surface; i.e. horizontally. Therefore, particles moving perpendicularly to the wave propagation direction move vertically.

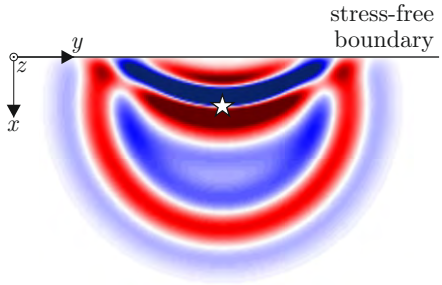

Fig. 2.2: Illustration of the propagation and interaction of the elastic wave with the surface of an isotropic homogeneous half-space. The location of an explosive Ricker-type source is marked with ☆.

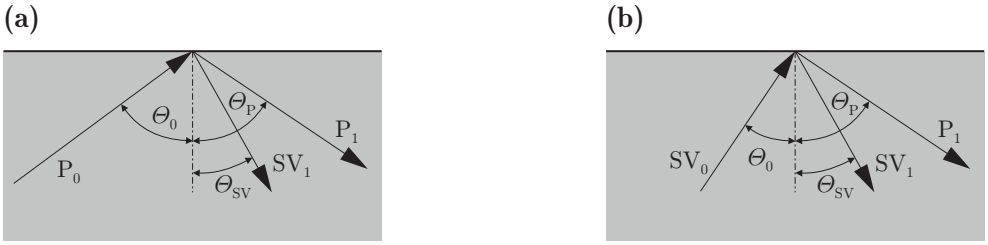

Fig. 2.3: Reflection and refraction at a free boundary of (a) a p-wave and (b) an sv-wave (adapted from [22])

limitation leads to a critical incident angle Θ_K for sv-waves, defined as

$$\Theta_K = \arcsin \frac{c_s}{c_p}. \tag{2.6}$$

Inserting Eq. (2.3) into Eq. (2.6) results in

$$\Theta_K = \arcsin \sqrt{\frac{1-2\nu_0}{2-2\nu_0}}. \tag{2.7}$$

The critical angle Θ_K is solely a function of ν_0. Using a Poisson's ratio of $\nu_0 = 0.2$ (approximate Poisson's ratio of concrete) leads to a critical angle of $\Theta_K = 37.8°$, as illustrated in Fig. 2.4 (b). If the incident angle of an sv-wave Θ_0 is smaller than the critical angle Θ_K, the wave is reflected and refracted as described above. If $\Theta_0 > \Theta_K$, the determination of the refraction angle Θ_P is complex. Instead of a p-wave, a surface wave occurs which carries no energy and only exists to fulfill the boundary conditions. Summarizing, the ratio of the angles Θ_P and Θ_S only depends on the Poisson's ratio and is independent of wave length and amplitude of all waves.

The assumption of a free surface leads to a stress-free surface/boundary. In this case, the ratio of the amplitudes of the reflected p-wave and the incident p-wave is defined as

$$\frac{A_{P_1}}{A_{P_0}} = -\frac{\cos(2\Theta_\mathrm{SV}) + (1-2\nu_0)\cos(2(\Theta_0 + \Theta_\mathrm{SV}))}{\cos(2\Theta_\mathrm{SV}) + (1-2\nu_0)\cos(2(\Theta_0 - \Theta_\mathrm{SV}))}. \tag{2.8}$$

The ratio of the amplitudes of the refracted sv-wave and the incident p-wave is defined as

$$\frac{A_{SV_1}}{A_{P_0}} = 2\sqrt{\frac{1-2\nu_0}{2-2\nu_0}}\frac{\sin(2\Theta_0)(1+(1-2\nu_0)\cos(2\Theta_0))}{\cos(2\Theta_\mathrm{SV}) + (1-2\nu_0)\cos(2(\Theta_0 - \Theta_\mathrm{SV}))}. \tag{2.9}$$

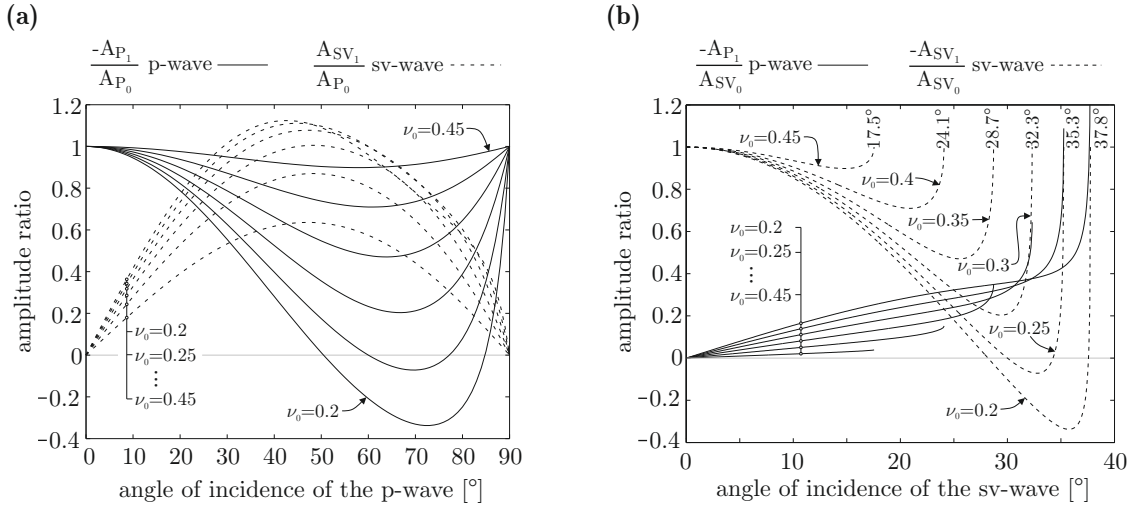

Fig. 2.4: Relative amplitude ratios of reflected (a) p-waves and (b) sv-waves as a function of the angle of incidence Θ_0 and various Poisson's ratios (adapted from [59]). The critical angles Θ_K are marked in (b).

The amplitude ratio for a refracted p-wave and its incident sv-wave is defined as

$$\frac{A_{P_1}}{A_{SV_0}} = -\sqrt{\frac{2-2\nu_0}{1-2\nu_0}}\frac{(1-2\nu_0)\sin(4\Theta_0)}{\cos(2\Theta_0)+(1-2\nu_0)\cos(2(\Theta_P-\Theta_0))} \tag{2.10}$$

for $\Theta_0 \leq \Theta_K$. The ratio of the amplitudes of the reflected sv-wave and the incident sv-wave is defined as

$$\frac{A_{SV_1}}{A_{SV_0}} = -\frac{\cos(2\Theta_0)+(1-2\nu_0)\cos(2(\Theta_P+\Theta_0))}{\cos(2\Theta_0)+(1-2\nu_0)\cos(2(\Theta_P-\Theta_0))}, \tag{2.11}$$

presupposing $\Theta_0 \leq \Theta_K$. These four equations, taken from [59], illustrate that the amplitudes of the reflected and refracted waves only depend on the amplitude of the incident wave, the angle of incidence and the Poisson's ratio, as both the reflection angle and the refraction angle are also a function of the angle of incidence and the Poisson's ratio. The amplitude ratios are frequency independent. The amplitude ratios for an incident p-wave are illustrated in Fig. 2.4 (a), and those for an incident sv-wave in Fig. 2.4 (b) as a function of the angle of incidence Θ_0 and for different Poisson's ratios. The considered angles of incidence for an incident sv-wave are limited to $\Theta_0 \leq \Theta_K$.

Eq. (2.8) and Fig. 2.4 (a) illustrate that the amplitude of a reflected p-wave does not exceed the amplitude of an incident p-wave ($A_{P_1}/A_{P_0} \leq 1$). For $\nu_o < 0.26$ and certain angles of incidence, the p-wave is entirely converted into an sv-wave, a phenomenon called mode conversion. However, the amplitude of the refracted sv-wave can be bigger than the amplitude of the incident p-wave (Eq. (2.9)). The amplitude of the reflected sv-wave of an incident sv-wave does not exceed the amplitude of the incident sv-wave itself ($A_{SV_1}/A_{SV_0} \leq 1$). For $\nu_0 < 0.26$ and certain angles of incidence, the sv-wave is converted entirely into a p-wave (mode conversion). Moreover, for $\nu_0 < 0.26$, the amplitude of the refracted p-wave can exceed the amplitude of the incident sv-wave, if the angle of incidence approaches the critical angle Θ_K.

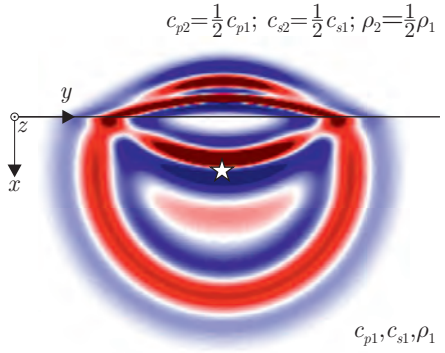

Fig. 2.5: Illustration of a wave propagating from a solid material 1 into a solid material 2, and its interaction with the boundary. The location of an explosive Ricker-type source is marked with ☆.

2.2 Elastic Wave Propagation in Heterogeneous Media

In heterogeneous materials and structures, the fastest wave may not propagate along a straight path. In reinforced concrete, a significant number of obstacles interferes with wave propagation. Some of these obstacles are considered impermeable (air in the form of cracks, voids, or honeycombing, etc.), while others may even speed up wave propagation. Materials with very high impedance contrasts have the most significant influence on the propagation behavior of elastic waves.

2.2.1 Wave interaction with boundaries

If a wave front interacts with the boundary between two different materials, the wave is partially reflected at this interface and partially transmitted to the other material, as visualized in Fig. 2.5. If the incident wave arrives at the interface at a right angle, the reflection coefficient K_r as well as the transmission coefficient K_t for a wave traveling from material i into material j can be determined as a function of the acoustic impedance coefficient of these two materials. The sound reflection and transmission coefficients [33] are defined as

$$K_{r(P)}(i,j) = \frac{Z_j - Z_i}{Z_j + Z_i} \tag{2.12}$$

$$K_{t(P)}(i,j) = \frac{2 \cdot Z_j}{Z_j + Z_i}. \tag{2.13}$$

The acoustic impedance coefficient

$$Z = \rho \cdot c \tag{2.14}$$

depends only on material properties, namely the density ρ and the considered wave velocity c. The greater the acoustic impedance contrast between two materials, the more wave energy is reflected at their interface. If an incident wave interacts with a free boundary ($Z_j/Z_i = 0$) it is reflected completely (see section 2.1.2). $K_{r(P)}$ and $K_{t(P)}$ in Eqs. (2.12) and (2.13) represent the relationship between the incident wave and reflected sound pressure. The coefficients with regard to energy are formulated as

$$K_{r(E)}(i,j) = \frac{(Z_j - Z_i)^2}{(Z_j + Z_i)^2} \tag{2.15}$$

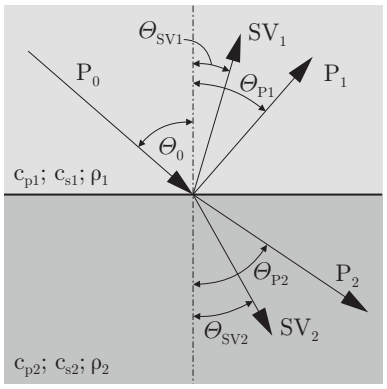

Fig. 2.6: Reflection, refraction, and transmission of a p-wave at a boundary between two solids (adapted from [22])

	c_p [m/s]	c_s [m/s]	ρ [kg/m^3]	$Z(c_p)$ [kg × s/m^2]
EEP concrete*	3912	2272	2200	8.61×10^6
Cement matrix	3950	2250	2050	8.10×10^6
Aggregate	4180	2475	2610	1.09×10^7
Reinforcement steel	5900	3200	7820	4.61×10^7
Air	0 (331)	-	0.0001 (1.29)	0 (4.27×10^2)

Tab. 2.1: Average material properties taken from [31] (values in parentheses taken from [33])

and

$$K_{t(E)}(i,j) = \frac{4\ Z_i\ Z_j}{(Z_j + Z_i)^2}. \tag{2.16}$$

If the incident wave interacts with the boundary between two solids, this boundary is not stress free; hence Eqs. (2.8) to (2.11) are not applicable. However, Snellius' relationship (Eq. (2.4)) remains valid (see Fig. 2.6).

All the source localization methods used in this research are arrival-time-based, which is why the behavior of p-waves is of particular interest (as $c_p > c_s$). The amplitude of the fastest wave is (almost) always reduced if the wave interacts with a boundary.

2.2.2 Wave propagation in concrete

Concrete is a commonly used heterogeneous building material. It consists of aggregate grains and air voids embedded in a cement matrix. Both, aggregate particles and air voids are distributed randomly within the concrete. Aggregates are a natural product whose material properties vary, usually within certain limits (see Section 4.3). Nevertheless, all three materials – the solids (cement matrix and aggregates) as well as the gas (air) – are considered homogeneous. The transmission and reflection behavior of a wave propagating from one material into another depends on the acoustic impedance contrast between these two materials (see Eqs. (2.12), (2.13), (2.15), and (2.16)). The acoustic impedance coefficient Z is the product of the density ρ and the considered wave velocity of the material (see Eq. (2.14)). The values of $Z(c_p)$ listed in Tab. 4.1

*Material properties of numerical homogenized concrete, referred to as concrete with effective elastic properties (EEP concrete) in [31] (see Section 4.3)

$K_{r(P)}(i,j)$ [%]		Material j			
		Cement matrix	Aggregate	Reinf. steel	Air
Material i	Cement matrix	0.00	-14.80	-70.14	99.99
	Aggregate	14.80	0.00	-61.75	99.99
	Reinforcement steel	70.14	61.75	0.00	100.00
	Air	-99.99	-99.99	-100.00	0.00

Tab. 2.2: Sound pressure reflection coefficient $K_{r(P)}(i,j)$ (Eq. (2.12)) determined for a wave propagating from material i into material j. The used material properties are shown in Tab. 4.1. For air, material properties taken from [33] are used (listed in brackets).

$K_{t(P)}(i,j)$ [%]		Material j			
		Cement matrix	Aggregate	Reinf. steel	Air
Material i	Cement matrix	100.00	85.20	29.86	199.99
	Aggregate	114.80	100.00	38.29	199.99
	Reinforcement steel	170.14	161.75	100.00	200.00
	Air	0.01	0.01	0.00	100.00

Tab. 2.3: Sound pressure transmission coefficient $K_{t(E)}(i,j)$ (Eq. (2.13)) determined for a wave propagating from material i into material j. The used material properties are shown in Tab. 4.1. For air, material properties taken from [33] are used (listed in brackets).

$K_{r(E)}(i,j)$ [%]		Material j			
		Cement matrix	Aggregate	Reinf. steel	Air
Material i	Cement matrix	0.00	2.19	49.20	99.98
	Aggregate	2.19	0.00	38.13	99.98
	Reinforcement steel	49.20	38.13	0.00	100.00
	Air	99.98	99.98	100.00	0.00

Tab. 2.4: Energy reflection coefficient $K_{r(E)}(i,j)$ (Eq. (2.15)) determined for a wave propagating from material i into material j. The used material properties are shown in Tab. 4.1. For air, material properties taken from [33] are used (listed in brackets).

$K_{t(E)}(i,j)$ [%]		Material j			
		Cement matrix	Aggregate	Reinf. steel	Air
Material i	Cement matrix	100.00	97.81	50.80	0.02
	Aggregate	97.81	100.00	61.87	0.02
	Reinforcement steel	50.80	61.87	100.00	0.00
	Air	0.02	0.02	0.00	100.00

Tab. 2.5: Energy transmission coefficient $K_{t(E)}(i,j)$ (Eq. (2.16)) determined for a wave propagating from material i into material j. The used material properties are shown in Tab. 4.1. For air, material properties taken from [33] are used (listed in brackets).

are obtained by inserting c_p into Eq. (2.14) and are used to determine the reflection/transmission behavior of p-waves. As mentioned above, p-waves are of particular interest in this dissertation, as arrival-time-based methods are used to estimate the source locations.

The two solid materials, cement matrix and aggregates, which are usually the main constituents of concrete, have roughly the same transmission coefficient ($\sim 10^7$ [kg $\times$ s/m^2]). Hence, only a small part of the wave energy is reflected at the boundary between these two materials. The reflection coefficient $K_{r(E)}$ calculated for a wave propagating from the cement matrix into the aggregate perpendicular to the cement–aggregate interface is about 2.19%, as shown in Tab. 2.4. However, as it is unlikely that the wave reaches the interface between the materials on a perpendicular travel path, a part of the wave is refracted. The Poisson's ratio of concrete and aggregate is about $\nu_0 = 0.2$ [15]. The amplitude of the reflected, transmitted and refracted waves can differ significantly from the amplitude of the incident wave with regard to the angle of incidence Θ_0 (see Fig. 2.4). The sound pressure reflection and transmission coefficients determined for a perpendicular wave interacting with a boundary between two components of concrete are listed in Tabs. 2.2 and 2.3 respectively. The corresponding energy reflection and transmission coefficients are listed in Tabs. 2.4 and 2.5 respectively.

The third main component of concrete is air. The acoustic impedance coefficient $Z(c_p)$ of air is significantly smaller than that of the solid materials. Almost no energy is transmitted from a solid to the air and vice versa. As a simplification, the wave velocity c_p as well as the density of the numerical air model can be set to zero* without any noticeable impact on the wave propagation behavior. Air in concrete can be categorized into air voids, air in cracks and air surrounding the concrete structure. All three "types" of air are physically identical, but due to their geometries and locations their impact on wave propagation is different. It is a common simplification to assume a straight wave propagation path, and most source location estimation algorithms rely on this simplification. An acoustic impedance coefficient of $Z \approx 0$ signifies that a surface, i.e. a boundary between solid and air, represents a free boundary, where almost the entire wave energy is reflected. A wave traveling from A to B has to bypass the air voids and hence a straight wave propagation path is not always possible. Air voids are a natural part of concrete. The diameters of air voids are usually in the millimeter range. The assumed straight wave propagation path is denoted as l_d. The effective wave travel path bypassing the air voids is denoted as l_{bp} (see Fig. 2.7 (a)). When air voids are present, the deviation from the straight path ($l_{bp} - l_d$) is usually negligible compared to the straight path between source and sensor l_d. The influence of air voids on the shortest wave propagation path can therefore be neglected. Depending on the frequencies of the acoustic emissions, the air voids still affect the wave front by reflecting and refracting the wave, resulting in distortion and damping of the wave signal.

In contrast to air voids, cracks have widths that are in the millimeter range or smaller, but their other dimensions are much larger. In Fig. 2.7 (b) it can be seen that the deviation from a straight path caused by a crack leads to a significantly longer wave travel path l_{bp}, compared to the direct distance between the source and sensor l_d. Hence, if a straight wave path is assumed, the wave appears to travel with a reduced velocity. This fact can be used to detect damaged areas [51, 52].

Other inclusions, such as aggregate particles or steel, also cause waves to be reflected. However, elastic wave energy is still transmitted at the wave velocity of the new material. This effect occurs every time the wave front arrives at the boundary to a new material that has a different acoustic impedance coefficient.

*The density of air is set to 0.0001. A density of exactly zero would lead to numerical problems in the used wave propagation software.

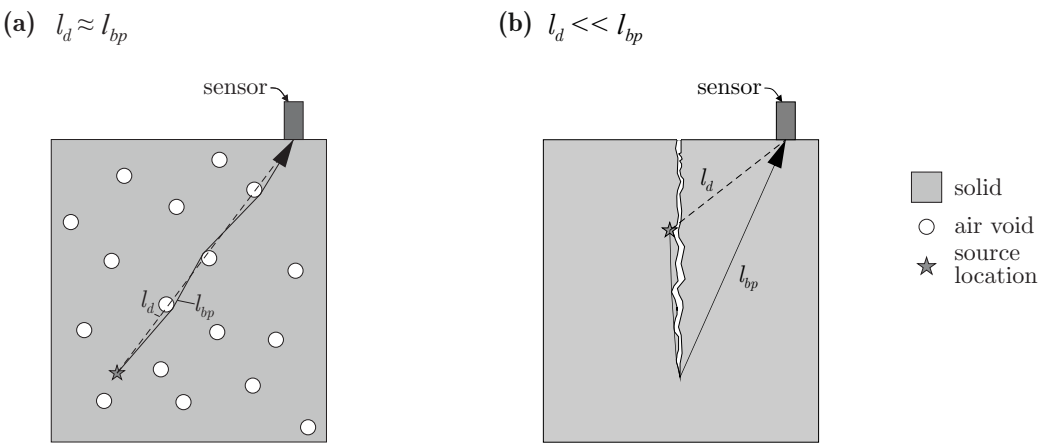

Fig. 2.7: Representations of the straight distance l_d (solid line) between source and sensor and the actual wave travel path l_{bp} (dashed line) for a medium (a) with air voids and (b) with a crack

2.2.3 Wave propagation in reinforced concrete

The tensile strength of concrete is significantly lower than its compressive strength. In order to increase the tensile resistance of a concrete structure, reinforcement can be added. The most common reinforcement type is steel bars. The material properties of steel differ considerably from those of the cement matrix, aggregates, and air (see Tab. 4.1). The p-wave velocity of steel ($c_{p(steel)} = 5900$ m/s^2) is about 1.5 times the p-wave velocity of the cement matrix ($c_{p(c-m)} = 3950$ m/s^2) (Tab. 4.1). Thus, reinforcements have a potentially significant influence on the wave propagation behavior. To discuss the potential influence of a steel reinforcement bar on the wave propagation behavior, a simplified two-dimensional ray-path model (see Fig. 2.8) is considered. The p-wave velocities of homogenized concrete and a reinforcement bar are denoted as c_1 and c_2, respectively. The reinforcement bar is modeled in one dimension. The p-wave velocity within the bar (c_2) is assumed to be constant. To simplify the approach, the angle of incidence from the source through the concrete into the bar and the exit angle from the bar to the sensor are assumed to be equal. Both angles are referred to as α_t. The suggested adapted wave travel path is indicated with the dotted line. In the presented model, the influence of the ratio of both p-wave velocities, and the dimensions of the specimen on the duration of wave propagation, is investigated. The calculation of the wave travel duration t_{norm} is normalized with respect to the case $l_2 = 0$, which leads to $l_1 = l/2$ (Eq. (2.17)). The case $l_2 = 0$ represents the shortest wave travel path if no reinforcement bar is present. Eqs. (2.18) and (2.19) describe geometrical relations. By introducing these equations into Eq. (2.17) and minimizing t_{norm} with respect to α_t, Eq. (2.20) can be derived. Eq. (2.20) shows that $\alpha_{t;\min}$ only depends on the ratio of the wave velocities c_1/c_2. For the previously mentioned p-wave velocities $\alpha_{t;\min} \approx 48°$ (see Fig. 2.9). However, this model is a rough simplification. The actual physics of a wave propagating in a steel rebar embedded in concrete are considerably more complex. Generally, the wave does not travel with the p-wave velocity of steel but with a guided mode speed, which is slower. A parameter study based on numerical simulations was performed in order to find an empirical guided wave velocity (see section 5.5).

Not only do the p-wave velocities of the steel rebar and the cement matrix (or the velocity of the guided wave in the steel rebar and the p-wave velocity of the cement matrix/concrete) differ, there are also other material properties that differ considerably. The great difference between both p-wave velocity and density of steel and the concrete constituents leads to a significant acoustic impedance coefficient contrast, too. The reflection coefficient $K_{r(E)}(i,j)$ determined

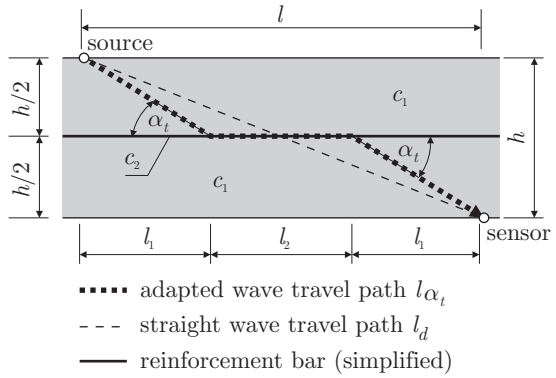

Fig. 2.8: Schematic setup for studying the influence of different parameters on the wave propagation behavior

$$t_{\text{norm}} = \frac{l_2/c_2 + \sqrt{(l_1 \cdot 2)^2 + h^2}/c_1}{\sqrt{l^2 + h^2}/c_1} \tag{2.17}$$

$$l_{\alpha_t} = l_2 + 2 \cdot \frac{l_1}{\cos \alpha_t} \tag{2.18}$$

$$\alpha_t = \arctan\left(\frac{h/2}{l_1}\right) \tag{2.19}$$

$$\alpha_{t;\min(t_{\text{norm}})} = \arccos\left(\frac{c_1}{c_2}\right) \tag{2.20}$$

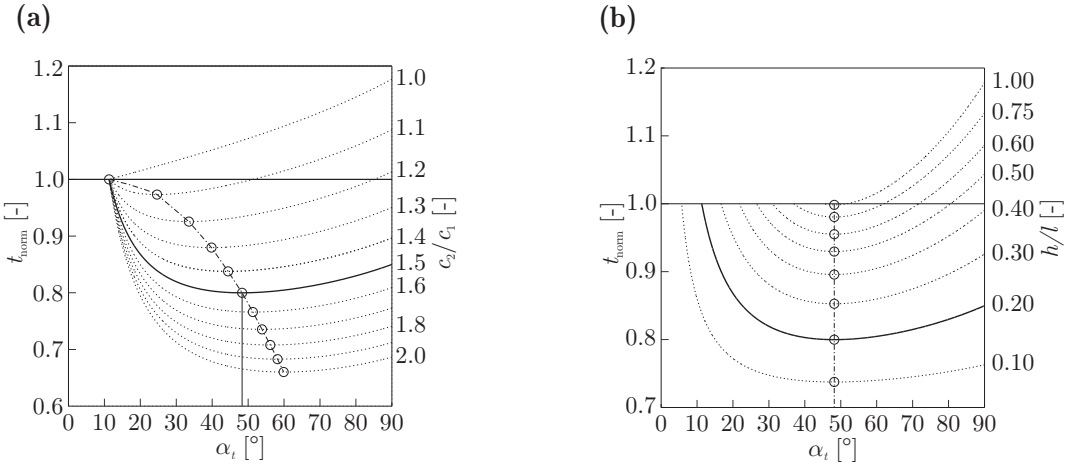

Fig. 2.9: Relationship between the wave travel path as a function of α_t and the normalized wave travel duration t_{norm} for (a) velocity ratios c_2/c_1 and a prescribed geometrical ratio of $h/l = 0.2$, (b) geometrical ratios h/l and a prescribed velocity ratio of $c_2/c_1 = 1.5$

for steel in combination with the other materials listed in Tab. 4.1 varies between 38.13% and 100.00%.

2.3 Numerical Wave Propagation Simulation

Since computer capacity and processor speed rapidly increase, the physical relation between AE and elastic wave propagation can be treated numerically. For example, solutions of elastodynamic equations can be calculated immensely faster and be visualized almost plastically [45]. Parallel processing and high-speed computer cluster enable the simulation of complex elastic wave propagation in different geometries and with variable material models. In concrete modelling, some promising simplifications have been made that allow taking into account heterogeneous material properties. In 1995 a sophisticated self-implemented, non-commercial tool for the numerical simulation of elastic wave propagation arises, called elastodynamic finite-integration technique (EFIT) [7]. The equations of motion are discretised on a numerical time domain scheme to model elastic wave propagation in isotropic, anisotropic, homogeneous and heterogeneous media, which is based on a velocity-stress formulation on a staggered-grid. The EFIT scheme is validated for isotropic, homogeneous and unbounded media by discussing dispersion relation

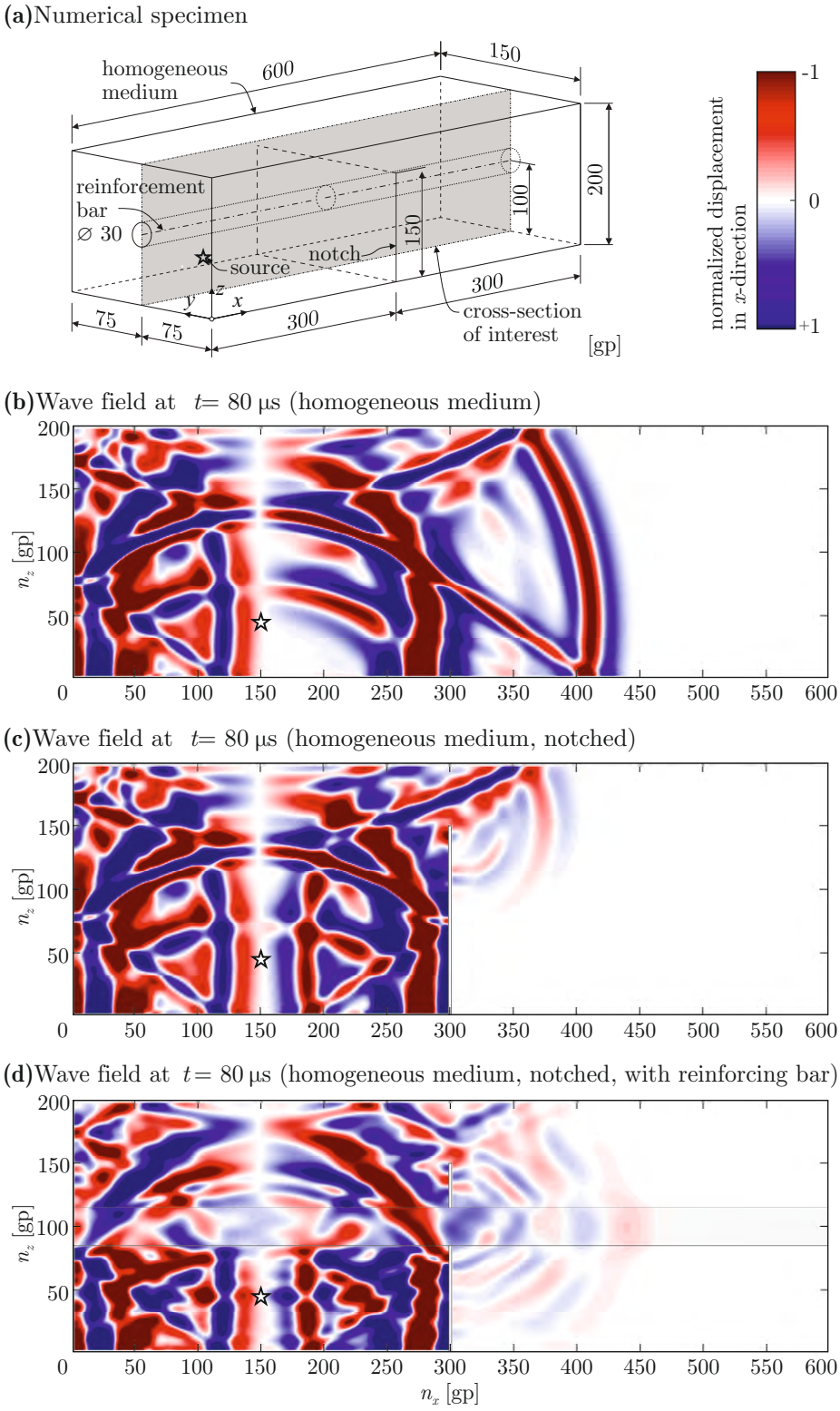

Fig. 2.10: Snapshots of the elastic wave field propagating due to an explosive Ricker-type source (marked with ☆) displayed at the mid-plane (cross-sections at $y = 75$ mm) of a three-dimensional numerical specimen at time step $t = 80$ µs; (a) Visualization of the numerical specimen consisting of a homogenized concrete, a steel reinforcement bar and a notch. Displaying the displacement field in the x-direction: (b) homogeneous medium, (c) homogeneous, notched medium, (d) homogeneous, notched, and reinforced medium.

and convergence criteria. Schubert [48] reconsiders the EFIT scheme and develops a randomly distributed concrete model. He is able to characterize scattering patterns for elastic waves by concrete aggregates and comes up with a robust numerical concrete model that is employed in a modified version in recent scientific works to be shown later. Saenger et al. [44] present in 2000 a modified version of the classic velocity-stress formulation, discretised on a staggered-grid with finite differences (FD) method [57, 58], the so-called rotated staggered-grid FD method. Neumann stability and the dispersion error are compared to the standard staggered-grid. This new approach is an alternative to EFIT and a reliable and robust tool for calculating the velocity and stress field based on the discretised equation of motion. Schubert [49] summarizes the EFIT applications for linear and non-linear elastic wave propagation in homogeneous and heterogeneous media. In particular, the randomly distributed concrete model is applied on AE modelling and discussed with respect to the scattering behaviour of large air voids. Applications of EFIT on the simulations of metallic pipes and mechanical parts in the railway industry are presented. Kocur et al. [29] apply the rotated staggered-grid FD method to simulate elastic wave propagation in numerical models obtained from X-ray computed tomography (CT) of real uncracked and cracked concrete [31] cuboids. Synergies are illustrated between numerical simulations in X-ray CT data for a concrete specimen and a self-developed purely numerical concrete model. The influence of concrete constituents such as aggregate grains and air voids on the wave propagation behaviour is studied.

For the numerical wave simulation in this documents a staggered grid finite-difference technique in the time domain was used. The same wave propagation simulation algorithms (see [44]) as in [27–30] was used. The used numerical modeling of elastic wave propagation is capable of considering all the effects on wave propagation mention in the previous sections of this chapter. The used numerical wave propagation simulations are described in detail in [44] and [27]. Fig. 2.10 shows the results of three different wave propagation simulations. It is clearly visible how a notch symbolizing a crack affects the wave propagation (compare Figs. 2.10 (b) and (c)). Reinforcements are influencing the wave propagation, too, as Fig. 2.10 (d) clearly shows. Numerical wave propagation simulations are an excellent to investigate and illustrate different influences on the wave propagation, see chapter 5.

Chapter 3

Source Localization Methods

One of the key objectives of AE analyses is to determine, or – to be more exact – estimate the source location. It is often of particular interest to locate areas with damage accumulations for structural monitoring and condition assessment. When it is a primary concern to determine the event location, which is generally unknown, a key issue for success is what approach is used to achieve the required source location estimation accuracy. The choice of the most suitable method depends on conditions such as the number and type of the recorded wave signals or the precision and availability of a velocity model of the investigated specimen. The more information is available about the investigated specimen, the more complex and elaborate the source estimation method can be. In this dissertation, the focus is on arrival-time-based source location estimation methods and the possible improvement of the estimation accuracy by incorporating multi-segmented wave travel paths based on a heterogeneous velocity model. Passages of this chapter have already been published in [17–21].

3.1 Basics of Source Localization

All AE source localization techniques aim at estimating the position of the source of a recorded acoustic emission. The result can be an estimated point location or an area in which the source is most likely located. Two input types are used by almost all source localization methods. The first type are the sensor coordinates. If the sensor layout is not rearranged during monitoring or the testing program, these input values are the same for every investigated event. The second type is obtained from the recorded wave signals. Most source location estimation methods process parameters obtained from the recorded signals instead of the entire recorded (and discretized) wave signal. The most commonly used parameter for source location estimation is the picked arrival time $t_{a,se}$ of the event-induced wave at the sensors. The input values determined from the recorded signals have to be obtained for each event and sensor. Besides the two described input types, a (wave travel) velocity model is needed for almost all source location estimation methods (see Section 3.2). Whether this velocity model stays constant for the whole monitoring process or should be updated depends on the used velocity model type and therefore on the used source location estimation method.

The relationship between the three input sets (sensor coordinates, input from the recorded wave signals, velocity model) is illustrated in Eq. (3.1), which is called the travel-time-difference approach:

$$\sqrt{(x_{se} - x_s)^2 + (y_{se} - y_s)^2 + (z_{se} - z_s)^2} = c(t_{a,se} - t_s). \tag{3.1}$$

This equation is the key function of almost all arrival-time-based point-location estimation methods (see Section 3.2.2). It links the aforementioned input values, the sensor coordinates (x_{se}, y_{se}, and z_{se}), arrival time of the wave at the sensor ($t_{a,se}$), and wave travel velocity (c), with the unknown and required values, the source coordinates (x_s, y_s, and z_s) and source time (t_s). As a simplification a constant global wave velocity c is assumed.

AE localization based on Eq. (3.1) uses the principle of trilateration. Both sides of the equation represent a distance. For a constant global wave velocity this distance is always the same, irrespective of the estimated wave propagation direction. Therefore, this distance is the radius of a sphere, with the sensor coordinates being at the center of this sphere. The source is located at the intersection of all the spheres with the radii

$$r_{se} = c(t_{a,se} - t_s) = c \cdot t_{a,se} - c \cdot t_s \tag{3.2}$$

and the center of the sphere at the corresponding sensor se. However, the absolute value of the radius r_{se} is unknown in an AE localization. The unknown part of the equations ($c \cdot t_s$) is a function of the unknown source time t_s. Combining two of the equations, for example those for sensors SE1 and SE2, eliminates the unknown part ($c \cdot t_s$):

$$r_{\mathrm{SE1}} = r_{\mathrm{SE2}} + c \cdot t_{\mathrm{SE1}} - c \cdot t_{\mathrm{SE2}}. \tag{3.3}$$

Generally, the arrival time of the wave at the sensors (t_{SE1} and t_{SE2}) as well as the wave velocity c are known values. The last two elements of Eq. (3.3) can be combined into one known value:

$$\Delta_{r_{\mathrm{SE1}};r_{\mathrm{SE2}}} = c \cdot t_{\mathrm{SE1}} - c \cdot t_{\mathrm{SE2}}. \tag{3.4}$$

Thus, by choosing the value of one of the radii, the other one is also defined:

$$r_{\mathrm{SE1}} = r_{SE2} + \Delta_{r_{\mathrm{SE1}};r_{\mathrm{SE2}}}. \tag{3.5}$$

In a two-dimensional localization problem the z-coordinates in Eq. (3.1) are eliminated. Replacing r_{SE1} and r_{SE2} in Eq. (3.5) with their counterparts from the left side of Eq. (3.1) and carrying out a transformation yields

$$\begin{aligned}\Delta_{r_{\mathrm{SE1}};r_{\mathrm{SE2}}} = &\sqrt{(x_{\mathrm{SE1}} - x_{s_{pot}})^2 + (y_{\mathrm{SE1}} - y_{s_{pot}})^2} \\ &- \sqrt{(x_{\mathrm{SE2}} - x_{s_{pot}})^2 + (y_{\mathrm{SE2}} - y_{s_{pot}})^2}.\end{aligned} \tag{3.6}$$

The unknown values in the equation are the coordinates $x_{s_{pot}}$ and $y_{s_{pot}}$ of a potential source location. Eq. (3.6) is a quadratic equation; hence, multiple solutions are possible. The equation can only be solved if

$$r_{\mathrm{SE1}} + r_{\mathrm{SE2}} \geq d_{\mathrm{SE1;SE2}}. \tag{3.7}$$

The distance between the two sensors is denoted as $d_{\mathrm{SE1;SE2}}$. For

$$r_{\mathrm{SE1}} + r_{\mathrm{SE2}} = d_{\mathrm{SE1;SE2}}, \tag{3.8}$$

only one coordinate pair fulfills Eq. (3.6). For

$$r_{\mathrm{SE1}} + r_{\mathrm{SE2}} > d_{\mathrm{SE1;SE2}}, \tag{3.9}$$

two coordinate pairs fulfill Eq. (3.6). The coordinates determined for different radii r_{SE1} and r_{SE2}, which fulfill Eqs. (3.5) and (3.7), form a hyperbolic curve, which is referred to as s_p(SE1,SE2).

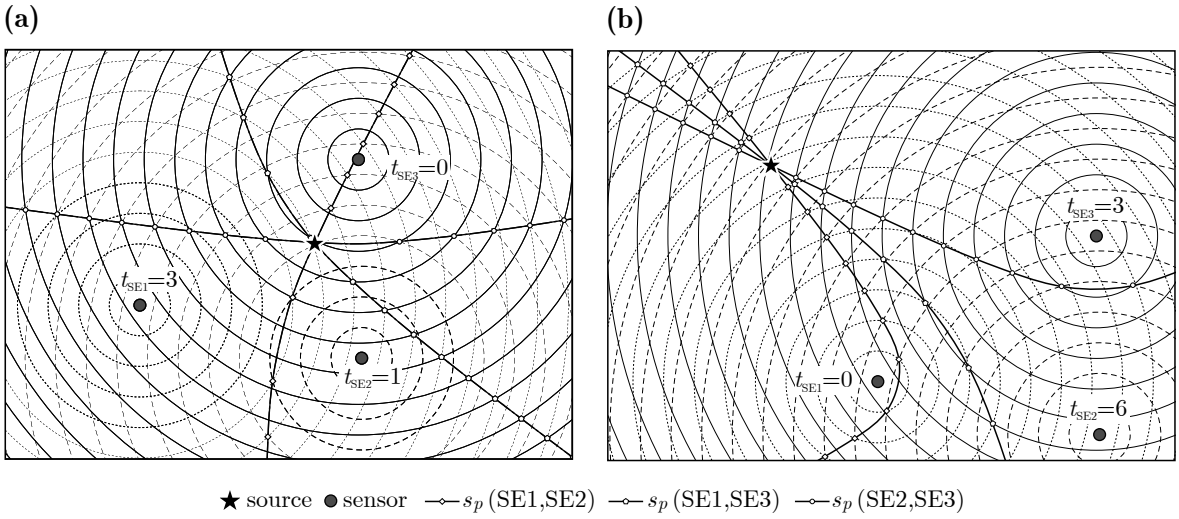

Fig. 3.1: Visualization of the (two-dimensional) travel-time-difference approach (Eq. (3.1)) including the visualization of the hyperbolic potential source location curves $s_p(i,j)$ determined for a three-sensor layout and (a) a source surrounded by sensors and (b) a source outside the sensor array.

The sensor locations are the focal points of this hyperbolic curve. The vertex is located on the line connecting the two sensors. Parameters d_{SE1} and d_{SE2} denote the distances of the two sensors from the vertex. The two distances are defined as:

$$d_{\mathrm{SE1}} = \frac{d_{\mathrm{SE1;SE2}} + \Delta_{r_{\mathrm{SE1}};r_{\mathrm{SE2}}}}{2} \tag{3.10}$$

$$d_{\mathrm{SE2}} = \frac{d_{\mathrm{SE1;SE2}} - \Delta_{r_{\mathrm{SE1}};r_{\mathrm{SE2}}}}{2}. \tag{3.11}$$

The $s_p(i,j)$ curves determined for all possible combinations of three sensors are visualized in Fig. 3.1 (a) and (b) for the same sensor layout and different source locations in a two-dimensional infinite space. The arrival time of the wave at the sensor is highlighted in the figure. The earliest arrival time is set to zero. The visualized circles have integer radii $r_i = 1, 2, ..., \mathbb{N}$. A wave velocity of $c = 1$ [length/time] leads to

$$\Delta_{r_i;r_j} = 1 \cdot t_i - 1 \cdot t_j. \tag{3.12}$$

The source is located at the intersection of the three curves (c_p(SE1,SE2), c_p(SE1,SE3), and c_p(SE2,SE3)), whose coordinates fulfill Eq. (3.6) for all possible sensor pairings.

For three-dimensional source localization Eq. (3.6) expands to

$$\begin{aligned}\Delta_{r_{\mathrm{SE1}};r_{SE2}} = &\sqrt{(x_{\mathrm{SE1}} - x_{s_{pot}})^2 + (y_{\mathrm{SE1}} - y_{s_{pot}})^2 + (z_{\mathrm{SE1}} - z_{s_{pot}})^2} \\ &- \sqrt{(x_{\mathrm{SE2}} - x_{s_{pot}})^2 + (y_{\mathrm{SE2}} - y_{s_{pot}})^2 + (z_{\mathrm{SE2}} - z_{s_{pot}})^2}.\end{aligned} \tag{3.13}$$

Again, if Eq. (3.8) applies, only one coordinate triple fulfills Eq. (3.13). If Eq. (3.9) applies, the coordinates fulfilling Eq. (3.13) will form a circle with the radius

$$r_{r_{\mathrm{SE1}};r_{\mathrm{SE2}}} = \sqrt{\left(d_{\mathrm{SE1;SE2}} \frac{r_{\mathrm{SE1}}}{r_{\mathrm{SE1}} + r_{\mathrm{SE2}}}\right)^2 - {r_{\mathrm{SE1}}}^2}. \tag{3.14}$$

Instead of forming hyperbolic potential source location curves $s_p(i,j)$, the potential source coordinates, fulfilling Eqs. (3.4), (3.7), and (3.13), form a hyperbolic surface $s_p(i,j)$. All hyperbolic surfaces determined for different sensor pairings intersect in one point, the source location. It is only in theory, however, that the two-dimensional curves $s_p(i,j)$ and three-dimensional surfaces $s_p(i,j)$ only intersect in one point.

Source localization errors do generally occur. These errors arise from a number of uncertainties. These uncertainties can be aleatory, like the heterogeneity of concrete, and epistemic like:

- sensor layout/geometry
- size of the sensor array and number of sensors
- accuracy of the sensor coordinates
- location of the source relative to the sensor array
- accuracy of the picked arrival time
- accuracy of the velocity model
- accuracy of the assumed wave travel path

3.1.1 Sensor layout

The sensor layout has a non-negligible influence on the source localization estimation accuracy. Most of the localization methods need a minimum number of input values determined from the signals recoded by the sensors, which means a minimum number of sensors (recording the acoustic emissions) is needed. For example, four values in Eq. (3.1) are unknown. Hence, at least four sensors have to provide reliable data. Reliable in terms of arrival-time-based methods means that it is possible to determine (a good estimation of) the arrival time of the wave at the sensor (see Section 3.1.2). The amplitude of the wave decreases on its way from the source due to damping. If a sensor is located too far from the source, the amplitude of the arriving (p-)wave may be too small for the sensor to detect. Hence, the distance between the monitoring sensors must not be too large. In structural concrete, the distance between the sensors should not exceed one meter [34], and often it needs to be even smaller. Consequently, the number of required sensors increases with increasing size of the monitored area. The input value "sensor coordinates" should be as accurate as possible. Inaccurate sensor coordinates distort all source location estimation results.

In addition, the sensor array should surround the monitored area [46]. It is possible to estimate the location of sources outside the sensor array. However, if the source is located outside the sensor array, any source localization error like the ones described above have a greater effect on the estimation of the source location because of the way the source location is usually estimated (see first part of Section 3.1). If, for example, the arrival time of the wave cannot be determined precisely (the arrival time is picked with an accuracy of ± 0.15), the resulting deviation between the real and estimated source location can range from negligibly small to surprisingly large, as visualized in Fig. 3.2. On the one hand, this is because the effect of the inaccuracy of the input value (in this case the picked arrival time) on the hyperbolic potential source locations curve $s_p(i,j)$ increases with increasing distance from the vertex of the curves. On the other hand, if the source is located outside the sensor array, the acute intersection angle $\alpha_{ij,ik}$ between curves $s_p(i,j)$ and $s_p(i,k)$ decreases. Thus, the area where the source might be located, defined by the intersection of the possible $s_p(i,j)$ curves, increases with the largest dimension oriented towards the center of the source array.

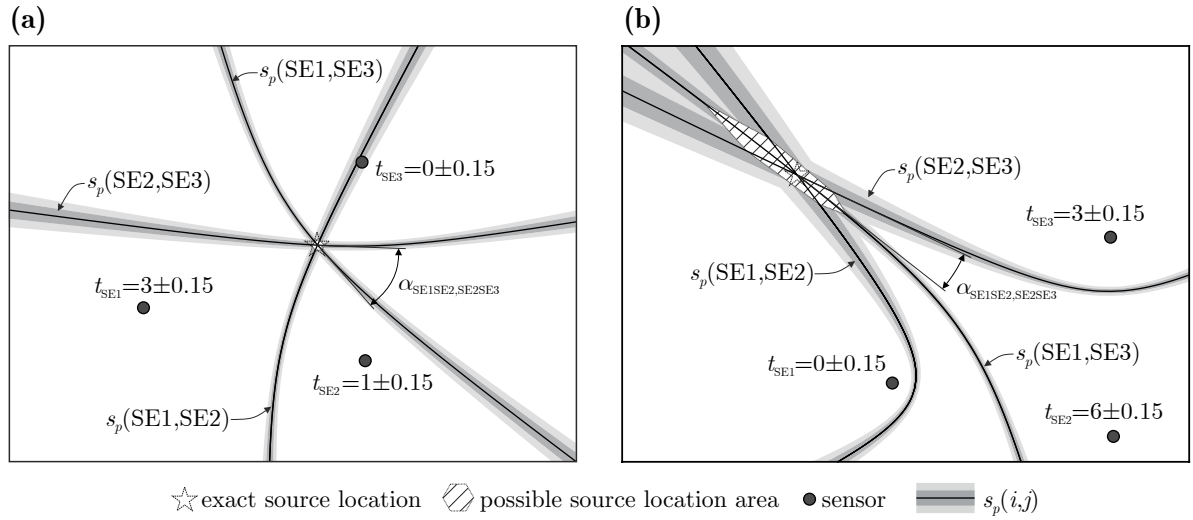

Fig. 3.2: Visualization of the influence of inaccurately picked arrival times on the potential hyperbolic source location curves $s_p(i,j)$, determined for a three-sensor layout and (a) a source surrounded by the sensors and (b) a source outside the sensor array.

The sensors should be positioned in a random fashion on the specimen so as to achieve a great variety of different source coordinates as (sensor) input values. For example, if all sensors are mounted on one surface of the specimen so that all sensors have, for example, the same y coordinate, it is impossible to estimate the y coordinate of the source. The x and z coordinates can still be estimated. Further, it is possible to estimate the third coordinate if beamforming array techniques are applied [39] and the distance between the sensor arrays is large enough for the beams of the different arrays to intersect at the source location at a sufficiently large acute angle.

Naturally, estimating the location of a source is impossible if there are impenetrable obstacles between the source and the sensors. Generally, if there are less than four sensors that receive wave energy, there is not enough input for a source location estimation. Some of the impenetrable obstacles can be bypassed, in which case the obstacles, such as cracks, have a significant influence on the wave propagation path (see Section 3.1.4). If, for example, a specimen has a complex shape, the obstacles on the wave propagation path can be parts of the specimen itself. It is not always possible to mount sensors on all surfaces of the specimen. The resulting effects on the source localization accuracy were investigated using numerical simulations and are described in Section 5.6.1.

3.1.2 Arrival time – arrival-time picking

The arrival time of the wave at the sensor is a crucial input value for all source location estimation methods. The arrival time of the wave at the sensor is determined from the signal recorded by the sensor. The recorded signal consists of the source-induced wave signal superimposed with white noise and other interfering signals.

In theory, the signal recorded before the arrival of the wave at the sensor should be zero. However, since white noise is always present, the sensors measure and record displacements even if there is no other acoustic signal. Hence, it is not possible to determine the arrival time of the fastest wave (the p-wave) at the sensor just by picking the first non-zero value of the recorded discretized wave signal.

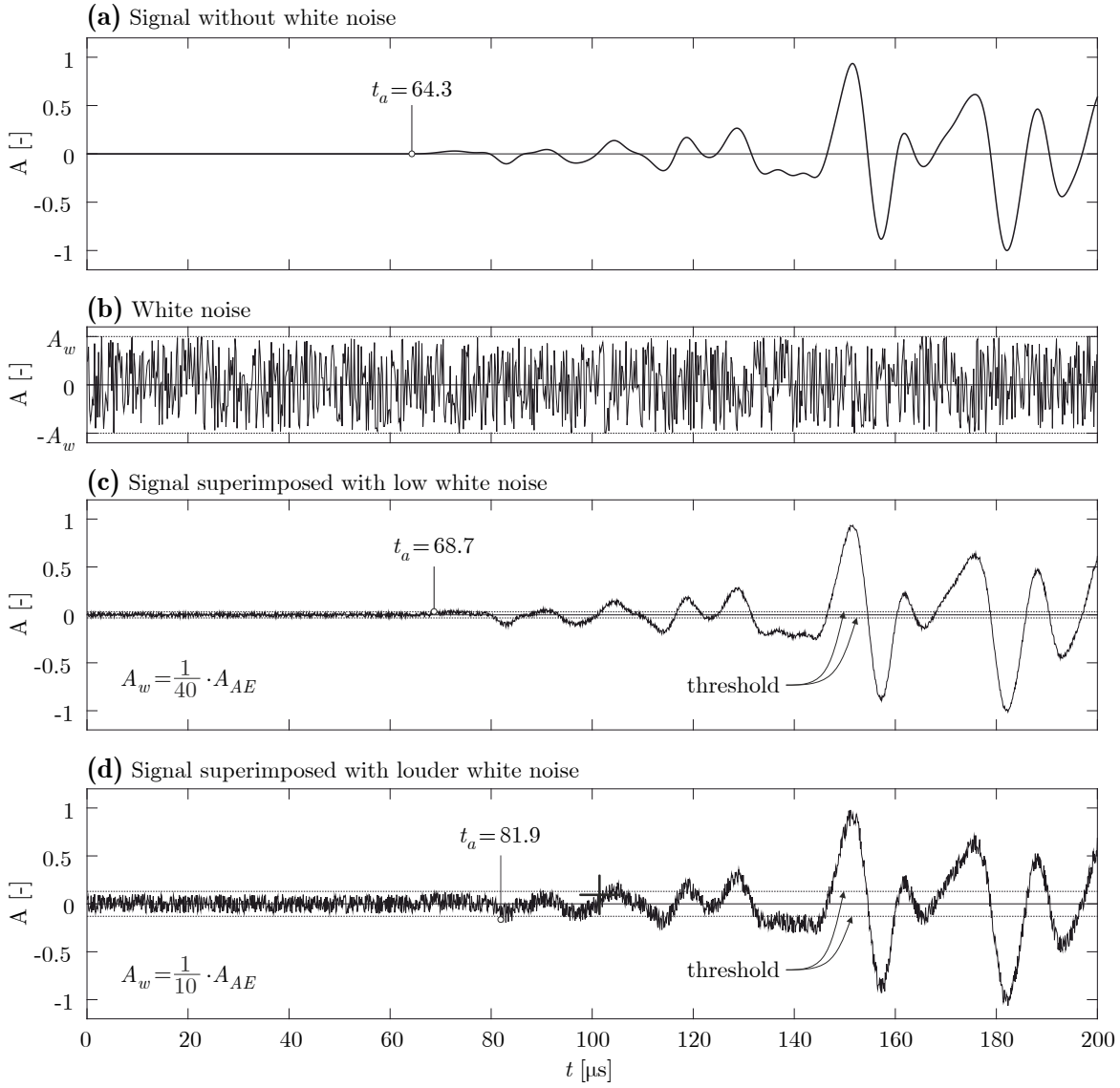

Fig. 3.3: Visualization of (a) a normalized signal recorded by a virtual sensor during a numerical wave propagation simulation in reinforced concrete without any white noise being present; (b) randomly generated white noise with a maximum amplitude of A_w; (c) superimposition of the normalized signal visualized in (a) and the white noise from (b) with a maximum amplitude of $A_w = 1/40 \cdot A_{AE}$; (d) superimposition of the normalized signal visualized in (a) and the white noise from (b) with a maximum amplitude of $A_w = 1/10 \cdot A_{AE}$. The arrival time of the wave, picked with a fixed threshold, is marked.

The amplitude of the event-induced signal must be larger than the amplitudes of the recorded white noise. If this is not the case, it is impossible to distinguish between the event-induced wave and the white noise, not to mention determine the arrival time of the wave. Various approaches for determining the arrival time of the wave at the sensors exist. If the amplitude of the arriving p-wave is larger than the constantly occurring white noise, the arrival time of the wave can be estimated by simply picking the first time at which the amplitude of the recorded signal exceeds the amplitude of the white noise. The exact maximum amplitude of the white noise, however, is an unknown value. Therefore, a threshold is needed to determine the onset time (the arrival time of the wave at the sensor). The value of the threshold depends on the amplitudes of the white noise and other interfering signals.

Fixed threshold

The simplest way to estimate the arrival time of wave t_a at the sensor is to apply a fixed threshold for the amplitude. However, this method has its limitations. On the one hand, the threshold has to be high enough to avoid that a large amplitude of the constantly recorded white noise superimposed with other interfering signals is picked. Moreover, the value of the maximum amplitude of the noise could change over time. On the other hand, the threshold should not be set too high, otherwise the arrival of a p-wave with a small amplitude will not be detected. The amplitude A_w of the recorded interfering noise is likely different for each sensor. A fixed threshold usually cannot fulfill the described requirements for all the recorded signals. For wave signals recorded during experiments, the wave onset time cannot be picked with satisfying accuracy even if a well-chosen threshold is used. Fig. 3.3 shows a visualization of the time delay caused by white noise if fixed-threshold-based arrival-time picking is used. Fig. 3.3 (a) shows the pure signal due to an acoustic emission. The signal is normalized with respect to the maximum absolute recorded amplitude (A_{AE}). The displayed signal includes no superimposed interfering signals such as white noise, which is possible only because the signal was recorded during a numerical simulation. The arrival time of the wave was determined at $t_a = 64.3\,\mu s$. The amplitude of the arriving wave is quite small; a significant deviation from the zero line is not visible until $t = 80\,\mu s$. Fig. 3.3 (b) is a visualization of randomly generated white noise. The maximum and minimum amplitudes of the white noise are denoted as A_w and $-A_w$, respectively. Fig. 3.3 (c) and (d) were generated by superimposing the pure signal caused by an acoustic emission (Fig. 3.3 (a)) with the randomly generated white noise (Fig. 3.3 (b)). A white-noise amplitude of $A_w = 1/40 \cdot A_{AE}$ was used for Fig. 3.3 (c), which means that the maximum absolute amplitude of the white noise was 1/40 of the maximum absolute amplitude of signal A_{AE} caused by the numerical acoustic emission. The fixed threshold was defined as ± 1.3 times A_w, yet it was still possible to estimate the arrival time of the wave accurately. The determined onset time $t_a = 68.7\,\mu s$ differs from the correct one by less than $5\,\mu s$. However, if the amplitude of the white noise were four times larger, as visualized in Fig. 3.3 (d), the absolute threshold would be larger than the absolute amplitude of the arriving wave and an almost $20\,\mu s$ late onset time would be determined.

There are approaches other than applying a fixed threshold to improve the picking accuracy, such as using different kinds of dynamic thresholds or following more complex approaches such as the AIC picker.

Dynamic threshold

Using a dynamic threshold does not eliminate the necessity of choosing a threshold larger than the noise amplitude. However, it allows (in theory) the use of a threshold that is as small as possible with respect to the recorded noise. However, small amplitudes of the arriving p-wave can be mistaken as louder noise. In that case, the dynamic threshold would increase, and the arrival of the p-wave would not be detected. Nevertheless, the picking accuracy can be improved significantly by applying a dynamic threshold. In Chapter 7, a multi-stage picking procedure including dynamic threshold picking is used.

AIC picker

The AIC (Akaike Information Criterion) picker is one of the most reliable advanced picking algorithms. No empirical values are needed for this algorithm [35]. Based on a first estimation of the onset time, determined for example with a fixed threshold picker, a time frame is chosen. The

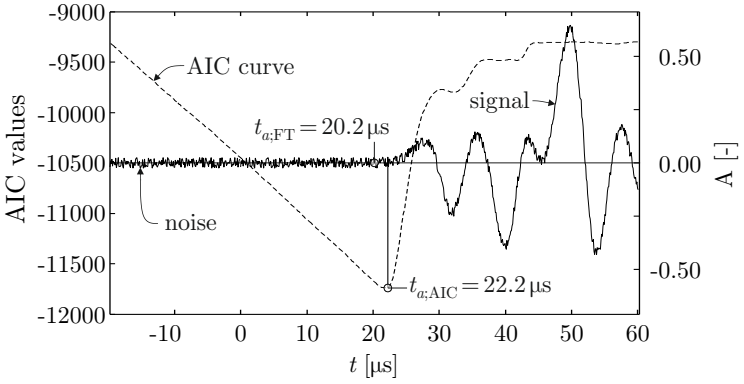

Fig. 3.4: Visualization of the result of an AIC picking process. The onset times determined with a fixed threshold ($t_{a;FT}$) and the AIC picker ($t_{a;AIC}$) are marked. The recorded signal and the calculated AIC curve for the applied time frame are visualized between $t_{a;FT} - 40\,\mu s$ and $t_{a;FT} + 40\,\mu s$.

waveform inside this time frame is transformed with the Hilbert transformation or the complex continuous transformation. Subsequently, an envelope of the transformed signal is computed and the AIC function is calculated. The minimum of the AIC function corresponds to the estimated arrival time of the wave (see Fig. 3.4). Hence, the arrival time determined with the AIC picker is limited to be within the chosen time frame (AIC window). In Chapter 7, a multi-stage picking procedure including AIC picking was used. The applied AIC picker including all the parameter settings is described in more detail in Section 7.3.1.

3.1.3 Velocity model

Most source location estimation methods assume that the wave travels with a global velocity c, as shown in Eq. (3.1). The wave travel velocity is a material property (see Section 2.1.1). Therefore, this assumption is only valid if the wave travels in a homogeneous, solid, and undamaged medium. As soon as the (assumed) wave travel path leads through more than one material, the assumption of a global wave velocity is no longer correct. Besides, some materials have direction-dependent material properties (for example wood or modern composites such as fiber-reinforced plastics).

Two kinds of velocity models can be distinguished: global models and discretized models.

Global wave velocity models

As the name indicates, in a global wave velocity model the same velocity is applied to each point in the specimen. Hence, the model neither reflects the effects of heterogeneous materials nor those of complex specimen shapes surrounded by air or other materials on wave propagation. Nevertheless, it is possible to implement different wave velocities for the entire specimen, for example a p-wave velocity and an s-wave velocity. It is also possible to implement direction-dependent wave velocities.

Discretized wave velocity models

If more realistic velocity models are needed, numerical discretized models of the specimens are used. Numerical models (see Section 4) and therefore also numerical velocity models (see Section 4.4) represent approximations of physical specimens. The accuracy, or, to be more precise, the resolution of the numerical model depends on the size of the voxel (or pixel for a two-dimensional model). Numerical models, including numerical velocity models, are described in more detail in Chapter 4. Instead of providing global velocity information, the velocities can be defined individually for every voxel. Hence, it is possible to incorporate heterogeneous materials, composite materials, as well as complex-shaped specimens surrounded by another material.

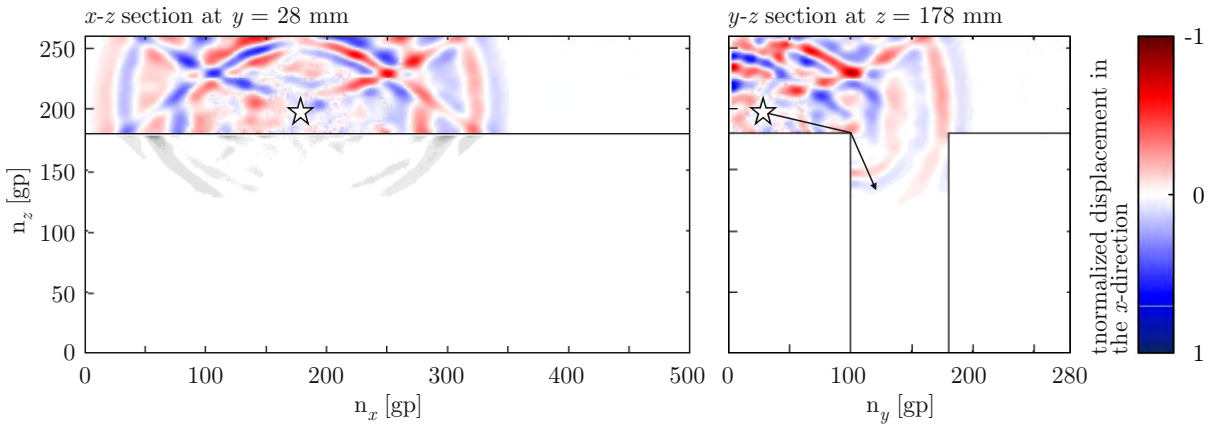

Fig. 3.5: Visualization of the wave field in a small T-shaped concrete beam; the source location is marked with ☆ (source S2 of the numerical simulation described in Section 5.6.1). The shown sections are located at the source location. [1 gp $\widehat{=}$ 1 mm]

3.1.4 Wave propagation path

In AE analysis and AE source localization the focus lies on elastic wave propagation (see Chapter 2). In a homogeneous infinite material, the wave always propagates along a straight path. In a heterogeneous material, the wave only travels on a straight wave propagation path as long as it stays within a single homogeneous component of the material. Whenever the wave reaches a boundary between two different materials, the wave interacts with this boundary (see Sections 2.1.2 and 2.2). It is transmitted partially across the boundary, but it is also reflected, refracted, and distorted. The part of the wave transmitted into the next homogeneous material generally adopts that material's wave velocity. Elastic wave propagation in heterogeneous materials is complex. It has to be pointed out that the wave usually does not travel along a straight wave propagation path in a heterogeneous or geometrically irregular specimen (see Sections 2.2.2 and 2.2.3). The influence of heterogeneity or geometrical irregularity on the wave propagation in general and the wave propagation path in particular depends on the material properties, size, and distribution of the homogeneous components within a heterogeneous material, as well as the size of the geometrical irregularities with respect to the length of the wave propagation path. Fig. 3.5 shows a visualization of the impact of the geometrical irregularities of a T-shaped cross-section on wave propagation.

In terms of source localization, three kinds of wave travel path approximations can be distinguished.

Straight wave propagation paths

In most cases, a straight wave propagation path from the source to the sensor is assumed. The only input data needed to compute such a propagation path are the coordinates of the source and the considered sensor. A straight wave propagation path is implemented in Eq. (3.1) and therefore forms the basis for the first part of Section 3.1. In most cases, the assumption of straight wave propagation paths is used in combination with a global wave velocity model. Probably the most important example is the traditional (homogeneous) Geiger method (Section 3.3.1). The assumption of straight wave propagation paths can also be combined with discretized, heterogeneous wave velocity models such as the heterogeneous Geiger method (Section 3.3.2). It has to be pointed out again that an assumed straight wave propagation path can differ significantly from the actual fastest wave propagation path.

Simulation-based wave propagation paths

The most realistic approximation of a wave propagation path is usually obtained by implementing wave propagation simulations combined with a high-resolution, highly realistic wave velocity model of the investigated specimen. In order to determine a realistic estimation of the actual wave propagation path in, for example, structural concrete, a high-resolution model, that includes small air voids and exhibits a density distribution within the aggregate, is required. Computed tomography (CT) and high-resolution X-ray are capable of providing such (three-dimensional) models. Based on the resulting highly sophisticated material properties model, which includes density and wave velocity information for each voxel, wave propagation simulations can be conducted. Time-reverse modeling (see Section 3.2.4) is an AE source localization method using reverse wave propagation simulations and therefore yields the most realistic wave propagation path approximations. However, running wave propagation simulations for every source localization requires a lot of computational power and time. The computed wave propagation path combined with the computed wave propagation is only accurate if the underlying discretized model is accurate. It has to be mentioned that such a wave propagation simulation is capable of determining the arrival time of the wave as well as the amplitudes of the ongoing signal at each voxel, but it is not capable of determining the travel path of the wave on its way to a certain voxel.

Multi-linear wave propagation paths

Assuming a multi-linear wave propagation path is significantly more realistic than assuming a straight wave propagation path. Nevertheless, a multi-linear wave propagation path still represents a simplification of the real propagation path. The multi-linear wave propagation path introduced in this section refers to the estimation of the fastest wave travel path between two points, which is a key element of the AE source localization method *FastWay* (see Section 3.4). The wave field visualized in Fig. 3.5 shows that the assumption of a bilinear (fastest) wave travel path, with the kink at the inner corner of the T-beam, is reasonably accurate. The process of determining such a multi-linear wave propagation path is described in detail in Section 3.4.2.

3.2 Existing Localization Methods – Overview

Over the past decades, a variety of source localization methods, or – more specifically – source location estimation methods, have been developed. Hardy outlined the general aspects of source localization techniques in the fifth chapter of his book *Acoustic Emission/Microseismic Activity; Volume 1: Principles, Techniques and Geotechnical Applications* [25]. He presented summaries of many of the existing methods [12] and divided them into two types of approaches, namely triaxial-sensor approaches and arrival-time approaches. The arrival-time approaches can be divided into point-location and zonal-location approaches [12]. Both approach types only use parameters derived from the recorded signal and not the entire recorded (discretized) signal. Approaches that process the entire signal also exist, for example time-reverse modeling [28].

3.2.1 Triaxial-sensor approach

The triaxial-sensor approach uses two types of physical data derived from the recorded signal – the amplitude and arrival time. Assuming straight wave propagation paths, the event location is defined by its relative distance and azimuth to the sensor, determined by the arrival-time difference of the p-wave and the s-wave combined with the amplitude information in three

orthogonal directions. This means that three-component transducers have to be used; hence the name "triaxial-sensor approach". However, three-component transducers are significantly more complex and therefore more expensive than the more commonly used piezo-electrical sensors, which measure only deformations perpendicular to the surface they are positioned on. Moreover, it is often difficult to determine the arrival time of p-waves and s-waves with this approach, especially if AE events occurring in (reinforced) concrete are investigated. Therefore, the triaxial-sensor approach is not considered further in this dissertation.

3.2.2 Arrival-time approach – point location

Arrival-time approaches determining a point location can be categorized into non-iterative [12] and iterative [13] methods. The arrival-time-based point localization methods, especially the iterative ones, are used most commonly. The basis of these methods is the following travel-time-difference approach [25] (see the first equation in Section 3.1):

$$\sqrt{(x_{se} - x_s)^2 + (y_{se} - y_s)^2 + (z_{se} - z_s)^2} = c(t_{a,se} - t_s), \tag{3.1}$$

with the unknown source coordinates x_c, y_c, z_c, and the source time t_c. The coordinates of the sensor s are x_s, y_s, and z_s, and the estimated arrival time of the wave at this sensor is $t_{a,se}$. The (wave travel) velocity in Eq. (3.1) is referred to as c. The equation illustrates that four values, the three source coordinates and the source time, are unknown. Therefore, at least four equations are needed to determine the unknown values, which means that the arrival times must be picked for a minimum of four sensors. The travel velocity of the wave propagating from the source to a sensor has to be known a priori. If more than four sensors provide input data, additional unknown values can be determined. It is possible to implement the wave velocity c as an unknown value if the wave velocity is not determined a priori. Moreover, if the system of equations is overdetermined, an error minimization can be performed, for example with the least-squares method (see Section 3.3). Considering the left side of Eq. (3.1), it can be seen that a straight wave propagation path is assumed. The right side of Eq. (3.1) indicates that a constant wave velocity is implemented.

Non-iterative methods are generally simple, and easy to apply. Computational problems connected with iterative computations, such as not meeting the convergence criterion, divergence, or guessing the correct start value, do not occur. However, these methods are incapable of processing (heterogeneous) velocity models [12].

Iterative methods are more flexible in processing arrival-time functions. Moreover, it is possible to implement a velocity model. The algorithms of the iterative approaches vary from empirically based sequential search methods to derivative systems [13]. Since iterative approaches are capable of handling a large range of practical problems, they are the most frequently applied approaches. The most common source localization method is the (homogeneous) Geiger method [13], which is described in more detail in Section 3.3.1. It is also possible to adopt Geiger's method to process a heterogeneous velocity model, since it is an iterative approach (see Section 3.3.2).

3.2.3 Arrival-time approach – zonal location

The zonal-location arrival-time approach is a special case within arrival-time-based approaches. As the name implies, the main difference between zonal location and point location is that in zonal location the zone that most likely contains the source is determined, whereas in point

location the point location or coordinates of the source are sought. The zonal-location methods can be used non-iteratively and iteratively.

Ge presented an iterative arrival-time-based zonal-location method which assumes straight wave propagation paths [12]. The monitored area is divided into so-called primary zones. Each zone is associated with one sensor. A zone extends half the distance between its associated sensor to the nearest surrounding sensors. The zone associated with the earliest picked arrival time most likely contains the source. Subsequently, the determined primary zone can be divided into smaller sub-zones The sub-zone most likely containing the source can be determined with the second-earliest picked arrival time. This sub-zone can be divided further into smaller sub-sub-zones, and so on, until the last picked arrival time has been used to narrow down the area of interest. This method, assumes straight wave propagation paths and that one single event is the cause of all the arrival times. There is no minimum required number of determined arrival times. Nevertheless, this iterative arrival-time-based zonal-location method is not considered further in this dissertation.

By definition, *FastWay* (see Section 3.4) is also a zonal-location method. The result of this novel source location estimation method is also an area that most likely contains the source. However, *FastWay* does not assume straight wave propagation paths. Instead, the fastest wave propagation paths from the source to each sensor are estimated. The method is non-iterative and requires as input the arrival time of the wave at a minimum of four sensors, as well as an accurate velocity model of the investigated specimen.

3.2.4 Time-reverse modeling

In 1997, Fink introduced time-reverse modeling (TRM) in *Time Reversed Acoustics* [8]. He pointed out that in fundamental physics time is generally irreversible. In the case of elastic waves, however, it is possible to emit one or more recorded signals in reverse to obtain (an estimation of) the time-reversed wave field. In order to emit a reversed wave field that is as accurate as possible, the entire specimen surface must be covered by sensors. Otherwise, not all of the possible reflected, refracted, or scattered signals at various locations in the medium would be considered in the time-reversed wave field.

TRM can be used to improve flaw detection in inhomogeneous and scattering media by working in pulse echo mode and using iterative time-reversal mirrors [43]. To visualize the results, an accurate high-resolution model of the specimen [29] is generally needed. The method can also be used for AE source localization [27].

3.2.5 Probabilistic source localization

By applying non-linear probabilistic methods, an improvement of the source location estimation accuracy can be achieved [56]. The result of such a non-linear localization method is a probability density function over the unknown source coordinates. The probability density function explicitly accounts for priori known data errors, which are assumed to be Gaussian. The coordinates of the estimated source location are the coordinates of the maximum likelihood point of the probability density function [23]. The accuracy of the estimated source location within heterogeneous specimens and outside the sensors array can be improved significantly [46].

3.3 Geiger's Method

Geiger's method is a stable, efficient and fast way to calculate the source location of an acoustic emission in three-dimensional space [14]. The method iteratively computes the best approximation of the source location using a least-squares approach, if signals recorded by more than four sensors are available. It was developed for AE source localization in solid homogeneous media but can also be adapted to process a heterogeneous velocity model. Geiger's method, however, always relies on the assumption of straight wave propagation paths.

The essence of the original Geiger method is formulated in the following equation, which relates the onset times $t_{a,se}$ to the source time t_s by assuming a straight wave propagation path between the source and sensors:

$$t_{a,se} = \frac{\sqrt{(x_{se} - x_s)^2 + (y_{se} - y_s)^2 + (z_{se} - z_s)^2}}{c_p} + t_s. \tag{3.15}$$

The spatial coordinates of the source location, x_s, y_s, and z_s, and the source time t_s are unknown parameters. The coordinates of the sensor se, x_{se}, y_{se}, and z_{se}, the arrival time of the p-wave at each sensor $t_{a,se}$, and the p-wave velocity c_p are known input parameters. The data of at least four sensors is needed to solve the system of equations. In general, more than four sensors are installed on a specimen, which leads to an overdetermined system of equations.

By assuming an initial source location with coordinates x_s, y_s, and z_s, as well as a source time t_s, Eq. (3.15) can be used to compute a theoretical arrival time $t_{a_t,se}$ at sensors se. The absolute value of the difference

$$\Delta t_{a,se} = t_{a_o,se} - t_{a_t,se} \tag{3.16}$$

between the observed arrival times $t_{a_o,se}$ and the theoretical arrival times $t_{a_t,se}$ at each sensor subsequently have to be minimized. The difference between the theoretical and observed arrival time can also be approximated with

$$\Delta t_{a,se} = \frac{\partial f(se)}{\partial x} \cdot \Delta x + \frac{\partial f(se)}{\partial y} \cdot \Delta y + \frac{\partial f(se)}{\partial z} \cdot \Delta z + \frac{\partial f(se)}{\partial t} \cdot \Delta t, \tag{3.17}$$

where $f(se)$ is the right side of Eq. (3.15). For N sensors, Eq. (3.17) can be written in matrix form as

$$\begin{bmatrix} \Delta t_{a,\mathrm{SE1}} \\ \Delta t_{a,\mathrm{SE2}} \\ \vdots \\ \Delta t_{a,\mathrm{SE\,N}} \end{bmatrix} = \begin{bmatrix} \frac{\partial f(\mathrm{SE1})}{\partial x} & \frac{\partial f(\mathrm{SE1})}{\partial y} & \frac{\partial f(\mathrm{SE1})}{\partial z} & \frac{\partial f(\mathrm{SE1})}{\partial t} \\ \frac{\partial f(\mathrm{SE2})}{\partial x} & \frac{\partial f(\mathrm{SE2})}{\partial y} & \frac{\partial f(\mathrm{SE2})}{\partial z} & \frac{\partial f(\mathrm{SE2})}{\partial t} \\ \vdots & \vdots & \vdots & \vdots \\ \frac{\partial f(\mathrm{SE\,N})}{\partial x} & \frac{\partial f(\mathrm{SE\,N})}{\partial y} & \frac{\partial f(\mathrm{SE\,N})}{\partial z} & \frac{\partial f(\mathrm{SE\,N})}{\partial t} \end{bmatrix} \cdot \begin{bmatrix} \Delta x \\ \Delta y \\ \Delta z \\ \Delta t \end{bmatrix}, \tag{3.18}$$

or in short matrix form as

$$\mathbf{t}_a = \mathbf{F} \cdot \Delta\mathbf{cor}, \tag{3.19}$$

where both $\Delta\mathbf{t}_a$ and $\mathbf{F}$ are assembled from known values. The correction values of $\Delta\mathbf{cor}$ are unknown. Only for the case of four sensors (N = 4) does a well-defined solution for determining

the correction array $\Delta\mathbf{cor}$ exist:

$$\Delta\mathbf{cor} = \mathbf{F}^{-1} \cdot \Delta\mathbf{t}_a. \tag{3.20}$$

It is impossible to solve the equation if less than four sensors are providing data. If N > 4, the equation is overdefined, in which case a least-squares approximation is used:

$$\Delta\mathbf{cor} = (\mathbf{F}^T \cdot \mathbf{F})^{-1} \cdot \mathbf{F}^T \cdot \Delta\mathbf{t}_a. \tag{3.21}$$

It is presupposed that the model parameters are independent and the data inaccuracies are normally distributed. Due to the linearization of the problem, the solution is calculated iteratively. The solution of Eq. (3.21) is used to update the source coordinates for the next iteration step, $k+1$.

$$\begin{aligned} {x_s}^{k+1} &= {x_s}^k + \Delta x \cdot R_x \\ {y_s}^{k+1} &= {y_s}^k + \Delta y \cdot R_y \\ {z_s}^{k+1} &= {z_s}^k + \Delta z \cdot R_z \\ {t_s}^{k+1} &= {t_s}^k + \Delta t \cdot R_t \end{aligned} \tag{3.22}$$

R are relaxation parameters. They can be defined individually for each source parameter (coordinates and time) and should be between zero and one. A relaxation parameter of $R = 0.1$ is commonly used. The iteration process stops when all four update parameters $\Delta i \cdot R_i$ are smaller than a certain value, denoted as ε. The described source localization algorithm has been published several times, for example in [13, 49].

Residuals, which indicate how well the calculated source locations and the recorded data agree with each other, can subsequently be computed. The residual for one event

$$s = \sqrt{\frac{\sum_i \Delta t_{a,i}}{i - m}} \tag{3.23}$$

depends on $\Delta t_{a,i}$, the deviations between the i observed arrival times and the i theoretical arrival times based on the final source location estimation, and on the number of unknown parameters m (source coordinates and time). It has to be mentioned that small residuals do not always signify that the localization error is small. However, big residuals generally indicate an incorrect source localization.

In order to visualize (an estimation of) the localization accuracy, error ellipsoids can be used. To do this, first the covariance matrix

$$\mathbf{C}' = \sigma_d^2 (\mathbf{F}^T \cdot \mathbf{F})^{-1} \tag{3.24}$$

has to be computed. However, the data variance is usually unknown. This is true for automatically picked arrival times; therefore, the variance σ_d^2 is substituted by s^2 (from Eq. (3.23)). The matrix $\mathbf{C}'$ is a symmetric 4×4 matrix. The eigenvalues of this matrix are the actual values for the variance of the four unknown source parameters x_c, y_c, z_c, and source time t_c. The visualization of the localization accuracy, the error ellipsoids, do not consider source-time errors. Hence, the 4×4 matrix can be reduced to a 3×3 matrix by excluding all elements with a time component. This matrix is denoted as $\mathbf{C}$. The size and orientation of an error ellipsoid can be determined by rotating $\mathbf{C}$ into normal form. The eigenvalues $\boldsymbol{w}_i$ correspond to the axis ratio, and the eigenvectors correspond to the orientation of the error ellipsoid [47]. 68% error ellipsoids as suggested by Schechinger [46] will be used in this dissertation. Therefore, the length

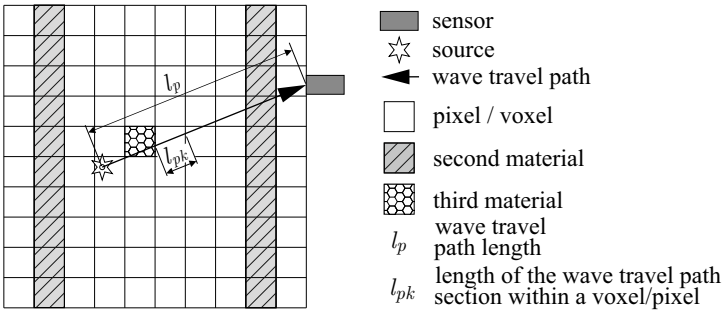

$$\bar{c}_{p\_het,se} = \sum_k \frac{l_{pk}(k) \cdot c_p(k)}{l_p} \tag{3.27}$$

Fig. 3.6: Two-dimensional scheme for determining the average wave travel velocity between the source and sensor, based on a heterogeneous velocity model and straight wave travel path

of each half-axis will be calculated with

$$l_i = \sqrt{3.53 \cdot \boldsymbol{w}_i}. \tag{3.25}$$

In her thesis, Schechinger points out that using s^2 instead of σ_d^2 leads to an overestimation of the error. This is especially true if the number of sensors providing data is between five and eight. In [46] it is suggested to use

$$s' = \frac{\sum_i \Delta t_{a,i}}{i} \tag{3.26}$$

as a substitution for σ_d^2. For the error ellipsoids in this dissertation (see Chapters 5, 6, and 7) s' is used.

3.3.1 Homogeneous Geiger method

For the traditional Geiger method, a global wave velocity model is used ($c_p = \text{const.}$). For that reason, the traditional Geiger method will be referred to as the homogeneous Geiger method in this dissertation.

3.3.2 Heterogeneous Geiger method

Geiger's method can be combined with a heterogeneous velocity model [37]. In that case, an average wave velocity $\bar{c}_{p\_het}$ (see Eq. (3.27)) substitutes the constant wave velocity c_p in Eq. (3.15). In order to compute $\bar{c}_{p\_het}$, the coordinates of sensor se and of the estimated source location s, as well as a discretized velocity model of the specimen are needed. The discretized model consists of pixels (2D) or voxels (3D). A p-wave velocity $c_p(k)$ is assigned to each of these pixels/voxels (see Section 3.1.3, Chapter 4, and in particular Section 4.4). The assumed straight wave travel path of length l_p, connecting the source and sensor, passes through k pixels (see Fig. 3.6). The length of the section of the wave travel path within a pixel $l_{pk}(k)$ varies for each pixel and therefore needs to be determined individually [54]. The average p-wave velocity $\bar{c}_{p\_het,se}$ of a wave traveling from the estimated source location to one sensor se can be computed according to Eq. (3.27). The process of computing the average wave velocity for a three-dimensional specimen is similar to the two-dimensional computation. Extending Geiger's method to process a heterogeneous velocity model has the potential to improve the accuracy of the estimated source location [19]. However, the average wave velocity $\bar{c}_{p\_het,se}$ has to be calculated for each iteration step and sensor, which increases the computational effort significantly. Moreover, the heterogeneous Geiger method assumes straight wave propagation

paths. Therefore, the influence of cracks on the wave propagation can not be considered satisfactorily. While the distance between an AE source and the sensors can range from centimeters to meters, the width of a crack usually does not exceed a few millimeters. Assigning a wave velocity of $0\,\mathrm{m\,s^{-1}}$ to the voxels representing the width of the cracks has a negligible influence on the average velocity calculated with Eq. (3.27). However, the real wave travel duration can be significantly longer than the duration determined with a heterogeneous velocity model assuming a straight wave propagation path, since the wave has to travel around the crack (see Section 2.2.2 and Fig. 2.7 (b)).

Summarizing, the heterogeneous Geiger method is able to incorporate a discretized velocity model in order to improve the localization accuracy, but assumes straight wave propagation paths, resulting in significant deviations between the estimated and real source location.

3.4 *FastWay*

FastWay is a novel approach for estimating the location of AE sources. The main difference between *FastWay* and other arrival-time-based localization methods is that the fastest wave travel path between the source and a sensor rather than the direct (shortest) one is used to estimate the source location. This is a refined way for a localization procedure to adapt to the geometry and material properties of the investigated specimen. The method is based on heterogeneous velocity models and multi-segment wave propagation analysis. In order to estimate the fastest multi-segmented wave travel path, a modified Dijkstra algorithm is used.

3.4.1 Dijkstra algorithm

The Dijkstra algorithm, published in 1959 [6], is a graph-searching algorithm for solving a single-source shortest-path problem. The input for the Dijkstra algorithm is a defined number of nodes and the length of the paths connecting them. Generally not all nodes are directly connected to each other. For *FastWay*, the wave travel time (generally of the p-wave) from one node to a connected node is used instead of the length of the connecting path between those nodes. The following node setup, which is suitable for the discretized numerical model (see Chapter 4), is suggested. The nodes used for the Dijkstra algorithm should be located in the center of the voxels of the numerical model. If the Dijkstra algorithm is applied to a node grid, a node is usually connected exclusively to its adjacent nodes, as shown in Fig. 3.7 (a). Thus, the center node n_c can be connected to a maximum of four other nodes in a two-dimensional node grid and to a maximum of six nodes in a three-dimensional node grid. Therefore, the modeled wave paths are limited to an unrealistic orthogonal system ($\omega = \pi/2 \cdot \mathbb{Z}$), as depicted in Fig. 3.7 (a). Connecting the center node with additional neighboring nodes reduces this limitation significantly. The area containing all the nodes connected to the center node is referred to as vicinity. The size of the vicinity is defined by the vicinity level v_{lev}. All nodes within distance v_{lev} from the center node n_c, in each direction of space, are located in the vicinity and are therefore connected to n_c. For $v_{\mathrm{lev}} = 1$ gp, the smallest possible angle between two potential wave travel paths ω decreases from $\pi/2$ to $\pi/4$, as illustrated in Fig. 3.7 (b). Connecting a node to additional nodes further decreases the minimum angle (see Fig. 3.7 (c)) but increases the computational effort. The number of nodes n connected to n_c, expressed as

$$n = (2 \cdot l_{\mathrm{lev}} + 1)^{\mathrm{dim}} - 1, \tag{3.28}$$

depends on the vicinity level v_{lev} and the dimension of the numerical model (dim). The resolution of the numerical discretization along with the limitations of ω introduce an error into the wave

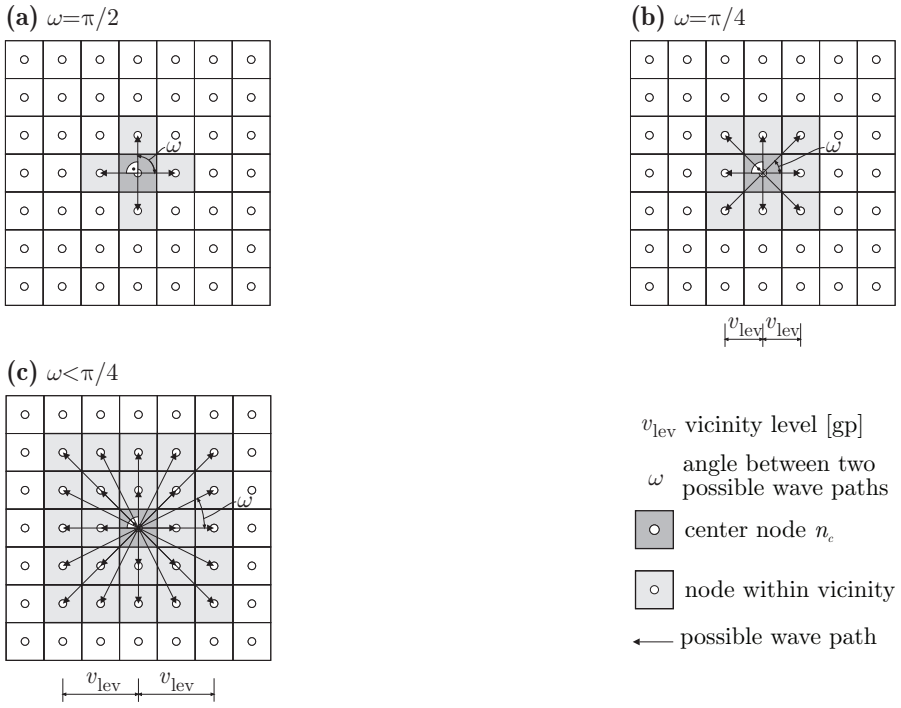

Fig. 3.7: Two-dimensional node grids in which the center point, the nodes connected with the center point (nodes in the vicinity), the possible wave paths, and ω, the angle between two possible wave travel paths, are marked: (a) the vicinity includes only direct-neighbor nodes; (b) the vicinity includes all nodes within a distance ≤ 1 gp in each direction of space; (c) the vicinity includes all nodes within a distance ≤ 2 gp in each direction of space

travel path, unless the nodes are aligned with the physical wave travel path. However, this error is small and can be minimized by decreasing the voxel size and increasing v_{lev}. The minimum size of the voxels is limited by the computational power needed to process the models. A parametric study was carried out and showed that choosing a vicinity level of $v_{\text{lev}} = 3\,\text{gp}$ allows the modeling of realistic wave paths without causing a tremendous increase in the required computational time. A vicinity level larger than 3 gp does not have a significant further positive effect on the determined wave travel time between two nodes, yet significantly increases the computational time. In a three-dimensional numerical model with a vicinity level of $v_{\text{lev}} = 3\,\text{gp}$, one node can be connected to up to 342 nodes. A vicinity level of 4 gp more than doubles this number to 728.

3.4.2 Fastest wave path between two nodes

The Dijkstra algorithm can be used to determine the fastest or shortest connection between two nodes. One of the nodes is the source or start node, n_s, while the other one is the receiving or end node, n_e. These two nodes are connected by a finite number of possible paths. Again, the possible paths are composed of a finite number of nodes and their direct connections. The execution of the Dijkstra algorithm can be divided into three steps (Step A, Step B, and Step B.1), as illustrated in Fig. 3.8. In order to determine the fastest wave path, an additional step (Step C) needs to be executed.

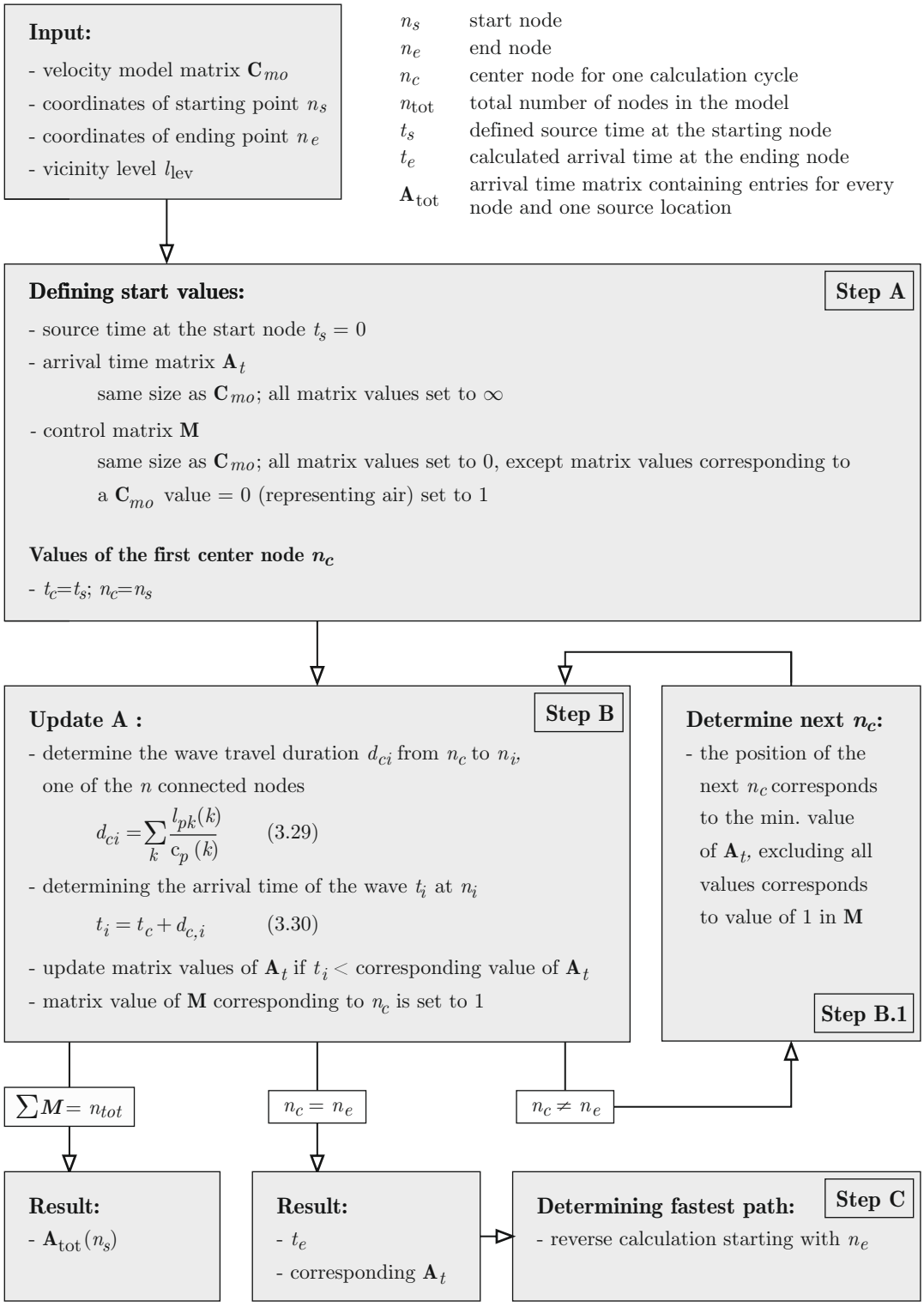

Fig. 3.8: Flowchart of the Dijkstra algorithm for determining the earliest possible arrival time and fastest wave propagation path, taken from [16]

Step A – Defining start values

To identify the fastest wave path between two nodes, the source time at n_s is set to $t_s = 0$. Two matrices with the same size and shape as the numerical velocity matrix $\mathbf{C}_{mo}$ (see Section 4.4) are generated. The first matrix is referred to as the arrival-time matrix $\mathbf{A}_t$. Each entry of $\mathbf{A}_t(n_s)$ represents the arrival time of the p-wave, which leaves node n_s at time t_s, at the node corresponding to the respective matrix entry. The position of the entry in the matrix corresponds to the node position in the numerical model of the specimen. Before initiation of the Dijkstra algorithm all values of this matrix are set to ∞*. During Step B the values of $\mathbf{A}_t$ are updated with the newly calculated arrival times. The second matrix is referred to as the control matrix $\mathbf{M} \ni \{0, 1\}$. A matrix entry of 1 means that the corresponding node must not be used as the center node n_c. Every node associated with a value of $\mathbf{M} \ni 0$ is suitable as the center node during the next execution of Step B. The p-wave velocity c_p assigned to air voxels is set to zero, as the air voxels cannot transmit wave energy. Therefore, the entries of $\mathbf{M}$ corresponding to air voxels are set to 1.

Step B – Update $\mathbf{A}_t$

For the first execution of step B, the starting node n_s is defined as the center node n_c. The arrival time of the p-wave at the center node is therefore identical with the defined source time $t_c = t_s = 0$. The time required for a p-wave to travel from node n_c to n connected nodes can be calculated using one of the numerical velocity models mentioned in Sections 3.1.3 and 4.4. Instead of using the average p-wave velocity $\bar{c}_{p\_het}$, the time duration of the wave propagation $d_{c,i}$ (see Eq. (3.27)) from node n_c to node n_i is calculated directly with

$$d_{c,i} = \sum_k \frac{l_{pk}(k)}{c_p(k)}. \tag{3.29}$$

The straight wave propagation path from n_c to n_i, illustrated in Fig. 3.9 (a), passes through k voxels. The numerical velocity matrix $\mathbf{C}_{mo}$ assigns a p-wave velocity to each of the k voxels. The length of the section of the wave travel path within a voxel is labeled $l_{pk}(k)$. To determine the arrival time of a p-wave at node n_i,

$$t_i = t_c + d_{c,i}, \tag{3.30}$$

the arrival time of the wave at node n_c and the duration of travel of the p-wave propagating from n_c to n_i are needed. Equations (3.27) and (3.29) use the same input values. However, the influence of a voxel representing air in Eq. (3.27) is by far smaller than in Eq. (3.29). The p-wave velocity of air is approximately zero (see Tab. 4.1). A very small denominator, approaching zero, leads to a very large result in Eq. (3.29). Therefore, the p-wave propagation duration $d_{c,i}$ is set to ∞ if the straight wave propagation path runs through an air voxel. Hence, the estimated arrival time of the p-wave at node n_i is $t_i = \infty$. If the calculated arrival time t_i at node n_i is smaller than the corresponding value in $\mathbf{A}_t$, the matrix entry is replaced with the smaller value t_i. With one execution of step B, the arrival time of the p-wave at n nodes is calculated. As the n nodes connected with n_c (i.e. in the vicinity) generally only represent a small part of all nodes within the numerical model of the specimen (see Fig. 3.9 (a)), step B has to be executed several times.

*The algorithms are implemented in MATLAB®. Therefore, the IEEE arithmetic representation for positive infinity as implemented in MATLAB® is used.

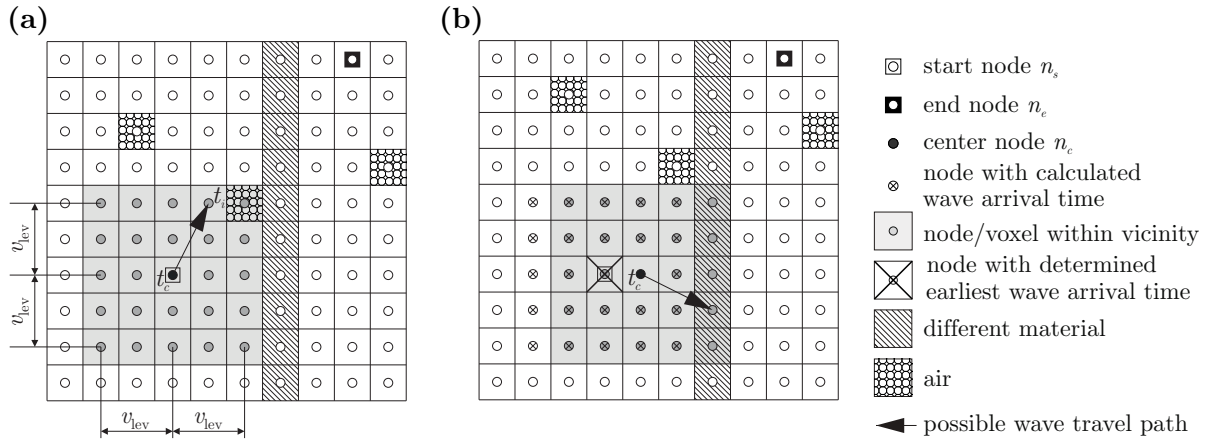

Fig. 3.9: Illustration of Step B: (a) First execution of step B ($t_c = t_s$) and (b) second execution of step B with updated center node n_c

Step B.1 – Determining the new center point n_c

A new center point n_c has to be determined for use in the subsequent execution of step B. The node in $\mathbf{A}_t$ with the smallest determined arrival time becomes the center node n_c for the next execution of step B, as long as its corresponding value $1 \in \mathbf{M}$ is not 1 (see Section 3.4.2). The calculated arrival time of the wave $t_{\min} = \min\{\mathbf{A}_t(i,j,k) | \mathbf{M}(i,j,k) = 0\}$ at the updated center node n_c is the earliest possible arrival time $t_c = t_{\min}$ of a wave emitted from n_s. The nodes in the vicinity of the new n_c overlap nodes in the vicinity of previous center nodes (see Fig. 3.9 (b)). The calculated arrival times of the wave at the nodes within the current vicinity replace the corresponding values in $\mathbf{A}_t$ only if they are smaller than the values stored in $\mathbf{A}_t$. In essence, it is always the smallest calculated arrival time value t_i that is stored in $\mathbf{A}_t$.

Results of the modified Dijkstra algorithm

The iteration is repeated until an ending criterion is fulfilled. If the result is used for the *FastWay* source localization (see Section 3.4.3), an arrival time for each node has to be determined. The ending criterion is hence defined as $\sum \mathbf{M} = n_{tot}$. The resulting arrival time matrix $\mathbf{A}_{\text{tot}}(s)$ contains the earliest arrival time of a wave propagating from source s to each of the nodes. If the fastest wave travel path and thus the smallest wave travel duration between two points/nodes is sought, an ending criterion formally written as $n_c = n_e$ can be used. This means that n_e would be used as the center node in the next iteration step and consequently that the earliest arrival time for n_e is determined. The results of the execution of the modified Dijkstra algorithm are the wave travel duration $d_{s,e}$ from the start node n_s to the end node n_e along the fastest possible wave propagation path, and the associated arrival time matrix $\mathbf{A}_t(n_s, n_e)$. However, at this point, the fastest wave propagation path between n_s and n_e is still unknown. Therefore, step C has to be executed.

Step C – Determining the fastest path between two nodes

Defining the previous start node as the end node and vice versa results in the same wave propagation duration $d_{n_1,n_2} = d_{n_2,n_1} = d_{n_s,n_e} = d_{n_e,n_s}$ and subsequently to the same fastest wave travel path connecting n_1 and n_2. To determine the nodes in the fastest wave travel path from n_1 to n_2, the Dijkstra algorithm has to be executed twice. For the first execution, n_1 is used as start node n_s, and n_2 as the end node n_e. The results are d_{n_1,n_2} and $\mathbf{A}_t(n_1, n_2)$. In the

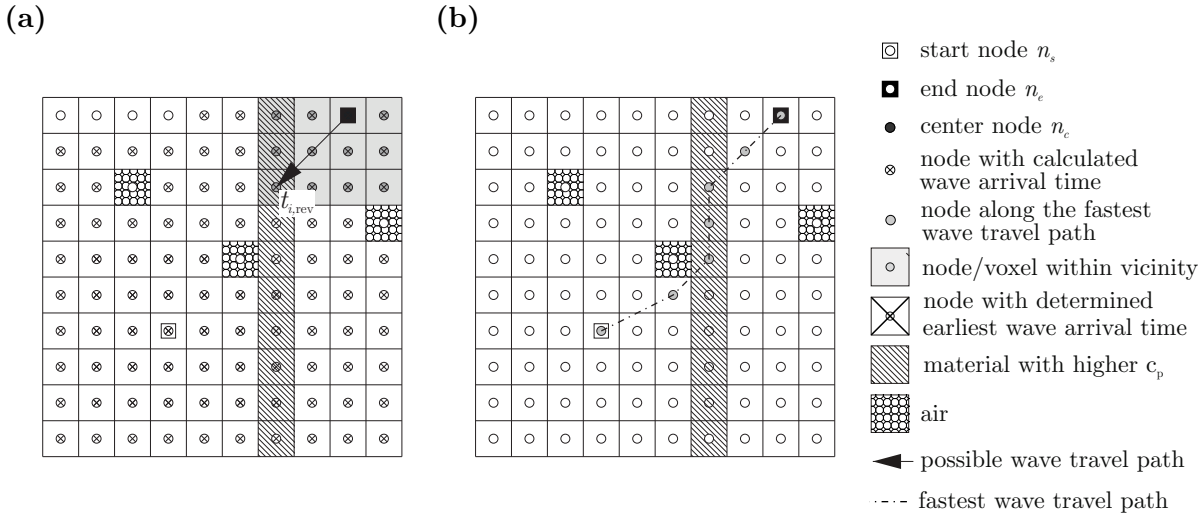

Fig. 3.10: (a) First reverse calculation of step B and (b) illustration of the fastest wave travel path between start and end node

second execution, which is a reverse calculation of step B, n_2 is used as the start node n_s, and n_1 as the end node n_e. The source time is defined as $t_s = d_{n_1,n_2}$. The (reverse) calculated arrival time of the wave at the connected nodes is written as

$$t_{i,\mathrm{rev}} = t_c - d_{c,i}. \tag{3.31}$$

After performing the reverse calculation for the first time, one entry of $\mathbf{A}_{t,\mathrm{rev}}(n_2, n_1)$ is identical to its counterpart in $\mathbf{A}_t(n_1, n_2)$. The node associated with this entry is the second-last node along the fastest wave travel path from n_1 to n_2 (see Fig. 3.10 (a)). The node is the new center node n_c for the subsequent execution of the reverse calculation of step B. All nodes along the fastest wave path can be determined this way. Visualizations of the fastest wave travel path between source and sensor are useful to illustrate how cracks and materials with different p-wave velocities influence the wave propagation path (see Fig. 3.10 (b)).

3.4.3 Source localization

The *FastWay* algorithm, used to calculate the estimated source location, is based on the assumption that the wave travel duration $d_{s,e}$ from node n_1 to node n_2 is independent of the wave propagation direction. This means that the result does not depend on which of these two nodes is chosen to be the emitting or start node n_s and which one is the receiving or end node n_e. This assumption was verified using numerical simulations of elastic wave propagation that are based on [31] and [44]. The specimen is discretized into a finite number of voxels $v_{\mathrm{tot}} = l_x \times l_y \times l_z$ (see Sections 4.2 and 4.4 and Fig. 4.2). The nodes used for the modified Dijkstra algorithm (see Section 3.4.1) are located at the center of this array of voxels. It is implied that the estimated source location must be exactly at the coordinates of one node. Hence, there are $n_{\mathrm{tot}} = v_{\mathrm{tot}}$ possible source locations within the numerical model of the specimen. The locations of the sensors as well as the coordinates of the receiving nodes are known from the experimental setup. Each receiving node, representing one sensor, is the end node n_e of the fastest wave path from the source to the sensor. The wave arrival times at the sensors $t_a(s)$ are also known. The location of the AE source, the source time, and the coordinates of the emitting node n_s are unknown. Hence, the fastest wave travel path and shortest wave travel duration between the source (node n_s) and the sensor (node n_e) cannot be determined. Moreover, the ending criterion $n_c = n_e$

cannot be applied for the execution of the modified Dijkstra algorithm (see Fig. 3.8 and Section 3.4.2). The wave travel duration $d_{se,xyz}$ for the journey between the node representing the sensor se and every other node is calculated instead. The source time is set to zero and therefore the value of the wave travel duration $d_{se,xyz}$ is equal to the arrival time of the wave $a_{xyz}(se)$ at node $[x\ y\ z]$. The calculated wave travel durations are stored in matrix $\mathbf{A}_{\mathrm{tot}}(se)$ and only depend on the numerical p-wave velocity model. The arrival time matrices $\mathbf{A}_{\mathrm{tot}}(se)$ have to be updated only if the numerical p-wave velocity model of the specimen changes, for example when a crack grows. A potential source time s_{pot} for each possible source location (every node in the numerical model of the specimen),

$$s_{\mathrm{pot};xyz}(se) = t_a(se) - d_{se,xyz}, \tag{3.32}$$

is calculated from the measured wave arrival time $t_a(se)$ at sensor se and the calculated wave travel durations $d_{xyz,se}$ stored in $\mathbf{A}_{\mathrm{tot}}(se)$. The matrix entry $s_{\mathrm{pot};xyz}(se) \in \mathbf{S}_{\mathrm{pot}}(se)$ represents the source time of an acoustic emission originating from the center of voxel $[x\ y\ z]$ (see Fig. 4.2), from which the arrival time of the wave $t_a(se)$ at sensor s can be determined. Equation (3.32) can also be written in matrix form:

$$\mathbf{S}_{\mathrm{pot}}(se) = t_a(se) \cdot \mathbf{J} - \mathbf{A}_{\mathrm{tot}}(se). \tag{3.33}$$

One specific entry of $\mathbf{S}_{\mathrm{pot}}(se)$ is the best estimation of the source time $t_{se,\mathrm{AE}}$ of the acoustic emission. The position (x, y, z) of $t_{se,\mathrm{AE}}$ in the potential source-time matrix $\mathbf{S}_{\mathrm{pot}}$ corresponds to node $n_{se,\mathrm{AE}}$, which represents the position of the estimated source location in the specimen. $\mathbf{J}$ is a three-dimensional all-ones matrix with the same size as matrices $\mathbf{S}_{\mathrm{pot}}(se)$ and $\mathbf{A}_{\mathrm{tot}}(se)$. Theoretically, $t_{se,\mathrm{AE}}$ and $n_{se,\mathrm{AE}}$ are identical regardless of which sensor se is used to determine $\mathbf{S}_{\mathrm{pot}}(se)$. Node $n_{se,\mathrm{AE}}$ located at $[x\ y\ z]$ fulfills

$$s_{\mathrm{pot};xyz}(se1) \approx s_{\mathrm{pot};xyz}(se2) \approx ... \approx s_{\mathrm{pot};xyz}(sen), \tag{3.34}$$

and therefore

$$t_a(se1) - a_{\mathrm{tot};xyz}(se1) \approx t_a(se2) - a_{\mathrm{tot};xyz}(se2) \approx ... \approx t_a(sen) - a_{\mathrm{tot};xyz}(sen). \tag{3.35}$$

The prerequisite for this is that the arrival time $t_a(se)$ of a wave detected at all sensors se is caused by the same acoustic emission. The estimated source location corresponds to the location of a node in the numerical model. All other values of matrices $\mathbf{S}_{\mathrm{pot}}(se)$ can differ. For geometrical reasons the data of at least four sensors have to be used. The estimated source location corresponds to the minimum value of

$$\mathbf{E}_{\mathrm{source}}(n) = \frac{\sum_{i=1}^{n} \left(\sum_{j=1}^{n} |\mathbf{S}_{\mathrm{pot}}(i) - \mathbf{S}_{\mathrm{pot}}(j)| \right)}{\max \left(\sum_{i=1}^{n} \left(\sum_{j=1}^{n} |\mathbf{S}_{\mathrm{pot}}(i) - \mathbf{S}_{\mathrm{pot}}(j)| \right) \right)}. \tag{3.36}$$

$\mathbf{E}_{\mathrm{source}}(n)$ is called the error matrix. The values of $\mathbf{E}_{\mathrm{source}}(n)$ represent the normalized deviations from the condition formulated in Eqs. (3.34) and (3.35) and range from 0 to 1.

Two remarks have to be made at this point. First, due to numerical and metrological inaccuracies, it is nearly impossible that $s_{\mathrm{pot};xyz}(se1) = s_{\mathrm{pot};xyz}(se2)$. Therefore, the condition is formulated as $s_{\mathrm{pot};xyz}(se1) \approx s_{\mathrm{pot};xyz}(se2)$. Consequently, the minimum value of $\mathbf{E}_{\mathrm{source}}(n)$ does not reach but only approaches zero. Secondly, it is possible that more than one node fulfills the conditions formulated in Eqs. (3.34) and (3.35), resulting in more than one value for which

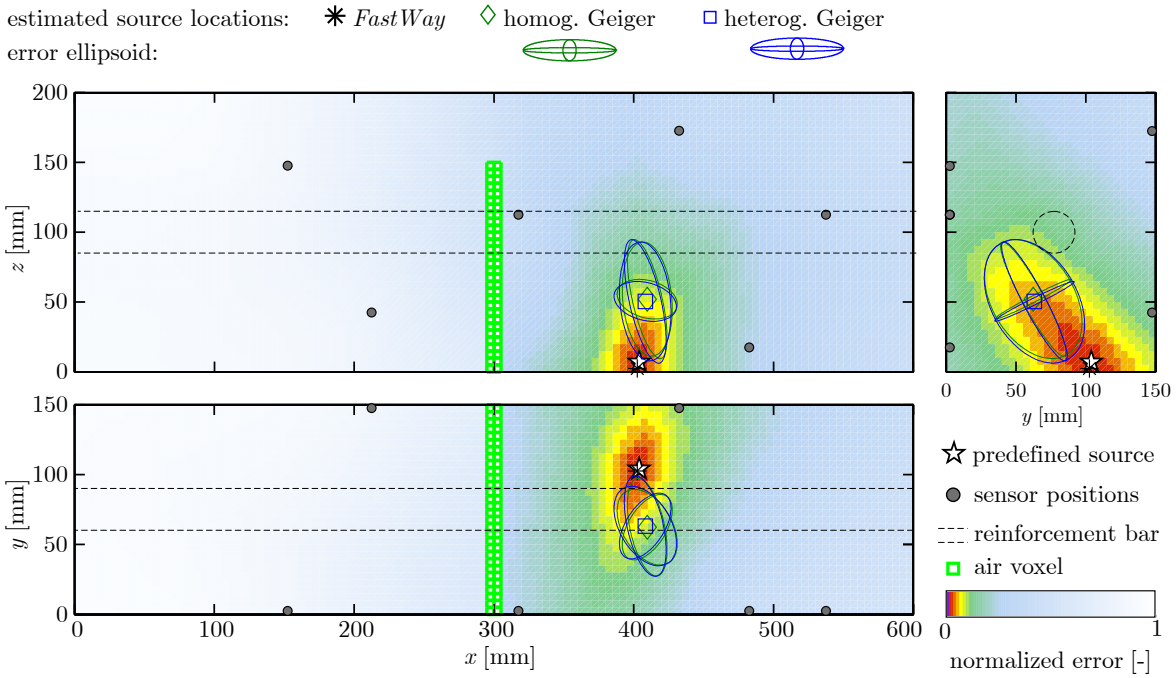

Fig. 3.11: Sample FastWay result for synthetic specimen. Cross-sections of the discretized specimen, including the visualization of $\mathbf{E}_{\text{source}}$. Error ellipsoids for the Geiger methods, locations of the sensors, estimated source locations, and predefined source location are marked. The shown cross-sections are at the location of the estimated source (using *FastWay*).

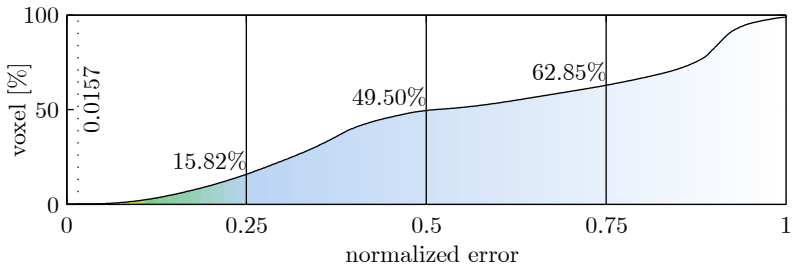

Fig. 3.12: Cumulative plot showing the normalized error of the voxels of the result presented in Fig. 3.11

$e_{\text{source};xyz}(n) \approx 0$. This can happen if all sensors are positioned on one surface of the specimen and the investigated specimen is homogeneous. The voxels corresponding to $0 \in \mathbf{E}_{\text{source}}(n)$ form a curved line. If the source is separated by a crack from the majority of the sensors, an exact source localization is impossible. Therefore, it is recommended to visualize the resulting $\mathbf{E}_{\text{source}}(n)$ as shown in Fig. 3.12.

FastWay also yields estimated source coordinates. They are the coordinates of the center of the voxel corresponding to the minimum value of $\mathbf{E}_{\text{source}}$. However, as mentioned above, *FastWay* is a zonal localization method. Therefore, the voxel corresponding to the minimum value of $\mathbf{E}_{\text{source}}$ is the real result. The coordinates of its center are only used to facilitate the comparison with results obtained with the Geiger methods.

Instead of error ellipsoids, the visualization of voxels corresponding to the minimum value of $\mathbf{E}_{\text{source}}$ (see Fig. 3.11) can be used to verify the estimated accuracy of the computed source location. Simply put, a small minimum normalized error, corresponding to the voxel most likely hosting the source ($e_{min} = 0.0157$ in Figs. 3.11 and 3.12), combined with a small number of other voxels with small $\mathbf{E}_{\text{source}}$ values indicates an accurate source location estimation. However, a

visual inspection of Figs. 3.11 and 3.12 for all estimated source locations is very time-consuming. Hence, an automatized evaluation process (see Section 7.3.4) was developed for the AE source location estimations performed in Chapter 7.

Chapter 4

Numerical Approximations of Physical Specimens

The foundation of the numerical simulations (e.g., the numerical wave propagation simulation) and the two source localization algorithms mentioned in this dissertation, namely the heterogeneous Geiger method (Section 3.3.2) and *FastWay* (Section 3.4), are numerical models that represent numerical approximations of physical specimens. In order to generate a precise numerical model, the interior of the specimen needs to be known a priori. Determining the interior structure of structural elements, especially those consisting of reinforced concrete, is an elaborate and difficult task (see Section 4.3).

4.1 Components of Numerical Models

The most commonly known numerical model component is the pixel. A pixel is the basic element of digital graphics; a physical point in a raster image. Hence, pixels are used for two-dimensional discretization (for example for pictures). In digital graphics, a pixel is defined by its edge length (pixels are generally square), color, and position. A synonym for a pixel in digital imaging is the dot. The resolution of graphics is usually given in *dpi*, dots per inch, and is therefore controlled by the edge length of the pixel. Voxels are the three-dimensional counterparts of pixels. They are generally cube-shaped. The edge length of a pixel (2D) or voxel (3D) is also referred to as grid point (gp). The resolution of a numerical model is defined by the number of grid points per unit length, similar to the aforementioned *dpi*. The smaller the edge length of the pixel, the higher (better) the resolution of a graphic. This means that if a higher resolution is desired, more pixels are needed in order to build a graphic of the same size. This rather trivial fact, connecting the resolution and number of voxels, shows that increasing the resolution may require increased computational power. There are examples of low-resolution pixel graphics within this dissertation. Every visualization of $\mathbf{E}_{\text{source}}$ (see Section 3.4.3) is such a low-resolution pixel graphic. The individual pixels are distinguishable, and the position of each visualized pixel corresponds to a voxel of the underlying numerical model. The color of each pixel represents the value of e_{source} of this voxel. All numerical models are composed of pixels for two-dimensional models and voxels for three-dimensional models. The type of information stored in the pixels or voxels can vary for each numerical model and is usually determined during a discretization process. In photography, the color that best reflects the colors of the part of an image conflated in one pixel is usually chosen as the stored information. The discretization is therefore an

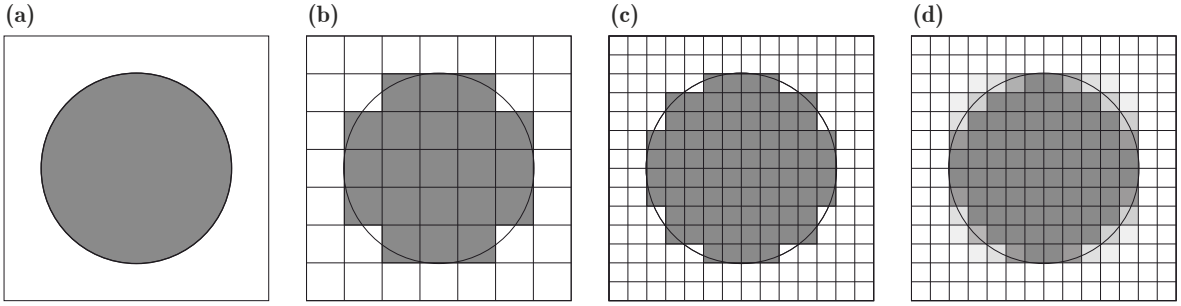

Fig. 4.1: Visualization of different discretization results of (a) a circle (b) with low resolution, (c) higher resolution, and (d) higher resolution combined with variable values for each pixel

approximation process associated with a loss of information. The resolution controls the amount of information loss and diametrically the amount of computational effort required to handle the numerical model.

4.2 Discretization

The result of a discretization depends on various parameters, the first of which is the aforementioned resolution. Fig. 4.1 shows the results of a two-dimensional discretization of a circle. The result visualized in Fig. 4.1 (b) does not resemble a circle. The resemblance can be improved significantly by simply halving the edge length of the pixels, as visualized in Fig. 4.1 (c). Both of these discretizations assume that the value of a voxel is either 1 – the voxel is part of the circle (gray) – or 0 – it is not part of the circle (white). In digital imaging, the value of pixels located partially inside and partially outside the circle would have a value between 0 and 1. Such a result is visualized in 4.1 (d). The grayscale of each pixel corresponds to the percentage of the voxel located inside the circle. The discretization process, leading to the result visualized in Fig. 4.1 (d), is significantly more complex than the one used for Figs. 4.1 (b) and 4.1 (c). For the discretization of structural concrete and especially cracked concrete this methode is, however, not suitable. Thin cracks in the physical specimens combined with a voxel size larger than the crack width would result only in a (small) reduction of the determined average wave velocity of all voxels representing the crack and the surrounding solid material, similar to the average velocity $\bar{c}_{p\_het,se}$ of the heterogeneous Geiger's method (see Eq. 3.27 and section 3.3.2). Therefore, a discretization that distinguishes between different materials and does not calculate average material properties for each voxel , as visualized in 4.1 (b) and (c), is used. It has to be mentioned that air voxels are treated in a special way in the discretization process. If a crack is located within the area represented by a voxel, the voxel used in the numerical model will be an air voxel, no matter how large, or small, the percentage of the air in the voxel area is.

Fig. 4.2 shows an example of how a cracked cuboid containing a single reinforcement bar can be discretized. The resolution of the numerical model displayed in Fig. 4.2 (b) is comparatively low, permitting fast computation. Nevertheless, it is possible to incorporate all heterogeneities of the specimen that are relevant for wave propagation simulations using this coarse resolution. Matrices can be used to store the information contained in each voxel or pixel of a numerical model, where each element of the matrix corresponds to one voxel or pixel. If the voxel or pixel contains more than one piece of information, cell arrays should be used instead of matrices. The structure of a cell array is identical to the structure of a matrix. However, each cell array

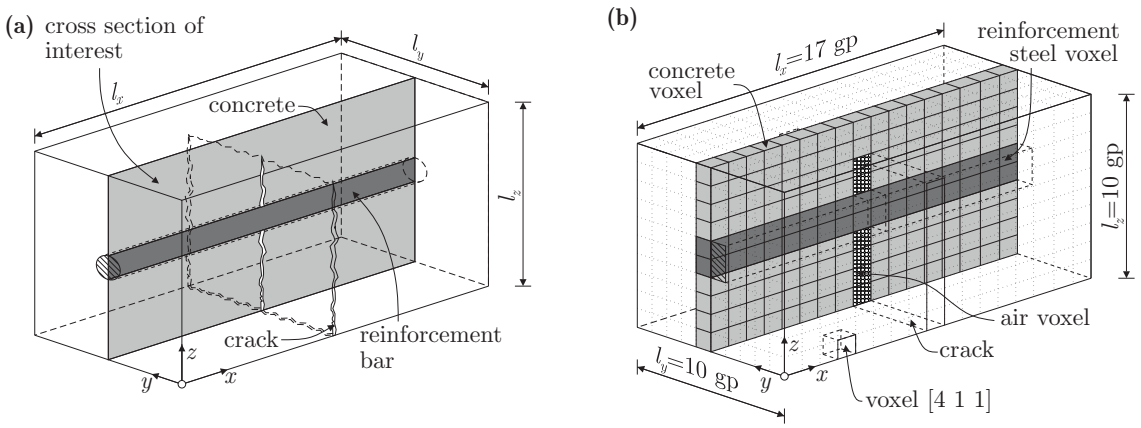

Fig. 4.2: (a) Representation of a cracked concrete cuboid with one reinforcing bar (one cross-section is highlighted) and (b) the discretization scheme of the cracked concrete cuboid (Figure taken from [16])

element can consist of multiple pieces of information. For numerical models, cell arrays are generally used rather than matrices. The cells can contain any type of information about the material assigned to the corresponding voxel, such as wave velocities, density, or an identification of the material. For example, cell [4 1 1] of the numerical model displayed in Fig. 4.2 (b) contains the information that the material assigned to voxel [x y z]=[4 1 1] is concrete, as well as the density and p-wave velocity of the concrete. If a cell contains only one value, the cell array reverts back to a three-dimensional matrix. If that one value is the p-wave velocity, the matrix represents a discretized p-wave velocity model and is referred to as $\mathbf{C}_{mo}$ (see Section 4.4).

Numerical models with different resolutions were used to obtain the results presented in this dissertation. For wave propagation simulations, high-resolution models were generally used. The edge length of the voxels was generally 1 mm. Using a higher resolution was not necessary because of the expected wavelengths of $\Lambda \approx 40$ mm [46]. A velocity model based on the wave propagation simulation input model was used for the heterogeneous Geiger method; hence the resolution was 1 gp $\widehat{=}$ 1 mm. Unfortunately, the existing *FastWay* algorithm is not capable of handling more than 250,000 voxels. For that reason, voxels with an edge length of 5 mm are used for the numerical simulations in Chapter 5 and the small-scale experiment in Chapter 6. For the large-scale experiment in Chapter 7 voxels with an edge length of $1/2'' \widehat{=} 12.7$ mm were used.

4.3 Numerical Concrete Model (NCM)

A homogeneous material is entirely uniform and does not have any irregularities. The focus of this dissertation was on concrete and reinforced concrete. Concrete is considered a heterogeneous material, as it consists of several different constituents – aggregate, water, and cement. However, homogeneity and therefore also heterogeneity are a function of the scale at which a material is observed. On a micro scale, even an apparently homogeneous material like steel is heterogeneous. It consists of iron (Fe) and other elements (mostly carbon (C)), as well as tiny air voids. Another example are rocks, which are heterogeneous on both the macro and mini level, and sometimes even on the micro level. However, in rock mechanics they can be considered an effective homogeneous material [24]. Consequently, aggregates (which are basically rock particles) are heterogeneous, but can be considered (effectively) homogeneous. The same theory applies to the hardened cement matrix. Different types of numerical concrete models (NCM) were used for the simulations and as input for the localization methods.

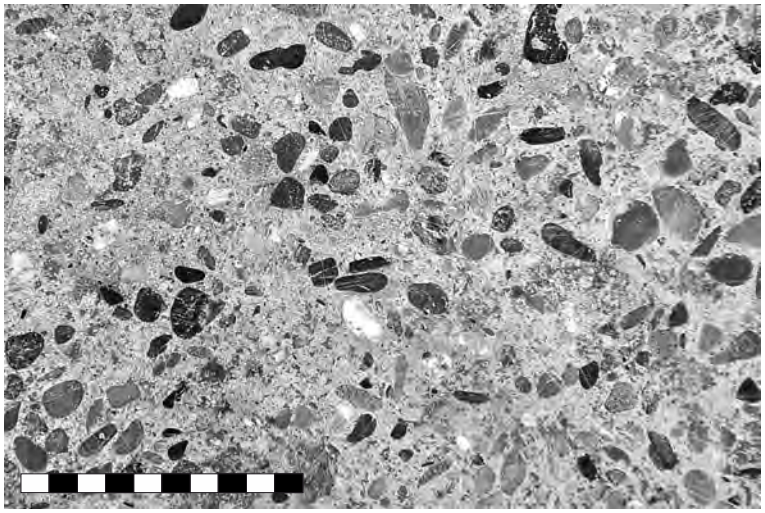

Fig. 4.3: Picture of a polished concrete cross-section. The scale bar has a total length of 10 cm.

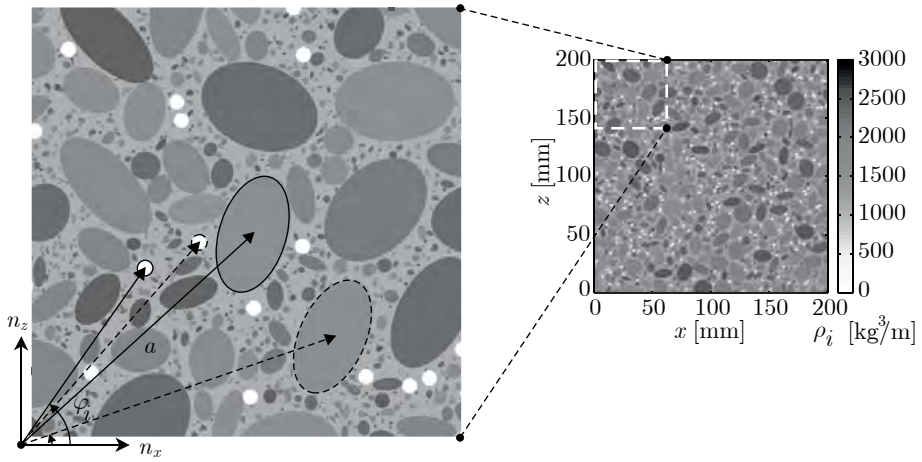

Fig. 4.4: Two-dimensional visualization of the NCM including aggregate particles (gray, max. ra = 8 mm), air voids (white, r = 0.5 mm), and cement matrix (light gray). The different shades of gray indicate the different density values of the materials. (Figure from [27])

4.3.1 Three-component NCM

The basic constituents of concrete are aggregate, cement, and air. Because of their small amounts and limited dimensions, additions and admixtures are not considered. Further, they have almost no effect on wave propagation. Fig. 4.3 shows a picture of a polished concrete cross-section. The aggregate grains and air voids as well as the cement matrix surrounding the other materials can be seen with the naked eye – the heterogeneity of the material is evident. Fig. 4.4 shows the visualization of a numerical model; a realistic numerical replica of concrete. The resemblance of the two shown cross-sections is apparent.

A numerical model like this can be used for realistic wave propagation simulations. The wave is reflected and scattered at every interface between two materials. This means that the wave is partially reflected and partially transmitted at the boundary between two different materials (see Section 2.2), for example at the surface of an aggregate particle covered by the cement matrix. This model is therefore a very realistic numerical replica of concrete. Of all numerical models

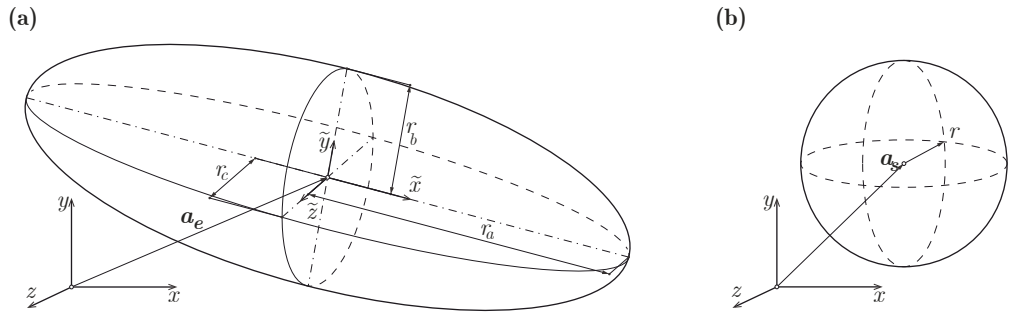

Fig. 4.5: Visualization of (a) an ellipsoid and its parameters (aggregate model), and (b) a sphere and its parameters (air-void model)

mentioned in this dissertation, this is the model best suited to predict and realistically simulate physical experiments. As mentioned above, the NCM consists of three (numerical) materials. It is compiled gradually. A working space with the material properties of air is created first. This working space is a cuboid and at least the same size as the future NCM model, which is defined subsequently. If the specimen is surrounded by a layer of air, the wave will be reflected completely at the surface of the specimen. The wave will not be transmitted to the outside of the specimen and will therefore also not be transmitted beyond the working space. It is also possible to define specimens without a surrounding air layer, which means that the voxels constituting the specimen may be at the boundary of the working space. If the wave reaches a voxel with at least one side touching the working-space boundary, the wave can be transmitted to the outside of the working space and there will be no reflection of the wave at this boundary. The wave energy diffuses outside the numerical model. In all the simulations mentioned in this dissertation the specimens are surrounded by an air layer. After defining the preliminary model, a homogeneous specimen with the physical properties of cement (see Table 1) and the overall dimensions of the final concrete model is generated inside the working space. Subsequently, most of the cement voxels are replaced by aggregate grains and air voxels. The air voids and aggregate particles are distributed randomly within the model. The generated aggregate particles and air voids do not overlap, although it is possible that the aggregate particles touch each other. The aggregate particles and air voids have to be placed one at a time to fulfill this requirement, starting with the biggest particle. In a first step, the dimensions of the particles are defined randomly within certain limits. Both aggregate particles and air voids generally have irregular shapes. As a simplification, the aggregate particles are modeled as ellipsoids and the air voids as spheres. The parameters needed to define these objects are marked in Fig. 4.5.

The size, position, and orientation of the ellipsoid representing one aggregate grain are primarily controlled by random numbers (X_i). To simplify the process, the two shorter half-axes of the ellipsoid are set to be equally long ($r_b = r_c$). The lengths of these half-axes are not controlled by a random number but by the diameter listed in grading curve diagrams, such as the Fuller curve or the EMPA curve [42]. These curves are two empirically developed grading curves used to achieve a high packing density. Grading curves like these are used in national and international standards and by concrete manufacturers to define the composition of concrete aggregates. The length of the longest half-axis (r_a) is determined randomly within the boundaries $r_c \leq r_a \leq 2.5 \cdot r_c$. At first, the center of each of the generated particles is at the origin of the coordinates. In a second step the new particle is translated, and rotated by a randomly chosen angle. The translation from the origin of the specimen coordinate system to the final position

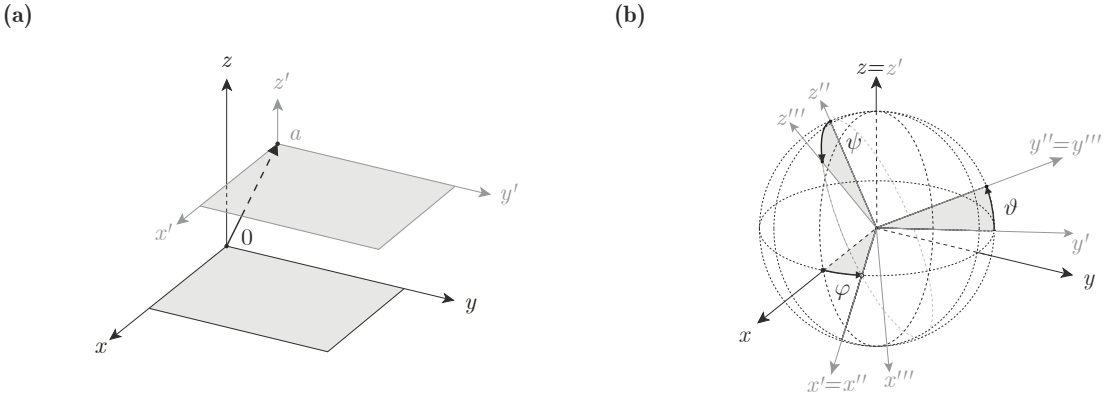

Fig. 4.6: Principle of (a) translation and (b) rotation of the Cartesian coordinate system, taken from [32]

of the ellipsoid is controlled by vector a_e, which is also determined using random numbers.

$$a_e = \begin{bmatrix} a_{e,x} \\ a_{e,y} \\ a_{e,z} \end{bmatrix} = \begin{bmatrix} l_x \cdot X_1 \\ l_y \cdot X_2 \\ l_z \cdot X_3 \end{bmatrix} + \begin{bmatrix} x_{min} \\ y_{min} \\ z_{min} \end{bmatrix} \tag{4.1}$$

One independent random number $0 \leq X_i \leq 1$ each is used for the x, y, and z-direction. In Eq. (4.1), the length of the specimen, for example in the x-direction, is taken into account with l_x. The last vector in Eq. (4.1) defines the point in the specimen with the smallest coordinate values.

In a three-dimensional space, rotation about the three axes of the Cartesian coordinate system is possible. The Euler angles (ψ, ϑ, and φ) can be used to determine the orientation of a body in space. A rotation matrix $\mathbf{R}$ based on the Euler angles is used for three-dimensional rotation.

$$\mathbf{R} = \begin{bmatrix} \cos\psi \cdot \cos\varphi - \cos\vartheta \cdot \sin\psi \cdot sin\varphi & -\sin\psi \cdot \cos\varphi - \cos\vartheta \cdot \cos\psi \cdot \sin\varphi & \sin\vartheta \cdot \sin\varphi \\ \cos\psi \cdot \sin\varphi + \cos\vartheta \cdot \sin\psi \cdot sin\varphi & -\sin\psi \cdot \sin\varphi + \cos\vartheta \cdot \sin\psi \cdot \cos\varphi & -\sin\vartheta \cdot \cos\varphi \\ \sin\psi \cdot \sin\vartheta & \cos\pi \cdot \sin\vartheta & \cos\vartheta \end{bmatrix} \tag{4.2}$$
$$\mathbf{R} = \begin{bmatrix} \xi & \eta & \zeta \end{bmatrix}$$

The Euler angles and the rotation are illustrated in Fig. 4.6 (b). The angle of nutation ϑ is defined as the angle between the y-axis and the y'-axis and is limited to $0 \leq \vartheta \leq \pi$. The axis of rotation is the x-axis. The angle of precision ψ is defined as the angle between the x-axis and the intersection line of the xy-plane and the $x'y'$-plane and is limited to $0 \leq \psi \leq \pi$. The axis of rotation is the z-axis. The angle φ is the angle between the positive x'-axis and the positive y'-axis. This angle is limited to $0 \leq \varphi \leq 2\pi$. The axis of rotation is the z'-axis. A vector r is transformed into the vector r' by multiplying r by the rotation matrix $\mathbf{R}$.

$$r' = \mathbf{R} \cdot r = \begin{bmatrix} x' \\ y' \\ z' \end{bmatrix} = \begin{bmatrix} \xi & \eta & \zeta \end{bmatrix} \cdot \begin{bmatrix} x \\ y \\ z \end{bmatrix} \tag{4.3}$$

The vectors ξ, η, and ζ, based on one independent random number $0 \leq X_i \leq 1$ for each Euler angle,

	c_p [m/s]	c_s [m/s]	ρ [kg/m^3]
EEP concrete*	3912	2272	2200
Reinforcement steel	5900	3200	7820
Cement matrix	3950	2250	2050
Aggregate	4180 ± 210	2475 ± 125	2610 ± 130
Air	0 (331)	-	0.0001 (1.29)

Tab. 4.1: Average material properties implemented in the numerical models (sources: [31] and [33])

$$\begin{aligned} \psi &= \pi \cdot X_i \\ \vartheta &= \pi \cdot X_i \\ \varphi &= 2\pi \cdot X_i \end{aligned} \tag{4.4}$$

are used as the rotation input for each aggregate grain of the NCM.

After inserting and randomly rotating the parametrically defined aggregate grain in the specimen, it is verified that the new particle does not overlap any previously inserted particle. If the aggregate grain does not overlap an existing one, it is discretized and included in the numerical model. Any cement voxel whose center point is located inside the new aggregate grain is converted into an aggregate voxel.
The surface of an ellipsoid is defined by

$$\left(\frac{\tilde{x}}{r_a}\right)^2 + \left(\frac{\tilde{y}}{r_b}\right)^2 + \left(\frac{\tilde{z}}{r_c}\right)^2 = 1, \tag{4.5}$$

where the coordinate system ($\tilde{x}$, $\tilde{y}$, and $\tilde{z}$) coincides with the main axes of the ellipsoid. The volume (as well as the surface) of an ellipsoid can be described by r_a, r_b and r_c with respect to the global coordinate system. It can be translated with a vector a_e and rotated with a rotation matrix $\mathbf{R}$ represented by the vectors ξ, η, and ζ.

$$\begin{aligned} &\left[\frac{\xi_1(x-a_{e;1}) + \eta_1(y-a_{e;2}) + \zeta_1(z-a_{e;3})}{r_a}\right]^2 + \\ &\left[\frac{\xi_2(x-a_{e;1}) + \eta_2(y-a_{e;2}) + \zeta_2(z-a_{e;3})}{r_a}\right]^2 + \\ &\left[\frac{\xi_3(x-a_{e;1}) + \eta_3(y-a_{e;2}) + \zeta_3(z-a_{e;3})}{r_a}\right]^2 \leq 1 \end{aligned} \tag{4.6}$$

In Eq. 4.6, ξ_1 represents the first row of ξ, $a_{e;1}$ represents the first value of a_e, and so on. Hence, cement voxels whose center coordinates fulfill Eq. 4.6 are converted into aggregate voxels.

The material properties of the aggregate particles usually vary within boundaries. The range of the material properties used in the numerical models is shown in Tab. 4.1. The range of variation is the same for each of the material properties. Hence, the same random number X_i is used to calculate each of the listed material properties of one aggregate particle. Only particles with $r_b = r_c \geq 0.5$ mm are considered in the numerical models (see Section 4.2).

Air voids are also inserted randomly into the cement matrix. All air voids are modeled parametrically as spheres with a diameter of 1 mm. Therefore, it is not necessary to rotate them randomly. Since voxels with an edge length of 1 mm are used (see Section 4.2), the discretized

*Material properties of a homogenized numerical model using concrete with effective elastic properties (EEP concrete) (see [31])

counterpart of an air void is one cube-shaped voxel. The air voids are inserted only after all aggregate grains with $r_b = r_c \geq 0.5$ mm have been included in the model. If a higher resolution than 1 gp $\widehat{=}$1 mm is used, all aggregate grains with $r_b = r_c < 0.5$ mm would be inserted into the model after the air voids. The used NCM and numerical reinforced concrete models (NRCM) are based on the NCM described in [27].

The creation of a NCM consisting of the three components cement, aggregate, and air voids (three-component NCM) is very time-consuming. Moreover, this type of model can generally only be used for (forward) wave propagation simulations. It is too sophisticated to represent an appropriate input for a source location estimation algorithm, not because it is too complex to be processed, but because the location of the individual concrete components is usually unknown. So far, one of the few available options for determining the location of aggregate grains and even air voids in concrete is a high-resolution X-ray scan [27].

4.3.2 Single-component NCM

It is usually impossible to create an accurate numerical model of the specimen for source localization purposes, since the distribution of air voids and aggregate grains is unknown. However, as air voids are randomly distributed, they can be considered to be evenly distributed. Moreover, their effect on the wave propagation path is very small and can therefore be neglected. Aggregate grains are also randomly distributed and can be considered to be evenly distributed as well. Hence, the influence of air voids and aggregate particles on wave propagation is approximately the same everywhere in the concrete structure and independent of the direction of wave propagation. As a simplification, the heterogeneous material concrete can hence be considered to be effectively homogeneous [24]. However, waves are still scattered at the interfaces between the different materials (see Section 2.2.2) and therefore the amplitude of a propagating wave is damped. In order to consider these effects of aggregate grains and air voids on wave propagation, in [31] a homogenized concrete with so-called effective elastic properties (EEP concrete) is used. The effective elastic properties are determined from numerical wave propagation simulations using the three-component NCM and later verified using experimental data [27].

The single-component NCM is the simplest numerical model in this context. Every voxel representing the specimen in the numerical model is assigned the same physical properties, the EEP. The influence of the shape and geometry of the specimen and/or cracks on wave propagation can be investigated using this model. The specimen consists of only one material; thus the wave is not scattered by reflection and diffraction inside the specimen. The wave is only influenced by the surfaces of the specimen, including crack surfaces. Therefore, this is the most suitable model for investigating geometrical influences. In most cases, a comparatively simple numerical model based on the EEPs is sufficiently accurate to be used for source localization. All source localization results presented in this dissertation are determined using a single-component NCM or a two-component NRCM. The more sophisticated three-component NCM is, for example, used for source localization in [28].

4.3.3 Numerical reinforced concrete model (NRCM)

Reinforcement steel was not present in the numerical models described so far. It differs significantly from the materials mentioned in Sections 4.3.1 and 4.3.2. The diameter of reinforcing bars is larger than that of air voids and can be larger than that of aggregate grains. The material properties of reinforcement steel differ significantly from the material properties of the aggregate, cement matrix, and therefore also from EEP concrete. Therefore, reinforcement steel

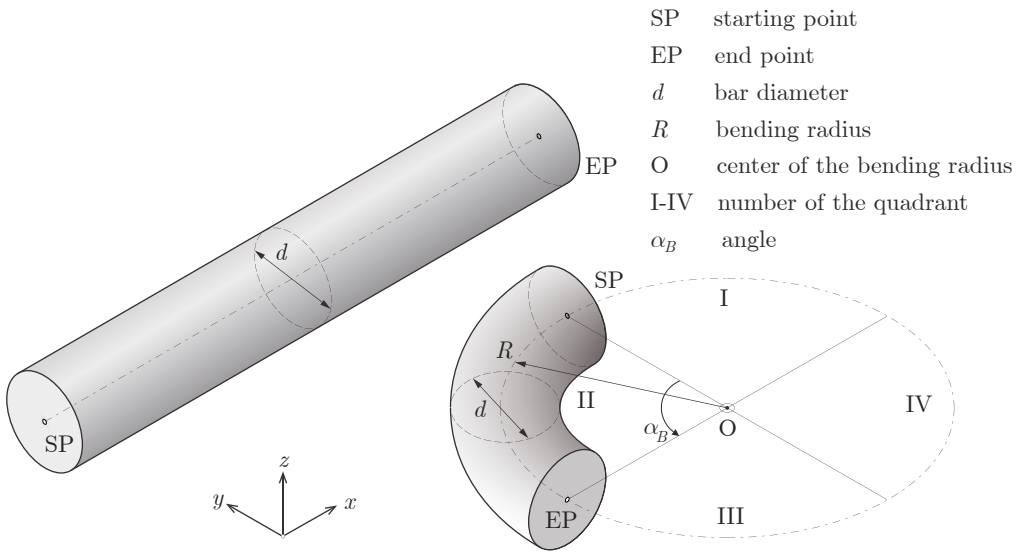

Fig. 4.7: Reinforcement components: bar and quarter torus (quadrant II) and the parameters for defining them

should be included as a separate material in numerical models of reinforced concrete specimens. Fortunately, the location of reinforcement bars can generally be obtained from construction plans (neglecting any construction-related deviation and the manufacturing tolerances).

The most common types of reinforcement are composed of cylinders and parts of tori. Hence, reinforcement bars are generally modeled as consisting of cylinder and quarter tori. No reinforcing-bar ribs are modeled – the surface of the reinforcement bars in the models is smooth. Stirrups are modeled without hooks at the end of the bars. They are modeled as self-contained elements and are continuous with neither beginning nor end. Reinforcing bars are defined by three parameters – the bar diameter, and the starting and end point of the bar. Bent reinforcements are modeled using quarter tori. Five parameters are needed to define quarter tori: the diameter of the reinforcement, the bending radius, the center of the torus, the orientation of the torus and the information in which quadrant – relative to the center of the torus and the orientation of the quarter torus – the quarter torus is located. If the bent shape of a reinforcing bar does not correspond to a series of quarter tori, the angle α_B can be used as an additional parameter. Using this information, the voxels assigned to the reinforcement can be determined. Numerical reinforcement models (NRM) are inserted into the existing numerical concrete specimen. The relevant existing voxels are changed to reinforcement steel voxels. If the NRM is combined with a three-component NCM, the result is a four-component NRCM. If the NRM is combined with a single-component NCM, the result is a two-component NRCM.

4.4 Numerical Velocity Models

The numerical velocity model (NVM) differs from the models mentioned above (NCM and NRCM) in only one point. The NVM only contains one piece of information, the wave velocity, while the NCM and NRCM contain a number of material properties (c_p, c_s, and ρ as a minimum). The NVM is used as input for source location estimation algorithms. The wave velocity stored in NVM is the p-wave velocity, since the source location estimation methods used in Chapters 5, 6, and 7 are arrival-time-based (see Sections 3.3 and 3.4), and the p-wave is the fastest body wave. If the arrival time of the s-wave can be determined reliably, the s-wave velocity instead of

the p-wave could be used for the source location estimation, or both of them could be used. In concrete specimens, however, a reliable determination of the s-wave arrival time is not possible. The information of the NVM is stored in a matrix, called the velocity matrix ($\mathbf{C}_{mo}$). The size and shape of this matrix correspond to the number of voxels and the shape of the numerical model of the specimen, respectively.

Chapter 5

Numerical Wave Propagation Simulation

Numerical wave propagation simulations proved extremely useful for all the investigative and developing steps in this dissertation. At the beginning of this research, they were simply used to investigate and visualize the influences of arbitrary heterogeneities on the wave propagation behavior. Subsequently, numerical wave propagation simulations were used to evaluate the accuracy of the heterogeneous Geiger method and *FastWay*, and to compare it with that of the homogeneous Geiger method.

All used source localization methods are based on a number of assumptions. These assumptions primarily relate to the used velocity model (see Sections 4.4, 3.3, and 3.4). The value of the p-wave velocity, whether chosen for a global velocity model or the velocity of each individual material, has a significant influence on the source location estimation accuracy. As a matter of fact, there is not always a p-wave velocity assigned to the different materials. For example, the observed wave propagation speed in a reinforcing bar is slower than the p-wave velocity of steel. The reinforcing bar in concrete acts as a wave guide and the wave velocity of the guided mode is lower than the p-wave velocity. Numerical wave propagation simulations are ideal tools for investigating these effects.

In numerical simulations, the exact source location, source time, wave velocities, and all other relevant material properties of each material, as well as the exact location of each virtual sensor are known. The wave signal computed at the virtual sensor location is a pure signal. In numerical simulations, there is no measurement chain and no white noise* that interfere with the recorded signal. The complexity and resolution of the numerical model used as input for the wave propagation simulation can easily be adapted in order to individually investigate different possible influences on the wave propagation behavior.

Most numerical simulations used in this dissertation consist of a numerical wave propagation simulation and the subsequent estimation of the source location using both Geiger methods and *FastWay*. A single numerical source was excited for each wave propagation simulation. It is technically possible to excite different wavelets and source types. However, for the simulation results presented in this dissertation, all numerical sources were modeled as an explosion and applied as a displacement at single grid nodes. The grid points adjacent to these nodes were smoothed to avoid numerical artifacts. The fundamental frequency of the Ricker wavelets was

*A hardly noticeable white noise with an extremely small amplitude and no impact on the arrival-time picking accuracy occurs due to the limited number of digits used during the computational process (double precision IEEE-754 standard).

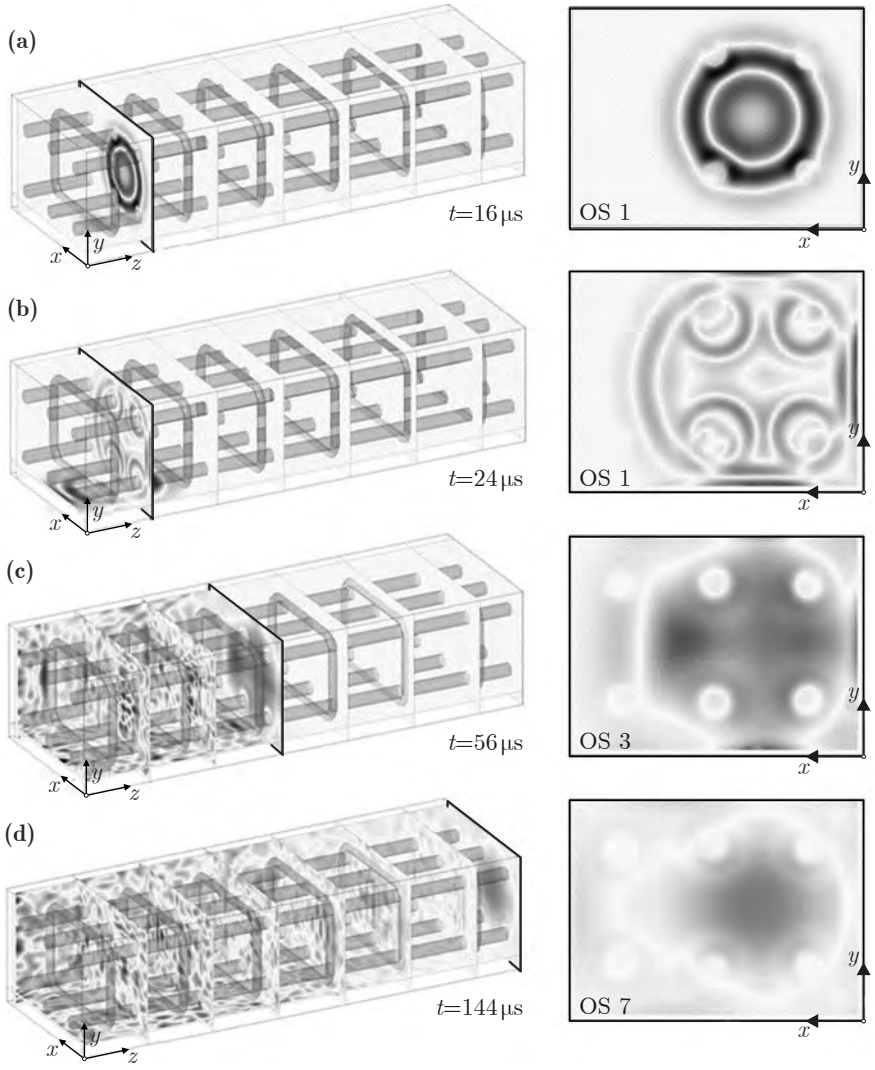

Fig. 5.1: Snapshots of displacement wave fields at different points in time. Left: 3D model of the specimen ($200 \times 150 \times 600$ mm) with seven xy ortho slices (OS), one yz OS, and one zx OS and including an illustration of the reinforcement. Right: Two-dimensional displacement wave field in different ortho slices.

100 kHz and the signal duration was 25 ms. Changing the source type has almost no influence on wave propagation. The frequency of 100 kHz was chosen because most of the signals recorded during the monitoring and testing of concrete structures have a fundamental frequency of 50–100 kHz.

Virtual sensors record signals induced by numerical acoustic emissions. Since these simulated signals are displacements calculated at the position of the virtual sensors, no white noise is contained in the signals, as would be the case for real AE signals. It is possible to subsequently superimpose artificial white noise onto the recorded wave signals. The displacements in all three directions of space are recorded at the positions of the sensors; however, only the displacement perpendicular to the specimen surface is processed. This is because the piezoelectric sensors that are applied to physical specimens only measure movements perpendicular to the surface they are located on.

Various numerical wave propagation configurations were used to investigate the wave propagation behavior in heterogeneous specimens in general, and structural concrete in

particular. They were primarily used to investigate the influences of the heterogeneity of concrete, reinforcing bars, cracks, and complex-shaped specimens on wave propagation. Moreover, the simulations were used to develop a source location estimation approach capable of taking into account the effects of cracks, air inclusions other than cracks, and the heterogeneity of materials on wave propagation, with the aim of achieving a significant improvement in the localization accuracy. The accuracy of the estimated source location achieved with the two Geiger methods and *FastWay* were compared with each other in order to evaluate the performance of *FastWay*. The most important numerical simulations are described in the following sections.

5.1 Wave Propagation in Reinforced Structural Concrete

A model of a numerical reinforced concrete beam with the dimensions $200 \times 150 \times 600$ mm was generated in order to visualize and investigate the impact of a realistic reinforcement layout on the wave propagation behavior. The resolution of the numerical model was 1 gp $\widehat{=}$1 mm. It was the first implementation of a realistic reinforcement layout in a numerical model. The implemented reinforcement layout consists of six longitudinal reinforcing bars ⌀ 16 mm and six stirrups ⌀ 12 mm. The stirrups were modeled as self-contained elements, as mentioned in Section 4.3.3. The concrete was modeled as a homogeneous material (see Section 4.3.2). The p-wave velocity of the reinforcement ($c_p = 5900$ m/s) was about 50% higher than the p-wave velocity of the homogenized concrete ($c_p = 3912.15$ m/s). The numerical source was a Ricker-type explosion source located at $x = 75$ mm, $y = 75$ mm, $z = 75$ mm. The fundamental frequency of the Ricker wavelets was 100 kHz and the signal duration was 25 ms.

Fig. 5.1 shows that the reinforcement influences the wave front in two ways by partially reflecting and refracting the wave at the boundary between the homogenized concrete and the reinforcement steel, and by its impact on the wave propagation velocity. It is clearly visible that the wave propagates faster in steel than in the homogenized concrete. The visualizations of the wave in Fig. 5.1 (a) to (d) show that both reinforcement elements, the longitudinal bars and the stirrups, significantly influence the wave propagation behavior. The wave front visualized in the ortho slices in Fig. 5.1 (a) and (b) is approximately circular, as would be expected in a homogeneous specimen. The wave front only deviates from this circular shape in the area of the longitudinal reinforcement and, in Fig. 5.1 (b), in the area near the surface of the specimen. The visualizations of the wave field of the ortho slices in Fig. 5.1 (c) and (d) clearly illustrate that the reinforcement has a significant influence on the wave propagation behavior and the wave front in areas farther away from the reinforcing bars (indicated by the irregular shape of the wave front in between the reinforcing bars on the left side). Consequently, reinforcement should be considered as a separate material in all numerical models concerned with elastic wave propagation in concrete, including wave propagation simulations and (elaborate) source location estimations.

The findings of this early numerical simulation were presented at the 10$^{\text{th}}$ *fib* International PhD Symposium in Civil Engineering in Quebec 2014, and published in [20].

5.2 Investigation of the Apparent Wave Velocity

After having created the model of a reinforced concrete beam, a simpler model was developed. To be more precise, three different numerical models were used for this investigation. The first one was a cuboid consisting of homogenized concrete (see Section 4.3.3) with the dimensions $200 \times 150 \times 600$ mm (NCM). The second model consisted of a single reinforcing bar with a

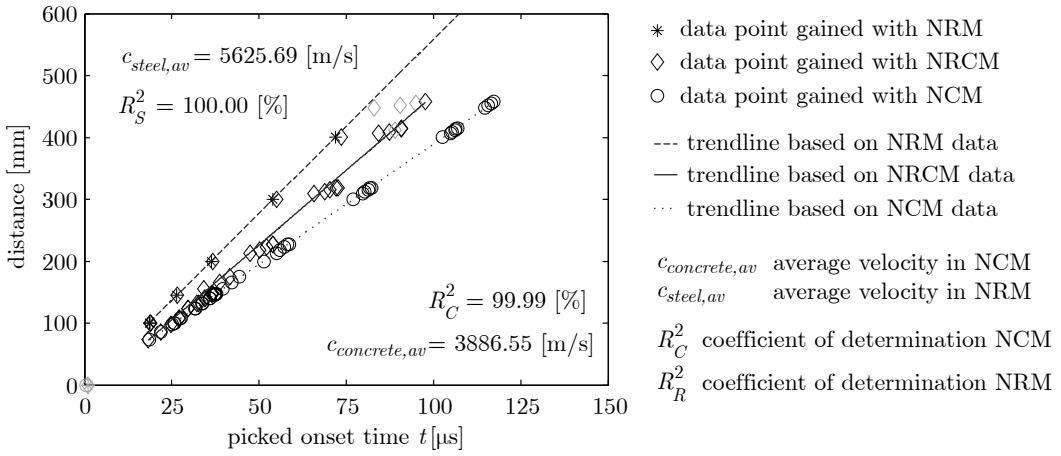

Fig. 5.2: Visualization of the distance between the source and a sensor at the picked onset time (the source time is 0 µs), including linear regression lines determined for each of the three material combinations

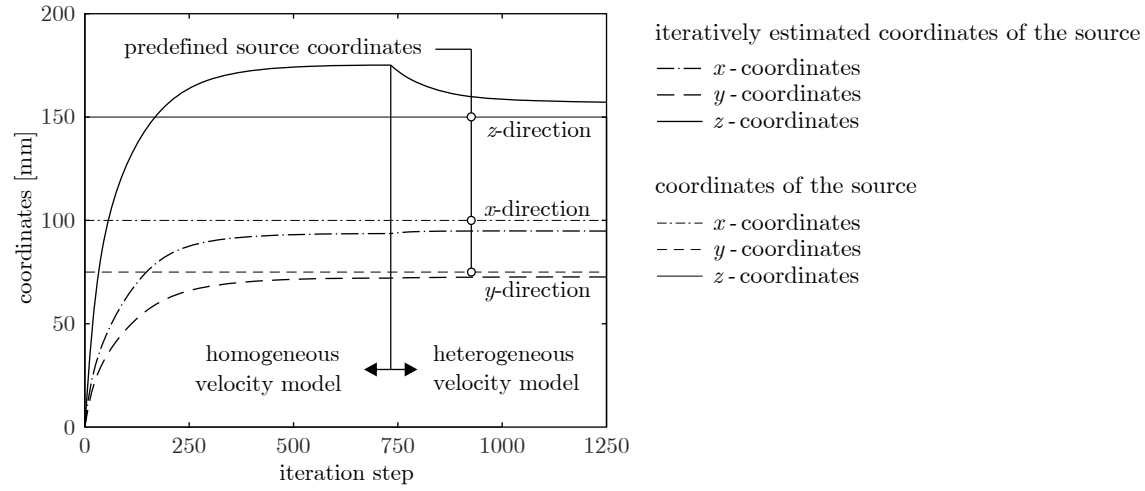

Fig. 5.3: Iterative development of the coordinates of the estimated source location using a combination of the homogeneous and heterogeneous Geiger methods. Taken from [19]

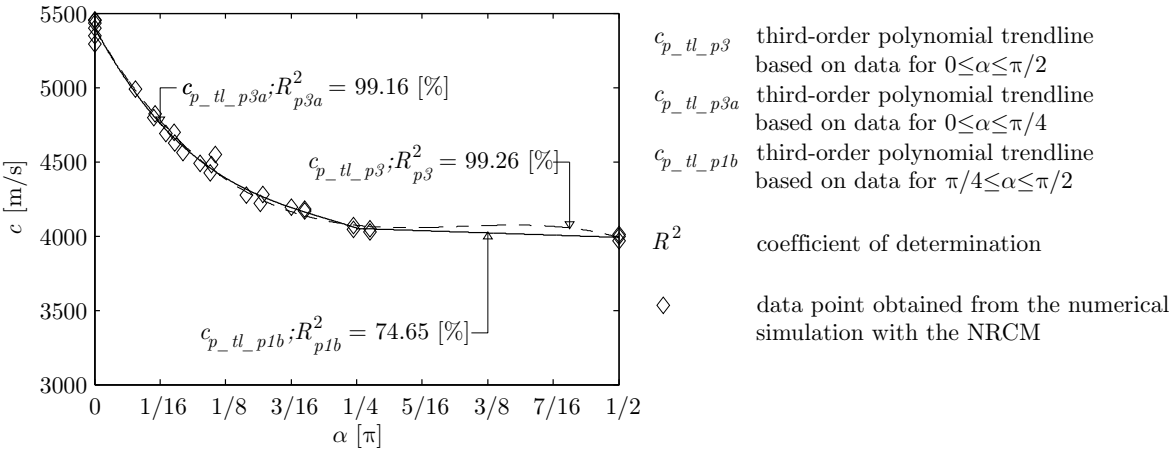

Fig. 5.4: Apparent relationship between the observed wave travel velocity (c) and the angle between the reinforcing bar and the straight connection between the source and the receiving sensor (α).

diameter of 30 mm and a length of 600 mm (NRM) positioned at the center of the *xy*-plane of an air cuboid with the same dimensions as the concrete-cuboid model. The last numerical model was a combination of the first two, resulting in a reinforced concrete cuboid consisting of two homogeneous materials (two-component NRCM). The models were used to investigate and compare the apparent wave travel velocities in a reinforcing bar, plain (homogenized) concrete, and reinforced concrete (two-component NRCM). It has to be mentioned that the *apparent* wave travel velocity was investigated, since straight wave propagation paths were assumed.

Unsurprisingly, it turned out that in the first two models, which consisted of only one material, the observed apparent wave travel velocity almost exactly matched the actual p-wave velocities of the modeled materials. In the two-component NRCM, the observed apparent wave travel velocity varied between the lower velocity of the homogenized concrete and the higher velocity of the reinforcement steel (see Fig. 5.2). The arrival times of the wave at the virtual sensors were used as input for the homogeneous Geiger method in order to estimate the location of the artificial numerical source and compare the results with the actual source locations. For the reinforcing bar, it was sufficient to use a one-dimensional source localization. The estimated and actual source location agreed well with each other. For the NCM model, a three-dimensional source location as described in Section 3.3 combined with a global (homogeneous) velocity model was used. Again, the estimated and actual source location were a close match. For the two-component NRCM, the homogeneous Geiger method did not yield sufficiently accurate source location estimations. Especially the deviation in the z-direction (the longitudinal direction of the reinforcing bar) was significant (see the visualization of the iterative development of the estimated source coordinates using a homogeneous velocity model in Fig. 5.3). Using the heterogeneous Geiger method, described in Section 3.3.2, improved the localization accuracy for the NRCM simulations.

However, the results of the numerical wave propagation simulation showed that the assumption of a straight wave propagation path might not even be suitable for an uncracked, heterogeneous specimen. The empirical evaluation of the data obtained from the numerical simulations showed that there was an apparent relationship between the observed wave travel velocity and the angle between the reinforcing bar and the straight path between the source and receiving sensor, denoted as α (see Fig. 5.4). In Section 2.2.3, a very simple model (see Fig. 2.8) was used to investigate the influence of a reinforcing bar on the wave propagation behavior. The results are based on Eqs. 2.17 to 2.20, visualized in Fig. 2.9, and confirm the observations made during the described numerical simulations. If the angle between the reinforcing bar and the straight path between source and sensor is $\alpha \approx \pi/4$ or larger, the reinforcing bar has no influence on the wave travel path. Hence, the observed wave travel velocity is equivalent to the (defined) wave travel velocity of the homogenized concrete ($c_{concrete} \approx 4000$ m/s^2). If α is smaller than approximately $\pi/4^*$, the reinforcing bar influences the wave travel path. The observed wave travel velocity increases with decreasing α. The polynomial trendlines shown in Fig. 5.4 reflect this relation surprisingly accurately. Only some of the data points are not located on or very near these trendlines. Neither the observed relationship between α and the observed wave travel velocity c nor the non-conforming data points could be reproduced by utilizing a heterogeneous velocity model in combination with assumed straight wave propagation paths. In addition, under the assumption of straight wave propagation paths it is impossible to reflect the impact of a crack on the wave travel duration and hence the observed wave travel velocity.

Parts of the findings were presented in 2014 at the 31st Conference of the European Working Group on Acoustic Emission (EWGAE) in Dresden and published in [19].

*The critical angle depends on the velocity ratio; see Section 2.2.3.

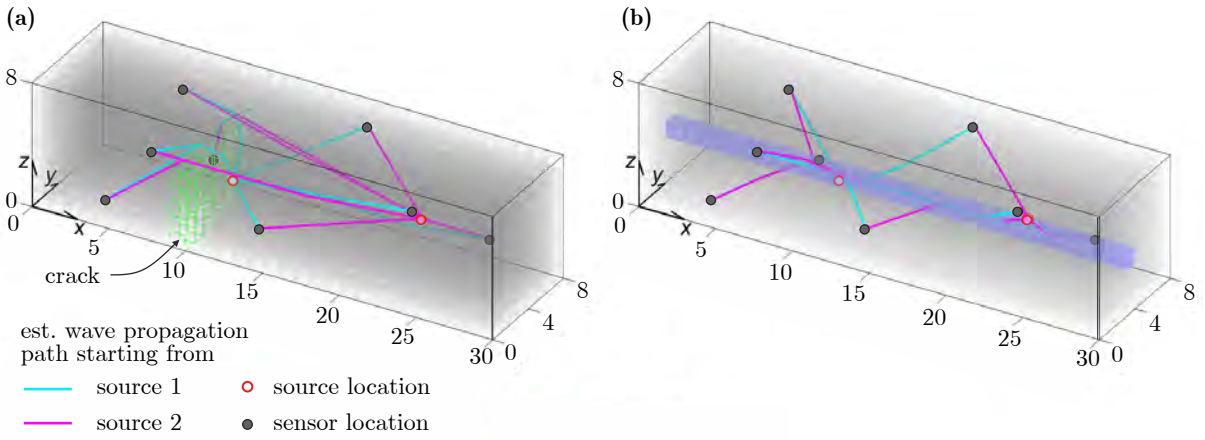

Fig. 5.5: Visualization of the estimated fastest wave propagation path between two sources and eight sensors in (a) a homogenized concrete specimen with a crack at $x = 10$ [gp], and (b) a homogenized concrete specimen with a single reinforcing bar.

5.3 Evaluation of *FastWay* Using Simple Numerical Models

FastWay is a novel source localization method capable of incorporating the effects of cracks and heterogeneous materials on the wave propagation behavior (see Section 3.4). In order to evaluate whether this novel method is capable of reflecting the influence of cracks and reinforcement on the wave propagation behavior, two very simple low-resolution numerical models were used. *FastWay* primarily reflects the effects of cracks and other air inclusions as well as heterogeneous materials on the (estimated) fastest wave travel path. Fig. 5.5 shows the visualization of some estimated fastest wave travel paths determined using the modified Dijkstra algorithm, which is included as a basic function in *FastWay*. The two low-resolution models show that it is possible to compute a realistic estimation of the fastest wave propagation path with *FastWay*. The wave bypasses the crack (Fig. 5.5 (a)), and the reinforcing bar has a significant influence on the (fastest) wave propagation path if $\alpha < \pi/4$.

5.4 Parameter Study of the Sensor Layout and Model Complexity

Reinforcing bars are considered to have the biggest influence on wave propagation in reinforced concrete specimens, apart from air inclusions (e.g., cracks or honeycombing) and the air surrounding the specimen (see Chapter 2). The reinforcement in a reinforced concrete specimen generally has a considerably more complex configuration than a single straight reinforcing bar and consists of longitudinal and transverse bars, stirrups etc. To apply *FastWay* to a more realistic specimen, a numerical model of a concrete cuboid with the dimensions $600 \times 150 \times 250$ [mm] including a complex reinforcement layout was generated. Six numerical source locations were investigated. Additionally, a crack was incorporated into the numerical model for the investigations of sources S3 to S6. The numerical model was used to investigate two independent things. The first aim of the parameter study was to figure out how accurate the numerical model of a reinforced concrete specimen needs to be. Three different configurations were used as input for the heterogeneous Geiger method and *FastWay*. The first model consisted

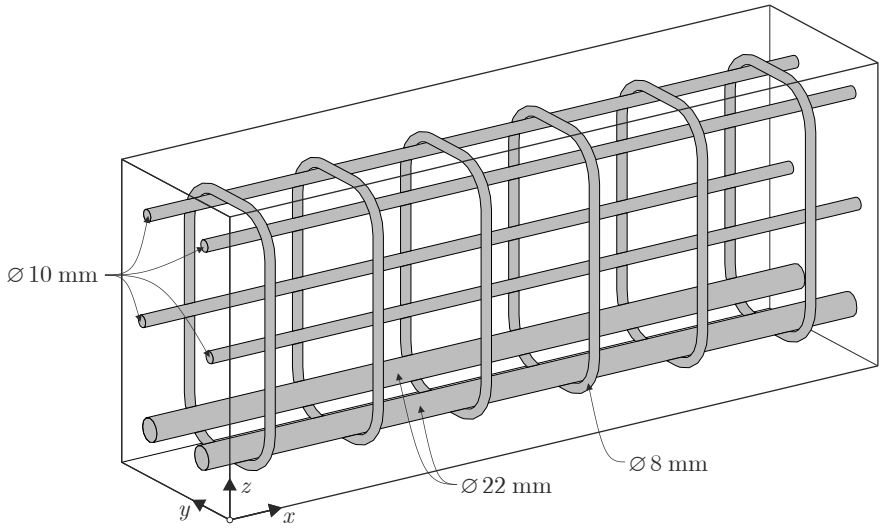

Fig. 5.6: Three-dimensional model of a concrete cuboid including longitudinal reinforcing bars, and stirrups with 100 mm spacings.

	SE1	SE2	SE3	SE4	SE5	SE6	SE7	SE8	SE9	SE10	SE11	SE12
x [mm]	4	4	4	4	4	4	4	4	4	4	4	4
y [mm]	50	100	50	100	50	100	150	200	150	200	150	200
z [mm]	50	150	250	350	450	550	50	150	250	350	450	550

	SE13	SE14	SE15	SE16	SE17	SE18	SE19	SE20	SE21	SE22	SE23	SE24
x [mm]	148	148	148	148	148	148	148	148	148	148	148	148
y [mm]	100	50	100	50	100	50	200	150	200	150	200	150
z [mm]	55	155	255	355	455	555	45	145	245	345	445	545

Tab. 5.1: Sensor coordinates*

of a homogenized concrete cuboid with longitudinal reinforcement, two ⌀20 mm bars near the bottom of the cuboid, two ⌀10 mm bars each near the top and in the middle of the cross-section, as well as ⌀8 mm stirrups with 100 mm spacings. It corresponds to the model used as input for the wave propagation simulation and is visualized in Fig. 5.6. The second model consisted of a homogenized concrete cuboid with longitudinal reinforcement and no stirrups. The last model was the plain homogenized concrete cuboid without any reinforcement (one-component NCM).

The second aim of the parameter study was to evaluate which sensors delivered the input (determined arrival time t_a and sensor location) that yielded the most accurate results. Despite the rather small size of the specimen a total of twenty-four numerical sensors were implemented in the model. Either all sensors or a subset of six or twelve sensors were used for source localization. After picking the arrival time of the wave for each sensor using an AIC picker (see Section 3.1.2), the determined arrival time was evaluated. Two criteria were used for this evaluation. The first

*The specimen was surrounded by a 3 mm $\widehat{=}$ 3 gp air layer. The virtual sensors were located in the surface concrete voxels at two relevant lateral surfaces.

	S1	S2	S3	S4	S5	S6
x [mm]	300	200	200	301	300	50
y [mm]	100	100	100	43	50	122
z [mm]	6	150	150	33	151	125

Tab. 5.2: Source coordinates

criterion was the signal-to-noise ratio. All signals were superimposed with artificial white noise of the same amplitude. Any sensors at which the maximum detected amplitude of the signal (the wave signal) was less than ten times the maximum amplitude of the recorded white noise were excluded from the subsequent localization process. The second verification criterion was the maximum deviation between the arrival time determined with a fixed threshold and that one determined with the AIC picker. The deviation was limited to 5 µs, which is a strict limit that is only suitable for numerical simulations. Subsequently, the evaluated arrival times were ranked using various ranking criteria. These criteria were:

- earliest arrival time,
- maximum amplitude,
- maximum amplitude in the first 10 µs after t_a,
- maximum amplitude in the first 20 µs after t_a, and
- fastest rise time.

The six to twenty-four arrival times were used as input for the three source localization methods (the homogeneous Geiger method, the heterogeneous Geiger method, and *FastWay*). For the homogeneous Geiger method, a global velocity model was used. The global velocity was identical to the implemented p-wave velocity of the homogenized EEP concrete (c_p = 3900 m/s). The resulting locations were considered only if they were within the (reinforced) concrete cuboid. Heterogeneous velocity models (see Section 4.4) were used for the other two methods. The model used as input for the heterogeneous Geiger method consisted of voxels with an edge length of 1 mm. The velocity model used for *FastWay* was composed of voxels with an edge length of 5 mm. Three different materials were included in both velocity models, namely EEP concrete ($c_{p,EEP}$ = 3900 m/s), reinforcement steel ($c_{p,steel}$ = 5900 m/s), and air ($c_{p,air}$ = 0 m/s). As mentioned before, for the numerical simulations with sources S3 to S6 the concrete model contained a notch which represented a crack. The notch was located at x = 300 mm, extended across the width of the beam, and ran from z = 0 mm to z = 150 mm. The notch width was 2 mm. The concrete voxels in the area of the notch were replaced by air voxels. Any steel voxels remained unchanged.

A total of twelve different sensor combinations, and three numerical velocity models for the uncracked specimen, as well as six numerical velocity models for the cracked specimen (three models with a notch, three models without a notch), combined with three source localization methods yielded a large number of results. Unfortunately, it was not possible to identify a numerical model or sensor combination that yielded universally optimal results (see Figs. A.1 to A.6). Nevertheless, some fundamental conclusions could be drawn.

First and foremost, an evaluation of the recorded signals (excluding signals with undetectable arrival time) can significantly improve the accuracy of the estimated source location. Moreover, such an evaluation never leads to a decrease in the source location estimation accuracy if at least six admissible signals are available. This is true for all three used localization methods. Secondly, a ranking of the evaluated signals is useful especially for more elaborated source localization methods. *FastWay*, and especially the heterogeneous Geiger method, generally require a significant amount of calculation time. Reducing the number of input parameters

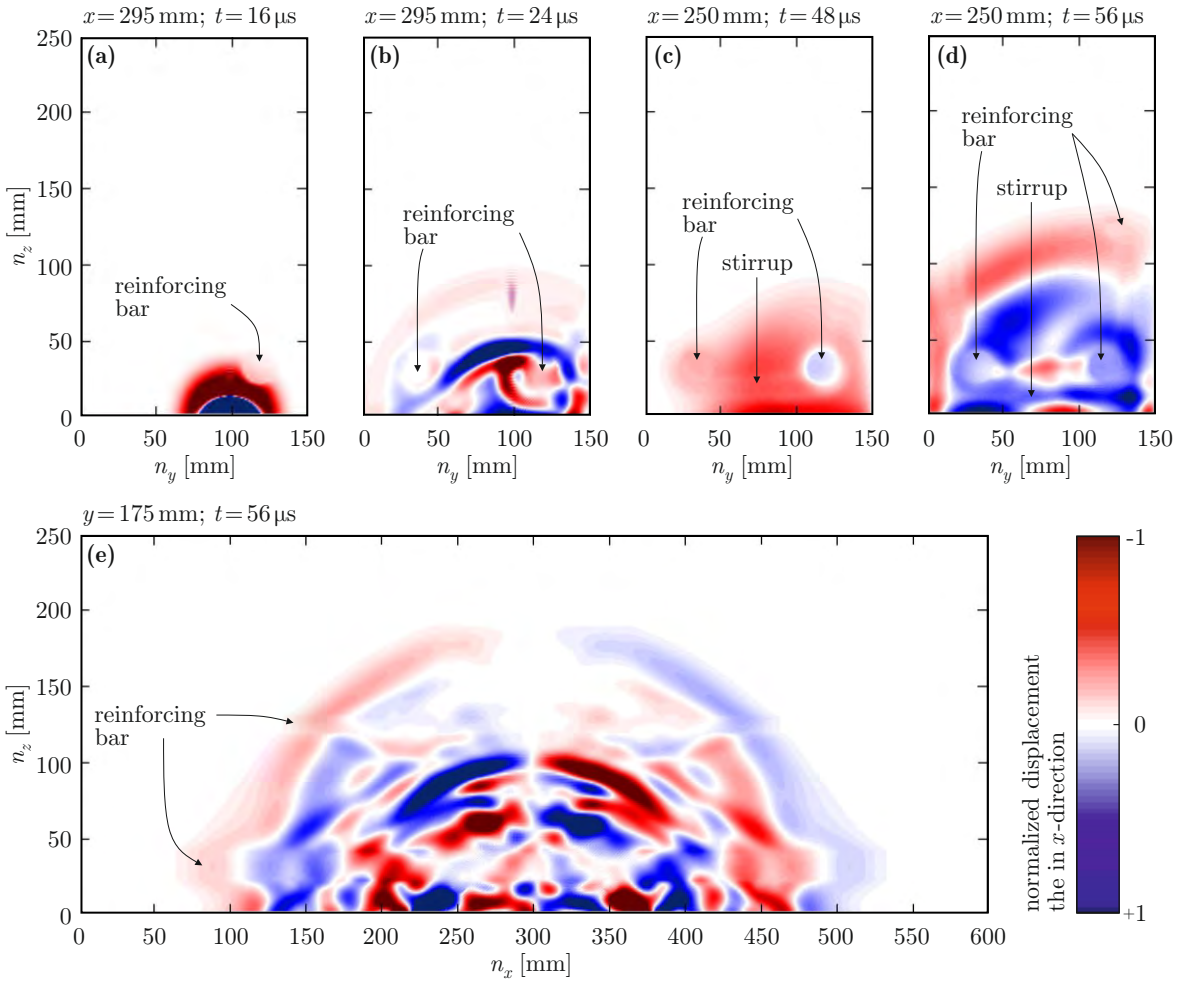

Fig. 5.7: Visualization of the normalized displacement in the x direction caused by source S1: (a)–(d) Four cross-sections over the time at two different locations; (e) longitudinal section.

(the used sensor locations) reduces the required calculation time substantially. This is especially true for *FastWay*. *FastWay* and the homogeneous Geiger method require approximately the same calculation time if the input is limited to the data obtained from six sensors. Ranking and limiting the number of input parameters (reducing the number of evaluated sensors) can improve the localization accuracy while speeding up the computational process. However, in the case of the six described simulations and the three localization methods, namely the homogeneous and teh heterogeneous Geiger's method as well as *FastWay*, ranking and limiting the number of input parameters had almost no influence on the source location estimation accuracy. This was mainly because all signals with undetectable arrival times had already been excluded, and the remaining signals had passed a comparatively strict evaluation process. Limiting the number of input parameters decreased the localization accuracy for sources S1 and S2 and both Geiger methods. On the other hand, the accuracy of estimating the location of source S6, determined with the Geiger methods, was improved by limiting the number of input parameters. The sensors were located only on two surfaces (y = 4 mm and y = 148 mm; see Tab. 5.1). It is, however, expedient to apply sensors to all accessible surfaces of the specimen. A great variety of sensor coordinates and surrounding as much as possible of the investigated area with sensors significantly improves the localization accuracy. Finally, the different velocity models had almost no influence on the localization results determined with the heterogeneous Geiger method. It was apparent that if a straight wave propagation path is assumed, comparatively small objects

such as the reinforcing bars and notch generally have almost no impact on the average wave velocity (see Eq. (3.27)). On the other hand, the influence of the different velocity models on the estimated source locations determined with *FastWay* was significant. The most precise velocity model consisted of the concrete cuboid with all reinforcing elements and is visualized in Fig. 5.6. Surprisingly, this NVM did not lead to the most accurate source location estimations determined with *FastWay*. On the contrary, it even yielded some of the most inaccurate source location estimations. Fig. 5.7 clearly shows that the reinforcement affects wave propagation. However, the impact on the apparent wave travel velocity seems limited. The wave front visualized in Fig. 5.7 (e) had advanced farther in the area around the reinforcing bars than in other areas, but the difference was not as significant as expected. The wave front in the reinforcing bars should be considerably further advanced compared to the wave front in the concrete, assuming that the wave front propagates with the p-wave velocity of the material it is traveling through ($c_{p,steel} \approx 1.5 \times c_{p,EEP}$). The reinforcing bars guide the wave through concrete and air. Hence, the wave front propagates with the velocity of the guided mode, which is considerably lower than the p-wave velocity.

It has to mentioned that the homogeneous Geiger method proved a reliable source localization estimation method. It provided accurate results whenever the source was in the middle of the area surrounded by the sensors. This was especially true for all simulations without a notch. However, it is recommended to use more elaborate source localization methods, such as *FastWay*, if cracks, notches, or similar air inclusions are present in the monitored specimen. The location of source S6 estimated with *FastWay* was far more accurate than the estimations determined with both Geiger methods. Cracks, notches, and similar air inclusions should be included in the NVM which is used as input for *FastWay*. Otherwise, it is not possible to consider their potentially significant effect on the propagation path of the fastest wave. The steel reinforcement should be considered too, especially if it could guide the wave through a crack or a similar air inclusion. However, the wave velocity of the guided mode, which is slower than the p-wave velocity of steel, should be implemented in the NVM.

5.5 Parameter Study of the Guided Wave in Reinforcing Elements

The main aim of this simulation was to evaluate the performance of *FastWay* and to investigate the apparent wave velocity in a reinforced bar using a numerical model of a reinforced concrete cuboid with dimensions 600 × 150 × 200 [mm]. The results of the numerical simulation were presented in [16].

5.5.1 Simulation setup

The concrete is modeled as a homogeneous material (see Section 4.3.2). The concrete cuboid is reinforced with a single ⌀30 mm steel bar. A notch, representing a crack, is incorporated into the model. In the y direction, the notch extends across the entire width of the specimen. In the z direction, the notch extends from the lower surface to $z = 150$ mm. The notch width is modeled to be 2 mm. In the x direction, the notch is positioned directly in the middle of the specimen, as shown in Fig. 5.8. The simulation was also used to find an expedient input value for the wave propagation velocity of reinforcement steel in the NVM that was used as input for the heterogeneous source localization methods. Therefore, a parameter study was used.

The wave propagation velocity assigned to the voxels representing the homogenized EEP concrete in all the numerical models was the p-wave velocity of the EEP concrete, $c_{p,\mathrm{EEP}} =$

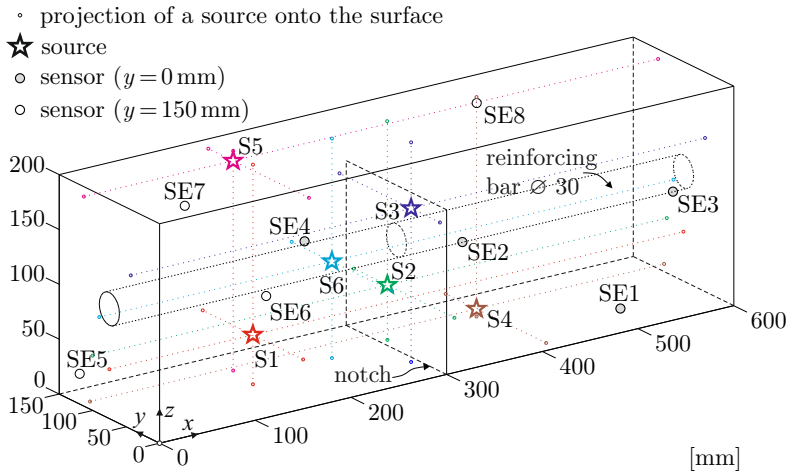

Fig. 5.8: Three-dimensional visualization of the source and sensor locations

	Sources						Sensors							
	S1	S2	S3	S4	S5	S6	SE1	SE2	SE3	SE4	SE5	SE6	SE7	SE8
x [mm]	150	308	293	404	156	243	485	320	540	155	20	215	130	435
y [mm]	75	100	43	104	113	90	5	5	5	5	148	148	148	148
z [mm]	45	50	140	7	191	88	20	115	115	150	15	45	145	175

Tab. 5.3: Source and sensor locations

3912.15 m/s. The models were the NRCM for the wave propagation simulation, and the NVM for both the heterogeneous Geiger method and *FastWay*. The wave propagation velocity assigned to the voxels representing air was $c_{air} = 0$ m/s in all the numerical models. The p-wave velocity of the voxels representing reinforcement steel was $c_{p,steel} = 5900$ m/s in the NRCM used for the wave propagation simulation. As mentioned above (particularly in Section 5.4), in reinforcing bars the wave front travels with the velocity of the guided mode. The velocity of the guided mode is limited by the p-wave velocity of concrete (lower boundary) and the p-wave velocity of steel (upper boundary). Therefore, the wave velocity of steel implemented in the NVM for the heterogeneous localization methods was varied between these boundaries according to

$$c_{steel} = c_{p,\mathrm{EEP}} + f_v \times (c_{p,steel} - c_{p,\mathrm{EEP}}). \tag{5.1}$$

Values from 0 to 1 in steps of 0.1 were assigned to the velocity factor f_v in Eq. (5.1).

Six sources were excited at different locations in the specimen (see Tab. 5.3). The fundamental frequency of the sources, the Ricker wavelets, was 100 kHz and the signal durations were 25 µs. The source was modeled as an explosion and applied as a displacement at the individual grid points. The adjacent grid points were smoothed to avoid numerical artifacts. To simulate the wave propagation caused by the six acoustic emissions, a numerical model consisting of 1.8×10^7 voxels with the dimensions 1 gp $\widehat{=}$ 1 mm was used. *FastWay* is not able to process such a large numerical model. For that reason, a lower resolution with larger voxels (1 gp $\widehat{=}$ 5 mm) was used. The resulting numerical model consisted of 1.44×10^5 voxels. Since the estimated source location is limited to be at the location of the nodes (see Section 3.4.1), a systematic error $err_s = \sqrt{3 \times (0.5 \text{ gp})^2} = 4.33$ mm was introduced. A total of eight virtual sensors were implemented in the numerical model. The coordinates of the sensors are listed in Tab. 5.3. No

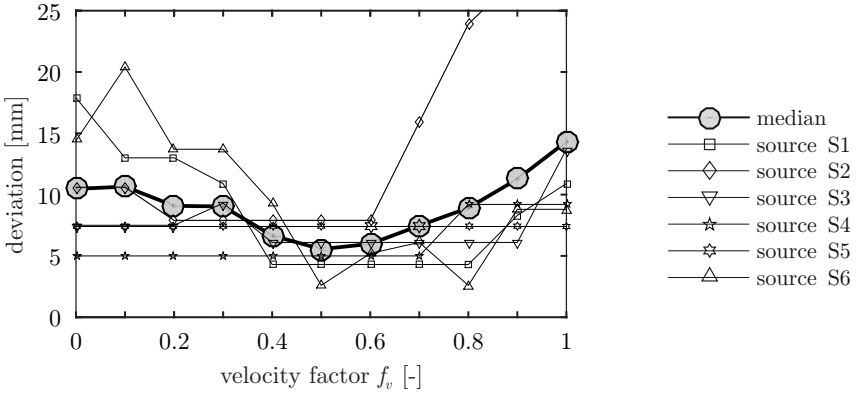

Fig. 5.9: Deviation between the actual and estimated (by *FastWay*) source locations as a function of the applied wave velocity $c_{steel}\{f_v\}$ (see Eq. (5.1)), including the median value of the six sources. Taken from [16]

white noise was superimposed onto the calculated wave signals. The six sensors that detected the earliest arrival times were used to determine the estimated source location. The three methods described in Chapter 3 (*FastWay*, the homogeneous Geiger method and the heterogeneous Geiger method) were used.

5.5.2 Investigation of the guided-mode velocity

The six source locations were estimated with eleven different NVMs. Only the wave velocity assigned to the steel voxels, c_{steel}, differed between these models (see Eq. (5.1)). As mentioned before, the six sensors with the earliest detected arrival times were used to determine the estimated source locations, using only *FastWay*. Hence, the same arrival times were used as input in all the NVMs. Some source locations were hardly affected by the variation of c_{steel} in the NVMs. The coordinates of the estimated source location of source S5 were the same for all eleven executions of *FastWay* with the input of the different NVMs, because the estimated fastest wave travel path from the source to the selected six sensors led only through concrete. In contrast, source S6 was located in the reinforcing bar, and source S2 was located near the reinforcing bar at the surface of the notch. The coordinates of their source location estimations were heavily influenced by the variation of the wave velocity of steel. A comparison of the deviation between the actual and estimated source locations for all six sources and eleven different NVMs as visualized in Fig. 5.9 shows that a velocity factor of $f_v = 0.5$ led to the most accurate source location estimations. The plot of the median value for all six sources clearly illustrates this. Therefore, the (guided) wave travel velocity of steel was set to $c_{steel} = 4900$ m/s. The velocity factor for the experiments was evaluated from pencil-lead breaks. A velocity factor of $f_v = 0.5$ was confirmed. The impact of the different NVMs on the source location accuracy was not as significant.

5.5.3 Localization results

All the results presented in this section were determined with an NVM using a steel velocity of $c_{steel} = 4900$ m/s. The results of the three used source localization methods for source S2 are visualized in Fig. 5.10. Source S2 is located near the notch. The voxels representing the air-filled notch are shown in white and have green borders, since no $\mathbf{E}_{\text{source}}$ value can be determined for a node located in a voxel representing air. The notch had a significant influence on the

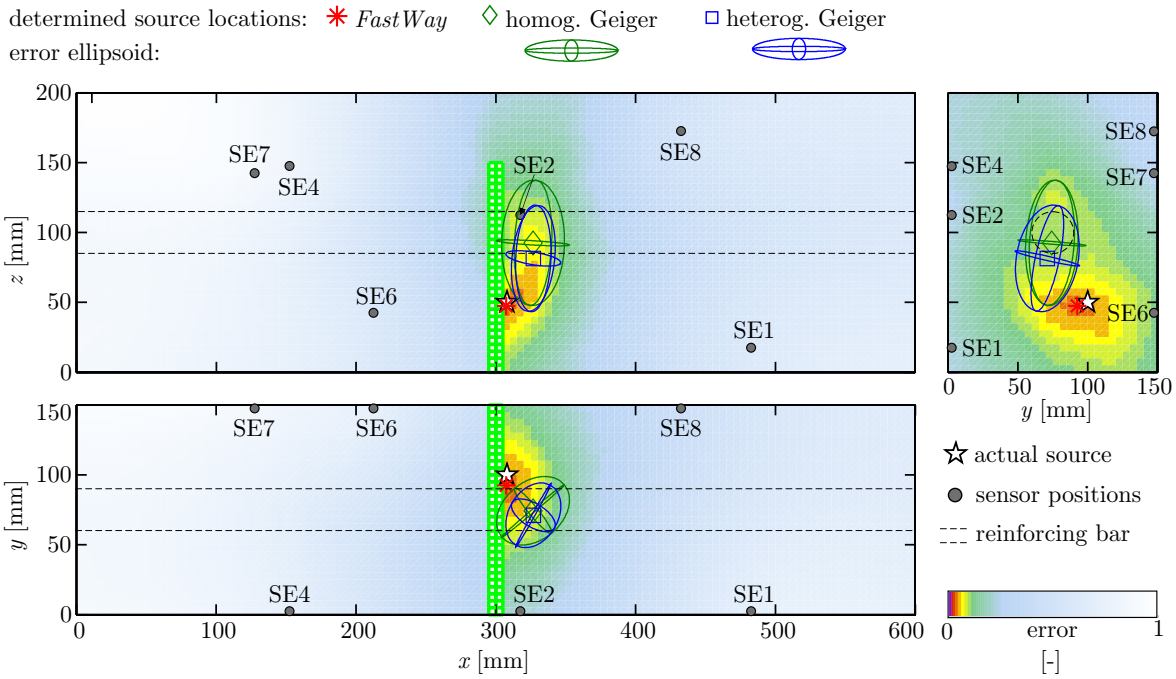

Fig. 5.10: Cross-sections of the specimen showing visualizations of $\mathbf{E}_{\text{source}}$ and the error ellipsoids for the Geiger methods. The locations of the sensors, estimated sources and actual source (S2) are marked. The shown cross-sections are at the location of the estimated source (determined using *FastWay*)

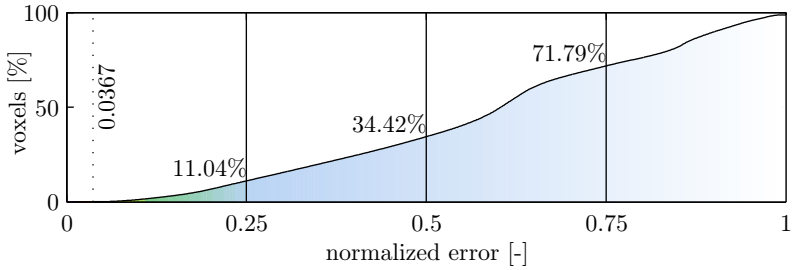

Fig. 5.11: Visualization of the cumulative distribution of the normalized error with respect to the voxels of $\mathbf{E}_{\text{source}}$, calculated for the *FastWay* localization of source S2

estimated source locations. Both traditional methods, the homogeneous Geiger method and the heterogeneous Geiger method, assume straight wave propagation paths and therefore do not consider that the elastic wave has to travel around the notch.

This resulted in a significantly larger deviation between the actual and estimated source location using the Geiger methods, compared with the deviation between the actual and estimated source location determined with *FastWay* (see Fig. 5.12). Both Geiger methods estimated the source location to be near the reinforcing bar on the same side of the notch as the actual source. The location and orientation of the respective error ellipsoids were nearly identical. Both error ellipsoids were relatively large; even so the actual source was located outside them. *FastWay* delivered a very accurate estimate of the source location; the deviation between the actual and estimated source location was minimal. The visualization of $\mathbf{E}_{\text{source}}$ in Fig. 5.10 illustrates that only a small number of voxels located near the source location was estimated to host the source. These voxels were located at the same side of the notch as the actual source. The cumulative distribution of the normalized error ($\mathbf{E}_{\text{source}}$) in regard to the voxels, visualized in

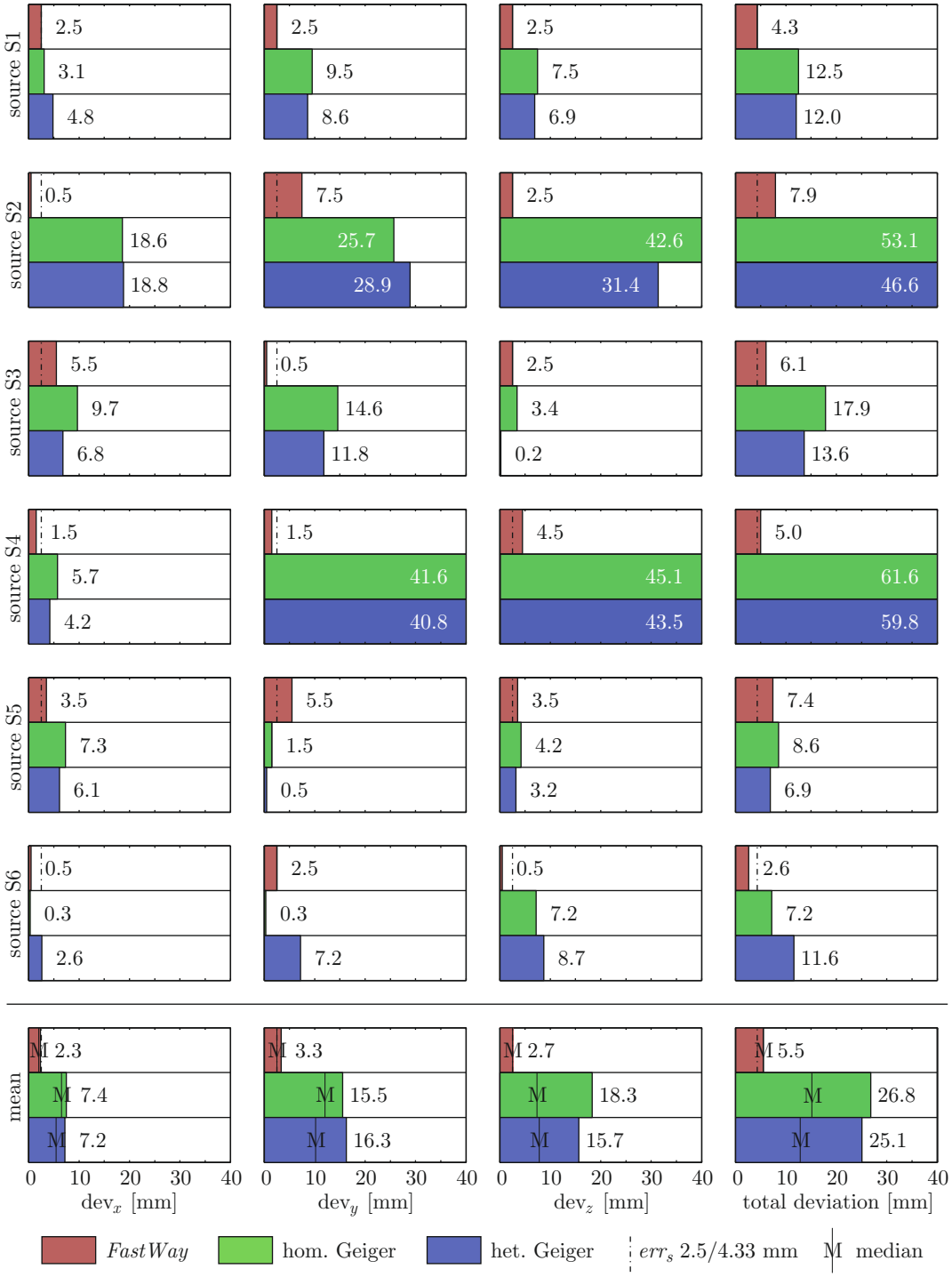

Fig. 5.12: Visualization of the deviation between the estimated and actual source locations. In the last row the mean (colored bar) and the median of the deviations are visualized for all six sources. The parameter err_s is marked in the bar representing the *FastWay* solution (2.5 mm in each direction; 4.33 mm in total)

Fig. 5.11, also confirms that the location of the source was estimated to be located in a very small area of the specimen. An $e_{\text{source};xyz}$ value of less than 0.25 was only determined for about 11% of the voxels. An $e_{\text{source};xyz}$ value of 0.10 or lower was calculated for less than 2% of the voxels. The smallest determined normalized error value was $e_{\text{source;AE}} = 0.0367$. The corresponding

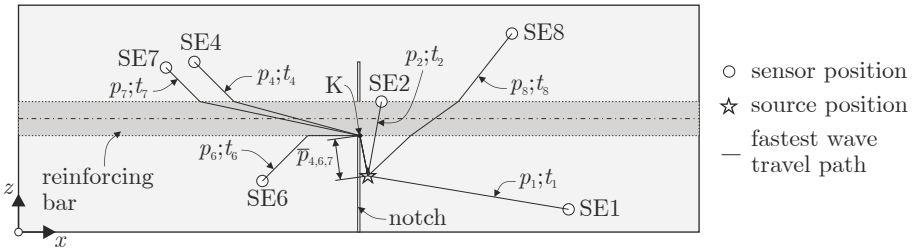

Fig. 5.13: An x–z cross-section of the investigated specimen including the location of source S2, locations of the sensors (SE1, SE2, SE4, SE6, SE7, and SE8), and simplified estimated fastest wave propagation paths p_i.

node represented the estimated source location visualized in Fig. 5.10. An accurate and reliable estimate of the source location goes hand in hand with a small $e_{\text{source;AE}}$ value and a small number of voxels with a normalized error of less than 0.25.

Fig. 5.12 shows the deviations between the estimated and actual source locations in the x direction, y direction, and z direction, as well as the absolute deviations of all six sources for the three source location estimation methods. The last row of Fig. 5.12 shows the mean deviations for all six sources. It is clearly visible that *FastWay* provided the most accurate estimations of the source location for five of the six sources. For source S5 the result determined with *FastWay* deviated by 0.5 mm more from the actual source location than the estimation determined with the heterogeneous Geiger method.

In Fig. 5.10 it can be seen that the wave paths between three of the six sensors and source S2 were significantly affected by the notch. The remaining three sensors were located on the same side of the notch as the source. The fastest wave travel paths connecting the three sensors on the left side of the notch (sensors SE4, SE6, and SE7) and the source had to lead around the notch. The three paths led through the reinforcing bar that bridged the notch (Fig. 5.8). Once the wave had passed the crack, the fastest wave travel path from the reinforcing bar (on the right side of the notch) to the source was almost the same for sensors SE4, SE6, and SE7. Fig. 5.13 shows a x–z cross-section of the investigated specimen including the location of source S2, the locations of sensors SE1, SE2, SE4, SE6, SE7, and SE8 (shown also in Fig. 5.10), and the simplified estimated fastest wave propagation paths p_{se} between the source and the sensors se determined with the *FastWay* algorithm. The sections of the wave travel paths p_4, p_6, and p_7 on the right side of the crack, marked with $\bar{p}_{4,6,7}$, are identical, which naturally affects the source localization. Assuming that the source time as well as the arrival times at the sensors are known, the wave travel duration d_{se} from the source to each sensor se can also be determined. The shortest wave travel durations between the sensors and the source are as unique as the lengths of the corresponding fastest wave travel paths. However, the determined wave travel duration $\bar{d}_{4,6,7}$ between the source and the kink point marked with K is identical for the three sensors on the left side of the notch. Hence, these three sensors all provide roughly the same information for the source location estimation. An accurate localization of the source is only possible by considering the three other sensors that are located at the same side of the notch as the source. It would be impossible to accurately estimate the source location if all the sensors were separated from the source by the same crack (notch). If, however, the sensors are separated from the source by different cracks, a source location estimation is possible as long as four unique (multi-)linear fastest wave propagation paths connect the sensors and source. The paths are only unique as long as no section of an estimated fastest path from the source to one sensor is identical with a section of an estimated fastest path connecting the source with another sensor, as it is the case with $\bar{p}_{4,6,7}$.

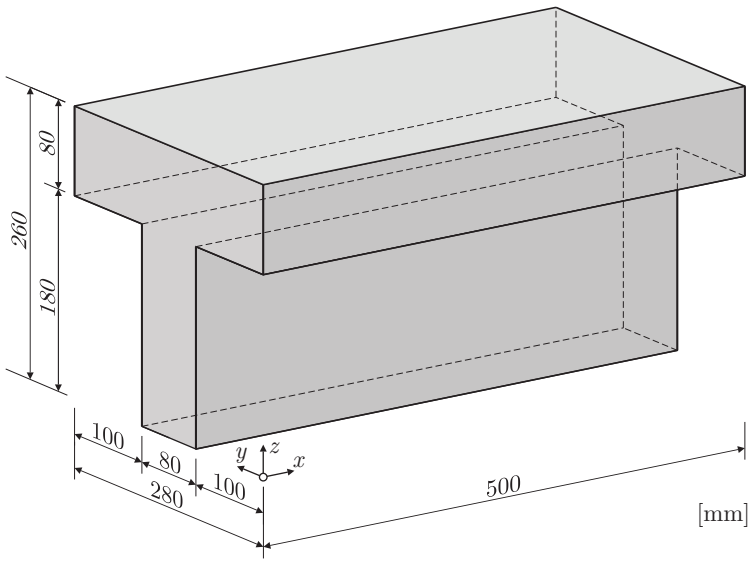

Fig. 5.14: Visualization of the numerical T-shaped concrete beam

5.5.4 Conclusions

Contrary to both the original Geiger method and the heterogeneous Geiger method, the *FastWay* method is capable of considering the influence of cracks on wave travel paths as long as they are represented in the velocity model, i.e. in the velocity matrix $\mathbf{C}_{mo}$ (see Section 4). The entire domain of the numerical model is considered by the $FastWay$ algorithm. In this way, the accuracy of the estimated source location can generally be improved. The improvement is particularly noticeable if the source is located near the crack or near the surface of the specimen. Looking at the estimates of the six simulated sources, it seems that the sensor locations have a significantly smaller influence on the accuracy of the estimated source location determined with *FastWay* than on that of the locations determined with the two Geiger methods.

5.6 T-shaped Concrete Beam

Numerical simulations of elastic wave propagation in a T-shaped beam were used to investigate the influence of a complex specimen shape on the wave propagation behavior and the accuracy of the estimated source locations. The source location was estimated using three arrival-time-based source localization methods: the homogeneous Geiger method, the heterogeneous Geiger method, and *FastWay*. As shown in Fig. 3.5 in Section 3.1.4, a wave propagating from the periphery of the flange to the bottom side of the web has to bypass the air surrounding the T-section. Hence, a linear wave propagation path is impossible. Only *FastWay* is able to consider this effect.

In many cases a monitored specimen or area is not surrounded by sensors. In some cases, not all the surfaces of the specimen are accessible. A T-shaped girder, for example, is generally loaded from the top and/or supports other structural elements. The flanges and/or the web might not be accessible. Therefore, sensors can sometimes only be applied to certain parts of the monitored specimen. The influence of sensors only covering part of the specimen on the

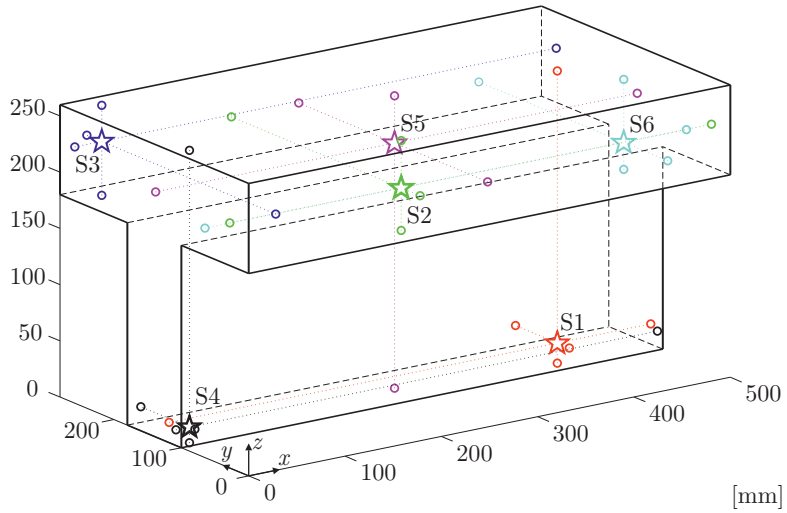

Fig. 5.15: Location of the six sources in the specimen (marked with ☆). Their projections onto the specimen surface are marked with ○.

	S1	S2	S3	S4	S5	S6
x [mm]	403	178	28	14	248	435
y [mm]	118	28	258	108	138	65
z [mm]	18	208	228	14	218	204

Tab. 5.4: Source coordinates

accuracy of the estimated source location was investigated by using five different sensor layouts. The numerical simulation and parts of the findings were published in [17].

5.6.1 Investigated numerical model

For the simulations of the elastic wave propagation, a numerical model of a T-shaped beam was used. The beam had a length of $l_x = 500$ mm, a 280 mm × 80 mm flange, and a 80 mm × 180 mm web, as shown in Fig. 5.14. The numerical specimen consisted of a three-component numerical concrete model (see Section 4.3.1). The NCM was composed of three different materials: the cement matrix, aggregate particles, and air voids. The aggregate had a maximum grain size of 16 mm. The material properties of aggregates usually vary within a certain range; this variation was implemented in the NCM. More information about the NCM and the used material properties listed in Tab. 4.1 is given in Section 4.3. In order to study the influence of a complex specimen shape (in this case a T-shaped cross-section) on the wave propagation behavior, the specimen was modeled as being uncracked and not having any reinforcement.

5.6.2 Sources

Two sources (S1 and S4) were located inside the web. Three sources (S2, S3, and S6) were located inside the flange, and the sixth source (S5) was located at the intersection of web and flange. The coordinates of the sources were selected randomly and are listed in Tab. 5.4. The source locations are displayed in Fig. 5.15.

	S1	S2	S3	S4	S5	S6	S7	S8	S9	S10	S11	S12	S13
x [mm]	50	130	210	290	370	450	55	135	215	295	375	455	80
y [mm]	100	100	100	100	100	100	180	180	180	180	180	180	80
z [mm]	50	130	60	115	55	125	150	35	155	35	160	35	180

	S14	S15	S16	S17	S18	S19	S20	S21	S22	S23	S24	S25	S26
x [mm]	250	420	90	240	400	150	350	90	255	425	70	230	410
y [mm]	20	70	260	210	230	140	150	20	80	30	205	270	240
z [mm]	180	180	180	180	180	260	260	260	260	260	260	260	260

Tab. 5.5: Sensor coordinates

5.6.3 Sensor layout

A total of 26 virtual sensors were implemented in the numerical model. Twelve sensors (S1–S12) were located on the lateral surfaces of the web, six sensors on each side. Six sensors (S13–S15 and S16–S18) were located on the bottom side of the flange, three on each side of the web. The remaining eight sensors (S19–S26) were located on the top surface of the flange. No sensors were placed on the end faces of the specimen or the bottom surface of the web. The coordinates of the sensor positions are listed in Section 5.5.

The calculated displacement history at the sensor locations was used to determine the arrival times of the wave at the sensors, which corresponds to arrival-time picking based on recorded wave signals. The arrival times were subsequently used as input for the source location estimation process. The five following sensor layouts were used to estimate the source location:

- Sensor layout A: eight sensors located at the upper surface of the flange (SE19–SE26)
- Sensor layout B: six sensors located at the lower surface of the flange (SE13–SE18)
- Sensor layout C: twelve sensors located on the web (SE1–SE12)
- Sensor layout D: 18 sensors located on the web and at the lower surface of the flange (SE1–SE18)
- Sensor layout E: 26 sensors located on all surfaces of the specimen (SE1–SE26)

The layouts are visualized schematically in Fig. 5.18. To estimate the source locations, the data of the six sensors recording the largest absolute amplitudes within the first 20 µs after the picked arrival time of the wave at the respective sensor were used. The used source localization methods were the heterogeneous Geiger method, the homogeneous Geiger method, and *FastWay*. These three methods need a velocity model as input. A global velocity model with a wave velocity of $c = 3912$ m/s (the p-wave velocity of EEP concrete) was used for the homogeneous Geiger method. The heterogeneous velocity model for the heterogeneous Geiger method and *FastWay* consisted of two different voxels types: air and EEP concrete. The entire beam was assembled from EEP-concrete voxels and surrounded by air voxels. The edge length of the voxels of the NVM for the heterogeneous Geiger method was 1 mm. The edge length of the voxels of the NVM for *FastWay* was 5 mm. The estimated source locations were restricted to locations within the specimen. The material properties of the voxels are listed in Tab. 4.1.

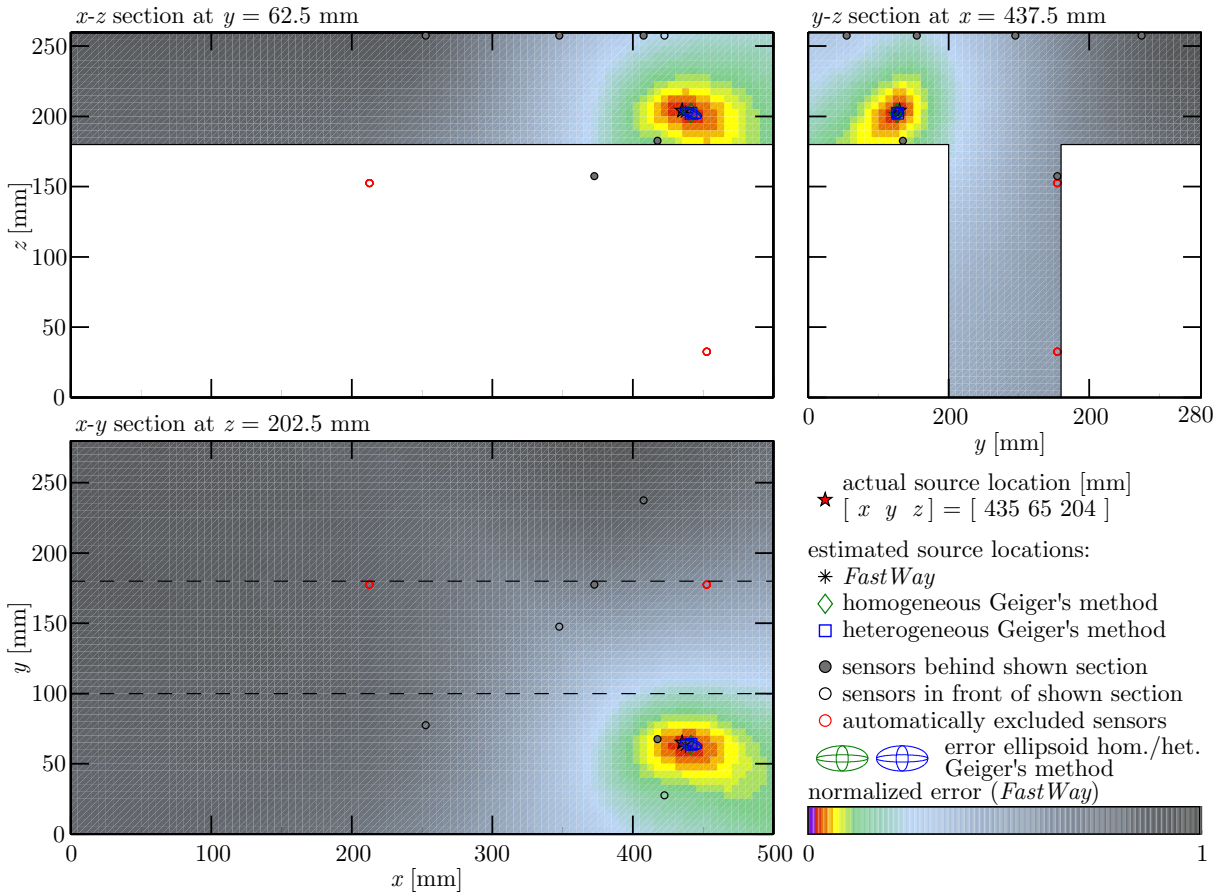

Fig. 5.16: Cross-sections of the T-beam specimen showing visualizations of $\mathbf{E}_{\text{source}}$ and the error ellipsoids for the Geiger methods (extremely small). The locations of the sensors (sensor layout E), estimated sources, and actual source (S6) are marked. The shown cross-sections are at the location of the estimated source (determined using *FastWay*)

5.6.4 Localization results

The location of the six sources (Tab. 5.4) was estimated with the three source localization methods mentioned above, using the data obtained with the five different sensor layouts. Hence, thirty source locations were estimated with each localization method. The results were subsequently visualized. Three cross-sections were used to visualize the projections of the three-dimensional error ellipsoids which were determined for the results obtained by the two Geiger methods. They were superimposed with the normalized error matrix determined for the results from *FastWay*. The shown cross-sections are at the source location estimated with *FastWay*. Only the error matrix for the voxels located in the displayed cross-section is shown. The error ellipsoids for the Geiger methods, the estimated source locations determined with the two Geiger methods, and the sensor locations were projected onto the sections.

Fig. 5.16 shows one of the best of the thirty results. The three methods estimated the source location within a maximum deviation of less than 7 mm (see Fig. 5.18). The determined error ellipsoids are very small, and the actual source location lies inside both error ellipsoids. The voxels with a normalized error matrix value ($e_{\text{source};xyz}$) of 0.11 or smaller form a volume in which the source is most likely located. In Fig. 5.16, the area most probably hosting the source is very small; it consists of the two voxels colored purple. One of the two voxels does actually host the actual source. In contrast, Fig. 5.17 represents an unsatisfactory result, at least at first

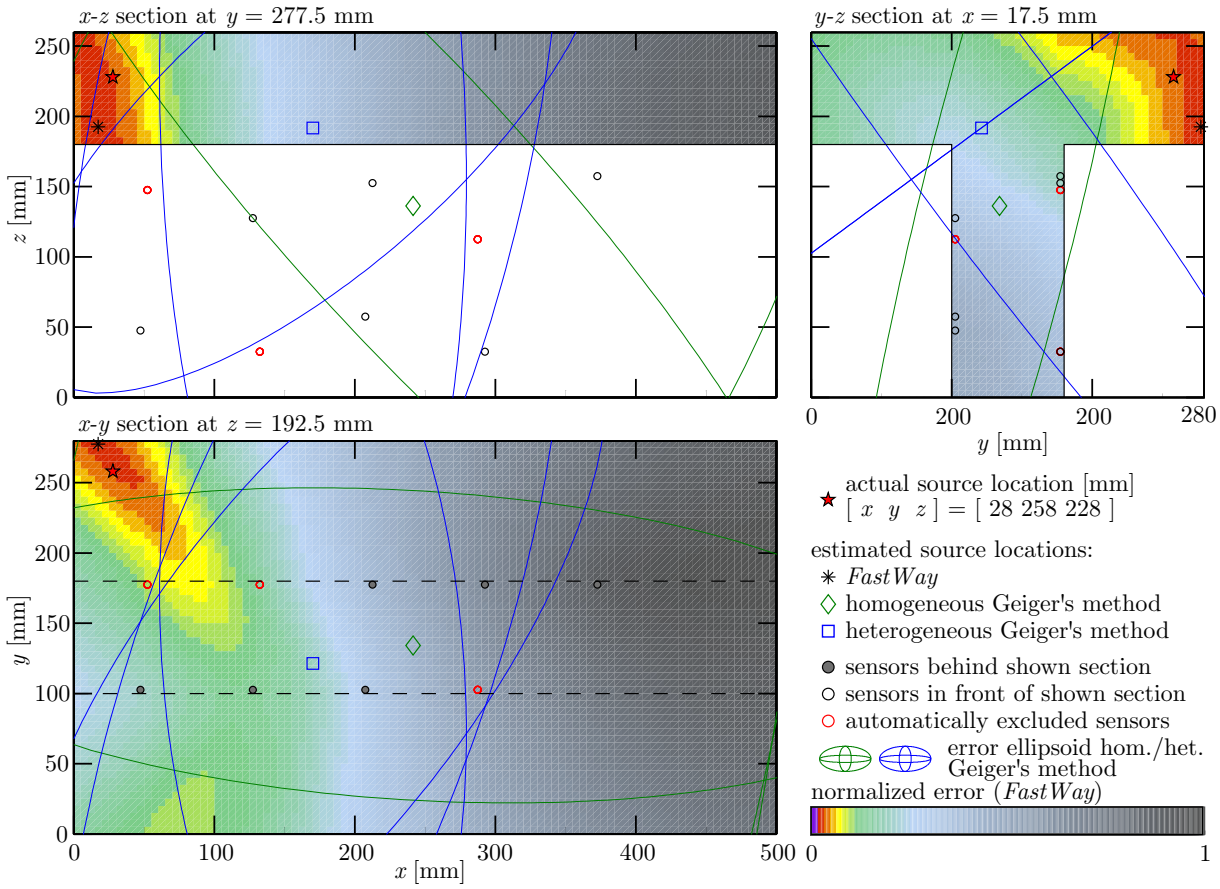

Fig. 5.17: Cross-sections of the T-beam specimen including visualizations of $\mathbf{E}_{\text{source}}$ and the error ellipsoids for the Geiger methods (very large). The locations of the sensors (sensor layout C), estimated sources, and actual source (S3) are marked. The cross-sections are at the location of the estimated source (determined using *FastWay*)

glance. It is clearly visible that the determined error ellipsoids are larger than the specimen itself. Hence, the actual source is obviously located inside both error ellipsoids. However, the large size of the error ellipsoids indicates that the accuracy of the determined source location is very low. The deviation between the actual and estimated source location is 263.3 mm and 200.6 mm for the homogeneous and the heterogeneous Geiger method, respectively. The estimated source locations determined with *FastWay* also differ considerably from the actual source locations. The deviation of 41.8 mm can, however, still be considered satisfactorily accurate. The visualization of the normalized error matrix in Fig. 5.17 indicates that the source is located in the upper-left corner of the flange (in the $y-x$ cross-section). The z location within the flange, however, cannot be clearly identified. The actual source is located inside the volume formed by the voxels with $e_{\text{source};xyz} \leq 0.11$. In Fig. 5.17, however, this area is significantly larger than in Fig. 5.16. Hence, the error ellipsoids and the visualization of the normalized error are a reliable way to estimate the expected accuracy of the determined source location.

The deviation between the estimated and actual source location is significantly lower if the estimated location is determined with *FastWay*. The mean deviation between the actual source location and the source location estimated with *FastWay* for the thirty source localization configurations is 20.7 mm. The homogeneous and heterogeneous Geiger methods provide estimated source locations with a mean deviation of 119.7 mm and 89.6 mm, respectively. The localization error of *FastWay* is approximately one fifth of the localization error of the Geiger methods. *FastWay* yielded 25 of the 30 estimated source locations with the smallest deviation

Fig. 5.18: Visualization of the deviation between the estimated and actual source locations. In the last row the mean (colored bar) and median of the deviations for all six sources are visualized.

from the actual source location. The homogeneous Geiger method yielded four of the most accurate source location predictions, while the heterogeneous Geiger method yielded only one. In the cases where *FastWay* did not provide the most accurate solution, the localization error of the source location predicted by *FastWay* was between 0.3 mm and 5.0 mm larger than the most accurate prediction. Fig. 5.18 shows the deviations between estimated and actual source locations for all six sources, five sensor layouts, and three localization methods. The bar diagram, which displays the deviation, is limited to show a maximum of 100 mm. A localization error of more than 100 mm is considered inadmissible. Determining a permissibly accurate source prediction of sources S2, S3, and S4 was not possible using the homogeneous Geiger method, regardless of the sensor layout. These sources were located in the web (S4) and the flange (S2 and S3). The localization error for S3 and S4 was about 250 mm, which is half of the largest specimen dimension ($l_x = 500$ mm). The heterogeneous Geiger method was not able to satisfactorily predict the source locations of S3 and S4, regardless of the sensor layout. Nevertheless, the localization error was smaller than that one of the homogeneous Geiger method. In addition, the localization error for source S1 for sensor layout A and B, as well as for source S2 for sensor layout E, is more than 100 mm if determined with the heterogeneous Geiger method.

5.6.5 Conclusion

The last row of Fig. 5.18 shows that *FastWay* provided significantly more accurate source predictions than the two Geiger methods for the investigated experimental setups. *FastWay* was the only method that provided a satisfactorily accurate estimation of the source location for every source and sensor layout. *FastWay* is based on a simplified wave propagation model and does not reflect the entire actual physical wave propagation behavior, which results in a mean source location deviation of 20.7 mm. However, the accuracy of the estimated source locations in a complex-shaped specimen can be improved significantly by using *FastWay*'s multi-segmented path analysis.

Chapter 6

Small Concrete Beam

The aim of this section is to test the performance of *FastWay* with data gained during an experiment. External and environmental influences affect the measurement chain and therefore the recorded signal. In experiments, the signal recorded by sensors consists of the wave signal emitted by the AE source superimposed with white noise and other interfering signals. Therefore, it is not always possible to accurately pick the arrival time of the wave at the sensor. This affects all arrival-time-based source estimation methods (e.g., Geiger's method, *FastWay*), since they rely on accurately picked arrival times as input (see Chapter 3). Generally, the first wave arriving at the sensor is a p-wave, as the velocity of the p-wave is higher than that of the other wave types (see Chapter 2). However, the amplitude of the p-wave is usually smaller than the amplitude of the slower s-wave. For numerical simulations, this presents no problem. The arrival of a p-wave with a small amplitude can easily be detected, as the amplitude "recorded" by the virtual sensor before the wave's arrival is equal to zero (see Chapter 5). Sometimes, the amplitude of white noise or other interfering signals can be as large as the amplitude of the arriving p-wave, or even greater. In such a case, picking the accurate arrival time of the wave is impossible. However, several onset-time picking techniques such as AIC picking [47] can be used to improve the reliability and accuracy of arrival-time picking. However, arrival-time picking is not the main focus here. Unreliably picked arrival times are generally excluded from the source location estimation processes mentioned in this dissertation.

Besides the arrival times of the wave at the sensors, a numerical model of the specimen (for *FastWay*, see Section 3.4) or at least the dimensions of the specimen and a constant global p-wave velocity (for the homogeneous Geiger method, see Section 3.3.1) are needed as input for the source location estimation. For experiments, this information cannot be adopted from an existing numerical model like the one used for the wave propagation simulation (see Chapter 4). The needed input values for the homogeneous Geiger method are easy to obtain. The dimensions of the specimen can generally be measured. The global constant wave velocity can be taken from literature or determined experimentally. Known notches, air inclusions, cracks, or reinforcement bars are not considered. *FastWay* and the heterogeneous Geiger method need a more elaborate numerical model as input. Therefore, the specimen has to be discretized numerically (see Section 4.3). The locations of twenty-six randomly selected artificial sources were estimated using two arrival-time-based methods, namely *FastWay* and the homogeneous Geiger method. In order to evaluate the reliability of *FastWay*, the results from both methods were compared with each other and with the actual source location.

Two types of physical experiments were performed – nondestructive and destructive. The nondestructive tests were pencil-lead break experiments. Artificial acoustic emissions, namely Hsu–Nielsen sources (pencil-lead breaks), were excited on the specimen surface. A pencil-lead

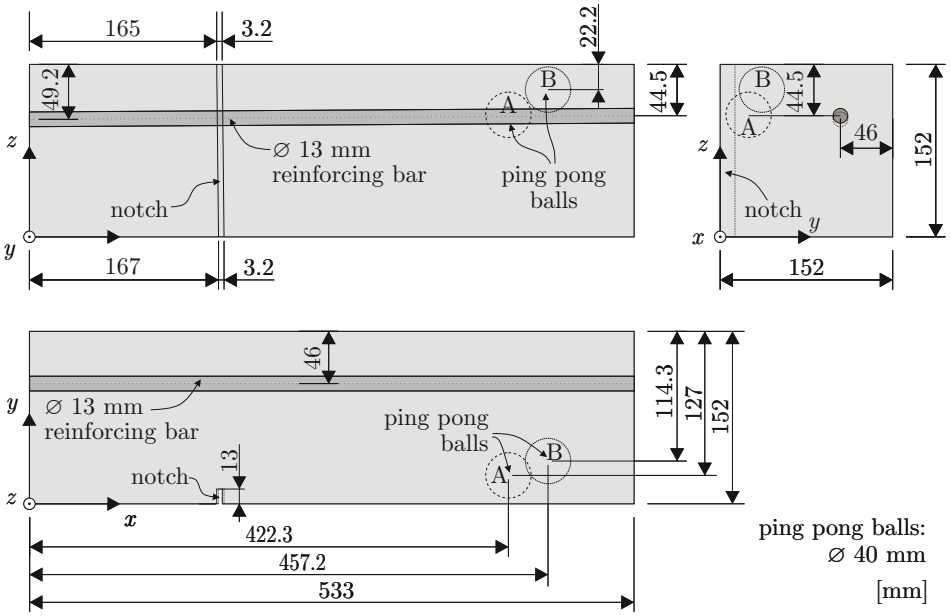

Fig. 6.1: The reinforced and notched concrete specimen. The positions of the ping pong balls, the notch, and the reinforcing bar are marked. Taken from [16]

break produces an intense acoustic signal similar to a natural AE source. The sensors detect such a signal as a strong burst of sound. The location of the source in these experiments is known; however, the (exact) source time is unknown. Hence, the estimated source location can easily be compared to the actual known source location. In the destructive experiment (see Chapter 7) a specimen was loaded, which led to deformations and damage (e.g., cracks). This caused acoustic emissions similar to those recorded during monitoring of a structure. In such an experiment, the actual locations and source times of the AE sources are unknown. The estimated source locations can only be compared to the positions of the cracks.

Passages of this chapter were published in [16] and [18].

6.1 Experimental Setup

The experimental work was performed in the laboratory at the University of Delaware, where a small concrete beam of dimensions 152.4 mm × 152.4 mm × 533.4 mm was cast, cured, and tested. A ⌀ 13 mm reinforcing bar as well as two identical ping pong balls with a diameter of 40 mm were placed in the beam during casting. The aim was to produce a very heterogeneous medium consisting of different components (concrete, steel, air). The positions of the ping pong balls and the steel reinforcing bar are shown in Fig. 6.1. A notch was cut into the hardened beam. The notch represented a crack and was used to create a more complex geometry of the propagation medium. The beam was then mapped with a 25.4 mm × 25.4 mm point grid placed on the whole surface, and pencil-lead breaks were performed at each grid point to generate acoustic emission sources. The coordinates of the twenty-six randomly selected sources that were the target of the two applied source localization methods are listed in Fig. 6.7. Twelve piezoelectric sensors were mounted on the surface of the beam to record the AE signals generated by the pencil-lead breaks. Their positions are visualized in Fig. 6.2 and their coordinates listed in Tab. 6.1. The recorded signals as well as the information about the source and sensor locations,

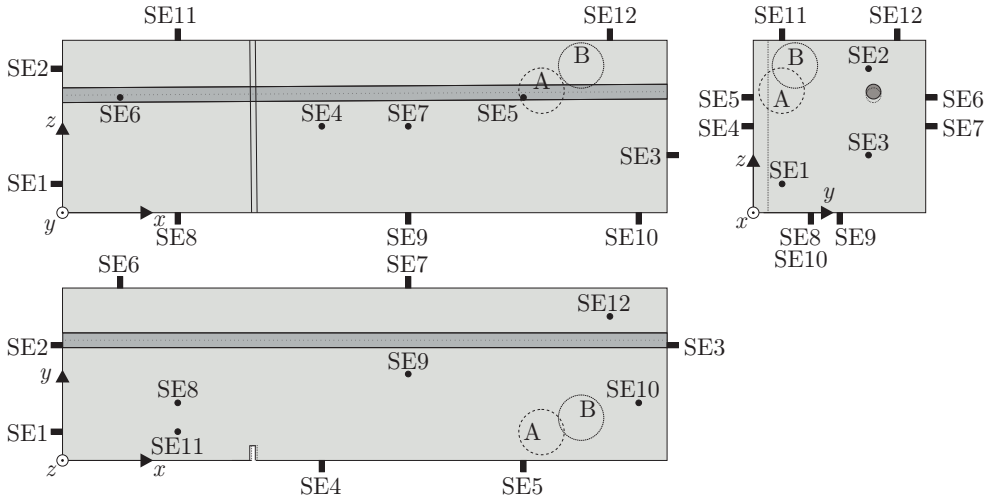

Fig. 6.2: Visualization of the location of the twelve sensors in the tested specimen. The coordinates of the sensors are listed in Tab. 6.1.

	S1	S2	S3	S4	S5	S6	S7	S8	S9	S10	S11	S12
x	0.0	0.0	533.4	288.6	406.4	50.8	304.8	101.6	304.8	508.0	101.6	482.6
y	25.4	101.6	101.6	0.0	0.0	152.0	152.0	50.8	76.2	50.8	25.4	127.0
z	25.4	127.0	50.8	76.2	101.6	101.6	76.2	0.0	0.0	0.0	152.0	152.0

Tab. 6.1: Sensor coordinates in mm

the dimensions of the specimen, as well as the locations of the notch, the reinforcing bar, and the two ping pong balls, were provided by the laboratory of the University of Delaware.

6.2 Preliminary Work

As mentioned above, two types of input are required for *FastWay* and the homogeneous Geiger method: (1) the wave arrival times at the sensors, and (2) the velocity model representing the specimen.

Ad (1): The arrival times were picked using a fixed amplitude threshold. This is probably the most elementary method, and it has its limitations. On the one hand, the threshold has to be high enough to avoid picking a large amplitude of the constantly present white noise. On the other hand, the threshold should not be set too high. Otherwise, the arrival of a p-wave with a small amplitude will not be detected. A fixed threshold usually cannot fulfill these requirements for all recorded signals. The wave onset time cannot be picked with 100% accuracy from wave signals recorded during experiments, even if a well-chosen threshold is applied. The human eye is presumed to be the best tool to detect mis-picked arrival times. Therefore, all picked arrival times were visually inspected and possible mis-picked arrival times excluded from the source location estimation process (see Figs. 6.3 and 6.4). Theoretically, the data of up to eight sensors can be excluded, as twelve sensors are used and both localization methods can be applied even if only data from four sensors is available. However, no more than six sensors had to be excluded for any of the experiments. If only the data of four sensors were available, the homogeneous Geiger method would determine one seemingly exact solution without any possibility to evaluate the accuracy with an error ellipsoid (see Section 3.3.1). Reducing the number of sensors could have a

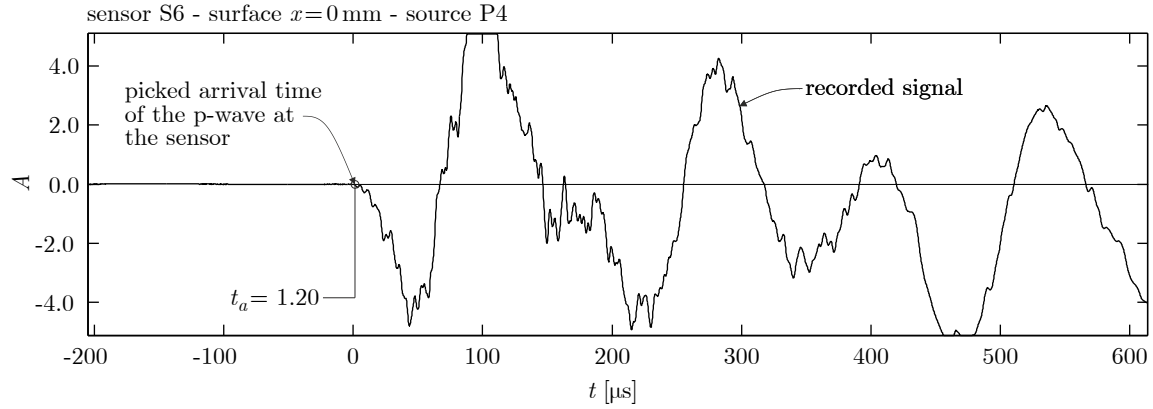

Fig. 6.3: Signal recorded by sensor S6, induced by source P4 on the specimen surface (at $x = 0$ mm). The arrival time of the p-wave at the sensor, picked with a fixed threshold of $A = 0.025$, is indicated. The arrival time is labeled t_a. This recorded data was not excluded during the visual inspection.

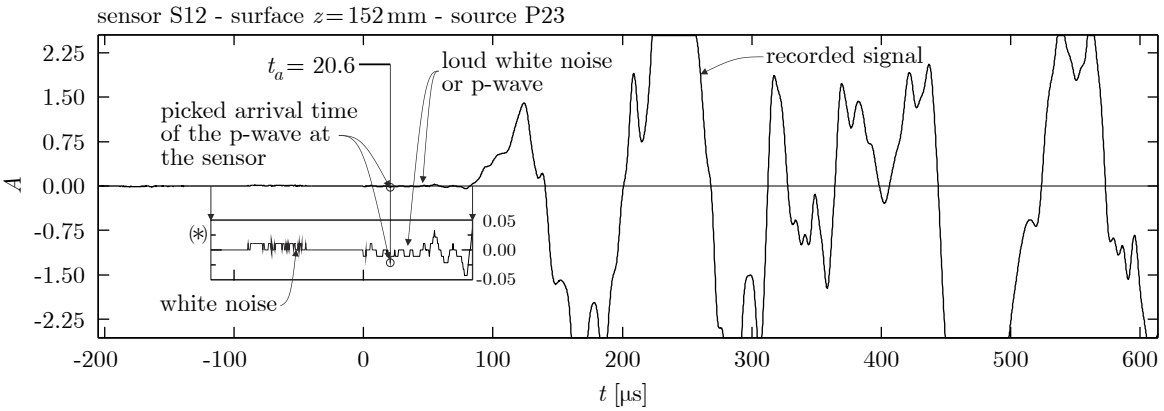

Fig. 6.4: Signal recorded by sensor S12, induced by source P23 on the specimen surface (at $z = 152$ mm). The arrival time of the p-wave at the sensor, picked with a fixed threshold of $A = 0.025$, is indicated. The picked arrival time is labeled t_a. This recorded data was excluded during the visual inspection. (*) Section of the recorded wave signal shown with ten times vertical exaggeration.

similar effect on the result determined with *FastWay*. The fewer sensors provide data, the more accurate the computed source location estimation appears to be. This is usually reflected in an exceptionally small $e_{\text{source;AE}}$ value (see Section 3.4.3). The data of five or more sensors should be processed in order to avoid this effect.

Ad (2): The heterogeneous numerical model of the specimen, implemented in *FastWay*, consists of three materials, namely air (e.g., the surrounding air, air inside the ping pong balls), steel (reinforcement), and EEP concrete (see Section 4.3.2). The p-wave velocity in air was assumed to be zero (see Section 2.2.2). The p-wave velocity in concrete was determined experimentally. The locations of the sensors and the source are known a priori. This information can be used to determine an average wave propagation velocity. If all sensors are excluded that cannot be reached by the waves via a direct (approximately straight) path, the average velocity obtained should be identical to the p-wave velocity in concrete. Hence, sensors that might first be reached by an elastic wave propagating through the reinforcing bar, as well as all sensors separated by air (notch or ping pong balls) from the source, are excluded. Fig. 6.5 shows the result of the velocity identification strategy performed for source P92, which is located on the plane $z = 0$ of the specimen. The signals shown as dotted lines are excluded for one of the

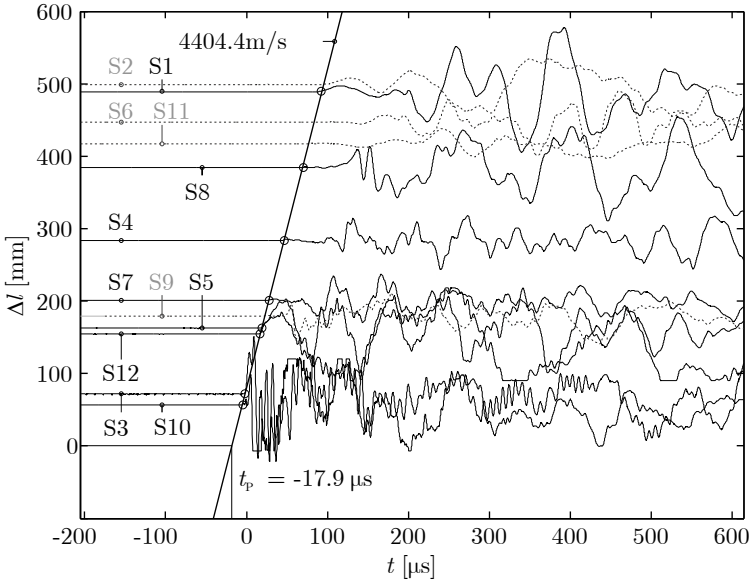

Fig. 6.5: AE signals recorded by the twelve sensors mounted on the beam and sorted with respect to their distance Δl to the location of the known source. Signals excluded from the velocity identification are plotted as dotted lines. The arrival time of the wave at the sensor is marked with ∘. The slope of the regression line corresponds to the average p-wave velocity in concrete c_p. Taken from [18]

reasons mentioned above. The regression line represents the average p-wave velocity in concrete ($c_p = 4,404$ m/s). Applying the same identification strategy to different sources results in an average p-wave velocity of $c_p \approx 4,400$ m/s. The p-wave velocity in steel was assumed to be $c_p = 5,900$ m/s (value taken from [31]). However, the reinforcing bar behaves as a wave guide. The velocity of the guided wave is usually lower than the p-wave velocity. Therefore, the wave travel velocity for steel implemented in *FastWay* is set to $c_{steel} = 5,150$ m/s (see Section 5.5). For the spatial discretization of the specimen a voxel size has to be defined. The edge length of the voxel is limited by two conditions. First, the voxel should be small enough to permit the creation of a realistic numerical model of the specimen. However, decreasing the edge length of the voxel results in an increasing number of voxels needed to build the numerical model, which in turn results in increasing computational effort (see Sections 3.4 and 4.2). A voxel edge length of 5 mm was chosen. This voxel size is small enough to allow the creation of a realistic numerical model and yet does not require too much computational effort. However, all dimensions of the numerical model must be multiples of the voxel edge length. Hence, it is impossible to generate a numerical model of the specimen with the dimensions 152.4 mm × 152.4 mm × 533.4 mm. The dimensions of the used numerical model are 30 gp × 30 gp × 106 gp, corresponding to 150 mm × 150 mm × 530 mm. The reinforcing bar, ping pong balls, and notch were incorporated into the numerical model that was used as input for *FastWay*. Naturally, the size and the shape of their numerical counterparts are approximations of the real objects (see Fig. 6.6). For the positions of the sensors within the numerical model the centers of the voxels closest to their real positions were chosen. The numerical notch is one voxel wide and three voxels deep, with a distance of 33 voxels to the surface $x = 0$. Only the air inside the ping pong balls was incorporated into the numerical model; the plastic ball itself was neglected.

The numerical model used for the homogeneous Geiger method consists of a homogeneous cuboid with the same dimensions as the specimen, namely 152.4 mm × 152.4 mm × 533.4 mm. The reinforcing bar, ping pong balls, and notch were not considered. The p-wave velocity in

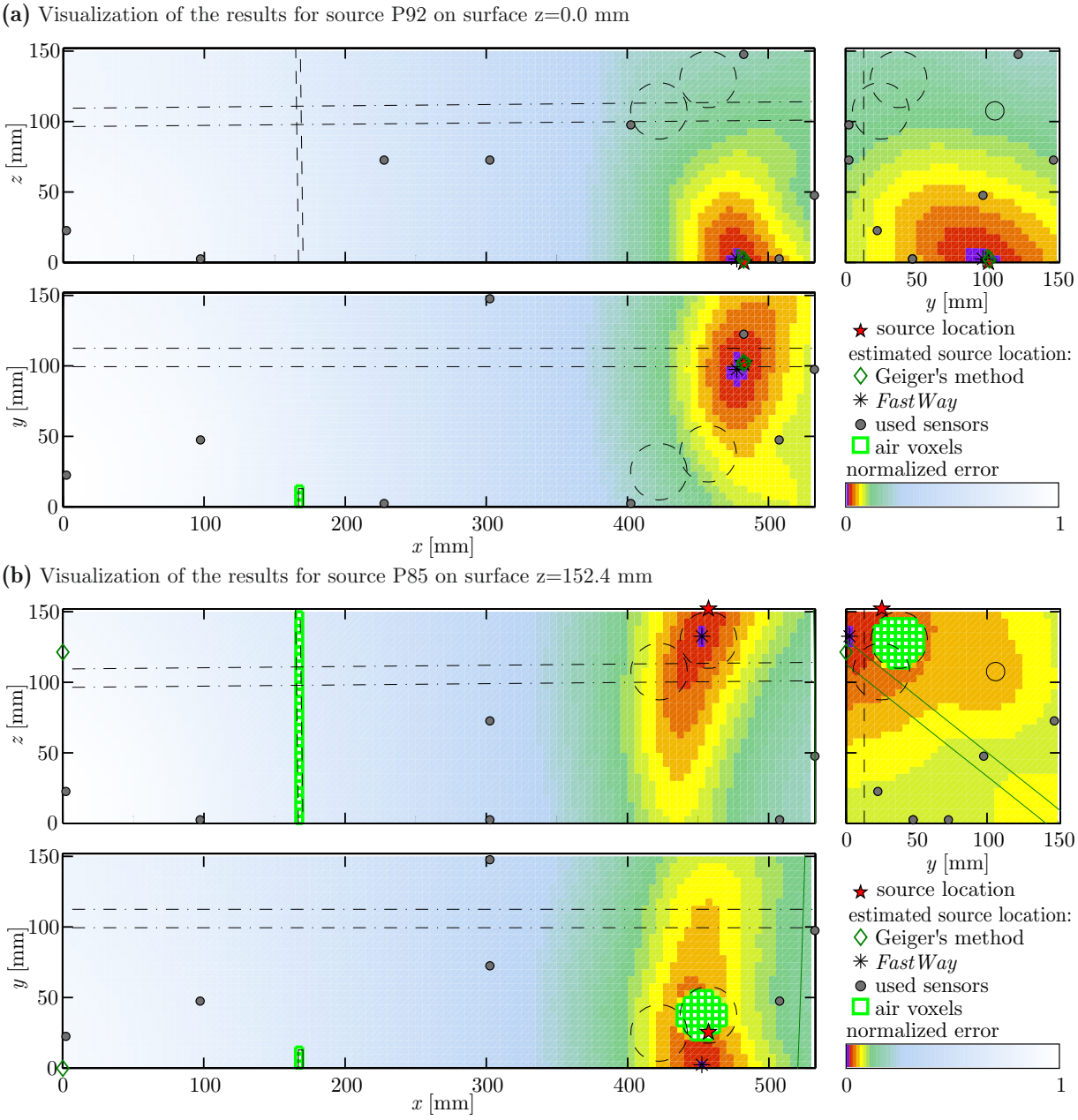

Fig. 6.6: Visualization of the location estimations of (a) source P92, located on the specimen surface at $z = 0$ mm, and (b) source P85, located on the specimen surface at $z = 152.4$ mm. The shown cross-sections include visualizations of $\mathbf{E}_{\text{source}}$ and the error ellipsoids for Geiger's method ((a) extreme small, (b) out of scale). They are positioned at the location of the source estimated with *FastWay*. Taken from [16].

the homogeneous cuboid was assumed to be $c_p = 4400$ m/s, just like the p-wave velocity in the homogenized concrete implemented in the *FastWay* model.

6.3 Results

Geiger's source localization algorithm yields the coordinates of an estimated source location. Error ellipsoids are calculated to visualize the estimated accuracy of the obtained solution. *FastWay* yields a normalized error matrix, $\mathbf{E}_{\text{source}}$ (see Section 3.4.3). These results can

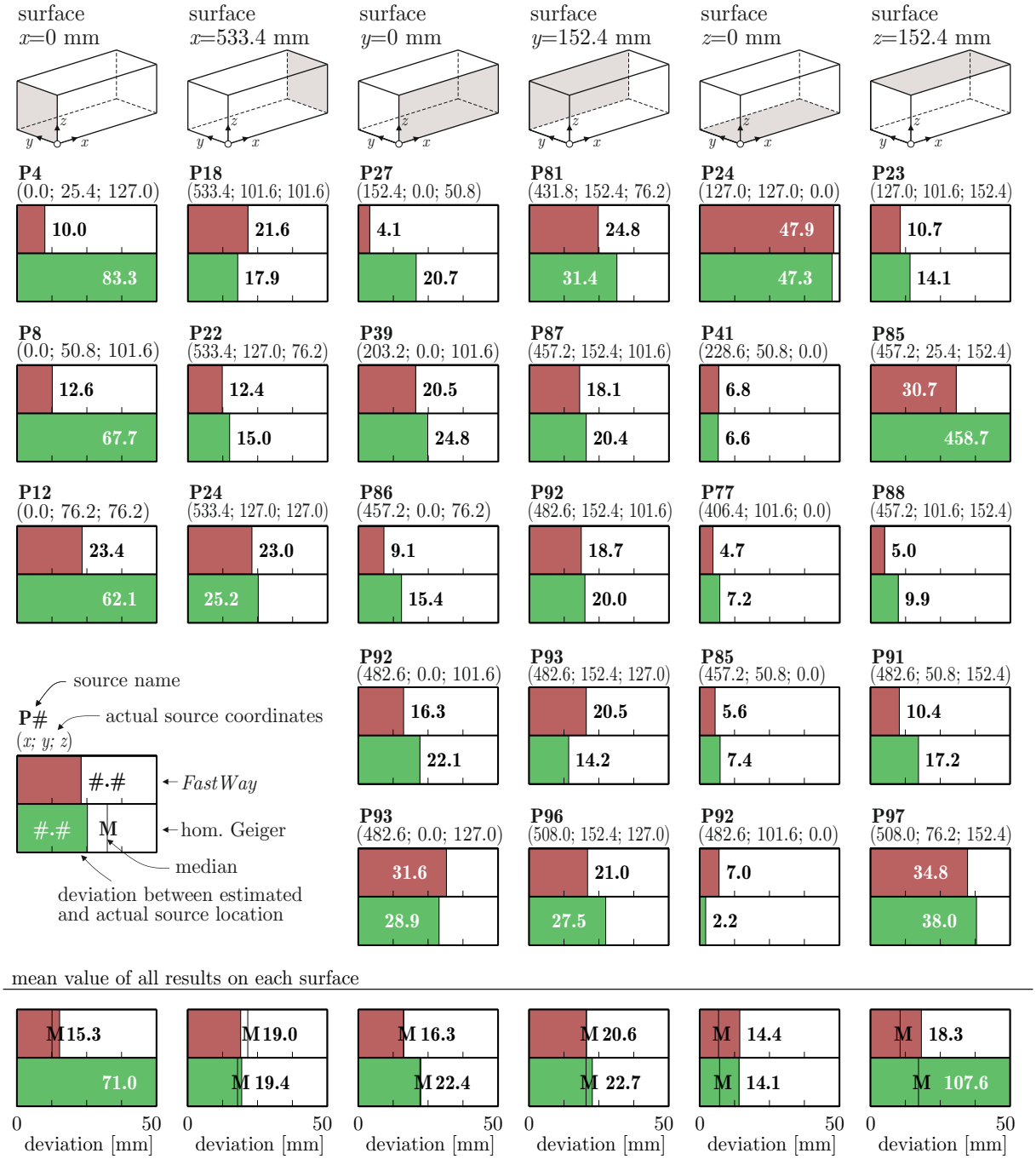

Fig. 6.7: Deviation between the estimated and actual source locations. In the last row, the mean (colored bar) and the median of the deviation computed separately for each specimen surface are shown. Previously published in [16]

be visualized as shown in Fig. 6.6. Both methods provide satisfactory location estimates. The deviation between the estimated and real source location is less than 25 mm for both methods. However, the real source is located outside the error ellipsoid computed for the results obtained from Geiger's method. The visualized result computed with *FastWay* is more accurate (4.1 mm error) than that one computed with Geiger's method (20.7 mm error). In the colored visualization, the area in which the source is most probably located is indicated. It is clearly

visible that the source is most likely located on the specimen surface with the coordinates $y = 0$. It has to be mentioned that not all results determined with *FastWay* and Geiger's method are as good as those shown in Figure 6.6 (a). For four sources *FastWay* was not able to compute the location with a localization error of less than 25 mm. The maximum error between the actual source location and the location estimated with *FastWay* is 47.9 mm. With Geiger's method the location of ten sources could only be determined with an error greater than 25 mm. The maximum error between the actual source location and the location estimated with this method is 458.7 mm (see Fig 6.6 (b)); however, this particular result is considered to be a rogue result. The second biggest error between the actual source location and the location estimated with Geiger's method is 83.3 mm. However, there were only three results with an error greater than 40 mm. It turned out that the results for sources below the ping pong balls could generally not be located accurately. The lowest determined $\mathbf{E}_{\text{source}}$ for these source location estimations was always greater than 0.1 (in the green area in the normalized error color scale), indicating that the estimated source location deviates from the actual one. A comparison of the deviation between the source locations estimated with the two methods (*FastWay* and Geiger's method) and the actual source location is shown in Fig. 6.7.

6.4 Conclusions

FastWay yielded more accurate source location estimations than the homogeneous Geiger method for twenty of the twenty-six studied cases. Only six of the twenty-six sources were localized more accurately with Geiger's method than *FastWay*. The sources located in the vicinity of the ping pong balls could not be estimated accurately with either method (e.g., P85 on the specimen surface at $z = 152.4$ mm; see Fig 6.6 (b)). The evaluation of the experimental data using the two used arrival-time-based source localization methods demonstrated that *FastWay* is capable of processing experimental data and is able to provide more satisfying results than the homogeneous Geiger method. The average deviation between the estimated and actual source location was 17.2 mm (median: 17.4 mm) for *FastWay*, and 42.6 mm (median: 20.6 mm) for Geiger's method. *FastWay* provided more accurate results for most of the investigated sources.

Chapter 7

Large T-shaped Concrete Beam

During a research visit at the Portland State University (Portland, Oregon, US) a large-scale experiment was performed. The objective of the large-scale experiment was to evaluate the performance of *FastWay* for artificial and generic acoustic emissions. The specimen was a T-shaped reinforced concrete beam with cuboid ends. The T-shaped cross-section was chosen because of its geometrical irregularities affecting the wave travel path from the flange to the web.

The specimen was used for two sets of experiments (SW I and SW II). Both sets consisted of a nondestructive part and a destructive part. The nondestructive part consisted of (a) the recording of the signals from Hsu–Nielsen sources (pencil-lead breaks) along a $4''$ (10.16 cm) grid on the undamaged specimen before loading and subsequent source localization, and (b) the repetition of the pencil-lead breaks on the cracked specimen after loading. For the destructive test the specimen was loaded with a hydraulic ram (three-point bending; see Section 7.2), in order to induce cracking in the concrete. The acoustic emissions occurring during the destructive test were recorded and subsequently used for the localization procedure.

Since the experiment was performed at a university in the United States all dimensions are in imperial units. The measurements are converted into the SI system wherever it is deemed useful.

7.1 Specimen – *SnowWhite*

The specimen, shown in Fig. 7.1, was a $16'$ (4.88 m) reinforced concrete beam. Its material properties are listed in Tab. 7.3. The standard cross-section was T-shaped. This geometrically complex cross-section which is commonly used in civil engineering, significantly affects the wave propagation path from (the outer parts of) the flange to the web and vice versa. The straight connection between the outer parts of the flange to the web would lead through air; hence, the wave propagation path (of interest) between these elements cannot be straight (see Chapter 2 and Section 5.6). The cross-section of the last feet at the respective ends of the beam was square with an edge length of $2'$ (60.96 cm). This cross-section shape was chosen so as to make the beam easier to support. There are three notches on the three free surfaces of the web in the middle section of the beam, as marked in Fig. 7.1. The two notches in the north are located at the positions of the stirrups. Their distances from the center of the beam, $5''$ (12.7 cm) and $15''$ (38.1 cm), respectively, correspond to the distance between the stirrups in the middle section of the beam. The third notch is located between two stirrups, $10''$ (25.4 cm) south of the center of the beam. The notches are small ($\sim 0.9'' = 2.3$ cm deep) and V-shaped. The purpose

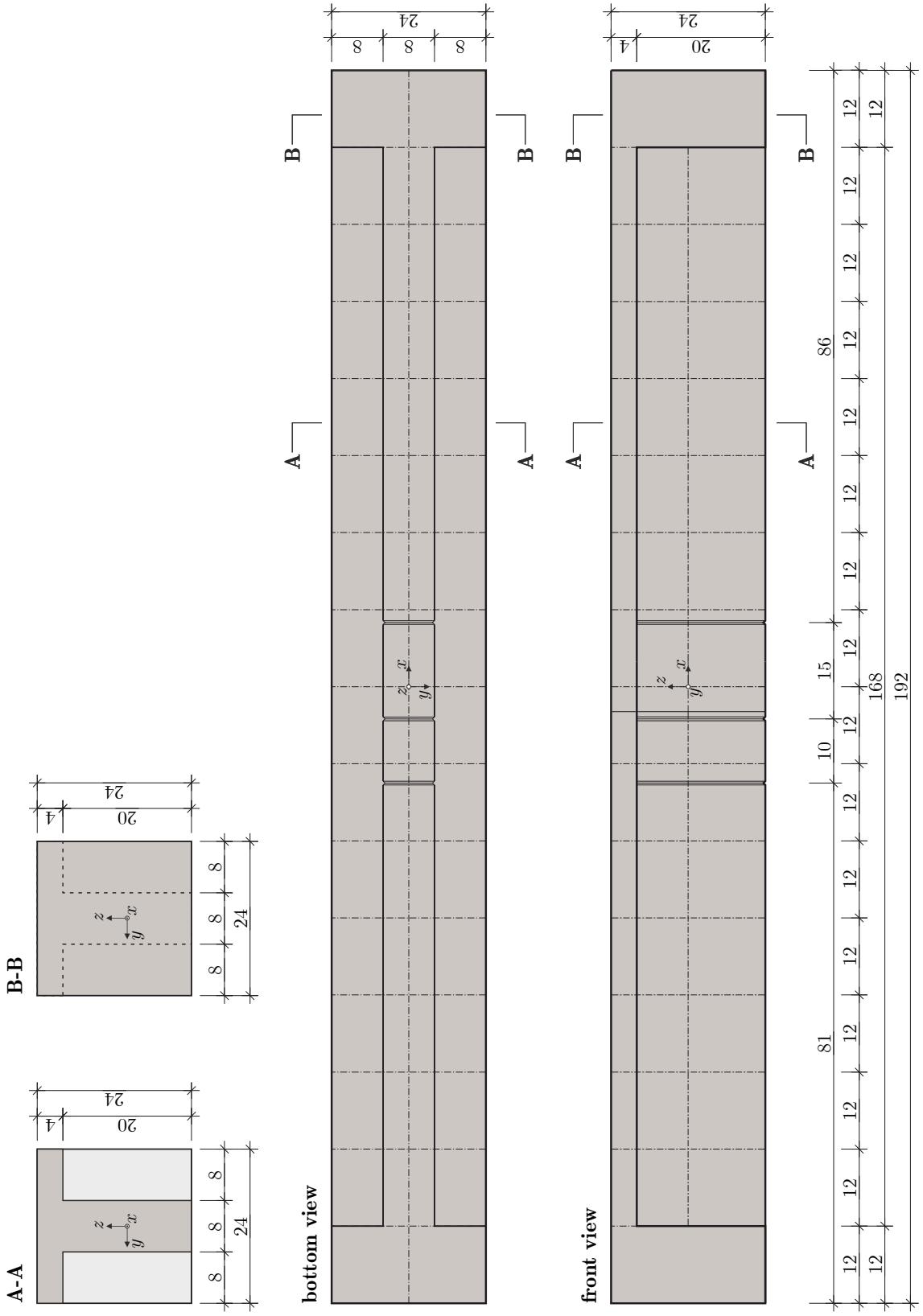

Fig. 7.1: Large T-shaped concrete beam *SnowWhite*. Dimensions in inches ($1'' = 25.4$ mm).

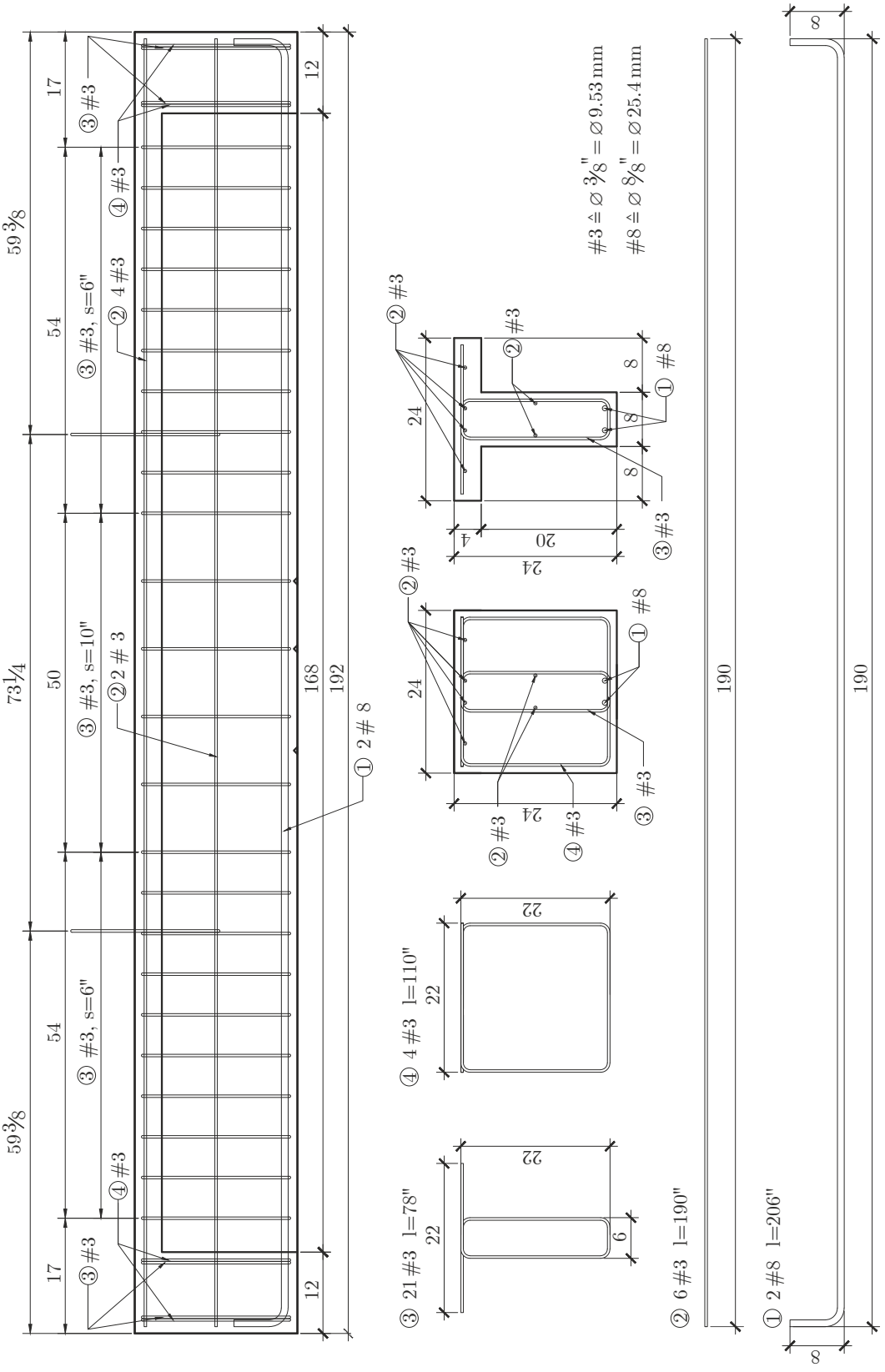

Fig. 7.2: Reinforcement plan of the large T-shaped concrete beam *SnowWhite*. Dimensions in inches ($1'' = 25.4$ mm).

of the notches was to decrease the (tensile zone of the) cross-section in order to facilitate the development of tensile cracks. The three notches are surrounded by the sensors of sensor layout SW I.

The beam was reinforced in order to allow the development of cracks before failure. The reinforcement consisted of two longitudinal #8 bars ($\varnothing 1'' = 25.4$ mm) at the bottom of the web, stirrups (#3 bars; $\varnothing 3/8'' = 9.53$ mm), and secondary reinforcing bars. The large diameter of the bending reinforcement was chosen in order to avoid early bending failure. The comparatively small spacing between the stirrups was chosen to avoid shear failure. The reinforcement layout is shown in Fig. 7.2.

The entire beam was painted with low-quality white paint. The color white was chosen to facilitate the localization of cracks with the naked eye. The lowest quality of wall paint was chosen to avoid paint covering the cracks. Square grids with the dimensions $1' \times 1'$ (30.5 cm $\times$ 30.5 cm) were drawn on all the surfaces of the specimen with a thick red marker. In addition, finer grids with the dimensions $2'' \times 2''$ (5.08 cm $\times$ 5.08 cm) were drawn with a pencil in the regions of the surface of the specimen where pencil-lead breaks were performed. Digital image correlation (DIC) was used to detect and visualize (micro) cracks. Therefore, a black spray pattern was applied to the areas with the drawn-on finer grids on the western surface of the web. The black pattern consisted of black spots at random locations, as well as random size and shape. Unfortunately, this pattern complicated the detection of cracks with the naked eye.

7.2 Test Setup

The experiments were carried out in the iSTAR laboratory of the Maseeh College of Engineering & Computer Science at Portland State University. As mentioned above, two sets of experiments were performed.

7.2.1 SW I – bending test

The test was a four-point bending test. The beam (marked with ① in Fig. 7.3) was supported on two neoprene strips ⑥ with the dimensions $24'' \times 2'' \times 1/2''$ (60.96 cm$\times$5.08 cm$\times$1.27 cm), which served as simple supports. The neoprene strips themselves were supported on steel I-beams ⑤. The steel beams were anchored into the strong floor of the lab in order to prevent them from tilting. The high location of the supports allowed access to the bottom of the beam. Additionally, the beam itself was located at a convenient height to perform any required work or measurements. The supports were located at the center of the wider end cross-section of the beam. The span of the $16'$ (4.55 m) long beam was therefore $15'$ (4.57 m).

The beam was loaded symmetrically using a hand-pump-controlled hydraulic ram ③. The applied load was measured with a load cell ④ positioned between the ram and the transverse beam ⑩. The hydraulic ram was a low-height cylinder, type RCS-1002 by Enerpac. The maximum cylinder capacity was 98.1 short tons (887 kN). The maximum stroke of the cylinder was $2.25''$ (57 mm). When the beam was loaded, the ram and load cell were pressed against the transverse beam, which was anchored into the strong floor ⑫ using four $\varnothing 1''$ threaded rods ⑪. The hydraulic ram applied load to a load transfer beam ⑦. The load transfer beam was supported on a rectangular hollow steel Section ⑨ with a length of $12''$ (30.48 cm) which was oriented in the y direction. A neoprene strip with the dimensions $12'' \times 2'' \times 1/2''$ (30.48 cm$\times$5.08 cm$\times$1.27 cm) was placed between the rectangular hollow section and the specimen. The load was applied to the test beam at two points with a distance of $48''$ (1.22 m) to each other (twice the height of

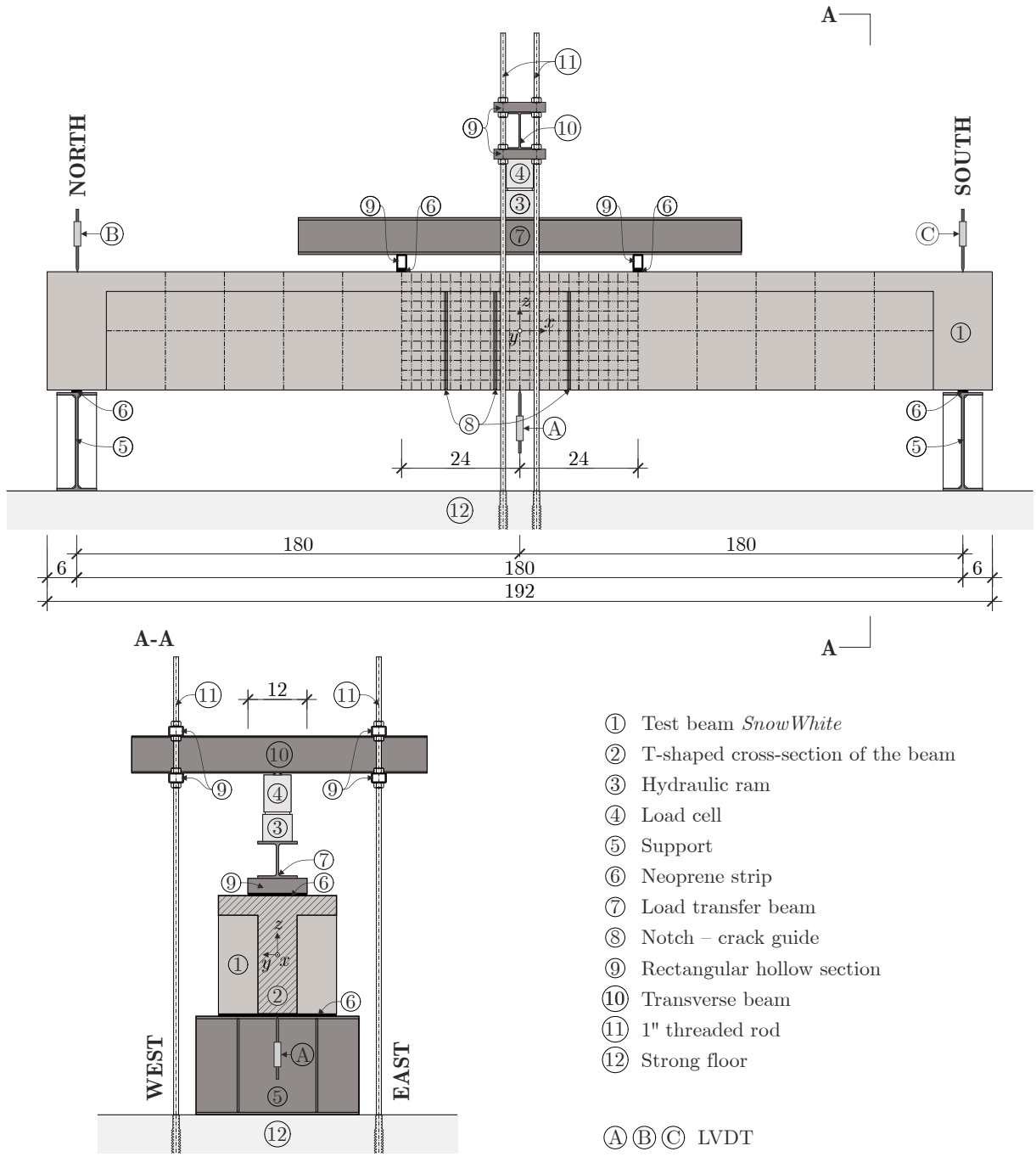

Fig. 7.3: Test setup of bending test SW I. The primary grid ($12'' \times 12''$; 30.48 cm×30.48 cm), as well as the finer grid ($2'' \times 2''$; 5.08 cm×5.08 cm) for the regions where pencil-lead breaks were performed, are shown. Dimensions in inches ($1'' = 25.4$ mm).

the beam). Each load introduction point was located at a distance of $24''$ (60.96 cm) from the hydraulic ram in the direction of the projection of the x-axis onto the top surface of the beam.

The load cell (④) measured the load in kips (1 kip = 4.448 kN). The time-history plot of force vs. time (see Fig. 7.26) was used for force-controlled load application on the beam. The load was applied in steps of 5 kips (22.24 kN). After reaching 10 kips (44.48 kN) the beam

Sensor	x	y	z	ID #
SE1	-18.0	8.0	12.0	1045388
SE2	-10.0	-2.0	12.0	1045391
SE3	6.0	6.0	12.0	1045385
SE4	20.0	-10.0	12.0	1045382
SE5	-8.0	8.0	8.0	1045387
SE6	10.0	10.0	8.0	1045389
SE7	20.0	4.0	0.0	1045384
SE8	0.0	4.0	4.0	1045393
SE9	-18.0	4.0	-6.0	1044999
SE10	-20.0	-10.0	8.0	1045383
SE11	12.0	-6.0	8.0	1045386
SE12	-18.0	-4.0	-2.0	1045390
SE13	-2.0	-4.0	-8.0	1045392
SE14	16.0	-4.0	-4.0	1045000

Tab. 7.1: Coordinates and IDs of the sensors used to detect acoustic emissions during test SW I.

was unloaded until a load of 5 kips (22.24 kN) was reached. When the number of new acoustic emissions decreased to almost zero, the beam was reloaded until the next load level was reached. The maximum applied force was 35 kips (155.69 kN). The first visible cracks occurred at the load level of 20 kips (88.96 kN). In the destructive part of "SW I – bending test" the beam was loaded for the first time. Prior to the test no cracks were visible on the specimen surface.

The acoustic emissions were recorded by 14 sensors which were mounted on the top and bottom surfaces of the flange, as well as the side surfaces of the web. The coordinates of the sensors are listed in Tab. 7.1. The sensors were glued directly onto the specimen surface using hot glue.

The deflection of the beam was measured at the center of the bottom surface of the web using a linear variable differential transformer (LVDT) (Ⓐ). Since the load application on the beam caused a compression of the neoprene strips, the whole beam moved to the negative z direction. In order to determine the actual deflection of the beam at the location of the LVDT (Ⓐ), the displacements of the top surface of the beam above the centers of the beam supports were measured with two additional LVDTs (Ⓑ and Ⓒ). These two LVDTs measured only translations. The mean value of the two measurements was subtracted from the measurement of the first LVDT (Ⓐ). Measuring the deflection of the beam at one point only was sufficient since the load-deformation behavior was not of particular interest for this research.

Prior to the destructive test, a set of non-destructive Hsu–Nielsen sources (pencil-lead breaks) were used to evaluate the accuracy of the applied source localization methods and the coverage of the sensor layout. Subsequently, the results were used to gain some information about the wave propagation behavior within the undisturbed (uncracked) specimen. The pencil-lead breaks were performed in the area of the fine pencil grid. The distance between these artificial sources was $4''\widehat{=}10.16$ cm (see Section 7.4.1). After completion of the destructive test, the beam was unloaded until a load of 20 kips (88.96 kN) was reached. The pencil-lead breaks were repeated, and the results compared to the localization results determined for the undamaged specimen (see Section 7.4.3).

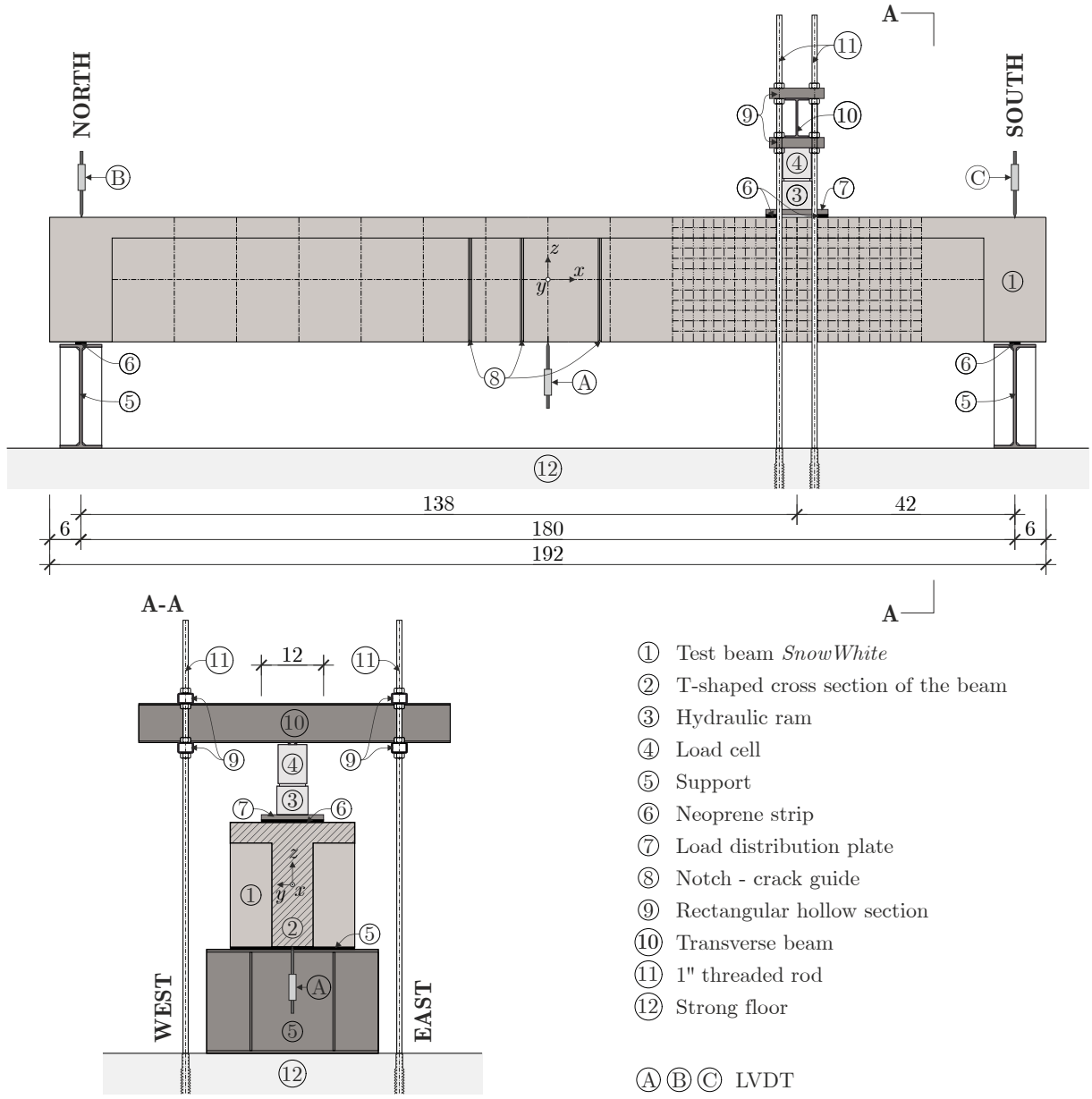

Fig. 7.4: Test setup of shear test SW II. The primary grid ($12'' \times 12''$; 30.48 cm×30.48 cm), as well as the finer grid ($2'' \times 2''$; 5.08 cm×5.08 cm) for the regions where pencil-lead breaks were performed, are shown. Dimensions in inches ($1'' = 25.4$ mm).

7.2.2 SW II – shear test

The test was a three-point bending test (Fig. 7.4). The support configuration was similar to that used in test SW I. The hydraulic ram ③ was positioned above the beam at the south quarter-span. Instead of a load transfer beam a $12'' \times 12''$ (30.48 cm×30.48 cm) steel plate (⑦), resting on two neoprene strips (⑥) with the dimensions $12'' \times 2'' \times 1/2''$ (30.48 cm×5.08 cm×1.27 cm), was used to apply the load to the test beam (①).

The load was applied in steps of 5 kips (22.24 kN) using a hand-pump-controlled hydraulic ram. As in test SW I, the beam was unloaded down to 5 kips (22.24 kN) after a load level

Sensor	x	y	z	ID #
SE1	70.0	-8.0	12.0	1045389
SE2	56.0	10.0	12.0	1045382
SE3	34.0	-8.0	12.0	1045384
SE4	28.0	4.0	12.0	1044999
SE5	30.0	-4.0	4.0	1045000
SE6	36.0	-7.5	8.0	1045392
SE7	54.0	-4.0	-6.0	1045387
SE8	60.0	-10.0	8.0	1045386
SE9	68.0	-4.0	4.0	1045383
SE10	44.0	4.0	4.0	1045393
SE11	52.0	4.0	-8.0	1045385
SE12	60.0	4.0	0.0	1045391
SE13	66.0	10.0	8.0	1045388
SE14	74.0	4.0	-2.0	1045390

Tab. 7.2: Coordinates and IDs of the sensors used to detect acoustic emissions during test SW II.

$>$ 10 kips ($>$ 44.48 kN) was reached. When almost no new acoustic emissions could be detected, the beam was reloaded until the next load level was reached. The maximum applied force was approximately 50 kips (222.4 kN). The acoustic emissions were recorded by 14 sensors, which were hot glued to the top and bottom surfaces of the flange as well as the side surfaces of the web. The coordinates of the sensors are listed in Tab. 7.2. The same LVDT setup as for test SW I was used.

Before and after the destructive test, pencil-lead breaks were performed at the intersections of the fine pencil grid (see Section 7.5.1). The post-loading pencil-lead breaks were performed at a load level of 30 kips $\widehat{=}$ 133.44 kN (see Section 7.5.3).

7.2.3 Measuring equipment

Sensors

The 14 used sensors were of type Panametrics V103 by Olympus. This sensor type has a videoscan transducer providing broadband performance. The sensors were attached to the surfaces of the specimen using hot glue. Prior to this, the surfaces of the specimen were sanded in order to remove the paint and provide a smooth surface. After connecting the sensors with the preamplifier and the data acquisition system, their bonds with the specimen were tested with pencil-lead breaks near each sensor. If the amplitude of the received signal was too low, or if no signal was recorded at a sensor, the sensor was reattached to the surface of the specimen. Thus it was assured that the sensors were able to detect the acoustic emissions and the data acquisition system was able to receive and record these signals.

Preamplifier

The preamplifier used for the 14 sensors was a custom-built 16-channel broadband preamplifier from KRN Services. In order to reduce the recorded noise, an external transformer set to 28 volt was plugged into the DC input of the preamplifier. The 14 AE sensors were connected with

Fig. 7.5: The AMSY-5 data acquisition setup consisting of a M16-2 master unit, PC tower, keyboard, mouse, and monitor

the AMSY-5 data acquisition system via this preamplifier. The 40 dB amplification setting was used.

Data acquisition system

The used data acquisition system was an AMSY-5 by Vallen Systeme GmbH. The AMSY-5 consists of one master unit and the connected PC. The master unit M16-2 provided slots for up to 16 ASIP-2 boards (acoustic signal processors), of which 14 were built in. Hence, the signals of 14 AE sensors could be processed. The master unit had four additional BNC connectors for four types of parametric input. The BNC connectors process measurements in volts, which can be converted just in time with Vallen software. In order to prevent memory overload, the used data acquisition system records only signals with an amplitude larger than a predefined constant threshold, t_{ct} (in decibels). For the destructive tests, this threshold was set to $t_{ct} = 37$ dB. For the first test, SW I, the sampling rate was set to 10 MHz, and the number of recorded discrete values was set to 8,192. Hence, the recorded signal length was 819.1 µs. The saved signal consisted of 4,000 discrete values even before the wave arrived (pretrigger samples), and the remaining discrete values were added after t_a. The high sampling rate combined with the low threshold led to memory overload. Therefore, the sampling rate for SW II was reduced to 5 MHz. The number of discrete values was reduced to 4,096 while maintaining the recorded signal length of 819.1 µs. The pretrigger sample consisted of 2,000 discrete values. The used Vallen software, R2015.0430.4, distinguished between hits (Ht), which are single recorded signals, events (Ev), which are composed of less than four hits (recorded signals), and localized events (LE), which are composed of at least four hits (recorded signals).

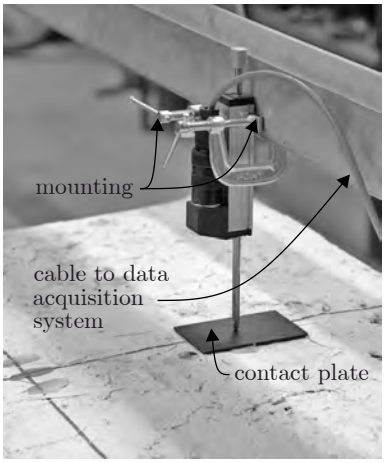

Fig. 7.6: LVDT including mounting and contact plate

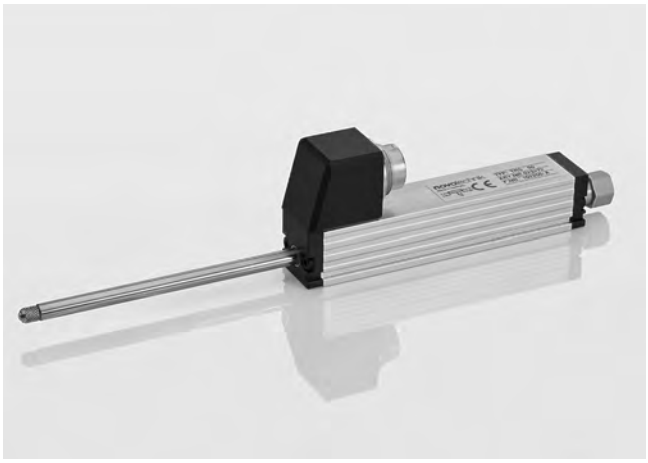

Fig. 7.7: Used LVDT type TRS-0050 by Novotechnik

Load cell

A BLH Electronics C2P1 100,000 lb compression load cell was used. The conversion of the measurement output (in volts) to a compressive force was evaluated using a calibrated compression testing system in the iSTAR lab. The load capacity of 100,000 lb $\widehat{=}$ 100 kips was never reached. The maximum applied load was 50.50 kips during the shear test (SW II) (see Tab. 7.5). The load cell was connected directly to the AE data acquisition system AMSY-5. The system software converted the measured voltage to a compressive force and displayed it in real time, in order to allow force-controlled load application.

LVDTs

Three linear variable differential transformers (LVDTs) were used for continuous measurements of the mid-span deflection of the beam. The positions of the three LVDTs (marked Ⓐ, Ⓑ, and Ⓒ in Fig. 7.6) are shown in Fig. 7.3, which illustrates the test setup of bending test SW I, as well as in Fig. 7.4 which shows the test setup of shear test SW II. The positions are the same for both setups (see Section 7.2). The three LVDTs were potentiometric short-way displacement transducers of type TRS-0050 by Novotechnik (Fig. 7.7). The defined measuring range is 50 mm (1.97″). The used electrical potential was 26.7 V. The maximum permitted electrical potential for this type of LVDT is 42 V. The three LVDTs were connected directly with three of the BNC connectors of the data acquisition system AMSY-5, such as the load cell. Hence, the time axes of all measurements gained during the experiment are identical. The unit of the input recorded by the data acquisition system was volts. The input was subsequently converted into mm and inches. The used conversion was 1 V $\widehat{=}$ 50/26.7 mm = 250/33, 909″. Due to the used transformer, minor voltage fluctuations occurred during all experiments. They can be seen as noise in the visualizations of the displacement (see for example Fig. 7.59).

DIC system

The used Digital Image Correlation (DIC) system consisted of one Canon DSLR camera on a fixed tripod in front of the beam. The camera was focused manually before load was applied to the beam in each of the two destructive tests. The autofocus function was turned off. The camera was focused on the lateral western surface of the web. A photo of this surface was taken

after every loading and unloading step of each load cycle. The photos were evaluated by the team of Neil Hoult at the Queen's University in Kingston, Ontario, Canada.

7.3 Source Localization

The two methods used to estimate the location of AE sources in the large-scale experiments were the (homogeneous) Geiger method and *FastWay*. These methods are described in Sections 3.3 and 3.4, respectively.

7.3.1 Arrival-time picking

Both used source localization methods are arrival-time-based methods; hence, the picked arrival time is of great importance. Various arrival-time picking methods are described in Section 3.1.2. As mentioned in subsection *Data acquisition system* in Section 7.2.3, a fixed amplitude threshold was used for a first picking. The resulting arrival time $t_a(t_{ct})$ was used to specify the section of the continuous signal to be discretized and stored. The length of the stored signal was 819.2 µs, including 400 µs of the signal before $t_a(t_{ct})$.

Dynamic threshold picking

A more accurate two-stage arrival-time picking method was subsequently used. All sensors and their cables are different and exposed to different environmental effects. Therefore, all sensors are measure white noise with different levels of intensity (different amplitudes). Naturally, these effects and therefore the amplitude of the recorded superimposed interfering signal can change over time. Hence, the first stage included using a dynamic threshold for a more exact arrival-time estimation. The first 200 µs of the recorded signal were used to determine the standard deviation of the recorded noise signal σ_N. The dynamic threshold was set to be $t_{dyn} = 10 \times \sigma_N$.

AIC picking

An AIC window was defined using the new estimated arrival time $t_a(t_{dyn})$ and its position within the recorded signal. The width of the AIC window corresponded to 60% of the length of the signal recorded before $t_a(t_{dyn})$. The AIC window was positioned symmetrically around $t_a(t_{dyn})$. The AIC values for the signal within this window were subsequently determined according to

$$\mathrm{AIC}(k) = k \cdot \log(\mathrm{Var}(x[1,k])) + (n-k-1) \cdot \log(\mathrm{Var}(x[k+1,n])). \tag{7.1}$$

In Eq. (7.1) n denotes the width of the AIC window and k denotes a point inside the AIC window ($1 \leq k \leq n$). The time corresponding to the lowest point of the resulting AIC value graph was selected as the final arrival time of the p-wave denoted as t_a. For the recorded signal visualized in Fig. 7.8 (a), t_a is very likely a satisfactory estimation of the real arrival time of the p-wave.

In order to estimate the accuracy of t_a, two criteria were used. The first criterion included verifying the signal-to-noise ratio S/N. S was the maximum absolute amplitude of the entire recorded signal, and N was the maximum absolute amplitude of the first 200 µs of the recorded noise (first 200 µs of the recorded signal). For the acoustic emissions recorded during the destructive tests, the ratio was required to be $S/N > 20$. The artificial pencil-lead breaks generate loud and clear AE signals. Therefore, this criterion was changed to $S/N > 50$. The second criterion concerned the shape of the AIC-value graph. The picked arrival time was

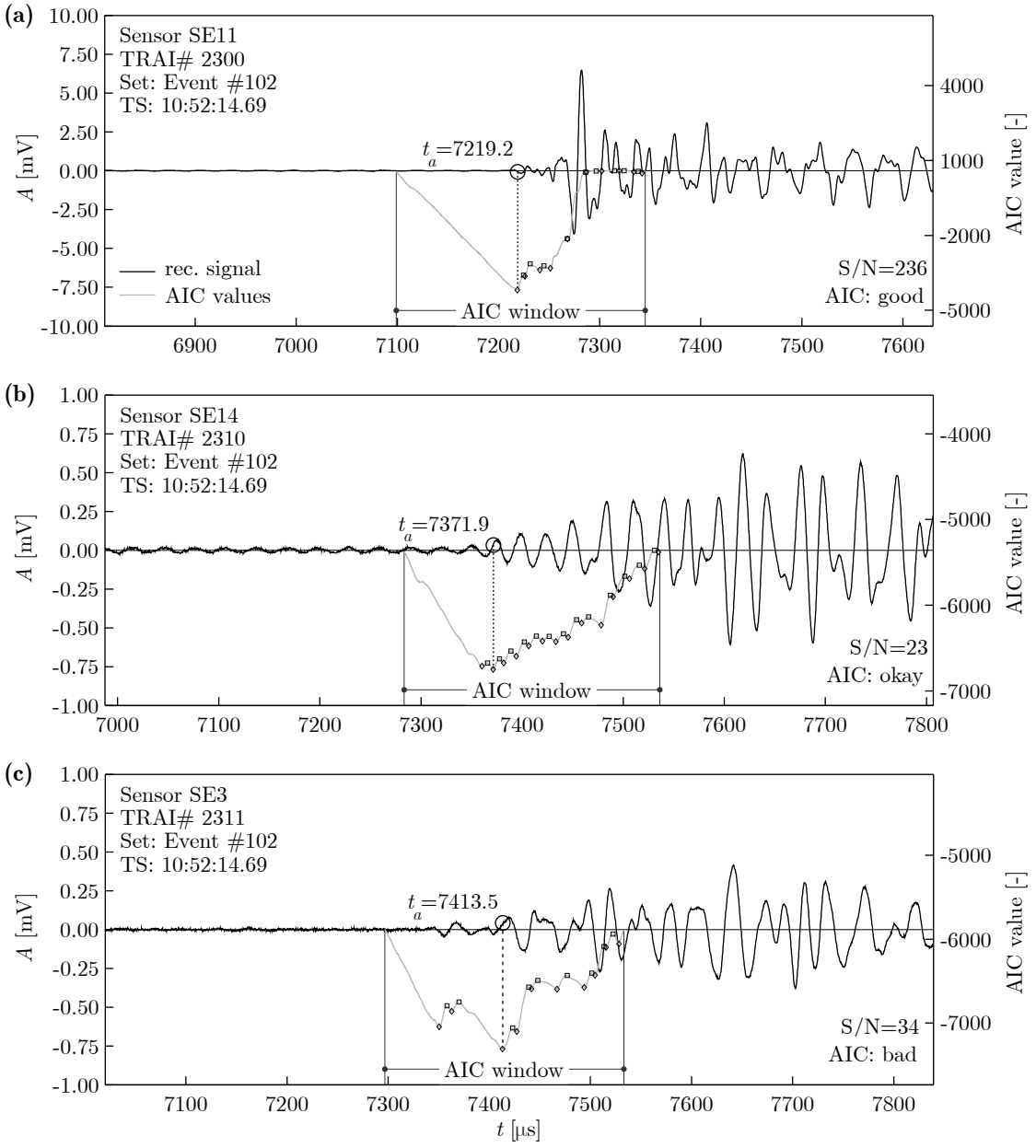

Fig. 7.8: Visualization of three recorded wave signals. (a) Signal with permissible S/N ratio and verified *good* AIC-picking result; (b) signal with AIC-picking result verified as *okay*. The global low point is not the first low point but the two low points do not differ by much. The S/N ratio is impermissibly low. (c) Signal with AIC-picking result verified as *bad*. The global low point is not the first low point, and the two low points differ too much. The S/N ratio is impermissibly low.

expected to be an accurate estimation of the actual arrival time of the p-wave if the lowest point of the AIC-value graph (almost) coincided with the first low point of the graph. If that was the case, the AIC picking result was denoted as *good*, like for the example visualized in Fig. 7.8 (a). If the two points did not coincide, it was checked whether the time difference between the first low point and the lowest point of the AIC-value graph was less than 50 µs. Additionally, it was confirmed that the difference in the AIC value between the first high point and the first low point was no greater than 1/50 of the difference between the lowest and the highest determined AIC value. In that case, the AIC picking result was denoted as *okay*, like

	[in/s]	[m/s]
Homogenized concrete	157,480	4,000
Reinforcement steel	196,850	5,000
Air	0	0

Tab. 7.3: Wave velocities implemented in the applied source localization algorithms

for the example visualized in Fig. 7.8 (b). In an *okay* result, the determined arrival time t_a still represents a reasonable estimation of the p-wave arrival time, but is most probably less accurate than that of a *good* AIC picking result. If the AIC picking result did not fulfill the two mentioned criteria it was denoted as *bad*, as for the example visualized in Fig. 7.8 (c).

Ranking of the determined arrival times

The determined arrival times were ranked with respect to their signal-to-noise ratio. Arrival times with an *okay* AIC-based arrival-time picking result were always ranked behind arrival times with a *good* AIC-based arrival-time picking result. Arrival-time picking results which did not fulfill one or both of the criteria mentioned above (the S/N ratio criterion and the AIC-value graph criterion) were excluded from the source localization process and therefore not included in the ranking.

7.3.2 Velocity models

Besides the estimated arrival times (t_a), both methods rely on velocity models as input (see Section 3.1.3). The tested specimen consisted of three materials, namely concrete, steel, and air. The concrete was considered to be homogeneous. Air surrounded the specimen, and air was present in the cracks. However, air-filled voids other than cracks were neglected. The velocities implemented in the source localization algorithms are listed in Tab. 7.3.

The homogeneous Geiger method assumes a constant wave velocity within the entire investigated volume. The implemented global velocity corresponds to the velocity of the homogenized concrete. However, the source location estimation calculated with Geiger's method was limited to being located within the specimen.

For *FastWay* a numerical velocity model was used (see Section 4.4). All materials listed in Tab. 7.3 were included in this model. It consisted of voxels with an edge length of $1/2''$ (12.7 mm). The voxels were considerably larger than those used for the numerical models implemented in the *FastWay* algorithm used for source localization in Chapters 5 and 6. However, in those cases the specimens were also considerably smaller. The applied Dijkstra algorithm is only able to process numerical modes consisting of a limited number of voxels, otherwise run-time errors occur. In this research, the critical number was found to be around 250,000 voxels. To avoid this type of problem, only part of the beam was represented in the numerical model. For test SW I the modeled section of the beam corresponded to the area where the pencil-lead breaks were performed. The model was $48''$ (121.92 cm) long and extended from $x = -24''$ to $x = 24''$. The cross-section of the model was $24'' \times 24''$ (60.96 cm $\times$ 60.96 cm), corresponding to the maximum cross-sectional dimensions of the beam. The result was a model consisting of 248,832 voxels. For SW II the modeled section of the beam corresponded to the area where the pencil-lead breaks were performed, plus an additional $6''$ in the x direction so as to include sensor SE14. The model was $54''$ (137.16 cm) long and extended from $x = 24''$ to $x = 78''$. The cross-section of the model was $24'' \times 24''$ (60.96 cm $\times$ 60.96 cm), corresponding to the maximum cross-sectional dimensions of the beam. The result was a model consisting of 221,184 voxels. The location of

the source in both SW I and SW II, estimated using *FastWay*, is limited to being located within the numerical model (excluding air). The T-shaped concrete beam could be recreated exactly since its dimensions were multiples of the edge length of the voxels. However, it was impossible to recreate the reinforcement with its exact dimensions. Hence, square shapes approximating the shapes of the reinforcing elements visualized in Fig. 7.2 were implemented in the numerical model.

7.3.3 Wave propagation path

The fastest wave propagation path is usually irregular and affected by various parameters (see Section 3.1.4). The two applied source location estimation methods approximate this path differently. Geiger's method assumes a straight wave propagation path. This, however, is only true if the wave propagates in a homogeneous, isotropic, and undamaged medium until the wave reaches a surface or boundary. Even if the concrete is considered homogeneous and the reinforcement is neglected, a straight wave propagation path is only possible if this straight path does not lead through air (or any other material besides concrete). Hence, a source, located for example in the bottom part of the web, would not be connected to a sensor applied to the outer side of the flange by a straight wave propagation path (see Fig. 3.5 and Section 5.6). For this reason, *FastWay* does not rely on straight wave propagation paths. Instead, a multi-linear approximation of the fastest wave propagation path connecting two points is determined using a modified Dijkstra algorithm (see Sections 3.4.1 and 3.4.2). For the large-scale experiments a vicinity level of $v_{\text{lev}} = 2$ was used.

7.3.4 Error estimation index *eei*

For numerical simulations and pencil-lead breaks it is always possible to compare the estimated and actual source locations. However, if the signals recorded during testing or monitoring are used for source location estimation, it is not possible to verify the accuracy of every localization. It is only possible to superimpose the estimated source location with photos of crack patterns or images obtained from DIC. However, both crack visualizations only show the location of the cracks on the surface. For that reason, only an estimated error can be determined. An error estimation index denoted as *eei* is therefore introduced. This index was calibrated using the evaluation of the localizations of the pencil-lead breaks for the uncracked specimen (see Sections 7.4.1 and 7.5.1).

The calibration process is demonstrated using the results of preloaded pencil-lead breaks of test SW II performed on the lateral western surface of the flange. Fig. 7.9 shows a scatter plot of *eei* vs. the deviation between the estimated and real source location (in inches). The plot is divided into different zones, which are shown in different colors. Six accuracy classes (*ac*) are shown from blue over yellow to red. The classifications of *ac* are shown next to the plot. A deviation of more than 7.5″ (19.05 cm) was considered imprecise. Any source location estimation with a deviation of more than 10″ (25.4 cm) from the real source location was considered inaccurate. Hence, results with a deviation greater than 7.5″ should correspond to $eei > 1$.

Error estimation index for Geiger's method

Error ellipsoids are commonly used to visualize the estimated accuracy of the source location estimation determined with Geiger's method. For that reason, the 68% error ellipsoid (see Section 3.3) forms the basis of the following equation for calculating the error estimation index

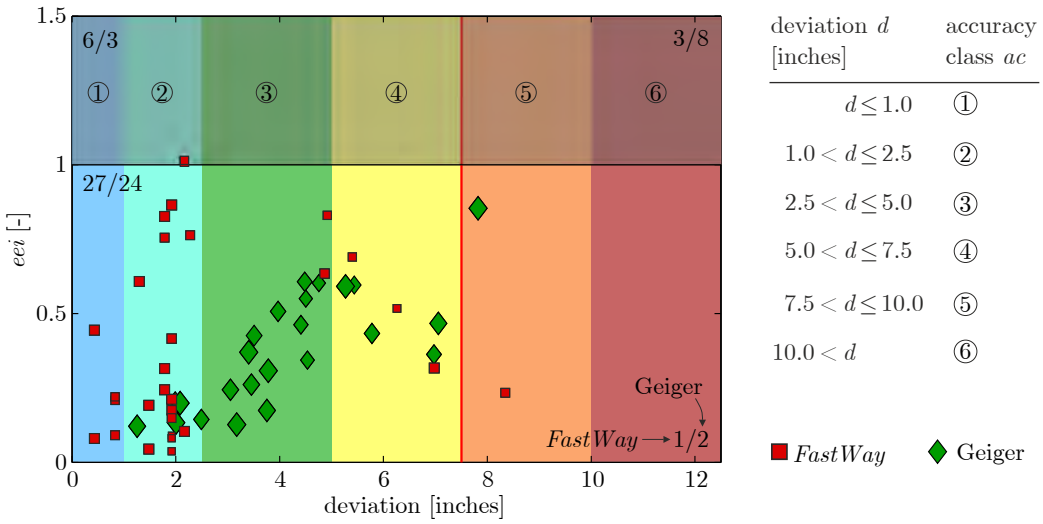

Fig. 7.9: Exemplary scatter plot of *eei* versus the deviation d in inches (results of the pencil-lead breaks PLB SW IIa performed on the "Top-Front" surface). The plot is divided into four sections by a line at $eei = 1$ and a line at $d = 7.5''$. Results with $d > 12.5''$ or $eei > 1.5$ are outside the visualized area. The number of results obtained with *FastWay* and Geiger's method in each of the four sections is shown as *FastWay*/Geiger.

eei_G.

$$eei_G = \frac{\sqrt{{e_1}^2 + {e_2}^2 + {e_3}^2}}{f_G} \tag{7.2}$$

In this equation, e_1, e_2, and e_3 are the lengths of the semi-axis of the error ellipsoid. The value of factor f_G, the scaling factor in the denominator, is chosen to minimize the results with a deviation of more than $7.5''$, while not excluding too many results with a deviation of $\leq 7.5''$ by increasing their corresponding error estimation index to 1 or greater. In Fig. 7.9 it appears that there is a linear correlation between *eei* and the real deviation. Even though this observation could not be confirmed for all the results, a factor of $f_G = 70$ leads to satisfactory results in terms of reliable *eei* values. For the results visualized in Fig. 7.9, eight inaccurate as well as three sufficiently accurate results were excluded, and two inaccurate results were not excluded. It has to mentioned that if less than five sensors provide signals fulfilling the criteria mentioned in paragraph *AIC picking* in Section 7.3.1, it is not possible to calculate an error ellipsoid. Since in that case *eei* is not defined, the results were reported as *eei* = NaN. Therefore, results based on data from exactly four sensors were also excluded.

Error estimation index for *FastWay*

As mentioned in Section 3.4, the normalized error distribution indicates the accuracy of the determined source location. The normalized error $e_{\text{source},AE}$, corresponding to the voxel hosting the estimated source location, should be very small. Therefore, the error estimation index for the source locations determined with *FastWay* is defined as

$$eei_{FW} = \frac{e_{\text{source},AE}}{f_{FW}}. \tag{7.3}$$

Again, a scaling factor (f_{FW}) is present in the denominator. In order to exclude all results fulfilling $e_{\text{source},AE} > 0.2$, this factor was set to $f_{FW} = 0.2$. Fig. 7.9 shows no apparent

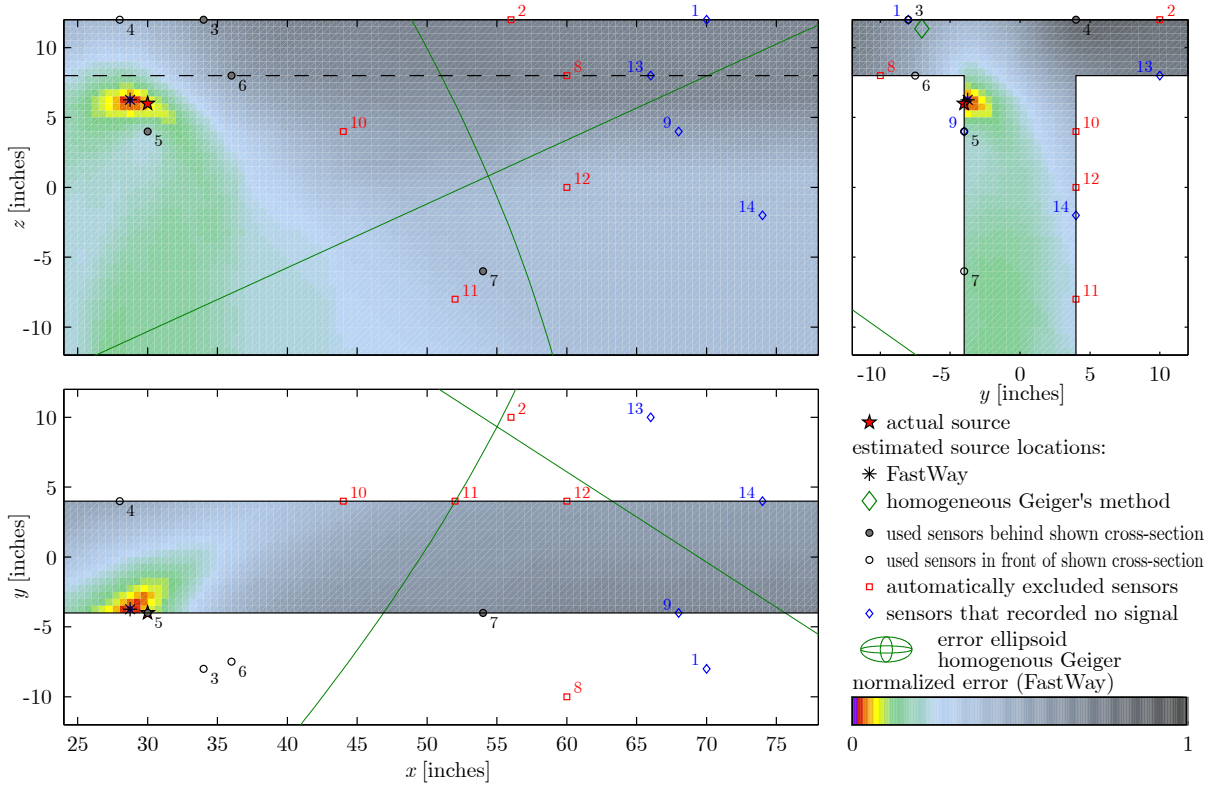

Fig. 7.10: Cross-sections of the specimen including the visualization of $\mathbf{E}_{\text{source}}$. Error ellipsoids for Geiger's method (out of scale), locations of sensors, and estimated and predefined source location are marked. The shown cross-sections are at the location of the estimated source (using *FastWay*).

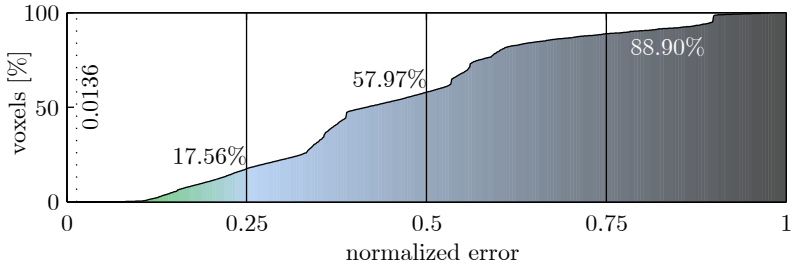

Fig. 7.11: Cumulative distribution of the normalized error values, determined with *FastWay* for the source location estimation of a pencil-lead break visualized in Fig. 7.10.

correlation between eei_{FW} and the deviation between the estimated and real source location. Good localizations, such as the *FastWay* localization result visualized in Fig. 7.10, (almost) always correspond to small eei_{FW} values. The corresponding cumulative distribution plot of the normalized error (see Fig. 7.11) shows that $e_{\text{source},AE} = 0.0136$, which is indeed a small value. The resulting error estimation index was $eei = 0.068$. Moreover, it can be seen that the percentage of voxels corresponding to $e_{\text{source};xyz} < 0.1$ is conspicuously small – almost zero.

At first glance, the cumulative distribution plot of the normalized error visualized in Fig. 7.13) again showed a very small normalized error for the estimated source location ($e_{\text{source},AE} = 0.0194$). The resulting error index was $eei = 0.097$. Hence, the determined source estimation appeared to be accurate. However, upon closer examination it could be seen that the percentage of voxels for which $e_{\text{source};xyz} < 0.05$ was true (visualized in Fig. 7.13) was significantly larger than that in Fig. 7.11. Fig. 7.12 shows that a higher percentage of voxels with corresponding

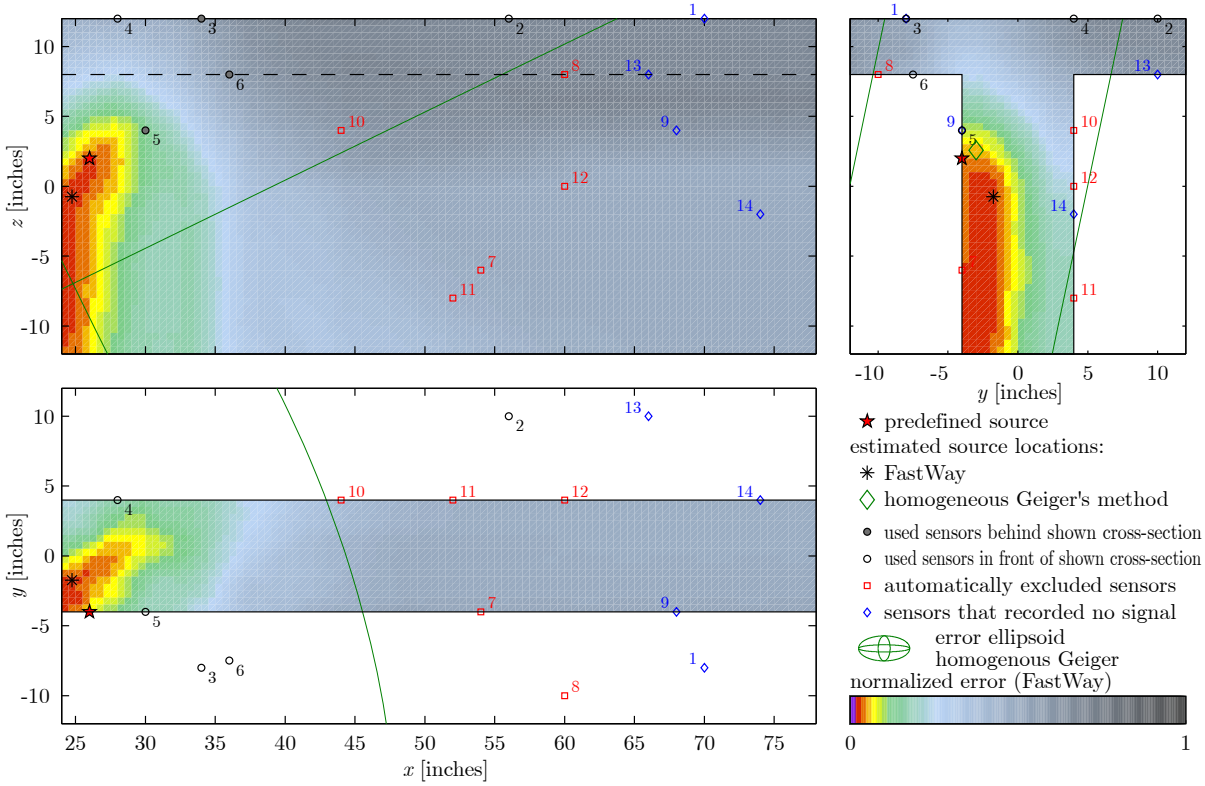

Fig. 7.12: Cross-sections of the specimen including the visualization of $\mathbf{E}_{\text{source}}$. Error ellipsoids for Geiger's method (out of scale), locations of sensors, and estimated and predefined source location are marked. The shown cross-sections are at the location of the estimated source (using *FastWay*).

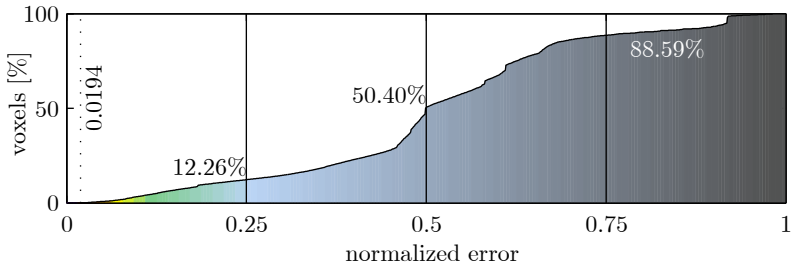

Fig. 7.13: Cumulative distribution of the normalized error values, determined with *FastWay* for the source location estimation of a pencil-lead break visualized in Fig. 7.12

$e_{\text{source};xyz} < 0.05$ means that there are more voxels that are likely to host the source, and a precise source location estimation is not possible. Therefore, additional criteria were needed to verify the results determined with *FastWay*. The ideal normalized error distribution resulting from *FastWay* would be one voxel corresponding to a value close to zero in the normalized error matrix $\mathbf{E}_{\text{source}}$. The normalized error values of the surrounding voxels should increase rapidly with increasing distance from the estimated source location. The result visualized in Fig. 7.10 is very close to this ideal. However, for an ideal result, the area formed by voxels shown in purple, red, orange, or yellow would be spherical with the source location at its center. The result visualized in Fig. 7.12 significantly deviates from this ideal result. This is because the percentage of voxels with $e_{\text{source};xyz} < 0.05$ is only one relevant characteristic, but the distribution of these voxels in the numerical model of the specimen might be even more important.

In an additional result verification the maximum distance between (the centers of) any two voxels fulfilling $e_{\text{source};xyz} < 0.05$ is determined. If the determined distance is greater than $8''$, the source location estimation determined with *FastWay* is excluded. Depending on the error estimation index, results fulfilling $e_{\text{source},AE} = 0.2$ are acceptable. However, if $e_{\text{source},AE} > 0.05$, the aforementioned verification is no longer useful. Therefore, the maximum distance between (the centers of) any two voxels fulfilling $e_{\text{source};xyz} < e_{\text{source},AE} + 0.04$ is determined for a second verification. If the determined distance is greater than $10''$, the source location estimation determined with *FastWay* is excluded. The maximum distances for the two verifications ($8''$ and $10''$) were determined empirically, based on the evaluation of the pencil-lead breaks on the uncracked specimen. If at least one of these two verifications is not fulfilled, eei = NEL (NEL = no exact localization). In the results visualized in Fig. 7.9 three inaccurate results and six sufficiently accurate results were excluded, while one inaccurate result was not excluded. It seemed that the evaluation process was too conservative. However, almost all of the six excluded but sufficiently accurate results looked similar to the one shown in Fig. 7.12 and were therefore rightfully excluded.

7.4 Results of Test SW I

The focus of this section is on the results obtained from the measurements of test SW I. Conclusions based on these results are listed in Section 7.7.

7.4.1 Pencil-lead breaks – SW Ia

The pencil-lead breaks (PLBs) of test SW Ia can be divided into four groups, based on the location of the PLBs. Pencil-lead breaks were performed on the top surface of the flange (referred to as "Top"), on the lateral western surface of the flange (referred to as "Top-Front"), on the lateral western surface of the web (referred to as "Front"), and on the lateral eastern surface of the web (referred to as "Back"). No PLBs were performed on the lateral eastern surface of the flange. PLBs were performed at each grid point of a $4''$ grid in the monitored area of the beam ($-24'' \leq x \leq 24''$). Between $x = -22''$ and $x = 22''$, $y = -10''$ and $y = 10''$, and $z = -10''$ and $z = 10''$ the grid lines of the $4''$ grid coincide with every other grid line of the $2''$ grid mentioned in Section 7.1. A minimum of three PLBs were performed at each grid point on the aforementioned beam surfaces. The locations of all (localized) PLBs are listed in the tables in Appendix B, Sections B.1 and B.3.

PLB "Top"

The signals of 338 AE events were recorded on the top surface during the execution of the PLBs. It was technically possible to compute an estimation of the source locations for 234 of these events. The results were subsequently verified (see Section 7.3.4) in order to exclude results which were deemed to be inaccurate. A possible explanation for the significant difference between the number of recorded events and the number of estimated source locations is that a number of undesirable signals was recorded. Such undesirable signals could be the AE of a second impact of the broken-off pencil lead, or an AE caused by the unintentional displacement of a sensor cable. These events were excluded during the data evaluation process wherever possible. However, most of the 104 dismissed events were excluded because less than four signals fulfilling the minimum criteria for the arrival-time picking process (see Section 7.3.1) were recorded. In an additional 13 cases exactly four signals fulfilled these criteria. Hence, it was not possible to determine an error ellipsoid, and consequently no error estimation index (eei) for the estimated source location could be calculated. The computed source location estimations for these cases were therefore also excluded. The corresponding eei values are reported as $eei = \text{NaN}$ in Tabs. B.1 to B.5. At least five permissible signals were recorded for each of the remaining 221 events. Nevertheless, the deviations (d) between the estimated and actual source locations for these 221 events was not always acceptable ($d < 7.5''$). Unfortunately, not all location estimations with $d \geq 7.5''$ were automatically excluded during the verification process. Fig. 7.14 illustrates the relationship between eei and the actual deviation d of the 234 events with an estimated source location. The two used source localization methods produce satisfactorily accurate results. For 195 source location estimations obtained with Geiger's method, $d < 7.5''$ and an eei value of less than 1 were computed. Additionally, twelve estimated source locations had an eei value of less than 1 but a deviation of $d \geq 7.5''$. Hence, these twelve inaccurate source location estimations were not excluded automatically. Even a reduction of factor f_G in Equation 7.2 would not have led to a noticeable improvement in the automatic exclusion process. However, in the eei_G verification process, 24 source location estimations with $d \geq 7.5''$ were successfully excluded, and only three results with $d < 7.5''$ were excluded (see Fig. 7.14). In the results obtained with *FastWay*, only 13 source location estimations deviated by more than 7.5" from the actual

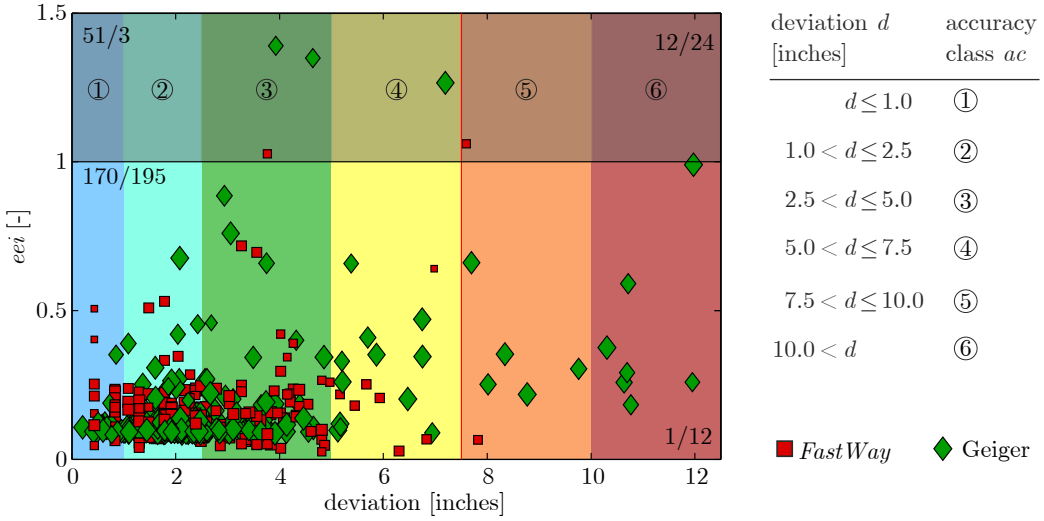

Fig. 7.14: Scatter plot of *eei* vs. deviation d in inches for the PLBs SW Ia performed on the "Top" surface. The deviation values are also listed in Tabs. B.1 to B.5. The plot is divided into four sections by a line at $eei = 1$ and a line at $d = 7.5''$. Results with $d > 12.5''$ or $eei > 1.5$ are outside the visualized area. The number of results obtained with *FastWay* and Geiger's method in each of these four sections is shown as *FastWay*/Geiger.

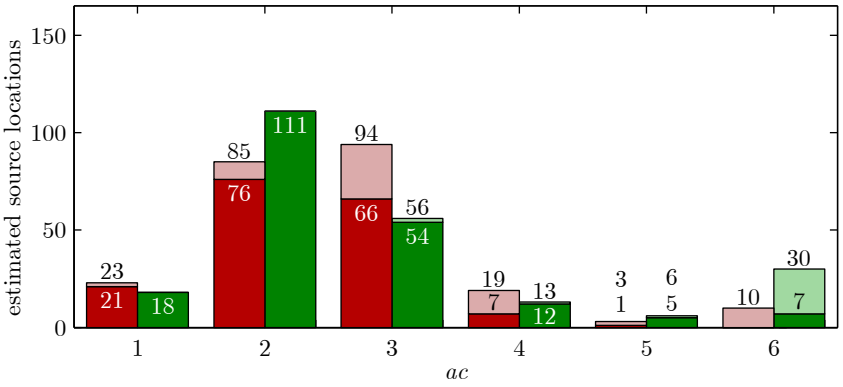

Fig. 7.15: Histogram of the estimated source locations obtained with *FastWay* (red) and Geiger's method (green) for the PLBs SW Ia – "Top". The excluded estimations are shown in light red and light green, respectively.

positions of the sources. Twelve of these estimations were excluded automatically during the evaluation process. Unfortunately, an additional 51 location estimations with $d < 7.5$ were also excluded. The majority (49) of these estimations were excluded because they did not fulfill the NEL criteria (see Section 7.3.4 – error estimation index for *FastWay*). A visual interpretation of the resulting localizations would generally also have led to an exclusion of these results. The histogram (Fig. 7.15) shows that Geiger's method yields more accurate verified source location estimations for test SW I than *FastWay*. However, it also yields more inaccurate verified source location estimations. However, if no verification process is carried out, *FastWay* produces better results than Geiger's method.

The estimated source locations and their deviations from the actual source locations (the PLBs) can be used to verify how well the sensors cover the area of the specimen where the PLBs were performed, and to visualize an estimated localization accuracy (*ela*). The *ela* based on the results determined with *FastWay* is visualized in Fig. 7.16 (a) and (b), and that for the results

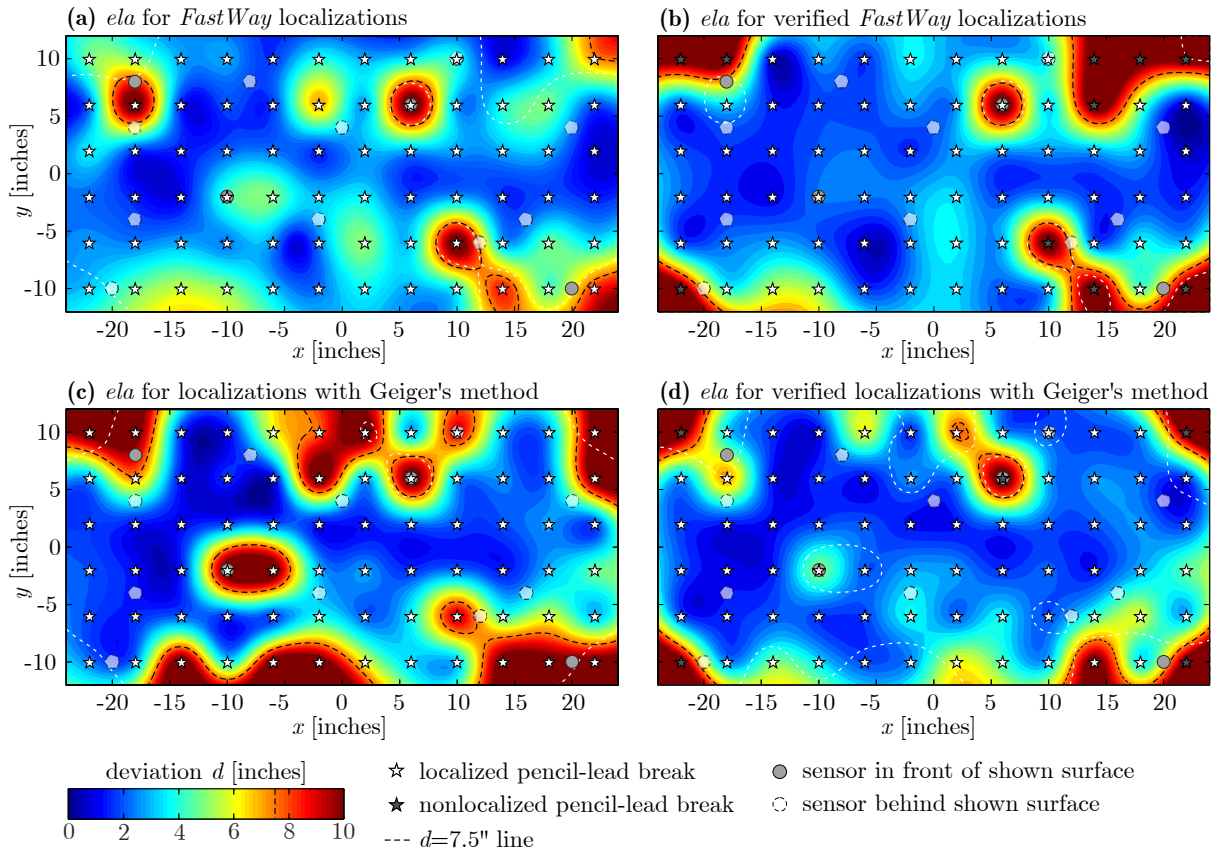

Fig. 7.16: Estimated localization accuracy (*ela*) at the top surface of the specimen, based on the source localization deviations for the pencil-lead breaks SW Ia "Top", and determined for the results obtained with *FastWay* and Geiger's method. The $d = 7.5''$ line of the figure based on all results is shown as a white dashed dotted line in the figure based on the verified results, and vice versa.

determined with Geiger's method is shown in Fig. 7.16 (c) and (d). The PLBs were distributed across the whole top surface of the flange of the investigated part of the beam ($-24'' \leq x \leq 24''$). Fig. 7.16 (b) and (d) show that the verification process generally improved the accuracy of the source location estimations in the central area of the top surface of the flange, but especially for the results from Geiger's method. Furthermore, a few PLB locations at the outer corners of the investigated area (marked with a gray ☆) could not be located with either method. In addition, the localization of the PLBs performed at the exact location of sensor SE3 (coordinates $x = 6''$, $y = 6''$, and $z = 12''$) was not possible. As the PLBs were executed directly on top of the sensor, the signal propagating in the reinforced concrete body was damped. It is assumed that an accurate source localization of an undamped signal in that area would still be possible. The results for all the PLBs are listed in Tabs. B.1 to B.5.

PLB "Top-Front"

Twenty-six PLBs were performed on the lateral western surface of the flange. For 25 of the 26 events, at least four signals fulfilling the arrival-time picking criteria mentioned in Section 7.3.1 were recorded. Only one event was excluded because of these criteria. One additional event was excluded from consideration with Geiger's method because only four signals were recorded

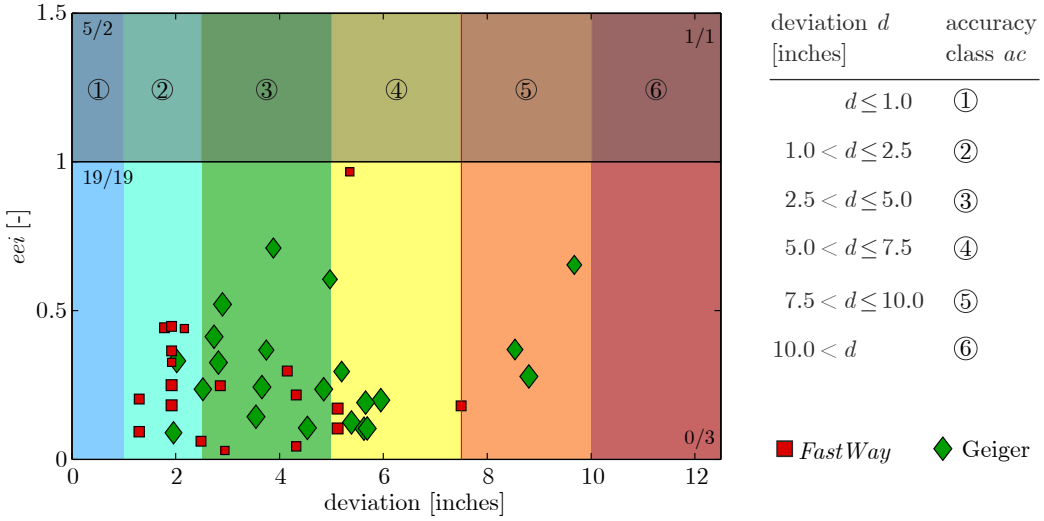

Fig. 7.17: Scatter plot of *eei* vs. deviation d in inches for the PLBs SW Ia performed on the "Top-Front" surface. The deviation values are also listed in Tab. B.6. The plot is divided into four sections by a line at $eei = 1$ and a line at $d = 7.5''$. Results with $d > 12.5''$ or $eei > 1.5$ are outside the visualized area. The number of results obtained with *FastWay* and Geiger's method in each of these four sections is shown as *FastWay*/Geiger.

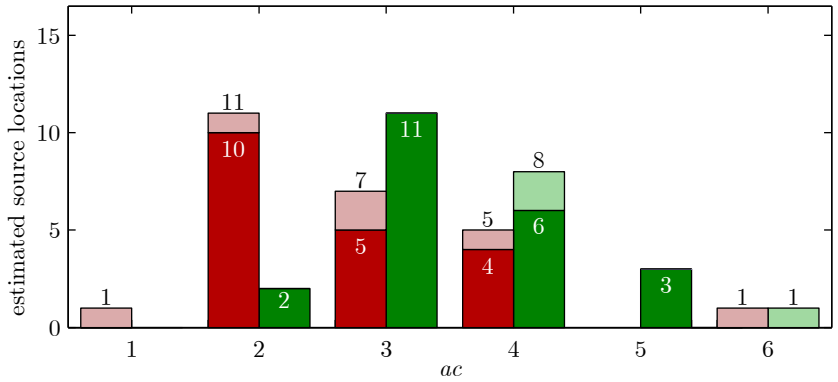

Fig. 7.18: Histogram of the estimated source locations obtained with *FastWay* (red) and Geiger's method (green) for the PLBs SW Ia – "Top-Front". The excluded estimations are shown in light red and light green, respectively.

and hence it is not possible to determine an error ellipsoid and the *eei* value. The source location estimations computed with *FastWay* were more accurate than those computed with Geiger's method. Three of the four inaccurate results ($d > 7.5''$) obtained with Geiger's method were not excluded automatically during the verification process. In contrast, the single inaccurate localization result obtained with *FastWay* was excluded automatically. However, an additional five accurate localizations computed with *FastWay* were excluded, as well as two accurate localizations computed with Geiger's method. The *ela* determined from the 25 source estimations is visualized in Fig. 7.21. It has to be mentioned that the number of localized events is comparatively low, as can be seen in Figs. 7.17 and 7.18. A meaningful interpretation of the results is therefore not possible.

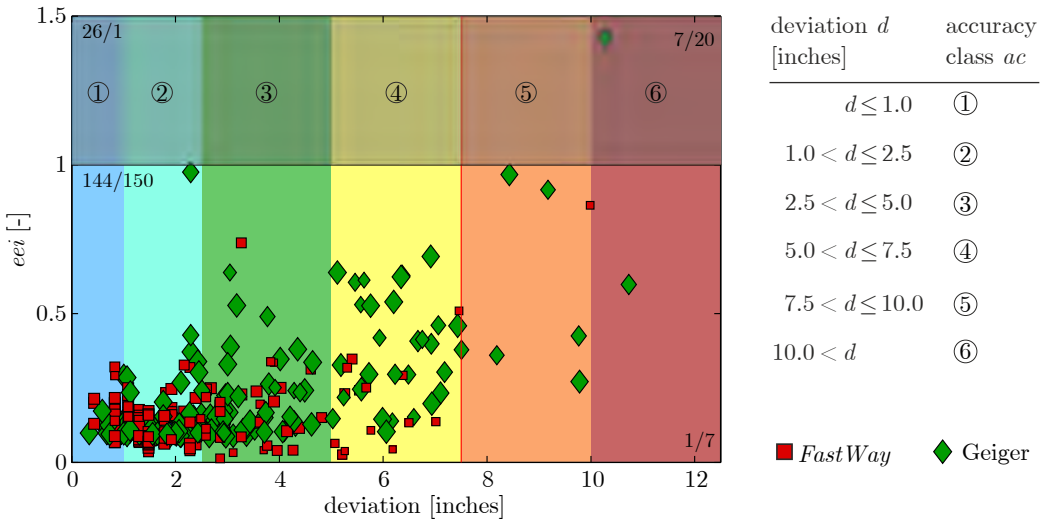

Fig. 7.19: Scatter plot of *eei* vs. deviation d in inches for the PLBs SW Ia performed on the "Front" surface. The deviation values are also listed in Tab. B.6. The plot is divided into four sections by a line at $eei = 1$ and a line at $d = 7.5''$. Results with $d > 12.5''$ or $eei > 1.5$ are outside the visualized area. The number of results obtained with *FastWay* and Geiger's method in each of these four sections is shown as *FastWay*/Geiger.

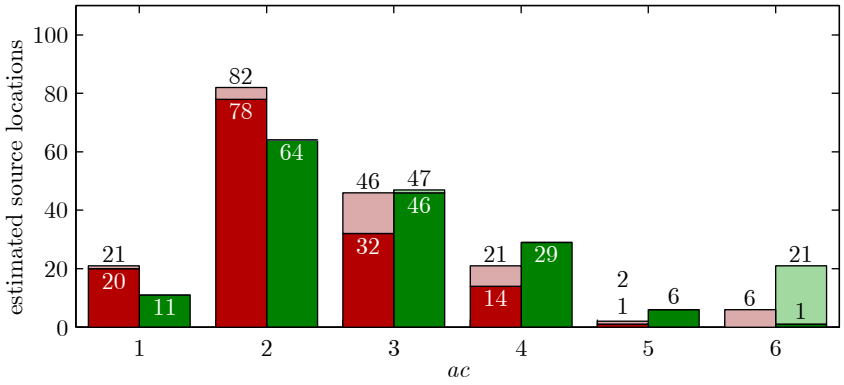

Fig. 7.20: Histogram of the estimated source locations "Front", obtained with *FastWay* (red) and Geiger's method (green). The excluded estimations are shown in light red and light green, respectively.

PLB "Front"

A total of 193 PLBs were performed on the lateral western surface of the flange. It was technically possible to estimate the locations of 178 events with either localization method. For the remaining 15 events, the arrival time of the wave according to Section 7.3.1 could not be determined for more than four signals. In an additional three cases only four arrival times per AE event could be determined. Therefore, it was impossible to determine an error ellipsoid and hence *eei* values. For these three events, the *eei* column for Geiger's method in Tabs. B.7 to B.10 shows the letters 'NaN'. 145 verified source location estimations computed with *FastWay* and 157 verified source location estimations computed with Geiger's method were considered to be accurate. 144 (> 99%) of the 145 results computed with *FastWay*, and 150 (96%) of the 157 verified source locations obtained with Geiger's method deviate less than 7.5" from the actual source locations. The percentages of inaccurate but verified source location estimations were therefore <1% and 4% for *FastWay* and Geiger's method, respectively, which is an exceptionally accurate result. During the evaluation process, 26 accurate *FastWay* results, and only one result determined

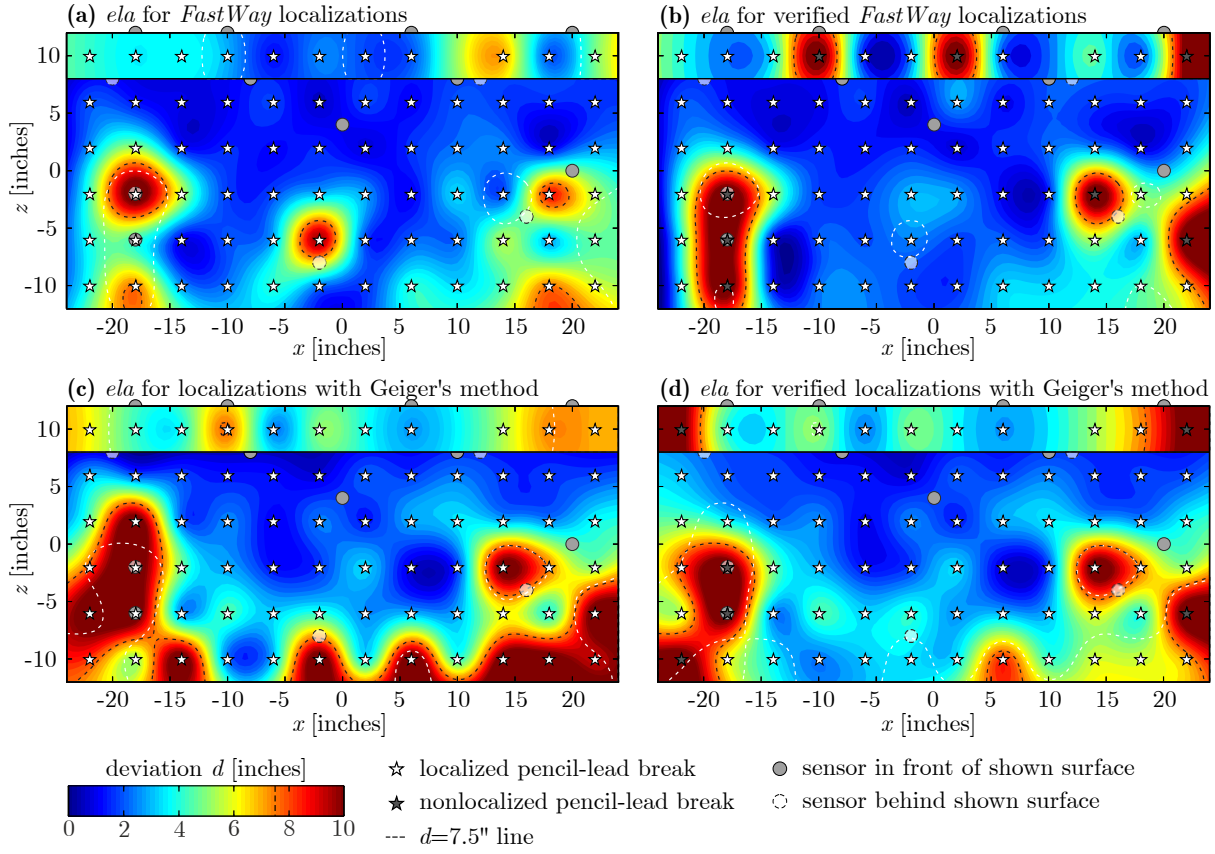

Fig. 7.21: Estimated localization accuracy (*ela*) at the western surface of the specimen, based on the source localization deviations for the pencil-lead breaks SW Ia "Front" and "Top-Front", and determined for the results obtained with *FastWay* and Geiger's method. The $d = 7.5''$ line of the figure based on all results is shown as a white dashed dotted line in the figure based on the verified results, and vice versa.

with Geiger's method were excluded. This seems to indicate that the evaluation process of the *FastWay* results was too conservative. However, the majority of the excluded *FastWay* source location estimations was dismissed because of the NEL criteria (see Section 7.3.4). A visual interpretation of the resulting localizations would generally also have led to an exclusion of these results.

As described above, the estimated source locations and their deviations from the actual source locations were used to verify how well the sensors cover the area of the specimen where the PLBs were performed, and to visualize an estimated localization accuracy (*ela*) of near-surface sources; see Fig. 7.21. This figure shows the *ela* for the lateral western surface of the flange and the web between $-12'' \leq x \leq 12''$. Unfortunately, the number of evaluated sources in the flange is insufficient to perform an informative interpretation. The *ela* based on the *FastWay* source location estimations visualized in Figs. 7.21 (a) and (b) shows a relatively good sensor coverage of the western surface of the web. There are only small areas in which PLBs could not be localized ($d > 7.5''$), especially for verified results shown in Fig. 7.21 (b). These areas are located at the edges of the cross-section. By checking the entries of the unlocatable PLBs listed in Tabs. B.7 to B.10, it can be seen that there are only a few PLBs, or even just one, with estimated source locations for the PLBs performed on the right-hand side of the beam. For the PLBs performed on the left-hand side of the specimen, the amplitude of the recorded signal was surprisingly low, even though the distance to the recording sensors was short. For sensor SE12 the reason might be that the PLB at $x = -18''$, $y = -4''$, and $z = -2''$ was performed directly on

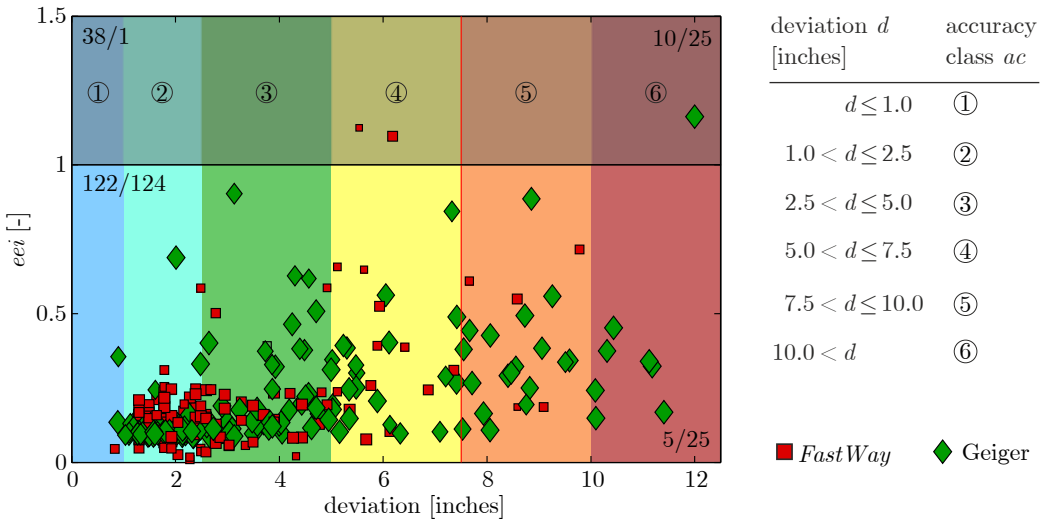

Fig. 7.22: Scatter plot of *eei* vs. deviation d in inches for the PLBs SW Ia performed on the "Back" surface. The plot is divided into for sections by a line at $eei = 1$ and a line at $d = 7.5''$. Results with $d > 12.5''$ or $eei > 1.5$ are outside the visualized area. The number of results obtained with *FastWay* and Geiger's method in each of these four sections is shown as *FastWay*/Geiger.

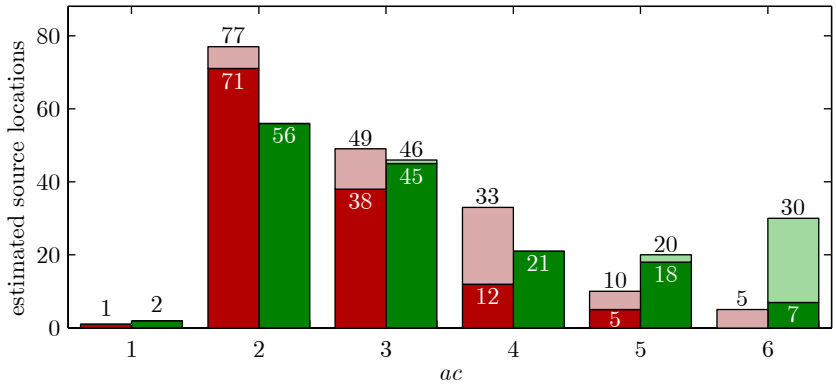

Fig. 7.23: Histogram of the estimated source locations obtained with *FastWay* (red) and Geiger's method (green) for the PLBs SW Ia – "Back". The excluded estimations are shown in light red and light green, respectively.

top of the sensor. This probably damped the signal that propagated into the reinforced-concrete body. The *ela* based on Geiger's method and visualized in Figs. 7.21 (c) and (d) shows that the evaluation process significantly improves the results. In Fig. 7.21 (c) PLBs close to the bottom edge of the flange seemed to be unlocatable. After the verification, the area in the plots with $d > 7.5''$ decreases to almost the same size as that in Fig. 7.21 (b).

PLB "Back"

202 PLBs were performed on the lateral eastern surface of the web. It was technically possible to calculate a source location estimation for 175 of the PLBs. For the remaining 27 events, less than four arrival times could be picked in accordance with Section 7.3.1. Exactly four arrival times were picked for an additional seven PLBs. It was therefore not possible to compute an error ellipsoid and hence an *eei* value during the verification process. Therefore, for these seven PLBs the letters 'NaN' are listed in the *eei* column for Geiger's method in Tabs. B.11 to B.14 . After completion of the evaluation process, 127 source location estimations computed with *FastWay*

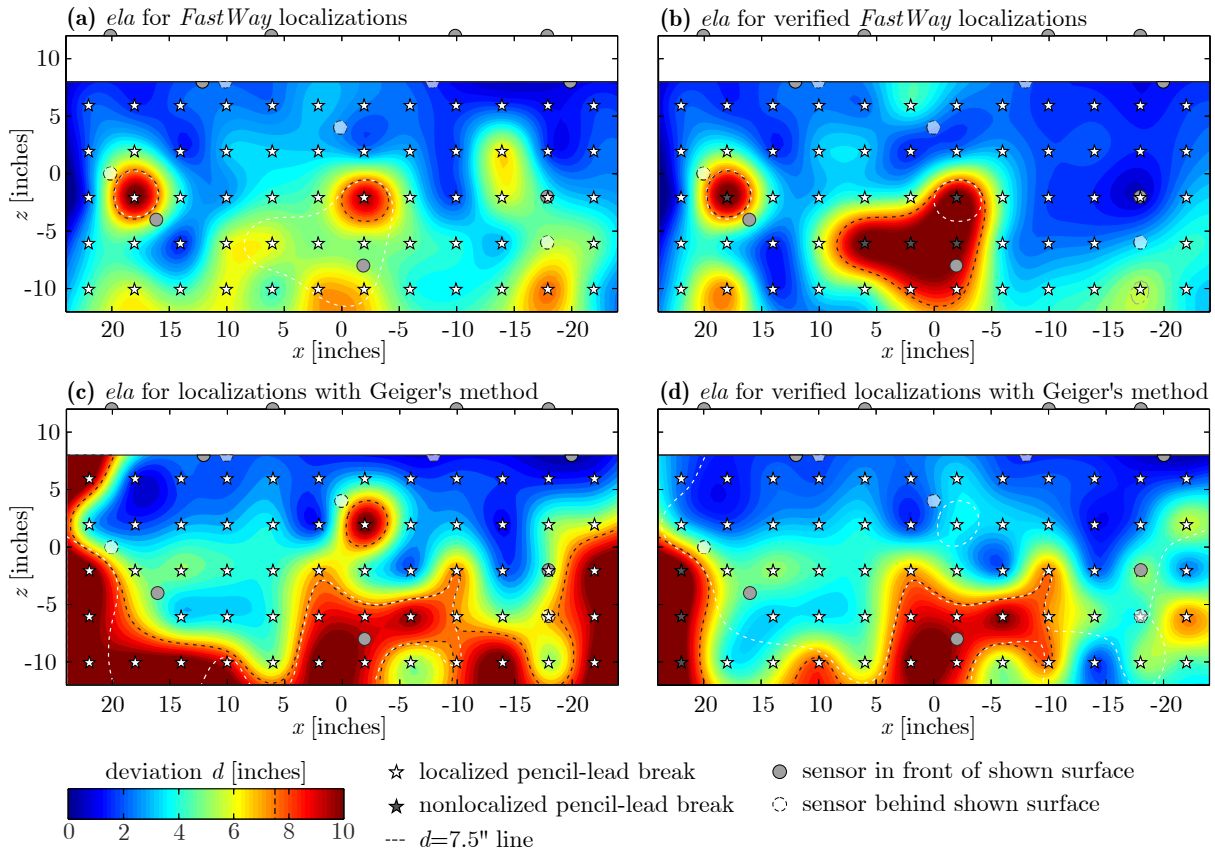

Fig. 7.24: Estimated localization accuracy (*ela*) at the top surface of the specimen, based on the source localization deviations for the pencil-lead breaks SW Ia "Back", and determined for the results obtained with *FastWay* and Geiger's method. The $d = 7.5''$ line of the figure based on all results is shown as a white dashed dotted line in the figure based on the verified results, and vice versa.

and 149 source location estimations computed with Geiger's method were considered to be accurate. 122 (96%) of the 127 results obtained with FastWay deviated by less than 7.5" from the actual source location, while only 124 (83%) of the 149 verified source locations computed with Geiger's method deviated by less than 7.5" from the actual source location. The percentages of inaccurate but verified source location estimations were therefore 4% and 17% for *FastWay* and Geiger's method, respectively. Again, 38 accurate *FastWay* results but only one accurate result determined with Geiger's method were excluded during the evaluation process. It seemed that the evaluation process of the *FastWay* results was too conservative. However, most of the excluded *FastWay* source location estimations were dismissed because they did not fulfill the NEL criteria (see Section 7.3.4). A visual interpretation of the results would also generally have led to their exclusion. Geiger's method yielded slightly more accurate verified source location estimations, but also significantly more verified inaccurate source location estimations. A significant percentage (24%) of the accurate results determined with *FastWay* were excluded during the verification process. However, the ratio between accurate and inaccurate verified results is clearly higher than that for the results obtained with Geiger's method.

The *ela* based on the source location estimations from *FastWay* is visualized in Fig. 7.24. Fig. 7.24 (a) shows that, for the unverified results, the *ela* for almost the entire bottom half of the eastern surface of the flange is $d > 5''$. After verification of the results the overall *ela* improves. However, at the center of the specimen surface there was a large area with unlocatable PLBs. A visual check of the localization results confirmed that the PLBs in this area could not be

accurately localized with *FastWay*. Almost all the results for this area were excluded during the verification process because they did not fulfill the NEL criteria (see Section 7.3.4). Fig. 7.24 (c) shows that, for the unverified results, the *ela* for almost the entire bottom half of the eastern surface of the flange is $d > 5''$, and $d > 7.5''$ for a major part of the area. It is also apparent that the PLBs at the center of the surface could not be located. The area with $d > 7.5''$ decreases significantly after the verification process. A comparison of Fig. 7.24 (b) and Fig. 7.24 (d) shows that overall *FastWay* yielded more accurate source location estimations for this surface than Geiger's method.

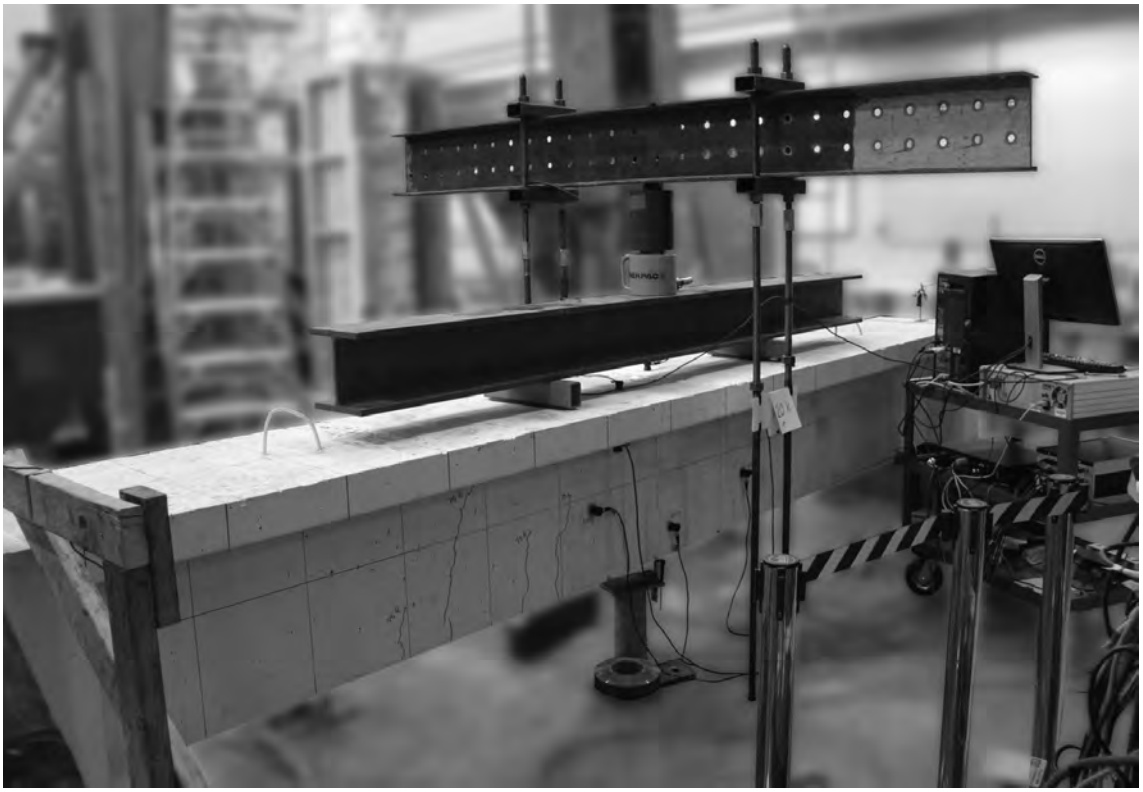

Fig. 7.25: Test setup of bending test SW I.

7.4.2 Bending Test – SW I

As mentioned above, the load was applied to the beam via a transverse beam, using a hand-pump-controlled hydraulic ram. The test was performed as a four-point bending test. The beam was loaded in six load cycles (see Tab. 7.4). The maximum load was 35.1 kips $\widehat{=}$ 156.1 kN.

Each of the load cycles consisted of four steps. During the first step, "load", the load was increased from A to B (see Tab. 7.4). After load B had been reached, no further hydraulic fluid was pumped into the ram. The applied force was then permitted to decrease slowly from B to C, during the step called "hold". When the number of recorded AEs (hits) had decreased to nearly zero, the beam was unloaded. In load cycle 1 the beam was unloaded completely. From load cycle 2 onwards, the beam was unloaded until a load of approximately 5 kips (22.24 kN) had been reached. This step from load C to D was called "unload". Subsequently, the load was held again until the number of recorded AE (hits) had decreased to nearly zero. This step from D of the load cycle to A of the next load cycle was also called "hold". Load cycles 1, 2, and 6 were slightly different from the other three cycles. In load cycle 1 the beam was loaded from 0 kips to 10 kips (44.5 kN). The load was applied in two steps of approximately 5 kips each, interrupted by a short phase in which the load was not increased (see Fig. 7.26). The two load steps were considered as one (1A to 1B). In load cycle 2 the load was applied in two steps of approximately 10 kips and 5 kips, respectively (2A to 2B). In load cycle 6, the beam was not unloaded down to 5 kips but to approximately 20 kips (89.0 kN). The load of 20 kips instead of 5 kips was chosen in order to keep the cracks open while the pencil-lead breaks SW II b were performed. The deflection of the beam remained low throughout the test. The maximum deflection, measured during load cycle 6, was about $w_{eff} = 11.6 \times 10^{-}2$ inches (less than 3 mm). Fig. 7.29 shows the deflection over time. The time axis of this figure corresponds to that in Fig. 7.26. After the

LS	t [s]	F [kips]	
1A	506.7	0.02	load
1B	836.3	10.03	hold
1C	891.7	9.65	unload
1D	907.7	0.03	hold
2A	1,020	0.04	load
2B	1,429	15.15	hold
2C	1,558	14.24	unload
2D	1,579	5.08	hold
3A	1,697	5.30	load
3B	1,892	20.50	hold
3C	2,203	18.54	unload
3D	2,263	4.85	hold
4A	2,299	5.07	load
4B	2,426	25.18	hold
4C	3,121	23.10	unload
4D	3,154	4.83	hold
5A	3,224	5.23	load
5B	3,373	29.95	hold
5C	3,846	28.27	unload
5D	3,901	4.84	hold
6A	3,955	5.22	load
6B	4,125	35.15	hold
6C	4,293	33.57	unload
6D	4,313	19.74	

Tab. 7.4: Load steps LS of load cycles 1–6 for bending test SW I

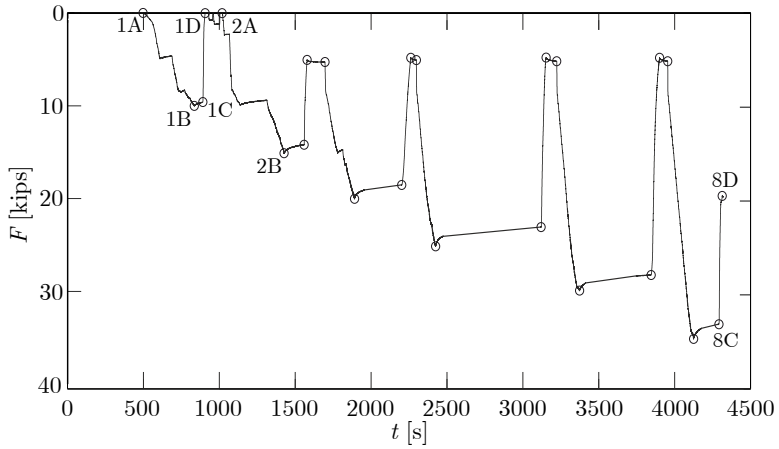

Fig. 7.26: Applied load (load cycles 1–6) in kips vs. time t [s]. Some of the points listed in Tab. 7.5 are marked on the load-time curve.

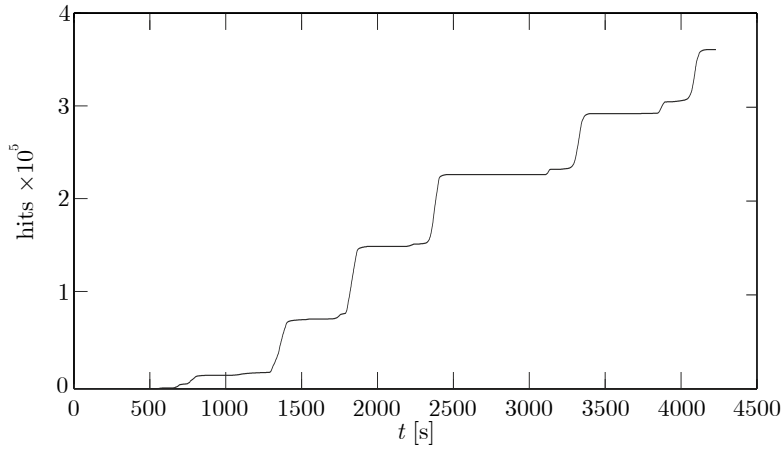

Fig. 7.27: Cumulative hits recorded over time. The time line corresponds to that of Fig. 7.26

beam had been loaded and the load had been held until almost no new hits were recorded, the data acquisition system was turned off for the visual inspection of the beam, in order to avoid recording artificial AEs (e.g., caused by touching the beam). During that time, no white noise was recorded and the graph shows a straight line connecting the last discrete point recorded before turning off the acquisition system to the first discrete point recorded after turning it on again (see Fig. 7.29). After completion of the test, a small plastic deformation of less than 0.1 mm remained. The compression of the neoprene support strips was less than 0.2 mm.

During bending test SW I, the wave signals of 363,300 hits (see Section 7.2.3 – Data acquisition system) were recorded. Fig. 7.57 shows the cumulative number of hits over time. Using the recorded signals, it was possible to estimate the locations of 224 AEs using *FastWay*, and of 101 AEs using Geiger's method. The source locations of 72 events could be estimated with both methods. The estimated source location coordinates and source times determined with both methods are listed in Tabs. B.15 to B.20. The ratio of hits to the number of estimated source locations for *FastWay* is approximately 1,622 to 1. Considering that generally a minimum of five signals (five hits) fulfilling the criteria formulated in Section 7.3.4 were needed to estimate

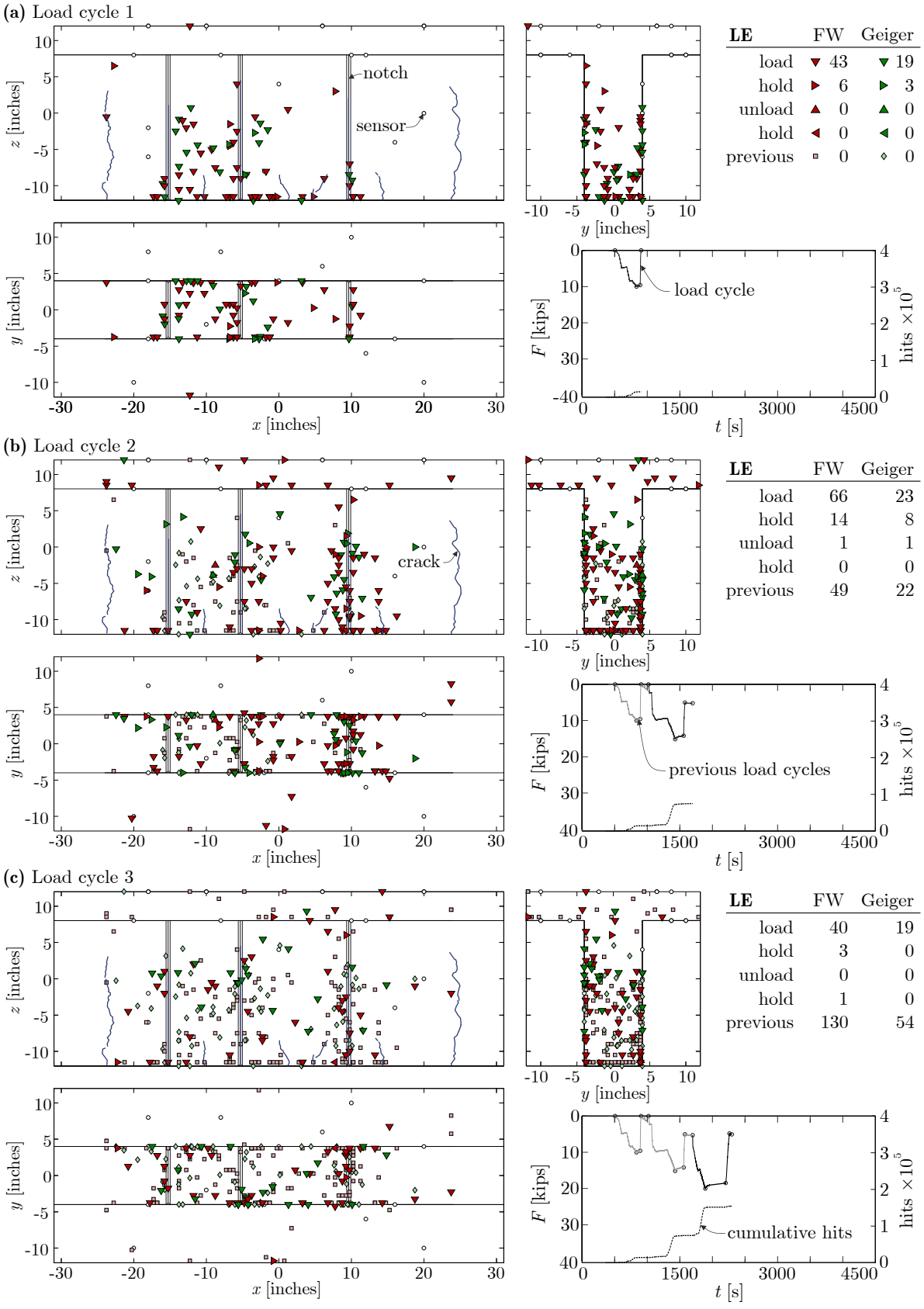

Fig. 7.28: Estimated source locations determined with *FastWay* and Geiger's method, shown for three cross-sections for load steps 1 to 3. The load steps and cumulative hits over time are shown at the bottom right. The numbers of localized sources are listed at the top right.

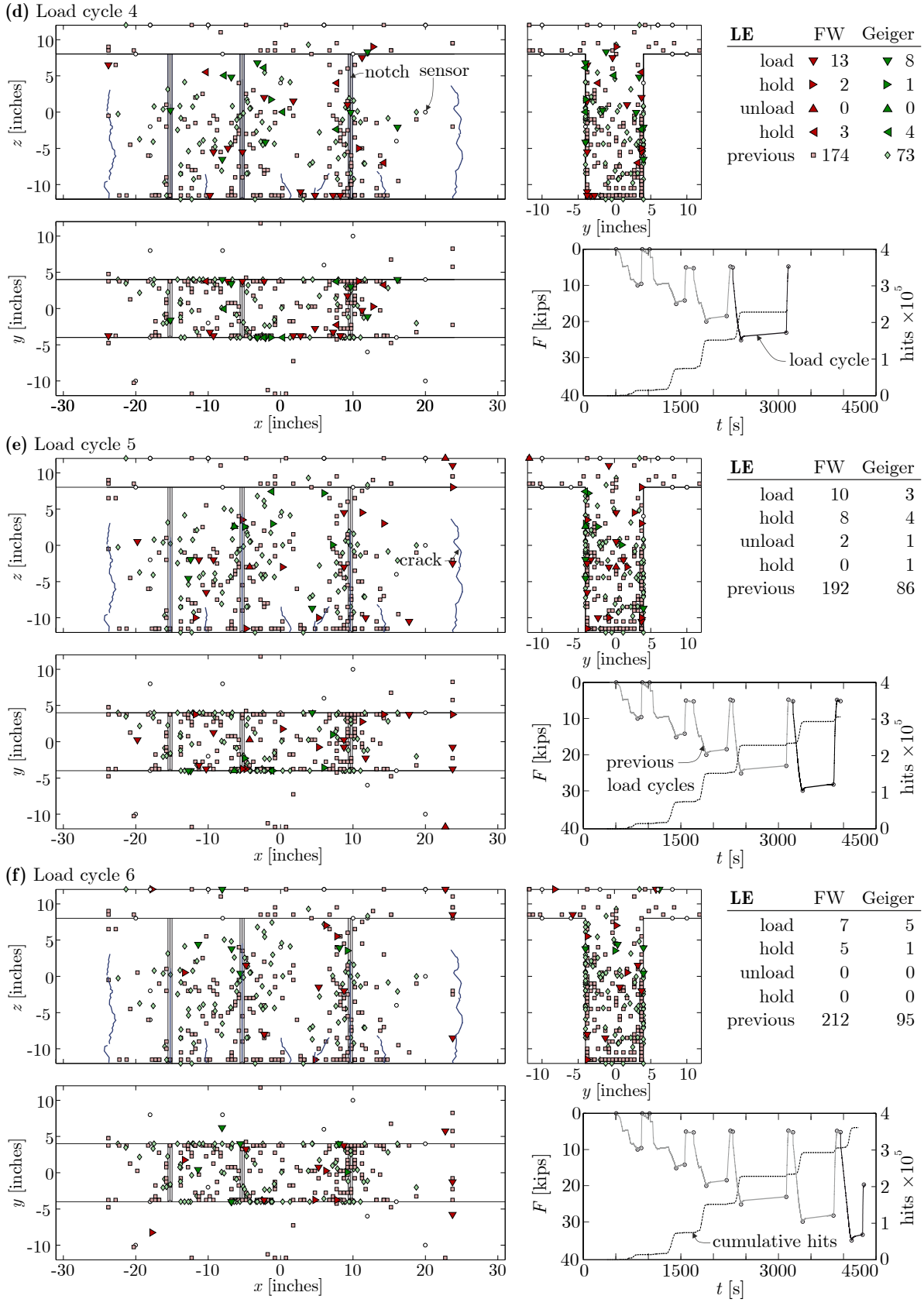

Fig. 7.28 (cont.)**:** Estimated source locations determined with *FastWay* and Geiger's method, shown for three cross-sections for load steps 4 to 6. The load steps and cumulative hits are are shown at the bottom right. The numbers of localized sources are listed at the top right.

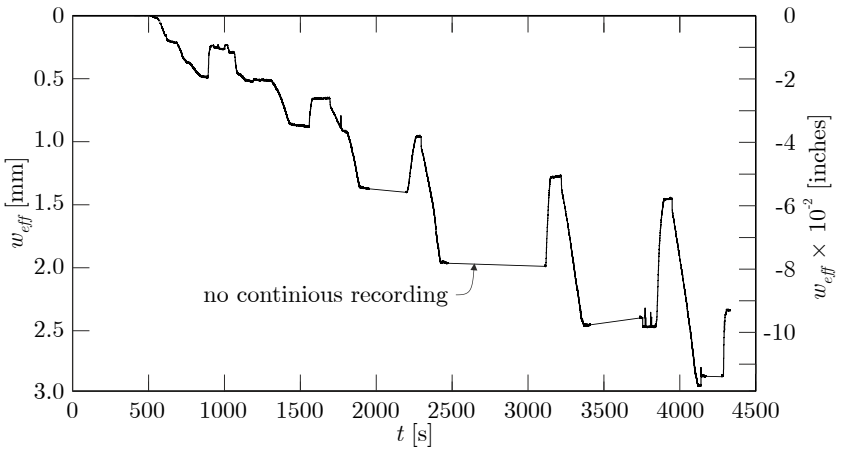

Fig. 7.29: Effective deflection of the beam at midd-span w_{eff} over the time t during bending test SW I

the location of an AE, this ratio seems reasonable. In addition, almost all of the localized AEs were recorded by 12 to 14 sensors (12 to 14 hits). The cumulative number of detected AEs does not completely reflect the development of the cumulative hits. Fig. 7.28 (a) to (f) show the development of AE localizations during the six load cycles. The positions of the estimated source locations are shown in three cross-sections (x–z section, y–z section, and x–y section). The source locations estimated with *FastWay* are labeled with green markers, while those estimated with Geiger's method are labeled with blue markers. The shape of the marker indicates if the AE occurred during loading ($\triangledown$), the hold phase after loading ($\triangleright$), unloading ($\triangle$), the hold phase after unloading ($\triangleleft$), or during a previous load cycle. In order to improve the legibility of the figure, a small table in the upper right corner shows a summary of the number of localized events (LE) for each phase of the load cycle, as well as the number of LEs during all previous load cycles for both applied source location estimation methods. In addition, the load cycles and cumulative number of hits over time are shown in the lower right corner of the figure. The relevant load cycle is highlighted.

The source location estimation results were not satisfactory. First, the estimated source locations do not seem to correspond to the visually localized crack locations. Only the crack located in the notch at $x = 10''$ corresponded to a localized AE pattern (see Fig. 7.28). Secondly, the signals were recorded with a frequency of 10 MHz for a signal length of 819.1 µs, resulting in 8,192 discrete values. It is evident that the number of source locations estimated for load cycles 4 to 6 does not reflect the number of hits in the cumulative hits plot. The memory of the data acquisition system was insufficient, hence not all the recorded wave signals could be saved. Even if all 14 sensors detected a wave signal induced by an AE, not all of the 14 wave signals were recorded, and sometimes even less than five. Performing verified source localizations using Geiger's method was therefore made impossible. Also, the recorded signals were not always ideally suited for use in the source localization process. A non-negligible share of the recorded signals was excluded during the picking process. In many cases where five or more signals were recorded, only four or fewer of the recorded signals fulfilled the picking criteria formulated in Section 7.3.1.

During load cycle 1 very few hits were recorded. Even so, 49 source locations were estimated using *FastWay*. Most of these AEs were located in the web between $x = -15''$ and $x = 0''$ (see Fig. 7.28 (a)). Additionally, a crack cluster occurred at $x = 10''$, i.e. in the region of the notch. During load cycle 2, AEs were determined to have occurred all over the monitored part of the specimen (including the flange) between $x = -24''$ and $x = 24''$. Most of the localized AEs were

estimated to be located in the area of the notch at $x = 10''$, indicating the formation of a crack at this location. However, up to a load of 20 kips (89.0 kN) no cracks were detected with the naked eye. All the cracks shown in Fig. 7.28 were detected after the load had been increased to 20 kips during load cycle 3. Crack growth during the subsequent load cycles was slow. It became apparent that the widths of the cracks were extremely small, which made detection with the naked eye very difficult, especially for the cracks located in the notches. It is hence quite likely that crack initiation occurred before load cycle 4. The cracks visualized in Fig. 7.28 show the final state of the beam after completion of load cycle 6. The number of hits detected during load cycle 2 increased significantly with respect to load cycle 1. During this load cycle, the number of estimated source locations determined with *FastWay* increased by 65% to 81. However, the increase in estimated source locations did not reflect the increase in detected hits, which indicates memory overload of the system. Although the number of hits remained approximately constant, the number of estimated locations decreased during load cycles 3 to 6. This phenomenon was probably caused by memory overload. A large part of the localized AEs was estimated to have occurred in the region around the notch (and the crack) at $x = 10''$. A significant number of the estimated AE locations were also estimated to be distributed over a larger area in the web between $x = -15''$ and $x = 0''$. There was no apparent correlation between the localized AEs and the cracks located in the notches at $x = -15''$ and $x = -5''$. Almost no AEs originating from the two large cracks at either end of the monitored area ($-24'' \leq x \leq 24''$) were localized.

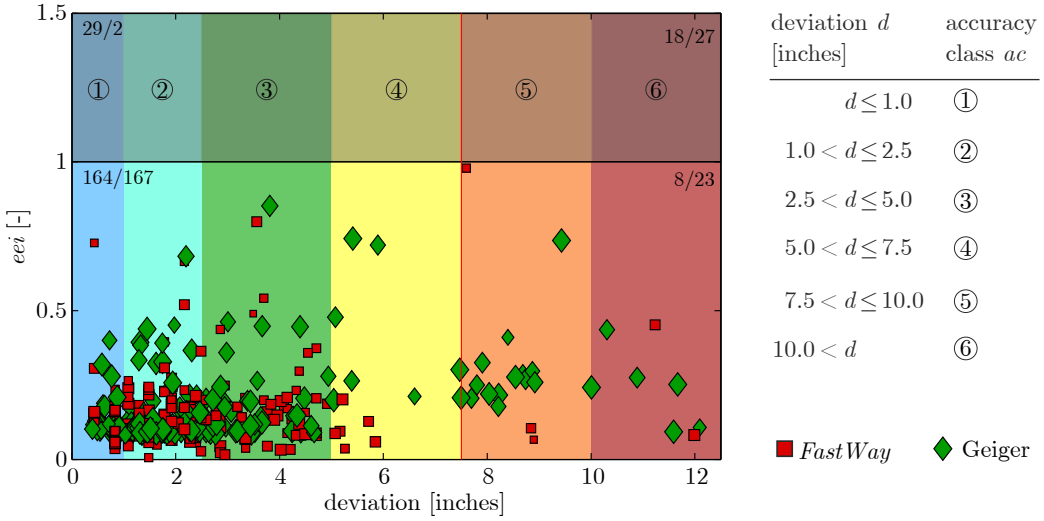

Fig. 7.30: Scatter plot of *eei* vs. deviation d in inches for the PLBs SW Ib performed on the "Top" surface. The plot is divided into four sections by a line at $eei = 1$ and a line at $d = 7.5''$. Results with $d > 12.5''$ or $eei > 1.5$ are outside the visualized area. The number of results obtained with *FastWay* and Geiger's method in each of these four section is shown as *FastWay*/Geiger.

7.4.3 Pencil-lead breaks – SW Ib

All the pencil-lead breaks of test SW Ia (see Section 7.4.1) were performed again after completion of the destructive bending test (see Sections 7.2.1 and 7.4.2). The pencil-lead breaks were again divided into the four groups described in Section 7.4.1, namely "Top", "Top-Front", "Front", and "Back". A load of 20 kips (89.0 kN) was applied to the beam to ensure that the cracks remained open. The velocity models used as input for *FastWay* did not take into account the presence of the cracks. The same model as for the PLBs SW Ia was used.

PLB "Top"

A total of 334 events were recorded while the PLBs were performed on the "Top" surface. It was technically possible to compute estimations for 234 source locations. They are listed in Tabs. B.21 to B.25. For the remaining 100 events, an arrival time that satisfied the arrival-time picking criteria listed in Section 7.3.1 could be picked only for four or fewer signals. Consequently, no source location estimations could be computed for these 100 events. The results of the 234 computed source location estimations were subsequently verified (see Section 7.3.4) in order to exclude results that were deemed to be inaccurate ($eei > 1$). For nine of the localized PLBs only four signals fulfilled the picking criteria. Therefore, it was not possible to determine an *eei* value for the results determined with Geiger's method ($eei = \text{NaN}$). These estimated source locations were excluded. At least five admissible signals were recorded for the remaining 229 events. 172 source locations estimated with *FastWay* were verified and deemed accurate. However, eight of these estimations deviated by more than $7.5''$ from the respective PLB locations. As mentioned above, source localization estimations with a deviation of $d > 7.5''$ ($d > 19.05$ cm) from the actual source location (*ac* 5 and 6) were considered inaccurate and inadmissible. 23 of the 190 verified source location estimations obtained with Geiger's method differed by more than $7.5''$ from the actual PLB location. During the verification process 18 and 27 inaccurate source location estimations determined with *FastWay* and Geiger's method, respectively, were excluded. An additional 29 and 2 source location estimations determined with *FastWay* and Geiger's method, respectively, were excluded during the verification process, even though they

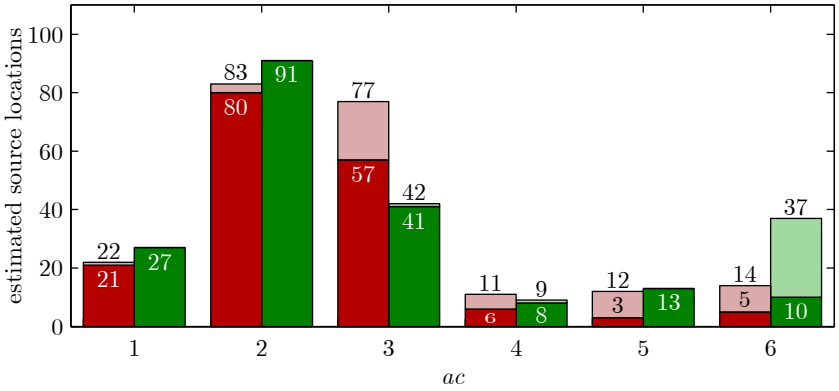

Fig. 7.31: Histogram of the estimated source locations obtained with *FastWay* (red) and Geiger's method (green) for the PLBs SW Ib – "Top". The excluded estimations are shown in light red and light green, respectively.

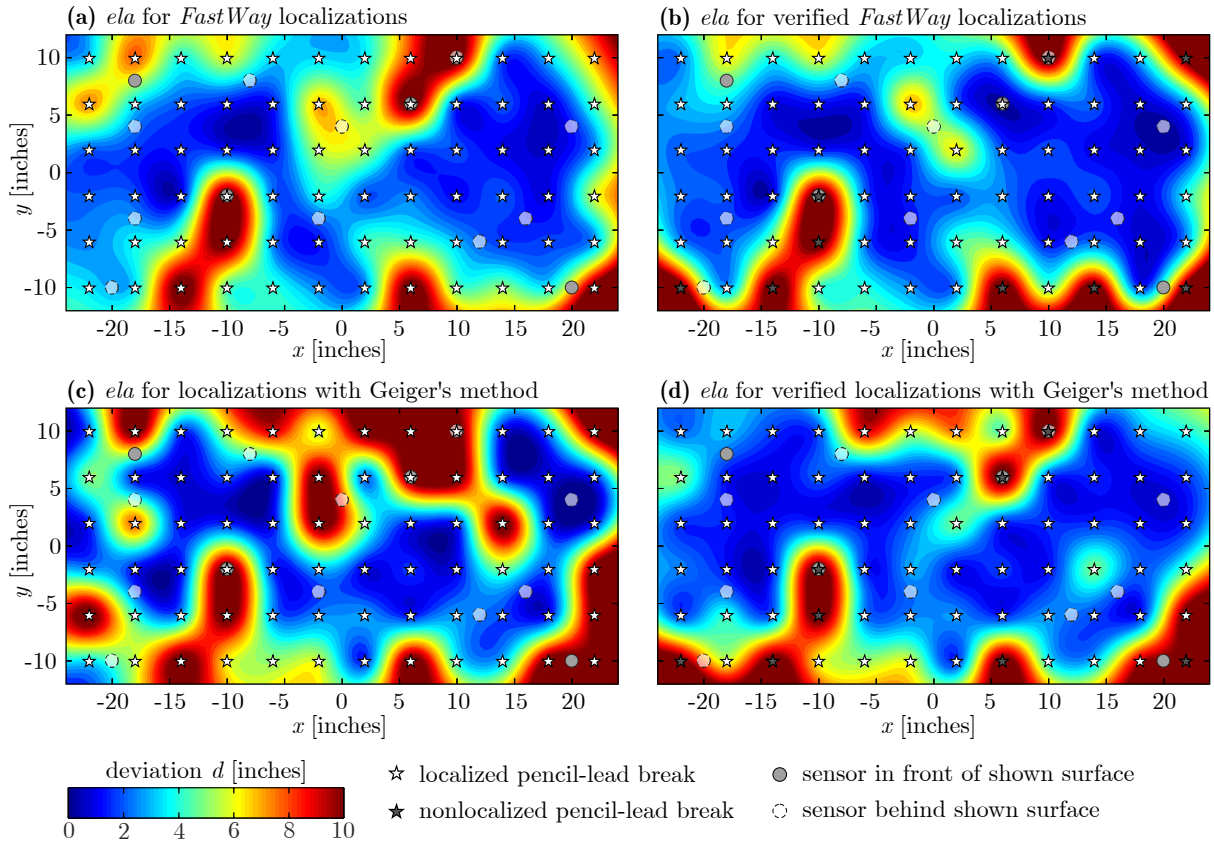

Fig. 7.32: Estimated localization accuracy (*ela*) at the top surface of the specimen, based on the source localization deviations for the pencil-lead breaks SW Ib "Top", and determined for the results obtained with *FastWay* and Geiger's method.

deviated by less than 7.5″ from the actual PLB locations. Most of the excluded and accurate *FastWay* results were excluded because they did not fulfill the NEL criteria (see Section 7.3.4). A visual interpretation of the visualization of $\mathbf{E}_{\text{source}}$ would generally also lead to the exclusion of most of these 29 results. Overall, both methods provide satisfactory source location estimations. At first glance it seems that Geiger's method performed better. However, 23 source location estimations were verified as accurate with *eei* values of less than 0.5. Therefore, *FastWay* seems

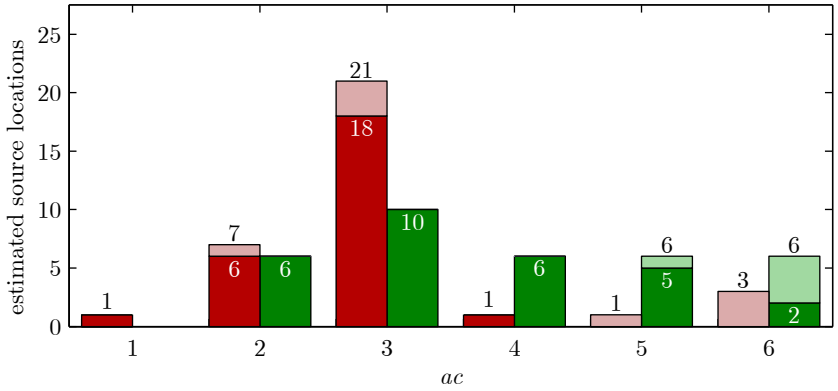

Fig. 7.33: Histogram of the estimated source locations obtained with *FastWay* (red) and Geiger's method (green) for the PLBs SW Ib – "Top-Front". The excluded estimations are shown in light red and light green, respectively.

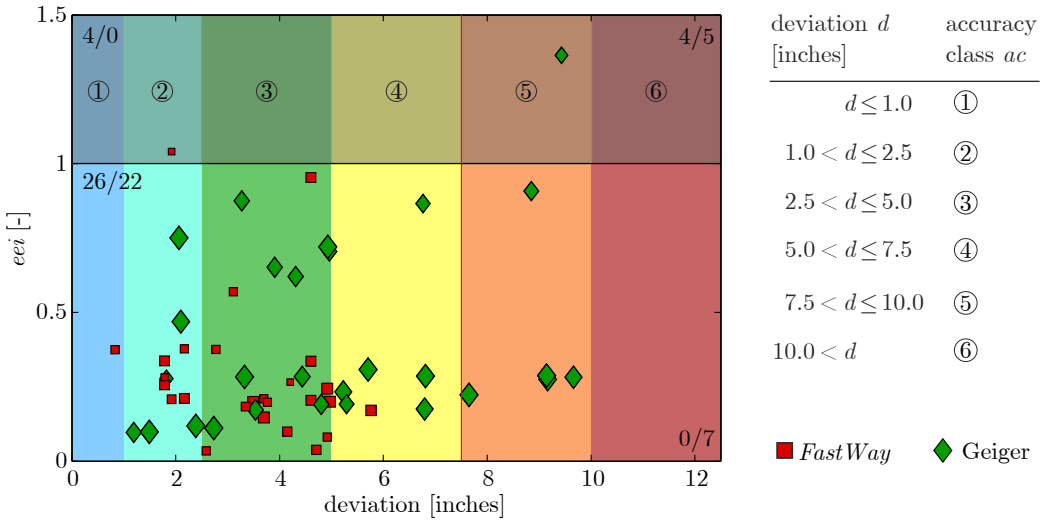

Fig. 7.34: Scatter plot of *eei* vs. deviation d in inches for the PLBs SW Ib performed on the "Top-Front" surface. The plot is divided into four sections by a line at $eei = 1$ and a line at $d = 7.5''$. Results with $d > 12.5''$ or $eei > 1.5$ are outside the visualized area. The number of results obtained with *FastWay* and Geiger's method in each of these four sections is shown as *FastWay*/Geiger.

to yield the more reliable results. Fig. 7.32 shows that the verification process improved the *ela* of both localization methods, but particularly that one of Geiger's method. It seems that the sensors were capable of detecting AEs from a large part of the top surface. Only PLBs in the periphery could not be localized.

PLB "Top-Front"

A total of 35 events were recorded while the PLBs were performed on the top western surface of the flange. It was technically possible to compute estimations for 34 source locations. They are listed in Tab. B.26. The results of the 34 computed source location estimations were subsequently verified (see Section 7.3.4) in order to exclude results which were deemed to be inaccurate ($eei > 1$). For three of the localized PLBs only four signals fulfilled the picking criteria. Therefore it was not possible to determine an *eei* value for the results determined with

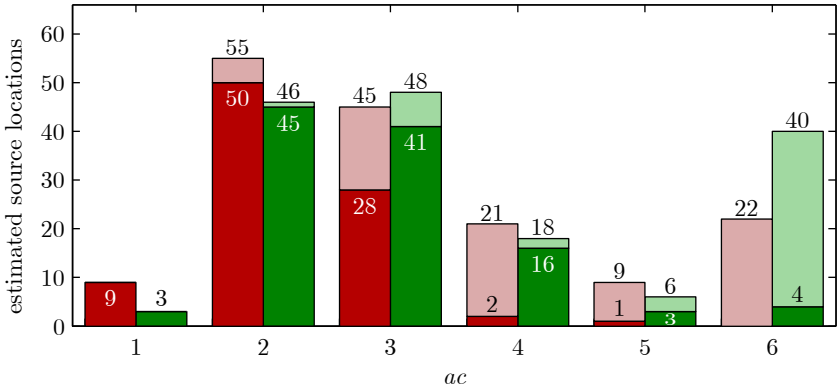

Fig. 7.35: Histogram of the estimated source locations obtained with *FastWay* (red) and Geiger's method (green) for the PLBs SW Ib – "Front". The excluded estimations are shown in light red and light green, respectively.

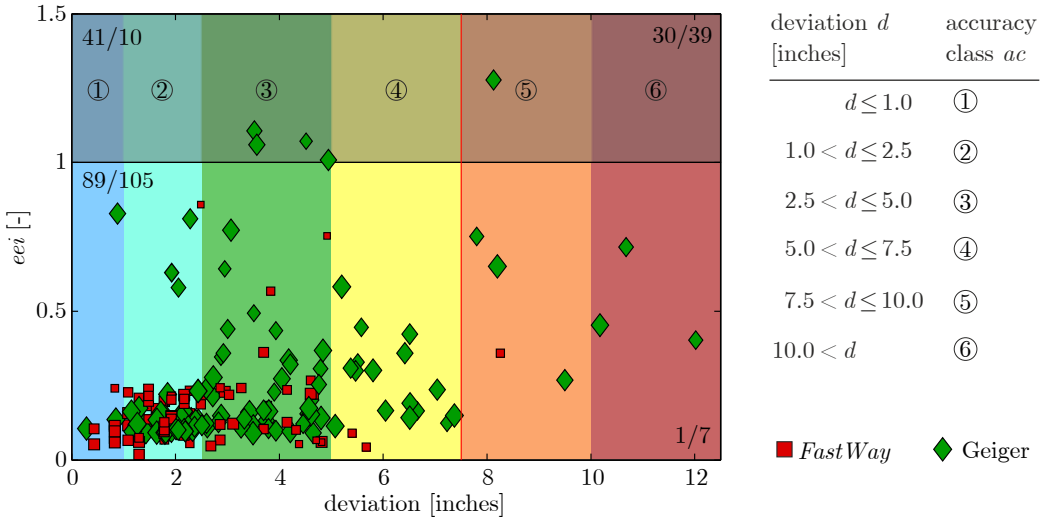

Fig. 7.36: Scatter plot of *eei* vs. deviation d in inches for the PLBs performed on the "Front" surface. The plot is divided into four sections by a line at $eei = 1$ and a line at $d = 7.5''$. Results with $d > 12.5''$ or $eei > 1.5$ are outside the visualized area. The number of results obtained with *FastWay* and Geiger's method in each of these four sections is shown as *FastWay*/Geiger.

Geiger's method (eei = NaN). These estimated source locations were excluded. At least five admissible signals were recorded for the remaining 29 events. 26 source locations estimated with *FastWay* were verified and deemed accurate. All of them deviated by less than $7.5''$ from the actual PLB locations. Seven of the 29 verified localizations determined with Geiger's method deviated by more than $7.5''$ from the actual PLB location. During the evaluation process five inaccurate localizations determined with Geiger's method, and four inaccurate localizations as well as four accurate localizations determined with *FastWay* were excluded. The number of PLBs performed on the western surface of the flange is too low for a reliable interpretation of the results. However, from the visualization of *ela* in Fig. 7.37, it appears that *FastWay* yielded more accurate localizations than Geiger's method.

PLB "Front"

A total of 208 events were recorded while the PLBs were performed on the top western surface of the flange. It was technically possible to compute estimations for 161 source locations. They

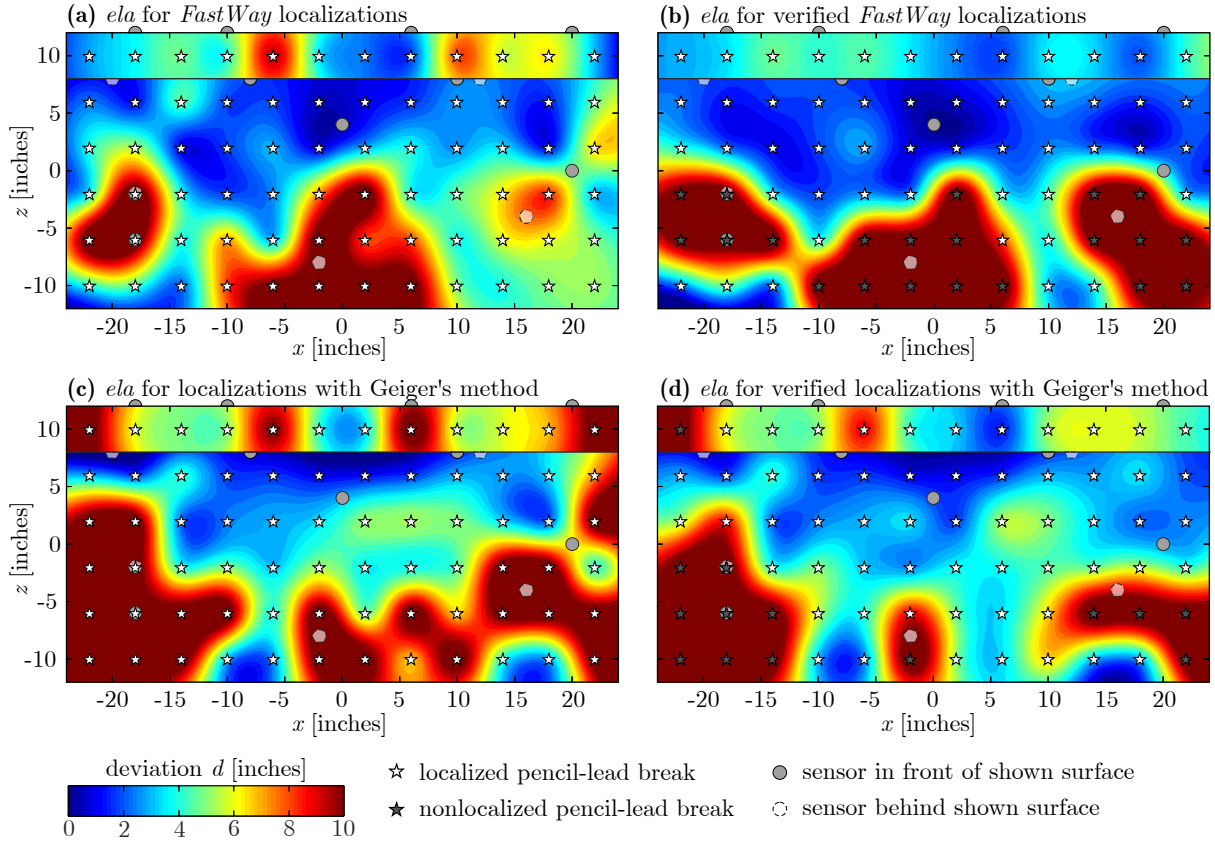

Fig. 7.37: Estimated localization accuracy (*ela*) at the top surface of the specimen, based on the source localization deviations for the pencil-lead breaks SW Ib "Front" and "Top-Front", and determined for the results obtained with *FastWay* and Geiger's method.

are listed in Tabs. B.27 to B.30. The remaining 47 events could not be localized because less than four picked arrival times for each event were available. The results of the 161 computed source location estimations were subsequently verified (see Section 7.3.4) in order to exclude results which were deemed to be inaccurate ($eei > 1$). For 22 of the localized PLBs, exactly four signals fulfilled the picking criteria. Therefore, it was not possible to determine *eei* values for the results determined with Geiger's method ($eei = \text{NaN}$). These estimated source locations were excluded. 90 source locations estimated with *FastWay* were verified and deemed accurate. Only one deviated by more than 7.5″ from the actual PLB location. 112 of the source locations estimated with Geiger's method were verified and deemed accurate. Only seven deviated by more than 7.5″ from the actual PLB locations. During the verification process 30 inaccurate localizations computed with *FastWay*, and 39 inaccurate localizations computed with Geiger's method were excluded (see Fig. 7.36). Additionally, 51 accurate localizations were excluded (41 computed with *FastWay*, 10 computed with Geiger's method). Geiger's method yielded a greater number of accurate source location estimations. However, *FastWay* yielded a greater number of localizations with *ac* 1 or 2, as shown in Fig. 7.35.

Fig. 7.37 shows that reliable localizations were likely not possible in the lower half of the web. However, it was possible to correctly estimate AE source locations in the middle part of the lower half of the web, according to the *ela* based on the verified results of Geiger's method.

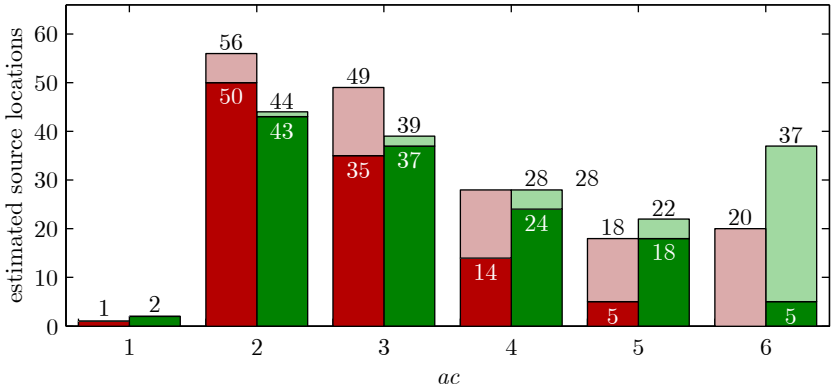

Fig. 7.38: Histogram of the estimated source locations obtained with *FastWay* (red) and Geiger's method (green) for the PLBs SW Ib – "Back". The excluded estimations are shown in light red and light green, respectively.

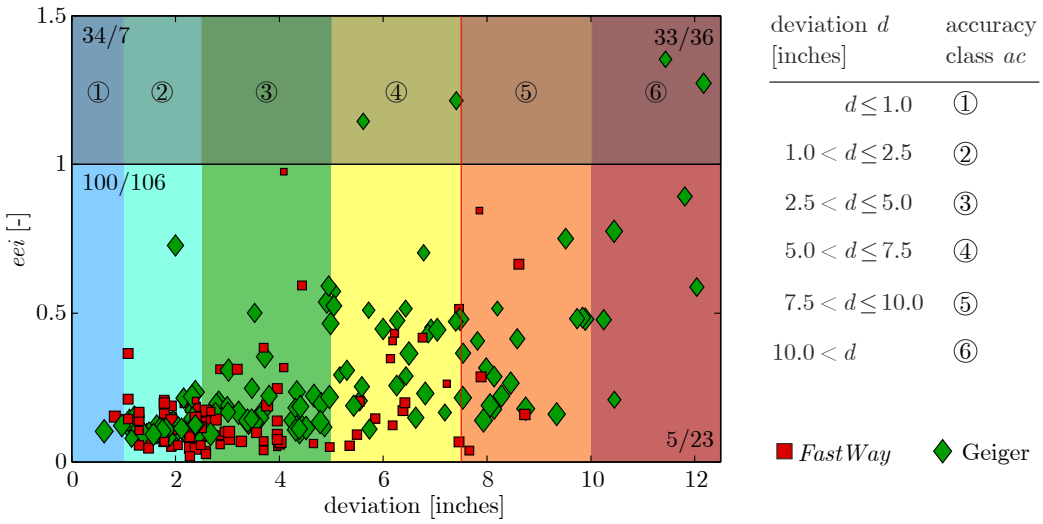

Fig. 7.39: Scatter plot of *eei* vs. deviation d in inches for the PLBs performed on the "Back" surface. The plot is divided into four sections by a line at $eei = 1$ and a line at $d = 7.5''$. Results with $d > 12.5''$ or $eei > 1.5$ are outside the visualized area. The number of results obtained with *FastWay* and Geiger's method in each of these four sections is shown as *FastWay*/Geiger.

PLB "Back"

A total of 423 events were recorded while the PLBs were excited on the top western surface of the flange. Estimated source locations were computed for 172 events. They are listed in Tabs. B.31 to B.34. For the PLBs on the eastern surface of the flange, a large number of unintentional AEs was recorded, which had to be excluded by hand. Only a fraction of the 251 events without an estimated source location were excluded due to an insufficient number of available picked arrival times. The results of the 172 computed source location estimations were subsequently verified (see Section 7.3.4) in order to exclude results that were deemed to be inaccurate ($eei > 1$). For 18 of the localized PLBs exactly four signals fulfilled the picking criteria; therefore it was not possible to determine *eei* values for the results determined with Geiger's method (eei = NaN). These estimated source locations were excluded. 105 source locations estimated with *FastWay* were verified and deemed accurate. Only five deviated by more than $7.5''$ from the actual PLB locations. 129 source locations estimated with Geiger's method were verified and deemed accurate, of which 23 deviated by more than $7.5''$ from the actual PLB locations. During

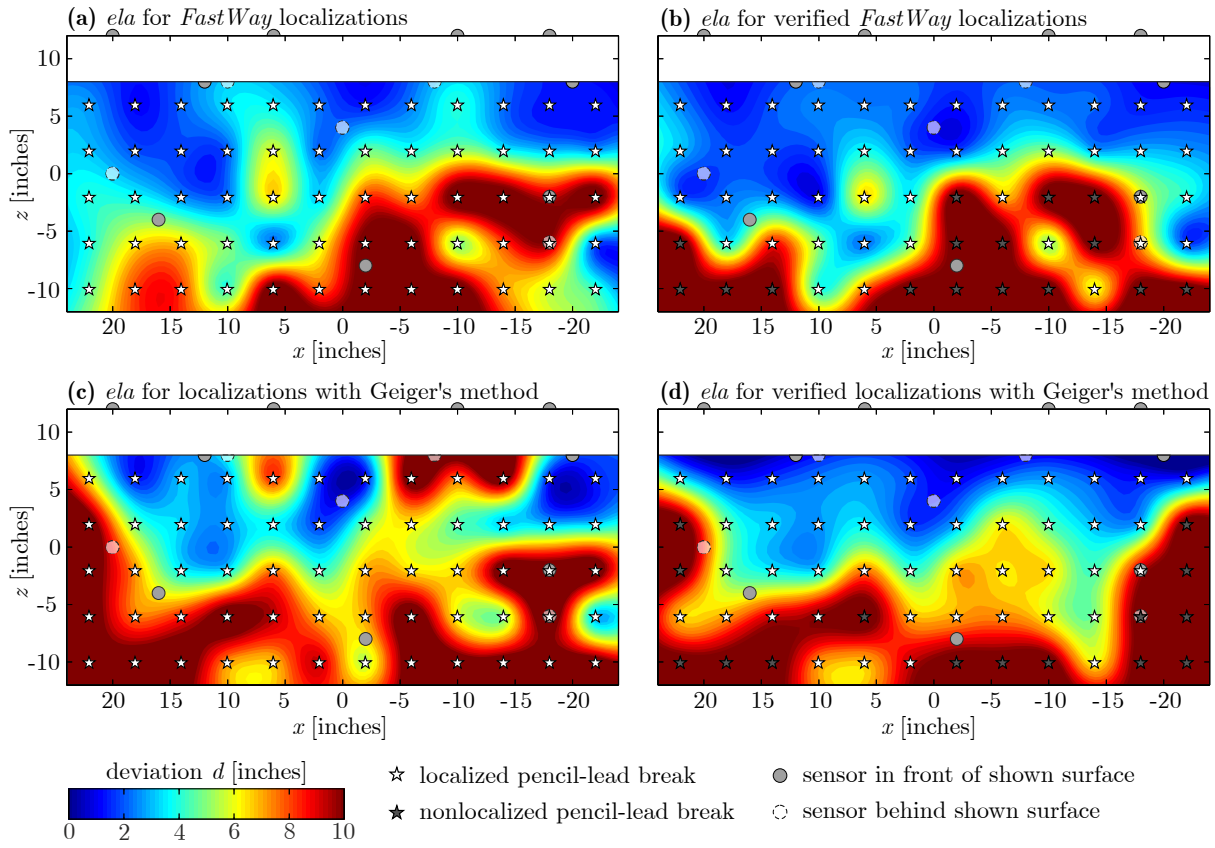

Fig. 7.40: Estimated localization accuracy (*ela*) at the back surface of the specimen, based on the source localization deviations of the pencil-lead breaks SW Ib "Back", and determined for the results obtained with *FastWay* and Geiger's method.

the verification process, 33 inaccurate localizations computed with *FastWay*, and 36 inaccurate localizations computed with Geiger's method were excluded (see Fig. 7.39). Additionally, 41 accurate localizations were excluded (34 computed with *FastWay*, seven computed with Geiger's method). Both methods yielded solid results, but *FastWay* performed a little better than Geiger's method (see Fig. 7.38).

Fig. 7.40 shows that reliable localizations of AEs located in the lower half of the web were unlikely with either of the methods.

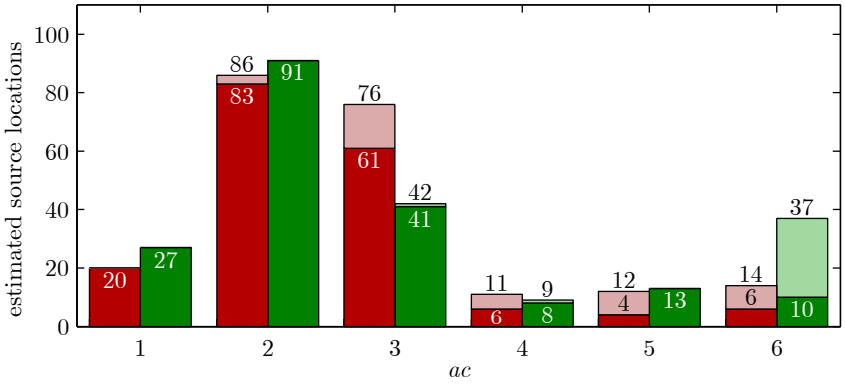

Fig. 7.41: Histogram of the estimated source locations obtained with *FastWay* (red) and Geiger's method (green) for the PLBs SW Ib – "Top", based on the NVM that includes cracks and the new NEL criteria. The excluded estimations are shown in light red and light green, respectively.

7.4.4 Pencil-lead breaks – SW Ib – Crack

An NVM incorporating the known cracks was generated and the source location estimation process was repeated. Although the NVM was a more accurate representation of the specimen than the velocity model used before (without cracks), the performance of *FastWay* did not improve significantly. Therefore, the results of the repeated localization process are not included in this document. Adapting the criteria for the NEL verification, however, had a more significant impact on the performance of *FastWay*. Therefore, the source localization was repeated using the NVM incorporating the cracks combined with the modified NEL criteria. The permissible distance between voxels corresponding to $e_{\text{source};xyz} < 0.05$ was increased from 8″ to 10″, and the permissible distance between voxels corresponding to $e_{\text{source};xyz} < e_{\text{source},AE} + 0.04$ was increased from 10″ to 12.5″ (see Section 7.3.4). All the known cracks were located in the web. The three large cracks correspond to the three notches (see Section 7.1 and Fig. 7.28). These three cracks were incorporated into the NVM, while the smaller cracks were neglected. Another two large cracks that are shown in Fig. 7.28 were located outside the NVM.

The NVM including the cracks had no noticeable effect on the coordinates of the estimated source locations on the surfaces of the flange. However, the new settings for the NEL verification process affected the verification of the results determined with *FastWay*. Therefore, the results of the localization process for all PLBs are presented in the following sections.

PLB "Top" – Crack

The number of technically locatable sources is the same as before, since the picking of the arrival times is not influenced by the NVM or the NEL verification process of the estimated source coordinates. Naturally, the results determined with Geiger's method were also not affected by using the NVM and the NEL verification and therefore did not change. The number of verified and accurate source location estimations computed with *FastWay* increased slightly, from 164 to 170. Unfortunately, the number of verified but inaccurate localizations also increased from eight to ten (see Figs. 7.31 and 7.41). The new NVM and the adapted NEL criteria only had a small effect on the *ela*, as can be seen in Fig. 7.42. Since only six sensors (or even fewer, but at least four) are needed for the localization with *FastWay*, it was not surprising that the cracks located in the web had almost no influence on the localization process. Also, the effect of the adapted NEL on the *ela* was very small. All localization results are listed in Tabs. B.35 to B.39.

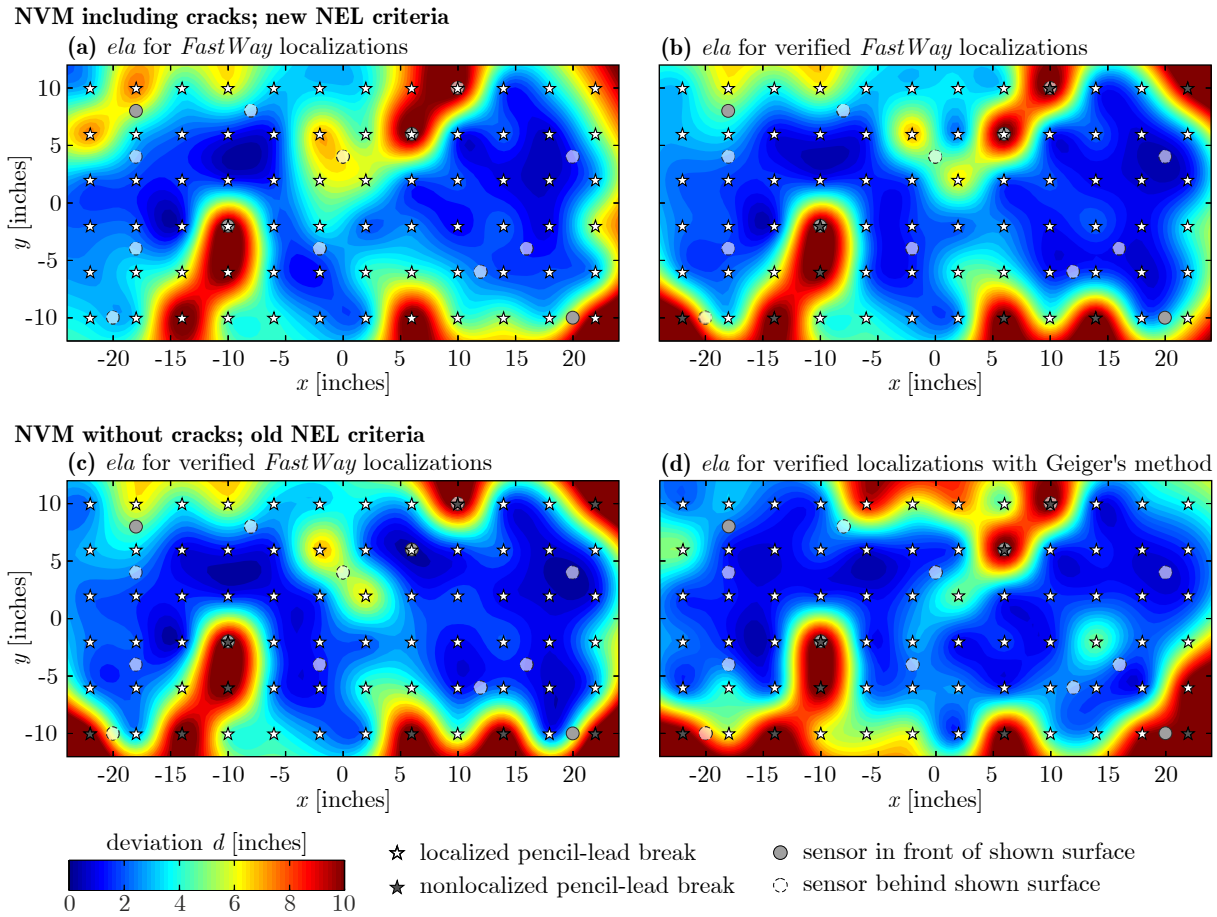

Fig. 7.42: Estimated localization accuracy (*ela*) at the top surface of the specimen, based on the source localization deviations of the pencil-lead breaks SW Ib "Top", and determined for the results obtained with *FastWay* and Geiger's method. Plots (a) and (b) are based on the NVM that includes cracks and the new NEL criteria and were determined with *FastWay*, while plots (c) and (d) were determined with *FastWay* and Geiger's method, respectively, and are also shown in Fig. 7.42.

PLB "Top-Front" – Crack

The new NVM had no impact on the estimated source locations. The adaptation of the NEL criteria resulted in an additional three verified source locations, two of which were accurate (*ac* 3), while the third one was inaccurate (*ac* 6). All localization results are listed in Tab. B.40.

PLB "Front" – Crack

The number of technically locatable sources was the same as before, since the picking of the arrival time is not influenced by the NVM or the NEL verification process of the estimated source coordinates. Naturally, the results determined with Geiger's method were also not affected by using the NVM and the NEL verification and therefore did not change. The number of verified and accurate source location estimations computed with *FastWay* increased slightly, from 90 to 97. Unfortunately, the number of verified but inaccurate localizations also increased from one to two (see Figs. 7.35 and 7.43). The new NVM and the adapted NEL criteria only had a small effect on the *ela*, as can be seen in Fig. 7.42. The *ela* in the region of the monitored area ($-24'' \leq x \leq 24''$) improved. All localization results are listed in Tabs. B.41 to B.44.

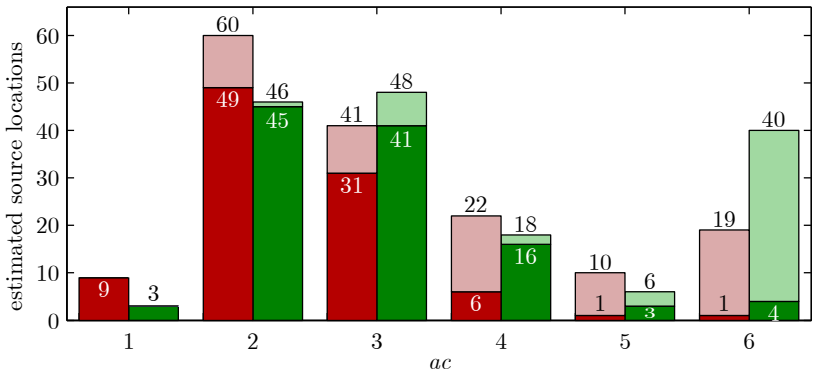

Fig. 7.43: Histogram of the estimated source locations obtained with *FastWay* (red) and Geiger's method (green) for the PLBs SW Ib – "Front", based on the NVM that includes cracks and the new NEL criteria. The excluded estimations are shown in light red and light green, respectively.

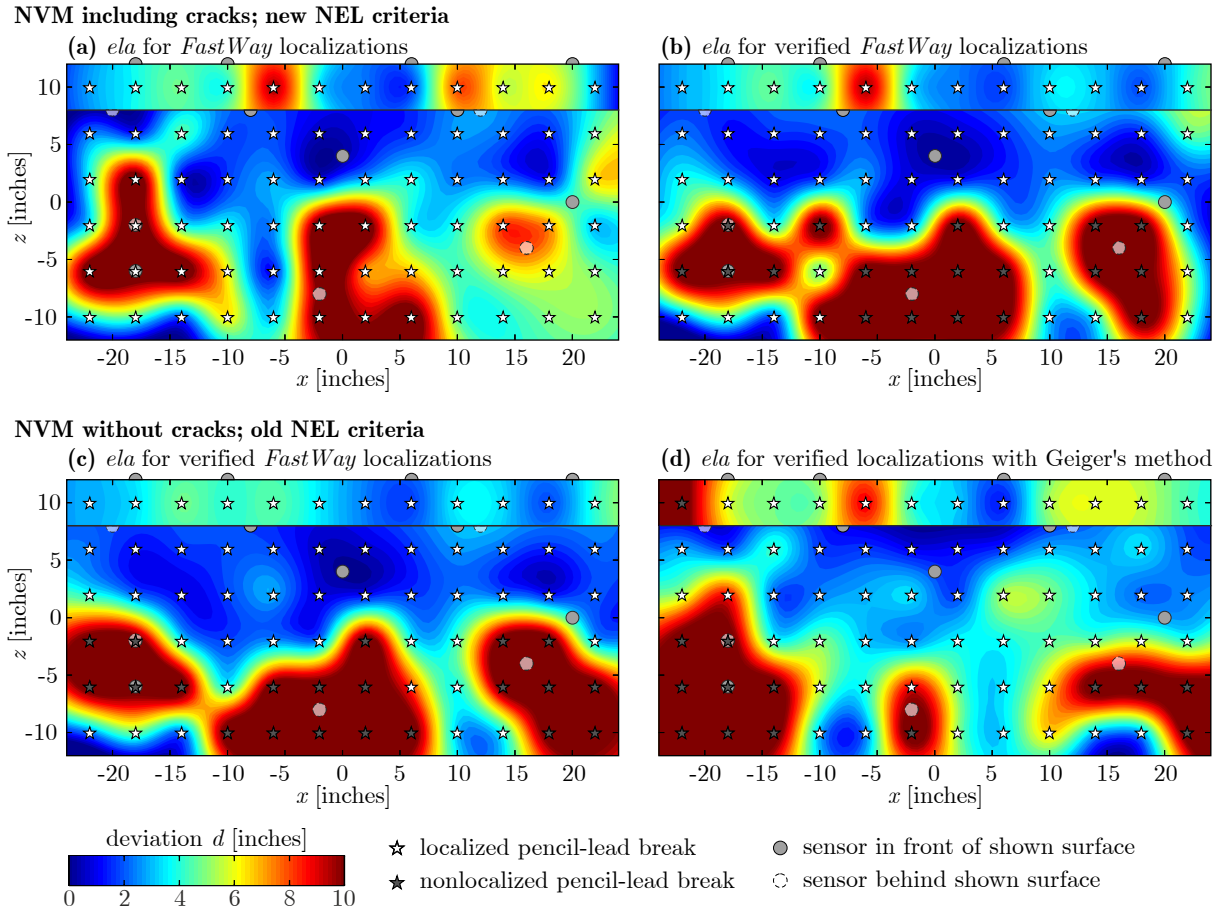

Fig. 7.44: Estimated localization accuracy (*ela*) at the western surface of the specimen, based on the source localization deviations of the pencil-lead breaks SW Ib "Front", and determined for the results obtained with *FastWay* and Geiger's method. Plots (a) and (b) are based on the NVM that includes cracks and the new NEL criteria and were determined with *FastWay*, while plots (c) and (d) were determined with *FastWay* and Geiger's method, respectively, and are also shown in Fig. 7.35.

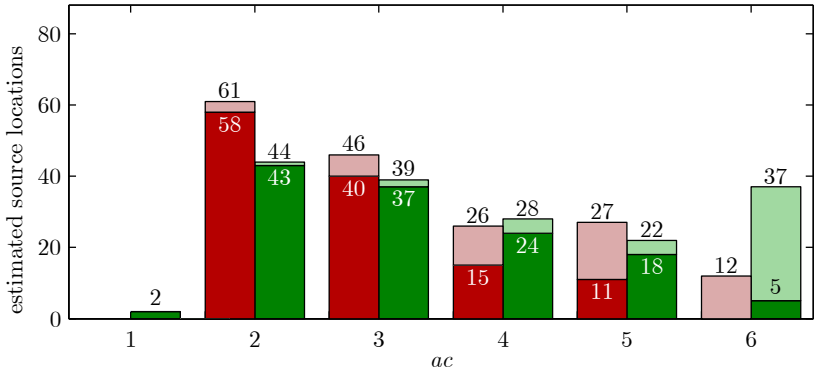

Fig. 7.45: Histogram of the estimated source locations obtained with *FastWay* (red) and Geiger's method (green) for the PLBs SW Ib – "Back", based on the NVM that includes cracks and the new NEL criteria. The excluded estimations are shown in light red and light green, respectively.

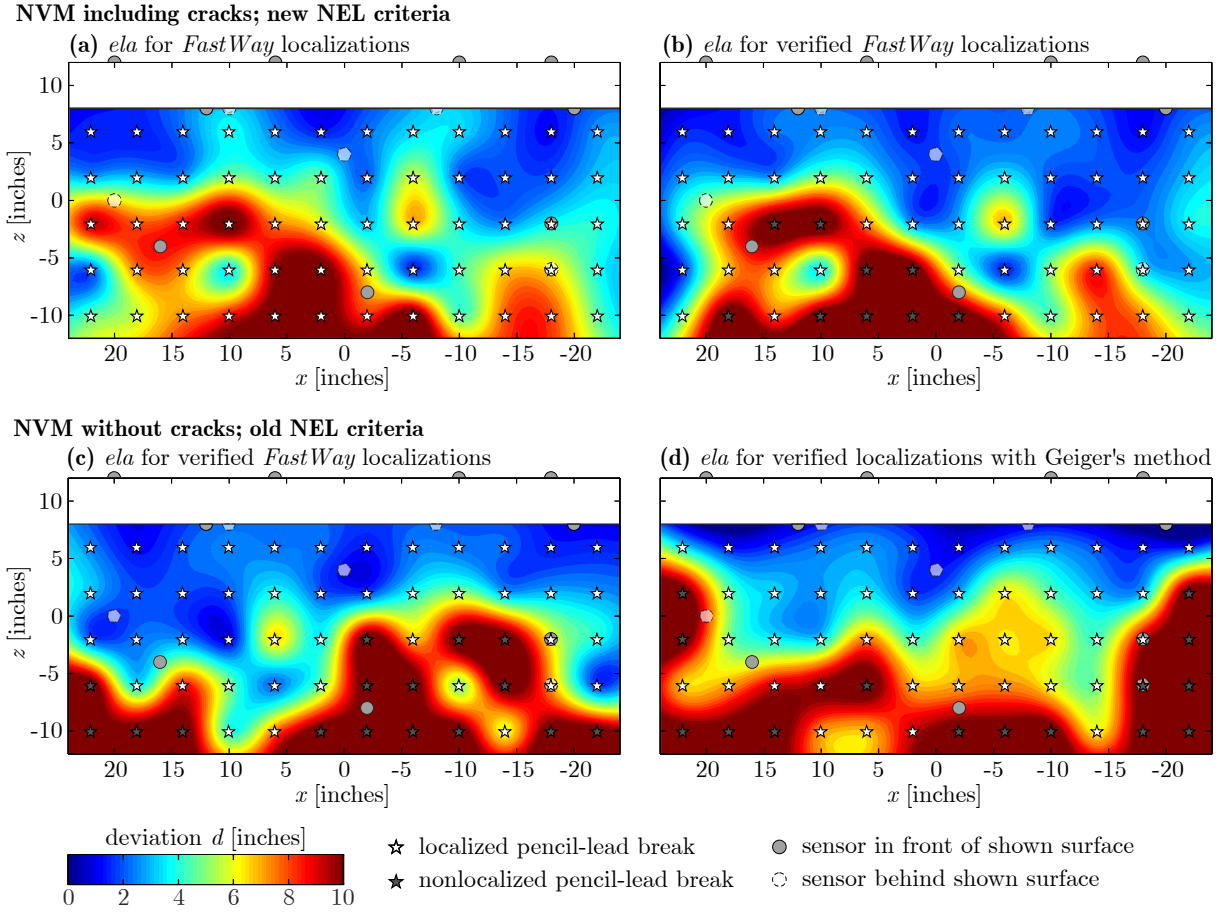

Fig. 7.46: Estimated localization accuracy (*ela*) at the eastern surface of the specimen, based on the source localization deviations of the pencil-lead breaks SW Ib "Back", and determined for the results obtained with *FastWay* and Geiger's method. Plots (a) and (b) are based on the NVM that includes cracks and the new NEL criteria and were determined with *FastWay*, while plots (c) and (d) were determined with *FastWay* and Geiger's method, respectively, and are also shown in Fig. 7.38.

PLB "Back" – Crack

Naturally, the number of technically locatable sources was the same as before. The results determined with Geiger's method did not change either. The number of verified and accurate *FastWay* localizations increased significantly, from 99 to 113. Unfortunately, the number of verified but inaccurate localizations also more than doubled from five to eleven (see Figs. 7.38 and 7.45). The new NVM and the adapted NEL criteria had a clearly visible effect on the *ela*, as shown in Fig. 7.42. The *ela* in the region $-24'' \leq x \leq 0''$ improved, while it decreased in the region $0'' \leq x \leq 24''$. All localization results are listed in Tabs. B.45 to B.48.

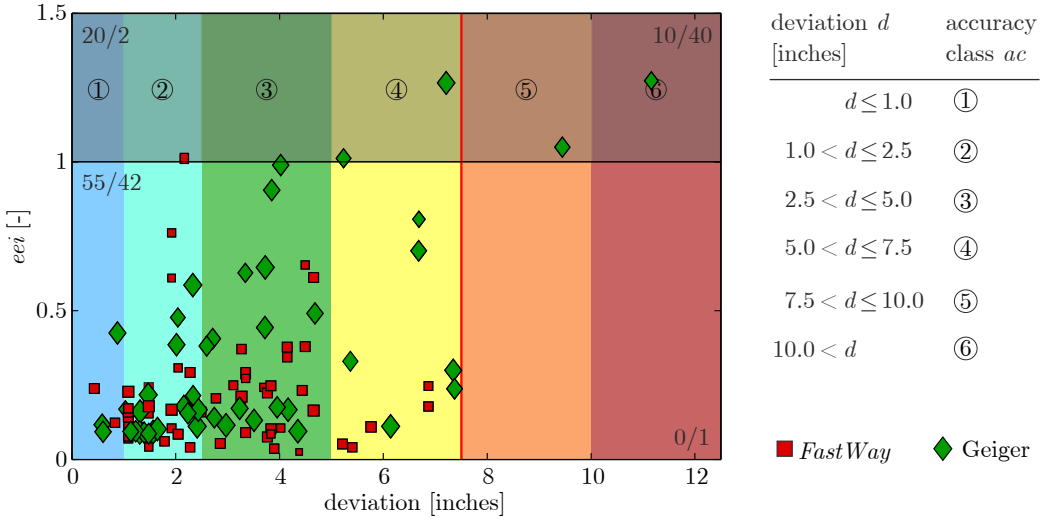

Fig. 7.47: Scatter plot of *eei* vs. deviation d in inches for the PLBs SW IIa on the "Top" surface. The plot is divided into four sections by a line at $eei = 1$ and a line at $d = 7.5''$. Results with $d > 12.5''$ or $eei > 1.5$ are outside the visualized area. The number of results obtained with *FastWay* and Geiger's method in each of the four sections is shown as *FastWay*/Geiger.

7.5 Results of Experimental Set SW II

The focus of this section is on the results from the measurements from test SW II. Conclusions based on these results are shown in Section 7.7.

7.5.1 Pencil-lead breaks – SW IIa

The pencil-lead breaks (PLBs) of this test can be divided into three groups based on their location. Pencil-lead breaks were performed on the western half of the top surface of the flange (referred to as "Top"), on the lateral western surface of the flange (referred to as "Top-Front"), and on the lateral western surface of the web (referred to as "Front"). The "Top" PLBs were performed at each grid point of a $4''$ grid located between $x = 24''$ and $x = 70''$, $y = 2''$ and $y = 10''$, and $z = 12''$. In the area of the load distribution plate, it was impossible to perform PLBs. Hence, no PLBs were performed between $x = 40''$ and $x = 56''$, and $y = 0''$ and $y = 16''$. The "Top-Front" PLBs were performed at each grid point of a $4''$ grid located between $x = 24''$ and $x = 70''$ at $y = 12''$ and $z = 10''$. The "Front" PLBs were performed at each grid point of a $4''$ grid located between $x = 24''$ and $x = 70''$, and $z = -10''$ and $z = 6''$, at $y = 4''$. At each PLB location a minimum of three PLBs was performed. The evaluation of the PLBs was also performed by group.

PLB "Top"

86 PLBs were executed on the western half of the top surface. It was technically possible to estimate the locations of 85 recorded events with both AE source localization methods. In one case, for a PLB located at $x = 62$, $y = -2$, and $z = 12$, the data acquisition system recorded eight sensor signals. However, only one of the recorded signals fulfilled the arrival-time picking criteria (see Section 7.3.1). In another case, the data acquisition system recorded twelve signals, induced by a PLB located at $x = 38$, $y = -2$, and $z = 12$, but only four of them fulfilled the arrival-time picking criteria. It was therefore impossible to compute an error ellipsoid for the source location

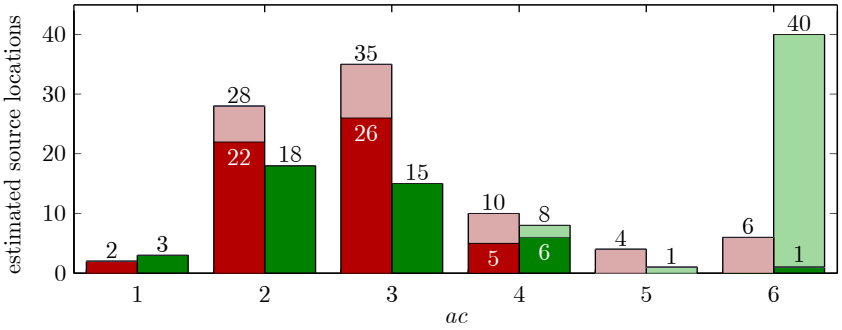

Fig. 7.48: Histogram of the estimated source locations obtained with *FastWay* (red) and Geiger's method (green). The excluded estimations are shown in light red and light green, respectively.

estimations obtained with Geiger's method. Consequently, it was not possible to determine the *eei* values (reported as *eei* = NaN in Tab. C.1), and the estimated source locations were excluded. For the remaining 84 events, at least five signals fulfilling the arrival-time picking criteria were recorded. However, not all of the estimated source locations were accurate, and the computed *eei* values for some of them were greater than 1. Fig. 7.47 shows a scatter plot of *eei* vs. deviation *d*. Unfortunately, there does not seem to be a clear correlation between *eei* and *d*. Nevertheless, the *eei* values were useful for the source location estimations determined with Geiger's method, resulting in the exclusion of 40 of the 41 location estimations with deviations greater than 7.5″. Moreover, only two Geiger source location estimations with $5.0'' < d < 7.5''$ and no results with a deviation of less than 5.0″ were excluded during the evaluation process, as visualized in Fig. 7.48. For the results obtained with *FastWay* the evaluation process seemed conservative. 30 of the 85 estimated source locations were excluded. The remaining 55 source locations had a deviation of $d < 7.5''$, which means that all estimated source locations with $d > 7.5''$ had been excluded in the evaluation process. An additional 20 source location estimations with $d < 7.5''$ were excluded. As mentioned in Section 7.3.4 and shown for example in Fig. 7.12, some of the estimated source locations had to be excluded because it was not possible to narrow down the area where the source was most likely located. Nevertheless, it seemed that *FastWay* was more suitable for estimating the source locations for the PLBs "Top", since more verified source locations (55) with a deviation of $d < 7.5''$ were estimated with this method than by using Geiger's method (42).

The estimated source locations and their deviations from the actual source locations (the PLBs) can be used to verify how well the sensors cover the area of the specimen where the PLB were performed, and to visualize an estimated localization accuracy (*ela*). The *ela* based on the results determined with *FastWay* is visualized in Fig. 7.49 (a) and (b), and that for the results determined with Geiger's method is shown in Fig. 7.49 (c) and (d). Areas where no PLBs were performed are shown in white. *FastWay* yielded more estimated PLB locations with a deviation of $d < 7.5''$. Even before applying the evaluation process described in Section 7.3.4, only two estimated source locations had deviations of $d > 7.5''$. The PLBs of four locations could no longer be localized after the evaluation process. The mean localization deviation of the 28 remaining PLB locations was smaller or remained the same after the evaluation process. 18 source locations estimated with Geiger's method had deviations of $d > 7.5''$. After the evaluation process this number decreased to nine. Eight of the PLBs were classified as unlocatable. Three of the four PLBs in the ninth PLB location with the coordinates $x = 66''$, $y = -6''$, and $z = 12''$ were also classified as unlocatable. Only one of the four source location estimations passed the verification process but still deviated by more than 21″ (53.34 cm) from the actual source location (see Tab. C.2 and Fig. 7.48).

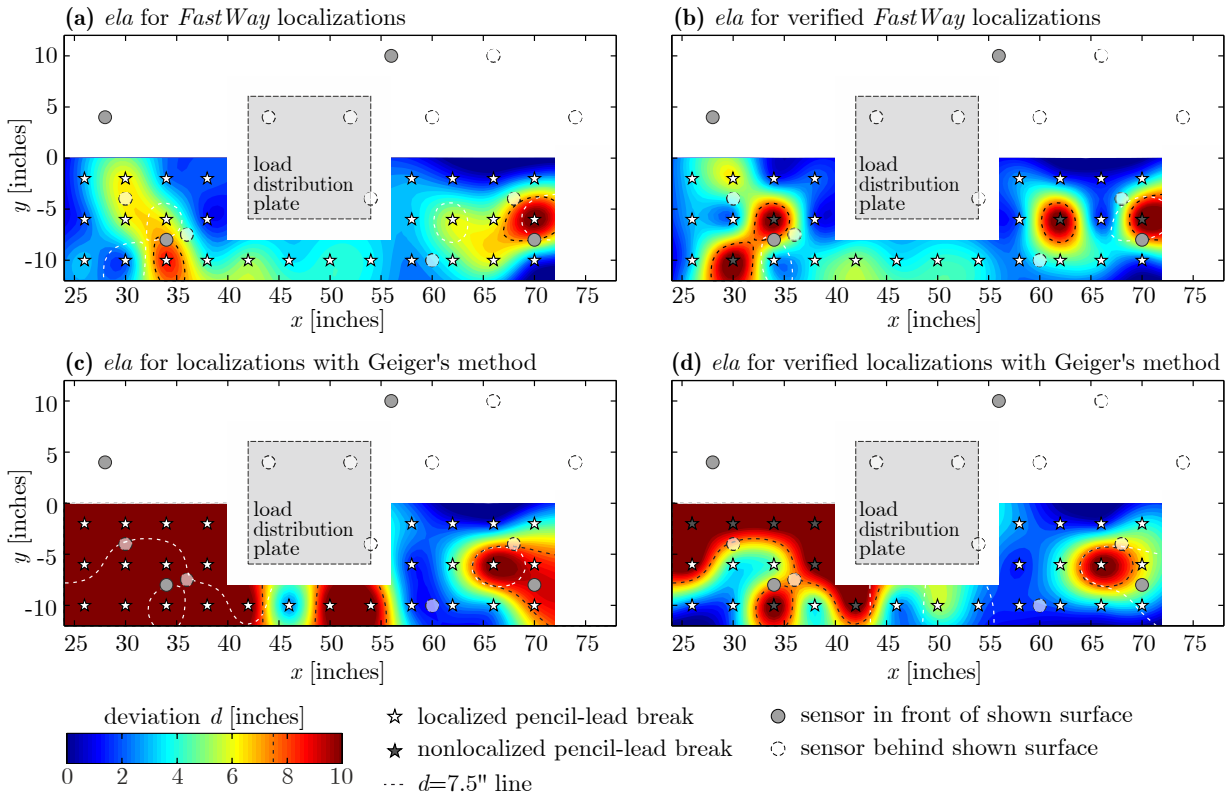

Fig. 7.49: Estimated localization accuracy (*ela*) at the top surface of the specimen, based on the source localization deviations of the pencil-lead breaks SW IIa "Top", and determined for the results obtained with *FastWay* and Geiger's method. The $d = 7.5''$ line of the figure based on all results is shown as a white dashed dotted line in the figure based on the verified results, and vice versa.

PLB "Top-Front"

37 PLBs were performed on the lateral western surface of the flange. It was technically possible to estimate the locations of all the events with either AE source localization method. For six PLBs, however, only four signals fulfilled the arrival-time picking criteria (see Section 7.3.1). Hence, it was not possible to compute an error ellipsoid, and therefore no *eei* values could be determined. For these six PLBs, the letters 'NaN' are shown in the eei_G column of Tab. C.3. At least five signals fulfilling the arrival-time picking criteria were recorded for the remaining 31 PLBs. For these 31 PLBs, Fig. 7.9 shows a scatter plot of *eei* vs. the deviations between the estimated and the actual source locations (see Section 7.3.4). No sensors were located on the same surface as this set of PLBs. The PLBs were performed at twelve locations (significantly fewer than at the "Top" and the "Front" surfaces). It was possible to compute source location estimations for all of the 36 recorded events using the *FastWay* algorithm. Exactly 75% of the estimated source locations had a deviation of $d < 7.5''$ and an *eei* value of less than 1. Only one of the four source location estimations with a deviation of $d > 7.5''$ had an *eei* value of less than 1 ($eei = 0.23$ and $d = 8.35'' = 21.2$ cm) and was therefore included, while the other three results were excluded. Additionally, six source location estimations with $d < 7.5''$ were excluded during the verification process (see Section 7.3.4). 24 source location estimations (66.7%) obtained with Geiger's method had a deviation of $d < 7.5''$ and an *eei* value of less than 1. Only two of the eight source location estimations with a deviation of $d > 7.5''$ had an *eei* value of less than 1 and were therefore not excluded; the other six results were excluded. Only three source location estimations with $d < 7.5''$ were excluded during the verification process. One of the

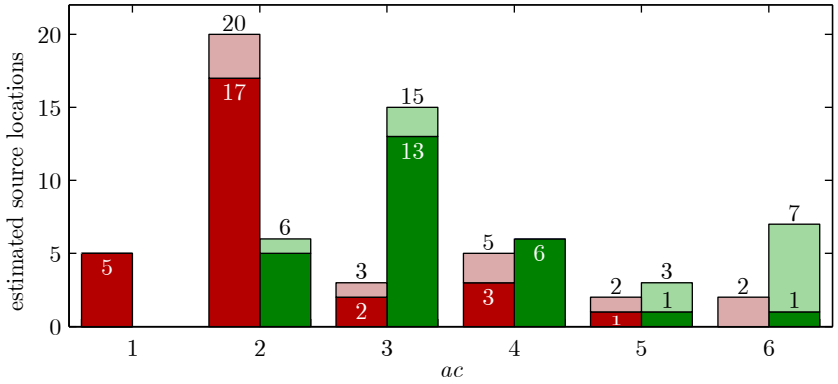

Fig. 7.50: Histogram of the estimated source locations obtained with *FastWay* (red) and Geiger's method (green) for the PLBs SW IIa – "Top-Front". The excluded estimations are shown in light red and light green, respectively.

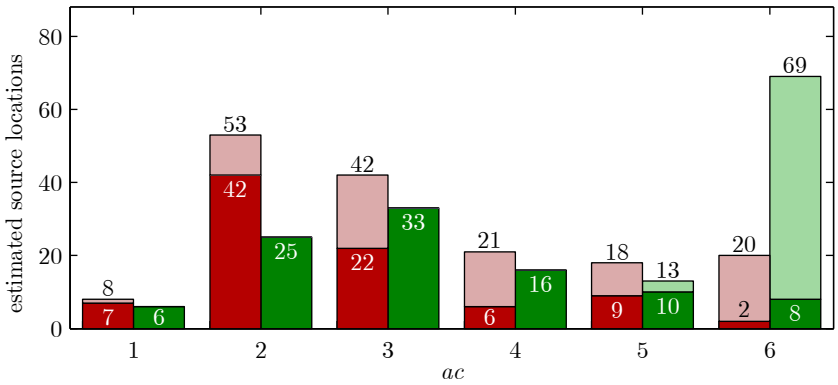

Fig. 7.51: Histogram of the estimated source locations obtained with *FastWay* (red) and Geiger's method (green) for the PLBs SW Ib – "Front". The excluded estimations are shown in light red and light green, respectively.

PLB locations could not be localized with either method. Surprisingly, this PLB was located in the central area of the monitored flange (coordinates $x = 46''$, $y = -12''$, $z = 10''$). Additionally, one PLB location estimation was excluded from the results of both methods (see Figs. 7.53 (b) and (d)). The overall localization accuracy of the results determined with Geiger's method is sufficient. The localization accuracy of the results determined with *FastWay* is satisfactory.

Again, the estimated source locations and their deviations from the actual source locations were used to verify how well the sensors covered the area of the specimen where the PLB were performed, and to visualize an estimated localization accuracy (see Fig. 7.53).

PLB "Front"

203 PLBs were performed on the lateral western surface of the web. It was technically possible to estimate the locations of 162 events with the two AE source localization methods. For the remaining 41 PLBs less than four signals fulfilled the arrival-time picking criteria (see Section 7.3.1); these results were therefore excluded. For 15 PLBs exactly four recorded signals fulfilled the arrival-time picking criteria. Consequently, it was not possible to compute an error ellipsoid and to determine *eei* values. For these PLBs the letters 'NaN' are listed in the eei_G column of Tabs. C.4 to C.6.

The computed localization estimations determined with both methods were verified in the same way as the estimations reported in Section 7.3.4). 64 source estimations determined with Geiger's method were excluded because they deviated from the real source location by more

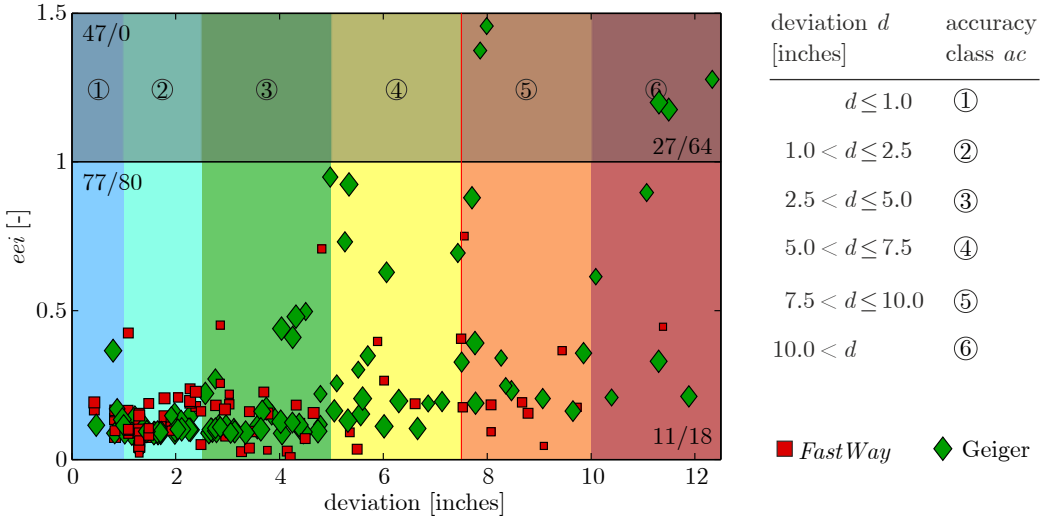

Fig. 7.52: Scatter plot of *eei* vs. deviation d in inches for the PLBs on the "Front" surface. The plot is divided into four sections by a line at $eei = 1$ and a line at $d = 7.5''$. Results with $d > 12.5''$ or $eei > 1.5$ are outside the visualized area. The number of results obtained with *FastWay* and Geiger's method in each of the four sections is shown as *FastWay*/Geiger.

than $7.5''$. However, 18 of the 98 verified results also deviated by more than $7.5''$ from the locations of the corresponding PLBs. None of source location estimations obtained with Geiger's method with $d < 7.5''$ were excluded. 74 source location estimations obtained with *FastWay* were excluded during the verification process. Only 27 of them deviated by more than $7.5''$ from the actual source locations (36.5% of the excluded results). Additionally, 11 of the 88 verified source locations deviated by more than $7.5''$ from the locations of the PLBs, leaving only 77 verified results with sufficient localization accuracy. It is remarkable that all exclusions of results determined with *FastWay* were made because the results did not satisfy the criteria described in the last paragraph of Section 7.3.4. Hence, *eei* values of less than 1 and the letters 'NEL' are listed in the *FastWay* - *eei* column in Tabs. C.4 to C.6.

Again, the estimated source locations and their deviations from the actual source locations were used to verify how well the sensors covered the area of the specimen where the PLBs were performed, and to visualize an estimated localization accuracy (see Fig. 7.53). Fig. 7.53 shows the *ela* for the western side of the flange and the web. Fig. 7.53 (c) shows that the estimated localization accuracy of Geiger's method (for the unverified results) is insufficient for most cases. The localization deviations in the left half of the investigated surface ($24'' \leq x \leq 43''$) and the lower part of the web ($-12'' \leq z \leq -5''$) are almost exclusively greater than $7.5''$. The areas representing an estimated localization accuracy of less than $2.5''$ (corresponding to *ac* 1 and 2; visualized in blue) are comparatively small and located mainly in the upper central section of the monitored area. The verification of the source location estimations led to a significant improvement in the *ela*. However, 17 PLB locations were identified as unlocatable. Most of these unlocatable PLB locations were located outside the area surrounded by the sensors, at the bottom edge of the web. The area with an estimated localization accuracy of $d \leq 2.5''$ remained comparatively small (see Fig. 7.53 (d)). The visualization of the *ela* based on the unverified *FastWay* results (shown in 7.53 (a)) exhibits a considerably smaller area with $d > 7.5''$ compared to that shown in Fig. 7.53 (c). The area representing an *ela* of $d \leq 2.5''$ in 7.53 (a) is significantly larger than that in 7.53 (c). The verification of the source location estimations determined with *FastWay* made it easier to distinguish between areas with poor and good *ela* (shown in red and in blue, respectively, in 7.53 (b)). During the verification process, almost the same number of PLB location estimations were excluded from the results obtained with *FastWay* and Geiger's method

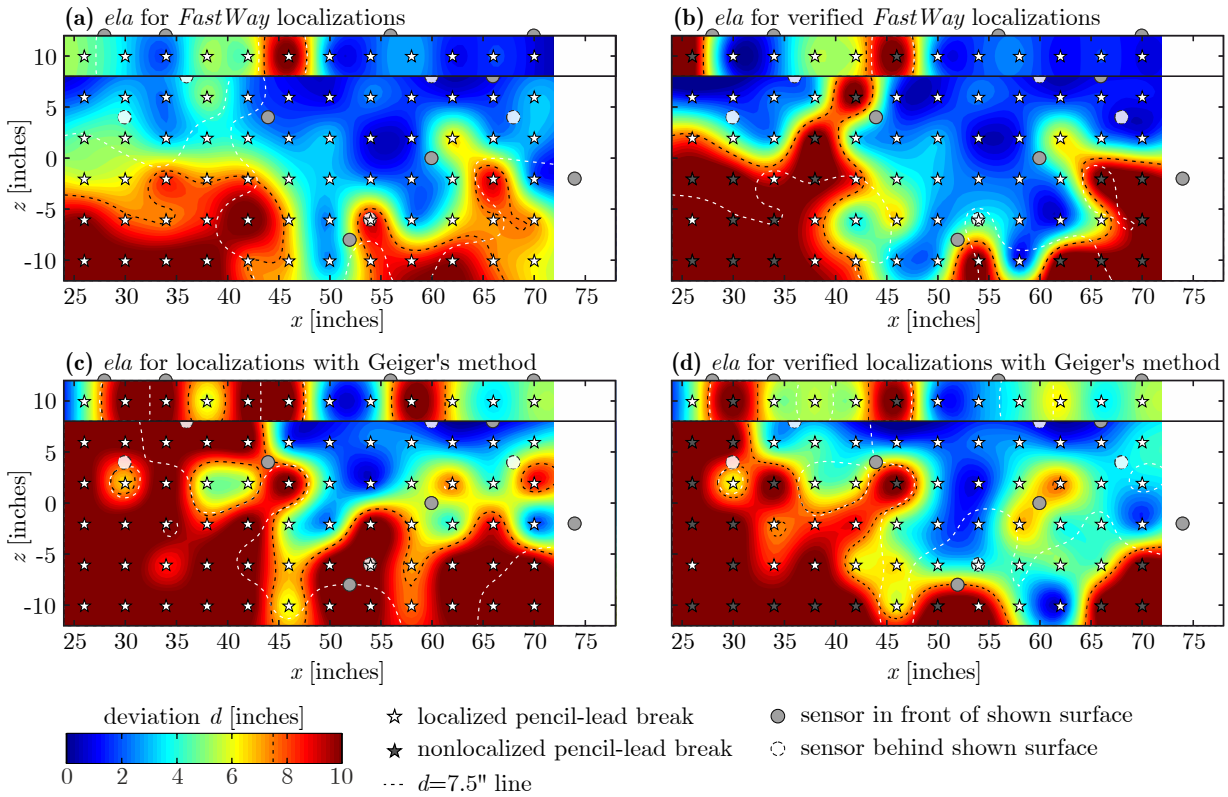

Fig. 7.53: Estimated localization accuracy (*ela*) at the top surface of the specimen, based on the source localization deviations of the pencil-lead breaks SW IIa "Top-Front" and "Front", and determined with *FastWay* and Geiger's method. The $d = 7.5''$ line of the figure based on all results is shown as a white dashed dotted line in the figure based on the verified results, and vice versa.

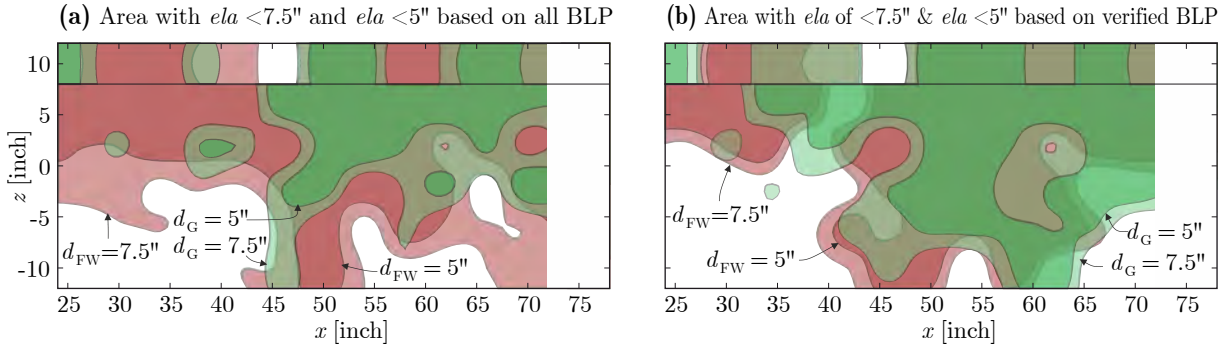

Fig. 7.54: Estimated localization accuracy (*ela*) based on the source localization deviations of the pencil-lead breaks (PLB), determined with *FastWay* (red) and Geiger's method (green).

(16 and 17, respectively). Unfortunately, during the verification process not all unlocatable PLB locations could be identified (marked with white source symbols in the red area of Figs. 7.53 (b) and (d), and listed in Tabs. C.4 to C.6).

In Fig. 7.54, the *ela* areas representing $d \leq 7.5''$ and $d \leq 5''$ for the two localization estimation methods were overlaid for (a) all the results and (b) only the verified results. Fig. 7.54 clearly shows that *FastWay* yielded more accurate source location estimations when the verification process was not applied. However, the performance of Geiger's method clearly improved due to the verification process. When the estimated source locations were verified the size of the *ela* area with $d < 7.5''$ seemed to be the same for both methods. However, if a more accurate source location estimation was required (e.g., with an ela of $d < 5''$), *FastWay* was more suitable.

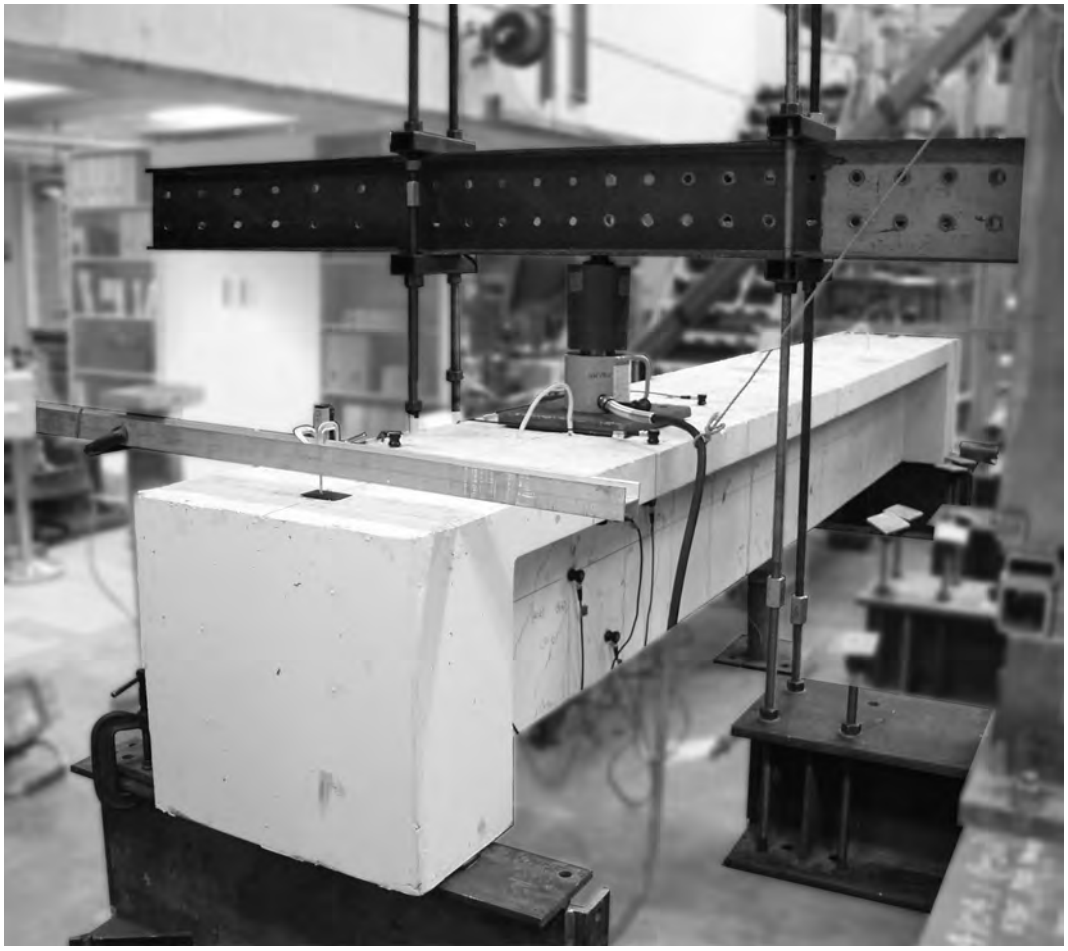

Fig. 7.55: Test setup of shear test SW II.

7.5.2 Shear Test – SW II

As mentioned above, the beam was loaded with a hand-pump-controlled hydraulic ram. The load was applied to the beam via a steel plate at a single load introduction point. Hence, the test was a three-point bending test. The beam was loaded in eight load cycles (listed in Tab. 7.5).

Each of the load cycles consisted of four steps. During the first step, "load", the load was increased from A to B (see Tab. 7.5). After load B had been reached, no further hydraulic fluid was pumped into the ram. The applied force was then permitted to decrease slowly from B to C, during the step called "hold". When the number of recorded AE (hits) had decreased to nearly zero, the beam was unloaded until a load of approximately 5 kips (22.24 kN) was reached. This step from load C to D was called "unload". Subsequently, the load was held again until the number of recorded AE (hits) had decreased to nearly zero. This step from D of the load cycle to A of the next load cycle was also called "hold". Load cycles 1 and 8 were slightly different from the other six cycles. In load cycle 1, the beam was loaded from 0 kips to 15.11 kips (67.21 kN). The load was applied in three steps of approximately 5 kips each, each step followed by a short phase in which the load was not increased (see Fig. 7.56). These three load steps were considered as one (A1 to A2). In load cycle 8, the beam was not unloaded down to 5 kips but to approximately 30 kips (133.4 kN). The load of 30 kips was chosen so as to keep the cracks open while the pencil-lead breaks SW IIb were performed. The deflection of the beam remained low throughout the test. The maximum deflection, measured during load cycle 8, was

LS	t [s]	F [kips]	
1A	2,551	-0.02	load
1B	2,771	-15.11	hold
1C	2,987	-14.37	unload
1D	3,002	-4.76	hold
2A	3,077	-5.01	load
2B	3,141	-20.37	hold
2C	3,370	-19.03	unload
2D	3,402	-5.00	hold
3A	3,459	-5.32	load
3B	3,547	-25.19	hold
3C	3,681	-23.97	unload
3D	3,765	-3.89	hold
4A	3,843	-4.33	load
4B	3,960	-30.07	hold
4C	4,192	-28.36	unload
4D	4,218	-4.40	hold
5A	4,267	-4.89	load
5B	4,391	-35.23	hold
5C	4,587	-33.51	unload
5D	4,628	-4.86	hold
6A	4,664	-5.20	load
6B	4,782	-40.11	hold
6C	5,161	-37.98	unload
6D	5,198	-4.81	hold
7A	5,247	-5.43	load
7B	5,397	-45.00	hold
7C	5,585	-43.19	unload
7D	5,615	-4.43	hold
8A	5,661	-5.13	load
8B	5,795	-50.50	hold
8C	6,264	-47.93	unload
8D	6,281	-29.27	

Tab. 7.5: Load steps LS of load cycles 1–8 of shear test SW II

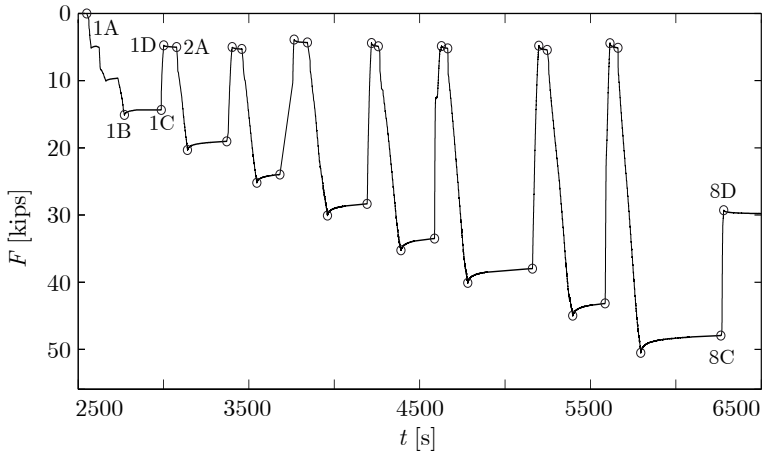

Fig. 7.56: Applied load (load cycles 1–8) in kips vs. time t [s]. Some of the points listed in Tab. 7.5 are marked on the load–time curve.

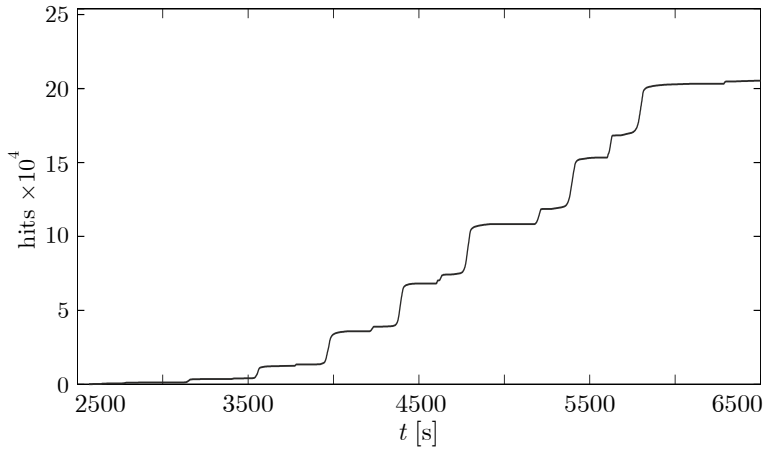

Fig. 7.57: Cumulative hits recorded over time. The time line corresponds to that of Fig. 7.56

about $w_{eff} = 7 \times 10^{-}2$ inches (less than 2 mm). Fig. 7.59 shows the deflection over time. The time axis of this figure corresponds to that of Fig. 7.56. After loading the beam and holding the load until almost no more hits were recorded, the data acquisition system was turned off for the visual inspection of the beam, in order to avoid recording artificial AEs (e.g., caused by touching the beam). During that time no white noise was recorded and the graph shows a straight line connecting the last discrete point recorded before turning off the acquisition system to the first discrete point recorded after turning it on again (see Fig. 7.59). After completion of the test a small plastic deformation of less than 0.1 mm remained. The maximum compression of the southern neoprene support strip (the strip closer to the load introduction point and the LVDT Ⓒ) was 0.2 mm.

During shear test SW II the wave signals of 234,369 hits (see Section 7.2.3 – Data acquisition system) were recorded. Fig. 7.57 shows the cumulative number of hits over time. From these

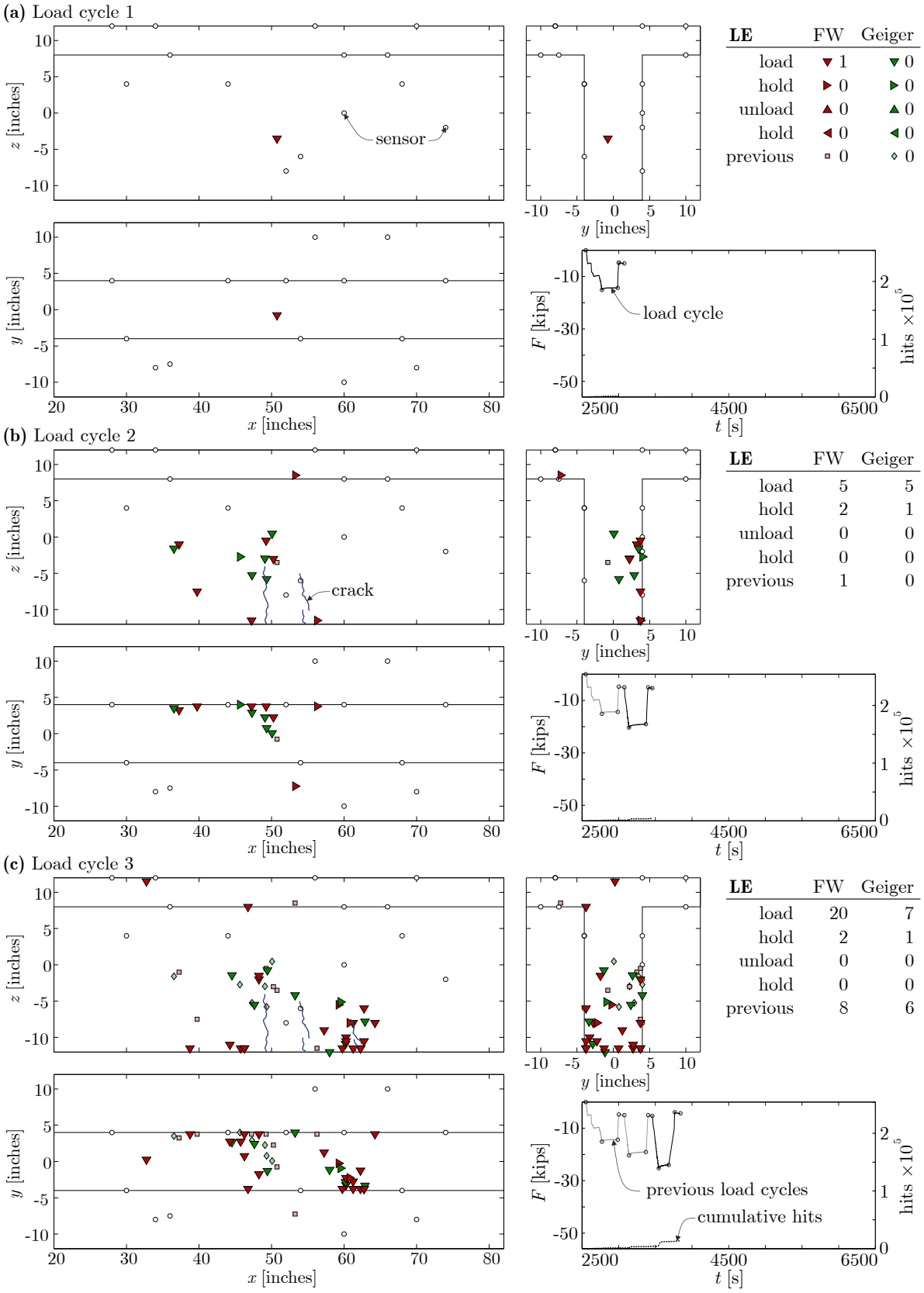

Fig. 7.58: Estimated source locations determined with *FastWay* and the Geiger's method, visualized in 3 sections for load steps 1 to 8. The load step and the cumulative hits are visualized in a small figure downright. The numbers of localized sources are listed top right.

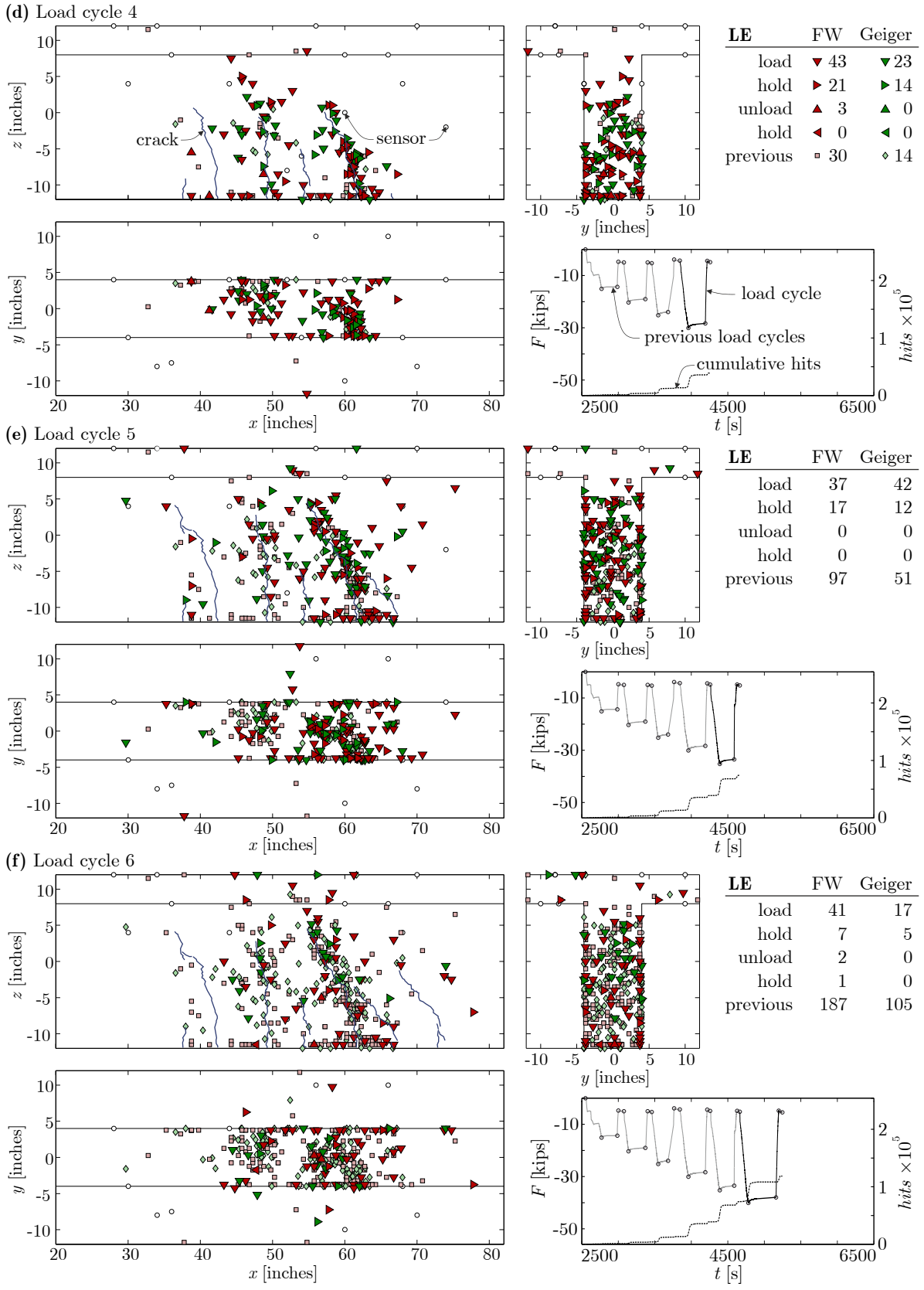

Fig. 7.58 (cont.)**:** Estimated source locations determined with *FastWay* and the Geiger's method, visualized in 3 sections for load steps 1 to 8. The load step and the cumulative hits are visualized in a small figure downright. The numbers of localized sources are listed top right.

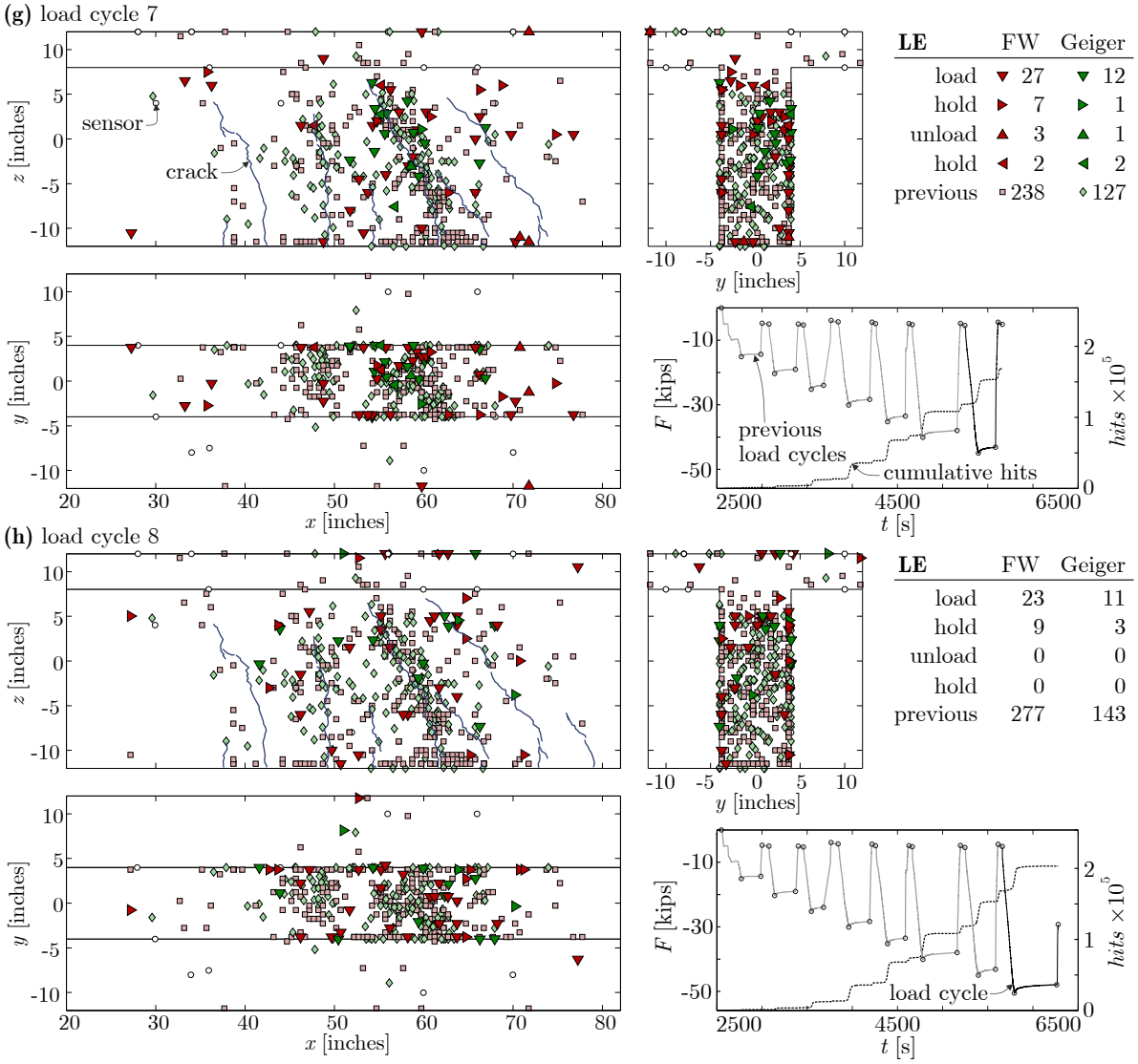

Fig. 7.57 (cont.)**:** Estimated source locations determined with *FastWay* and the Geiger's method, visualized in 3 sections for load steps 1 to 8. The load step and the cumulative hits are visualized in a small figure downright. The numbers of localized sources are listed top right.

results it was possible to estimate the locations of 309 AEs using *FastWay*, and of 157 AEs using Geiger's method. The source locations of 103 events could be estimated with both methods. The estimated source location coordinates and source times determined with both methods are listed in Tabs. C.8 to C.16. The ratio of hits to the number of estimated source locations for *FastWay* is 758 to 1. Considering that generally a minimum of five signals (five hits) fulfilling the criteria formulated in Section 7.3.4 were needed to estimate the location of an AE, this ratio seems reasonable. In addition, almost all of the localized AEs were recorded by 12 to 14 sensors (12 to 14 hits). The cumulative number of detected AEs does not completely reflect the development of the cumulative hits.

Fig. 7.58 (a) to (h) shows the development of AE localizations during the eight load cycles. The positions of the estimated source locations are shown in three cross-sections (x–z section, y–z section, and x–y section). The source locations estimated with *FastWay* are labeled with green markers, while those estimated with Geiger's method are labeled with blue markers. The

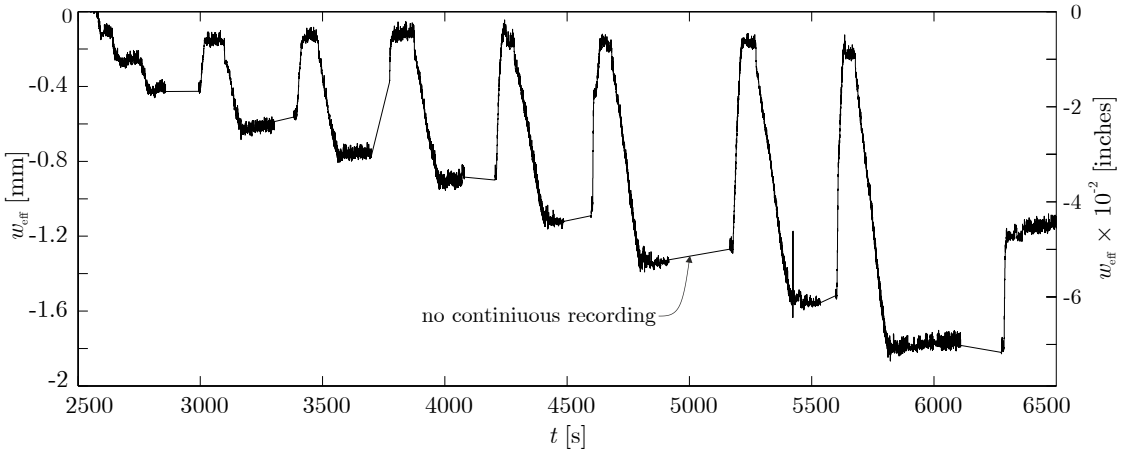

Fig. 7.59: Effective deflection of the beam at midd-span w_{eff} over the time t during shear test SW II

shape of the marker indicates if the AE occurred during loading ($\triangledown$), the hold phase after loading ($\triangleright$), unloading ($\triangle$), the hold phase after unloading ($\triangleleft$), or during a previous load cycle. In order to improve the legibility of the figure, a small table in the upper right corner shows a summary of the number of localized events (LE) for each phase of the load cycle, as well as the number of LEs during all previous load cycles for both applied source location estimation methods. In addition, the load cycles and cumulative number of hits over time is shown in the lower right corner of the figure. The relevant load cycle is highlighted.

During load cycle 1, very few hits were recorded, and only one source location could be estimated using *FastWay*. The location of this AE was estimated as being almost at the center of the monitored part of the web, and not in an area under maximum tensile stress (see Fig. 7.58 (a)). Additional AEs occurred during load cycle 2 in the area around the first localized AE. The AEs occurred mainly in the eastern part of the web. During load cycle 2, the hit activity was slightly greater than during load cycle 1. During load cycle 3 the first AEs in the lower part of the web that could be localized. These AEs were spread across the entire width of the web. Besides an increasing number of localized AEs, the number of hits also increased significantly during this load cycle. Load cycle 4 saw the most AE action of all eight load cycles. The locations of 67 AEs could be estimated using *FastWay*. Using Geiger's method, only 37 AE locations could be estimated. The x–y section in Fig. 7.58 (d) shows that most of the estimated sources determined with both methods are clustered around an almost horizontal line which starts at the bottom of the web at $x \approx 60''$, which indicates the development of a crack. During load cycles 5 to 8, additional AEs were localized alongside this line which eventually reached the web. Some additional, more scattered and isolated AEs were also detected.

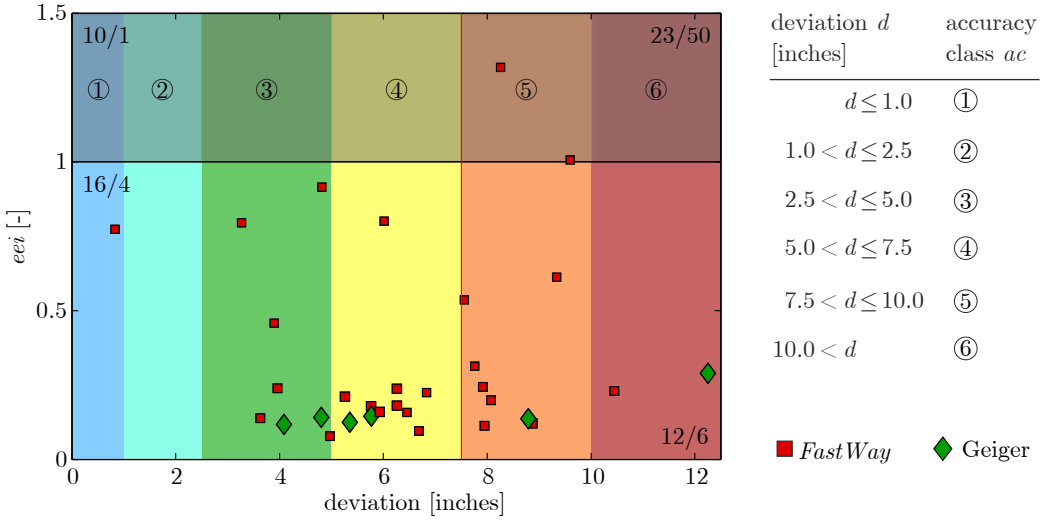

Fig. 7.60: Scatter plot of *eei* vs. deviation d in inches for the PLBs SW IIb on the "Top" surface. The plot is divided into four sections by a line at $eei = 1$ and a line at $d = 7.5''$. Results with $d > 12.5''$ or $eei > 1.5$ are outside the visualized area. The number of results obtained with *FastWay* and Geiger's method in each of the four sections is shown as *FastWay*/Geiger.

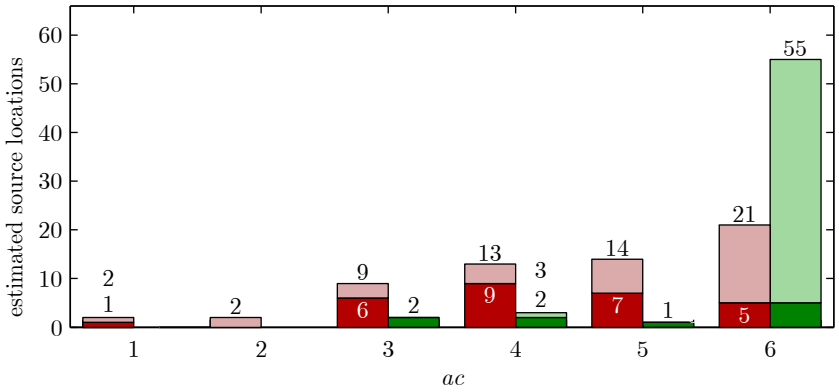

Fig. 7.61: Histogram of the estimated source locations obtained with *FastWay* (red) and Geiger's method (green) for the PLBs SW IIb – "Top". The excluded estimations are shown in light red and light green, respectively.

7.5.3 Pencil-lead breaks – SW IIb

All the pencil-lead breaks of test SW IIa (see Section 7.5.1) were performed again after completion of the destructive shear test (see Sections 7.2.2 and 7.5.2). The pencil-lead breaks were again divided into the three groups described in Section 7.5.1, namely "Top", "Top-Front", and "Front". A load of 30 kips (133.5 kN) was applied to the beam in order to ensure that the cracks remained open. The velocity models used as input for *FastWay* did not take into account the presence of the cracks. The same model as for the PLBs SW IIa was used.

PLB "Top"

84 PLBs were performed on the western half of the top surface. It was technically possible to estimate the location of 61 recorded events with both AE source localization methods. For all of the 61 events at least five signals fulfilling the arrival-time picking criteria were recorded. However, not all of the estimated source locations were accurate, and the computed *eei* values

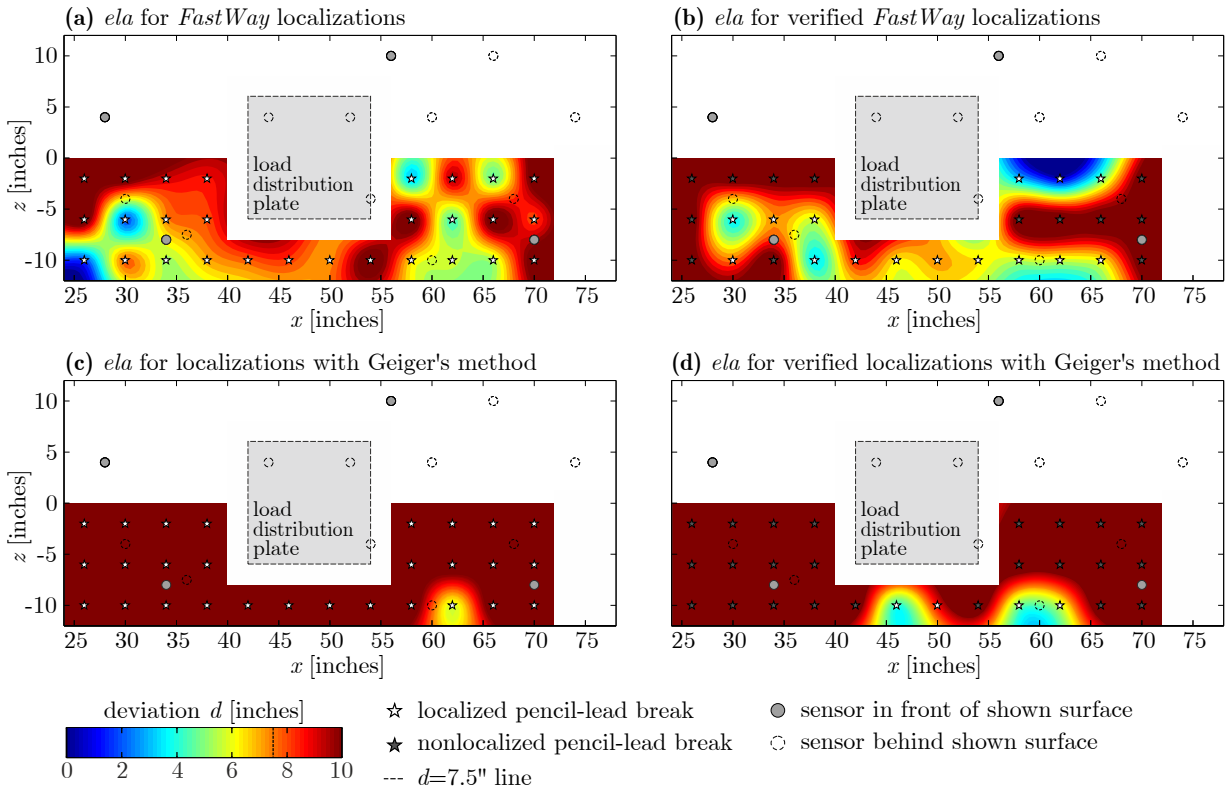

Fig. 7.62: Estimated localization accuracy (*ela*) at the top surface of the specimen, based on the source localization deviations of the pencil-lead breaks SW IIb – "Top", and determined for the results obtained with *FastWay* and Geiger's method.

for some of them were greater than 1. Fig. 7.60 shows a scatter plot of *eei* vs. deviation *d*. Unfortunately, there does not seem to be a clear correlation between *eei* and *d*. The cracks seemed to have a significant impact on wave propagation and the wave propagation path, and hence also on the picking accuracy. Only a small fraction of the estimated source locations were verified and deemed accurate. 16 ($\approx$ 19%) of the 84 localizations determined with *FastWay* had corresponding *eei* values of less than 1 and deviations of less than 7.5″. Four ($\approx$ 5%) of the 84 localizations obtained with Geiger's method had corresponding *eei* values of less than 1 and deviations of less than 7.5″. In total, 18 inaccurate estimations (twelve estimated with *Fastway*, six estimated with Geiger's method) were not excluded during the verification process. On the other hand, 11 estimations (ten estimated with *Fastway*, one estimated with Geiger's method) were excluded, even though they deviated by less than 7.5″ from the actual PLB locations. However, 73 inaccurate estimations were excluded during the verification process (see Fig. 7.60 and 7.61). Fig. 7.61 also shows that most of those estimated source locations were inaccurate and therefore rightfully excluded. Comparing these results with those for the PLBs SW IIa "Top", the uncracked specimen, it can be seen that the number of accurate and verified source location estimations decreased significantly for PLBs SW IIb. For the results determined with *FastWay* the number dropped from 55 to 16 (29%). For Geiger's method the number dropped from 42 to 4 (9.5%).

The visualization of the *ela* in Fig. 7.62 shows that accurate localizations were possible only in individual, isolated small areas. Satisfactory source location estimations were impossible with either method. *FastWay* yielded more verified source location estimations, both accurate and inaccurate. All localization results are listed in Tabs. C.18 and C.19.

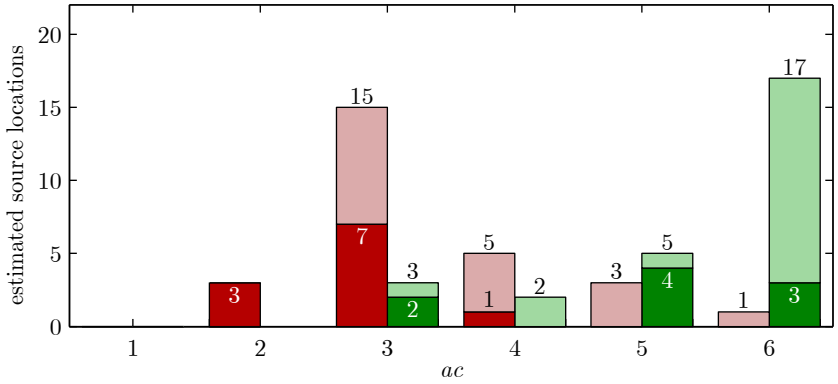

Fig. 7.63: Histogram of the estimated source locations obtained with *FastWay* (red) and Geiger's method (green) for the PLBs SW IIb – "Top-Front". The excluded estimations are shown in light red and light green, respectively.

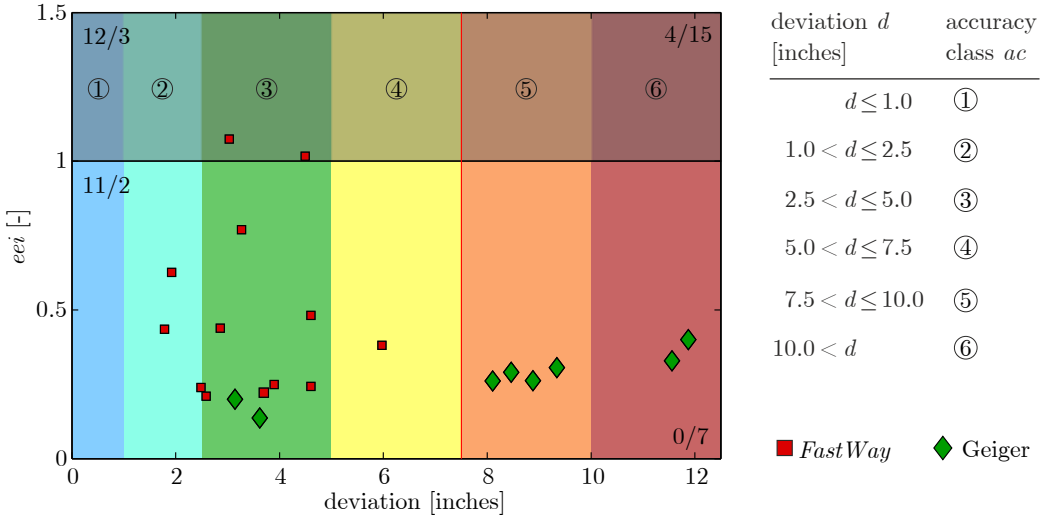

Fig. 7.64: Scatter plot of *eei* vs. deviation d in inches for the PLBs SW IIb on the "Top-Front" surface. The plot is divided into four sections by a line at $eei = 1$ and a line at $d = 7.5''$. Results with $d > 12.5''$ or $eei > 1.5$ are outside the visualized area. The number of results obtained with *FastWay* and Geiger's method in each of the four sections is shown as *FastWay*/Geiger.

PLB "Top-Front"

It was technically possible to estimate 27 PLB locations, which is ten fewer than for the PLBs SW IIa "Top-Front". At least five signals fulfilling the arrival-time picking criteria were recorded for all PLBs. During the verification process, all inaccurate *FastWay* localizations, and 12 of the 23 accurate source location estimations determined with *FastWay* were excluded (see Figs. 7.63 and 7.64). Three of the five accurate localizations but only 15 of the 22 inaccurate source location estimations obtained with Geiger's method were excluded. A comparison of the results of the two localization methods shows that all the verified source location estimations determined with *FastWay* were accurate, while seven (78%) of the nine verified source location estimations determined with Geiger's method were inaccurate.

The visualization of the *ela* in 7.67 shows that accurate near-surface localizations should be possible in the center part of the flange using *FastWay*, but seems unlikely when using Geiger's method. For both localization methods, the *ela* decreased due to the evaluation process, because

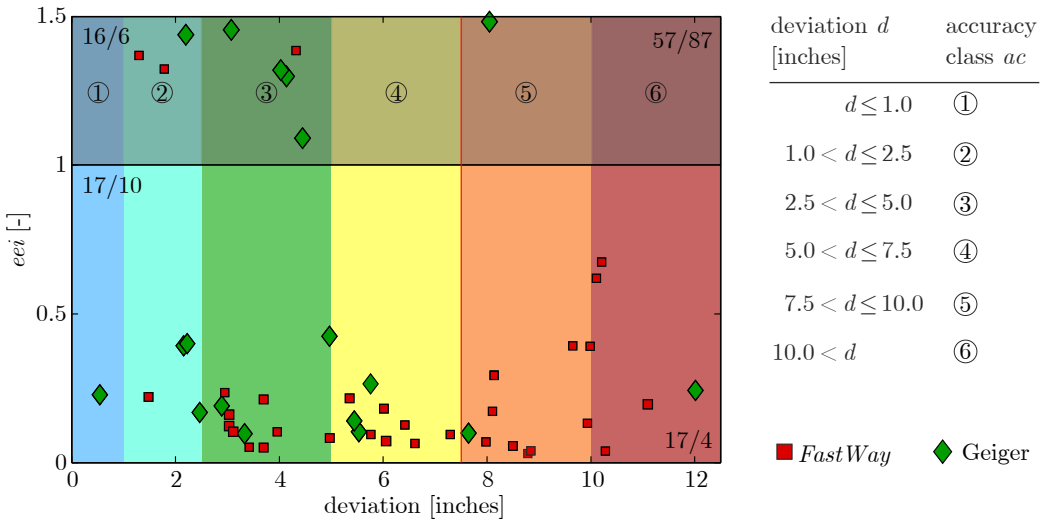

Fig. 7.65: Scatter plot of *eei* vs. deviation d in inches for the PLBs SW IIb on the "Front" surface. The plot is divided into four sections by a line at $eei = 1$ and a line at $d = 7.5''$. Results with $d > 12.5''$ or $eei > 1.5$ are outside the visualized area. The number of results obtained with *FastWay* and Geiger's method in each of the four sections is shown as *FastWay*/Geiger.

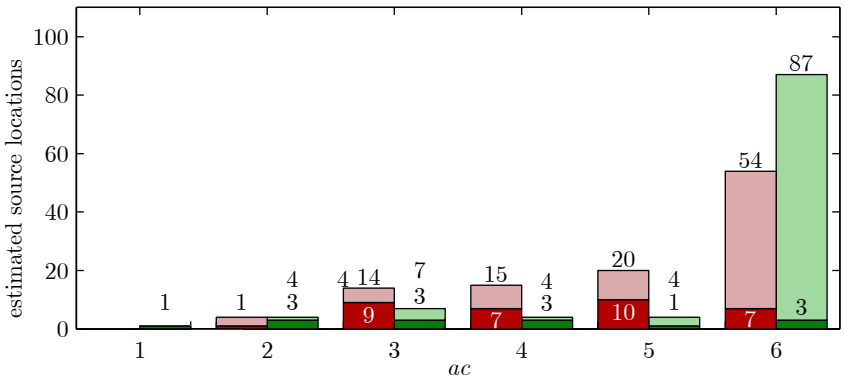

Fig. 7.66: Histogram of the estimated source locations obtained with *FastWay* (red) and Geiger's method (green) for the PLBs SW IIb – "Front". The excluded estimations are shown in light red and light green, respectively.

some source localizations with a satisfactory *ac* were also excluded. The localization results are listed in Tab. C.20.

PLB "Front"

It was technically possible to estimate 107 PLB locations, as opposed to the 162 source location estimations computed for PLBs SW IIa. At least five signals fulfilling the arrival-time picking criteria were recorded for all 107 PLBs. However, most of the estimated source locations were excluded during the verification process, as shown in Fig. 7.66. Only 22 of the 166 excluded results (both localization methods) were accurate. Moreover, 21 inaccurate results were not excluded during the verification process. Hence, only 27 accurate and verified results remained, as shown in Fig. 7.65. Exactly one half of the 34 verified localizations obtained with *Fastway* deviated by more than $7.5''$ from the actual PLB locations and were therefore deemed inaccurate. Additionally, 16 of the 73 excluded source location estimations deviated by less than $7.5''$ from the actual PLB locations and were therefore considered accurate. At least one of the ten PLBs that could not be

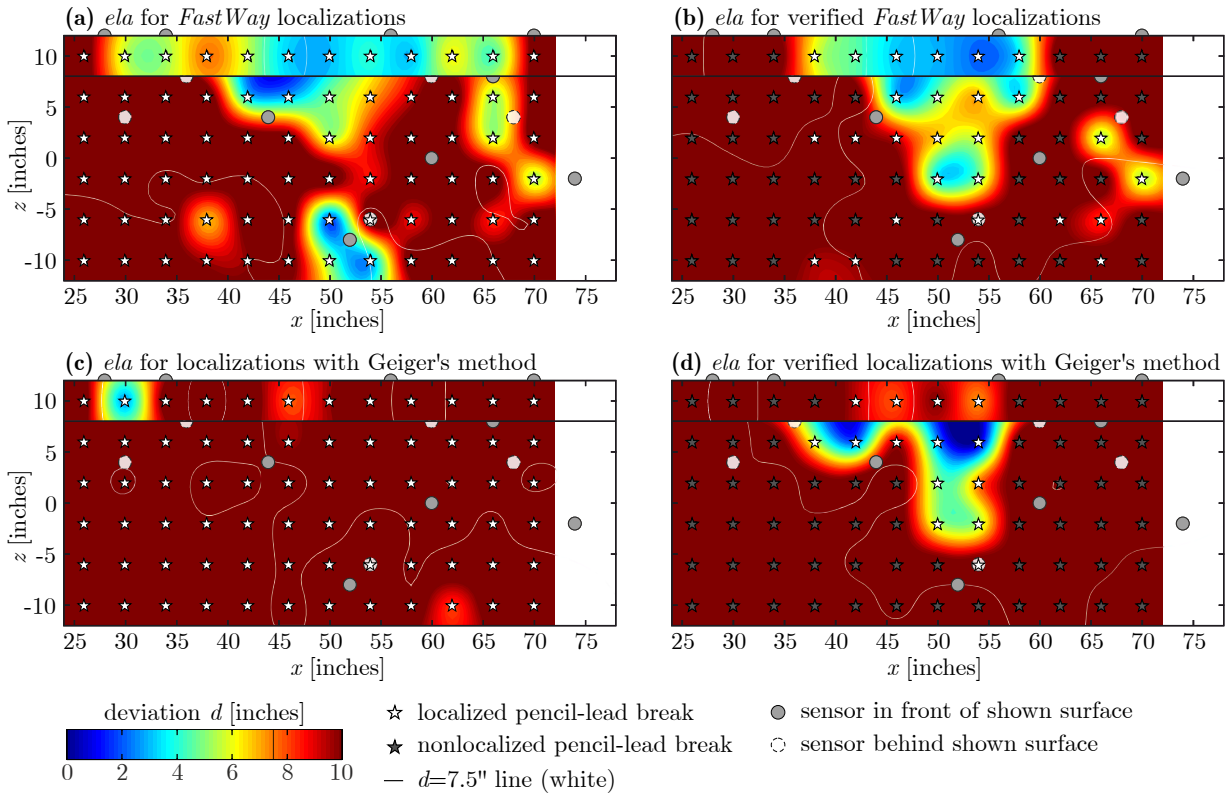

Fig. 7.67: Estimated localization accuracy (*ela*) at the western surface of the specimen (flange and web), based on the source localization deviations of the pencil-lead breaks SW IIb "Top-Front" and "Front", and determined for the results obtained with *FastWay* and Geiger's method. The $d = 7.5''$ line from the PLBs SW Ia visualized in Fig. 7.53 is shown as a white line.

accurately localized with *FastWay* was not excluded, as shown in Fig. 7.67. Only PLBs located in the upper central part of the monitored web area were accurately localized. Similar observations are true for Geiger's method. Only 16 of the 107 events were accurately localized with Geiger's method. Only 10 of those 16 localizations were verified and deemed accurate. Additionally, four inaccurate localizations obtained with Geiger's method were verified and deemed accurate, even though they deviated by more than $7.5''$ from the actual source locations. The remaining 87 inaccurate Geiger localizations were correctly excluded.

The visualization of the *ela* in Fig. 7.67 shows that the area where successful source localizations are likely shrank in comparison with that for the PLBs performed before the destructive test (see Fig. 7.53, and white line in Fig. 7.67). The rather small area where accurate source location estimations were possible was uncracked and surrounded by sensors. Hence, it can be concluded that the cracks have no influence on the wave propagation behavior. Any PLBs located in the leftmost third of the web (visualized in Figs. 7.67 (a) to (d)) were not locatable even for PLBs SW IIa "Front", as the white $d = 7.5''$ line indicates. However, accurate source location estimations were possible in the rightmost third of the web where only two sensors had been mounted. Consequently, the elastic wave induced by a PLB performed in this area had to bypass the crack, or bridge the crack via a reinforcing bar on its way to the other sensors, which resulted in significant damping of the p-wave amplitude. All localization results are listed in Tabs. C.21 to C.23.

7.5.4 Pencil-lead breaks – SW IIb – Crack

An NVM incorporating any cracks visible in pictures of the monitored area was created. The source locations of PLBs SW IIb were estimated a second time using this more precise NVM, and *FastWay*. However, no significant improvement of the estimation accuracy occurred. An adaptation of the NEL verification limits did also not improve the results. Therefore, these results are not presented.

7.6 Results of the Digital Image Correlation (DIC)

It can be stated that the DIC system did not yield the desired results. During bending test SW I, the camera lost focus after load cycle 2, making it impossible to use the pictures of this set. During shear test SW II, the sensors and cables attached to the sensors interfered with the used DIC algorithm. Only small sections of the specimen, where there were no mounted sensors or crossing cables, could therefore be evaluated. The cracks that could be identified from the resulting DIC plots matched the localization results and the photographed crack patterns but did not lead to the identification of any additional cracks. The additional expense for the DIC system did not seem justified for the SW tests, as it did not yield any additional information that had not already been gained through AE analysis and visual inspection of the beam.

7.7 Conclusions

The large-scale experiments showed that *FastWay* can be used successfully for monitoring a large-scale specimen. However, it also showed some limitations of *FastWay*, and AE analysis in general. The two experiments, SW I and SW II, led to different observations, most likely because of the different data acquisition settings and the different sensor layouts (see Section 7.2).

For test SW Ia, the locations of most PLBs could be estimated with satisfactory accuracy with either Geiger's method or *FastWay*. Nevertheless, the overall performance of *FastWay* was better. However, the results also show that it was almost impossible to obtain source location estimations of *ac* 1 even when accurate NVMs were used. The large voxel size (edge length $1/2''$) and low vicinity level (v_{lev}) led to inaccurate estimations of the fastest wave propagation paths.

The data acquisition settings for bending test SW I caused memory overload, and a large part of the measured wave signals were not saved. Because of this, the informative value of SW I is limited. Nevertheless, one large crack (located close to the notch at $x = 10''$) could be identified from the estimated source locations. A large number of AEs could be detected in the area around the cracks developed from the other two notches. However, it was impossible to estimate the crack locations based on these AEs (see Fig. 7.28).

Surprisingly, the cracks only had a minor effect on the source localization results of PLB set SW Ib. For all PLB sets, the area with an *ela* of $d < 7.5$ shrank due to the cracks, but the PLBs on the flange and the upper half of the web were still locatable. However, most of the PLBs performed on the lower half of the web could not be localized.

The results of the PLB set SW IIa showed that the sensors in the chosen sensor layout did not seem to be able to detect AEs occurring in the entire web (see Fig. 7.53) and parts of the flange (see Fig. 7.49). In this more challenging situation *FastWay* performed significantly better than Geiger's method.

In shear test SW II, it was possible to estimate the locations of two large cracks from the estimated AE locations. The two used methods yielded satisfactory results, but using *FastWay* it was possible to estimate almost twice as many AE locations than using Geiger's method (see

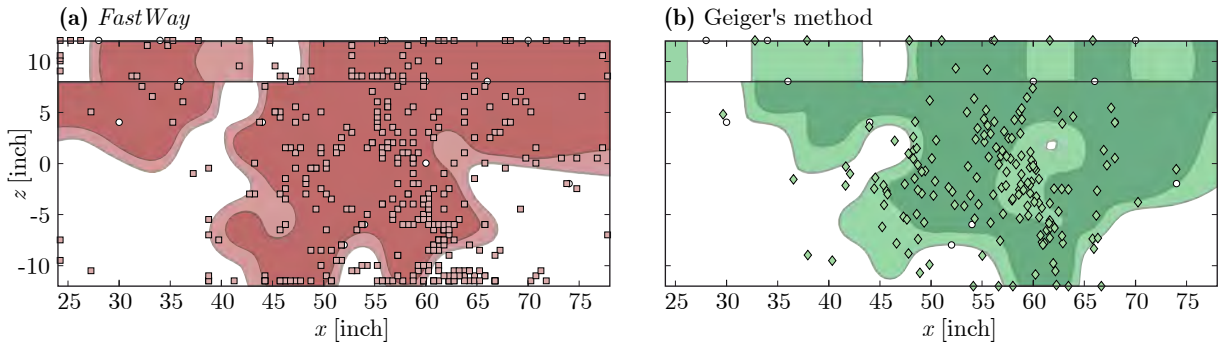

Fig. 7.68: Estimated localization accuracy (*ela*) based on the source localization deviations of the pencil-lead breaks (PLBs SW IIa – "Top-Front" and "Front"), determined with *FastWay* (red) and Geiger's method (green) superimposed with the source locations estimated during the shear test SW II.

Fig. 7.58). Superimposing the estimated localization accuracy visualized in Fig. 7.54 with that in Fig. 7.68 shows that most of the estimated source locations were within the boundaries of the areas with $d < 7.5''$. Hence, the estimated source locations are probably accurate. However, this also means that sources located outside the $d < 7.5''$ boundaries might have been excluded during the verification process (see Section 7.3.4). There might have been more acoustic emissions in the monitored part of the beam ($-24'' \leq x \leq 24''$), but the used sensor configuration was not able to detect them, or the recorded signals were not sufficiently strong to allow source location estimations.

It was almost impossible to obtain accurate source location estimations for PLB set SW IIb, regardless of the used method. The cracks nearly reached the top of the web and physically separated the sensors from each other. The amplitude of the fastest p-wave seemed to be damped significantly due to the wave having to bypass the crack, or bridge the crack via a reinforcing bar. It seemed that AE analysis is of limited usefulness for a severely cracked specimen.

Chapter 8

Conclusion and Outlook

8.1 Conclusion

The effects of heterogeneity in general, and reinforcement and air inclusions in concrete in particular on the wave propagation behavior were investigated and visualized with numerical wave propagation simulations. It was demonstrated that particularly air inclusions such as cracks or a complex specimen shape have a significant impact on the wave propagation path. For elastic wave propagation in solids, air can be considered impenetrable because of the high impedance contrast between air and any solid material. Consequently, it is not always possible for a wave to travel along a straight wave propagation path. Even if a straight path between source and sensor does not lead through air, the fastest wave travel path might still not be straight, because the effective wave travel velocities in a heterogeneous specimen affect the wave front.

For (arrival-time-based) source location estimations, this fact should be taken into account. Therefore, a novel arrival-time-based source location estimation method, called *FastWay*, was developed. In this method, an estimation of the fastest wave travel path is used instead of a straight (i.e. the shortest) wave propagation path. A modified Dijkstra algorithm is used to estimate the fastest wave travel path based on an NVM of the specimen. Any geometrical parameters included in the NVM in form of a discretized velocity distribution are taken into account during the estimation of the fastest wave travel path.

Numerical simulations were used to evaluate and adjust *FastWay*. One key finding of these numerical simulations was that less sensors are needed for *FastWay* than for Geiger's method to yield accurate estimations of source locations . Moreover, *FastWay* generally performed better than Geiger's method if the source was located outside the area surrounded by the sensors. It was found that the velocity assigned to the different materials in the NVM used as input for *FastWay* should not necessarily be the p-wave velocity, although *FastWay* performs estimations based on the fastest wave travel path. However, for example reinforcing elements act as wave guides. Hence, in the presence of reinforcement the wave velocity of the guided mode, which is considerably slower than the p-wave velocity, should be used as the input value.

FastWay is well suited for monitoring homogeneous and heterogeneous specimens with complex shapes, in addition to improving the localization accuracy in heterogeneous closed-volume specimens. Using numerical simulations, it was demonstrated that it is possible to estimate the location of a source even if there is no straight connection between the source and the sensor. Hence, it is possible to estimate the location of sources in the flange of a T-beam even if the sensors can only be mounted on the surfaces of the web (see Section 5.6).

The small-scale experiment demonstrated that *FastWay* is well suited for evaluating the AE data gained during the monitoring of heterogeneous lab-sized specimens. The deviations between estimated and actual source locations determined with *FastWay* were generally smaller or almost the same as the corresponding deviations for the results determined with Geiger's method. For 15% of the investigated PLBs it was not possible to determine a source location estimation with Geiger's method. The source location estimations for all PLBs determined with *FastWay* satisfied the accuracy criteria.

FastWay also performed well in evaluating the data gained during a large-scale experiment. The large-scale experiment highlighted a couple of limitations of AE analysis in general, and of the novel source localization method in particular. The initial reason for developing *FastWay* had been to provide a source location estimation method capable of estimating source locations in cracked materials. However, cracks not only affect the wave propagation path, they also have a significant impact on the wave amplitude. The results for the PLBs performed after completion of the destructive tests (SW Ib and SW IIb) show that it is almost impossible to localize an AE source if the wave has to change direction on its way from the source to the sensor, mainly because of the damping of the amplitude associated with changes of direction. Neither of the used localization methods takes this effect into account. Besides, due to computational limitations, the voxel size used for the NVM for *FastWay* increases for larger specimens. Hence, the systematic err_s increases, too. Naturally, this leads to more inaccurate localizations, especially if large voxels are combined with a low vicinity level, v_{lev}. Nevertheless, the deviations between estimated and actual source locations determined with *FastWay* were still generally smaller or similar to those obtained with Geiger's method. Especially in cases with less than ideal sensor layouts, *FastWay* performed better than Geiger's method. Finally, for the AEs recorded during the destructive tests, nearly twice the number of events could be localized with *FastWay* than with Geiger's method.

FastWay generally yielded more accurate source location estimations than Geiger's method. It is possible to include all known heterogeneities in the underlying NVM. The normalized error plot is a useful way for visualizing the estimated localization accuracy. The accuracy of a source location estimated with *FastWay* depends less on the sensor positions relative to the source location than the estimated localization accuracy determined with Geiger's method. Additionally, *FastWay* needs less sensors in order to perform accurate localizations. However, the applicability of *FastWay* is limited by the maximum size of the NVM and the maximum size of the vicinity. *FastWay* is only capable of considering known heterogeneities (e.g., reinforcing bars and cracks), and these heterogeneities have to be included in the NVM. The overall computational effort for *FastWay* is significantly greater than that for Geiger's method. For a monitored specimen consisting of a solid, heterogeneous material (or that can be considered to be effectively heterogeneous), Geiger's method is most probably the better method. However, if the geometry of the monitored specimen is more complex, *FastWay* yields significantly more accurate source location estimations.

8.2 Outlook

The greatest limitation of *FastWay* is the limitation with respect to the size of the NVM (the maximum total number of voxels), and the computationally possible vicinity level. *FastWay* was developed and used with MATLAB®. MATLAB® is not designed to handle matrices with millions of entries rapidly. Moreover, saving or loading such matrices is extremely time-consuming. Until MATLAB® R2006b it was impossible to save MAT files larger than 2 GB. From MATLAB® R2006b onwards, MAT files of version 7.3, which can be larger than

2 GB, can be handled by a 64-bit computer. However, these files are not compatible with older versions of MATLAB®. In order to make *FastWay* more efficient, the algorithm should be translated into a high-level, general-purpose, interpreted, dynamic programming language such as Python or Fortran.

So far, *FastWay* only takes into account the wave propagation path based on the NVM. The NVM is based on a numerical model of the specimen containing more information than just the wave propagation velocity. Using this numerical model, it is possible to estimate the decrease in wave amplitude as the wave makes its way from the source to the sensor. The amplitude of the source is usually unknown. However, it is possible to estimate the amplitude of the source from the recorded wave amplitudes (reverse calculation). Moreover, based on a initial source location estimation, the estimated decrease in amplitude can be used to identify the most suitable sensors for a more accurate source localization. In any case, the estimated decrease in amplitude can be used to evaluate and improve sensor layouts before testing.

Concrete elements have been investigated with AE for a long time. Cracks are common in reinforced concrete structures. However, they hamper elastic wave propagation and are therefore responsible for damping the signal on its way to the sensor. Thus, AE analysis in general, and AE localization in particular, is sometimes simply not possible. However, *FastWay* seems to be predestined to be used for the evaluation of AEs recorded during the monitoring of structures with complex shapes, such as steel truss nodes. The usability of *FastWay* in non-civil engineering applications should be investigated. This method could be used to improve the localization accuracy of AEs in medicine (e.g., bone fractures) or the automotive industry (e.g., non-destructive testing).

Appendix A

Parameter study of the sensor layout and model complexity

Deviation between the determined and the actual source location

Extreme values:

smallest deviation = 3.84 mm

-) FastWay; MC: 3

-) first 6 sensors sorted by max. A. within 10 µs

largest deviation = 316.28 mm

-) homogeneous Geiger's method

-) first 6 sensors sorted by max. A. within 10 µs

	Geiger		Fast
	homog.	heterog.	Way
No. of smallest deviations	0	2	10
No. of largest deviations	1	3	8

largest deviation considered, only if bigger than 5 mm

sensor setting	MC	Geiger homog.	Geiger heterog.	Fast Way
all sensors	1	6.73	6.73	4.97
	2	6.73	7.82	14.31
	3	6.73	7.82	22.91
all sensors with auto exclusion	1	6.31	6.31	4.97
	2	6.31	8.73	14.31
	3	6.31	8.73	18.30
first 6 sensors sorted by onset time	1	6.83	6.83	8.65
	2	6.83	10.58	8.05
	3	6.83	10.58	10.23
first 12 sensors sorted by onset time	1	6.57	6.57	4.97
	2	6.57	6.40	8.65
	3	6.57	6.40	18.30
first 6 sensors sorted by max. amplitude	1	100.25	100.25	13.22
	2	100.25	100.25	86.98
	3	100.25	100.25	42.60
first 12 sensors sorted by max. amplitude	1	100.19	100.19	8.65
	2	100.19	100.19	21.09
	3	100.19	100.19	42.01
first 6 sensors sorted by max. A. within 10 µs	1	316.28	316.28	4.97
	2	316.28	316.28	10.23
	3	316.28	316.28	3.84
first 12 sensors sorted by max. A. within 10 µs	1	6.81	6.81	4.97
	2	6.81	6.45	8.05
	3	6.81	6.45	13.96
first 6 sensors sorted by max. A. within 20 µs	1	6.93	6.93	4.97
	2	6.93	6.90	8.05
	3	6.93	6.90	4.97
first 12 sensors sorted by max. A. within 20 µs	1	6.59	6.59	4.97
	2	6.59	8.07	10.23
	3	6.59	8.07	16.87
first 6 sensors sorted by fastest rise time	1	7.59	7.59	4.97
	2	7.59	4.42	17.17
	3	7.59	4.42	10.23
first 12 sensors sorted by fastest rise time	1	7.56	7.56	4.97
	2	7.56	6.77	14.31
	3	7.56	6.77	18.30

MC ... material configuration

1 ... EEP concrete; no cracks; no reinforcement
2 ... EEP concrete; no cracks; all reinforcement
3 ... EEP concrete; no cracks; main bars
4 ... EEP concrete; known cracks; no reinforcement
5 ... EEP concrete; known cracks; all reinforcement
6 ... EEP concrete; known cracks; main bars

Fig. A.1: Deviation between the determined and actual location of source I estimated for different sensor layouts and material configurations

Deviation between the determined and the actual source location

Extreme values:

Smallest deviation = 1.86 mm

-) homogeneous Geiger's method

-) first 6 sensors sorted by max. A. within 20 µs

Largest deviation = 269.26 mm

-) homogeneous Geiger's method

-) first 6 sensors sorted by max. amplitude

	Geiger		Fast
	homog.	heterog.	Way
No. of smallest deviations	6	2	4
No. of largest deviations	2	0	9

largest deviation considered, only if bigger than 5 mm

sensor setting	MC	Geiger homog.	Geiger heterog.	Fast Way
all	1	4.84	4.83	4.33
sensors	2	4.84	7.86	22.78
	3	4.84	7.86	20.46
all sensors	1	4.57	4.57	4.33
with	2	4.57	7.56	14.79
auto exclusion	3	4.57	7.56	14.79
first 6 sensors	1	2.01	2.00	4.33
sorted by	2	2.01	2.13	8.29
onset time	3	2.01	2.13	4.33
first 12 sensors	1	2.64	2.64	4.33
sorted by	2	2.64	4.98	8.29
onset time	3	2.64	4.98	8.29
first 6 sensors	1	269.26	269.26	4.33
sorted by	2	269.26	3.06	8.29
max. amplitude	3	269.26	3.06	4.33
first 12 sensors	1	3.08	3.09	4.33
sorted by	2	3.08	3.55	10.90
max. amplitude	3	3.08	3.55	8.29
first 6 sensors	1	269.26	269.26	4.33
sorted by max.	2	269.26	269.26	8.29
A. within 10 µs	3	269.26	269.26	8.29
first 12 sensors	1	2.58	2.58	4.33
sorted by max.	2	2.58	4.81	8.29
A. within 10 µs	3	2.58	4.81	8.29
first 6 sensors	1	1.86	1.87	4.33
sorted by max.	2	1.86	1.87	8.29
A. within 20 µs	3	1.86	1.87	4.33
first 12 sensors	1	2.75	2.75	4.33
sorted by max.	2	2.75	2.75	4.33
A. within 20 µs	3	2.75	2.75	4.33
first 6 sensors	1	2.83	2.84	4.33
sorted by	2	2.83	2.89	10.90
fastest rise time	3	2.83	2.89	10.90
first 12 sensors	1	4.95	4.94	4.33
sorted by	2	4.95	6.65	8.29
fastest rise time	3	4.95	6.65	4.33

MC ... material configuration

1 ... EEP concrete; no cracks; no reinforcement
2 ... EEP concrete; no cracks; all reinforcement
3 ... EEP concrete; no cracks; main bars
4 ... EEP concrete; known cracks; no reinforcement
5 ... EEP concrete; known cracks; all reinforcement
6 ... EEP concrete; known cracks; main bars

Fig. A.2: Deviation between the determined and actual location of source II estimated for different sensor layouts and material configurations

Deviation between the determined and the actual source location

Extreme values:
Smallest deviation = 0.84 mm
-) homogeneous Geiger's method
-) first 6 sensors sorted by max. amplitude
Largest deviation = 39.61 mm
-) FastWay; MC: 2 6
-) first 12 sensors sorted by fastest RT

	Geiger		Fast
	homog.	heterog.	Way
No. of smallest deviations	3	6	3
No. of largest deviations	0	0	4

largest deviation considered, only if bigger than 5 mm

sensor setting	M C	Geiger homog.	Geiger heterog.	Fast Way
all sensors	1	6.44	6.44	4.33
	2	6.44	8.09	28.61
	3	6.44	8.09	26.81
	4	6.44	6.68	4.33
	5	6.44	6.94	26.81
	6	6.44	6.68	26.81
all sensors with auto exclusion	1	5.11	5.11	4.33
	2	5.11	7.10	28.61
	3	5.11	7.10	26.81
	4	5.11	5.35	4.33
	5	5.11	6.28	26.81
	6	5.11	5.35	26.81
first 6 sensors sorted by onset time	1	1.41	1.40	4.33
	2	1.41	1.08	4.33
	3	1.41	1.08	4.33
	4	1.41	1.13	4.33
	5	1.41	1.08	4.33
	6	1.41	1.13	4.33
first 12 sensors sorted by onset time	1	1.02	1.03	4.33
	2	1.02	2.27	10.90
	3	1.02	2.27	4.33
	4	1.02	1.94	4.33
	5	1.02	2.27	4.33
	6	1.02	1.94	4.33
first 6 sensors sorted by max. amplitude	1	0.84	0.84	4.33
	2	0.84	1.77	4.33
	3	0.84	1.77	4.33
	4	0.84	1.42	4.33
	5	0.84	1.77	4.33
	6	0.84	1.42	4.33
first 12 sensors sorted by max. amplitude	1	2.16	2.17	4.33
	2	2.16	2.90	4.33
	3	2.16	2.90	4.33
	4	2.16	2.68	4.33
	5	2.16	2.90	4.33
	6	2.16	2.68	4.33

sensor setting	M C	Geiger homog.	Geiger heterog.	Fast Way
first 6 sensors sorted by max. A. within 10 µs	1	1.87	1.87	4.33
	2	1.87	2.21	4.33
	3	1.87	2.21	4.33
	4	1.87	1.66	4.33
	5	1.87	2.21	4.33
	6	1.87	1.66	4.33
first 12 sensors sorted by max. A. within 10 µs	1	1.78	1.79	4.33
	2	1.78	0.91	4.33
	3	1.78	0.91	4.33
	4	1.78	0.96	4.33
	5	1.78	0.91	4.33
	6	1.78	0.96	4.33
first 6 sensors sorted by max. A. within 20 µs	1	1.15	1.16	4.33
	2	1.15	1.07	4.33
	3	1.15	1.07	4.33
	4	1.15	1.09	4.33
	5	1.15	1.07	4.33
	6	1.15	1.09	4.33
first 12 sensors sorted by max. A. within 20 µs	1	1.78	1.79	4.33
	2	1.78	0.91	4.33
	3	1.78	0.91	4.33
	4	1.78	0.96	4.33
	5	1.78	0.91	4.33
	6	1.78	0.96	4.33
first 6 sensors sorted by fastest rise time	1	1.99	1.99	4.33
	2	1.99	1.99	4.33
	3	1.99	1.99	4.33
	4	1.99	1.99	4.33
	5	1.99	1.99	4.33
	6	1.99	1.99	4.33
first 12 sensors sorted by fastest rise time	1	6.22	6.22	4.33
	2	6.22	6.61	39.61
	3	6.22	6.61	37.00
	4	6.22	7.52	4.33
	5	6.22	8.72	37.00
	6	6.22	7.52	39.61

MC ... material configuration
1 ... EEP concrete; no cracks; no reinforcement
2 ... EEP concrete; no cracks; all reinforcement
3 ... EEP concrete; no cracks; main bars
4 ... EEP concrete; known cracks; no reinforcement
5 ... EEP concrete; known cracks; all reinforcement
6 ... EEP concrete; known cracks; main bars

Fig. A.3: Deviation between the determined and actual location of source III estimated for different sensor layouts and material configurations

Deviation between the determined and the actual source location

Extreme values:
Smallest deviation = 1.66 mm
-) FastWay; MC: 2 5
-) first 12 sensors sorted by max. A. within 20 µs
Largest deviation = 117.53 mm
-) FastWay; MC: 4
-) first 6 sensors sorted by onset time

	Geiger		Fast
	homog.	heterog.	Way
No. of smallest deviations	0	0	12
No. of largest deviations	0	0	12

largest deviation considered, only if bigger than 5 mm

sensor setting	MC	Geiger homog.	Geiger heterog.	Fast Way
all sensors	1	35.40	35.40	34.25
	2	35.40	34.71	5.72
	3	35.40	34.71	11.08
	4	35.40	34.83	100.71
	5	35.40	33.84	5.72
	6	35.40	34.83	5.72
all sensors with auto exclusion	1	33.46	33.46	27.80
	2	33.46	32.37	7.26
	3	33.46	32.37	6.54
	4	33.46	33.10	88.67
	5	33.46	32.31	4.77
	6	33.46	33.10	4.77
first 6 sensors sorted by onset time	1	25.40	25.40	28.33
	2	25.40	25.06	10.14
	3	25.40	25.06	8.53
	4	25.40	25.48	117.53
	5	25.40	25.00	5.72
	6	25.40	25.48	5.72
first 12 sensors sorted by onset time	1	19.47	19.48	23.08
	2	19.47	13.20	3.57
	3	19.47	13.20	10.14
	4	19.47	14.18	93.45
	5	19.47	17.62	3.57
	6	19.47	14.18	5.72
first 6 sensors sorted by max. amplitude	1	13.38	13.39	16.82
	2	13.38	6.25	8.53
	3	13.38	6.25	11.08
	4	13.38	11.15	99.96
	5	13.38	11.70	3.57
	6	13.38	11.15	3.57
first 12 sensors sorted by max. amplitude	1	20.46	20.46	25.74
	2	20.46	20.56	5.72
	3	20.46	20.56	5.72
	4	20.46	23.49	94.94
	5	20.46	20.32	5.72
	6	20.46	23.49	5.72

sensor setting	MC	Geiger homog.	Geiger heterog.	Fast Way
first 6 sensors sorted by max. A. within 10 µs	1	34.21	34.21	32.29
	2	34.21	34.04	10.14
	3	34.21	34.04	5.72
	4	34.21	29.91	107.90
	5	34.21	33.45	3.57
	6	34.21	29.91	3.57
first 12 sensors sorted by max. A. within 10 µs	1	19.51	19.51	23.08
	2	19.51	18.52	6.54
	3	19.51	18.52	5.72
	4	19.51	18.58	92.05
	5	19.51	17.88	3.57
	6	19.51	18.58	5.72
first 6 sensors sorted by max. A. within 20 µs	1	34.21	34.21	32.29
	2	34.21	34.04	10.14
	3	34.21	34.04	5.72
	4	34.21	29.91	107.90
	5	34.21	33.45	3.57
	6	34.21	29.91	3.57
first 12 sensors sorted by max. A. within 20 µs	1	21.38	21.38	27.62
	2	21.38	16.83	1.66
	3	21.38	16.83	6.54
	4	21.38	15.93	112.40
	5	21.38	19.70	1.66
	6	21.38	15.93	5.72
first 6 sensors sorted by fastest rise time	1	12.43	12.45	16.21
	2	12.43	11.83	10.14
	3	12.43	11.83	5.72
	4	12.43	10.89	35.54
	5	12.43	10.61	31.67
	6	12.43	10.89	3.57
first 12 sensors sorted by fastest rise time	1	13.12	13.13	12.36
	2	13.12	4.59	3.57
	3	13.12	4.59	4.77
	4	13.12	11.21	68.21
	5	13.12	10.95	1.66
	6	13.12	11.21	1.66

MC ... material configuration
1 ... EEP concrete; no cracks; no reinforcement
2 ... EEP concrete; no cracks; all reinforcement
3 ... EEP concrete; no cracks; main bars
4 ... EEP concrete; known cracks; no reinforcement
5 ... EEP concrete; known cracks; all reinforcement
6 ... EEP concrete; known cracks; main bars

Fig. A.4: Deviation between the determined and actual location of source IV estimated for different sensor layouts and material configurations

Deviation between the determined and the actual source location

Extreme values:
Smallest deviation = 0.22 mm
-) heterogeneous Geiger's method; MC: 1
-) all sensors
Largest deviation = 11.61 mm
-) FastWay; MC: 3
-) first 6 sensors sorted by max. amplitude

	Geiger		Fast
	homog.	heterog.	Way
No. of smallest deviations	1	11	0
No. of largest deviations	0	0	8

largest deviation considered, only if bigger than 5 mm

sensor setting	MC	Geiger homog.	Geiger heterog.	Fast Way
all sensors	1	0.22	0.22	3.84
	2	0.22	2.95	3.84
	3	0.22	2.95	3.84
	4	0.22	2.43	3.84
	5	0.22	2.84	7.40
	6	0.22	2.43	7.40
all sensors with auto exclusion	1	0.55	0.56	3.84
	2	0.55	3.43	3.84
	3	0.55	3.43	3.84
	4	0.55	3.99	3.84
	5	0.55	4.28	3.84
	6	0.55	3.99	3.84
first 6 sensors sorted by onset time	1	1.68	1.69	4.97
	2	1.68	1.80	3.84
	3	1.68	1.80	3.84
	4	1.68	1.60	3.84
	5	1.68	1.65	3.84
	6	1.68	1.60	3.84
first 12 sensors sorted by onset time	1	0.50	0.50	3.84
	2	0.50	3.71	7.40
	3	0.50	3.71	3.84
	4	0.50	2.69	3.84
	5	0.50	2.75	7.40
	6	0.50	2.69	7.40
first 6 sensors sorted by max. amplitude	1	2.76	2.75	3.84
	2	2.76	5.24	4.97
	3	2.76	5.24	11.61
	4	2.76	5.67	3.84
	5	2.76	5.65	3.84
	6	2.76	5.67	3.84
first 12 sensors sorted by max. amplitude	1	1.42	1.42	3.84
	2	1.42	3.47	3.84
	3	1.42	3.47	3.84
	4	1.42	2.37	3.84
	5	1.42	2.82	3.84
	6	1.42	2.37	3.84

sensor setting	MC	Geiger homog.	Geiger heterog.	Fast Way
first 6 sensors sorted by max. A. within 10µs	1	2.16	2.17	3.84
	2	2.16	2.08	7.40
	3	2.16	2.08	4.97
	4	2.16	1.95	3.84
	5	2.16	1.98	3.84
	6	2.16	1.95	3.84
first 12 sensors sorted by max. A. within 10µs	1	1.05	1.04	3.84
	2	1.05	3.62	3.84
	3	1.05	3.62	3.84
	4	1.05	3.66	3.84
	5	1.05	3.10	3.84
	6	1.05	3.66	3.84
first 6 sensors sorted by max. A. within 20µs	1	1.56	1.58	4.97
	2	1.56	1.51	7.40
	3	1.56	1.51	4.97
	4	1.56	1.33	3.84
	5	1.56	1.29	7.40
	6	1.56	1.33	7.40
first 12 sensors sorted by max. A. within 20µs	1	1.66	1.67	3.84
	2	1.66	3.08	3.84
	3	1.66	3.08	3.84
	4	1.66	1.59	3.84
	5	1.66	1.60	7.40
	6	1.66	1.59	3.84
first 6 sensors sorted by fastest rise time	1	1.78	1.76	8.65
	2	1.78	3.83	3.84
	3	1.78	3.83	3.84
	4	1.78	2.50	3.84
	5	1.78	3.83	3.84
	6	1.78	2.50	3.84
first 12 sensors sorted by fastest rise time	1	0.50	0.49	4.97
	2	0.50	4.37	7.40
	3	0.50	4.37	3.84
	4	0.50	3.61	3.84
	5	0.50	4.38	7.40
	6	0.50	3.61	7.40

MC ... material configuration
1 ... EEP concrete; no cracks; no reinforcement
2 ... EEP concrete; no cracks; all reinforcement
3 ... EEP concrete; no cracks; main bars
4 ... EEP concrete; known cracks; no reinforcement
5 ... EEP concrete; known cracks; all reinforcement
6 ... EEP concrete; known cracks; main bars

Fig. A.5: Deviation between the determined and actual location of source V estimated for different sensor layouts and material configurations

Deviation between the determined and the actual source location

Extreme values:

Smallest deviation = 2.25 mm

-) heterogeneous Geiger's method; MC: 1

-) first 6 sensors sorted by max. A within 10 µs

Largest deviation = 100.27 mm

-) homogeneous Geiger's method

-) all sensors

	Geiger		Fast
	homog.	heterog.	Way
No. of smallest deviations	0	2	10
No. of largest deviations	1	0	11

largest deviation considered, only if bigger than 5 mm

sensor setting	MC	Geiger homog.	Geiger heterog.	Fast Way
all sensors	1	100.27	88.87	33.36
	2	100.27	89.56	65.37
	3	100.27	89.56	68.65
	4	100.27	89.66	30.21
	5	100.27	89.65	62.95
	6	100.27	89.66	68.65
all sensors with auto exclusion	1	21.59	10.24	3.57
	2	21.59	9.77	21.28
	3	21.59	9.77	21.97
	4	21.59	13.93	3.57
	5	21.59	9.77	24.14
	6	21.59	13.93	26.13
first 6 sensors sorted by onset time	1	7.05	2.25	3.57
	2	7.05	4.78	13.52
	3	7.05	4.78	12.76
	4	7.05	6.39	3.57
	5	7.05	4.78	13.88
	6	7.05	6.39	13.88
first 12 sensors sorted by onset time	1	21.59	10.24	3.57
	2	21.59	9.77	21.28
	3	21.59	9.77	21.97
	4	21.59	13.93	3.57
	5	21.59	9.77	24.14
	6	21.59	13.93	26.13
first 6 sensors sorted by max. amplitude	1	4.77	6.94	3.57
	2	4.77	10.00	9.10
	3	4.77	10.00	13.52
	4	4.77	6.07	6.54
	5	4.77	10.00	9.10
	6	4.77	6.07	13.88
first 12 sensors sorted by max. amplitude	1	21.59	10.24	3.57
	2	21.59	9.77	21.28
	3	21.59	9.77	21.97
	4	21.59	13.93	3.57
	5	21.59	9.77	24.14
	6	21.59	13.93	26.13

sensor setting	MC	Geiger homog.	Geiger heterog.	Fast Way
first 6 sensors sorted by max. A. within 10µs	1	7.05	2.25	3.57
	2	7.05	4.78	13.52
	3	7.05	4.78	12.76
	4	7.05	6.39	3.57
	5	7.05	4.78	13.88
	6	7.05	6.39	13.88
first 12 sensors sorted by max. A. within 10µs	1	34.29	25.13	3.57
	2	34.29	28.85	36.09
	3	34.29	28.85	31.67
	4	34.29	31.41	3.57
	5	34.29	28.19	36.09
	6	34.29	31.41	36.09
first 6 sensors sorted by max. A. within 20µs	1	12.00	3.92	3.57
	2	12.00	8.37	9.10
	3	12.00	8.37	9.10
	4	12.00	10.73	3.57
	5	12.00	8.37	11.95
	6	12.00	10.73	13.88
first 12 sensors sorted by max. A. within 20µs	1	34.29	25.13	3.57
	2	34.29	28.85	36.09
	3	34.29	28.85	31.67
	4	34.29	31.41	3.57
	5	34.29	28.19	36.09
	6	34.29	31.41	36.09
first 6 sensors sorted by fastest rise time	1	19.83	11.77	9.63
	2	19.83	4.10	53.97
	3	19.83	4.10	50.62
	4	19.83	16.45	3.57
	5	19.83	4.10	30.38
	6	19.83	16.45	30.38
first 12 sensors sorted by fastest rise time	1	21.59	10.24	3.57
	2	21.59	9.77	21.28
	3	21.59	9.77	21.97
	4	21.59	13.93	3.57
	5	21.59	9.77	24.14
	6	21.59	13.93	26.13

MC ... material configuration

1 ... EEP concrete; no cracks; no reinforcement
2 ... EEP concrete; no cracks; all reinforcement
3 ... EEP concrete; no cracks; main bars
4 ... EEP concrete; known cracks; no reinforcement
5 ... EEP concrete; known cracks; all reinforcement
6 ... EEP concrete; known cracks; main bars

Fig. A.6: Deviation between the determined and actual location of source VI estimated for different sensor layouts and material configurations

Appendix B

Large T-shaped concrete beam SW I

B.1 Pencil-lead breaks SW Ia

B.1.1 Top

PLB			Set	Geiger's method						*FastWay*					
x [in]	y [in]	z [in]	#	x [in]	y [in]	z [in]	d [in]	eei [-]	ac [-]	x [in]	y [in]	z [in]	d [in]	eei [-]	ac [-]
-22.0	-10.0	12.0	10-12	-25.8	-8.8	10.4	4.32	0.40	3	-23.3	-9.3	8.8	3.56	0.05	3
-22.0	-10.0	12.0	10-19	-20.6	-10.7	11.9	1.56	0.17	2	-21.3	-9.3	10.3	2.05	0.10	2
-22.0	-10.0	12.0	12-7	-20.4	-9.2	12.0	1.77	0.23	2	-21.8	-8.3	8.3	4.15	NEL	3
-22.0	-6.0	12.0	11-10	-21.8	-5.7	10.9	1.15	0.13	2	-21.8	-5.8	9.8	2.28	0.28	2
-22.0	-6.0	12.0	12-5	-24.3	-6.4	11.8	2.39	0.14	2	-21.3	-5.8	10.3	1.92	0.19	2
-22.0	-6.0	12.0	12-6	-21.4	-4.8	8.6	3.64	0.18	3	-23.8	-3.3	8.3	4.97	NEL	3
-22.0	-6.0	12.0	12-13	-21.8	-5.7	11.2	0.85	0.11	1	-21.8	-5.8	10.3	1.79	0.19	2
-22.0	-2.0	12.0	11-1	-19.4	-2.0	10.6	3.00	0.10	3	-20.8	-2.3	10.3	2.17	0.19	2
-22.0	-2.0	12.0	11-7	-21.2	-2.0	10.4	1.79	0.09	2	-22.8	-2.3	9.8	2.38	0.23	2
-22.0	-2.0	12.0	12-1	-21.0	-2.0	10.4	1.91	0.09	2	-22.8	-2.3	9.8	2.38	0.24	2
-22.0	-2.0	12.0	12-22	-21.1	-1.9	10.4	1.80	0.09	2	-22.8	-2.3	9.8	2.38	0.23	2
-22.0	2.0	12.0	11-33	-21.5	1.6	10.6	1.52	0.10	2	-23.3	1.3	10.8	1.92	0.16	2
-22.0	2.0	12.0	11-37	-24.2	1.8	11.0	2.39	0.12	2	-23.8	2.8	5.3	7.01	NEL	4
-22.0	2.0	12.0	11-50	-21.5	1.8	10.4	1.69	0.09	2	-23.3	1.8	10.3	2.17	0.14	2
-22.0	6.0	12.0	11-39	-23.2	5.6	11.4	1.38	0.17	2	-22.8	4.8	11.8	1.48	0.51	2
-22.0	6.0	12.0	11-53	-25.1	7.7	9.4	4.39	0.18	3	-20.3	4.3	10.8	2.77	NEL	3
-22.0	6.0	12.0	12-63	-19.8	4.2	11.0	2.99	0.09	3	-20.8	4.3	10.8	2.49	0.06	2
-22.0	10.0	12.0	10-31	-26.3	8.3	11.4	4.64	1.35	3	-20.3	5.8	11.8	4.60	NEL	3
-22.0	10.0	12.0	11-46	-96.0	-12.0	12.0	77.20	>10.00	6	-23.8	3.8	11.8	6.50	NEL	4
-22.0	10.0	12.0	11-56	-96.0	12.0	12.0	74.03	>10.00	6	-20.8	6.8	11.8	3.49	NEL	3
-18.0	-10.0	12.0	12-8	-19.4	-10.0	12.0	1.37	0.25	2	-20.3	-7.3	8.3	5.17	NEL	4
-18.0	-10.0	12.0	12-18	-23.0	-8.0	11.5	5.38	0.66	4	-20.3	-7.3	8.3	5.17	NEL	4
-18.0	-10.0	12.0	12-32	-18.8	-10.8	12.0	1.09	0.39	2	-15.8	-10.8	8.8	4.02	0.16	3
-18.0	-6.0	12.0	12-14	-18.0	-6.1	11.8	0.21	0.11	1	-17.8	-6.3	10.8	1.30	0.10	2
-18.0	-6.0	12.0	12-15	-16.7	-3.8	12.0	2.55	0.16	3	-17.8	-2.8	11.8	3.27	0.25	3
-18.0	-6.0	12.0	12-28	-17.7	-5.7	10.8	1.24	0.13	2	-17.8	-6.3	11.3	0.83	0.13	1
-18.0	-6.0	12.0	13-4	-18.5	-6.0	10.6	1.51	0.14	2	-17.3	-6.3	8.3	3.83	0.07	3
-18.0	-6.0	12.0	14-17	-16.5	-3.6	12.0	2.78	0.13	3	-17.8	-2.8	11.8	3.27	0.23	3
-18.0	-2.0	12.0	12-2	-17.6	-2.0	10.6	1.43	0.09	2	-18.8	-2.3	10.3	1.92	0.14	2
-18.0	-2.0	12.0	12-3	-16.5	-1.7	10.7	1.96	0.11	2	-17.8	-2.3	10.8	1.30	0.23	2
-18.0	-2.0	12.0	12-11	-18.1	-1.9	11.0	0.97	0.09	1	-18.8	-2.3	10.8	1.48	0.12	2
-18.0	-2.0	12.0	12-23	-17.9	-1.9	11.0	1.02	0.09	2	-18.8	-2.3	10.8	1.48	0.11	2
-18.0	2.0	12.0	12-61	-17.9	1.6	10.6	1.44	0.10	2	-18.8	1.3	10.8	1.64	0.07	2
-18.0	2.0	12.0	12-77	-18.2	1.7	10.8	1.31	0.10	2	-19.3	1.3	10.8	1.92	0.10	2
-18.0	2.0	12.0	14-230	-17.9	1.6	10.7	1.35	0.09	2	-18.8	1.3	10.8	1.64	0.07	2
-18.0	6.0	12.0	14-239	-16.6	3.4	12.0	2.96	0.21	3	-15.8	3.3	11.8	3.56	0.70	3
-18.0	6.0	12.0	14-261	-7.6	12.0	12.0	11.97	0.99	6	-10.3	2.3	-11.8	25.26	2.26	6
-18.0	10.0	12.0	11-35	-96.0	4.0	-12.0	81.83	>10.00	6	-21.8	10.3	11.8	3.77	1.03	3
-18.0	10.0	12.0	11-47	-18.1	6.9	12.0	3.11	0.20	3	-21.3	9.3	11.8	3.34	NEL	3
-18.0	10.0	12.0	11-57	-96.0	12.0	12.0	78.03	>10.00	6	-15.8	2.8	11.8	7.60	1.06	5
-18.0	10.0	12.0	12-80	-15.9	8.9	8.9	3.91	0.19	3	-16.3	7.3	8.3	4.97	NEL	3
-14.0	-10.0	12.0	14-33	-14.6	-8.6	10.3	2.35	0.11	2	-16.3	-6.8	8.3	5.45	NEL	4
-14.0	-10.0	12.0	14-34	96.0	-12.0	12.0	110.02	>10.00	6	-12.3	-7.8	8.3	4.71	NEL	3
-14.0	-10.0	12.0	14-63	-15.6	-11.3	12.0	2.04	0.42	2	-19.3	-5.3	11.8	7.08	NEL	4
-14.0	-10.0	12.0	14-92	-14.5	-4.0	3.2	10.64	0.26	6	-16.8	-6.8	8.3	5.67	0.25	4

Tab. B.1: SW I PLB a - "Top", part 1: Coordinates of the pencil-lead breaks and estimated source locations determined using Geiger's method and *FastWay*. Estimated source locations excluded during the verification process (see Section 7.3.4) are shown in gray.

PLB			Set	Geiger's method						*FastWay*					
x [in]	y [in]	z [in]	#	x [in]	y [in]	z [in]	d [in]	eei [-]	ac [-]	x [in]	y [in]	z [in]	d [in]	eei [-]	ac [-]
-14.0	-6.0	12.0	12-29	-15.1	-4.9	10.5	2.16	0.12	2	-12.8	-6.8	8.3	4.02	0.04	3
-14.0	-6.0	12.0	14-16	-15.8	-5.7	11.4	1.98	0.13	2	-15.8	-6.3	10.3	2.49	0.17	2
-14.0	-6.0	12.0	14-57	-12.3	-4.5	11.7	2.28	0.11	2	-12.3	-4.8	11.3	2.28	0.17	2
-14.0	-2.0	12.0	12-4	-13.5	-2.1	10.2	1.87	0.10	2	-13.8	-2.8	10.3	1.92	0.12	2
-14.0	-2.0	12.0	13-11	-13.6	-1.9	11.1	1.00	0.09	2	-13.8	-2.3	11.3	0.83	0.17	1
-14.0	-2.0	12.0	14-78	-13.8	-1.5	10.6	1.44	0.10	2	-14.3	-2.3	11.3	0.83	0.24	1
-14.0	2.0	12.0	12-73	-13.8	1.7	10.6	1.43	0.12	2	-13.8	1.3	10.3	1.92	0.19	2
-14.0	2.0	12.0	14-212	-13.8	1.7	10.8	1.28	0.09	2	-13.8	1.3	10.3	1.92	0.18	2
-14.0	2.0	12.0	14-253	-13.7	1.8	10.9	1.14	0.10	2	-13.8	1.8	11.3	0.83	0.19	1
-14.0	6.0	12.0	11-54	-13.4	5.8	12.0	0.64	0.12	1	-13.8	6.3	11.8	0.43	0.21	1
-14.0	6.0	12.0	12-64	-13.5	5.9	11.7	0.58	0.11	1	-13.8	6.3	11.3	0.83	0.23	1
-14.0	6.0	12.0	14-221	-15.2	3.7	12.0	2.56	0.27	3	-15.8	3.3	11.8	3.27	0.72	3
-14.0	10.0	12.0	12-70	-14.7	8.7	10.6	2.07	0.27	2	-16.8	11.8	8.3	4.97	NEL	3
-14.0	10.0	12.0	14-246	-12.9	9.1	12.0	1.42	0.16	2	-13.8	9.3	11.8	0.83	0.15	1
-10.0	-10.0	12.0	14-64	-11.7	-8.5	9.5	3.39	0.11	3	-13.3	-6.8	8.3	5.93	0.21	4
-10.0	-10.0	12.0	14-65	-10.4	-6.6	10.5	3.74	0.11	3	-10.3	-7.3	8.8	4.26	0.24	3
-10.0	-10.0	12.0	14-93	-6.8	-12.0	12.0	3.75	0.66	3	-12.3	-7.3	8.3	5.17	0.22	4
-10.0	-6.0	12.0	13-5	-10.7	-7.2	11.1	1.68	0.13	2	-9.3	-8.8	8.8	4.32	0.15	3
-10.0	-6.0	12.0	13-6	-8.3	-7.8	12.0	2.45	0.12	2	-9.8	-6.3	11.8	0.43	0.15	1
-10.0	-6.0	12.0	14-18	-10.5	-6.2	11.9	0.58	0.11	1	-11.8	-5.8	11.8	1.79	0.23	2
-10.0	-6.0	12.0	14-86	-8.0	-7.3	11.6	2.41	0.15	2	-7.8	-7.3	9.8	3.42	NEL	3
-10.0	-2.0	12.0	10-16	-96.0	-12.0	-12.0	89.84	NaN	6	-11.3	3.8	8.3	6.98	0.64	4
-10.0	-2.0	12.0	12-24	-2.4	-5.7	12.0	8.48	NaN	5	-10.3	-2.3	11.8	0.43	0.51	1
-10.0	-2.0	12.0	13-1	-11.3	-1.6	9.7	2.68	0.46	3	-10.3	-2.3	11.8	0.43	0.40	1
-10.0	-2.0	12.0	13-12	-18.5	4.5	12.0	10.71	0.59	6	-4.8	8.8	11.8	11.97	NEL	6
-10.0	-2.0	12.0	14-2	-9.6	-1.3	10.2	1.98	0.09	2	-10.3	-1.3	10.3	1.92	0.15	2
-10.0	2.0	12.0	14-213	-10.2	1.7	10.1	1.91	0.09	2	-10.8	1.3	9.8	2.49	0.13	2
-10.0	2.0	12.0	14-231	-10.5	1.7	10.5	1.62	0.09	2	-11.3	1.8	11.3	1.48	0.22	2
-10.0	2.0	12.0	14-254	-10.3	1.7	9.9	2.12	0.09	2	-10.8	1.3	9.8	2.49	0.12	2
-10.0	6.0	12.0	13-65	-10.5	5.5	9.9	2.24	0.09	2	-10.8	5.3	9.8	2.49	0.10	2
-10.0	6.0	12.0	14-222	-10.6	5.6	9.8	2.27	0.09	2	-10.8	5.3	9.8	2.49	0.09	2
-10.0	6.0	12.0	14-241	-10.2	5.6	11.4	0.76	0.11	1	-10.8	5.8	11.3	1.09	0.19	2
-10.0	10.0	12.0	14-226	-10.1	8.7	12.0	1.29	0.13	2	-11.3	8.3	11.8	2.17	0.23	2
-10.0	10.0	12.0	14-247	-10.2	10.3	11.1	0.95	0.09	1	-11.3	8.8	9.8	2.86	0.11	3
-10.0	10.0	12.0	14-267	-10.7	9.4	10.9	1.38	0.09	2	-11.3	7.8	9.3	3.77	0.08	3
-6.0	-10.0	12.0	14-35	-6.2	-12.0	12.0	2.01	0.24	2	-7.3	-11.3	11.8	1.79	0.15	2
-6.0	-10.0	12.0	14-94	96.0	-12.0	12.0	102.02	>10.00	6	-9.8	-7.3	10.8	4.82	NEL	3
-6.0	-6.0	12.0	14-19	-6.4	-7.4	11.9	1.44	0.12	2	-6.8	-6.8	9.8	2.49	NEL	2
-6.0	-6.0	12.0	14-20	-5.5	-6.1	12.0	0.51	0.12	1	-6.3	-6.3	11.8	0.43	0.25	1
-6.0	-6.0	12.0	14-58	-5.6	-6.3	12.0	0.47	0.09	1	-6.3	-5.8	10.8	1.30	0.12	2
-6.0	-6.0	12.0	14-59	-1.4	-3.9	11.5	5.12	0.10	4	-0.8	-2.3	10.3	6.68	NEL	4
-6.0	-2.0	12.0	12-25	-96.0	-12.0	-12.0	93.68	NaN	6	-15.8	0.3	4.3	12.66	NEL	6
-6.0	-2.0	12.0	14-3	-6.8	-1.8	10.2	1.94	0.10	2	-7.8	-1.3	10.3	2.59	0.18	3
-6.0	-2.0	12.0	14-50	-7.8	-1.3	9.3	3.30	0.10	3	-8.8	-0.8	9.3	4.09	0.14	3
-6.0	-2.0	12.0	14-79	-5.9	-2.1	10.9	1.10	0.09	2	-6.8	-1.8	11.8	0.83	0.19	1
-6.0	2.0	12.0	14-215	-6.5	2.4	10.0	2.12	0.09	2	-7.3	2.3	9.8	2.59	0.09	3
-6.0	2.0	12.0	14-233	-6.5	2.2	9.8	2.23	0.10	2	-7.3	2.3	9.8	2.59	0.12	3
-6.0	2.0	12.0	14-255	-6.2	1.9	9.9	2.06	0.10	2	-6.8	1.8	10.3	1.92	0.17	2
-6.0	6.0	12.0	14-223	-5.5	6.5	12.0	0.67	0.11	1	-6.3	5.3	11.3	1.09	0.17	2
-6.0	6.0	12.0	14-242	-6.0	5.6	10.2	1.81	0.09	2	-6.3	5.3	9.8	2.38	0.14	2

Tab. B.2: SW I PLB a - "Top", part 2: Coordinates of the pencil-lead breaks and estimated source locations determined using Geiger's method and *FastWay*. Estimated source locations excluded during the verification process (see Section 7.3.4) are shown in gray.

PLB			Set	Geiger's method						*FastWay*					
x [in]	y [in]	z [in]	#	x [in]	y [in]	z [in]	d [in]	eei [-]	ac [-]	x [in]	y [in]	z [in]	d [in]	eei [-]	ac [-]
-6.0	6.0	12.0	14-262	-5.6	6.0	11.1	0.96	0.09	1	-5.8	5.3	10.3	1.92	0.11	2
-6.0	10.0	12.0	14-248	-6.8	4.0	1.7	11.95	0.26	6	-6.3	9.3	11.8	0.83	0.11	1
-6.0	10.0	12.0	14-268	-6.4	9.9	11.9	0.42	0.09	1	-6.8	7.8	10.8	2.68	0.11	3
-4.0	-6.0	12.0	14-21	-3.8	-7.0	9.1	3.07	0.12	3	-3.8	-6.8	11.8	0.83	0.16	1
-2.0	-10.0	12.0	14-36	-0.6	-9.8	9.7	2.76	0.16	3	-1.3	-11.3	11.8	1.48	NEL	2
-2.0	-10.0	12.0	14-66	-0.7	-7.8	12.0	2.60	0.23	3	-1.8	-11.8	11.8	1.79	0.33	2
-2.0	-10.0	12.0	14-95	-65.5	-4.0	-12.0	68.19	>10.00	6	-2.3	-10.8	8.3	3.83	0.15	3
-2.0	-6.0	12.0	14-22	-1.4	-6.9	9.7	2.55	0.09	3	-1.3	-6.3	11.8	0.83	0.18	1
-2.0	-6.0	12.0	14-88	-2.2	-4.0	7.2	5.20	0.33	4	-2.3	-10.3	11.8	4.26	0.39	3
-2.0	-2.0	12.0	14-4	-3.6	-4.9	10.9	3.52	0.14	3	-4.8	-5.3	11.3	4.32	NEL	3
-2.0	-2.0	12.0	14-5	-2.2	-2.2	10.7	1.31	0.10	2	-2.3	-1.8	10.8	1.30	0.11	2
-2.0	-2.0	12.0	14-52	-1.8	-2.2	10.6	1.47	0.10	2	-1.8	-1.8	10.3	1.79	0.13	2
-2.0	-2.0	12.0	14-80	-2.3	-3.0	10.4	1.91	0.11	2	-2.3	-2.3	10.3	1.79	0.15	2
-2.0	-2.0	12.0	14-81	-1.8	4.5	9.5	6.94	0.09	4	-1.8	4.3	9.3	6.83	0.07	4
-2.0	2.0	12.0	14-216	-1.6	2.0	10.9	1.12	0.10	2	-1.8	2.3	10.8	1.30	0.20	2
-2.0	2.0	12.0	14-234	-1.7	1.9	10.5	1.52	0.10	2	-1.8	1.3	10.3	1.92	0.15	2
-2.0	6.0	12.0	11-34	64.4	12.0	12.0	66.63	NaN	6	15.3	-3.8	11.8	19.82	NEL	6
-2.0	6.0	12.0	14-224	-2.2	7.8	12.0	1.83	0.10	2	-2.3	6.3	10.8	1.30	0.09	2
-2.0	6.0	12.0	14-243	-1.5	4.0	7.8	4.65	0.11	3	-1.8	5.3	8.3	3.83	0.07	3
-2.0	6.0	12.0	14-263	-1.8	6.0	10.0	2.04	0.10	2	-1.8	5.3	8.3	3.83	0.05	3
-2.0	10.0	12.0	14-227	-1.8	10.8	12.0	0.85	0.35	1	-2.8	11.8	10.8	2.28	0.18	2
-2.0	10.0	12.0	14-249	-2.2	10.6	9.8	2.27	0.11	2	-1.8	8.3	8.3	4.15	0.12	3
-2.0	10.0	12.0	14-269	-2.0	10.7	10.7	1.50	0.09	2	-1.8	8.8	8.3	3.96	0.10	3
-2.0	10.0	12.0	14-270	9.4	4.0	-12.0	27.23	1.97	6	1.8	8.8	8.3	5.45	0.18	4
2.0	-10.0	12.0	14-37	4.5	-8.4	9.8	3.69	0.13	3	4.3	-7.8	8.3	4.92	NEL	3
2.0	-10.0	12.0	14-38	3.6	-3.5	12.0	6.75	0.47	4	2.3	-11.8	11.8	1.79	0.53	2
2.0	-10.0	12.0	14-39	1.5	-4.0	3.6	10.30	0.38	6	1.3	-11.8	8.3	4.21	0.22	3
2.0	-10.0	12.0	14-67	2.7	-4.0	6.2	8.34	0.35	5	2.8	-11.8	8.3	4.21	0.19	3
2.0	-10.0	12.0	14-96	2.8	-8.2	12.0	1.92	0.26	2	1.3	-11.3	8.3	4.02	0.30	3
2.0	-6.0	12.0	14-23	1.1	-4.5	12.0	1.73	0.13	2	0.3	-5.3	11.8	1.92	NEL	2
2.0	-6.0	12.0	14-24	2.2	-5.8	10.2	1.78	0.09	2	2.3	-4.8	9.3	3.03	0.08	3
2.0	-6.0	12.0	14-25	4.2	-6.3	9.6	3.28	0.10	3	3.3	-8.8	8.3	4.82	0.07	3
2.0	-6.0	12.0	14-60	1.7	-6.1	8.7	3.31	0.09	3	1.3	-5.8	8.3	3.83	0.16	3
2.0	-6.0	12.0	14-89	2.4	-5.4	11.2	1.06	0.11	2	2.3	-3.8	-0.3	12.46	NEL	6
2.0	-2.0	12.0	14-6	0.2	-2.4	10.5	2.36	0.14	2	0.3	-2.3	9.8	2.86	0.09	3
2.0	-2.0	12.0	14-7	2.0	-3.4	11.0	1.77	0.09	2	2.3	-3.3	9.3	3.03	0.07	3
2.0	-2.0	12.0	14-53	3.5	-1.4	9.1	3.30	0.09	3	3.3	-1.8	8.3	3.96	NEL	3
2.0	-2.0	12.0	14-82	1.5	-2.0	7.9	4.13	0.09	3	1.3	-2.3	7.3	4.82	0.10	3
2.0	2.0	12.0	14-217	2.0	0.3	11.7	1.74	0.10	2	2.3	-0.8	11.3	2.86	0.12	3
2.0	2.0	12.0	14-235	2.1	2.1	10.9	1.09	0.10	2	0.8	4.3	10.8	2.86	0.11	3
2.0	2.0	12.0	14-257	2.0	2.3	10.6	1.39	0.10	2	1.8	2.8	8.8	3.34	0.06	3
2.0	6.0	12.0	14-244	1.6	6.5	10.1	1.98	0.09	2	1.8	5.8	9.3	2.77	0.24	3
2.0	6.0	12.0	14-264	3.5	7.2	8.8	3.74	0.19	3	1.8	5.3	9.3	2.86	0.05	3
2.0	10.0	12.0	14-228	21.2	-4.0	-12.0	33.77	4.23	6	1.8	11.8	11.8	1.79	0.15	2
2.0	10.0	12.0	14-250	2.2	4.0	6.7	8.02	0.25	5	2.3	8.3	8.3	4.15	0.22	3
6.0	-6.0	12.0	14-26	7.5	-4.7	12.0	2.03	0.09	2	7.8	-4.8	11.8	2.17	0.16	2
6.0	-6.0	12.0	14-61	5.4	-4.0	3.5	8.77	0.22	5	4.8	-8.3	8.3	4.55	0.19	3
6.0	-6.0	12.0	14-62	9.7	-5.9	12.0	3.73	0.10	3	9.8	-5.8	11.3	3.83	NEL	3

Tab. B.3: SW I PLB a - "Top", part 3: Coordinates of the pencil-lead breaks and estimated source locations determined using Geiger's method and *FastWay*. Estimated source locations excluded during the verification process (see Section 7.3.4) are shown in gray.

PLB			Set	Geiger's method						*FastWay*					
x [in]	y [in]	z [in]	#	x [in]	y [in]	z [in]	d [in]	eei [-]	ac [-]	x [in]	y [in]	z [in]	d [in]	eei [-]	ac [-]
6.0	-6.0	12.0	14-90	6.0	-5.4	11.8	0.60	0.10	1	5.3	-6.8	9.8	2.49	0.25	2
6.0	-2.0	12.0	14-8	4.7	-1.6	10.1	2.38	0.09	2	5.3	-1.8	8.8	3.34	0.07	3
6.0	-2.0	12.0	14-54	6.5	-1.3	10.4	1.84	0.10	2	6.3	-1.3	10.3	1.92	0.15	2
6.0	-2.0	12.0	14-83	6.0	-1.9	11.1	0.88	0.09	1	5.8	-2.3	11.8	0.43	0.12	1
6.0	2.0	12.0	14-218	7.7	2.4	9.4	3.15	0.11	3	6.8	1.8	9.8	2.38	0.07	2
6.0	2.0	12.0	14-236	6.2	1.8	10.2	1.79	0.09	2	7.3	2.3	9.3	3.03	0.19	3
6.0	2.0	12.0	14-258	6.7	1.9	10.3	1.79	0.09	2	7.3	2.3	9.3	3.03	0.21	3
6.0	6.0	12.0	11-44	56.9	12.0	12.0	51.28	NaN	6	16.8	-5.3	11.8	15.56	NEL	6
6.0	6.0	12.0	12-79	96.0	-12.0	12.0	91.78	NaN	6	4.3	-11.8	11.8	17.84	NEL	6
6.0	10.0	12.0	14-229	5.5	9.0	9.6	2.64	0.10	3	5.3	8.3	8.8	3.77	0.05	3
6.0	10.0	12.0	14-271	8.9	11.1	12.0	3.06	0.76	3	5.8	8.3	9.3	3.27	0.05	3
10.0	-10.0	12.0	14-40	10.3	-6.5	12.0	3.52	0.08	3	9.3	-7.3	11.8	2.86	NEL	3
10.0	-10.0	12.0	14-68	11.2	-5.7	11.2	4.56	0.09	3	10.8	-5.8	11.3	4.38	0.18	3
10.0	-10.0	12.0	14-69	9.5	-10.4	10.3	1.84	0.11	2	10.3	-9.3	11.3	1.09	0.24	2
10.0	-10.0	12.0	14-97	9.8	-6.7	11.3	3.41	0.10	3	8.8	-6.8	10.3	3.90	0.23	3
10.0	-10.0	12.0	14-98	11.2	-9.3	9.8	2.60	0.27	3	14.8	-5.8	8.3	7.40	NEL	4
10.0	-6.0	12.0	12-30	-14.0	-3.7	10.7	24.13	NaN	6	-23.8	-1.8	9.3	34.13	NEL	6
10.0	-6.0	12.0	14-27	8.5	-5.3	11.6	1.65	0.10	2	8.8	-4.8	10.8	2.17	NEL	2
10.0	-6.0	12.0	14-28	11.7	-4.2	11.6	2.48	0.15	2	11.8	-4.3	11.8	2.49	NEL	2
10.0	-2.0	12.0	14-10	7.0	-1.0	9.3	4.14	0.12	3	9.3	0.3	7.8	4.87	0.05	3
10.0	-2.0	12.0	14-11	8.2	-1.6	10.8	2.20	0.09	2	8.3	-1.3	10.3	2.59	0.12	3
10.0	-2.0	12.0	14-12	8.3	-1.8	10.4	2.32	0.09	2	8.3	-1.8	10.3	2.49	0.08	2
10.0	-2.0	12.0	14-13	11.5	-1.6	10.2	2.36	0.10	2	12.3	-1.3	9.3	3.63	0.13	3
10.0	-2.0	12.0	14-56	9.7	-2.0	10.8	1.23	0.10	2	9.8	-2.3	10.8	1.30	0.14	2
10.0	-2.0	12.0	14-84	10.2	-1.6	10.8	1.32	0.09	2	9.8	-1.8	10.8	1.30	0.13	2
10.0	2.0	12.0	14-219	9.6	1.7	9.9	2.13	0.10	2	9.3	1.3	9.3	2.95	0.09	3
10.0	2.0	12.0	14-237	9.9	1.9	9.9	2.05	0.09	2	9.8	1.8	9.3	2.77	0.16	3
10.0	6.0	12.0	14-225	9.3	5.3	9.6	2.61	0.09	3	9.3	5.3	9.8	2.49	0.14	2
10.0	6.0	12.0	14-245	9.5	5.1	9.8	2.48	0.09	2	10.8	4.8	11.8	1.48	NEL	2
10.0	6.0	12.0	14-265	8.5	5.1	8.8	3.64	0.09	3	8.3	4.8	8.3	4.32	0.14	3
10.0	10.0	12.0	12-81	38.2	12.0	12.0	28.29	2.95	6	12.3	9.3	11.8	2.38	0.21	2
10.0	10.0	12.0	13-60	11.6	9.0	10.8	2.23	0.10	2	10.8	8.3	10.8	2.28	0.21	2
10.0	10.0	12.0	14-251	10.6	12.0	12.0	2.08	0.68	2	5.3	8.3	8.3	6.30	0.03	4
10.0	10.0	12.0	14-252	13.4	12.0	12.0	3.93	1.39	3	8.8	7.3	8.3	4.82	0.02	3
14.0	-10.0	12.0	12-33	10.7	0.8	12.0	11.27	NaN	6	17.3	-3.3	11.8	7.50	NEL	4
14.0	-10.0	12.0	13-9	20.6	-3.8	6.4	10.69	0.29	6	18.8	-7.3	8.3	6.65	NEL	4
14.0	-10.0	12.0	14-41	15.9	-4.0	3.3	10.77	0.18	6	18.8	-3.8	3.3	11.76	NEL	6
14.0	-6.0	12.0	13-8	15.5	-3.7	8.5	4.46	0.14	3	14.3	-3.8	9.3	3.56	0.05	3
14.0	-6.0	12.0	13-14	17.5	-2.8	11.0	4.86	0.34	3	14.3	-4.8	11.8	1.30	0.06	2
14.0	-6.0	12.0	13-20	16.8	-4.0	6.5	6.47	0.20	4	15.8	-5.8	8.3	4.15	NEL	3
14.0	-6.0	12.0	14-29	15.6	-4.8	11.2	2.09	0.14	2	14.8	-6.8	10.3	2.05	0.35	2
14.0	-6.0	12.0	14-30	17.5	-4.1	8.7	5.16	0.12	4	15.3	-5.3	11.8	1.48	0.08	2
14.0	-6.0	12.0	14-91	13.6	-3.5	10.1	3.18	0.15	3	13.8	-3.8	7.8	4.82	NEL	3
14.0	-2.0	12.0	13-13	13.8	-1.4	10.5	1.65	0.09	2	13.8	-1.3	10.3	1.92	0.10	2
14.0	-2.0	12.0	13-18	14.2	-1.4	11.1	1.10	0.09	2	14.3	-1.3	10.8	1.48	0.10	2
14.0	2.0	12.0	14-220	13.4	1.9	10.5	1.65	0.11	2	13.3	1.8	10.8	1.48	0.12	2
14.0	2.0	12.0	14-238	13.6	1.9	10.0	2.09	0.09	2	13.3	1.8	9.8	2.38	0.16	2
14.0	2.0	12.0	14-259	12.7	2.7	11.3	1.61	0.21	2	9.8	1.8	10.3	4.60	0.09	3

Tab. B.4: SW I PLB a - "Top", part 4: Coordinates of the pencil-lead breaks and estimated source locations determined using Geiger's method and *FastWay*. Estimated source locations excluded during the verification process (see Section 7.3.4) are shown in gray.

PLB			Set	Geiger's method						*FastWay*					
x [in]	y [in]	z [in]	#	x [in]	y [in]	z [in]	d [in]	eei [-]	ac [-]	x [in]	y [in]	z [in]	d [in]	eei [-]	ac [-]
14.0	2.0	12.0	14-260	12.5	1.9	9.4	3.03	0.09	3	11.8	1.8	9.3	3.56	0.14	3
14.0	6.0	12.0	13-58	15.8	5.6	10.1	2.67	0.22	3	12.8	4.8	8.3	4.15	NEL	3
14.0	6.0	12.0	13-62	12.9	5.1	9.6	2.85	0.09	3	12.8	5.3	8.3	4.02	NEL	3
14.0	10.0	12.0	11-48	15.9	9.5	10.9	2.24	0.20	2	14.3	9.8	11.8	0.43	NEL	1
14.0	10.0	12.0	12-71	14.8	5.3	9.7	5.31	NaN	4	14.3	10.3	11.8	0.43	NEL	1
14.0	10.0	12.0	12-82	14.8	9.1	10.9	1.70	0.12	2	15.3	11.8	11.8	2.17	NEL	2
18.0	-10.0	12.0	11-6	18.9	-8.4	12.0	1.86	0.24	2	19.8	-10.3	8.3	4.15	0.34	3
18.0	-10.0	12.0	11-8	96.0	4.0	-12.0	82.80	>10.00	6	20.3	-9.3	8.3	4.44	NEL	3
18.0	-10.0	12.0	12-19	17.7	-6.4	8.3	5.17	0.11	4	16.8	-7.3	8.3	4.82	0.27	3
18.0	-6.0	12.0	10-11	27.7	-5.4	12.0	9.76	0.30	5	23.8	-6.8	10.3	6.06	NEL	4
18.0	-6.0	12.0	12-31	19.8	-4.4	11.7	2.38	0.14	2	18.8	-7.3	8.3	4.02	0.42	3
18.0	-6.0	12.0	14-31	23.1	-3.5	12.0	5.70	0.41	4	18.3	-8.3	8.3	4.38	NEL	3
18.0	-2.0	12.0	12-12	23.5	0.1	12.0	5.87	0.35	4	18.3	-2.3	10.8	1.30	0.05	2
18.0	-2.0	12.0	13-19	17.5	-2.0	10.3	1.79	0.10	2	17.8	-2.3	10.3	1.79	0.13	2
18.0	-2.0	12.0	14-14	15.6	-1.7	11.0	2.61	0.09	3	16.3	-2.3	10.3	2.49	0.15	2
18.0	-2.0	12.0	14-15	17.4	-2.0	10.0	2.11	0.10	2	17.3	-2.3	9.8	2.38	0.15	2
18.0	2.0	12.0	12-62	17.6	2.1	8.1	3.91	0.09	3	17.8	2.3	8.3	3.77	0.08	3
18.0	2.0	12.0	13-57	16.5	1.7	9.3	3.10	0.10	3	15.8	1.8	8.3	4.38	0.23	3
18.0	2.0	12.0	13-61	17.2	1.8	10.3	1.89	0.10	2	18.3	2.3	11.3	0.83	0.21	1
18.0	2.0	12.0	13-64	16.9	1.8	9.9	2.35	0.09	2	16.8	1.3	9.3	3.11	0.15	3
18.0	6.0	12.0	11-45	17.2	5.0	11.3	1.44	0.10	2	15.8	3.8	8.8	4.55	NEL	3
18.0	6.0	12.0	11-55	16.5	4.7	10.3	2.59	0.10	3	15.8	4.8	9.8	3.42	0.16	3
18.0	6.0	12.0	12-67	16.4	4.6	10.2	2.79	0.10	3	15.3	4.3	9.8	3.96	0.16	3
18.0	6.0	12.0	14-266	20.4	4.9	10.7	2.94	0.89	3	11.3	4.8	8.3	7.82	0.07	5
18.0	10.0	12.0	11-59	16.8	8.3	10.5	2.60	0.09	3	18.3	9.8	9.8	2.28	NEL	2
18.0	10.0	12.0	12-72	16.2	8.6	10.9	2.47	0.13	2	16.8	8.8	8.3	4.15	NEL	3
18.0	10.0	12.0	12-76	16.8	6.8	11.2	3.50	0.34	3	16.3	7.8	11.3	2.95	NEL	3
22.0	-10.0	12.0	10-13	9.5	-7.0	12.0	12.82	NaN	6	23.8	-10.3	11.3	1.92	NEL	2
22.0	-10.0	12.0	10-20	-96.0	-4.0	-12.0	120.57	NaN	6	23.8	-0.3	0.8	14.99	NEL	6
22.0	-6.0	12.0	10-3	21.9	-3.6	12.0	2.42	0.45	2	20.3	-8.8	8.3	4.97	0.26	3
22.0	-6.0	12.0	10-18	22.2	-5.3	12.0	0.73	0.19	1	20.8	-6.3	11.3	1.48	0.17	2
22.0	-6.0	12.0	12-17	22.0	-4.8	11.0	1.61	0.31	2	19.3	-5.8	8.3	4.66	NEL	3
22.0	-6.0	12.0	14-32	28.1	-1.3	12.0	7.70	0.66	5	23.8	-7.8	9.8	3.34	0.15	3
22.0	-2.0	12.0	10-2	27.1	-1.4	11.1	5.21	0.26	4	22.3	-1.8	11.3	0.83	0.06	1
22.0	-2.0	12.0	12-27	28.6	-1.3	10.9	6.75	0.35	4	22.8	-1.3	11.3	1.30	0.04	2
22.0	-2.0	12.0	13-3	19.8	-1.7	11.0	2.45	0.09	2	19.8	-1.8	11.3	2.38	0.12	2
22.0	2.0	12.0	11-52	20.8	1.8	10.7	1.79	0.10	2	22.3	2.3	11.3	0.83	0.18	1
22.0	2.0	12.0	12-74	20.6	1.8	10.7	1.92	0.09	2	21.8	2.3	11.3	0.83	0.18	1
22.0	6.0	12.0	12-68	19.8	4.8	10.7	2.83	0.10	3	21.3	5.3	11.3	1.30	0.17	2
22.0	6.0	12.0	12-75	96.0	12.0	12.0	74.24	>10.00	6	23.8	6.8	8.3	4.21	NEL	3
22.0	6.0	12.0	13-66	21.3	6.2	12.0	0.77	0.08	1	21.8	5.8	11.8	0.43	0.05	1
22.0	10.0	12.0	11-36	96.0	12.0	12.0	74.03	NaN	6	14.8	4.8	8.3	9.71	NEL	5
22.0	10.0	12.0	11-60	-6.9	1.6	-8.1	36.18	NaN	6	18.8	11.3	8.3	5.12	NEL	4

Tab. B.5: SW I PLB a - "Top", part 5: Coordinates of the pencil-lead breaks and estimated source locations determined using Geiger's method and *FastWay*. Estimated source locations excluded during the verification process (see Section 7.3.4) are shown in gray.

B.1.2 Top-Front

PLB			Set	Geiger's method						*FastWay*					
x [in]	y [in]	z [in]	#	x [in]	y [in]	z [in]	d [in]	eei [-]	ac [-]	x [in]	y [in]	z [in]	d [in]	eei [-]	ac [-]
-22.0	-12.0	10.0	11-9	-28.0	-11.5	12.0	6.36	1.53	4	-21.3	-9.3	9.3	2.95	0.03	3
-22.0	-12.0	10.0	12-9	-22.0	-8.3	10.1	3.75	0.37	3	-23.8	-7.3	8.3	5.36	0.97	4
-22.0	-12.0	10.0	13-15	-20.8	-4.0	7.3	8.54	0.37	5	-19.8	-8.8	8.3	4.32	0.04	3
-18.0	-12.0	10.0	12-10	-19.8	-9.0	10.8	3.55	0.14	3	-17.8	-10.3	8.3	2.49	0.06	2
-18.0	-12.0	10.0	12-20	-22.5	-11.3	12.0	4.97	0.60	3	-20.3	-8.3	8.3	4.71	NEL	3
-14.0	-12.0	10.0	14-42	-15.8	-11.4	12.0	2.74	0.41	3	-13.3	-11.8	8.3	1.92	0.25	2
-14.0	-12.0	10.0	14-70	-16.0	-12.0	12.0	2.82	0.32	3	-16.3	-8.8	8.3	4.32	0.22	3
-14.0	-12.0	10.0	14-71	-15.5	-6.6	12.0	5.95	0.20	4	-14.8	-7.3	11.8	5.12	0.17	4
-10.0	-12.0	10.0	14-43	-19.9	-12.0	12.0	10.11	3.10	6	-10.3	-11.8	10.8	0.83	NEL	1
-10.0	-12.0	10.0	14-72	-11.7	-7.1	11.4	5.39	0.12	4	-11.8	-7.3	8.3	5.36	NEL	4
-6.0	-12.0	10.0	14-44	-4.5	-12.0	12.0	2.52	0.24	3	-6.3	-11.8	8.8	1.30	0.09	2
-2.0	-12.0	10.0	14-45	-1.8	-4.0	6.3	8.80	0.28	5	-2.3	-11.3	11.8	1.92	0.18	2
-2.0	-12.0	10.0	14-73	-2.3	-12.0	12.0	2.02	0.33	2	-2.3	-11.8	11.8	1.79	0.44	2
-2.0	-12.0	10.0	14-74	2.2	-10.4	10.0	4.53	0.11	3	1.8	-11.8	8.3	4.15	0.30	3
2.0	-12.0	10.0	14-46	0.6	-9.0	12.0	3.88	0.71	3	1.3	-11.8	8.3	1.92	NEL	2
6.0	-12.0	10.0	14-47	7.3	-9.2	12.0	3.66	0.24	3	6.3	-11.8	11.3	1.30	0.20	2
6.0	-12.0	10.0	14-75	8.1	-11.7	12.0	2.90	0.52	3	5.3	-11.8	8.3	1.92	0.36	2
6.0	-12.0	10.0	14-76	7.9	-11.8	9.7	1.96	0.09	2	8.3	-11.8	8.3	2.86	0.25	3
14.0	-12.0	10.0	13-16	15.9	-7.1	12.0	5.66	0.19	4	23.8	-3.8	4.3	14.01	NEL	6
14.0	-12.0	10.0	14-48	13.5	-6.8	12.0	5.63	0.10	4	15.8	-4.8	9.3	7.50	0.18	4
14.0	-12.0	10.0	14-49	15.0	-7.7	12.0	4.85	0.24	3	13.3	-11.8	11.8	1.92	0.45	2
14.0	-12.0	10.0	14-77	13.8	-6.7	12.0	5.69	0.10	4	13.3	-7.3	11.8	5.12	0.10	4
18.0	-12.0	10.0	12-21	20.8	-3.0	12.0	9.68	0.65	5	18.8	-11.8	8.3	1.92	0.33	2
18.0	-12.0	10.0	13-10	18.9	-7.3	12.0	5.20	0.30	4	19.3	-11.8	8.3	2.17	0.44	2
22.0	-12.0	10.0	10-5	20.4	-5.4	12.0	7.03	NaN	4	19.3	-8.3	11.8	4.97	NEL	3

Tab. B.6: SW I PLB a - "Top-Front", part 1: Coordinates of the pencil-lead breaks and estimated source locations determined using Geiger's method and *FastWay*. Estimated source locations excluded during the verification process (see Section 7.3.4) are shown in gray.

B.1.3 Front

PLB			Set	Geiger's method						*FastWay*					
x [in]	y [in]	z [in]	#	x [in]	y [in]	z [in]	d [in]	eei [-]	ac [-]	x [in]	y [in]	z [in]	d [in]	eei [-]	ac [-]
-22.0	-4.0	-10.0	12-37	-17.8	1.4	-5.5	8.19	0.36	5	-18.3	-0.8	-6.8	5.93	NEL	4
-22.0	-4.0	-10.0	12-39	-18.0	0.8	-5.8	7.51	0.38	5	-21.3	-1.8	-8.8	2.68	NEL	3
-22.0	-4.0	-10.0	13-26	-31.0	-4.0	-12.0	9.18	0.92	5	-23.8	-1.8	-7.8	3.63	0.20	3
-22.0	-4.0	-6.0	12-36	-16.7	-2.4	-5.5	5.57	0.53	4	-23.3	-3.8	-7.3	1.79	0.24	2
-22.0	-4.0	-6.0	12-38	-37.2	-4.0	-12.0	16.30	4.64	6	-17.3	-0.8	-3.8	6.18	0.04	4
-22.0	-4.0	-6.0	12-41	-40.9	-4.0	-12.0	19.83	NaN	6	-23.8	-1.8	-3.3	3.96	NEL	3
-22.0	-4.0	-2.0	11-16	-31.0	-4.0	-5.8	9.78	0.27	5	-20.3	-1.8	-2.3	2.86	0.19	3
-22.0	-4.0	-2.0	11-17	-16.4	-1.7	-0.8	6.18	0.14	4	-16.8	-1.8	-1.3	5.76	0.11	4
-22.0	-4.0	2.0	10-23	-19.3	-2.1	3.2	3.52	0.12	3	-20.3	-0.8	1.8	3.70	0.04	3
-22.0	-4.0	2.0	12-40	-19.2	-0.8	1.4	4.31	0.12	3	-21.8	-2.8	1.3	1.48	0.11	2
-22.0	-4.0	2.0	13-24	-19.7	-0.8	1.0	4.10	0.10	3	-21.3	-1.8	1.8	2.38	0.12	2
-22.0	-4.0	2.0	14-106	-27.5	0.2	0.2	7.10	0.23	4	-23.8	-1.3	1.8	3.27	0.74	3
-22.0	-4.0	6.0	13-22	-20.3	-1.7	5.3	2.94	0.09	3	-21.3	-2.3	5.3	2.05	0.12	2
-22.0	-4.0	6.0	13-23	-20.3	-1.6	5.0	3.11	0.09	3	-21.3	-2.3	5.3	2.05	0.08	2
-22.0	-4.0	6.0	13-25	-19.5	-1.9	5.0	3.37	0.09	3	-21.3	-2.3	5.3	2.05	0.09	2
-18.0	-4.0	-10.0	13-28	-13.9	0.5	-8.0	6.37	0.63	4	-5.8	-2.8	-11.8	12.44	NEL	6
-18.0	-4.0	-10.0	13-30	-13.8	-3.9	-10.6	4.22	NaN	3	-18.3	-1.3	-9.8	2.77	NEL	3
-18.0	-4.0	-6.0	14-108	-96.0	-12.0	12.0	80.45	>10.00	6	-22.3	-3.8	-6.3	4.26	NEL	3
-18.0	-4.0	-2.0	10-24	-96.0	-12.0	12.0	79.65	>10.00	6	-22.3	-3.3	-6.3	6.06	NEL	4
-18.0	-4.0	-2.0	11-19	-38.2	-12.0	12.0	25.83	8.25	6	-2.8	-11.8	11.8	21.95	NEL	6
-18.0	-4.0	2.0	13-32	-96.0	-12.0	12.0	79.04	>10.00	6	-16.8	0.8	3.3	5.07	0.06	4
-18.0	-4.0	2.0	14-107	-15.9	-1.9	0.1	3.52	0.11	3	-16.8	-3.3	1.8	1.48	0.14	2
-18.0	-4.0	2.0	14-109	-74.8	-12.0	12.0	58.26	>10.00	6	-13.3	-11.8	9.3	11.63	NEL	6
-18.0	-4.0	2.0	14-110	-96.0	-12.0	12.0	79.04	>10.00	6	-16.8	0.8	3.8	5.21	0.03	4
-18.0	-4.0	2.0	14-111	-16.1	-1.3	-0.3	4.06	0.10	3	-17.3	-1.3	1.3	2.95	0.11	3
-18.0	-4.0	6.0	13-27	-17.6	-2.0	5.9	2.03	0.10	2	-18.8	-2.8	5.8	1.48	0.14	2
-18.0	-4.0	6.0	13-29	-17.0	-2.2	5.6	2.11	0.09	2	-17.8	-2.8	5.8	1.30	0.18	2
-18.0	-4.0	6.0	13-31	-17.5	-2.0	6.0	2.02	0.09	2	-18.8	-2.8	5.8	1.48	0.11	2
-14.0	-4.0	-10.0	13-37	-96.0	-4.0	-12.0	82.02	>10.00	6	-14.3	-2.8	-9.8	1.30	0.13	2
-14.0	-4.0	-10.0	13-40	-12.5	-0.7	-11.1	3.77	0.49	3	-13.3	-0.8	-11.8	3.77	NEL	3
-14.0	-4.0	-10.0	13-42	-96.0	-4.0	-12.0	82.02	>10.00	6	-16.8	-3.8	-11.8	3.27	NEL	3
-14.0	-4.0	-6.0	13-36	-13.7	-3.3	-6.7	1.00	0.14	1	-14.3	-3.3	-6.3	0.83	0.10	1
-14.0	-4.0	-6.0	14-116	-15.5	-0.3	-10.7	6.20	0.54	4	-13.8	-2.8	-5.8	1.30	0.07	2
-14.0	-4.0	-6.0	14-119	-13.9	-3.4	-6.6	0.84	0.14	1	-13.8	-2.8	-6.3	1.30	0.07	2
-14.0	-4.0	-2.0	13-35	-12.9	-0.8	-3.6	3.80	0.26	3	-15.8	-3.8	-7.3	5.54	0.24	4
-14.0	-4.0	-2.0	13-39	-11.7	2.0	-1.2	6.49	0.29	4	-16.8	-3.8	-7.8	6.38	0.29	4
-14.0	-4.0	-2.0	13-41	-13.7	-0.2	-4.4	4.49	0.24	3	-16.3	-3.8	-6.8	5.26	0.23	4
-14.0	-4.0	2.0	13-34	-13.6	-1.1	1.2	3.03	0.17	3	-13.8	-1.8	1.3	2.38	0.22	2
-14.0	-4.0	2.0	13-38	-13.5	-1.8	1.3	2.35	0.15	2	-14.3	-3.3	1.8	0.83	0.20	1
-14.0	-4.0	2.0	14-113	-13.4	-3.1	2.0	1.12	0.10	2	-13.8	-3.3	2.3	0.83	0.16	1
-14.0	-4.0	2.0	14-118	-13.4	-2.0	3.3	2.49	0.11	2	-14.3	-3.3	3.8	1.92	0.18	2
-14.0	-4.0	6.0	14-112	-13.6	-2.2	5.3	1.94	0.10	2	-14.3	-3.3	5.3	1.09	0.16	2
-14.0	-4.0	6.0	14-114	-13.6	-2.3	5.2	1.97	0.11	2	-14.3	-3.3	5.3	1.09	0.16	2
-14.0	-4.0	6.0	14-115	-13.6	-2.3	5.4	1.88	0.11	2	-14.3	-3.3	5.8	0.83	0.17	1
-14.0	-4.0	6.0	14-117	-13.5	-2.1	5.3	2.06	0.10	2	-13.8	-3.3	5.3	1.09	0.20	2
-10.0	-4.0	-10.0	13-43	-10.8	-4.0	-10.6	1.00	0.29	2	-10.3	-3.3	-9.8	0.83	0.32	1
-10.0	-4.0	-10.0	13-44	-10.7	-4.0	-10.8	1.07	0.28	2	-10.3	-2.3	-8.8	2.17	0.10	2

Tab. B.7: SW I PLB a - "Front", part 1: Coordinates of the pencil-lead breaks and estimated source locations determined using Geiger's method and *FastWay*. Estimated source locations excluded during the verification process (see Section 7.3.4) are shown in gray.

PLB			Set	Geiger's method						*FastWay*					
x [in]	y [in]	z [in]	#	x [in]	y [in]	z [in]	d [in]	eei [-]	ac [-]	x [in]	y [in]	z [in]	d [in]	eei [-]	ac [-]
-10.0	-4.0	-10.0	13-45	-14.7	-4.0	-12.0	5.12	0.64	4	-9.8	-0.8	-7.3	4.26	0.04	3
-10.0	-4.0	-6.0	14-123	-8.1	2.7	-7.7	7.18	0.30	4	-9.8	-1.8	-5.8	2.28	0.04	2
-10.0	-4.0	-6.0	14-127	-9.7	-1.8	-5.1	2.39	0.11	2	-10.3	-1.8	-5.3	2.38	0.10	2
-10.0	-4.0	-6.0	14-131	-11.5	-4.0	-9.7	4.02	0.35	3	-10.3	-2.3	-5.8	1.79	0.08	2
-10.0	-4.0	-2.0	14-122	-9.8	-1.2	-2.9	2.96	0.22	3	-10.3	-1.8	-1.3	2.38	0.06	2
-10.0	-4.0	-2.0	14-126	-10.9	-1.2	-1.7	2.95	0.17	3	-10.3	-2.3	-1.8	1.79	0.11	2
-10.0	-4.0	-2.0	14-130	-9.6	-1.2	-3.0	3.01	0.23	3	-10.3	-2.8	-1.8	1.30	0.16	2
-10.0	-4.0	2.0	14-121	-9.5	-0.3	1.9	3.71	0.15	3	-10.3	-1.8	1.8	2.28	0.12	2
-10.0	-4.0	2.0	14-125	-10.7	-3.5	2.1	0.87	0.11	1	-10.3	-3.3	1.8	0.83	0.18	1
-10.0	-4.0	2.0	14-129	-10.1	-0.7	1.6	3.37	0.12	3	-10.3	-2.3	1.8	1.79	0.11	2
-10.0	-4.0	6.0	14-120	-9.9	-2.4	6.1	1.62	0.09	2	-10.3	-2.8	5.8	1.30	0.08	2
-10.0	-4.0	6.0	14-124	-9.1	-2.8	5.8	1.53	0.13	2	-9.8	-2.8	5.8	1.30	0.15	2
-10.0	-4.0	6.0	14-128	-9.6	-2.9	6.1	1.19	0.11	2	-9.8	-3.3	6.3	0.83	0.09	1
-6.0	-4.0	-10.0	14-136	-7.1	-4.0	-12.0	2.30	0.37	2	-6.8	-3.3	-10.3	1.09	0.25	2
-6.0	-4.0	-10.0	14-141	-9.0	-3.8	-10.5	3.06	0.39	3	-6.8	-1.3	-7.3	3.96	0.04	3
-6.0	-4.0	-10.0	14-145	-7.7	-0.5	-8.1	4.35	0.38	3	-4.8	2.3	-6.8	7.15	NEL	4
-6.0	-4.0	-10.0	14-146	-7.5	-1.6	-11.5	3.18	0.53	3	-6.3	0.3	-11.8	4.60	NEL	3
-6.0	-4.0	-6.0	14-135	-7.7	-4.0	-7.7	2.43	0.34	2	-6.8	-3.3	-5.3	1.30	0.15	2
-6.0	-4.0	-6.0	14-140	-6.8	-1.9	-5.1	2.46	0.12	2	-7.3	-1.8	-5.3	2.68	0.25	3
-6.0	-4.0	-6.0	14-144	-9.5	-1.4	-3.2	5.18	0.33	4	-10.3	-3.8	-3.8	4.82	NEL	3
-6.0	-4.0	-2.0	14-134	-6.5	-3.7	-1.6	0.75	0.12	1	-6.8	-2.3	-1.8	1.92	0.25	2
-6.0	-4.0	-2.0	14-139	-6.6	-2.3	-1.4	1.94	0.15	2	-6.8	-2.3	-1.8	1.92	0.17	2
-6.0	-4.0	2.0	14-133	-5.3	-4.0	4.1	2.18	0.10	2	-6.8	-3.3	4.3	2.49	0.13	2
-6.0	-4.0	2.0	14-138	-6.0	-3.7	2.1	0.34	0.10	1	-6.3	-3.8	2.3	0.43	0.20	1
-6.0	-4.0	2.0	14-143	-6.3	-3.1	2.0	0.96	0.10	1	-6.8	-3.3	2.3	1.09	0.23	2
-6.0	-4.0	6.0	14-132	-6.7	-2.7	6.2	1.47	0.12	2	-7.3	-2.3	5.8	2.17	0.17	2
-6.0	-4.0	6.0	14-137	-5.8	-3.0	6.1	1.05	0.14	2	-6.8	-2.8	6.3	1.48	0.08	2
-6.0	-4.0	6.0	14-142	-6.3	-2.5	6.5	1.57	0.12	2	-6.8	-2.3	6.3	1.92	0.16	2
-2.0	-4.0	-10.0	14-151	96.0	4.0	-12.0	98.35	>10.00	6	-1.8	-2.8	-9.3	1.48	0.04	2
-2.0	-4.0	-10.0	14-155	4.0	-3.4	-8.0	6.34	0.62	4	-0.3	-2.3	-6.8	4.09	NEL	3
-2.0	-4.0	-10.0	14-156	-1.1	-1.9	-10.0	2.27	0.09	2	-1.3	-1.8	-9.8	2.38	0.06	2
-2.0	-4.0	-10.0	14-161	-1.5	-2.2	-10.4	1.92	0.10	2	-1.8	-2.3	-10.3	1.79	0.07	2
-2.0	-4.0	-6.0	14-150	0.4	0.5	-8.6	5.73	0.30	4	22.3	-2.3	-9.8	24.60	NEL	6
-2.0	-4.0	-6.0	14-154	-1.4	1.4	-4.8	5.58	0.25	4	-2.3	-0.3	-3.8	4.38	0.12	3
-2.0	-4.0	-6.0	14-160	-1.6	-3.4	-5.3	1.07	0.09	2	-2.3	-3.3	-5.8	0.83	0.07	1
-2.0	-4.0	-2.0	14-149	-2.8	-2.5	-1.6	1.76	0.20	2	-3.3	-1.8	-2.3	2.59	0.24	3
-2.0	-4.0	-2.0	14-159	-2.0	-2.4	-2.7	1.76	0.15	2	-2.3	-0.8	-3.3	3.49	0.13	3
-2.0	-4.0	2.0	14-148	-2.2	-1.9	1.8	2.11	0.27	2	-4.3	-1.8	1.3	3.27	0.23	3
-2.0	-4.0	2.0	14-153	-2.6	-1.4	0.7	3.00	0.33	3	-2.3	-3.3	2.3	0.83	0.22	1
-2.0	-4.0	2.0	14-158	-2.2	-1.6	1.2	2.50	0.16	2	-2.3	-3.3	1.8	0.83	0.16	1
-2.0	-4.0	6.0	14-147	-2.0	-2.9	6.0	1.07	0.15	2	-2.3	-3.3	5.8	0.83	0.08	1
-2.0	-4.0	6.0	14-152	-2.4	-3.5	5.9	0.64	0.12	1	-2.3	-3.8	5.8	0.43	0.13	1
-2.0	-4.0	6.0	14-157	-2.6	-3.3	5.6	1.02	0.12	2	-2.3	-3.3	5.8	0.83	0.09	1
2.0	-4.0	-10.0	14-166	3.1	-4.0	-12.0	2.30	0.98	2	1.3	-3.8	-11.8	1.92	NEL	2
2.0	-4.0	-10.0	14-171	3.3	1.5	-11.3	5.75	0.53	4	3.3	-3.3	-11.8	2.28	0.32	2
2.0	-4.0	-10.0	14-176	3.8	-4.0	-11.7	2.51	0.24	3	2.8	-3.3	-9.8	1.09	0.11	2
2.0	-4.0	-6.0	14-165	2.5	-3.6	-5.8	0.68	0.10	1	1.8	-2.8	-6.3	1.30	0.15	2
2.0	-4.0	-6.0	14-170	2.8	-4.0	-4.9	1.35	0.10	2	1.8	-3.8	-5.3	0.83	0.12	1
2.0	-4.0	-6.0	14-175	2.0	0.7	-9.7	5.99	0.15	4	1.3	-0.8	-7.3	3.56	0.24	3

Tab. B.8: SW I PLB a - "Front", part 2: Coordinates of the pencil-lead breaks and estimated source locations determined using Geiger's method and *FastWay*. Estimated source locations excluded during the verification process (see Section 7.3.4) are shown in gray.

PLB			Set	Geiger's method						*FastWay*					
x [in]	y [in]	z [in]	#	x [in]	y [in]	z [in]	d [in]	eei [-]	ac [-]	x [in]	y [in]	z [in]	d [in]	eei [-]	ac [-]
2.0	-4.0	-2.0	14-164	2.9	-2.1	-3.7	2.67	0.16	3	2.3	-2.8	-2.8	1.48	0.05	2
2.0	-4.0	-2.0	14-169	4.4	1.7	-5.1	6.94	0.20	4	2.8	-2.3	-3.3	2.28	0.04	2
2.0	-4.0	-2.0	14-174	1.8	-3.7	-1.4	0.71	0.12	1	2.3	0.3	-4.3	4.82	0.15	3
2.0	-4.0	2.0	14-163	1.9	-2.9	1.8	1.13	0.23	2	1.8	-3.3	1.8	0.83	0.07	1
2.0	-4.0	2.0	14-168	1.8	-3.6	2.4	0.59	0.17	1	1.8	-3.8	2.3	0.43	0.21	1
2.0	-4.0	2.0	14-173	2.8	-1.5	1.1	2.75	0.14	3	2.3	-2.8	1.3	1.48	0.17	2
2.0	-4.0	6.0	14-162	3.1	-1.8	4.8	2.78	0.15	3	2.8	-1.8	4.3	2.95	0.15	3
2.0	-4.0	6.0	14-167	0.8	-3.6	6.8	1.53	0.11	2	1.3	-3.8	5.8	0.83	NEL	1
2.0	-4.0	6.0	14-172	0.4	-3.1	7.0	2.07	0.13	2	0.3	-3.8	6.8	1.92	NEL	2
6.0	-4.0	-10.0	14-181	-5.7	4.0	-12.0	14.29	5.32	6	4.3	1.3	-11.3	5.67	NEL	4
6.0	-4.0	-10.0	14-186	4.2	4.0	-12.0	8.43	0.97	5	5.8	0.3	-11.8	4.60	0.31	3
6.0	-4.0	-10.0	14-191	-6.1	4.0	-12.0	14.64	5.56	6	5.8	-2.8	-11.8	2.17	0.33	2
6.0	-4.0	-6.0	14-179	6.2	2.0	-5.2	6.06	0.10	4	6.3	-0.3	-4.3	4.15	0.10	3
6.0	-4.0	-6.0	14-180	5.8	-2.2	-5.9	1.80	0.11	2	5.8	-2.8	-6.3	1.30	0.14	2
6.0	-4.0	-6.0	14-185	6.0	-1.1	-6.8	2.97	0.09	3	5.8	-2.3	-7.3	2.17	NEL	2
6.0	-4.0	-6.0	14-190	6.0	-2.8	-5.5	1.30	0.10	2	5.8	-2.8	-6.3	1.30	0.14	2
6.0	-4.0	-2.0	14-184	6.2	-3.4	-1.3	1.00	0.10	2	5.8	-2.8	-2.3	1.30	0.12	2
6.0	-4.0	-2.0	14-189	6.1	-4.0	-1.3	0.73	0.09	1	5.3	-3.8	-1.3	1.09	0.15	2
6.0	-4.0	2.0	14-178	6.1	-1.5	-0.2	3.30	0.11	3	5.8	-2.3	1.3	1.92	0.09	2
6.0	-4.0	2.0	14-183	6.6	-1.1	0.3	3.44	0.14	3	5.8	-2.8	1.3	1.48	0.06	2
6.0	-4.0	2.0	14-188	6.3	-2.5	0.3	2.27	0.16	2	6.3	-2.8	0.8	1.79	0.08	2
6.0	-4.0	6.0	14-177	5.6	-2.4	5.5	1.76	0.11	2	5.8	-2.8	5.3	1.48	0.10	2
6.0	-4.0	6.0	14-182	5.3	-3.1	6.0	1.12	0.11	2	5.8	-3.3	5.8	0.83	0.09	1
6.0	-4.0	6.0	14-187	6.3	-1.8	5.2	2.40	0.12	2	5.8	-2.8	5.3	1.48	0.16	2
10.0	-4.0	-10.0	13-47	9.9	-4.0	-7.7	2.29	0.43	2	10.3	-1.3	-9.3	2.86	0.01	3
10.0	-4.0	-10.0	14-196	9.4	3.1	-12.0	7.43	0.46	4	9.3	-0.3	-11.3	4.02	0.25	3
10.0	-4.0	-10.0	14-204	10.5	-1.9	-12.0	2.95	0.15	3	9.8	-1.3	-11.8	3.27	0.09	3
10.0	-4.0	-6.0	13-48	10.2	-4.0	-8.4	2.45	0.30	2	9.8	-1.8	-7.3	2.59	NEL	3
10.0	-4.0	-6.0	14-194	8.9	-1.0	-6.1	3.21	0.22	3	9.3	-1.3	-3.8	3.63	0.13	3
10.0	-4.0	-6.0	14-195	10.8	0.5	-7.0	4.64	0.34	3	9.3	-3.8	-4.8	1.48	0.06	2
10.0	-4.0	-6.0	14-200	9.6	-3.7	-4.3	1.75	0.09	2	9.3	-3.3	-5.3	1.30	0.09	2
10.0	-4.0	-2.0	14-199	10.4	-2.5	-1.2	1.78	0.09	2	10.3	-2.8	-1.3	1.48	0.07	2
10.0	-4.0	-2.0	14-203	9.6	-2.2	-1.9	1.88	0.09	2	9.8	0.8	-4.8	5.49	NEL	4
10.0	-4.0	2.0	14-193	9.5	-2.2	0.1	2.69	0.11	3	9.8	-3.3	0.8	1.48	0.09	2
10.0	-4.0	2.0	14-198	10.2	-0.7	0.3	3.74	0.17	3	9.8	-1.3	1.3	2.86	0.20	3
10.0	-4.0	2.0	14-202	10.1	0.0	0.5	4.29	0.14	3	9.8	-1.8	0.8	2.59	0.22	3
10.0	-4.0	6.0	14-192	10.5	-2.0	5.6	2.10	0.09	2	10.3	-2.3	5.8	1.79	0.06	2
10.0	-4.0	6.0	14-197	10.6	-1.4	5.9	2.69	0.11	3	10.3	-1.8	5.8	2.28	0.06	2
10.0	-4.0	6.0	14-201	10.7	-1.5	5.9	2.65	0.09	3	10.3	-1.8	5.8	2.28	0.05	2
14.0	-4.0	-10.0	12-47	96.0	-12.0	-12.0	82.41	NaN	6	12.8	2.8	-10.8	6.91	NEL	4
14.0	-4.0	-10.0	12-48	12.1	0.7	-12.0	5.46	0.60	4	10.8	-2.8	-11.8	3.90	0.34	3
14.0	-4.0	-10.0	12-49	96.0	-4.0	-12.0	82.02	>10.00	6	12.8	-1.8	-7.3	3.77	0.06	3
14.0	-4.0	-10.0	12-51	14.3	1.9	-12.0	6.23	0.30	4	14.8	-0.3	-10.3	3.83	0.34	3
14.0	-4.0	-6.0	12-50	14.1	-0.6	-8.6	4.29	0.24	3	18.8	-3.8	-10.8	6.72	NEL	4
14.0	-4.0	-6.0	13-49	16.9	-4.0	-12.0	6.67	0.41	4	17.8	-3.8	-10.3	5.67	0.25	4
14.0	-4.0	-6.0	14-208	13.9	-0.6	-12.0	6.92	0.69	4	13.3	-0.8	-10.3	5.40	0.35	4
14.0	-4.0	-6.0	14-210	11.7	-1.4	-12.0	6.93	0.40	4	13.3	-3.3	-1.8	4.38	NEL	3
14.0	-4.0	-2.0	12-46	13.6	-0.1	-12.0	10.73	0.60	6	15.8	-3.8	-1.3	1.92	NEL	2

Tab. B.9: SW I PLB a - "Front", part 3: Coordinates of the pencil-lead breaks and estimated source locations determined using Geiger's method and *FastWay*. Estimated source locations excluded during the verification process (see Section 7.3.4) are shown in gray.

PLB			Set	Geiger's method						*FastWay*					
x [in]	y [in]	z [in]	#	x [in]	y [in]	z [in]	d [in]	eei [-]	ac [-]	x [in]	y [in]	z [in]	d [in]	eei [-]	ac [-]
14.0	-4.0	2.0	13-50	13.0	-0.3	-0.6	4.62	0.13	3	12.8	-0.8	0.3	3.90	0.20	3
14.0	-4.0	2.0	14-206	13.5	-1.9	0.9	2.46	0.12	2	12.8	-2.3	1.3	2.28	0.14	2
14.0	-4.0	2.0	14-209	14.1	-2.3	0.8	2.07	0.10	2	13.3	-2.8	1.8	1.48	0.07	2
14.0	-4.0	6.0	13-51	14.3	-2.4	5.7	1.65	0.10	2	13.8	-2.3	6.3	1.79	0.15	2
14.0	-4.0	6.0	14-205	14.5	-2.2	5.8	1.89	0.11	2	14.3	-2.3	6.3	1.79	0.09	2
14.0	-4.0	6.0	14-207	14.2	-2.3	5.6	1.79	0.10	2	14.3	-2.3	6.3	1.79	0.08	2
18.0	-4.0	-10.0	11-23	16.1	1.4	-8.4	5.93	0.42	4	16.3	3.3	-11.3	7.56	NEL	5
18.0	-4.0	-10.0	11-24	96.0	-12.0	12.0	81.44	>10.00	6	15.3	-3.8	6.8	16.98	NEL	6
18.0	-4.0	-10.0	12-52	29.0	-4.0	-12.0	11.22	4.51	6	18.3	-3.8	-10.8	0.83	0.29	1
18.0	-4.0	-10.0	12-55	14.6	0.0	-12.0	5.63	0.61	4	14.3	-0.8	-11.8	5.26	0.04	4
18.0	-4.0	-10.0	12-57	11.9	4.0	-12.0	10.27	1.43	6	10.8	-3.8	-11.8	7.46	0.51	4
18.0	-4.0	-6.0	11-22	16.6	-0.3	-6.0	3.92	0.25	3	16.8	-1.8	-4.3	3.11	0.03	3
18.0	-4.0	-6.0	12-56	16.9	-0.5	-3.9	4.21	0.15	3	20.8	-3.8	-5.3	2.86	0.08	3
18.0	-4.0	-2.0	11-21	13.0	4.0	-4.6	9.77	0.42	5	15.8	0.3	-4.3	5.31	0.32	4
18.0	-4.0	-2.0	12-54	16.9	0.1	-5.1	5.24	0.22	4	13.3	1.3	-11.8	12.05	NEL	6
18.0	-4.0	2.0	12-53	16.6	-1.5	1.3	2.92	0.10	3	17.3	-3.3	1.8	1.09	0.19	2
18.0	-4.0	2.0	13-55	17.1	-1.9	1.2	2.46	0.10	2	17.3	-3.3	1.8	1.09	0.15	2
18.0	-4.0	2.0	14-211	17.0	-1.9	1.3	2.43	0.10	2	17.8	-3.3	1.8	0.83	0.14	1
18.0	-4.0	6.0	13-52	17.9	-2.1	6.0	1.91	0.10	2	17.8	-2.3	6.3	1.79	0.14	2
18.0	-4.0	6.0	13-53	17.6	-2.1	6.0	1.98	0.10	2	17.8	-2.3	6.3	1.79	0.16	2
18.0	-4.0	6.0	13-54	17.5	-2.6	5.6	1.56	0.10	2	17.3	-2.8	5.8	1.48	0.16	2
22.0	-4.0	-10.0	10-28	33.3	-2.0	-11.2	11.58	3.15	6	23.8	0.3	-11.3	4.76	NEL	3
22.0	-4.0	-10.0	11-32	23.0	2.7	-11.9	7.06	0.46	4	18.3	-1.3	-4.8	7.01	0.14	4
22.0	-4.0	-6.0	12-58	96.0	-12.0	12.0	76.58	>10.00	6	23.8	0.3	-7.3	4.76	NEL	3
22.0	-4.0	-2.0	9-10	18.1	0.9	-4.0	6.59	0.15	4	17.3	0.3	-3.3	6.50	0.13	4
22.0	-4.0	-2.0	9-11	16.1	-0.9	-2.8	6.75	0.41	4	14.3	2.3	-1.3	9.98	0.86	5
22.0	-4.0	-2.0	11-27	24.7	-3.3	-0.8	3.05	0.64	3	19.8	-3.3	-0.3	2.95	NEL	3
22.0	-4.0	-2.0	12-60	19.5	-0.7	-3.5	4.40	0.23	3	23.8	-3.8	-3.8	2.49	0.15	2
22.0	-4.0	2.0	11-26	17.3	-2.6	1.0	5.03	0.15	4	19.8	-2.8	1.8	2.59	0.09	3
22.0	-4.0	2.0	11-29	19.6	-1.2	1.6	3.71	0.10	3	20.3	-1.8	2.3	2.86	0.17	3
22.0	-4.0	2.0	11-31	19.6	-2.4	1.9	2.93	0.10	3	19.8	-2.8	2.3	2.59	0.11	3
22.0	-4.0	6.0	11-25	21.0	-2.5	5.6	1.87	0.10	2	20.8	-2.8	5.8	1.79	0.10	2
22.0	-4.0	6.0	11-28	21.1	-2.2	6.0	2.00	0.10	2	21.3	-2.8	5.8	1.48	0.09	2
22.0	-4.0	6.0	11-30	21.1	-2.4	6.3	1.84	0.09	2	21.3	-2.3	6.3	1.92	0.08	2

Tab. B.10: SW I PLB a - "Front", part 4: Coordinates of the pencil-lead breaks and estimated source locations determined using Geiger's method and *FastWay*. Estimated source locations excluded during the verification process (see Section 7.3.4) are shown in gray.

B.1.4 Back

PLB			Set	Geiger's method						*FastWay*					
x [in]	y [in]	z [in]	#	x [in]	y [in]	z [in]	d [in]	eei [-]	ac [-]	x [in]	y [in]	z [in]	d [in]	eei [-]	ac [-]
-22.0	4.0	-10.0	9-19	-96.0	-4.0	-12.0	74.46	>10.00	6	-23.8	2.8	-11.8	2.77	0.50	3
-22.0	4.0	-10.0	9-20	-96.0	-4.0	-12.0	74.46	>10.00	6	-18.8	1.3	-7.8	4.82	0.24	3
-22.0	4.0	-10.0	9-22	-96.0	-4.0	-12.0	74.46	>10.00	6	-19.8	1.3	-8.8	3.77	0.39	3
-22.0	4.0	-6.0	9-17	96.0	-4.0	-12.0	118.42	NaN	6	-23.8	3.8	-0.8	5.54	1.12	4
-22.0	4.0	-6.0	9-21	-18.7	2.9	-4.1	4.01	NaN	3	-18.3	2.8	-4.3	4.32	0.02	3
-22.0	4.0	-2.0	10-40	-96.0	-4.0	-12.0	75.10	>10.00	6	-18.8	2.8	-2.3	3.49	0.08	3
-22.0	4.0	-2.0	12-83	-96.0	-4.0	-12.0	75.10	>10.00	6	-18.8	3.3	-2.3	3.34	0.06	3
-22.0	4.0	-2.0	12-84	-20.9	1.7	-2.5	2.61	0.14	3	-19.8	3.3	-2.3	2.38	0.25	2
-22.0	4.0	2.0	11-61	-18.4	2.3	1.2	4.05	0.10	3	-20.3	2.3	1.3	2.59	0.16	3
-22.0	4.0	2.0	13-69	-18.7	2.9	1.5	3.50	0.10	3	-20.3	2.8	1.8	2.17	0.17	2
-22.0	4.0	2.0	13-71	-19.0	3.1	1.7	3.11	0.09	3	-20.8	2.8	1.8	1.79	0.11	2
-22.0	4.0	6.0	13-67	-20.0	2.8	5.7	2.35	0.09	2	-20.8	2.8	5.3	1.92	0.10	2
-22.0	4.0	6.0	13-68	-20.0	2.8	5.7	2.38	0.09	2	-20.8	2.8	5.3	1.92	0.10	2
-22.0	4.0	6.0	13-70	-96.0	-12.0	12.0	75.95	>10.00	6	-21.3	2.8	5.3	1.64	0.21	2
-18.0	4.0	-10.0	10-42	-6.4	3.3	-3.4	13.37	NaN	6	-21.3	-0.3	-11.8	5.63	0.65	4
-18.0	4.0	-10.0	11-62	-96.0	-4.0	-12.0	78.43	>10.00	6	-23.8	-1.8	4.3	16.41	NEL	6
-18.0	4.0	-10.0	12-85	-96.0	-4.0	-12.0	78.43	>10.00	6	-21.8	-0.8	-11.8	6.30	NEL	4
-18.0	4.0	-10.0	13-81	-18.0	4.0	-6.0	4.00	0.12	3	-19.8	3.8	-7.8	2.86	NEL	3
-18.0	4.0	-2.0	13-77	-22.9	3.7	0.5	5.49	0.30	4	-20.8	0.8	-7.8	7.15	NEL	4
-18.0	4.0	-2.0	13-80	-22.6	3.3	-0.1	5.03	0.20	4	-17.3	3.8	-1.8	0.83	0.05	1
-18.0	4.0	2.0	13-73	-16.2	2.8	1.6	2.16	0.10	2	-17.3	2.8	1.8	1.48	0.17	2
-18.0	4.0	2.0	13-74	-18.7	4.0	0.9	1.28	0.15	2	-18.8	3.8	0.3	1.92	0.24	2
-18.0	4.0	2.0	13-76	-16.2	3.0	1.6	2.13	0.09	2	-17.3	2.8	1.8	1.48	0.19	2
-18.0	4.0	2.0	13-79	-16.2	2.8	1.6	2.19	0.10	2	-17.3	2.8	1.8	1.48	0.17	2
-18.0	4.0	6.0	13-72	-18.0	2.3	6.3	1.71	0.10	2	-17.8	2.8	5.8	1.30	0.16	2
-18.0	4.0	6.0	13-75	-18.1	2.8	6.2	1.20	0.13	2	-18.3	2.8	5.8	1.30	0.21	2
-18.0	4.0	6.0	13-78	-17.9	3.0	5.6	1.10	0.10	2	-17.8	2.8	5.8	1.30	0.16	2
-14.0	4.0	-10.0	13-82	-96.0	-4.0	-12.0	82.41	>10.00	6	-16.8	-0.8	-11.8	5.76	NEL	4
-14.0	4.0	-10.0	13-84	-96.0	-4.0	-12.0	82.41	>10.00	6	-16.3	-1.8	-11.8	6.42	0.39	4
-14.0	4.0	-10.0	13-87	-13.5	-0.6	-11.9	5.02	0.34	4	-12.8	3.3	-8.3	2.28	0.01	2
-14.0	4.0	-6.0	13-83	-13.3	2.1	-9.1	3.73	0.37	3	-13.8	2.8	-7.8	2.17	NEL	2
-14.0	4.0	-6.0	13-86	-12.4	4.0	-6.3	1.61	0.24	2	-12.8	2.8	-4.3	2.49	0.05	2
-14.0	4.0	-6.0	14-275	-13.7	-0.4	-7.2	4.56	0.23	3	-14.3	-0.8	-7.3	4.92	NEL	3
-14.0	4.0	-2.0	14-274	-13.3	0.0	-3.1	4.19	0.18	3	-5.8	-3.8	-11.8	14.94	NEL	6
-14.0	4.0	-2.0	14-278	-16.8	-1.0	-4.1	6.12	0.40	4	-13.3	3.3	-1.3	1.30	0.05	2
-14.0	4.0	-2.0	14-280	-15.3	-0.4	-4.9	5.47	0.33	4	-12.8	2.8	-2.3	1.79	0.31	2
-14.0	4.0	2.0	14-273	-13.1	1.3	1.0	3.00	0.14	3	-13.8	2.3	1.8	1.79	0.24	2
-14.0	4.0	2.0	14-277	-13.4	2.0	1.7	2.16	0.10	2	-13.3	1.8	1.8	2.38	0.18	2
-14.0	4.0	2.0	14-279	-13.1	0.5	1.4	3.70	0.13	3	-2.8	-3.3	-6.3	15.72	NEL	6
-14.0	4.0	6.0	13-85	-13.2	2.1	5.6	2.05	0.10	2	-13.8	2.3	5.8	1.79	0.08	2
-14.0	4.0	6.0	14-272	-13.6	2.4	6.1	1.70	0.09	2	-13.3	2.3	6.3	1.92	0.15	2
-14.0	4.0	6.0	14-276	-12.4	1.5	5.4	3.07	0.10	3	-15.3	3.3	6.3	1.48	0.15	2
-10.0	4.0	-10.0	13-89	-12.9	-3.7	-8.4	8.41	0.29	5	-11.8	0.3	-9.3	4.21	0.23	3
-10.0	4.0	-10.0	14-285	-12.3	-4.0	-12.0	8.56	0.32	5	-9.3	3.3	-7.8	2.49	0.04	2
-10.0	4.0	-10.0	14-290	-18.7	-4.0	-12.0	12.00	1.16	6	-12.8	-0.8	-11.8	5.76	0.26	4
-10.0	4.0	-10.0	14-294	-11.3	-3.2	-11.9	7.55	0.38	5	-10.8	1.3	-9.8	2.86	0.08	3
-10.0	4.0	-6.0	13-90	-11.3	0.6	-8.6	4.48	0.38	3	-11.3	-1.8	-6.3	5.89	NEL	4

Tab. B.11: SW I PLB a - "Back", part 1: Coordinates of the pencil-lead breaks and estimated source locations determined using Geiger's method and *FastWay*. Estimated source locations excluded during the verification process (see Section 7.3.4) are shown in gray.

PLB			Set	Geiger's method						*FastWay*					
x [in]	y [in]	z [in]	#	x [in]	y [in]	z [in]	d [in]	eei [-]	ac [-]	x [in]	y [in]	z [in]	d [in]	eei [-]	ac [-]
-10.0	4.0	-6.0	14-284	-10.3	1.8	-7.4	2.64	0.40	3	-9.3	3.8	-8.3	2.38	0.18	2
-10.0	4.0	-2.0	14-283	-11.3	-1.7	-2.7	5.89	0.21	4	-9.8	2.8	-1.8	1.30	0.08	2
-10.0	4.0	-2.0	14-288	-10.0	-0.8	-2.4	4.77	0.16	3	-10.3	2.3	-3.8	2.49	0.19	2
-10.0	4.0	-2.0	14-289	-10.1	-1.0	-2.4	5.03	0.18	4	-10.3	2.3	-2.3	1.79	0.06	2
-10.0	4.0	-2.0	14-293	-9.6	1.9	-2.0	2.16	0.12	2	-10.3	2.3	-1.8	1.79	0.13	2
-10.0	4.0	2.0	14-282	-9.9	-0.0	1.6	4.03	0.13	3	-10.3	2.3	1.8	1.79	0.15	2
-10.0	4.0	2.0	14-287	-9.9	0.2	1.7	3.80	0.11	3	-10.3	1.8	1.8	2.28	0.22	2
-10.0	4.0	2.0	14-292	-10.0	2.6	2.0	1.41	0.12	2	-10.3	2.3	2.3	1.79	0.08	2
-10.0	4.0	6.0	14-281	-9.7	1.9	5.7	2.12	0.11	2	-10.3	2.3	5.8	1.79	0.09	2
-10.0	4.0	6.0	14-286	-9.9	2.1	5.4	2.00	0.09	2	-10.3	2.3	5.8	1.79	0.07	2
-10.0	4.0	6.0	14-291	-10.2	2.1	6.1	1.88	0.10	2	-10.3	2.8	5.8	1.30	0.11	2
-6.0	4.0	-10.0	13-91	-7.0	0.9	-8.5	3.58	0.13	3	-7.8	-0.3	-7.3	5.36	0.18	4
-6.0	4.0	-10.0	14-303	-6.8	-0.2	-12.0	4.71	0.51	3	-7.3	0.3	-11.8	4.32	NEL	3
-6.0	4.0	-10.0	14-308	-7.7	-3.1	-8.9	7.41	0.27	4	-6.3	2.8	-7.8	2.59	0.03	3
-6.0	4.0	-6.0	14-297	-4.4	-3.9	0.1	10.10	0.15	6	-5.8	-1.8	0.3	8.50	NEL	5
-6.0	4.0	-6.0	14-298	-6.4	2.1	-5.4	2.03	0.13	2	-7.8	0.8	-4.8	3.90	0.14	3
-6.0	4.0	-6.0	14-302	-6.2	1.9	-5.3	2.27	0.12	2	-7.3	1.3	-4.8	3.27	0.20	3
-6.0	4.0	-6.0	14-307	-6.8	1.2	-5.0	3.09	0.11	3	-7.3	0.8	-4.8	3.70	0.16	3
-6.0	4.0	-2.0	14-301	-4.9	-1.1	-1.1	5.35	0.15	4	-4.8	-1.8	-0.3	6.14	0.11	4
-6.0	4.0	-2.0	14-306	-6.0	0.8	-2.7	3.24	0.18	3	-7.3	1.3	-1.8	3.03	0.06	3
-6.0	4.0	2.0	14-296	-6.2	0.5	1.7	3.48	0.14	3	-6.8	1.8	1.8	2.38	0.11	2
-6.0	4.0	2.0	14-300	-5.6	0.5	1.6	3.57	0.18	3	-6.8	0.3	2.8	3.90	0.23	3
-6.0	4.0	2.0	14-305	-5.4	-0.3	1.1	4.43	0.20	3	-7.3	1.8	2.3	2.59	0.24	3
-6.0	4.0	6.0	14-295	-6.1	1.4	5.6	2.68	0.13	3	-6.3	1.8	5.8	2.28	0.08	2
-6.0	4.0	6.0	14-299	-5.6	1.4	5.7	2.66	0.09	3	-6.3	1.8	5.8	2.28	0.09	2
-6.0	4.0	6.0	14-304	-5.8	1.0	5.5	3.04	0.10	3	-6.8	1.8	5.8	2.38	0.11	2
-2.0	4.0	-10.0	13-92	-4.0	-4.0	1.0	13.71	NaN	6	1.3	-3.8	-11.8	8.58	0.19	5
-2.0	4.0	-10.0	13-94	5.3	-4.0	-0.6	14.35	NaN	6	1.8	-3.8	-11.8	8.79	NEL	5
-2.0	4.0	-10.0	14-321	0.9	-4.0	-4.0	10.44	0.45	6	-0.8	3.3	-11.8	2.28	NEL	2
-2.0	4.0	-6.0	14-316	-2.5	-4.0	-2.3	8.82	0.25	5	-4.8	3.3	-10.3	5.12	NEL	4
-2.0	4.0	-2.0	14-311	0.9	-3.0	-0.4	7.71	0.27	5	21.3	-3.8	1.8	24.79	NEL	6
-2.0	4.0	-2.0	14-312	-1.5	-3.0	-2.7	7.10	0.10	4	-1.3	-3.3	-2.8	7.33	NEL	4
-2.0	4.0	-2.0	14-315	-3.9	-0.9	-0.4	5.48	0.25	4	-3.8	0.8	-1.8	3.70	NEL	3
-2.0	4.0	-2.0	14-319	-3.6	-3.0	-0.1	7.42	0.49	4	-8.3	3.8	-1.3	6.30	NEL	4
-2.0	4.0	-2.0	14-320	-1.1	-4.0	-1.7	8.06	0.11	5	-1.3	-2.8	-2.8	6.83	NEL	4
-2.0	4.0	2.0	14-310	-2.2	3.4	1.4	0.89	0.14	1	-2.3	2.3	1.8	1.79	0.11	2
-2.0	4.0	2.0	14-314	-1.6	2.0	2.0	2.06	0.12	2	-1.8	1.3	2.3	2.77	0.12	3
-2.0	4.0	2.0	14-318	-1.8	2.0	2.1	1.98	0.13	2	-1.8	1.3	2.3	2.77	0.07	3
-2.0	4.0	6.0	14-309	-1.8	1.1	5.7	2.90	0.19	3	-2.3	1.3	5.8	2.77	0.13	3
-2.0	4.0	6.0	14-313	-2.6	2.0	6.6	2.11	0.12	2	-2.8	1.3	6.8	2.95	0.18	3
-2.0	4.0	6.0	14-317	-2.1	2.4	6.1	1.57	0.09	2	-2.3	2.3	6.3	1.79	0.20	2
2.0	4.0	-10.0	14-325	2.4	-4.0	-1.9	11.41	0.17	6	3.3	-0.3	-5.3	6.50	NEL	4
2.0	4.0	-10.0	14-326	4.4	-2.9	-6.8	7.93	0.16	5	4.3	-1.8	-8.3	6.42	NEL	4
2.0	4.0	-10.0	14-331	5.2	-4.0	-12.0	8.86	0.89	5	5.3	-3.8	-11.8	8.58	0.55	5
2.0	4.0	-10.0	14-337	4.8	-4.0	-6.3	9.26	0.56	5	2.8	-1.3	-5.8	6.80	NEL	4
2.0	4.0	-6.0	14-336	2.9	-4.0	-2.6	8.76	0.19	5	3.3	-0.8	-5.3	4.97	NEL	3
2.0	4.0	-2.0	14-324	3.4	-0.2	-1.3	4.50	0.22	3	2.3	-0.8	-0.8	4.92	0.19	3

Tab. B.12: SW I PLB a - "Back", part 2: Coordinates of the pencil-lead breaks and estimated source locations determined using Geiger's method and *FastWay*. Estimated source locations excluded during the verification process (see Section 7.3.4) are shown in gray.

PLB			Set	Geiger's method						*FastWay*					
x [in]	y [in]	z [in]	#	x [in]	y [in]	z [in]	d [in]	eei [-]	ac [-]	x [in]	y [in]	z [in]	d [in]	eei [-]	ac [-]
2.0	4.0	-2.0	14-329	1.8	0.3	-0.7	3.92	0.32	3	0.8	-0.3	-0.3	4.76	0.13	3
2.0	4.0	-2.0	14-330	1.6	-3.5	-2.6	7.53	0.11	5	1.8	-2.8	-3.3	6.87	0.24	4
2.0	4.0	-2.0	14-335	1.6	2.5	-1.7	1.62	0.11	2	0.8	0.8	-0.8	3.70	0.16	3
2.0	4.0	2.0	13-95	-96.0	12.0	12.0	98.83	NaN	6	3.8	0.3	2.3	4.15	NEL	3
2.0	4.0	2.0	14-323	1.8	2.7	1.9	1.31	0.10	2	1.8	2.3	1.8	1.79	0.13	2
2.0	4.0	2.0	14-328	2.0	2.5	2.0	1.52	0.13	2	2.3	2.8	1.8	1.30	0.11	2
2.0	4.0	2.0	14-334	8.2	2.5	-4.0	8.73	0.49	5	7.3	3.8	-1.3	6.18	1.10	4
2.0	4.0	6.0	14-327	-0.8	0.6	7.4	4.62	0.12	3	-1.3	1.3	7.3	4.44	0.08	3
2.0	4.0	6.0	14-332	1.4	1.6	6.3	2.48	0.33	2	1.8	1.8	5.3	2.38	NEL	2
6.0	4.0	-10.0	13-100	6.9	1.8	-12.0	3.13	0.90	3	6.8	2.3	-11.3	2.28	0.02	2
6.0	4.0	-10.0	14-341	5.9	-4.0	-2.2	11.18	0.32	6	6.3	2.3	-7.3	3.27	NEL	3
6.0	4.0	-10.0	14-342	5.8	4.0	-12.0	2.01	0.69	2	6.3	-2.3	-8.8	6.38	NEL	4
6.0	4.0	-10.0	14-346	6.4	-0.9	-9.1	5.00	0.31	3	6.3	1.8	-5.8	4.82	NEL	3
6.0	4.0	-10.0	14-347	5.1	-4.0	-10.6	8.07	0.43	5	6.3	-3.3	-8.8	7.36	0.31	4
6.0	4.0	-10.0	14-351	6.5	4.0	-7.7	2.34	0.09	2	6.8	3.8	-8.3	1.92	NEL	2
6.0	4.0	-6.0	14-350	5.3	-4.0	0.1	10.09	0.24	6	5.8	-1.3	-2.8	6.18	NEL	4
6.0	4.0	-2.0	14-345	6.0	1.8	-2.7	2.27	0.16	2	5.8	-0.3	-1.8	4.26	0.08	3
6.0	4.0	2.0	14-339	4.8	-0.8	2.5	4.95	0.14	3	4.8	-0.3	2.3	4.44	0.19	3
6.0	4.0	2.0	14-344	5.5	2.5	1.3	1.70	0.12	2	4.8	0.8	1.8	3.49	0.19	3
6.0	4.0	2.0	14-349	4.7	0.4	2.1	3.82	0.13	3	5.8	1.8	1.3	2.38	0.23	2
6.0	4.0	6.0	13-98	7.3	5.5	8.4	3.13	0.09	3	7.3	5.3	8.3	2.86	0.08	3
6.0	4.0	6.0	14-338	5.6	2.4	6.0	1.65	0.10	2	5.3	2.3	5.8	1.92	0.16	2
6.0	4.0	6.0	14-343	5.5	2.1	6.1	1.97	0.10	2	5.3	1.8	5.8	2.38	0.12	2
6.0	4.0	6.0	14-348	5.8	2.1	6.2	1.88	0.11	2	5.8	2.3	5.3	1.92	0.07	2
10.0	4.0	-10.0	14-355	9.6	-4.0	-2.3	11.12	0.34	6	11.3	0.8	-11.8	3.90	0.14	3
10.0	4.0	-10.0	14-356	9.1	0.4	-8.9	3.86	0.12	3	8.8	-0.8	-8.3	5.21	NEL	4
10.0	4.0	-10.0	14-361	8.0	-1.2	-6.9	6.33	0.10	4	7.8	-2.3	-6.8	7.40	NEL	4
10.0	4.0	-10.0	14-366	6.9	-4.0	-4.3	10.31	0.37	6	7.8	-3.3	-6.3	8.47	NEL	5
10.0	4.0	-6.0	14-360	8.4	-0.7	-4.4	5.16	0.10	4	8.3	-1.3	-4.8	5.67	0.08	4
10.0	4.0	-6.0	14-365	7.5	-4.0	-1.4	9.59	0.34	5	8.3	-1.8	-7.8	6.26	NEL	4
10.0	4.0	-2.0	14-354	9.2	-4.0	2.2	9.06	0.38	5	8.8	0.8	-2.3	3.49	0.07	3
10.0	4.0	-2.0	14-359	9.8	0.8	-6.3	5.34	0.25	4	9.3	3.8	-3.8	1.92	NEL	2
10.0	4.0	-2.0	14-364	9.0	-4.0	0.6	8.47	0.30	5	8.8	1.3	-2.3	3.03	0.06	3
10.0	4.0	2.0	14-353	7.5	-1.6	1.9	6.13	0.13	4	6.8	0.3	0.8	5.12	0.24	4
10.0	4.0	2.0	14-358	9.5	1.9	2.0	2.17	0.11	2	9.3	1.8	2.3	2.38	0.10	2
10.0	4.0	2.0	14-363	9.5	3.1	0.9	1.47	0.09	2	8.8	1.8	1.8	2.59	0.13	3
10.0	4.0	6.0	14-352	9.4	2.0	5.9	2.14	0.10	2	9.3	1.8	5.8	2.38	0.15	2
10.0	4.0	6.0	14-357	9.3	2.0	6.3	2.17	0.12	2	8.8	1.8	5.8	2.59	0.15	3
10.0	4.0	6.0	14-362	9.5	2.0	5.4	2.13	0.11	2	9.3	1.8	5.3	2.49	0.15	2
14.0	4.0	-10.0	12-90	24.1	-4.0	-12.0	13.05	2.90	6	11.3	-0.3	-11.8	5.36	NEL	4
14.0	4.0	-10.0	13-102	13.6	2.6	-11.0	1.77	0.10	2	13.3	2.8	-9.3	1.64	0.11	2
14.0	4.0	-10.0	13-104	96.0	-4.0	-12.0	82.41	>10.00	6	14.3	-1.8	-11.3	5.89	NEL	4
14.0	4.0	-6.0	14-371	13.7	-0.4	-9.0	5.30	0.38	4	13.8	3.8	-7.8	1.79	0.05	2
14.0	4.0	-6.0	14-374	14.0	-0.1	-9.2	5.23	0.39	4	13.8	3.8	-7.3	1.30	0.08	2
14.0	4.0	-2.0	12-89	13.1	3.5	-2.6	1.13	0.13	2	12.8	3.8	-3.3	1.79	0.25	2
14.0	4.0	-2.0	13-101	14.5	0.5	-3.5	3.87	0.25	3	18.8	3.8	-9.8	9.09	0.19	5
14.0	4.0	-2.0	13-103	12.6	3.6	-1.7	1.46	0.10	2	12.8	3.8	-2.3	1.30	0.18	2

Tab. B.13: SW I PLB a - "Back", part 3: Coordinates of the pencil-lead breaks and estimated source locations determined using Geiger's method and *FastWay*. Estimated source locations excluded during the verification process (see Section 7.3.4) are shown in gray.

PLB			Set	Geiger's method						*FastWay*					
x [in]	y [in]	z [in]	#	x [in]	y [in]	z [in]	d [in]	eei [-]	ac [-]	x [in]	y [in]	z [in]	d [in]	eei [-]	ac [-]
14.0	4.0	2.0	14-368	13.3	3.5	1.2	1.19	0.12	2	12.8	2.8	1.3	1.92	0.25	2
14.0	4.0	2.0	14-370	13.6	3.2	1.3	1.11	0.10	2	13.3	2.8	1.8	1.48	0.14	2
14.0	4.0	2.0	14-373	13.0	4.0	0.9	1.50	0.09	2	12.8	3.8	1.3	1.48	0.13	2
14.0	4.0	6.0	14-367	14.1	2.3	5.6	1.81	0.10	2	13.8	2.3	5.8	1.79	0.19	2
14.0	4.0	6.0	14-369	13.8	2.8	5.6	1.27	0.10	2	13.3	2.3	5.3	2.05	0.13	2
14.0	4.0	6.0	14-372	13.4	1.5	5.4	2.60	0.12	3	12.8	1.8	5.3	2.68	0.24	3
18.0	4.0	-10.0	11-68	21.1	1.9	-12.0	4.25	0.46	3	16.8	1.3	-4.8	6.06	NEL	4
18.0	4.0	-10.0	11-69	18.7	-3.0	-12.0	7.32	0.84	4	22.8	-1.8	-11.8	7.66	0.61	5
18.0	4.0	-10.0	11-70	19.0	0.3	-12.0	4.30	0.63	3	13.8	3.8	-10.3	4.26	NEL	3
18.0	4.0	-6.0	12-92	22.0	4.0	-12.0	7.20	0.29	4	17.8	3.8	-7.3	1.30	NEL	2
18.0	4.0	-6.0	12-95	31.1	-4.0	-12.0	16.49	1.30	6	23.8	-0.3	-8.8	7.66	NEL	5
18.0	4.0	-6.0	12-97	20.1	1.1	-4.5	3.86	0.33	3	23.8	3.8	-7.3	5.89	0.39	4
18.0	4.0	-6.0	12-98	18.0	4.0	-6.9	0.90	0.36	1	17.3	3.8	-4.8	1.48	0.14	2
18.0	4.0	-2.0	12-91	12.6	4.0	0.7	6.05	0.56	4	6.8	3.8	-6.8	12.21	NEL	6
18.0	4.0	-2.0	12-94	13.6	4.0	-1.7	4.39	0.38	3	9.8	3.8	-6.3	9.28	NEL	5
18.0	4.0	2.0	12-96	14.3	1.9	4.1	4.71	0.18	3	12.8	1.3	1.8	5.93	0.52	4
18.0	4.0	2.0	13-106	17.2	12.0	12.0	12.83	1.69	6	8.3	3.8	1.3	9.78	0.72	5
18.0	4.0	2.0	13-107	17.1	3.2	1.5	1.27	0.10	2	17.3	2.8	1.8	1.48	0.13	2
18.0	4.0	2.0	13-108	17.2	3.1	1.4	1.37	0.10	2	17.3	2.8	1.8	1.48	0.15	2
18.0	4.0	6.0	12-93	18.3	2.7	6.2	1.33	0.09	2	18.3	2.8	6.3	1.30	0.17	2
18.0	4.0	6.0	13-105	18.5	2.5	6.2	1.58	0.10	2	18.8	2.3	5.8	1.92	0.09	2
22.0	4.0	-10.0	9-30	20.6	0.1	-8.0	4.57	0.62	3	23.8	3.8	-8.3	2.49	0.59	2
22.0	4.0	-10.0	9-34	26.8	-4.0	-12.0	9.52	2.01	5	23.8	-0.3	-8.3	4.92	0.59	3
22.0	4.0	-10.0	10-47	27.9	-2.9	-12.0	9.26	1.67	5	23.8	-0.8	-9.3	5.12	0.66	4
22.0	4.0	-10.0	11-71	-0.7	-4.0	-12.0	24.13	4.61	6	23.8	-0.3	-8.3	4.92	NEL	3
22.0	4.0	-6.0	9-32	27.6	-0.8	-8.1	7.66	0.44	5	23.8	3.8	-3.3	3.27	0.14	3
22.0	4.0	-6.0	10-46	13.3	-0.4	2.1	12.69	NaN	6	23.8	0.8	-5.8	3.70	NEL	3
22.0	4.0	-2.0	9-29	20.0	2.6	-1.6	2.48	0.11	2	23.8	3.8	-3.3	2.17	0.20	2
22.0	4.0	-2.0	10-45	2.7	4.0	-12.0	21.70	3.06	6	21.3	2.3	-1.3	2.05	0.03	2
22.0	4.0	2.0	9-35	15.4	4.0	-4.8	9.51	0.34	5	21.3	2.3	2.3	1.92	0.05	2
22.0	4.0	2.0	10-44	20.2	2.5	2.1	2.31	0.10	2	19.8	2.8	2.3	2.59	0.15	3
22.0	4.0	6.0	12-99	20.4	1.9	5.4	2.73	0.11	3	19.8	2.3	5.3	2.95	0.23	3
22.0	4.0	6.0	12-100	22.5	3.1	6.2	1.03	0.09	2	23.3	3.3	6.8	1.64	0.16	2
22.0	4.0	6.0	12-101	21.8	2.4	6.2	1.60	0.10	2	22.3	2.3	6.3	1.79	0.22	2

Tab. B.14: SW I PLB a - "Back", part 4: Coordinates of the pencil-lead breaks and estimated source locations determined using Geiger's method and *FastWay*. Estimated source locations excluded during the verification process (see Section 7.3.4) are shown in gray.

B.2 Bending Test SW I

B.2.1 Localized events

Event	Geiger's method					*FastWay*				
#	x [in]	y [in]	z [in]	t_s [hh:mm:ss]	*eei* [-]	x [in]	y [in]	z [in]	t_s [hh:mm:ss]	*eei* [-]
26	-96.0	4.0	-12.0	14:10:02.896985	>10.00	-13.8	2.8	-8.5	14:10:02.910037	0.03
28	-13.8	-1.2	-12.0	14:10:06.050798	0.51	-13.8	-0.8	-10.5	14:10:06.050815	0.10
39	-13.8	-4.0	-0.8	14:10:11.314643	0.33	-12.8	0.8	-2.0	14:10:11.314650	0.35
45	-13.3	3.6	-1.1	14:10:14.160252	NaN	-13.3	3.8	-1.0	14:10:14.160257	0.07
70	-1.5	-2.4	-2.3	14:11:42.322289	0.54	-6.3	3.8	-4.5	14:11:42.322296	NEL
78	-16.0	-0.9	-9.7	14:11:44.824630	0.47	-15.8	0.8	-9.0	14:11:44.824633	0.31
83	-9.0	3.3	-4.8	14:11:45.557905	0.25	-9.3	3.8	-5.0	14:11:45.557911	0.10
87	-15.4	4.0	-12.0	14:11:46.201862	3.54	-10.8	3.8	-5.5	14:11:46.201909	0.63
100	96.0	12.0	12.0	14:11:48.122834	NaN	-12.3	-11.8	12.0	14:11:48.131758	0.97
129	0.1	4.0	-12.0	14:11:57.832653	1.96	-6.3	-3.8	-4.0	14:11:57.832721	0.38
139	-12.1	1.8	-11.9	14:12:00.089350	NaN	-12.3	2.3	-10.5	14:12:00.089359	0.01
140	10.1	0.5	-9.2	14:12:00.129279	0.14	9.8	-2.3	-7.0	14:12:00.129294	0.21
160	-15.6	-1.5	-12.0	14:12:03.892923	1.29	-11.8	3.8	-8.0	14:12:03.892945	0.64
164	-12.7	4.0	-5.4	14:12:04.906870	0.54	-6.8	0.8	-11.5	14:12:04.906829	0.29
169	9.7	-4.0	-8.5	14:12:05.147388	0.63	9.8	-3.8	-10.0	14:12:05.147390	0.64
172	9.2	4.0	-12.0	14:12:06.145327	NaN	10.3	2.8	-11.5	14:12:06.145371	0.47
207	-15.7	-2.0	-11.5	14:12:10.095496	0.51	-17.3	-3.8	-11.5	14:12:10.095495	0.10
282	-3.0	4.0	-12.0	14:12:59.974924	1.60	-6.3	0.8	-11.5	14:12:59.974963	0.38
283	-0.8	-4.0	-12.0	14:13:01.504567	4.51	-10.3	2.3	-11.5	14:13:01.504654	0.22
291	-13.7	0.7	-7.3	14:13:05.413169	0.22	-15.8	-1.3	-10.0	14:13:05.413159	0.48
296	-14.2	4.0	-2.5	14:13:06.981187	0.36	-13.3	3.8	-1.5	14:13:06.981186	1.16
325	-5.9	-2.4	-3.7	14:13:11.670793	NaN	-5.8	-1.8	-2.5	14:13:11.670789	0.01
356	-13.2	-0.1	-10.9	14:13:17.697990	1.13	-16.8	-3.8	-11.5	14:13:17.697984	0.32
375	10.8	-4.0	7.4	14:13:21.646355	4.21	11.3	-0.8	-11.5	14:13:21.646393	0.22
390	-4.4	-4.0	-12.0	14:13:22.285542	2.57	-7.3	0.8	-11.5	14:13:22.285593	0.31
394	-8.1	0.1	-8.1	14:13:22.401170	0.19	-8.8	-1.3	-7.5	14:13:22.401172	0.10
399	6.3	4.0	-12.0	14:13:22.512051	1.67	-5.8	0.3	-7.5	14:13:22.512130	0.28
402	-3.5	1.2	-12.0	14:13:22.605010	0.82	-2.8	3.3	-11.0	14:13:22.605012	NEL
431	-4.5	3.2	-8.4	14:13:24.404234	0.13	-5.3	3.3	-9.0	14:13:24.404229	0.19
440	-13.0	-3.5	-12.0	14:13:25.085812	2.66	-11.3	-3.8	-11.5	14:13:25.085823	0.40
451	4.3	-4.0	1.0	14:13:26.231292	1.39	6.3	2.8	-9.0	14:13:26.231294	0.21
455	3.1	4.0	-12.0	14:13:26.266108	0.83	3.3	3.8	-11.5	14:13:26.266109	0.28
458	0.1	4.0	-11.4	14:13:26.562464	NaN	1.3	-1.8	0.5	14:13:26.562543	0.22
464	13.2	-4.0	-12.0	14:13:26.952974	NaN	-1.8	-3.8	-8.0	14:13:26.953106	0.41
486	96.0	-4.0	-12.0	14:13:30.617261	>10.00	-1.3	-3.8	-11.5	14:13:30.618195	0.72
493	-2.1	-4.0	-12.0	14:13:32.241097	1.67	-2.8	-3.8	-11.5	14:13:32.241131	0.24
523	-5.2	3.1	2.3	14:13:36.588353	1.19	-5.8	-3.8	4.0	14:13:36.588397	0.46
533	-2.5	-3.7	-1.4	14:13:39.146307	0.32	-3.3	-3.8	-0.5	14:13:39.146306	0.12
567	-18.3	4.0	-12.0	14:13:45.236713	>10.00	-3.8	3.8	-11.5	14:13:45.236832	0.27

Tab. B.15: SW I - localized events, part 1: Coordinates of the estimated source locations determined using Geiger's method and *FastWay*. Estimated source locations excluded during the verification process (see Section 7.3.4) are shown in gray.

Event	Geiger's method					*FastWay*				
#	x [in]	y [in]	z [in]	t_s [hh:mm:ss]	*eei* [-]	x [in]	y [in]	z [in]	t_s [hh:mm:ss]	*eei* [-]
592	-14.3	-0.4	-4.7	14:13:47.924620	1.58	-0.8	-1.3	-11.5	14:13:47.924531	0.63
603	-12.1	4.0	0.7	14:13:49.312770	0.45	-11.8	3.8	-1.5	14:13:49.312776	0.21
614	-6.0	4.0	-8.7	14:13:50.692400	1.25	-6.3	-0.8	-9.0	14:13:50.692413	0.03
619	-2.7	-4.0	-4.1	14:13:51.093474	0.65	-3.3	3.8	-11.5	14:13:51.093455	0.27
661	-6.6	4.0	-12.0	14:13:55.271399	4.53	-1.3	-3.8	-11.5	14:13:55.271483	0.41
666	6.9	4.0	-12.0	14:13:55.609552	4.30	10.3	0.8	-11.5	14:13:55.609627	0.36
668	-11.2	4.0	-4.4	14:13:55.791364	0.44	-23.8	3.8	-0.5	14:13:55.791382	0.46
676	-4.7	2.3	-8.5	14:13:56.601357	0.36	-4.3	-3.8	-3.0	14:13:56.601367	NEL
694	-17.9	4.0	-12.0	14:13:58.598257	>10.00	4.8	0.3	-11.5	14:13:58.598422	0.39
697	-6.9	-4.0	-4.3	14:13:59.364539	0.21	-6.8	-2.3	-4.5	14:13:59.364539	0.24
699	-9.9	-2.0	11.7	14:13:59.906279	2.37	-6.8	-3.8	-1.5	14:13:59.906285	0.59
741	35.2	-12.0	12.0	14:14:12.964479	>10.00	7.8	-1.3	3.0	14:14:12.964735	0.05
755	-3.3	-4.0	-2.7	14:14:28.536102	0.63	-0.3	3.8	-11.5	14:14:28.536103	0.38
767	-9.5	-4.0	-9.7	14:14:43.107960	2.74	-22.8	-3.8	6.5	14:14:43.108022	0.36
784	-4.1	0.8	-2.9	14:18:43.549893	1.42	-4.8	-2.8	-3.0	14:18:43.549919	0.61
793	-13.8	1.1	-8.5	14:18:51.712964	0.47	-17.3	-3.3	-11.5	14:18:51.712948	0.18
800	-5.2	3.5	-12.0	14:18:59.361544	1.20	-4.8	-2.8	-7.5	14:18:59.361578	0.37
803	51.9	-12.0	12.0	14:19:01.128763	>10.00	10.3	1.8	-11.5	14:19:01.129159	0.14
806	-68.5	-4.0	-12.0	14:19:04.071432	>10.00	10.3	-0.8	-11.5	14:19:04.071978	0.48
813	-6.0	-4.0	-1.1	14:19:07.392600	0.33	-6.3	-3.8	-3.5	14:19:07.392610	0.24
815	-27.1	4.0	-12.0	14:19:10.112640	>10.00	-2.8	2.8	-11.5	14:19:10.112911	0.87
822	0.0	4.0	3.8	14:19:12.229405	2.11	1.8	-1.8	-0.5	14:19:12.229433	0.58
828	96.0	12.0	12.0	14:19:15.933635	>10.00	-8.3	2.8	11.0	14:19:15.938977	0.47
829	-12.3	-0.3	-12.0	14:19:16.630415	0.85	-11.3	2.3	-9.0	14:19:16.630428	NEL
830	-5.5	4.0	-0.7	14:19:16.781258	1.04	-0.8	-1.8	0.0	14:19:16.781314	0.38
840	96.0	-4.0	-12.0	14:19:23.549137	>10.00	11.3	1.3	-11.5	14:19:23.551651	0.39
861	-45.0	-4.0	-12.0	14:19:44.888163	>10.00	-21.3	3.8	-11.5	14:19:44.888468	0.44
872	96.0	4.0	-12.0	14:19:53.616706	NaN	16.3	3.8	-9.5	14:19:53.625831	0.50
879	-11.1	-1.1	-9.8	14:20:08.724227	NaN	-11.3	-0.3	-9.0	14:20:08.724232	0.06
885	96.0	12.0	12.0	14:20:14.703115	NaN	23.8	5.8	9.5	14:20:14.714262	0.63
892	96.0	-4.0	-12.0	14:20:17.877993	>10.00	7.8	1.8	-8.5	14:20:18.569614	0.34
907	4.4	4.0	-6.9	14:20:41.108341	0.80	6.3	-2.8	-11.5	14:20:41.108354	0.15
914	-56.4	4.0	-12.0	14:20:54.439791	>10.00	-15.3	3.8	-11.5	14:20:54.440189	0.87
934	-7.5	0.2	-3.3	14:22:00.809449	1.74	-17.3	-1.8	-11.5	14:22:00.809444	0.39
995	10.9	-12.0	11.7	14:22:29.999757	2.35	8.3	-3.8	5.5	14:22:29.999810	0.95
1019	8.8	-4.0	-5.9	14:22:31.753545	0.69	6.8	-3.8	-5.0	14:22:31.753558	0.41
1028	8.6	-4.0	-1.1	14:22:32.124801	0.44	7.3	-3.8	-0.5	14:22:32.124794	0.62
1059	11.0	-4.0	-1.4	14:22:33.537626	0.42	11.3	-3.8	-1.5	14:22:33.537631	1.04
1080	7.4	4.0	-12.0	14:22:34.304392	NaN	6.8	3.8	-7.5	14:22:34.304421	0.28
1093	2.3	-11.1	12.0	14:22:34.598583	NaN	1.8	-7.3	8.5	14:22:34.598590	0.41
1097	96.0	-4.0	-12.0	14:22:34.808364	>10.00	13.3	-3.8	-11.5	14:22:34.815687	0.89
1106	-53.5	4.0	-12.0	14:22:35.242449	>10.00	0.3	3.8	-11.5	14:22:35.242885	0.31
1113	96.0	-12.0	-12.0	14:22:35.474671	NaN	8.8	-2.8	-11.5	14:22:35.482743	0.60
1115	10.5	-4.0	-2.4	14:22:35.517128	1.01	8.3	0.3	-3.5	14:22:35.517129	0.08
1118	10.1	-4.0	-0.8	14:22:35.610212	0.92	10.3	3.8	-3.5	14:22:35.610204	0.15

Tab. B.16: SW I - localized events, part 2: Coordinates of the estimated source locations determined using Geiger's method and *FastWay*. Estimated source locations excluded during the verification process (see Section 7.3.4) are shown in gray.

Event	Geiger's method					*FastWay*				
#	x [in]	y [in]	z [in]	t_s [hh:mm:ss]	*eei* [-]	x [in]	y [in]	z [in]	t_s [hh:mm:ss]	*eei* [-]
1129	9.7	2.5	-9.8	14:22:35.980224	0.50	8.3	-3.8	-2.5	14:22:35.980238	0.03
1146	11.5	-1.3	-7.1	14:22:36.825182	0.61	9.3	0.8	-5.5	14:22:36.825177	0.06
1147	14.1	4.0	-12.0	14:22:36.880242	4.37	8.3	3.8	-10.0	14:22:36.880302	0.19
1149	3.9	-12.0	12.0	14:22:37.006088	NaN	6.8	-0.3	8.5	14:22:37.006238	0.05
1161	13.3	4.0	-10.1	14:22:37.495628	1.46	11.8	3.8	-1.0	14:22:37.495662	0.61
1176	96.0	12.0	-12.0	14:22:38.220049	NaN	9.3	3.8	-11.5	14:22:38.227619	0.29
1182	-5.0	0.0	-3.4	14:22:38.446687	NaN	-5.8	-0.8	-3.0	14:22:38.446695	0.28
1184	10.4	4.0	-12.0	14:22:38.521702	NaN	9.8	3.8	-9.5	14:22:38.521734	0.41
1191	-0.1	4.0	-12.0	14:22:38.845377	NaN	-2.8	3.8	-7.5	14:22:38.845411	0.13
1231	-0.2	4.0	-8.2	14:22:40.136348	1.73	-3.8	3.8	-3.0	14:22:40.136406	0.32
1238	9.0	3.0	-4.5	14:22:40.781623	0.29	9.8	3.8	-7.5	14:22:40.781618	0.40
1245	-1.3	4.0	-0.3	14:22:41.023190	5.67	-0.8	2.8	-1.5	14:22:41.023282	0.06
1269	9.0	-4.0	0.6	14:22:41.808389	0.37	13.3	-3.8	-1.5	14:22:41.808375	0.25
1284	25.8	-4.0	-12.0	14:22:42.457856	NaN	14.3	-3.8	-11.5	14:22:42.457949	0.59
1291	14.6	-4.0	-12.0	14:22:42.733783	2.11	14.8	-3.8	-11.5	14:22:42.733800	0.61
1381	-17.7	1.6	-12.0	14:22:46.204391	7.86	-16.8	-3.8	-11.5	14:22:46.204435	0.37
1476	-2.4	4.0	-4.5	14:22:51.859326	0.94	-3.8	3.8	-5.0	14:22:51.859340	0.28
1504	-10.6	-2.8	2.6	14:22:53.496865	NaN	-10.8	-2.8	2.5	14:22:53.496870	0.07
1515	-12.0	4.0	-9.3	14:22:54.040342	0.53	-12.8	3.3	-7.5	14:22:54.040349	0.24
1543	-81.6	-2.0	12.0	14:22:55.803760	>10.00	-23.8	-4.8	8.5	14:22:55.804112	0.52
1572	-6.1	-0.9	-2.1	14:22:57.372772	0.89	-6.8	2.8	-4.5	14:22:57.372762	NEL
1621	12.3	-3.6	-11.3	14:22:59.640777	NaN	9.8	-2.8	-6.0	14:22:59.640790	0.03
1656	-2.0	4.0	-12.0	14:23:00.996791	2.48	0.3	0.3	-10.5	14:23:00.996830	0.03
1679	-96.0	-4.0	-12.0	14:23:01.741734	NaN	23.8	8.3	9.5	14:23:01.764905	0.40
1695	-21.3	3.5	12.0	14:23:02.235972	0.22	-23.8	4.8	9.0	14:23:02.235965	0.24
1755	20.2	4.0	-12.0	14:23:05.140084	>10.00	13.8	3.8	-6.0	14:23:05.140142	0.25
1865	10.3	2.3	-3.2	14:23:11.131005	NaN	10.3	1.3	-1.5	14:23:11.131012	0.05
1877	13.7	-4.0	6.5	14:23:11.701887	NaN	15.3	-4.8	8.5	14:23:11.701896	0.24
1924	-96.0	-4.0	-12.0	14:23:13.169722	>10.00	-20.3	-10.3	8.5	14:23:13.175310	0.86
1981	-6.7	4.0	-12.0	14:23:15.459875	2.05	-13.8	-1.8	-11.5	14:23:15.459907	0.13
1997	8.0	4.0	-6.4	14:23:16.157089	0.60	8.3	-2.8	-1.5	14:23:16.157099	0.12
2065	-22.4	4.0	-0.3	14:23:19.787916	0.63	-6.8	3.8	-11.0	14:23:19.787883	0.25
2142	7.6	1.4	-4.1	14:23:22.266236	0.35	13.8	3.8	-7.5	14:23:22.266202	0.22
2155	0.2	0.1	4.6	14:23:22.561066	0.70	-0.8	-2.3	9.5	14:23:22.561077	0.07
2237	-4.6	-3.2	1.7	14:23:24.376057	0.64	-1.8	-11.3	8.5	14:23:24.376063	0.03
2438	10.6	0.4	0.1	14:23:28.984461	0.50	5.8	0.8	1.0	14:23:28.984486	NEL
2513	0.2	4.3	12.0	14:23:30.650951	1.40	-4.8	4.3	12.0	14:23:30.650984	0.16
2523	6.6	4.0	-12.0	14:23:30.980403	NaN	8.8	3.8	-11.0	14:23:30.980446	0.31
2670	-3.5	4.0	-12.0	14:23:35.173959	NaN	-3.8	1.8	-11.5	14:23:35.173988	0.19
2834	7.9	0.6	-9.2	14:23:39.557507	0.30	10.3	-2.8	-0.5	14:23:39.557535	NEL
3194	-17.6	3.3	-4.1	14:23:51.248427	0.80	-15.3	2.3	-5.0	14:23:51.248428	NEL
3204	11.4	3.7	-10.9	14:23:51.499581	NaN	11.3	3.8	-9.5	14:23:51.499589	0.03
3215	-4.1	-4.0	0.5	14:23:52.409658	0.25	-2.8	-3.8	0.0	14:23:52.409659	0.50
3255	-15.6	2.3	3.1	14:23:53.996773	0.86	-16.8	3.8	4.5	14:23:53.996760	NEL
3483	0.2	12.0	12.0	14:24:01.481085	NaN	-2.8	11.8	8.5	14:24:01.481167	0.31

Tab. B.17: SW I - localized events, part 3: Coordinates of the estimated source locations determined using Geiger's method and *FastWay*. Estimated source locations excluded during the verification process (see Section 7.3.4) are shown in gray.

Event	Geiger's method					*FastWay*				
#	x [in]	y [in]	z [in]	t_s [hh:mm:ss]	*eei* [-]	x [in]	y [in]	z [in]	t_s [hh:mm:ss]	*eei* [-]
3529	96.0	-12.0	12.0	14:24:03.857657	>10.00	0.8	-11.8	12.0	14:24:03.865710	0.70
3745	2.8	3.0	-12.0	14:24:12.408932	1.61	2.8	0.3	-11.5	14:24:12.408941	0.43
3792	95.1	4.0	-12.0	14:24:15.701477	>10.00	10.3	3.3	6.5	14:24:15.702110	0.05
3816	9.5	-4.0	1.9	14:24:18.626387	0.34	7.8	-0.3	-1.0	14:24:18.626395	0.04
3821	-13.2	-4.0	4.1	14:24:19.148499	0.80	-8.3	2.3	-5.5	14:24:19.148489	0.03
3855	10.6	4.0	-12.0	14:24:26.496184	NaN	9.3	3.8	-8.5	14:24:26.496208	0.16
3860	18.7	-2.0	-0.0	14:24:27.136963	0.38	13.3	3.8	-5.5	14:24:27.136948	NEL
3876	-96.0	-4.0	-12.0	14:24:35.058957	NaN	-18.3	3.8	-6.0	14:24:35.065311	0.59
3879	-16.3	4.0	-12.0	14:24:35.855435	9.03	-2.8	0.3	-11.5	14:24:35.855492	0.77
3889	96.0	-12.0	12.0	14:24:40.799223	>10.00	13.8	-0.3	-11.5	14:24:40.806256	0.56
3892	-4.4	-0.5	-1.5	14:24:46.518745	NaN	-2.3	3.8	-4.0	14:24:46.518685	0.10
3894	9.4	-1.2	0.5	14:24:49.313900	0.13	9.3	-2.8	1.5	14:24:49.313906	0.45
3904	-19.4	2.2	-3.7	14:24:57.682101	0.41	-18.3	0.8	-4.0	14:24:57.682103	NEL
3934	-9.1	4.0	-3.9	14:26:04.500920	0.84	-8.8	3.3	-2.5	14:26:04.500942	0.04
3969	-96.0	-4.0	-12.0	14:29:17.082997	NaN	-2.3	-3.8	-8.0	14:29:17.107038	0.83
3981	-13.9	0.8	0.8	14:29:26.507929	0.27	-15.8	-0.8	1.0	14:29:26.507926	0.33
3982	-11.7	-4.0	0.5	14:29:26.743312	1.28	-17.8	-3.8	-11.5	14:29:26.743298	0.54
3983	-96.0	12.0	-12.0	14:29:26.766259	NaN	-12.8	3.8	-11.5	14:29:26.767710	0.44
4009	-17.4	4.0	0.8	14:29:36.657159	0.44	-16.8	2.8	-1.0	14:29:36.657178	0.07
4018	0.2	-4.0	1.1	14:29:39.193345	1.89	2.3	0.8	-6.0	14:29:39.193354	0.36
4026	5.4	1.7	-2.8	14:29:41.465110	0.62	8.8	-0.8	-4.5	14:29:41.465121	0.06
4039	-11.5	-3.2	2.1	14:29:45.463090	0.10	-11.8	-2.8	2.0	14:29:45.463090	0.16
4046	12.3	-5.7	11.9	14:29:46.980965	NaN	14.3	-3.8	12.0	14:29:46.980968	0.08
4063	5.6	-4.0	-2.0	14:29:49.081873	1.63	9.3	2.8	-10.5	14:29:49.081862	0.34
4066	-15.6	0.9	-2.6	14:29:49.775326	NaN	-15.8	1.3	-2.0	14:29:49.775328	0.06
4080	-4.5	-3.0	1.4	14:29:50.952647	0.13	-4.8	-3.8	2.5	14:29:50.952652	0.19
4085	1.3	-4.0	4.1	14:29:51.436593	0.55	9.3	3.3	-2.5	14:29:51.436597	0.02
4090	16.5	4.0	-12.0	14:29:52.380587	NaN	13.3	3.8	-10.5	14:29:52.380639	0.33
4098	-96.0	-4.0	-12.0	14:29:54.125052	>10.00	-12.3	2.8	-8.0	14:29:54.134522	0.04
4112	-96.0	-12.0	12.0	14:29:55.521804	>10.00	8.8	-3.8	-3.0	14:29:55.526918	0.39
4128	10.1	-4.0	1.6	14:29:57.443257	0.28	9.8	0.8	-7.5	14:29:57.443266	0.06
4135	8.3	-4.4	9.1	14:29:58.230854	NaN	7.8	-4.3	9.5	14:29:58.230850	0.04
4140	-5.6	-4.0	2.1	14:29:58.520671	NaN	-5.8	-3.8	-0.5	14:29:58.520686	0.52
4142	7.0	4.0	-3.6	14:29:58.662145	NaN	6.8	3.3	1.0	14:29:58.662176	0.52
4187	-96.0	4.0	-12.0	14:30:03.468668	>10.00	-2.3	-3.8	-8.5	14:30:03.484775	0.66
4197	-1.8	-12.0	12.0	14:30:07.403061	NaN	6.8	-3.8	6.5	14:30:07.403317	0.57
4204	96.0	4.0	-12.0	14:30:09.854458	NaN	11.3	3.8	-5.0	14:30:09.859008	0.43
4210	-16.2	-2.1	0.4	14:30:13.668205	0.25	-15.8	1.3	-11.0	14:30:13.668156	NEL
4230	-1.1	4.0	-12.0	14:30:22.755900	4.05	-20.8	1.3	-4.5	14:30:22.756028	0.09
4231	4.0	-4.0	-7.2	14:30:22.992035	0.72	3.3	-3.8	-11.5	14:30:22.992018	0.24
4241	-4.5	-2.7	2.5	14:30:32.351206	NaN	-3.8	-2.8	3.0	14:30:32.351207	0.03
4243	-10.2	3.8	-2.7	14:30:33.529381	NaN	-9.8	3.8	-1.5	14:30:33.529387	0.58
4251	8.9	0.3	-4.1	14:30:38.624052	NaN	8.3	0.3	-4.0	14:30:38.624053	0.04
4304	13.4	-0.1	1.8	14:30:41.419676	NaN	23.8	-2.3	-2.0	14:30:41.419772	0.43
4313	-5.6	-4.0	-0.6	14:30:42.413652	0.43	-8.8	-2.8	-1.0	14:30:42.413656	0.36

Tab. B.18: SW I - localized events, part 4: Coordinates of the estimated source locations determined using Geiger's method and *FastWay*. Estimated source locations excluded during the verification process (see Section 7.3.4) are shown in gray.

Event	Geiger's method					*FastWay*				
#	x [in]	y [in]	z [in]	t_s [hh:mm:ss]	*eei* [-]	x [in]	y [in]	z [in]	t_s [hh:mm:ss]	*eei* [-]
4315	8.3	-12.0	12.0	14:30:42.515761	NaN	9.3	1.3	-10.5	14:30:42.515943	0.24
4326	-14.6	-0.7	-9.7	14:30:43.372714	1.69	-15.3	-1.8	-11.5	14:30:43.372695	0.39
4331	-2.2	-2.3	5.4	14:30:43.750628	0.95	-0.8	0.3	7.0	14:30:43.750654	NEL
4332	-10.7	4.0	-3.9	14:30:43.757938	0.65	-5.3	2.8	-8.5	14:30:43.757908	NEL
4340	11.6	4.0	-7.1	14:30:44.155004	0.24	9.8	3.8	-10.0	14:30:44.155001	0.19
4389	22.1	-4.0	-3.0	14:30:46.648528	1.08	18.8	-3.3	-1.0	14:30:46.648539	0.02
4403	-0.9	-1.5	-4.4	14:30:47.295354	0.27	-4.3	-3.3	-4.5	14:30:47.295360	0.08
4435	-4.2	-4.0	0.5	14:30:48.088269	0.58	-10.8	-3.8	-2.5	14:30:48.088254	NEL
4485	-6.6	4.0	0.8	14:30:49.497628	0.34	-9.3	2.8	-0.5	14:30:49.497618	0.28
4496	5.0	-4.0	-12.0	14:30:49.874263	2.87	3.3	-3.8	-11.5	14:30:49.874310	0.62
4528	-5.1	-1.9	-0.2	14:30:50.759527	0.57	-2.8	3.8	-8.5	14:30:50.759498	NEL
4594	14.8	2.8	-0.9	14:30:52.397020	0.18	14.3	3.8	-1.5	14:30:52.397020	NEL
4914	-4.8	-4.0	-11.0	14:30:58.831127	1.37	-6.8	-3.8	-10.5	14:30:58.831131	0.55
5167	3.8	0.3	9.3	14:31:05.517193	0.18	4.3	0.3	8.0	14:31:05.517198	0.03
5393	-96.0	4.0	-12.0	14:31:10.406263	>10.00	15.3	6.8	8.5	14:31:10.417060	0.67
7348	-6.2	-12.0	12.0	14:31:57.889777	2.08	-0.8	-11.8	8.5	14:31:57.889755	0.70
7406	-18.3	4.0	-12.0	14:32:05.523420	2.57	-22.3	3.8	-11.5	14:32:05.523431	0.48
7473	9.6	0.5	6.1	14:32:28.398329	NaN	9.3	-0.3	6.0	14:32:28.398334	0.06
7588	-5.0	-12.0	8.0	14:38:04.252773	NaN	7.8	3.8	-11.5	14:38:04.252733	0.52
7635	96.0	-4.0	-12.0	14:39:23.400836	NaN	-23.8	-3.8	6.5	14:39:23.414121	0.67
7714	17.3	-4.0	-12.0	14:39:36.639187	>10.00	7.3	-3.3	-11.5	14:39:36.639261	0.24
7802	-14.1	4.0	-12.0	14:39:45.584943	1.78	-9.3	-3.8	-5.5	14:39:45.584996	0.62
7810	28.2	-4.0	-12.0	14:39:45.893315	>10.00	2.8	-3.8	-11.0	14:39:45.893517	0.82
7849	12.0	-1.1	8.3	14:39:47.090486	0.22	11.3	-0.3	7.5	14:39:47.090495	0.21
7860	0.1	-3.1	0.2	14:39:47.578205	2.62	1.8	-3.8	1.5	14:39:47.578272	0.47
7901	2.1	4.0	-12.0	14:39:49.668982	2.10	-7.3	3.8	-5.0	14:39:49.669053	0.25
7910	-15.2	-1.6	0.2	14:39:50.347665	0.79	-9.8	-3.3	-11.5	14:39:50.347590	0.59
7927	9.7	3.0	-0.1	14:39:51.608948	0.18	9.3	1.8	1.0	14:39:51.608957	0.13
7931	-8.0	4.0	-6.5	14:39:51.820301	0.36	-7.8	3.8	0.0	14:39:51.820331	NEL
7933	-2.1	-4.0	-4.1	14:39:51.944585	0.57	4.8	-2.8	-11.5	14:39:51.944544	0.71
7939	16.1	4.0	-2.1	14:39:52.049349	0.80	15.8	3.8	1.5	14:39:52.049360	NEL
8015	-3.2	-4.0	6.8	14:39:53.980940	1.00	-5.3	3.8	-5.5	14:39:53.980968	0.74
8032	-96.0	-12.0	-12.0	14:39:54.539290	NaN	8.3	-3.8	-11.5	14:39:54.543682	0.83
8081	-6.8	3.4	4.8	14:39:55.982290	0.57	-10.8	8.8	8.5	14:39:55.982275	NEL
8248	4.3	-1.8	12.0	14:39:59.495038	1.81	-2.3	3.8	2.0	14:39:59.495028	0.39
11567	96.0	12.0	12.0	14:40:56.128560	>10.00	12.8	0.3	9.0	14:40:56.148814	0.06
11575	-1.4	-4.0	1.7	14:40:56.727878	0.77	-1.8	-3.8	6.5	14:40:56.727878	NEL
11654	17.9	-7.1	9.0	14:41:14.541769	NaN	10.8	3.8	-5.0	14:41:14.541837	0.27
11768	7.7	3.7	-2.4	14:52:39.651538	0.14	7.8	-2.3	4.0	14:52:39.651532	0.03
11850	-7.8	-0.1	5.0	14:52:46.930401	0.32	-10.3	3.8	5.5	14:52:46.930414	0.38
11853	0.3	-4.0	0.0	14:52:47.854041	0.60	11.8	0.3	-8.5	14:52:47.854007	NEL
11890	-2.3	-4.0	6.1	14:52:55.238133	0.39	14.3	3.3	-7.0	14:52:55.238098	0.20
11908	0.6	-4.0	-12.0	14:54:17.427156	1.40	8.8	-0.8	-3.0	14:54:17.427227	0.06
11957	17.8	4.0	-12.0	14:55:05.240730	2.92	17.8	3.8	-10.5	14:55:05.240755	0.44
12029	-12.4	-4.0	-2.0	14:55:18.706332	0.39	-11.3	-3.3	-2.0	14:55:18.706332	0.91

Tab. B.19: SW I - localized events, part 5: Coordinates of the estimated source locations determined using Geiger's method and *FastWay*. Estimated source locations excluded during the verification process (see Section 7.3.4) are shown in gray.

Event	Geiger's method					*FastWay*				
#	x [in]	y [in]	z [in]	t_s [hh:mm:ss]	*eei* [-]	x [in]	y [in]	z [in]	t_s [hh:mm:ss]	*eei* [-]
12040	96.0	-4.0	-12.0	14:55:19.510627	NaN	23.8	-3.8	-2.5	14:55:19.511237	0.79
12323	-28.7	2.4	-1.9	14:55:36.162540	1.13	-19.8	0.3	0.5	14:55:36.162566	0.07
12434	9.1	0.1	3.8	14:55:39.442002	NaN	8.8	0.3	4.5	14:55:39.442000	0.06
12460	-12.7	-4.0	-4.6	14:55:39.886504	0.78	-10.3	-3.8	-6.5	14:55:39.886519	0.26
12520	13.0	-4.0	1.0	14:55:41.533772	1.46	23.8	-0.8	11.0	14:55:41.533778	0.22
12618	4.4	4.0	-8.7	14:55:44.066656	0.99	15.3	3.3	12.0	14:55:44.066648	NEL
12631	-10.7	4.0	-3.5	14:55:44.165066	NaN	-9.3	1.3	-2.0	14:55:44.165079	0.22
13791	-96.0	-4.0	-12.0	14:56:06.574344	NaN	11.8	-2.3	-10.0	14:56:06.582113	0.64
14901	-1.1	-4.0	3.0	14:56:37.443681	0.80	0.3	1.8	-3.0	14:56:37.443703	0.04
14927	-14.3	-4.0	-9.0	14:56:39.425737	1.42	-4.8	-3.8	-11.5	14:56:39.425781	0.98
14977	6.0	-3.6	7.2	14:56:44.599979	0.59	11.3	2.8	4.5	14:56:44.599960	0.04
14979	-10.3	4.0	-12.0	14:56:44.764425	2.35	-11.8	3.8	-10.0	14:56:44.764455	0.46
15045	-5.0	-2.3	2.6	14:56:54.560374	0.27	-5.3	-3.8	3.5	14:56:54.560374	0.21
15053	96.0	12.0	12.0	14:56:58.219284	>10.00	23.8	3.8	8.0	14:56:58.224753	0.31
15073	-23.4	4.0	-12.0	14:57:06.765165	>10.00	5.3	-0.8	-10.0	14:57:06.765363	0.04
15080	7.2	1.0	0.1	14:57:10.850349	0.49	14.3	3.8	3.0	14:57:10.850379	0.77
15167	-6.4	-4.0	2.6	15:04:46.672500	0.37	-4.3	0.3	-3.0	15:04:46.672528	0.35
15215	-13.6	-12.0	12.0	15:04:51.531542	>10.00	22.8	-11.8	12.0	15:04:51.531736	0.81
15502	-1.2	-4.0	7.4	15:05:14.310459	0.76	1.3	-2.8	-2.5	15:05:14.310460	NEL
15689	-8.1	6.2	12.0	15:07:46.861834	0.48	-13.8	1.3	-6.5	15:07:46.861780	NEL
15822	-5.5	4.0	0.4	15:08:02.004838	0.31	-4.8	3.3	1.5	15:08:02.004847	0.27
15922	0.5	-4.0	3.3	15:08:07.733089	1.30	8.8	3.8	-2.0	15:08:07.733108	0.41
15971	96.0	-4.0	-12.0	15:08:10.506800	>10.00	23.8	-1.3	-8.5	15:08:10.514475	0.42
16094	96.0	12.0	12.0	15:08:16.189539	>10.00	22.8	5.8	12.0	15:08:16.191113	0.27
16119	-6.8	-4.0	3.8	15:08:16.902336	0.70	-6.3	3.8	6.0	15:08:16.902323	NEL
16199	96.0	-12.0	12.0	15:08:19.792863	>10.00	23.8	-5.8	8.5	15:08:19.801092	0.74
16205	-96.0	-4.0	-12.0	15:08:20.125754	NaN	-2.3	-3.8	-8.0	15:08:20.138234	0.81
16269	8.1	4.0	3.9	15:08:21.443854	0.48	5.3	0.8	-1.5	15:08:21.443859	0.04
16375	-11.4	0.4	4.4	15:08:24.011882	0.66	8.8	-3.8	2.0	15:08:24.011765	NEL
18511	-96.0	-12.0	12.0	15:09:10.568541	>10.00	7.8	-3.8	5.5	15:09:10.576537	0.13
18566	-96.0	10.6	12.0	15:09:14.960157	>10.00	-17.8	-8.3	12.0	15:09:14.960962	0.56
18601	-37.3	-4.0	2.5	15:09:19.702721	4.19	-13.3	1.8	0.5	15:09:19.702811	0.03
18627	5.7	-4.0	-8.1	15:09:24.692975	NaN	4.8	-3.8	-11.5	15:09:24.692989	0.60
18673	9.2	0.1	3.5	15:09:35.068423	0.25	6.3	0.3	7.0	15:09:35.068437	0.02

Tab. B.20: SW I - localized events, part 6: Coordinates of the estimated source locations determined using Geiger's method and *FastWay*. Estimated source locations excluded during the verification process (see Section 7.3.4) are shown in gray.

B.3 Pencil-lead breaks SW I b

B.3.1 Top

PLB			Set	Geiger's method						*FastWay*					
x [in]	y [in]	z [in]	#	x [in]	y [in]	z [in]	d [in]	eei [-]	ac [-]	x [in]	y [in]	z [in]	d [in]	eei [-]	ac [-]
-22.0	-10.0	12.0	12-8	-22.1	-9.3	12.0	0.73	0.40	1	-20.8	-11.8	11.8	2.17	0.67	2
-22.0	-10.0	12.0	12-9	-19.7	-9.8	12.0	2.27	0.21	2	-20.3	-6.8	8.3	5.26	NEL	4
-22.0	-10.0	12.0	12-20	-19.7	-4.0	3.9	10.31	0.44	6	-23.8	-8.3	8.8	4.09	0.18	3
-22.0	-10.0	12.0	12-36	-19.4	-9.9	10.5	2.96	0.11	3	-21.8	-8.3	8.3	4.15	0.17	3
-22.0	-10.0	12.0	12-37	-21.8	-11.5	12.0	1.56	0.20	2	-19.8	-9.8	11.8	2.28	0.18	2
-22.0	-6.0	12.0	12-5	-23.7	-6.0	9.5	3.07	0.16	3	-20.3	-5.8	8.3	4.15	0.09	3
-22.0	-6.0	12.0	12-16	-61.7	-12.0	12.0	40.17	2.47	6	-23.8	-7.3	11.8	2.17	0.52	2
-22.0	-6.0	12.0	12-29	-22.1	-6.0	11.4	0.60	0.12	1	-22.3	-5.8	10.3	1.79	0.23	2
-22.0	-2.0	12.0	12-1	-26.4	-2.4	11.3	4.48	0.21	3	-23.8	-2.8	11.8	1.92	NEL	2
-22.0	-2.0	12.0	12-12	-21.8	-2.0	10.5	1.52	0.09	2	-23.8	-2.3	9.8	2.86	0.16	3
-22.0	-2.0	12.0	12-24	-23.2	-1.3	10.5	2.08	0.17	2	-22.8	-2.3	10.3	1.92	0.27	2
-22.0	2.0	12.0	12-79	-21.2	1.8	10.3	1.89	0.09	2	-23.3	1.8	10.3	2.17	0.12	2
-22.0	2.0	12.0	12-94	-22.1	1.6	10.7	1.37	0.09	2	-23.8	1.3	10.8	2.28	0.12	2
-22.0	2.0	12.0	12-106	-21.3	1.8	10.4	1.78	0.09	2	-23.3	1.8	10.3	2.17	0.16	2
-22.0	6.0	12.0	11-59	-19.3	3.9	11.4	3.49	0.10	3	-19.3	3.8	10.8	3.77	0.16	3
-22.0	6.0	12.0	12-87	-21.4	4.3	11.4	1.87	0.23	2	-19.8	3.8	11.8	3.19	0.18	3
-22.0	6.0	12.0	12-101	-22.6	5.1	11.7	1.12	0.18	2	-20.8	4.3	10.8	2.49	0.03	2
-22.0	6.0	12.0	13-54	-19.5	5.8	11.6	2.59	0.20	3	-20.8	5.8	11.8	1.30	NEL	2
-22.0	6.0	12.0	13-63	-6.0	1.0	12.0	16.81	0.61	6	-8.3	3.8	-10.8	26.68	NEL	6
-22.0	10.0	12.0	11-43	-20.3	8.1	11.8	2.51	3.68	3	-20.3	6.3	11.8	4.15	NEL	3
-22.0	10.0	12.0	13-76	-23.8	8.5	12.0	2.31	0.37	2	-23.8	8.3	11.8	2.49	0.36	2
-18.0	-10.0	12.0	12-21	-20.8	-11.0	12.0	3.01	0.46	3	-16.3	-11.8	10.8	2.77	0.16	3
-18.0	-10.0	12.0	14-59	-13.7	-4.0	7.5	8.69	0.29	5	-18.3	-5.8	11.8	4.26	NEL	3
-18.0	-6.0	12.0	11-7	-25.2	3.7	11.8	12.09	0.11	6	-17.8	1.8	11.3	7.79	NEL	5
-18.0	-6.0	12.0	12-17	-18.1	-4.0	7.5	4.94	0.28	3	-17.3	-6.3	10.8	1.48	0.15	2
-18.0	-6.0	12.0	12-31	-17.6	-6.0	11.0	1.06	0.12	2	-17.3	-6.3	8.8	3.34	0.21	3
-18.0	-6.0	12.0	13-4	-17.3	-6.1	11.5	0.85	0.13	1	-17.3	-6.3	10.3	1.92	0.21	2
-18.0	-6.0	12.0	14-52	-16.4	-4.1	12.0	2.51	0.15	3	-19.3	-2.3	9.8	4.55	NEL	3
-18.0	-2.0	12.0	14-1	-17.4	-2.1	10.6	1.54	0.09	2	-18.3	-2.3	10.3	1.79	0.14	2
-18.0	-2.0	12.0	14-23	-18.1	-1.8	10.6	1.41	0.09	2	-19.8	-1.8	10.3	2.49	0.13	2
-18.0	-2.0	12.0	14-45	-17.9	-1.8	10.9	1.15	0.09	2	-19.3	-1.8	10.3	2.17	0.12	2
-18.0	2.0	12.0	12-80	-36.6	11.6	11.6	20.91	2.06	6	-17.8	2.8	9.8	2.38	0.06	2
-18.0	2.0	12.0	12-95	-17.8	1.4	10.5	1.62	0.10	2	-18.8	1.3	10.8	1.64	0.12	2
-18.0	2.0	12.0	12-107	-17.9	1.5	10.7	1.42	0.11	2	-18.8	1.3	10.8	1.64	0.08	2
-18.0	6.0	12.0	13-71	-18.5	4.8	12.0	1.31	0.39	2	-15.8	3.3	11.8	3.56	0.80	3
-18.0	10.0	12.0	11-44	-96.0	12.0	12.0	78.03	>10.00	6	-23.8	-1.3	11.8	12.64	NEL	6
-18.0	10.0	12.0	12-105	-17.0	6.8	12.0	3.38	0.20	3	-17.3	7.3	11.8	2.86	0.44	3
-18.0	10.0	12.0	12-115	-32.1	-3.6	12.0	19.61	2.04	6	-15.8	2.8	11.8	7.60	0.98	5
-18.0	10.0	12.0	13-59	-10.8	4.0	0.8	14.63	NaN	6	-10.3	7.8	8.3	8.90	0.07	5
-14.0	-6.0	12.0	12-6	-13.5	-4.0	7.4	5.08	NaN	4	-13.3	-7.8	8.3	4.21	0.13	3
-14.0	-6.0	12.0	14-9	-13.9	-5.9	11.5	0.56	0.12	1	-11.3	-8.3	8.3	5.17	0.09	4
-14.0	-6.0	12.0	14-30	-13.6	-6.0	9.7	2.29	0.10	2	-11.8	-7.8	8.3	4.71	0.08	3
-14.0	-6.0	12.0	14-31	-13.6	-4.4	12.0	1.62	0.32	2	-6.3	-10.3	11.8	8.84	0.10	5
-14.0	-6.0	12.0	14-53	-14.6	-1.8	12.0	4.26	0.15	3	-14.8	-1.8	11.3	4.38	0.30	3

Tab. B.21: SW I PLB b - "Top", part 1: Coordinates of the pencil-lead breaks and estimated source locations determined using Geiger's method and *FastWay*. Estimated source locations excluded during the verification process (see Section 7.3.4) are shown in gray.

PLB			Set	Geiger's method						*FastWay*					
x	y	z	#	x	y	z	d	eei	ac	x	y	z	d	eei	ac
[in]	[in]	[in]		[in]	[in]	[in]	[in]	[-]	[-]	[in]	[in]	[in]	[in]	[-]	[-]
-14.0	-2.0	12.0	14-2	-13.6	-1.9	11.0	1.08	0.09	2	-13.8	-2.3	10.8	1.30	0.18	2
-14.0	-2.0	12.0	14-24	-15.7	-0.6	12.0	2.18	0.13	2	-15.3	-1.3	11.8	1.48	0.22	2
-14.0	-2.0	12.0	14-46	-14.0	-1.8	11.3	0.73	0.10	1	-14.3	-2.3	11.8	0.43	0.16	1
-14.0	2.0	12.0	13-62	-13.8	1.7	11.1	0.95	0.10	1	-14.3	1.3	11.8	0.83	0.20	1
-14.0	2.0	12.0	14-168	-13.9	1.7	11.0	1.06	0.10	2	-14.3	1.3	10.3	1.92	0.25	2
-14.0	2.0	12.0	14-206	-14.8	1.6	10.5	1.74	0.12	2	-14.3	1.3	9.8	2.38	0.07	2
-14.0	6.0	12.0	13-55	-13.9	5.6	12.0	0.43	0.12	1	-15.3	4.3	8.3	4.32	NEL	3
-14.0	6.0	12.0	13-64	-14.3	5.5	10.2	1.87	0.09	2	-13.8	5.8	10.3	1.79	0.08	2
-14.0	6.0	12.0	14-213	-13.8	5.6	12.0	0.47	0.13	1	-13.8	5.8	11.8	0.43	0.31	1
-14.0	10.0	12.0	14-181	-13.9	9.1	10.9	1.45	0.12	2	-15.8	7.8	8.3	4.71	0.37	3
-14.0	10.0	12.0	14-200	-14.0	8.8	10.9	1.63	0.12	2	-15.3	7.8	8.3	4.55	0.36	3
-14.0	10.0	12.0	14-218	-13.3	7.7	12.0	2.43	0.09	2	-13.8	7.3	11.8	2.77	0.18	3
-10.0	-10.0	12.0	14-37	-13.6	-4.0	6.7	8.74	0.27	5	-11.3	-11.8	8.3	4.32	0.23	3
-10.0	-10.0	12.0	14-38	-10.5	-4.0	6.9	7.91	0.33	5	-12.3	-7.8	8.3	4.92	0.19	3
-10.0	-10.0	12.0	14-60	-11.6	-11.8	12.0	2.40	0.22	2	-11.8	-8.3	8.3	4.49	0.16	3
-10.0	2.0	12.0	14-188	-11.4	1.6	10.7	1.94	0.12	2	-10.3	1.8	10.8	1.30	0.14	2
-10.0	2.0	12.0	14-207	-10.4	1.9	10.9	1.17	0.10	2	-11.3	1.8	11.3	1.48	0.13	2
-10.0	6.0	12.0	14-175	-11.1	5.6	10.2	2.16	0.12	2	-10.8	5.3	10.8	1.64	0.05	2
-10.0	6.0	12.0	14-194	-10.3	5.7	11.0	1.05	0.09	2	-10.8	5.3	10.8	1.64	0.08	2
-10.0	6.0	12.0	14-214	-12.9	5.2	10.3	3.44	0.19	3	-10.8	5.8	11.3	1.09	0.05	2
-10.0	10.0	12.0	14-182	-11.3	8.1	10.3	2.89	0.20	3	-11.3	8.8	9.8	2.86	0.04	3
-10.0	10.0	12.0	14-201	-10.4	9.4	11.0	1.18	0.09	2	-11.3	8.8	9.8	2.86	0.10	3
-10.0	10.0	12.0	14-219	2.0	4.0	7.3	14.23	NaN	6	2.3	11.8	8.3	12.93	0.28	6
-8.0	-2.0	12.0	14-47	-4.1	1.7	12.0	5.41	0.74	4	-4.8	8.8	11.8	11.23	0.45	6
-8.0	-2.0	12.0	14-48	-5.5	-2.6	12.0	2.59	0.09	3	-6.3	-2.8	10.8	2.28	0.18	2
-6.0	-10.0	12.0	14-17	-2.8	-12.0	12.0	3.81	0.85	3	-8.3	-11.8	8.3	4.71	0.09	3
-6.0	-10.0	12.0	14-18	-6.2	-10.5	12.0	0.58	0.32	1	-5.8	-9.8	8.3	3.77	0.04	3
-6.0	-10.0	12.0	14-39	-6.0	-4.0	5.9	8.54	0.28	5	-7.3	-9.3	8.3	4.02	0.20	3
-6.0	-10.0	12.0	14-61	-6.2	-4.0	6.1	8.40	0.41	5	-8.3	-9.3	8.3	4.44	0.08	3
-6.0	-6.0	12.0	14-10	-6.9	-11.0	12.0	5.08	0.48	4	-7.3	-7.3	9.3	3.27	NEL	3
-6.0	-6.0	12.0	14-11	-5.8	-6.5	12.0	0.60	0.19	1	-6.8	-5.8	8.8	3.34	0.04	3
-6.0	-6.0	12.0	14-32	-2.7	-9.0	12.0	4.40	0.45	3	-5.3	-7.3	11.8	1.48	0.23	2
-6.0	-6.0	12.0	14-54	-5.4	-6.2	12.0	0.63	0.18	1	-7.3	-8.3	11.8	2.59	0.20	3
-6.0	-2.0	12.0	14-4	-6.3	-2.4	9.4	2.67	0.09	3	-6.8	-2.3	8.8	3.34	0.07	3
-6.0	-2.0	12.0	14-25	-5.5	-2.5	11.8	0.73	0.10	1	-6.3	-2.8	10.8	1.48	0.16	2
-6.0	2.0	12.0	14-170	-6.4	2.4	10.7	1.45	0.10	2	-6.8	2.3	11.3	1.09	0.09	2
-6.0	2.0	12.0	14-189	-6.0	1.9	11.2	0.83	0.10	1	-6.3	1.8	11.3	0.83	0.15	1
-6.0	2.0	12.0	14-208	-6.4	1.8	10.6	1.50	0.10	2	-6.8	1.8	10.3	1.92	0.19	2
-6.0	6.0	12.0	14-176	-5.7	6.1	11.2	0.85	0.09	1	-5.8	5.8	10.8	1.30	0.11	2
-6.0	6.0	12.0	14-195	-5.6	6.2	11.3	0.81	0.09	1	-5.8	5.3	10.3	1.92	0.12	2
-6.0	6.0	12.0	14-196	-5.0	7.1	11.9	1.49	0.14	2	-4.8	7.3	11.8	1.79	0.23	2
-6.0	6.0	12.0	14-215	-5.9	6.9	12.0	0.93	0.09	1	-6.3	5.8	11.3	0.83	0.04	1
-6.0	10.0	12.0	14-183	-6.7	4.0	2.9	10.89	0.27	6	-6.3	7.8	10.3	2.86	0.14	3
-6.0	10.0	12.0	14-202	-6.6	4.0	2.0	11.67	0.25	6	-5.8	7.8	10.8	2.59	0.12	3
-6.0	10.0	12.0	14-220	-10.3	9.7	11.2	4.41	0.09	3	-11.3	8.8	9.8	5.85	0.06	4
-6.0	10.0	12.0	14-221	-6.0	4.0	4.0	10.01	0.24	6	-6.8	8.3	10.8	2.28	0.16	2
-2.0	-10.0	12.0	14-19	-0.7	-4.0	7.8	7.47	0.30	4	-1.3	-11.3	11.8	1.48	0.24	2
-2.0	-10.0	12.0	14-40	-0.9	-9.9	11.1	1.39	0.16	2	-1.3	-8.3	9.8	2.95	0.25	3

Tab. B.22: SW I PLB b - "Top", part 2: Coordinates of the pencil-lead breaks and estimated source locations determined using Geiger's method and *FastWay*. Estimated source locations excluded during the verification process (see Section 7.3.4) are shown in gray.

PLB			Set	Geiger's method						*FastWay*					
x [in]	y [in]	z [in]	#	x [in]	y [in]	z [in]	d [in]	*eei* [-]	*ac* [-]	x [in]	y [in]	z [in]	d [in]	*eei* [-]	*ac* [-]
-2.0	-10.0	12.0	14-62	-2.6	-4.0	5.5	8.87	0.30	5	-3.3	-11.3	8.8	3.70	0.20	3
-2.0	-6.0	12.0	14-12	-2.2	-6.7	9.5	2.64	0.10	3	-2.8	-5.8	9.3	2.86	0.11	3
-2.0	-6.0	12.0	14-33	-1.6	-6.9	9.4	2.77	0.09	3	-1.8	-5.8	11.8	0.43	0.15	1
-2.0	-6.0	12.0	14-55	-1.3	-7.1	9.9	2.46	0.10	2	-1.3	-6.8	11.8	1.09	0.19	2
-2.0	-2.0	12.0	14-5	-2.0	-2.3	10.4	1.67	0.11	2	-2.3	-1.8	10.3	1.79	0.15	2
-2.0	-2.0	12.0	14-26	-2.1	-2.4	8.7	3.31	0.10	3	-2.3	-2.3	7.3	4.76	NEL	3
-2.0	-2.0	12.0	14-49	-2.1	-1.8	7.8	4.24	0.10	3	-2.3	-2.3	6.8	5.26	NEL	4
-2.0	2.0	12.0	12-108	96.0	12.0	-12.0	101.39	NaN	6	7.3	-1.3	7.3	10.89	NEL	6
-2.0	2.0	12.0	14-171	-1.6	2.3	9.9	2.19	0.10	2	-1.8	1.8	9.3	2.77	0.20	3
-2.0	2.0	12.0	14-190	-1.5	1.8	11.0	1.14	0.12	2	-1.8	1.3	10.8	1.48	0.16	2
-2.0	2.0	12.0	14-209	-1.9	2.1	8.5	3.53	0.10	3	-2.3	2.8	4.3	7.79	NEL	5
-2.0	6.0	12.0	14-177	-1.9	6.1	10.4	1.59	0.10	2	-1.8	5.3	8.8	3.34	0.07	3
-2.0	6.0	12.0	14-198	31.1	-12.0	12.0	37.68	NaN	6	-3.3	-9.8	11.8	15.80	0.80	6
-2.0	6.0	12.0	14-216	-1.9	6.7	10.6	1.55	0.10	2	-1.8	5.8	9.8	2.28	0.10	2
-2.0	10.0	12.0	14-184	-1.7	4.0	6.4	8.22	0.22	5	-1.8	8.8	8.3	3.96	0.15	3
-2.0	10.0	12.0	14-203	-1.7	4.0	7.2	7.70	0.21	5	-1.8	7.8	8.3	4.38	0.15	3
-2.0	10.0	12.0	14-222	-2.1	11.4	11.4	1.55	0.10	2	-2.3	11.8	11.8	1.79	0.15	2
2.0	-10.0	12.0	14-20	3.4	-11.0	12.0	1.75	0.33	2	3.3	-11.8	8.3	4.32	0.08	3
2.0	-10.0	12.0	14-41	3.9	-9.5	12.0	1.94	0.26	2	1.8	-11.8	11.8	1.79	0.31	2
2.0	-10.0	12.0	14-63	3.3	-10.0	12.0	1.32	0.38	2	2.3	-11.8	11.8	1.79	0.39	2
2.0	-6.0	12.0	14-13	2.1	-6.4	9.9	2.10	0.10	2	1.8	-5.3	8.3	3.83	NEL	3
2.0	-6.0	12.0	14-34	2.4	-5.6	11.4	0.85	0.10	1	1.3	-5.8	8.3	3.83	0.19	3
2.0	-6.0	12.0	14-35	1.5	-5.5	8.6	3.46	0.09	3	1.3	-5.3	8.3	3.90	0.13	3
2.0	-6.0	12.0	14-56	1.9	-4.0	7.4	5.04	0.20	4	1.3	-10.3	8.3	5.72	0.13	4
2.0	-2.0	12.0	14-6	2.2	-2.6	11.1	1.05	0.10	2	2.3	-2.8	9.8	2.38	0.11	2
2.0	-2.0	12.0	14-27	1.3	-3.1	12.0	1.35	0.09	2	1.3	-3.3	10.8	1.92	0.10	2
2.0	-2.0	12.0	14-50	1.8	-2.2	11.2	0.81	0.11	1	1.8	-2.8	10.3	1.92	0.07	2
2.0	2.0	12.0	14-169	-10.7	1.9	11.0	12.77	0.09	6	-11.3	1.8	11.3	13.27	0.15	6
2.0	2.0	12.0	14-172	1.6	3.1	9.6	2.63	0.10	3	1.8	2.8	8.8	3.34	0.07	3
2.0	2.0	12.0	14-191	2.0	2.2	10.2	1.86	0.10	2	1.8	2.3	9.3	2.77	0.13	3
2.0	2.0	12.0	14-210	1.8	2.0	9.3	2.72	0.11	3	1.8	1.8	8.8	3.27	NEL	3
2.0	6.0	12.0	14-179	1.7	6.1	10.3	1.73	0.09	2	2.3	5.8	9.3	2.77	0.21	3
2.0	6.0	12.0	14-197	1.8	6.6	9.6	2.46	0.12	2	-6.3	8.8	8.3	9.47	NEL	5
2.0	6.0	12.0	14-217	1.5	6.5	9.8	2.34	0.12	2	2.3	4.8	10.8	1.79	0.08	2
2.0	10.0	12.0	14-185	9.5	4.0	-12.0	25.86	2.18	6	2.3	10.8	11.3	1.09	0.24	2
2.0	10.0	12.0	14-204	1.3	4.0	7.6	7.50	0.21	4	1.8	7.8	8.3	4.38	0.12	3
2.0	10.0	12.0	14-205	35.9	12.0	12.0	33.94	8.45	6	5.3	8.3	8.3	5.26	0.04	4
2.0	10.0	12.0	14-223	1.9	4.0	6.6	8.04	0.22	5	2.3	8.3	8.3	4.15	0.21	3
6.0	-6.0	12.0	14-57	4.8	-6.8	12.0	1.41	0.11	2	4.3	-7.8	8.3	4.49	0.08	3
6.0	-2.0	12.0	14-7	5.7	-2.4	12.0	0.54	0.10	1	5.8	-2.3	11.8	0.43	0.16	1
6.0	-2.0	12.0	14-28	7.9	-1.3	9.6	3.16	0.09	3	8.8	-0.8	7.8	5.21	0.20	4
6.0	-2.0	12.0	14-51	6.6	-1.1	10.3	1.98	0.11	2	6.8	-0.8	10.3	2.28	0.17	2
6.0	2.0	12.0	14-173	5.9	1.5	12.0	0.49	0.10	1	5.3	1.3	11.8	1.09	0.12	2
6.0	2.0	12.0	14-192	6.9	2.6	9.4	2.78	0.12	3	8.8	2.3	11.8	2.77	0.15	3
6.0	2.0	12.0	14-211	6.4	1.9	10.5	1.57	0.09	2	6.3	1.8	9.8	2.28	0.06	2
6.0	6.0	12.0	13-56	9.0	-12.0	12.0	18.25	2.09	6	5.8	5.8	11.8	0.43	0.73	1
6.0	6.0	12.0	13-65	96.0	-4.0	-12.0	93.68	>10.00	6	23.8	-8.3	11.8	22.76	NEL	6
6.0	6.0	12.0	13-72	68.2	-12.0	9.3	64.77	>10.00	6	21.3	-8.3	11.3	20.89	NEL	6
6.0	10.0	12.0	13-68	35.6	12.0	12.0	29.67	1.69	6	23.8	8.8	9.3	18.01	1.14	6
6.0	10.0	12.0	13-77	6.2	4.0	7.0	7.80	0.25	5	6.3	8.3	9.3	3.27	0.14	3

Tab. B.23: SW I PLB b - "Top", part 3: Coordinates of the pencil-lead breaks and estimated source locations determined using Geiger's method and *FastWay*. Estimated source locations excluded during the verification process (see Section 7.3.4) are shown in gray.

PLB			Set	Geiger's method						*FastWay*					
x [in]	y [in]	z [in]	#	x [in]	y [in]	z [in]	d [in]	eei [-]	ac [-]	x [in]	y [in]	z [in]	d [in]	eei [-]	ac [-]
6.0	10.0	12.0	14-186	6.0	11.5	12.0	1.45	0.44	2	5.3	8.3	8.3	4.21	0.03	3
10.0	-10.0	12.0	14-21	11.2	-5.5	11.8	4.67	0.09	3	10.8	-5.8	11.8	4.32	0.14	3
10.0	-10.0	12.0	14-64	9.7	-6.9	11.5	3.19	0.10	3	11.8	-5.3	11.8	5.07	0.09	4
10.0	-6.0	12.0	13-19	12.7	-3.6	12.0	3.64	0.14	3	9.8	-5.3	11.8	0.83	0.18	1
10.0	-6.0	12.0	14-14	8.1	-4.3	9.4	3.66	0.12	3	10.8	-3.8	3.8	8.58	NEL	5
10.0	-6.0	12.0	14-15	11.4	-4.7	11.6	1.98	0.09	2	10.3	-5.3	11.8	0.83	0.10	1
10.0	-6.0	12.0	14-36	9.2	-4.0	12.0	2.20	0.10	2	9.8	-3.8	11.3	2.38	0.21	2
10.0	-2.0	12.0	14-8	10.6	-1.6	10.6	1.61	0.09	2	10.3	-1.8	10.8	1.30	0.13	2
10.0	-2.0	12.0	14-29	9.3	-2.2	11.7	0.82	0.09	1	9.8	-1.8	10.8	1.30	0.14	2
10.0	2.0	12.0	13-52	9.9	1.8	10.4	1.66	0.10	2	9.8	1.8	10.3	1.79	0.08	2
10.0	2.0	12.0	14-193	9.9	1.9	10.2	1.83	0.09	2	9.8	1.8	9.8	2.28	0.12	2
10.0	2.0	12.0	14-212	10.6	2.1	10.6	1.56	0.13	2	9.8	1.8	9.8	2.28	0.07	2
10.0	6.0	12.0	13-57	9.6	5.2	9.9	2.27	0.10	2	9.8	4.8	10.3	2.17	0.17	2
10.0	6.0	12.0	13-73	58.1	12.0	12.0	48.46	5.36	6	10.8	5.3	11.8	1.09	0.10	2
10.0	6.0	12.0	14-199	9.9	5.2	10.6	1.63	0.09	2	9.8	4.8	10.8	1.79	0.10	2
14.0	-10.0	12.0	13-21	14.1	-11.8	8.8	3.67	0.45	3	16.3	-8.3	8.3	4.71	NEL	3
14.0	-10.0	12.0	14-43	13.3	-8.3	9.7	2.94	0.18	3	15.3	-5.8	8.3	5.80	NEL	4
14.0	-6.0	12.0	13-7	15.5	-4.5	11.6	2.20	0.16	2	13.8	-5.8	11.8	0.43	NEL	1
14.0	-6.0	12.0	13-14	12.6	-4.0	11.6	2.43	0.11	2	12.3	-4.3	11.3	2.59	0.13	3
14.0	-6.0	12.0	13-15	14.4	-4.9	12.0	1.19	0.11	2	15.3	-4.8	9.8	2.86	0.02	3
14.0	-6.0	12.0	14-58	15.1	-4.2	12.0	2.17	0.12	2	14.3	-4.8	11.3	1.48	0.06	2
14.0	-2.0	12.0	12-26	22.9	1.1	11.4	9.43	0.74	5	13.8	-1.8	10.8	1.30	0.08	2
14.0	-2.0	12.0	13-2	13.9	0.1	8.2	4.34	0.15	3	10.8	-1.3	9.8	4.02	0.03	3
14.0	-2.0	12.0	13-11	14.0	-1.6	10.9	1.17	0.10	2	13.8	-1.8	10.8	1.30	0.12	2
14.0	2.0	12.0	12-99	13.8	2.0	10.7	1.36	0.09	2	13.3	1.8	10.8	1.48	0.07	2
14.0	2.0	12.0	13-53	96.0	12.0	12.0	82.61	>10.00	6	14.3	1.8	11.8	0.43	0.12	1
14.0	2.0	12.0	13-70	13.6	1.9	10.2	1.88	0.09	2	13.3	1.8	10.8	1.48	0.10	2
14.0	6.0	12.0	12-103	14.1	5.5	10.3	1.76	0.10	2	13.3	5.3	10.3	2.05	0.12	2
14.0	6.0	12.0	13-74	12.8	4.7	10.5	2.30	0.10	2	12.8	4.8	10.8	2.17	0.10	2
14.0	6.0	12.0	14-180	13.9	5.4	11.4	0.91	0.11	1	12.8	4.8	10.3	2.49	0.14	2
14.0	10.0	12.0	13-78	13.3	10.6	11.1	1.29	0.33	2	12.3	9.3	11.8	1.92	0.20	2
18.0	-10.0	12.0	12-23	41.4	-4.9	12.0	23.93	1.20	6	18.8	-10.8	11.8	1.09	0.26	2
18.0	-10.0	12.0	12-41	32.9	-7.6	12.0	15.09	0.84	6	19.3	-11.8	11.8	2.17	0.23	2
18.0	-10.0	12.0	13-8	16.1	-4.9	8.3	6.60	0.21	4	15.3	-5.8	8.3	6.30	NEL	4
18.0	-10.0	12.0	13-9	19.1	-4.0	5.5	8.92	0.26	5	17.8	-7.3	8.3	4.66	NEL	3
18.0	-10.0	12.0	13-16	19.0	-4.0	6.5	8.21	0.18	5	16.8	-7.3	8.3	4.82	NEL	3
18.0	-6.0	12.0	12-7	20.4	-4.9	11.3	2.72	0.20	3	19.3	-7.8	8.3	4.32	NEL	3
18.0	-6.0	12.0	12-18	17.7	-5.5	12.0	0.56	0.10	1	17.3	-6.3	11.8	0.83	0.17	1
18.0	-6.0	12.0	12-34	18.0	-5.3	12.0	0.71	0.12	1	17.3	-6.3	11.8	0.83	0.24	1
18.0	-2.0	12.0	12-3	18.4	-1.7	10.9	1.21	0.10	2	18.8	-1.8	11.3	1.09	0.21	2
18.0	-2.0	12.0	12-14	20.0	-0.6	12.0	2.47	0.16	2	18.8	-1.3	11.3	1.30	0.16	2
18.0	-2.0	12.0	12-27	20.3	-1.7	10.3	2.86	0.24	3	18.3	-1.8	11.3	0.83	0.09	1
18.0	2.0	12.0	12-111	17.8	1.7	10.8	1.30	0.09	2	18.3	1.8	11.3	0.83	0.09	1
18.0	6.0	12.0	13-58	18.0	5.7	11.8	0.39	0.10	1	17.8	5.3	11.8	0.83	0.05	1
18.0	6.0	12.0	13-66	17.5	5.0	11.4	1.28	0.11	2	17.8	5.3	11.8	0.83	0.05	1
18.0	6.0	12.0	13-75	17.4	5.0	11.4	1.30	0.12	2	17.8	5.3	11.8	0.83	0.06	1
18.0	10.0	12.0	11-53	20.0	11.6	10.4	2.98	0.36	3	17.3	10.8	9.8	2.49	NEL	2
18.0	10.0	12.0	11-54	18.8	6.7	10.8	3.57	0.26	3	16.8	6.3	11.3	4.02	NEL	3

Tab. B.24: SW I PLB b - "Top", part 4: Coordinates of the pencil-lead breaks and estimated source locations determined using Geiger's method and *FastWay*. Estimated source locations excluded during the verification process (see Section 7.3.4) are shown in gray.

PLB			Set	Geiger's method						*FastWay*					
x [in]	y [in]	z [in]	#	x [in]	y [in]	z [in]	d [in]	eei [-]	ac [-]	x [in]	y [in]	z [in]	d [in]	eei [-]	ac [-]
18.0	10.0	12.0	11-60	15.5	7.6	11.5	3.52	0.12	3	16.8	9.8	10.3	2.17	0.17	2
18.0	10.0	12.0	12-92	16.2	5.8	11.1	4.61	0.11	3	15.8	6.3	10.3	4.71	0.20	3
18.0	10.0	12.0	12-116	18.3	6.6	12.0	3.44	0.11	3	18.8	6.3	11.8	3.83	NEL	3
18.0	10.0	12.0	13-79	17.3	11.6	12.0	1.74	0.39	2	15.3	11.8	11.8	3.27	NEL	3
18.0	10.0	12.0	14-187	18.3	10.8	11.9	0.87	0.21	1	17.8	9.3	8.3	3.83	NEL	3
22.0	-10.0	12.0	12-10	43.4	-4.0	-3.8	27.22	2.02	6	20.3	-9.3	8.3	4.21	NEL	3
22.0	-10.0	12.0	12-11	-96.0	-12.0	-12.0	120.43	NaN	6	23.8	-0.8	10.3	9.58	NEL	5
22.0	-10.0	12.0	12-40	96.0	-4.0	-12.0	78.03	>10.00	6	20.3	-9.3	8.3	4.21	NEL	3
22.0	-10.0	12.0	13-20	14.3	-4.0	0.8	14.87	NaN	6	14.8	-7.8	8.3	8.47	NEL	5
22.0	-10.0	12.0	14-16	-20.9	-12.0	12.0	42.99	1.02	6	-17.8	-9.8	11.8	39.75	NEL	6
22.0	-10.0	12.0	14-44	-96.0	-12.0	8.0	118.08	NaN	6	-5.3	2.3	9.3	30.00	NEL	6
22.0	-6.0	12.0	10-4	29.2	4.7	12.0	12.92	NaN	6	23.3	-2.8	11.8	3.49	0.49	3
22.0	-6.0	12.0	12-19	96.0	12.0	12.0	76.16	>10.00	6	20.8	-6.3	11.3	1.48	0.01	2
22.0	-6.0	12.0	12-35	31.5	3.0	12.0	13.10	0.72	6	23.8	-2.8	11.8	3.70	0.54	3
22.0	-2.0	12.0	12-4	27.3	-1.3	11.2	5.39	0.26	4	22.3	-1.8	11.3	0.83	0.10	1
22.0	-2.0	12.0	12-15	23.0	-1.3	11.6	1.31	0.09	2	23.8	-1.3	11.8	1.92	0.13	2
22.0	-2.0	12.0	12-28	22.1	-1.6	11.1	1.03	0.08	2	22.8	-1.8	10.8	1.48	0.12	2
22.0	-2.0	12.0	13-10	96.0	4.0	-12.0	78.03	>10.00	6	8.8	1.8	9.8	13.95	NEL	6
22.0	-2.0	12.0	13-18	10.6	-1.3	10.3	11.59	0.09	6	10.3	-1.3	9.8	11.99	0.08	6
22.0	2.0	12.0	12-85	22.6	2.5	12.0	0.77	0.28	1	15.3	1.8	8.3	7.73	NEL	5
22.0	2.0	12.0	12-86	21.0	1.9	11.0	1.45	0.09	2	22.8	2.3	11.8	0.83	0.16	1
22.0	2.0	12.0	12-100	21.0	1.5	10.6	1.77	0.09	2	22.3	1.3	10.3	1.92	0.17	2
22.0	2.0	12.0	12-112	20.7	1.9	10.9	1.74	0.09	2	21.8	2.3	11.3	0.83	0.16	1
22.0	6.0	12.0	12-89	20.5	5.1	11.6	1.75	0.10	2	21.3	5.3	9.3	2.95	0.02	3
22.0	6.0	12.0	12-114	23.7	7.1	12.0	1.97	0.45	2	23.8	6.8	8.3	4.21	NEL	3
22.0	6.0	12.0	13-67	20.7	5.3	11.8	1.51	0.10	2	17.8	1.8	8.3	7.08	NEL	4
22.0	10.0	12.0	12-93	25.9	5.6	11.9	5.89	0.72	4	18.8	3.8	5.3	9.76	NEL	5
22.0	10.0	12.0	13-61	58.0	12.0	12.0	36.06	6.55	6	14.3	11.8	11.8	7.95	NEL	5
22.0	10.0	12.0	13-69	22.6	12.0	11.3	2.20	0.68	2	19.8	10.8	8.3	4.44	NEL	3

Tab. B.25: SW I PLB b - "Top", part 5: Coordinates of the pencil-lead breaks and estimated source locations determined using Geiger's method and *FastWay*. Estimated source locations excluded during the verification process (see Section 7.3.4) are shown in gray.

B.3.2 Top-Front

PLB			Set	Geiger's method						*FastWay*					
x	y	z	#	x	y	z	d	eei	ac	x	y	z	d	eei	ac
[in]	[in]	[in]		[in]	[in]	[in]	[in]	[-]	[-]	[in]	[in]	[in]	[in]	[-]	[-]
-22.0	-12.0	10.0	12-44	-25.5	-10.4	9.7	3.91	0.65	3	-23.8	-10.3	8.8	2.77	NEL	3
-22.0	-12.0	10.0	12-47	-89.3	-12.0	12.0	67.29	7.38	6	-23.3	-9.8	8.3	3.11	0.57	3
-22.0	-12.0	10.0	12-49	-35.1	-4.0	-8.5	23.99	0.74	6	-23.8	-10.3	8.8	2.77	0.38	3
-18.0	-12.0	10.0	12-45	-26.6	-12.0	12.0	8.85	0.91	5	-20.8	-8.8	8.3	4.60	0.33	3
-18.0	-12.0	10.0	12-50	-21.8	-11.8	12.0	4.31	0.62	3	-19.3	-11.8	11.8	2.17	0.38	2
-18.0	-12.0	10.0	13-24	-22.4	-11.0	12.0	4.96	0.71	3	-20.3	-8.3	8.3	4.71	NEL	3
-14.0	-12.0	10.0	13-26	-15.4	-9.8	12.0	3.28	0.88	3	-15.8	-9.3	8.3	3.70	0.21	3
-14.0	-12.0	10.0	14-65	-14.2	-4.0	5.5	9.16	0.28	5	-16.8	-7.3	8.3	5.76	0.17	4
-14.0	-12.0	10.0	14-72	-14.8	-10.8	11.9	2.39	0.12	2	-17.3	-8.8	11.8	4.92	0.24	3
-10.0	-12.0	10.0	14-66	-11.5	-4.0	5.8	9.14	0.29	5	-12.8	-8.3	8.3	4.97	0.20	3
-10.0	-12.0	10.0	14-73	-12.6	-11.4	12.0	3.33	0.28	3	-12.8	-10.8	11.8	3.49	0.20	3
-10.0	-12.0	10.0	14-79	-11.8	-11.6	12.0	2.73	0.11	3	-12.8	-10.3	11.8	3.70	0.15	3
-6.0	-12.0	10.0	14-67	-7.2	-4.0	4.7	9.66	0.28	5	-8.8	-8.8	8.3	4.60	0.20	3
-6.0	-12.0	10.0	14-68	-3.2	-4.0	-0.9	13.78	NaN	6	-2.3	-10.3	10.8	4.21	0.27	3
-6.0	-12.0	10.0	14-74	-2.8	2.6	11.2	15.03	0.57	6	-10.3	-10.3	11.8	4.92	0.08	3
-6.0	-12.0	10.0	14-80	-6.6	-12.0	12.0	2.10	0.47	2	-21.8	6.3	11.8	24.17	NEL	6
-2.0	-12.0	10.0	14-69	2.5	-11.9	12.0	4.93	0.72	3	2.3	-11.8	11.8	4.60	0.95	3
-2.0	-12.0	10.0	14-75	0.5	-7.3	12.0	5.70	0.31	4	-2.3	-10.8	8.3	2.17	0.21	2
-2.0	-12.0	10.0	14-81	-1.7	-11.1	11.6	1.82	0.28	2	-2.3	-8.3	9.8	3.77	0.20	3
2.0	-12.0	10.0	14-70	7.8	-9.0	12.0	6.81	0.29	4	6.3	-11.8	8.3	4.60	0.34	3
2.0	-12.0	10.0	14-76	2.7	-11.1	9.8	1.19	0.10	2	2.3	-11.8	9.3	0.83	0.37	1
2.0	-12.0	10.0	14-82	2.5	-12.0	12.0	2.06	0.75	2	1.8	-11.8	8.3	1.79	0.26	2
6.0	-12.0	10.0	14-77	6.8	-4.0	-10.8	22.28	NaN	6	5.8	-11.8	8.3	1.79	0.28	2
6.0	-12.0	10.0	14-83	6.2	-11.1	11.1	1.49	0.10	2	6.3	-11.8	8.3	1.79	0.34	2
10.0	-12.0	10.0	13-23	15.5	-7.1	12.0	7.65	0.22	5	23.8	-3.8	4.3	17.03	NEL	6
10.0	-12.0	10.0	14-78	11.7	-7.5	12.0	5.23	0.23	4	12.3	-8.3	11.8	4.71	0.04	3
10.0	-12.0	10.0	14-84	12.0	-9.3	11.2	3.54	0.17	3	10.8	-10.3	11.8	2.59	0.03	3
14.0	-12.0	10.0	12-46	17.7	-8.8	12.0	5.29	0.19	4	17.3	-11.8	10.8	3.34	0.18	3
14.0	-12.0	10.0	13-27	16.6	-5.8	11.1	6.80	0.18	4	19.3	-6.3	8.3	7.98	NEL	5
18.0	-12.0	10.0	11-18	20.6	-8.5	12.0	4.80	0.19	3	18.8	-11.8	11.8	1.92	0.21	2
18.0	-12.0	10.0	12-48	14.2	-6.8	12.0	6.76	0.87	4	23.8	0.8	11.8	14.10	NEL	6
18.0	-12.0	10.0	12-51	25.2	-6.2	12.0	9.43	1.36	5	17.8	-9.3	11.8	3.27	NEL	3
22.0	-12.0	10.0	11-20	22.4	-8.1	12.0	4.44	0.28	3	18.3	-11.8	11.8	4.15	0.10	3
22.0	-12.0	10.0	11-21	4.0	-4.0	-6.7	25.88	NaN	6	21.8	-11.3	11.8	1.92	1.04	2

Tab. B.26: SW I PLB b - "Top-Front", part 1: Coordinates of the pencil-lead breaks and estimated source locations determined using Geiger's method and *FastWay*. Estimated source locations excluded during the verification process (see Section 7.3.4) are shown in gray.

B.3.3 Front

PLB			Set	Geiger's method						*FastWay*					
x	y	z	#	x	y	z	d	eei	ac	x	y	z	d	eei	ac
[in]	[in]	[in]		[in]	[in]	[in]	[in]	[-]	[-]	[in]	[in]	[in]	[in]	[-]	[-]
-22.0	-4.0	-10.0	9-12	96.0	-4.0	-12.0	118.02	NaN	6	-23.8	-3.8	-11.8	2.49	0.86	2
-22.0	-4.0	-10.0	10-15	-11.6	2.4	1.5	16.74	NaN	6	-18.3	0.3	-9.3	5.72	NEL	4
-22.0	-4.0	-2.0	10-12	2.2	-1.1	-8.3	25.23	0.85	6	-17.3	-1.3	-1.8	5.49	NEL	4
-22.0	-4.0	-2.0	10-16	-96.0	-12.0	12.0	75.74	>10.00	6	-23.8	-3.3	-2.8	2.05	NEL	2
-22.0	-4.0	2.0	10-13	-78.0	-4.0	-12.0	57.75	6.11	6	-18.8	-1.3	-1.8	5.67	0.04	4
-22.0	-4.0	2.0	11-22	-16.1	0.0	0.8	7.23	0.12	4	-17.8	-0.8	1.3	5.40	0.09	4
-22.0	-4.0	2.0	12-53	-49.0	2.8	2.8	27.85	2.24	6	-23.8	-1.3	0.3	3.70	0.36	3
-22.0	-4.0	2.0	12-56	-19.8	-1.0	1.3	3.75	0.13	3	-22.3	-2.8	1.8	1.30	0.21	2
-22.0	-4.0	6.0	12-52	-21.8	-1.8	5.4	2.27	0.12	2	-23.8	-2.3	5.3	2.59	0.22	3
-22.0	-4.0	6.0	12-55	-20.5	-2.0	5.2	2.61	0.11	3	-21.8	-2.8	5.3	1.48	0.20	2
-22.0	-4.0	6.0	12-59	-21.6	-1.9	5.4	2.23	0.11	2	-23.8	-2.8	5.3	2.28	0.23	2
-22.0	-4.0	6.0	13-28	-17.8	-2.1	5.6	4.65	0.09	3	-18.8	-2.8	5.8	3.49	0.11	3
-18.0	-4.0	-10.0	9-16	-18.4	-3.8	-11.6	1.64	NaN	2	-18.3	-0.3	-9.3	3.83	NEL	3
-18.0	-4.0	-10.0	10-19	-6.7	2.9	4.5	19.68	NaN	6	-18.3	0.8	-10.8	4.82	NEL	3
-18.0	-4.0	-10.0	12-63	-9.9	-4.0	-3.0	10.67	1.73	6	-22.8	-3.8	-11.3	4.92	0.75	3
-18.0	-4.0	-6.0	12-61	96.0	-12.0	-12.0	114.44	NaN	6	-13.3	-9.8	11.8	19.25	NEL	6
-18.0	-4.0	2.0	12-60	-44.6	-5.4	8.6	27.45	3.39	6	-23.8	-1.3	-2.3	7.66	NEL	5
-18.0	-4.0	2.0	12-62	-27.0	4.0	1.6	12.02	0.40	6	-15.3	1.8	2.3	6.38	NEL	4
-18.0	-4.0	2.0	12-64	-21.3	0.2	0.5	5.51	0.33	4	-17.3	-2.3	0.8	2.28	0.06	2
-18.0	-4.0	6.0	13-29	-17.7	-2.2	5.7	1.88	0.10	2	-18.8	-2.8	5.8	1.48	0.18	2
-18.0	-4.0	6.0	13-30	-17.5	-2.3	5.7	1.84	0.10	2	-18.3	-2.8	5.8	1.30	0.12	2
-18.0	-4.0	6.0	14-85	-17.4	-2.2	5.6	1.92	0.09	2	-18.3	-2.8	5.8	1.30	0.17	2
-14.0	-4.0	-10.0	11-26	-88.9	-4.0	-12.0	74.92	9.52	6	-14.8	-2.3	-8.8	2.28	0.08	2
-14.0	-4.0	-6.0	11-25	6.3	-4.0	-12.0	21.17	NaN	6	-15.8	-1.3	-3.8	3.96	NEL	3
-14.0	-4.0	-2.0	11-24	-16.3	-1.8	-3.2	3.41	0.13	3	-16.3	-1.3	-3.3	3.77	0.18	3
-14.0	-4.0	-2.0	12-67	-16.7	-1.1	0.4	4.63	0.20	3	-10.3	-3.3	-3.8	4.21	NEL	3
-14.0	-4.0	2.0	14-87	-13.7	-1.3	1.9	2.72	0.21	3	-12.8	-3.8	2.3	1.30	0.15	2
-14.0	-4.0	2.0	14-88	-14.7	-2.4	2.6	1.85	0.12	2	-14.3	-3.3	2.8	1.09	0.12	2
-14.0	-4.0	6.0	13-32	-17.4	-0.3	10.0	6.42	0.36	4	-16.8	-0.3	11.8	7.40	NEL	4
-14.0	-4.0	6.0	14-86	-13.7	-1.9	5.8	2.08	0.12	2	-14.3	-2.3	5.8	1.79	0.20	2
-10.0	-4.0	-10.0	13-33	-12.0	-2.8	-12.0	3.07	0.77	3	-3.3	-3.8	-5.3	8.26	NEL	5
-10.0	-4.0	-6.0	13-34	-96.0	-4.0	-12.0	86.21	>10.00	6	-15.3	-3.3	-11.8	7.82	NEL	5
-10.0	-4.0	-6.0	13-35	-9.4	-2.9	-3.4	2.87	0.35	3	-6.8	-3.8	-0.8	6.18	NEL	4
-10.0	-4.0	-6.0	14-92	-14.4	3.2	-1.7	9.50	0.27	5	-20.8	-3.3	-3.3	11.12	NEL	6
-10.0	-4.0	-6.0	14-96	-10.5	0.8	-5.9	4.80	0.31	3	-13.8	-3.8	-5.3	3.83	0.57	3
-10.0	-4.0	-2.0	14-91	-9.0	-0.7	-2.1	3.42	0.16	3	-9.3	-1.3	-1.3	2.95	0.23	3
-10.0	-4.0	-2.0	14-99	-14.6	-0.9	1.7	6.66	0.17	4	-10.3	-3.8	-1.3	0.83	0.24	1
-10.0	-4.0	2.0	14-90	-11.0	-2.4	3.1	2.19	0.13	2	-11.3	-3.3	2.8	1.64	0.17	2
-10.0	-4.0	2.0	14-98	-8.9	-1.9	3.6	2.88	0.15	3	-9.8	-2.3	3.3	2.17	0.22	2
-10.0	-4.0	6.0	14-89	-9.9	-2.5	6.3	1.55	0.12	2	-10.3	-2.3	6.3	1.79	0.12	2
-10.0	-4.0	6.0	14-93	-9.9	-2.6	6.6	1.59	0.11	2	-10.3	-2.3	6.3	1.79	0.08	2
-10.0	-4.0	6.0	14-94	-10.1	-2.7	3.5	2.83	0.13	3	-10.3	-2.3	3.3	3.27	0.24	3
-10.0	-4.0	6.0	14-97	-9.7	-2.8	6.6	1.39	0.12	2	-9.8	-3.3	6.3	0.83	0.11	1
-6.0	-4.0	-10.0	11-28	-8.2	-4.0	-9.6	2.28	0.81	2	-13.3	-3.8	-11.8	7.46	NEL	4
-6.0	-4.0	-10.0	12-68	-7.6	-4.0	-9.0	1.93	0.63	2	1.3	3.8	-4.8	11.84	NEL	6
-6.0	-4.0	-10.0	12-69	-3.1	-4.0	-7.3	3.93	0.43	3	22.3	3.8	-9.3	29.30	NEL	6

Tab. B.27: SW I PLB b - "Front", part 1: Coordinates of the pencil-lead breaks and estimated source locations determined using Geiger's method and *FastWay*. Estimated source locations excluded during the verification process (see Section 7.3.4) are shown in gray.

PLB			Set	Geiger's method						*FastWay*					
x [in]	y [in]	z [in]	#	x [in]	y [in]	z [in]	d [in]	eei [-]	ac [-]	x [in]	y [in]	z [in]	d [in]	eei [-]	ac [-]
-6.0	-4.0	-10.0	13-37	-3.1	-4.0	-8.1	3.52	1.11	3	-4.3	-3.8	-10.3	1.79	NEL	2
-6.0	-4.0	-10.0	13-39	-4.9	-3.4	-8.4	2.06	0.58	2	-4.3	-3.8	-9.3	1.92	NEL	2
-6.0	-4.0	-6.0	14-109	-2.8	-1.7	-5.2	4.05	0.27	3	-3.3	-3.3	-4.8	3.11	NEL	3
-6.0	-4.0	-2.0	14-105	-8.4	-0.6	-2.7	4.18	0.33	3	-6.8	-3.8	-0.8	1.48	0.24	2
-6.0	-4.0	-2.0	14-108	-5.6	-3.1	0.1	2.30	0.14	2	-3.3	-3.8	0.8	3.90	0.11	3
-6.0	-4.0	2.0	14-101	-2.6	-3.0	4.9	4.57	0.16	3	-2.3	-3.8	4.8	4.66	0.22	3
-6.0	-4.0	2.0	14-104	-6.2	-2.2	3.0	2.09	0.13	2	-7.3	-2.3	2.8	2.28	0.16	2
-6.0	-4.0	2.0	14-107	-5.6	-1.8	3.0	2.44	0.13	2	-6.3	-2.3	3.3	2.17	0.22	2
-6.0	-4.0	6.0	14-100	-6.7	-2.2	6.9	2.16	0.12	2	-6.8	-2.8	6.8	1.64	0.12	2
-6.0	-4.0	6.0	14-103	-5.7	-3.1	7.1	1.43	0.09	2	-6.3	-2.8	7.3	1.79	0.14	2
-6.0	-4.0	6.0	14-106	-6.6	-2.5	6.8	1.80	0.15	2	-6.8	-2.3	7.3	2.28	0.14	2
-2.0	-4.0	-10.0	14-118	-80.3	-4.0	-12.0	78.34	6.55	6	-19.8	0.3	-11.8	18.34	NEL	6
-2.0	-4.0	-10.0	14-119	1.7	-1.6	-9.2	4.52	1.07	3	-5.8	-2.3	-11.3	4.32	NEL	3
-2.0	-4.0	-10.0	14-124	2.1	-0.8	-2.7	9.02	NaN	5	-14.8	3.8	-10.8	14.94	NEL	6
-2.0	-4.0	-6.0	14-113	65.5	4.0	-12.0	68.27	>10.00	6	-17.8	0.3	-11.8	17.30	NEL	6
-2.0	-4.0	-6.0	14-117	-10.1	1.8	-3.9	10.18	0.45	6	-11.3	3.8	-4.8	12.13	NEL	6
-2.0	-4.0	-6.0	14-123	-8.8	-1.0	-8.4	7.80	0.75	5	-7.3	1.3	-11.8	9.39	NEL	5
-2.0	-4.0	-2.0	14-112	-2.5	-1.5	-2.7	2.59	0.24	3	-2.8	-1.8	-2.8	2.49	0.19	2
-2.0	-4.0	-2.0	14-122	-3.0	3.9	-3.5	8.13	1.28	5	-11.3	3.8	-4.8	12.38	NEL	6
-2.0	-4.0	2.0	14-111	-1.9	-4.0	2.3	0.28	0.11	1	-2.3	-3.3	1.8	0.83	0.12	1
-2.0	-4.0	2.0	14-116	-1.9	-2.5	3.6	2.16	0.16	2	-2.3	-2.8	3.3	1.79	0.11	2
-2.0	-4.0	2.0	14-121	5.2	-4.0	5.9	8.20	0.65	5	-1.8	-3.8	1.8	0.43	0.10	1
-2.0	-4.0	6.0	14-110	-1.5	-2.8	6.0	1.26	0.12	2	-1.8	-3.3	5.8	0.83	0.07	1
-2.0	-4.0	6.0	14-115	-1.6	-2.9	6.1	1.18	0.10	2	-1.8	-3.8	5.8	0.43	0.05	1
-2.0	-4.0	6.0	14-120	-2.0	-3.2	6.2	0.85	0.14	1	-1.8	-3.3	5.8	0.83	0.11	1
2.0	-4.0	-10.0	14-129	2.6	-0.2	-6.5	5.20	0.58	4	14.3	0.3	-10.8	12.99	NEL	6
2.0	-4.0	-10.0	14-130	-96.0	4.0	-12.0	98.35	>10.00	6	-17.8	0.8	-11.8	20.39	NEL	6
2.0	-4.0	-10.0	14-136	-96.0	-4.0	-12.0	98.02	NaN	6	-10.8	-3.8	-6.3	13.29	NEL	6
2.0	-4.0	-10.0	14-141	-1.4	-4.0	-8.8	3.57	1.06	3	1.3	-3.8	-11.8	1.92	NEL	2
2.0	-4.0	-6.0	14-128	0.9	-0.5	-2.9	4.84	0.37	3	2.8	2.3	-5.8	6.30	NEL	4
2.0	-4.0	-6.0	14-135	-3.1	-2.7	-4.7	5.47	0.30	4	-6.8	1.3	-9.8	10.87	NEL	6
2.0	-4.0	-6.0	14-140	-1.4	-4.0	-3.5	4.21	0.32	3	7.3	-3.3	-11.3	7.46	NEL	4
2.0	-4.0	-2.0	14-134	-1.6	-3.2	-1.2	3.80	0.16	3	-23.8	-3.3	4.3	26.51	NEL	6
2.0	-4.0	2.0	14-126	1.2	-2.3	1.9	1.85	0.22	2	1.3	-3.3	1.8	1.09	0.16	2
2.0	-4.0	2.0	14-132	-3.9	-0.9	-12.0	15.53	NaN	6	-1.3	-3.8	-5.8	8.41	NEL	5
2.0	-4.0	2.0	14-133	0.9	-2.2	2.2	2.11	0.15	2	0.8	-3.3	2.3	1.48	0.14	2
2.0	-4.0	2.0	14-138	1.0	-2.6	2.2	1.71	0.16	2	1.3	-3.3	1.8	1.09	0.07	2
2.0	-4.0	6.0	14-125	1.7	-2.8	6.2	1.30	0.17	2	1.8	-3.3	5.8	0.83	0.06	1
2.0	-4.0	6.0	14-131	1.5	-3.0	6.4	1.15	0.16	2	1.8	-3.3	5.8	0.83	0.10	1
2.0	-4.0	6.0	14-137	1.3	-3.1	6.6	1.27	0.12	2	2.8	-2.8	4.8	1.92	NEL	2
6.0	-4.0	-10.0	14-147	3.8	-4.0	-8.0	2.92	0.36	3	-11.8	-3.3	-6.3	18.16	NEL	6
6.0	-4.0	-10.0	14-152	-7.6	4.0	0.9	19.19	NaN	6	-0.3	3.8	-3.3	12.03	NEL	6
6.0	-4.0	-10.0	14-153	5.3	-4.0	-10.5	0.89	0.83	1	7.8	-0.3	-11.3	4.32	NEL	3
6.0	-4.0	-10.0	14-157	5.1	2.2	-8.3	6.51	0.42	4	1.8	3.8	-8.3	9.01	NEL	5
6.0	-4.0	-10.0	14-158	4.8	0.7	-8.9	4.94	1.01	3	-0.8	3.8	-11.8	10.43	NEL	6
6.0	-4.0	-6.0	14-145	80.0	4.0	-12.0	74.63	>10.00	6	3.3	3.8	-5.3	8.26	0.36	5
6.0	-4.0	-6.0	14-146	4.4	-1.3	-4.4	3.51	0.49	3	1.8	2.8	-6.3	7.98	NEL	5
6.0	-4.0	-2.0	14-151	3.8	-1.4	-0.3	3.79	0.11	3	3.3	-1.8	-1.3	3.63	0.11	3

Tab. B.28: SW I PLB b - "Front", part 2: Coordinates of the pencil-lead breaks and estimated source locations determined using Geiger's method and *FastWay*. Estimated source locations excluded during the verification process (see Section 7.3.4) are shown in gray.

PLB			Set	Geiger's method						*FastWay*					
x [in]	y [in]	z [in]	#	x [in]	y [in]	z [in]	d [in]	eei [-]	ac [-]	x [in]	y [in]	z [in]	d [in]	eei [-]	ac [-]
6.0	-4.0	-2.0	14-156	3.9	-1.5	0.2	3.94	0.10	3	3.8	-0.8	-0.8	4.15	0.24	3
6.0	-4.0	2.0	14-143	9.8	4.0	-4.0	10.68	0.72	6	6.8	1.3	0.3	5.58	NEL	4
6.0	-4.0	2.0	14-150	5.7	-1.6	1.5	2.43	0.23	2	5.8	-2.3	1.8	1.79	0.12	2
6.0	-4.0	2.0	14-155	3.9	-1.3	2.7	3.50	0.12	3	4.8	0.3	1.3	4.49	NEL	3
6.0	-4.0	6.0	14-142	5.9	-2.4	5.7	1.64	0.13	2	5.8	-2.8	5.8	1.30	0.06	2
6.0	-4.0	6.0	14-148	5.0	-2.6	6.3	1.78	0.10	2	5.8	-2.3	5.3	1.92	0.15	2
6.0	-4.0	6.0	14-154	5.0	-2.6	6.3	1.74	0.09	2	5.8	-2.3	5.3	1.92	0.14	2
10.0	-4.0	-10.0	11-30	96.0	4.0	-12.0	86.39	>10.00	6	20.3	-3.3	-11.8	10.43	NEL	6
10.0	-4.0	-10.0	12-72	96.0	-4.0	-12.0	86.02	>10.00	6	9.8	-2.8	-9.8	1.30	0.02	2
10.0	-4.0	-10.0	12-73	12.2	1.5	-7.2	6.52	0.19	4	10.3	-0.8	-11.8	3.70	0.10	3
10.0	-4.0	-10.0	13-41	12.0	2.7	-9.4	7.04	0.24	4	10.3	0.3	-11.8	4.60	0.27	3
10.0	-4.0	-6.0	13-42	11.8	1.1	-8.7	6.05	0.17	4	11.3	-1.3	-6.3	3.03	0.22	3
10.0	-4.0	-6.0	14-167	7.6	2.7	-7.9	7.37	0.15	4	7.8	0.3	-6.3	4.82	0.06	3
10.0	-4.0	-2.0	14-161	8.5	-1.9	-2.9	2.73	0.28	3	8.8	-0.3	-4.8	4.82	NEL	3
10.0	-4.0	-2.0	14-164	10.5	2.0	-4.5	6.51	0.14	4	10.3	0.3	-3.8	4.60	0.22	3
10.0	-4.0	2.0	13-43	14.1	-0.2	3.6	5.81	0.30	4	10.3	-2.3	3.3	2.17	0.08	2
10.0	-4.0	2.0	14-160	10.7	0.9	1.1	5.08	0.11	4	11.3	-3.8	4.8	3.03	NEL	3
10.0	-4.0	2.0	14-163	10.8	0.7	1.1	4.81	0.14	3	11.3	-1.8	0.8	2.86	0.12	3
10.0	-4.0	2.0	14-166	11.0	0.4	1.0	4.60	0.15	3	11.3	-1.8	0.8	2.86	0.07	3
10.0	-4.0	6.0	14-159	12.9	-2.1	6.0	3.49	0.09	3	12.3	-1.8	6.8	3.27	0.11	3
10.0	-4.0	6.0	14-162	11.4	-2.2	5.7	2.33	0.10	2	11.3	-2.3	5.8	2.17	0.19	2
10.0	-4.0	6.0	14-165	11.6	-1.2	6.5	3.27	0.11	3	11.3	-1.3	6.8	3.11	0.12	3
14.0	-4.0	-10.0	10-20	16.2	-4.0	-12.0	3.01	0.44	3	11.8	-3.8	-11.8	2.86	0.24	3
14.0	-4.0	-10.0	10-21	14.1	-1.7	-5.7	4.92	NaN	3	13.8	-1.8	-5.8	4.82	0.06	3
14.0	-4.0	-10.0	10-24	14.1	-1.7	-6.4	4.28	NaN	3	13.8	-1.8	-6.3	4.38	0.05	3
14.0	-4.0	-6.0	10-23	-24.0	-4.0	-12.0	38.43	8.14	6	18.8	-3.8	-9.8	6.06	NEL	4
14.0	-4.0	-2.0	10-22	-5.8	-4.0	-12.0	22.21	5.13	6	10.8	-2.3	-8.3	7.26	NEL	4
14.0	-4.0	-2.0	11-32	2.7	0.7	-12.0	15.79	NaN	6	11.3	-1.3	-6.3	5.76	NEL	4
14.0	-4.0	-2.0	11-33	18.5	-2.7	-1.2	4.76	0.25	3	11.3	-1.8	-7.3	6.34	NEL	4
14.0	-4.0	2.0	13-45	15.2	-1.9	2.0	2.39	0.13	2	12.8	-2.8	1.8	1.79	0.09	2
14.0	-4.0	2.0	13-47	17.6	-1.9	3.8	4.57	0.17	3	12.8	-1.8	1.3	2.68	0.05	3
14.0	-4.0	2.0	13-49	14.3	-1.0	0.6	3.33	0.14	3	10.3	-0.3	-1.3	6.22	NEL	4
14.0	-4.0	6.0	13-44	14.3	-2.4	5.9	1.64	0.09	2	13.8	-2.3	6.3	1.79	0.11	2
14.0	-4.0	6.0	13-46	16.1	-1.5	7.6	3.70	0.17	3	13.8	-2.3	6.3	1.79	0.07	2
14.0	-4.0	6.0	13-48	14.2	-2.2	6.0	1.79	0.09	2	13.8	-2.3	6.3	1.79	0.09	2
14.0	-4.0	6.0	13-50	17.8	-2.3	6.0	4.21	0.10	3	17.8	-2.3	6.3	4.15	0.13	3
18.0	-4.0	-10.0	9-20	17.1	-1.7	-8.5	2.95	0.64	3	16.8	0.8	-11.3	5.07	NEL	4
18.0	-4.0	-6.0	10-27	-13.1	-4.0	-12.0	31.63	9.84	6	15.3	0.3	-9.3	6.02	NEL	4
18.0	-4.0	-6.0	10-28	7.9	-2.9	2.4	13.14	NaN	6	20.3	-3.8	-1.8	4.82	NEL	3
18.0	-4.0	-6.0	10-31	7.6	-4.0	5.2	15.25	NaN	6	13.3	-3.8	-11.8	7.46	NEL	4
18.0	-4.0	-2.0	10-26	23.4	-2.7	-1.1	5.58	0.45	4	11.8	-0.3	-11.8	12.17	NEL	6
18.0	-4.0	-2.0	10-30	86.7	-0.8	2.1	68.94	4.26	6	22.8	-3.8	-2.3	4.76	NEL	3
18.0	-4.0	2.0	12-74	17.4	-1.9	1.4	2.25	0.11	2	17.3	-2.8	1.8	1.48	0.20	2
18.0	-4.0	2.0	12-76	17.5	-2.2	1.3	2.02	0.12	2	17.3	-3.3	1.8	1.09	0.23	2
18.0	-4.0	2.0	12-77	17.2	-1.8	1.5	2.36	0.11	2	17.3	-2.8	1.8	1.48	0.22	2
18.0	-4.0	6.0	12-75	22.3	-1.4	7.8	5.38	0.31	4	17.8	-2.8	5.8	1.30	0.07	2
18.0	-4.0	6.0	13-51	17.7	-2.2	6.0	1.81	0.09	2	17.3	-2.3	6.3	1.92	0.14	2
22.0	-4.0	-10.0	8-7	96.0	4.0	-12.0	74.46	NaN	6	23.8	3.8	-11.8	8.14	NEL	5

Tab. B.29: SW I PLB b - "Front", part 3: Coordinates of the pencil-lead breaks and estimated source locations determined using Geiger's method and *FastWay*. Estimated source locations excluded during the verification process (see Section 7.3.4) are shown in gray.

PLB			Set	Geiger's method						*FastWay*					
x [in]	y [in]	z [in]	#	x [in]	y [in]	z [in]	d [in]	eei [-]	ac [-]	x [in]	y [in]	z [in]	d [in]	eei [-]	ac [-]
22.0	-4.0	-10.0	9-23	27.8	-0.2	-12.0	7.20	3.19	4	23.8	-0.3	-11.3	4.32	NEL	3
22.0	-4.0	-10.0	10-35	96.0	12.0	-12.0	75.74	NaN	6	20.3	0.8	-11.8	5.36	NEL	4
22.0	-4.0	-10.0	10-38	17.2	-1.5	0.4	11.72	NaN	6	23.8	-0.3	-11.3	4.32	NEL	3
22.0	-4.0	-10.0	10-50	29.5	-0.5	-2.2	11.40	1.84	6	23.8	-0.3	-10.8	4.21	NEL	3
22.0	-4.0	-6.0	10-45	22.9	-0.8	-11.9	6.72	5.15	4	23.8	-0.8	-10.3	5.63	NEL	4
22.0	-4.0	-6.0	10-49	92.1	-1.5	12.0	72.40	6.26	6	20.8	-2.3	-2.3	4.32	NEL	3
22.0	-4.0	-2.0	10-34	18.9	-0.8	-2.0	4.46	0.12	3	18.8	-1.3	-1.3	4.32	0.10	3
22.0	-4.0	-2.0	10-40	20.0	-0.6	-2.0	3.90	0.23	3	23.8	-3.8	-2.8	1.92	0.21	2
22.0	-4.0	2.0	9-24	96.0	4.0	-12.0	75.74	NaN	6	22.3	-0.8	-7.8	10.28	NEL	6
22.0	-4.0	2.0	10-36	20.9	-1.7	1.4	2.60	0.12	3	21.3	-2.3	1.8	1.92	0.20	2
22.0	-4.0	2.0	10-39	1.0	-0.5	2.9	21.33	NaN	6	14.8	3.8	-3.8	12.07	NEL	6
22.0	-4.0	2.0	10-48	20.7	-1.9	1.7	2.51	0.12	3	20.8	-2.3	2.3	2.17	0.21	2
22.0	-4.0	6.0	9-22	25.7	-2.0	-2.6	9.57	NaN	5	23.8	-0.8	-10.8	17.15	NEL	6
22.0	-4.0	6.0	10-41	22.0	-2.0	6.1	2.01	0.10	2	21.8	-2.3	5.8	1.79	0.09	2
22.0	-4.0	6.0	10-43	19.6	-1.7	2.3	4.97	NaN	3	19.8	-2.3	2.3	4.71	0.07	3
22.0	-4.0	6.0	10-46	50.1	2.3	12.0	29.41	1.54	6	23.8	-0.8	8.3	4.32	NEL	3
22.0	-4.0	6.0	11-37	22.4	-1.9	6.5	2.17	0.10	2	22.3	-2.3	6.3	1.79	0.11	2
22.0	-4.0	6.0	11-38	22.4	-1.9	6.5	2.19	0.10	2	22.3	-2.3	6.3	1.79	0.10	2
22.0	-4.0	6.0	12-78	22.0	-2.0	6.5	2.05	0.10	2	21.8	-2.3	6.3	1.79	0.13	2

Tab. B.30: SW I PLB b - "Front", part 4: Coordinates of the pencil-lead breaks and estimated source locations determined using Geiger's method and *FastWay*. Estimated source locations excluded during the verification process (see Section 7.3.4) are shown in gray.

B.3.4 Back

PLB			Set	Geiger's method						*FastWay*					
x [in]	y [in]	z [in]	#	x [in]	y [in]	z [in]	d [in]	eei [-]	ac [-]	x [in]	y [in]	z [in]	d [in]	eei [-]	ac [-]
-22.0	4.0	-10.0	8-10	-56.9	3.5	3.0	37.18	NaN	6	-20.3	0.3	-11.3	4.32	NEL	3
-22.0	4.0	-6.0	10-67	-21.4	3.5	-4.6	1.63	NaN	2	-23.3	3.8	-4.8	1.79	0.10	2
-22.0	4.0	-6.0	10-69	-17.9	2.3	-5.0	4.56	NaN	3	-20.3	2.8	-4.8	2.49	NEL	2
-22.0	4.0	-2.0	11-63	-16.5	2.3	-2.7	5.78	NaN	4	-17.8	2.8	-2.3	4.44	NEL	3
-22.0	4.0	-2.0	11-65	96.0	-4.0	-12.0	118.69	NaN	6	-23.8	2.3	1.3	4.09	0.98	3
-22.0	4.0	-2.0	11-67	-96.0	-4.0	-12.0	75.10	>10.00	6	0.8	-3.8	-6.3	24.41	NEL	6
-22.0	4.0	2.0	11-62	-23.8	2.1	0.8	2.83	0.20	3	-20.3	2.8	1.3	2.28	0.18	2
-22.0	4.0	2.0	11-66	-17.8	2.8	1.3	4.39	0.09	3	-20.3	2.8	1.8	2.17	0.20	2
-22.0	4.0	2.0	12-117	-23.7	2.1	1.0	2.79	0.20	3	-23.8	0.8	0.3	4.09	0.32	3
-22.0	4.0	6.0	11-61	-21.1	2.7	5.9	1.58	0.11	2	-21.8	2.8	5.8	1.30	0.15	2
-22.0	4.0	6.0	11-64	-21.6	2.6	5.7	1.45	0.09	2	-21.8	2.3	5.8	1.79	0.21	2
-22.0	4.0	6.0	12-118	-21.5	2.5	6.0	1.62	0.10	2	-21.8	2.3	5.8	1.79	0.13	2
-18.0	4.0	-10.0	10-71	-29.9	-4.0	-12.0	14.47	4.06	6	-20.8	-0.8	-11.8	5.76	NEL	4
-18.0	4.0	-6.0	9-26	-96.0	-4.0	-12.0	78.64	>10.00	6	-23.3	-3.8	2.3	12.48	NEL	6
-18.0	4.0	-6.0	9-29	14.1	3.3	-12.0	32.67	NaN	6	-20.3	0.3	-11.8	7.22	0.26	4
-18.0	4.0	-2.0	11-68	-9.0	-4.0	-12.0	15.65	1.40	6	-23.8	3.3	-4.3	6.22	0.43	4
-18.0	4.0	-2.0	11-70	-24.0	-0.9	-7.5	9.51	0.75	5	-8.8	0.8	-9.8	12.50	NEL	6
-18.0	4.0	2.0	12-120	-19.9	2.2	1.1	2.77	0.17	3	-17.3	2.8	1.3	1.64	0.12	2
-18.0	4.0	2.0	12-122	-21.1	2.0	1.6	3.68	0.17	3	-23.8	3.3	1.3	5.85	0.15	4
-18.0	4.0	2.0	12-123	-15.3	2.8	1.3	2.99	0.19	3	-17.3	2.3	1.8	1.92	0.14	2
-18.0	4.0	6.0	12-119	-18.5	2.5	6.2	1.63	0.11	2	-17.8	2.8	5.8	1.30	0.10	2
-18.0	4.0	6.0	12-121	-18.1	2.8	6.3	1.23	0.10	2	-18.3	2.3	6.3	1.79	0.19	2
-14.0	4.0	-10.0	11-71	-7.4	-4.0	-12.0	10.56	5.09	6	-16.3	-1.8	-11.8	6.42	NEL	4
-14.0	4.0	-10.0	11-72	-18.1	1.7	-5.9	6.27	0.48	4	-15.3	-1.8	-11.8	6.14	0.35	4
-14.0	4.0	-10.0	11-74	-96.0	-4.0	-12.0	82.41	>10.00	6	-19.3	-2.8	-6.8	9.15	NEL	5
-14.0	4.0	-6.0	12-124	-17.3	0.8	-3.6	5.16	0.29	4	-13.3	-2.3	-11.3	8.20	NEL	5
-14.0	4.0	-6.0	12-126	-18.1	1.3	-5.2	4.99	0.46	3	-15.3	-1.8	-11.8	8.23	NEL	5
-14.0	4.0	-2.0	12-125	-14.0	1.8	-2.2	2.16	0.21	2	-5.3	-3.8	-11.8	15.22	NEL	6
-14.0	4.0	-2.0	12-127	-10.3	-0.6	-5.6	6.92	0.45	4	-6.3	-3.8	-11.3	14.34	NEL	6
-14.0	4.0	-2.0	13-81	96.0	-4.0	-12.0	110.74	NaN	6	-5.3	-3.8	-11.8	15.22	NEL	6
-14.0	4.0	2.0	14-225	-18.2	2.2	3.0	4.67	0.22	3	-19.8	3.3	2.8	5.85	NEL	4
-14.0	4.0	2.0	14-227	-14.9	2.0	2.8	2.33	0.17	2	-12.3	1.8	2.3	2.86	0.09	3
-14.0	4.0	2.0	14-229	-13.8	1.7	2.9	2.47	0.12	2	-13.3	1.3	2.8	2.95	0.10	3
-14.0	4.0	6.0	13-80	-96.0	-12.0	-12.0	85.46	NaN	6	-13.8	4.8	8.3	2.38	NEL	2
-14.0	4.0	6.0	14-224	-14.2	2.5	6.9	1.75	0.10	2	-14.3	2.3	6.8	1.92	0.12	2
-14.0	4.0	6.0	14-226	-14.0	2.1	4.7	2.37	0.10	2	-13.8	1.8	4.8	2.59	0.09	3
-14.0	4.0	6.0	14-228	-14.2	2.2	6.7	1.93	0.09	2	-14.3	1.8	6.8	2.38	0.18	2
-10.0	4.0	-10.0	13-83	-96.0	-4.0	-12.0	86.39	>10.00	6	-23.8	-1.8	-9.8	14.91	NEL	6
-10.0	4.0	-6.0	13-82	-10.1	0.5	-5.7	3.47	0.25	3	-9.8	2.3	-3.8	2.86	0.31	3
-10.0	4.0	-6.0	13-84	-10.1	-4.0	-4.5	8.13	0.18	5	-10.3	-3.3	-4.3	7.46	0.51	4
-10.0	4.0	-6.0	13-85	-3.3	4.0	-3.5	7.19	0.17	4	-4.3	3.8	-3.8	6.18	0.41	4
-10.0	4.0	-6.0	13-87	-12.8	-1.0	-5.5	5.72	0.51	4	-9.3	1.3	-3.3	3.96	0.05	3
-10.0	4.0	-2.0	14-232	-12.8	-3.4	-1.1	7.98	0.32	5	-23.8	-3.3	-5.8	15.99	NEL	6
-10.0	4.0	-2.0	14-235	-10.6	-2.5	-0.8	6.63	0.15	4	-10.8	-0.3	-0.8	4.49	NEL	3
-10.0	4.0	-2.0	14-238	-8.6	-1.3	-1.2	5.55	0.21	4	-23.8	1.8	6.8	16.45	NEL	6
-10.0	4.0	2.0	14-234	-11.7	-0.0	4.1	4.81	0.20	3	-13.3	-0.8	4.8	6.38	0.17	4
-10.0	4.0	2.0	14-237	-12.5	1.1	4.0	4.36	0.14	3	-12.3	1.3	3.8	3.96	0.25	3

Tab. B.31: SW I PLB b - "Back", part 1: Coordinates of the pencil-lead breaks and estimated source locations determined using Geiger's method and *FastWay*. Estimated source locations excluded during the verification process (see Section 7.3.4) are shown in gray.

PLB			Set	Geiger's method						*FastWay*					
x [in]	y [in]	z [in]	#	x [in]	y [in]	z [in]	d [in]	eei [-]	ac [-]	x [in]	y [in]	z [in]	d [in]	eei [-]	ac [-]
-10.0	4.0	6.0	13-86	15.9	12.0	12.0	27.73	NaN	6	-4.8	8.3	11.8	8.87	NEL	5
-10.0	4.0	6.0	14-230	-9.8	2.0	7.1	2.26	0.10	2	-9.8	1.8	7.3	2.59	0.14	3
-10.0	4.0	6.0	14-231	-12.2	0.6	4.9	4.24	0.14	3	-13.3	1.3	4.3	4.60	NEL	3
-10.0	4.0	6.0	14-233	-9.4	2.0	6.5	2.18	0.10	2	-9.3	2.3	6.3	1.92	0.19	2
-10.0	4.0	6.0	14-236	-11.5	2.8	7.5	2.47	0.12	2	-11.8	2.8	7.8	2.77	0.14	3
-6.0	4.0	-10.0	12-129	96.0	12.0	-12.0	102.33	NaN	6	9.3	3.3	-5.8	15.85	NEL	6
-6.0	4.0	-10.0	12-131	3.3	-3.4	2.6	17.34	NaN	6	-3.8	-3.8	-6.8	8.70	NEL	5
-6.0	4.0	-6.0	14-243	-6.7	-4.0	-3.3	8.46	0.27	5	-5.3	-3.8	-3.8	8.10	NEL	5
-6.0	4.0	-6.0	14-248	96.0	-4.0	-12.0	102.49	>10.00	6	-12.8	-2.8	-9.3	10.08	NEL	6
-6.0	4.0	-6.0	14-252	-10.1	-0.2	-3.4	6.43	0.52	4	-18.8	-2.3	-7.3	14.25	NEL	6
-6.0	4.0	-2.0	14-242	-5.2	-3.5	0.5	7.93	0.14	5	-3.8	-2.8	0.3	7.46	0.07	4
-6.0	4.0	-2.0	14-247	-7.3	-0.1	-1.8	4.34	0.24	3	-13.3	2.8	-5.8	8.26	NEL	5
-6.0	4.0	-2.0	14-251	-6.3	0.6	2.6	5.74	0.11	4	-7.3	0.8	2.3	5.49	0.09	4
-6.0	4.0	-2.0	14-253	-5.0	-4.0	-2.0	8.06	0.19	5	-5.3	-3.8	-3.3	7.89	0.29	5
-6.0	4.0	2.0	14-241	-5.8	-0.1	3.2	4.31	0.11	3	-7.3	0.3	2.3	3.96	0.09	3
-6.0	4.0	2.0	14-246	-0.6	-3.7	6.6	10.46	0.21	6	-7.3	0.3	2.8	4.02	0.06	3
-6.0	4.0	2.0	14-250	-6.7	-0.4	2.8	4.51	0.11	3	-7.3	0.3	2.8	4.02	0.07	3
-6.0	4.0	6.0	14-239	-6.4	1.8	6.1	2.19	0.10	2	-6.8	2.3	5.8	1.92	0.15	2
-6.0	4.0	6.0	14-240	-96.0	12.0	12.0	90.55	NaN	6	-4.8	5.8	8.3	3.11	0.17	3
-6.0	4.0	6.0	14-244	-6.9	1.9	5.7	2.33	0.14	2	-6.8	1.8	6.3	2.38	NEL	2
-6.0	4.0	6.0	14-249	-7.5	2.0	5.4	2.52	0.11	3	-7.8	2.3	5.3	2.59	0.09	3
-2.0	4.0	-10.0	14-263	-3.6	0.3	-6.1	5.62	1.14	4	-21.8	-3.8	-9.8	21.22	NEL	6
-2.0	4.0	-6.0	14-257	-8.8	0.8	-6.6	7.54	0.37	5	-13.8	3.8	-7.8	11.88	NEL	6
-2.0	4.0	-6.0	14-262	-4.6	-3.0	-5.5	7.48	0.48	4	-0.3	-0.3	-8.3	5.12	NEL	4
-2.0	4.0	-6.0	14-267	-3.4	-2.3	-6.0	6.44	0.29	4	-16.3	3.8	-10.8	15.02	NEL	6
-2.0	4.0	-2.0	14-256	2.4	-0.7	-2.8	6.50	0.36	4	4.8	3.8	-5.3	7.50	NEL	4
-2.0	4.0	-2.0	14-261	-5.0	-4.0	6.2	11.81	0.89	6	-14.8	-3.3	-1.8	14.67	NEL	6
-2.0	4.0	-2.0	14-266	-4.6	3.3	-0.6	3.02	0.31	3	-3.3	1.8	-1.8	2.59	NEL	3
-2.0	4.0	2.0	14-255	-0.1	0.8	2.3	3.72	0.35	3	-1.3	2.3	1.8	1.92	0.05	2
-2.0	4.0	2.0	14-260	-4.0	4.0	3.2	2.38	0.24	2	-10.8	3.8	7.3	10.21	NEL	6
-2.0	4.0	2.0	14-265	-9.8	1.7	6.1	9.11	2.34	5	-0.3	2.8	1.3	2.28	NEL	2
-2.0	4.0	6.0	14-254	-2.1	2.9	6.4	1.20	0.10	2	-2.8	3.3	6.3	1.09	0.21	2
-2.0	4.0	6.0	14-259	-1.4	2.5	6.2	1.64	0.10	2	-1.8	1.8	5.8	2.28	0.10	2
-2.0	4.0	6.0	14-264	-2.3	3.5	6.3	0.63	0.10	1	-2.8	3.8	6.8	1.09	0.36	2
2.0	4.0	-10.0	12-132	-0.3	-4.0	-1.3	12.04	0.59	6	-5.8	2.8	-10.3	7.85	NEL	5
2.0	4.0	-10.0	13-89	-1.5	-0.7	-6.5	6.87	0.43	4	6.8	-2.3	-9.8	7.85	NEL	5
2.0	4.0	-6.0	13-90	0.0	-3.5	-7.3	7.82	0.41	5	-0.3	-2.3	-7.3	6.76	NEL	4
2.0	4.0	-6.0	14-276	2.0	-1.8	-3.5	6.26	0.26	4	0.8	-0.3	-3.8	4.97	0.05	3
2.0	4.0	-6.0	14-282	1.5	-3.0	-6.1	7.04	0.44	4	-0.3	-1.3	-6.8	5.76	NEL	4
2.0	4.0	-2.0	14-271	2.0	0.6	-1.0	3.52	0.50	3	1.3	1.8	-1.3	2.49	0.05	2
2.0	4.0	-2.0	14-272	-2.6	-1.0	-2.6	6.81	0.23	4	-2.8	1.8	-3.8	5.54	0.20	4
2.0	4.0	-2.0	14-275	1.0	2.5	-1.2	2.00	0.10	2	0.8	1.3	-0.8	3.27	0.07	3
2.0	4.0	-2.0	14-281	1.1	-0.6	-0.5	4.91	0.54	3	3.3	3.8	-3.3	1.79	NEL	2
2.0	4.0	2.0	14-270	1.7	1.9	2.9	2.32	0.22	2	1.8	1.8	2.8	2.38	0.05	2
2.0	4.0	2.0	14-274	1.7	2.1	2.3	1.95	0.13	2	1.8	1.8	2.3	2.28	0.05	2
2.0	4.0	2.0	14-279	2.1	2.9	2.3	1.11	0.14	2	1.8	2.3	2.3	1.79	0.07	2
2.0	4.0	6.0	14-269	1.9	2.4	6.0	1.64	0.12	2	1.8	2.3	5.8	1.79	0.16	2
2.0	4.0	6.0	14-273	1.4	1.7	6.5	2.44	0.09	2	0.8	1.3	6.3	3.03	0.08	3
2.0	4.0	6.0	14-277	1.7	2.1	6.3	1.89	0.09	2	1.8	1.8	5.8	2.28	0.10	2

Tab. B.32: SW I PLB b - "Back", part 2: Coordinates of the pencil-lead breaks and estimated source locations determined using Geiger's method and *FastWay*. Estimated source locations excluded during the verification process (see Section 7.3.4) are shown in gray.

PLB			Set	Geiger's method						*FastWay*					
x	y	z	#	x	y	z	d	eei	ac	x	y	z	d	eei	ac
6.0	4.0	-10.0	13-93	1.2	2.7	-9.0	5.08	0.57	4	-14.3	1.3	-3.3	21.52	NEL	6
6.0	4.0	-10.0	13-94	4.3	-4.0	-9.6	8.20	0.52	5	4.8	-3.8	-9.8	7.85	0.84	5
[in]	[in]	[in]		[in]	[in]	[in]	[in]	[-]	[-]	[in]	[in]	[in]	[in]	[-]	[-]
6.0	4.0	-10.0	13-95	3.8	-3.0	-9.7	7.40	0.47	4	-13.8	1.3	-4.3	20.75	NEL	6
6.0	4.0	-6.0	13-92	-1.4	4.0	-12.0	9.52	2.10	5	3.8	3.8	-5.3	2.38	0.21	2
6.0	4.0	-2.0	14-291	1.7	-2.4	0.6	8.14	0.29	5	-0.8	3.8	-2.3	6.76	0.42	4
6.0	4.0	-2.0	14-293	2.5	-4.0	-1.9	8.75	0.18	5	2.3	-3.8	-2.3	8.61	0.66	5
6.0	4.0	-2.0	14-297	3.7	-3.6	0.5	8.28	0.22	5	4.3	-0.8	-0.3	5.36	0.05	4
6.0	4.0	-2.0	14-299	3.6	-0.8	-2.6	5.43	0.19	4	3.3	-1.8	-2.8	6.42	0.20	4
6.0	4.0	2.0	14-285	5.5	2.6	2.2	1.49	0.09	2	4.8	1.3	2.3	3.03	0.10	3
6.0	4.0	2.0	14-286	3.5	1.3	-1.2	4.87	0.12	3	2.8	-0.8	-0.3	6.18	0.12	4
6.0	4.0	2.0	14-289	4.1	-0.4	2.4	4.79	0.13	3	-2.3	-3.3	7.8	12.40	NEL	6
6.0	4.0	2.0	14-296	4.4	0.8	2.5	3.63	0.15	3	4.8	1.8	1.8	2.59	0.17	3
6.0	4.0	6.0	14-283	4.6	1.1	7.2	3.40	0.13	3	4.3	0.8	6.8	3.77	0.19	3
6.0	4.0	6.0	14-284	5.5	5.2	9.1	3.41	0.12	3	5.3	5.3	8.3	2.68	0.17	3
6.0	4.0	6.0	14-287	5.5	2.4	7.0	1.96	0.13	2	5.3	2.3	6.3	1.92	0.14	2
6.0	4.0	6.0	14-288	35.5	12.0	12.0	31.12	5.83	6	11.8	5.8	11.8	8.32	NEL	5
6.0	4.0	6.0	14-294	4.8	1.8	6.8	2.68	0.09	3	5.8	2.8	5.3	1.48	0.09	2
10.0	4.0	-10.0	13-96	10.0	4.0	-12.0	2.00	0.73	2	9.8	0.8	-11.8	3.70	0.38	3
10.0	4.0	-10.0	13-98	10.4	-4.0	-3.6	10.25	0.48	6	9.8	-0.3	-11.3	4.44	0.59	3
10.0	4.0	-10.0	14-311	9.3	-4.0	-4.2	9.89	0.48	5	9.8	-0.3	-11.8	4.60	NEL	3
10.0	4.0	-6.0	12-136	13.0	-4.0	-12.0	10.45	0.78	6	9.8	3.8	-8.3	2.28	0.09	2
10.0	4.0	-6.0	14-303	8.9	-4.0	-0.4	9.84	0.49	5	8.3	-0.8	-7.3	5.21	NEL	4
10.0	4.0	-6.0	14-307	96.0	-4.0	-12.0	86.58	>10.00	6	15.8	-0.3	-3.3	7.66	0.04	5
10.0	4.0	-2.0	14-302	9.9	4.0	-4.1	2.06	0.11	2	9.8	3.8	-2.8	0.83	0.15	1
10.0	4.0	-2.0	14-306	9.8	3.1	-2.2	0.97	0.12	1	9.3	2.8	-2.3	1.48	0.07	2
10.0	4.0	-2.0	14-310	7.2	-3.0	-1.9	7.53	0.22	5	7.8	0.3	-4.3	4.92	NEL	3
10.0	4.0	2.0	14-301	9.6	1.0	1.0	3.22	0.17	3	9.3	2.8	1.8	1.48	0.05	2
10.0	4.0	2.0	14-305	9.5	1.4	-0.3	3.52	0.13	3	8.8	2.8	0.3	2.49	0.13	2
10.0	4.0	2.0	14-309	9.1	2.5	1.5	1.82	0.11	2	8.3	2.3	1.8	2.49	0.12	2
10.0	4.0	6.0	13-97	6.5	2.8	6.0	3.73	NaN	3	12.3	3.8	11.8	6.18	NEL	4
10.0	4.0	6.0	14-300	9.9	1.6	3.7	3.39	0.14	3	10.3	1.8	3.8	3.19	0.31	3
10.0	4.0	6.0	14-304	9.8	2.3	6.0	1.69	0.10	2	9.3	1.8	5.8	2.38	0.04	2
10.0	4.0	6.0	14-308	9.4	1.7	6.0	2.39	0.13	2	9.3	1.8	6.3	2.38	0.15	2
14.0	4.0	-10.0	10-77	-96.0	-4.0	-12.0	110.31	>10.00	6	11.8	-3.8	-11.8	8.26	NEL	5
14.0	4.0	-6.0	10-76	9.0	4.0	-12.0	7.78	NaN	5	16.8	3.8	-9.8	4.66	NEL	3
14.0	4.0	-6.0	12-140	21.7	-1.2	-6.4	9.34	0.16	5	20.8	-1.3	-4.3	8.73	0.16	5
14.0	4.0	-2.0	10-78	16.5	0.7	-1.0	4.30	0.18	3	14.3	1.8	-0.8	2.59	0.03	3
14.0	4.0	-2.0	10-80	14.6	3.0	-1.9	1.21	0.16	2	14.3	1.8	-0.8	2.59	0.04	3
14.0	4.0	-2.0	11-77	17.5	-0.2	-0.9	5.59	0.25	4	14.3	1.8	-0.8	2.59	0.03	3
14.0	4.0	2.0	12-138	15.9	0.0	2.0	4.41	0.19	3	14.3	1.8	2.3	2.28	0.02	2
14.0	4.0	2.0	12-139	15.1	1.9	2.1	2.38	0.13	2	14.3	2.3	2.3	1.79	0.08	2
14.0	4.0	2.0	12-142	15.8	1.1	2.3	3.47	0.14	3	14.8	2.3	2.8	2.05	0.11	2
14.0	4.0	6.0	12-137	19.7	6.1	10.3	7.41	1.21	4	14.3	4.8	8.8	2.86	0.06	3
14.0	4.0	6.0	12-141	14.1	2.3	5.8	1.70	0.11	2	13.8	2.3	5.8	1.79	0.19	2
14.0	4.0	6.0	13-99	14.3	1.9	6.2	2.11	0.11	2	12.3	2.8	4.8	2.49	NEL	2
14.0	4.0	6.0	13-100	14.2	2.3	5.8	1.75	0.10	2	13.8	2.3	5.8	1.79	0.20	2
18.0	4.0	-10.0	9-33	26.0	-4.0	-8.2	11.44	1.35	6	23.8	-2.3	-7.3	8.93	NEL	5
18.0	4.0	-10.0	9-34	-39.5	-4.0	-12.0	58.13	9.04	6	23.8	-0.8	-10.3	7.46	NEL	4

Tab. B.33: SW I PLB b - "Back", part 3: Coordinates of the pencil-lead breaks and estimated source locations determined using Geiger's method and *FastWay*. Estimated source locations excluded during the verification process (see Section 7.3.4) are shown in gray.

PLB			Set	Geiger's method						*FastWay*					
x	y	z	#	x	y	z	d	eei	ac	x	y	z	d	eei	ac
[in]	[in]	[in]		[in]	[in]	[in]	[in]	[-]	[-]	[in]	[in]	[in]	[in]	[-]	[-]
18.0	4.0	-6.0	9-32	21.1	-1.0	-5.1	6.00	0.45	4	18.3	1.3	-3.8	3.56	0.10	3
18.0	4.0	-6.0	9-36	13.3	-0.0	-0.3	8.46	NaN	5	23.8	-2.3	-7.8	8.67	NEL	5
18.0	4.0	-6.0	10-85	24.4	-1.3	-3.7	8.58	0.41	5	23.8	-0.3	-6.8	7.19	NEL	4
18.0	4.0	-2.0	9-35	28.2	-2.6	-1.2	12.17	1.27	6	21.3	-0.3	-3.8	5.63	NEL	4
18.0	4.0	-2.0	10-84	21.4	0.4	-2.2	4.95	0.59	3	18.8	1.8	-1.3	2.49	0.06	2
18.0	4.0	-2.0	10-87	21.5	0.4	-2.4	5.05	0.52	4	19.8	1.3	-1.3	3.34	NEL	3
18.0	4.0	2.0	10-82	20.4	1.1	-1.8	5.30	0.31	4	17.8	2.3	-1.3	3.70	0.07	3
18.0	4.0	2.0	11-82	19.4	1.4	1.5	3.01	0.17	3	17.8	2.8	2.3	1.30	0.06	2
18.0	4.0	2.0	11-84	18.2	2.8	2.2	1.24	0.11	2	17.8	2.8	2.3	1.30	0.09	2
18.0	4.0	2.0	11-87	27.2	4.0	5.2	9.73	0.48	5	18.3	2.3	2.3	1.79	0.07	2
18.0	4.0	6.0	12-143	18.2	2.7	6.2	1.36	0.10	2	18.3	2.8	6.3	1.30	0.16	2
18.0	4.0	6.0	12-144	18.0	2.6	5.9	1.38	0.09	2	17.8	2.8	5.8	1.30	0.14	2
18.0	4.0	6.0	12-145	18.3	2.5	6.4	1.57	0.09	2	18.3	2.8	6.3	1.30	0.17	2
22.0	4.0	-10.0	8-13	96.0	4.0	-12.0	74.03	NaN	6	23.8	0.3	-8.3	4.49	NEL	3
22.0	4.0	-10.0	9-38	13.6	1.0	0.0	13.47	NaN	6	23.8	-0.3	-8.3	4.92	NEL	3
22.0	4.0	-6.0	10-90	45.8	-4.0	-10.5	25.56	1.82	6	23.8	3.8	-8.3	2.86	NEL	3
22.0	4.0	-6.0	10-96	23.8	-2.0	-8.7	6.78	0.70	4	23.8	-0.3	-8.3	5.12	NEL	4
22.0	4.0	-2.0	9-37	20.3	-2.0	1.1	6.98	NaN	4	23.8	3.3	-7.3	5.58	NEL	4
22.0	4.0	-2.0	10-89	96.0	4.0	-12.0	74.67	>10.00	6	23.8	3.3	-2.8	2.05	0.06	2
22.0	4.0	-2.0	10-95	33.4	-2.8	-8.6	14.79	1.21	6	23.8	1.3	-5.3	4.60	NEL	3
22.0	4.0	2.0	10-88	65.3	4.0	-3.4	43.63	2.44	6	22.8	3.3	2.8	1.30	0.05	2
22.0	4.0	2.0	10-92	96.0	4.0	-12.0	75.31	>10.00	6	21.8	2.3	-1.3	3.70	0.04	3
22.0	4.0	2.0	10-94	96.0	4.0	-12.0	75.31	>10.00	6	23.8	3.3	-2.3	4.66	0.06	3
22.0	4.0	6.0	10-91	39.5	4.0	6.6	17.55	1.18	6	21.8	2.8	2.3	3.96	0.08	3
22.0	4.0	6.0	10-93	23.8	3.2	2.1	4.38	0.11	3	22.3	2.8	2.3	3.96	0.14	3
22.0	4.0	6.0	11-89	25.6	3.3	6.9	3.80	0.22	3	21.8	3.3	6.8	1.09	0.14	2
22.0	4.0	6.0	12-146	26.5	2.2	5.0	4.96	0.22	3	22.3	0.8	4.8	3.49	NEL	3
22.0	4.0	6.0	12-147	21.5	3.2	6.6	1.16	0.08	2	22.3	3.8	7.3	1.30	0.11	2

Tab. B.34: SW I PLB b - "Back", part 4: Coordinates of the pencil-lead breaks and estimated source locations determined using Geiger's method and *FastWay*. Estimated source locations excluded during the verification process (see Section 7.3.4) are shown in gray.

B.4 Pencil-lead breaks SW I b - Crack

B.4.1 Top

PLB			Set	Geiger's method						*FastWay*					
x [in]	y [in]	z [in]	#	x [in]	y [in]	z [in]	d [in]	eei [-]	ac [-]	x [in]	y [in]	z [in]	d [in]	eei [-]	ac [-]
-22.0	-10.0	12.0	12-8	-22.1	-9.3	12.0	0.73	0.40	1	-20.8	-11.8	11.8	2.17	0.67	2
-22.0	-10.0	12.0	12-9	-19.7	-9.8	12.0	2.27	0.21	2	-20.3	-6.8	8.3	5.26	NEL	4
-22.0	-10.0	12.0	12-20	-19.7	-4.0	3.9	10.31	0.44	6	-23.8	-8.3	8.8	4.09	0.18	3
-22.0	-10.0	12.0	12-36	-19.4	-9.9	10.5	2.96	0.11	3	-21.8	-8.3	8.3	4.15	0.17	3
-22.0	-10.0	12.0	12-37	-21.8	-11.5	12.0	1.56	0.20	2	-19.8	-9.8	11.8	2.28	0.18	2
-22.0	-6.0	12.0	12-5	-23.7	-6.0	9.5	3.07	0.16	3	-20.3	-5.8	8.3	4.15	0.09	3
-22.0	-6.0	12.0	12-16	-61.7	-12.0	12.0	40.17	2.47	6	-23.8	-7.3	11.8	2.17	0.52	2
-22.0	-6.0	12.0	12-29	-22.1	-6.0	11.4	0.60	0.12	1	-22.3	-5.8	10.3	1.79	0.23	2
-22.0	-2.0	12.0	12-1	-26.4	-2.4	11.3	4.48	0.21	3	-23.8	-2.8	11.8	1.92	NEL	2
-22.0	-2.0	12.0	12-12	-21.8	-2.0	10.5	1.52	0.09	2	-23.8	-2.3	9.8	2.86	0.16	3
-22.0	-2.0	12.0	12-24	-23.2	-1.3	10.5	2.08	0.17	2	-22.8	-2.3	10.3	1.92	0.27	2
-22.0	2.0	12.0	12-79	-21.2	1.8	10.3	1.89	0.09	2	-23.3	1.8	10.3	2.17	0.12	2
-22.0	2.0	12.0	12-94	-22.1	1.6	10.7	1.37	0.09	2	-23.8	1.3	10.8	2.28	0.12	2
-22.0	2.0	12.0	12-106	-21.3	1.8	10.4	1.78	0.09	2	-23.3	1.8	10.3	2.17	0.16	2
-22.0	6.0	12.0	11-59	-19.3	3.9	11.4	3.49	0.10	3	-19.3	3.8	10.8	3.77	0.16	3
-22.0	6.0	12.0	12-87	-21.4	4.3	11.4	1.87	0.23	2	-19.8	3.8	11.8	3.19	0.18	3
-22.0	6.0	12.0	12-101	-22.6	5.1	11.7	1.12	0.18	2	-20.8	4.3	10.8	2.49	0.03	2
-22.0	6.0	12.0	13-54	-19.5	5.8	11.6	2.59	0.20	3	-20.8	5.8	11.8	1.30	NEL	2
-22.0	6.0	12.0	13-63	-6.0	1.0	12.0	16.81	0.61	6	-7.8	3.3	-11.3	27.41	NEL	6
-22.0	10.0	12.0	11-43	-20.3	8.1	11.8	2.51	3.68	3	-20.3	6.3	11.8	4.15	0.74	3
-22.0	10.0	12.0	13-76	-23.8	8.5	12.0	2.31	0.37	2	-23.8	8.3	11.8	2.49	0.36	2
-18.0	-10.0	12.0	12-21	-20.8	-11.0	12.0	3.01	0.46	3	-16.3	-11.8	10.8	2.77	0.16	3
-18.0	-10.0	12.0	14-59	-13.7	-4.0	7.5	8.69	0.29	5	-18.3	-5.8	11.8	4.26	0.15	3
-18.0	-6.0	12.0	11-7	-25.2	3.7	11.8	12.09	0.11	6	-17.8	1.8	11.3	7.79	NEL	5
-18.0	-6.0	12.0	12-17	-18.1	-4.0	7.5	4.94	0.28	3	-17.3	-6.3	10.8	1.48	0.15	2
-18.0	-6.0	12.0	12-31	-17.6	-6.0	11.0	1.06	0.12	2	-17.3	-6.3	8.8	3.34	0.20	3
-18.0	-6.0	12.0	13-4	-17.3	-6.1	11.5	0.85	0.13	1	-17.3	-6.3	10.3	1.92	0.21	2
-18.0	-6.0	12.0	14-52	-16.4	-4.1	12.0	2.51	0.15	3	-19.3	-2.3	9.8	4.55	NEL	3
-18.0	-2.0	12.0	14-1	-17.4	-2.1	10.6	1.54	0.09	2	-18.3	-2.3	10.3	1.79	0.14	2
-18.0	-2.0	12.0	14-23	-18.1	-1.8	10.6	1.41	0.09	2	-19.8	-1.8	10.3	2.49	0.12	2
-18.0	-2.0	12.0	14-45	-17.9	-1.8	10.9	1.15	0.09	2	-19.3	-1.8	10.3	2.17	0.12	2
-18.0	2.0	12.0	12-80	-36.6	11.6	11.6	20.91	2.06	6	-17.8	2.8	9.8	2.38	0.06	2
-18.0	2.0	12.0	12-95	-17.8	1.4	10.5	1.62	0.10	2	-18.8	1.3	10.8	1.64	0.12	2
-18.0	2.0	12.0	12-107	-17.9	1.5	10.7	1.42	0.11	2	-18.8	1.3	10.8	1.64	0.08	2
-18.0	6.0	12.0	13-71	-18.5	4.8	12.0	1.31	0.39	2	-15.8	3.3	11.8	3.56	0.80	3
-18.0	10.0	12.0	11-44	-96.0	12.0	12.0	78.03	>10.00	6	-23.8	-1.3	11.8	12.64	NEL	6
-18.0	10.0	12.0	12-105	-17.0	6.8	12.0	3.38	0.20	3	-16.3	8.8	11.8	2.17	0.42	2
-18.0	10.0	12.0	12-115	-32.1	-3.6	12.0	19.61	2.04	6	-15.8	2.8	11.8	7.60	0.98	5
-18.0	10.0	12.0	13-59	-10.8	4.0	0.8	14.63	NaN	6	-10.3	7.8	8.3	8.90	0.07	5
-14.0	-6.0	12.0	12-6	-13.5	-4.0	7.4	5.08	NaN	4	-13.3	-7.8	8.3	4.21	0.13	3
-14.0	-6.0	12.0	14-9	-13.9	-5.9	11.5	0.56	0.12	1	-11.3	-8.3	8.3	5.17	0.09	4
-14.0	-6.0	12.0	14-30	-13.6	-6.0	9.7	2.29	0.10	2	-11.8	-7.8	8.3	4.71	0.09	3
-14.0	-6.0	12.0	14-31	-13.6	-4.4	12.0	1.62	0.32	2	-6.3	-10.3	11.8	8.84	0.10	5
-14.0	-6.0	12.0	14-53	-14.6	-1.8	12.0	4.26	0.15	3	-14.8	-1.8	11.3	4.38	0.29	3

Tab. B.35: SW I PLB b - "Top" - Crack, part 1: Coordinates of the pencil-lead breaks and estimated source locations determined using Geiger's method and *FastWay*. Estimated source locations excluded during the verification process (see Section 7.3.4) are shown in gray.

PLB			Set	Geiger's method						*FastWay*					
x	y	z	#	x	y	z	d	eei	ac	x	y	z	d	eei	ac
[in]	[in]	[in]		[in]	[in]	[in]	[in]	[-]	[-]	[in]	[in]	[in]	[in]	[-]	[-]
-14.0	-2.0	12.0	14-2	-13.6	-1.9	11.0	1.08	0.09	2	-13.8	-2.3	10.8	1.30	0.18	2
-14.0	-2.0	12.0	14-24	-15.7	-0.6	12.0	2.18	0.13	2	-15.3	-1.3	11.8	1.48	0.22	2
-14.0	-2.0	12.0	14-46	-14.0	-1.8	11.3	0.73	0.10	1	-14.3	-2.3	11.8	0.43	0.16	1
-14.0	2.0	12.0	13-62	-13.8	1.7	11.1	0.95	0.10	1	-14.3	1.3	11.3	1.09	0.17	2
-14.0	2.0	12.0	14-168	-13.9	1.7	11.0	1.06	0.10	2	-14.3	1.3	10.3	1.92	0.20	2
-14.0	2.0	12.0	14-206	-14.8	1.6	10.5	1.74	0.12	2	-14.3	1.3	9.8	2.38	0.07	2
-14.0	6.0	12.0	13-55	-13.9	5.6	12.0	0.43	0.12	1	-15.3	4.3	8.3	4.32	NEL	3
-14.0	6.0	12.0	13-64	-14.3	5.5	10.2	1.87	0.09	2	-13.8	5.8	10.3	1.79	0.08	2
-14.0	6.0	12.0	14-213	-13.8	5.6	12.0	0.47	0.13	1	-13.8	5.8	11.8	0.43	0.27	1
-14.0	10.0	12.0	14-181	-13.9	9.1	10.9	1.45	0.12	2	-15.8	7.8	8.3	4.71	0.37	3
-14.0	10.0	12.0	14-200	-14.0	8.8	10.9	1.63	0.12	2	-15.3	7.8	8.3	4.55	0.36	3
-14.0	10.0	12.0	14-218	-13.3	7.7	12.0	2.43	0.09	2	-13.8	7.3	11.8	2.77	0.18	3
-10.0	-10.0	12.0	14-37	-13.6	-4.0	6.7	8.74	0.27	5	-11.3	-11.8	8.3	4.32	0.23	3
-10.0	-10.0	12.0	14-38	-10.5	-4.0	6.9	7.91	0.33	5	-12.3	-7.8	8.3	4.92	0.19	3
-10.0	-10.0	12.0	14-60	-11.6	-11.8	12.0	2.40	0.22	2	-11.8	-8.3	8.3	4.49	0.16	3
-10.0	2.0	12.0	14-188	-11.4	1.6	10.7	1.94	0.12	2	-10.3	1.8	10.8	1.30	0.13	2
-10.0	2.0	12.0	14-207	-10.4	1.9	10.9	1.17	0.10	2	-11.3	1.8	11.3	1.48	0.13	2
-10.0	6.0	12.0	14-175	-11.1	5.6	10.2	2.16	0.12	2	-10.8	5.3	10.8	1.64	0.05	2
-10.0	6.0	12.0	14-194	-10.3	5.7	11.0	1.05	0.09	2	-10.8	5.3	10.8	1.64	0.08	2
-10.0	6.0	12.0	14-214	-12.9	5.2	10.3	3.44	0.19	3	-10.8	5.8	11.3	1.09	0.05	2
-10.0	10.0	12.0	14-182	-11.3	8.1	10.3	2.89	0.20	3	-11.3	8.8	9.8	2.86	0.04	3
-10.0	10.0	12.0	14-201	-10.4	9.4	11.0	1.18	0.09	2	-11.3	8.8	9.8	2.86	0.10	3
-10.0	10.0	12.0	14-219	2.0	4.0	7.3	14.23	NaN	6	2.3	11.8	8.3	12.93	0.28	6
-8.0	-2.0	12.0	14-47	-4.1	1.7	12.0	5.41	0.74	4	-4.8	8.8	11.8	11.23	0.45	6
-8.0	-2.0	12.0	14-48	-5.5	-2.6	12.0	2.59	0.09	3	-6.3	-2.8	10.8	2.28	0.18	2
-6.0	-10.0	12.0	14-17	-2.8	-12.0	12.0	3.81	0.85	3	-8.3	-11.8	8.3	4.71	0.08	3
-6.0	-10.0	12.0	14-18	-6.2	-10.5	12.0	0.58	0.32	1	-5.8	-9.8	8.3	3.77	0.04	3
-6.0	-10.0	12.0	14-39	-6.0	-4.0	5.9	8.54	0.28	5	-7.3	-9.3	8.3	4.02	0.20	3
-6.0	-10.0	12.0	14-61	-6.2	-4.0	6.1	8.40	0.41	5	-8.3	-9.3	8.3	4.44	0.08	3
-6.0	-6.0	12.0	14-10	-6.9	-11.0	12.0	5.08	0.48	4	-7.3	-7.3	8.8	3.70	1.09	3
-6.0	-6.0	12.0	14-11	-5.8	-6.5	12.0	0.60	0.19	1	-6.8	-5.8	8.8	3.34	0.04	3
-6.0	-6.0	12.0	14-32	-2.7	-9.0	12.0	4.40	0.45	3	-5.3	-7.3	11.8	1.48	0.19	2
-6.0	-6.0	12.0	14-54	-5.4	-6.2	12.0	0.63	0.18	1	-7.3	-8.3	11.8	2.59	0.20	3
-6.0	-2.0	12.0	14-4	-6.3	-2.4	9.4	2.67	0.09	3	-6.8	-2.3	8.8	3.34	0.07	3
-6.0	-2.0	12.0	14-25	-5.5	-2.5	11.8	0.73	0.10	1	-6.3	-2.8	10.8	1.48	0.14	2
-6.0	2.0	12.0	14-170	-6.4	2.4	10.7	1.45	0.10	2	-6.8	2.3	10.8	1.48	0.07	2
-6.0	2.0	12.0	14-189	-6.0	1.9	11.2	0.83	0.10	1	-6.3	1.3	10.8	1.48	0.13	2
-6.0	2.0	12.0	14-208	-6.4	1.8	10.6	1.50	0.10	2	-6.8	1.8	10.3	1.92	0.19	2
-6.0	6.0	12.0	14-176	-5.7	6.1	11.2	0.85	0.09	1	-5.8	5.8	10.8	1.30	0.11	2
-6.0	6.0	12.0	14-195	-5.6	6.2	11.3	0.81	0.09	1	-5.8	5.3	10.3	1.92	0.12	2
-6.0	6.0	12.0	14-196	-5.0	7.1	11.9	1.49	0.14	2	-4.8	7.3	11.8	1.79	0.23	2
-6.0	6.0	12.0	14-215	-5.9	6.9	12.0	0.93	0.09	1	-6.3	5.8	11.3	0.83	0.04	1
-6.0	10.0	12.0	14-183	-6.7	4.0	2.9	10.89	0.27	6	-6.3	7.8	10.3	2.86	0.14	3
-6.0	10.0	12.0	14-202	-6.6	4.0	2.0	11.67	0.25	6	-5.8	7.8	10.8	2.59	0.12	3
-6.0	10.0	12.0	14-220	-10.3	9.7	11.2	4.41	0.09	3	-11.3	8.8	9.8	5.85	0.06	4
-6.0	10.0	12.0	14-221	-6.0	4.0	4.0	10.01	0.24	6	-6.8	8.3	10.8	2.28	0.16	2
-2.0	-10.0	12.0	14-19	-0.7	-4.0	7.8	7.47	0.30	4	-1.3	-11.3	11.8	1.48	0.24	2
-2.0	-10.0	12.0	14-40	-0.9	-9.9	11.1	1.39	0.16	2	-1.3	-8.3	9.8	2.95	0.25	3

Tab. B.36: SW I PLB b - "Top" - Crack, part 2: Coordinates of the pencil-lead breaks and estimated source locations determined using Geiger's method and *FastWay*. Estimated source locations excluded during the verification process (see Section 7.3.4) are shown in gray.

PLB			Set	Geiger's method						*FastWay*					
x [in]	y [in]	z [in]	#	x [in]	y [in]	z [in]	d [in]	eei [-]	ac [-]	x [in]	y [in]	z [in]	d [in]	eei [-]	ac [-]
-2.0	-10.0	12.0	14-62	-2.6	-4.0	5.5	8.87	0.30	5	-3.3	-11.3	8.8	3.70	0.20	3
-2.0	-6.0	12.0	14-12	-2.2	-6.7	9.5	2.64	0.10	3	-2.8	-5.8	9.3	2.86	0.11	3
-2.0	-6.0	12.0	14-33	-1.6	-6.9	9.4	2.77	0.09	3	-1.8	-5.8	11.8	0.43	0.15	1
-2.0	-6.0	12.0	14-55	-1.3	-7.1	9.9	2.46	0.10	2	-1.3	-6.8	11.8	1.09	0.19	2
-2.0	-2.0	12.0	14-5	-2.0	-2.3	10.4	1.67	0.11	2	-2.3	-1.8	10.3	1.79	0.15	2
-2.0	-2.0	12.0	14-26	-2.1	-2.4	8.7	3.31	0.10	3	-2.3	-2.3	7.3	4.76	NEL	3
-2.0	-2.0	12.0	14-49	-2.1	-1.8	7.8	4.24	0.10	3	-2.3	-2.3	6.8	5.26	NEL	4
-2.0	2.0	12.0	12-108	96.0	12.0	-12.0	101.39	NaN	6	7.3	-1.3	7.3	10.89	NEL	6
-2.0	2.0	12.0	14-171	-1.6	2.3	9.9	2.19	0.10	2	-1.8	1.8	9.3	2.77	0.20	3
-2.0	2.0	12.0	14-190	-1.5	1.8	11.0	1.14	0.12	2	-1.8	1.3	10.8	1.48	0.16	2
-2.0	2.0	12.0	14-209	-1.9	2.1	8.5	3.53	0.10	3	-2.3	2.8	4.3	7.79	NEL	5
-2.0	6.0	12.0	14-177	-1.9	6.1	10.4	1.59	0.10	2	-1.8	5.3	8.8	3.34	0.07	3
-2.0	6.0	12.0	14-198	31.1	-12.0	12.0	37.68	NaN	6	-3.3	-9.8	11.8	15.80	0.80	6
-2.0	6.0	12.0	14-216	-1.9	6.7	10.6	1.55	0.10	2	-1.8	5.8	9.8	2.28	0.10	2
-2.0	10.0	12.0	14-184	-1.7	4.0	6.4	8.22	0.22	5	-1.8	8.8	8.3	3.96	0.15	3
-2.0	10.0	12.0	14-203	-1.7	4.0	7.2	7.70	0.21	5	-1.8	7.8	8.3	4.38	0.15	3
-2.0	10.0	12.0	14-222	-2.1	11.4	11.4	1.55	0.10	2	-2.3	11.8	11.8	1.79	0.15	2
2.0	-10.0	12.0	14-20	3.4	-11.0	12.0	1.75	0.33	2	3.3	-11.8	8.3	4.32	0.08	3
2.0	-10.0	12.0	14-41	3.9	-9.5	12.0	1.94	0.26	2	1.8	-11.8	11.8	1.79	0.31	2
2.0	-10.0	12.0	14-63	3.3	-10.0	12.0	1.32	0.38	2	2.3	-11.8	11.8	1.79	0.39	2
2.0	-6.0	12.0	14-13	2.1	-6.4	9.9	2.10	0.10	2	1.8	-5.3	8.3	3.83	NEL	3
2.0	-6.0	12.0	14-34	2.4	-5.6	11.4	0.85	0.10	1	1.3	-5.8	8.3	3.83	0.19	3
2.0	-6.0	12.0	14-35	1.5	-5.5	8.6	3.46	0.09	3	1.3	-5.3	8.3	3.90	0.13	3
2.0	-6.0	12.0	14-56	1.9	-4.0	7.4	5.04	0.20	4	1.3	-10.3	8.3	5.72	0.13	4
2.0	-2.0	12.0	14-6	2.2	-2.6	11.1	1.05	0.10	2	2.3	-2.8	9.8	2.38	0.11	2
2.0	-2.0	12.0	14-27	1.3	-3.1	12.0	1.35	0.09	2	1.3	-3.3	10.8	1.92	0.10	2
2.0	-2.0	12.0	14-50	1.8	-2.2	11.2	0.81	0.11	1	1.8	-2.8	10.3	1.92	0.07	2
2.0	2.0	12.0	14-169	-10.7	1.9	11.0	12.77	0.09	6	-11.3	1.8	11.3	13.27	0.15	6
2.0	2.0	12.0	14-172	1.6	3.1	9.6	2.63	0.10	3	1.8	2.8	8.8	3.34	0.07	3
2.0	2.0	12.0	14-191	2.0	2.2	10.2	1.86	0.10	2	1.8	2.3	9.3	2.77	0.13	3
2.0	2.0	12.0	14-210	1.8	2.0	9.3	2.72	0.11	3	1.8	1.8	8.8	3.27	NEL	3
2.0	6.0	12.0	14-179	1.7	6.1	10.3	1.73	0.09	2	2.3	5.8	9.3	2.77	0.20	3
2.0	6.0	12.0	14-197	1.8	6.6	9.6	2.46	0.12	2	-6.3	8.8	8.3	9.47	NEL	5
2.0	6.0	12.0	14-217	1.5	6.5	9.8	2.34	0.12	2	2.3	4.8	10.8	1.79	0.08	2
2.0	10.0	12.0	14-185	9.5	4.0	-12.0	25.86	2.18	6	2.3	10.8	11.3	1.09	0.24	2
2.0	10.0	12.0	14-204	1.3	4.0	7.6	7.50	0.21	4	1.8	7.8	8.3	4.38	0.12	3
2.0	10.0	12.0	14-205	35.9	12.0	12.0	33.94	8.45	6	5.3	8.3	8.3	5.26	0.04	4
2.0	10.0	12.0	14-223	1.9	4.0	6.6	8.04	0.22	5	2.3	8.3	8.3	4.15	0.21	3
6.0	-6.0	12.0	14-57	4.8	-6.8	12.0	1.41	0.11	2	4.3	-7.8	8.3	4.49	0.08	3
6.0	-2.0	12.0	14-7	5.7	-2.4	12.0	0.54	0.10	1	5.8	-2.3	11.8	0.43	0.16	1
6.0	-2.0	12.0	14-28	7.9	-1.3	9.6	3.16	0.09	3	8.8	-0.8	7.8	5.21	0.20	4
6.0	-2.0	12.0	14-51	6.6	-1.1	10.3	1.98	0.11	2	6.8	-0.8	10.3	2.28	0.17	2
6.0	2.0	12.0	14-173	5.9	1.5	12.0	0.49	0.10	1	5.3	1.3	11.8	1.09	0.12	2
6.0	2.0	12.0	14-192	6.9	2.6	9.4	2.78	0.12	3	8.8	2.3	11.8	2.77	0.15	3
6.0	2.0	12.0	14-211	6.4	1.9	10.5	1.57	0.09	2	6.3	1.8	9.8	2.28	0.06	2
6.0	6.0	12.0	13-56	9.0	-12.0	12.0	18.25	2.09	6	5.8	5.8	11.8	0.43	0.73	1
6.0	6.0	12.0	13-65	96.0	-4.0	-12.0	93.68	>10.00	6	23.8	-8.3	11.8	22.76	0.39	6
6.0	6.0	12.0	13-72	68.2	-12.0	9.3	64.77	>10.00	6	21.3	-8.3	11.3	20.89	NEL	6
6.0	10.0	12.0	13-68	35.6	12.0	12.0	29.67	1.69	6	23.8	8.8	9.3	18.01	1.14	6
6.0	10.0	12.0	13-77	6.2	4.0	7.0	7.80	0.25	5	6.3	8.3	9.3	3.27	0.14	3

Tab. B.37: SW I PLB b - "Top" - Crack, part 3: Coordinates of the pencil-lead breaks and estimated source locations determined using Geiger's method and *FastWay*. Estimated source locations excluded during the verification process (see Section 7.3.4) are shown in gray.

PLB			Set	Geiger's method						*FastWay*					
x [in]	y [in]	z [in]	#	x [in]	y [in]	z [in]	d [in]	eei [-]	ac [-]	x [in]	y [in]	z [in]	d [in]	eei [-]	ac [-]
6.0	10.0	12.0	14-186	6.0	11.5	12.0	1.45	0.44	2	5.3	8.3	8.3	4.21	0.03	3
10.0	-10.0	12.0	14-21	11.2	-5.5	11.8	4.67	0.09	3	10.8	-5.8	11.8	4.32	0.14	3
10.0	-10.0	12.0	14-64	9.7	-6.9	11.5	3.19	0.10	3	11.8	-5.3	11.8	5.07	0.09	4
10.0	-6.0	12.0	13-19	12.7	-3.6	12.0	3.64	0.14	3	9.8	-5.3	11.8	0.83	0.18	1
10.0	-6.0	12.0	14-14	8.1	-4.3	9.4	3.66	0.12	3	10.8	-3.8	3.8	8.58	NEL	5
10.0	-6.0	12.0	14-15	11.4	-4.7	11.6	1.98	0.09	2	10.3	-5.3	11.8	0.83	0.10	1
10.0	-6.0	12.0	14-36	9.2	-4.0	12.0	2.20	0.10	2	9.8	-3.8	11.3	2.38	0.21	2
10.0	-2.0	12.0	14-8	10.6	-1.6	10.6	1.61	0.09	2	10.3	-1.8	10.8	1.30	0.13	2
10.0	-2.0	12.0	14-29	9.3	-2.2	11.7	0.82	0.09	1	9.8	-1.8	10.8	1.30	0.14	2
10.0	2.0	12.0	13-52	9.9	1.8	10.4	1.66	0.10	2	9.8	1.8	10.3	1.79	0.08	2
10.0	2.0	12.0	14-193	9.9	1.9	10.2	1.83	0.09	2	9.8	1.8	9.8	2.28	0.12	2
10.0	2.0	12.0	14-212	10.6	2.1	10.6	1.56	0.13	2	9.8	1.8	9.8	2.28	0.07	2
10.0	6.0	12.0	13-57	9.6	5.2	9.9	2.27	0.10	2	9.8	4.8	10.3	2.17	0.17	2
10.0	6.0	12.0	13-73	58.1	12.0	12.0	48.46	5.36	6	10.8	5.3	11.8	1.09	0.10	2
10.0	6.0	12.0	14-199	9.9	5.2	10.6	1.63	0.09	2	9.8	4.8	10.8	1.79	0.10	2
14.0	-10.0	12.0	13-21	14.1	-11.8	8.8	3.67	0.45	3	16.3	-8.3	8.3	4.71	NEL	3
14.0	-10.0	12.0	14-43	13.3	-8.3	9.7	2.94	0.18	3	15.3	-5.8	8.3	5.80	NEL	4
14.0	-6.0	12.0	13-7	15.5	-4.5	11.6	2.20	0.16	2	13.8	-5.8	11.8	0.43	0.39	1
14.0	-6.0	12.0	13-14	12.6	-4.0	11.6	2.43	0.11	2	12.3	-4.3	11.3	2.59	0.13	3
14.0	-6.0	12.0	13-15	14.4	-4.9	12.0	1.19	0.11	2	15.3	-4.8	9.8	2.86	0.02	3
14.0	-6.0	12.0	14-58	15.1	-4.2	12.0	2.17	0.12	2	14.3	-4.8	11.3	1.48	0.06	2
14.0	-2.0	12.0	12-26	22.9	1.1	11.4	9.43	0.74	5	13.8	-1.8	10.8	1.30	0.08	2
14.0	-2.0	12.0	13-2	13.9	0.1	8.2	4.34	0.15	3	10.8	-1.3	9.8	4.02	0.03	3
14.0	-2.0	12.0	13-11	14.0	-1.6	10.9	1.17	0.10	2	13.8	-1.8	10.8	1.30	0.12	2
14.0	2.0	12.0	12-99	13.8	2.0	10.7	1.36	0.09	2	13.3	1.8	10.8	1.48	0.07	2
14.0	2.0	12.0	13-53	96.0	12.0	12.0	82.61	>10.00	6	14.3	1.8	11.8	0.43	0.12	1
14.0	2.0	12.0	13-70	13.6	1.9	10.2	1.88	0.09	2	13.3	1.8	10.8	1.48	0.10	2
14.0	6.0	12.0	12-103	14.1	5.5	10.3	1.76	0.10	2	13.3	5.3	10.3	2.05	0.12	2
14.0	6.0	12.0	13-74	12.8	4.7	10.5	2.30	0.10	2	12.8	4.8	10.8	2.17	0.10	2
14.0	6.0	12.0	14-180	13.9	5.4	11.4	0.91	0.11	1	12.8	4.8	10.3	2.49	0.14	2
14.0	10.0	12.0	13-78	13.3	10.6	11.1	1.29	0.33	2	12.3	9.3	11.8	1.92	0.20	2
18.0	-10.0	12.0	12-23	41.4	-4.9	12.0	23.93	1.20	6	18.8	-10.8	11.8	1.09	0.26	2
18.0	-10.0	12.0	12-41	32.9	-7.6	12.0	15.09	0.84	6	19.3	-11.8	11.8	2.17	0.23	2
18.0	-10.0	12.0	13-8	16.1	-4.9	8.3	6.60	0.21	4	15.3	-5.8	8.3	6.30	NEL	4
18.0	-10.0	12.0	13-9	19.1	-4.0	5.5	8.92	0.26	5	17.8	-7.3	8.3	4.66	NEL	3
18.0	-10.0	12.0	13-16	19.0	-4.0	6.5	8.21	0.18	5	16.8	-7.3	8.3	4.82	0.38	3
18.0	-6.0	12.0	12-7	20.4	-4.9	11.3	2.72	0.20	3	19.3	-7.8	8.3	4.32	NEL	3
18.0	-6.0	12.0	12-18	17.7	-5.5	12.0	0.56	0.10	1	17.3	-6.3	11.8	0.83	0.17	1
18.0	-6.0	12.0	12-34	18.0	-5.3	12.0	0.71	0.12	1	17.3	-6.3	11.8	0.83	0.24	1
18.0	-2.0	12.0	12-3	18.4	-1.7	10.9	1.21	0.10	2	18.8	-1.8	11.3	1.09	0.21	2
18.0	-2.0	12.0	12-14	20.0	-0.6	12.0	2.47	0.16	2	18.8	-1.3	11.3	1.30	0.16	2
18.0	-2.0	12.0	12-27	20.3	-1.7	10.3	2.86	0.24	3	18.3	-1.8	11.3	0.83	0.09	1
18.0	2.0	12.0	12-111	17.8	1.7	10.8	1.30	0.09	2	18.3	1.8	11.3	0.83	0.09	1
18.0	6.0	12.0	13-58	18.0	5.7	11.8	0.39	0.10	1	17.8	5.3	11.8	0.83	0.05	1
18.0	6.0	12.0	13-66	17.5	5.0	11.4	1.28	0.11	2	17.8	5.3	11.8	0.83	0.05	1
18.0	6.0	12.0	13-75	17.4	5.0	11.4	1.30	0.12	2	17.8	5.3	11.8	0.83	0.06	1
18.0	10.0	12.0	11-53	20.0	11.6	10.4	2.98	0.36	3	17.3	10.8	9.8	2.49	NEL	2
18.0	10.0	12.0	11-54	18.8	6.7	10.8	3.57	0.26	3	16.8	6.3	11.3	4.02	NEL	3

Tab. B.38: SW I PLB b - "Top" - Crack, part 4: Coordinates of the pencil-lead breaks and estimated source locations determined using Geiger's method and *FastWay*. Estimated source locations excluded during the verification process (see Section 7.3.4) are shown in gray.

PLB			Set	Geiger's method						*FastWay*					
x [in]	y [in]	z [in]	#	x [in]	y [in]	z [in]	d [in]	eei [-]	ac [-]	x [in]	y [in]	z [in]	d [in]	eei [-]	ac [-]
18.0	10.0	12.0	11-60	15.5	7.6	11.5	3.52	0.12	3	16.8	9.8	10.3	2.17	0.17	2
18.0	10.0	12.0	12-92	16.2	5.8	11.1	4.61	0.11	3	15.8	6.3	10.3	4.71	0.20	3
18.0	10.0	12.0	12-116	18.3	6.6	12.0	3.44	0.11	3	18.8	6.3	11.8	3.83	NEL	3
18.0	10.0	12.0	13-79	17.3	11.6	12.0	1.74	0.39	2	15.3	11.8	11.8	3.27	NEL	3
18.0	10.0	12.0	14-187	18.3	10.8	11.9	0.87	0.21	1	17.8	9.3	8.3	3.83	NEL	3
22.0	-10.0	12.0	12-10	43.4	-4.0	-3.8	27.22	2.02	6	20.3	-9.3	8.3	4.21	0.38	3
22.0	-10.0	12.0	12-11	-96.0	-12.0	-12.0	120.43	NaN	6	23.8	-0.8	10.3	9.58	NEL	5
22.0	-10.0	12.0	12-40	96.0	-4.0	-12.0	78.03	>10.00	6	20.3	-9.3	8.3	4.21	0.38	3
22.0	-10.0	12.0	13-20	14.3	-4.0	0.8	14.87	NaN	6	14.8	-7.8	8.3	8.47	0.08	5
22.0	-10.0	12.0	14-16	-20.9	-12.0	12.0	42.99	1.02	6	-17.8	-9.8	11.8	39.75	NEL	6
22.0	-10.0	12.0	14-44	-96.0	-12.0	8.0	118.08	NaN	6	-5.3	2.3	9.3	30.00	NEL	6
22.0	-6.0	12.0	10-4	29.2	4.7	12.0	12.92	NaN	6	23.3	-2.8	11.8	3.49	0.49	3
22.0	-6.0	12.0	12-19	96.0	12.0	12.0	76.16	>10.00	6	20.8	-6.3	11.3	1.48	0.01	2
22.0	-6.0	12.0	12-35	31.5	3.0	12.0	13.10	0.72	6	23.8	-2.8	11.8	3.70	0.54	3
22.0	-2.0	12.0	12-4	27.3	-1.3	11.2	5.39	0.26	4	22.3	-1.8	11.3	0.83	0.10	1
22.0	-2.0	12.0	12-15	23.0	-1.3	11.6	1.31	0.09	2	23.8	-1.3	11.8	1.92	0.13	2
22.0	-2.0	12.0	12-28	22.1	-1.6	11.1	1.03	0.08	2	22.8	-1.8	10.8	1.48	0.12	2
22.0	-2.0	12.0	13-10	96.0	4.0	-12.0	78.03	>10.00	6	8.8	1.8	9.8	13.95	NEL	6
22.0	-2.0	12.0	13-18	10.6	-1.3	10.3	11.59	0.09	6	10.3	-1.3	9.8	11.99	0.08	6
22.0	2.0	12.0	12-85	22.6	2.5	12.0	0.77	0.28	1	15.3	1.8	8.3	7.73	NEL	5
22.0	2.0	12.0	12-86	21.0	1.9	11.0	1.45	0.09	2	22.8	2.3	11.8	0.83	0.16	1
22.0	2.0	12.0	12-100	21.0	1.5	10.6	1.77	0.09	2	22.3	1.3	10.3	1.92	0.17	2
22.0	2.0	12.0	12-112	20.7	1.9	10.9	1.74	0.09	2	21.8	2.3	11.3	0.83	0.16	1
22.0	6.0	12.0	12-89	20.5	5.1	11.6	1.75	0.10	2	21.3	5.3	9.3	2.95	0.02	3
22.0	6.0	12.0	12-114	23.7	7.1	12.0	1.97	0.45	2	23.8	6.8	8.3	4.21	NEL	3
22.0	6.0	12.0	13-67	20.7	5.3	11.8	1.51	0.10	2	17.8	1.8	8.3	7.08	NEL	4
22.0	10.0	12.0	12-93	25.9	5.6	11.9	5.89	0.72	4	18.8	3.8	5.3	9.76	NEL	5
22.0	10.0	12.0	13-61	58.0	12.0	12.0	36.06	6.55	6	14.3	11.8	11.8	7.95	NEL	5
22.0	10.0	12.0	13-69	22.6	12.0	11.3	2.20	0.68	2	19.8	10.8	8.3	4.44	NEL	3

Tab. B.39: SW I PLB b - "Top" - Crack, part 5: Coordinates of the pencil-lead breaks and estimated source locations determined using Geiger's method and *FastWay*. Estimated source locations excluded during the verification process (see Section 7.3.4) are shown in gray.

B.4.2 Top-Front

PLB			Set	Geiger's method						*FastWay*					
x	y	z	#	x	y	z	d	eei	ac	x	y	z	d	eei	ac
[in]	[in]	[in]		[in]	[in]	[in]	[in]	[-]	[-]	[in]	[in]	[in]	[in]	[-]	[-]
-22.0	-12.0	10.0	12-44	-25.5	-10.4	9.7	3.91	0.65	3	-23.8	-10.3	8.8	2.77	0.77	3
-22.0	-12.0	10.0	12-47	-89.3	-12.0	12.0	67.29	7.38	6	-23.3	-9.8	8.3	3.11	0.57	3
-22.0	-12.0	10.0	12-49	-35.1	-4.0	-8.5	23.99	0.74	6	-23.8	-10.3	8.8	2.77	0.38	3
-18.0	-12.0	10.0	12-45	-26.6	-12.0	12.0	8.85	0.91	5	-20.8	-8.8	8.3	4.60	0.33	3
-18.0	-12.0	10.0	12-50	-21.8	-11.8	12.0	4.31	0.62	3	-19.3	-11.8	11.8	2.17	0.38	2
-18.0	-12.0	10.0	13-24	-22.4	-11.0	12.0	4.96	0.71	3	-20.3	-8.3	8.3	4.71	0.37	3
-14.0	-12.0	10.0	13-26	-15.4	-9.8	12.0	3.28	0.88	3	-15.8	-9.3	8.3	3.70	0.21	3
-14.0	-12.0	10.0	14-65	-14.2	-4.0	5.5	9.16	0.28	5	-16.8	-7.3	8.3	5.76	0.17	4
-14.0	-12.0	10.0	14-72	-14.8	-10.8	11.9	2.39	0.12	2	-17.3	-8.8	11.8	4.92	0.24	3
-10.0	-12.0	10.0	14-66	-11.5	-4.0	5.8	9.14	0.29	5	-12.8	-8.3	8.3	4.97	0.20	3
-10.0	-12.0	10.0	14-73	-12.6	-11.4	12.0	3.33	0.28	3	-12.8	-10.8	11.8	3.49	0.19	3
-10.0	-12.0	10.0	14-79	-11.8	-11.6	12.0	2.73	0.11	3	-12.8	-10.3	11.8	3.70	0.15	3
-6.0	-12.0	10.0	14-67	-7.2	-4.0	4.7	9.66	0.28	5	-8.8	-8.8	8.3	4.60	0.20	3
-6.0	-12.0	10.0	14-68	-3.2	-4.0	-0.9	13.78	NaN	6	-2.3	-10.3	10.8	4.21	0.27	3
-6.0	-12.0	10.0	14-74	-2.8	2.6	11.2	15.03	0.57	6	-10.3	-10.3	11.8	4.92	0.08	3
-6.0	-12.0	10.0	14-80	-6.6	-12.0	12.0	2.10	0.47	2	-22.3	6.3	11.8	24.50	0.11	6
-2.0	-12.0	10.0	14-69	2.5	-11.9	12.0	4.93	0.72	3	2.3	-11.8	11.8	4.60	0.95	3
-2.0	-12.0	10.0	14-75	0.5	-7.3	12.0	5.70	0.31	4	-2.3	-10.8	8.3	2.17	0.21	2
-2.0	-12.0	10.0	14-81	-1.7	-11.1	11.6	1.82	0.28	2	-2.3	-8.3	9.8	3.77	0.20	3
2.0	-12.0	10.0	14-70	7.8	-9.0	12.0	6.81	0.29	4	6.3	-11.8	8.3	4.60	0.34	3
2.0	-12.0	10.0	14-76	2.7	-11.1	9.8	1.19	0.10	2	2.3	-11.8	9.3	0.83	0.37	1
2.0	-12.0	10.0	14-82	2.5	-12.0	12.0	2.06	0.75	2	1.8	-11.8	8.3	1.79	0.26	2
6.0	-12.0	10.0	14-77	6.8	-4.0	-10.8	22.28	NaN	6	5.8	-11.8	8.3	1.79	0.28	2
6.0	-12.0	10.0	14-83	6.2	-11.1	11.1	1.49	0.10	2	6.3	-11.8	8.3	1.79	0.34	2
10.0	-12.0	10.0	13-23	15.5	-7.1	12.0	7.65	0.22	5	23.8	-3.8	4.3	17.03	NEL	6
10.0	-12.0	10.0	14-78	11.7	-7.5	12.0	5.23	0.23	4	12.3	-8.3	11.8	4.71	0.04	3
10.0	-12.0	10.0	14-84	12.0	-9.3	11.2	3.54	0.17	3	10.8	-10.3	11.8	2.59	0.03	3
14.0	-12.0	10.0	12-46	17.7	-8.8	12.0	5.29	0.19	4	17.3	-11.8	10.8	3.34	0.18	3
14.0	-12.0	10.0	13-27	16.6	-5.8	11.1	6.80	0.18	4	19.3	-6.3	8.3	7.98	NEL	5
18.0	-12.0	10.0	11-18	20.6	-8.5	12.0	4.80	0.19	3	18.8	-11.8	11.8	1.92	0.21	2
18.0	-12.0	10.0	12-48	14.2	-6.8	12.0	6.76	0.87	4	23.8	0.8	11.8	14.10	NEL	6
18.0	-12.0	10.0	12-51	25.2	-6.2	12.0	9.43	1.36	5	17.8	-9.3	11.8	3.27	NEL	3
22.0	-12.0	10.0	11-20	22.4	-8.1	12.0	4.44	0.28	3	18.3	-11.8	11.8	4.15	0.10	3
22.0	-12.0	10.0	11-21	4.0	-4.0	-6.7	25.88	NaN	6	21.8	-11.3	11.8	1.92	1.04	2

Tab. B.40: SW I PLB b - "Top-Front" - Crack, part 1: Coordinates of the pencil-lead breaks and estimated source locations determined using Geiger's method and *FastWay*. Estimated source locations excluded during the verification process (see Section 7.3.4) are shown in gray.

B.4.3 Front

		PLB	Set	Geiger's method						*FastWay*					
x	y	z	#	x	y	z	d	eei	ac	x	y	z	d	eei	ac
[in]	[in]	[in]		[in]	[in]	[in]	[in]	[-]	[-]	[in]	[in]	[in]	[in]	[-]	[-]
-22.0	-4.0	-10.0	9-12	96.0	-4.0	-12.0	118.02	NaN	6	-23.8	-3.8	-11.8	2.49	0.85	2
-22.0	-4.0	-10.0	10-15	-11.6	2.4	1.5	16.74	NaN	6	-18.3	0.3	-9.3	5.72	NEL	4
-22.0	-4.0	-2.0	10-12	2.2	-1.1	-8.3	25.23	0.85	6	-17.3	-1.3	-1.8	5.49	0.13	4
-22.0	-4.0	-2.0	10-16	-96.0	-12.0	12.0	75.74	>10.00	6	-23.8	-3.3	-2.8	2.05	NEL	2
-22.0	-4.0	2.0	10-13	-78.0	-4.0	-12.0	57.75	6.11	6	-18.8	-1.3	-1.8	5.67	0.04	4
-22.0	-4.0	2.0	11-22	-16.1	0.0	0.8	7.23	0.12	4	-17.8	-0.8	1.3	5.40	0.09	4
-22.0	-4.0	2.0	12-53	-49.0	2.8	2.8	27.85	2.24	6	-23.8	-1.3	0.3	3.70	0.36	3
-22.0	-4.0	2.0	12-56	-19.8	-1.0	1.3	3.75	0.13	3	-22.3	-2.8	1.8	1.30	0.21	2
-22.0	-4.0	6.0	12-52	-21.8	-1.8	5.4	2.27	0.12	2	-23.8	-2.3	5.3	2.59	0.22	3
-22.0	-4.0	6.0	12-55	-20.5	-2.0	5.2	2.61	0.11	3	-21.8	-2.8	5.3	1.48	0.20	2
-22.0	-4.0	6.0	12-59	-21.6	-1.9	5.4	2.23	0.11	2	-23.8	-2.8	5.3	2.28	0.23	2
-22.0	-4.0	6.0	13-28	-17.8	-2.1	5.6	4.65	0.09	3	-18.8	-2.8	5.8	3.49	0.10	3
-18.0	-4.0	-10.0	9-16	-18.4	-3.8	-11.6	1.64	NaN	2	-18.3	-0.3	-9.3	3.83	NEL	3
-18.0	-4.0	-10.0	10-19	-6.7	2.9	4.5	19.68	NaN	6	-18.3	0.8	-11.3	4.92	NEL	3
-18.0	-4.0	-10.0	12-63	-9.9	-4.0	-3.0	10.67	1.73	6	-22.8	-3.8	-11.3	4.92	0.74	3
-18.0	-4.0	-6.0	12-61	96.0	-12.0	-12.0	114.44	NaN	6	-13.3	-9.8	11.8	19.25	NEL	6
-18.0	-4.0	2.0	12-60	-44.6	-5.4	8.6	27.45	3.39	6	-21.3	-3.3	-1.8	5.02	NEL	4
-18.0	-4.0	2.0	12-62	-27.0	4.0	1.6	12.02	0.40	6	10.8	-0.8	0.8	28.96	NEL	6
-18.0	-4.0	2.0	12-64	-21.3	0.2	0.5	5.51	0.33	4	-15.8	-3.3	0.3	2.95	0.05	3
-18.0	-4.0	6.0	13-29	-17.7	-2.2	5.7	1.88	0.10	2	-18.8	-2.8	5.8	1.48	0.18	2
-18.0	-4.0	6.0	13-30	-17.5	-2.3	5.7	1.84	0.10	2	-18.3	-2.8	5.8	1.30	0.12	2
-18.0	-4.0	6.0	14-85	-17.4	-2.2	5.6	1.92	0.09	2	-18.3	-2.8	5.8	1.30	0.17	2
-14.0	-4.0	-10.0	11-26	-88.9	-4.0	-12.0	74.92	9.52	6	-14.8	-2.3	-9.3	2.05	0.24	2
-14.0	-4.0	-6.0	11-25	6.3	-4.0	-12.0	21.17	NaN	6	-23.8	-0.8	-1.3	11.32	NEL	6
-14.0	-4.0	-2.0	11-24	-16.3	-1.8	-3.2	3.41	0.13	3	-15.8	-1.8	-4.3	3.63	0.30	3
-14.0	-4.0	-2.0	12-67	-16.7	-1.1	0.4	4.63	0.20	3	-11.3	-3.8	-5.3	4.26	0.14	3
-14.0	-4.0	2.0	14-87	-13.7	-1.3	1.9	2.72	0.21	3	-12.8	-3.8	2.3	1.30	0.16	2
-14.0	-4.0	2.0	14-88	-14.7	-2.4	2.6	1.85	0.12	2	-14.3	-3.3	2.3	0.83	0.11	1
-14.0	-4.0	6.0	13-32	-17.4	-0.3	10.0	6.42	0.36	4	-16.8	-0.3	11.8	7.40	NEL	4
-14.0	-4.0	6.0	14-86	-13.7	-1.9	5.8	2.08	0.12	2	-14.3	-2.3	5.8	1.79	0.19	2
-10.0	-4.0	-10.0	13-33	-12.0	-2.8	-12.0	3.07	0.77	3	-4.8	-3.3	-6.3	6.50	NEL	4
-10.0	-4.0	-6.0	13-34	-96.0	-4.0	-12.0	86.21	>10.00	6	-14.8	-3.3	-11.8	7.50	NEL	4
-10.0	-4.0	-6.0	13-35	-9.4	-2.9	-3.4	2.87	0.35	3	-9.8	-3.8	-4.8	1.30	NEL	2
-10.0	-4.0	-6.0	14-92	-14.4	3.2	-1.7	9.50	0.27	5	-20.8	-3.3	-3.3	11.12	NEL	6
-10.0	-4.0	-6.0	14-96	-10.5	0.8	-5.9	4.80	0.31	3	-14.8	-3.8	-6.8	4.82	0.47	3
-10.0	-4.0	-2.0	14-91	-9.0	-0.7	-2.1	3.42	0.16	3	-5.8	-3.8	-5.8	5.67	NEL	4
-10.0	-4.0	-2.0	14-99	-14.6	-0.9	1.7	6.66	0.17	4	-10.3	-3.8	-4.3	2.28	NEL	2
-10.0	-4.0	2.0	14-90	-11.0	-2.4	3.1	2.19	0.13	2	-11.3	-3.3	2.3	1.48	0.18	2
-10.0	-4.0	2.0	14-98	-8.9	-1.9	3.6	2.88	0.15	3	-9.8	-2.3	3.3	2.17	0.22	2
-10.0	-4.0	6.0	14-89	-9.9	-2.5	6.3	1.55	0.12	2	-10.3	-2.3	5.8	1.79	0.13	2
-10.0	-4.0	6.0	14-93	-9.9	-2.6	6.6	1.59	0.11	2	-10.3	-2.3	6.3	1.79	0.08	2
-10.0	-4.0	6.0	14-94	-10.1	-2.7	3.5	2.83	0.13	3	-11.3	-1.8	3.8	3.42	0.27	3
-10.0	-4.0	6.0	14-97	-9.7	-2.8	6.6	1.39	0.12	2	-9.8	-3.3	6.3	0.83	0.11	1
-6.0	-4.0	-10.0	11-28	-8.2	-4.0	-9.6	2.28	0.81	2	-8.3	-3.8	-9.3	2.38	NEL	2
-6.0	-4.0	-10.0	12-68	-7.6	-4.0	-9.0	1.93	0.63	2	-4.8	1.8	-5.8	7.26	NEL	4
-6.0	-4.0	-10.0	12-69	-3.1	-4.0	-7.3	3.93	0.43	3	-3.8	-3.3	-9.3	2.49	NEL	2

Tab. B.41: SW I PLB b - "Front" - Crack, part 1: Coordinates of the pencil-lead breaks and estimated source locations determined using Geiger's method and *FastWay*. Estimated source locations excluded during the verification process (see Section 7.3.4) are shown in gray.

PLB			Set	Geiger's method						*FastWay*					
x [in]	y [in]	z [in]	#	x [in]	y [in]	z [in]	d [in]	eei [-]	ac [-]	x [in]	y [in]	z [in]	d [in]	eei [-]	ac [-]
-6.0	-4.0	-10.0	13-37	-3.1	-4.0	-8.1	3.52	1.11	3	-4.3	-3.8	-10.3	1.79	NEL	2
-6.0	-4.0	-10.0	13-39	-4.9	-3.4	-8.4	2.06	0.58	2	-4.3	-3.3	-11.8	2.59	NEL	3
-6.0	-4.0	-6.0	14-109	-2.8	-1.7	-5.2	4.05	0.27	3	-4.8	-3.8	-5.3	1.48	NEL	2
-6.0	-4.0	-2.0	14-105	-8.4	-0.6	-2.7	4.18	0.33	3	-6.8	-3.8	-3.3	1.48	0.31	2
-6.0	-4.0	-2.0	14-108	-5.6	-3.1	0.1	2.30	0.14	2	-3.3	-3.8	0.8	3.90	0.11	3
-6.0	-4.0	2.0	14-101	-2.6	-3.0	4.9	4.57	0.16	3	-2.3	-3.8	4.8	4.66	0.21	3
-6.0	-4.0	2.0	14-104	-6.2	-2.2	3.0	2.09	0.13	2	-7.3	-2.3	2.8	2.28	0.16	2
-6.0	-4.0	2.0	14-107	-5.6	-1.8	3.0	2.44	0.13	2	-6.3	-2.3	2.8	1.92	0.22	2
-6.0	-4.0	6.0	14-100	-6.7	-2.2	6.9	2.16	0.12	2	-7.3	-2.3	6.3	2.17	0.11	2
-6.0	-4.0	6.0	14-103	-5.7	-3.1	7.1	1.43	0.09	2	-6.3	-2.8	7.3	1.79	0.14	2
-6.0	-4.0	6.0	14-106	-6.6	-2.5	6.8	1.80	0.15	2	-6.8	-2.3	7.3	2.28	0.14	2
-2.0	-4.0	-10.0	14-118	-80.3	-4.0	-12.0	78.34	6.55	6	-6.8	-1.3	-8.3	5.76	NEL	4
-2.0	-4.0	-10.0	14-119	1.7	-1.6	-9.2	4.52	1.07	3	-14.3	-2.8	-11.8	12.44	NEL	6
-2.0	-4.0	-10.0	14-124	2.1	-0.8	-2.7	9.02	NaN	5	-13.8	3.8	-10.3	14.08	NEL	6
-2.0	-4.0	-6.0	14-113	65.5	4.0	-12.0	68.27	>10.00	6	-14.3	0.3	-11.3	13.99	NEL	6
-2.0	-4.0	-6.0	14-117	-10.1	1.8	-3.9	10.18	0.45	6	-19.8	3.3	-5.3	19.19	NEL	6
-2.0	-4.0	-6.0	14-123	-8.8	-1.0	-8.4	7.80	0.75	5	-6.8	1.3	-11.8	9.12	NEL	5
-2.0	-4.0	-2.0	14-112	-2.5	-1.5	-2.7	2.59	0.24	3	-2.8	-1.8	-2.8	2.49	0.19	2
-2.0	-4.0	-2.0	14-122	-3.0	3.9	-3.5	8.13	1.28	5	-19.8	3.3	-5.3	19.45	NEL	6
-2.0	-4.0	2.0	14-111	-1.9	-4.0	2.3	0.28	0.11	1	-2.3	-3.3	1.8	0.83	0.12	1
-2.0	-4.0	2.0	14-116	-1.9	-2.5	3.6	2.16	0.16	2	-2.3	-2.8	3.3	1.79	0.11	2
-2.0	-4.0	2.0	14-121	5.2	-4.0	5.9	8.20	0.65	5	-1.8	-3.8	1.8	0.43	0.10	1
-2.0	-4.0	6.0	14-110	-1.5	-2.8	6.0	1.26	0.12	2	-1.8	-3.3	5.8	0.83	0.07	1
-2.0	-4.0	6.0	14-115	-1.6	-2.9	6.1	1.18	0.10	2	-1.8	-3.8	5.8	0.43	0.05	1
-2.0	-4.0	6.0	14-120	-2.0	-3.2	6.2	0.85	0.14	1	-1.8	-3.3	5.8	0.83	0.11	1
2.0	-4.0	-10.0	14-129	2.6	-0.2	-6.5	5.20	0.58	4	10.8	0.3	-10.3	9.73	NEL	5
2.0	-4.0	-10.0	14-130	-96.0	4.0	-12.0	98.35	>10.00	6	-15.8	0.3	-11.3	18.29	NEL	6
2.0	-4.0	-10.0	14-136	-96.0	-4.0	-12.0	98.02	NaN	6	-4.8	-3.3	-5.8	8.01	NEL	5
2.0	-4.0	-10.0	14-141	-1.4	-4.0	-8.8	3.57	1.06	3	0.8	-3.8	-11.8	2.17	NEL	2
2.0	-4.0	-6.0	14-128	0.9	-0.5	-2.9	4.84	0.37	3	3.3	-1.8	-3.3	3.77	NEL	3
2.0	-4.0	-6.0	14-135	-3.1	-2.7	-4.7	5.47	0.30	4	-4.8	2.8	-11.3	10.89	NEL	6
2.0	-4.0	-6.0	14-140	-1.4	-4.0	-3.5	4.21	0.32	3	7.3	-3.3	-11.3	7.46	NEL	4
2.0	-4.0	-2.0	14-134	-1.6	-3.2	-1.2	3.80	0.16	3	-23.8	-3.8	3.8	26.39	NEL	6
2.0	-4.0	2.0	14-126	1.2	-2.3	1.9	1.85	0.22	2	1.3	-3.3	1.8	1.09	0.16	2
2.0	-4.0	2.0	14-132	-3.9	-0.9	-12.0	15.53	NaN	6	-1.3	-3.8	-5.8	8.41	NEL	5
2.0	-4.0	2.0	14-133	0.9	-2.2	2.2	2.11	0.15	2	0.8	-3.3	2.3	1.48	0.14	2
2.0	-4.0	2.0	14-138	1.0	-2.6	2.2	1.71	0.16	2	1.3	-3.3	1.8	1.09	0.07	2
2.0	-4.0	6.0	14-125	1.7	-2.8	6.2	1.30	0.17	2	1.8	-3.3	5.8	0.83	0.06	1
2.0	-4.0	6.0	14-131	1.5	-3.0	6.4	1.15	0.16	2	1.8	-3.3	5.8	0.83	0.10	1
2.0	-4.0	6.0	14-137	1.3	-3.1	6.6	1.27	0.12	2	2.8	-2.8	4.8	1.92	NEL	2
6.0	-4.0	-10.0	14-147	3.8	-4.0	-8.0	2.92	0.36	3	-17.8	-3.8	-6.3	24.05	NEL	6
6.0	-4.0	-10.0	14-152	-7.6	4.0	0.9	19.19	NaN	6	-0.8	3.8	-3.3	12.30	NEL	6
6.0	-4.0	-10.0	14-153	5.3	-4.0	-10.5	0.89	0.83	1	7.8	-0.3	-11.3	4.32	NEL	3
6.0	-4.0	-10.0	14-157	5.1	2.2	-8.3	6.51	0.42	4	1.8	3.8	-8.3	9.01	NEL	5
6.0	-4.0	-10.0	14-158	4.8	0.7	-8.9	4.94	1.01	3	-0.8	3.3	-11.8	10.06	NEL	6
6.0	-4.0	-6.0	14-145	80.0	4.0	-12.0	74.63	>10.00	6	3.3	3.8	-7.3	8.32	NEL	5
6.0	-4.0	-6.0	14-146	4.4	-1.3	-4.4	3.51	0.49	3	3.3	0.8	-5.8	5.49	NEL	4

Tab. B.42: SW I PLB b - "Front" - Crack, part 2: Coordinates of the pencil-lead breaks and estimated source locations determined using Geiger's method and *FastWay*. Estimated source locations excluded during the verification process (see Section 7.3.4) are shown in gray.

PLB			Set	Geiger's method						*FastWay*					
x [in]	y [in]	z [in]	#	x [in]	y [in]	z [in]	d [in]	eei [-]	ac [-]	x [in]	y [in]	z [in]	d [in]	eei [-]	ac [-]
6.0	-4.0	-2.0	14-151	3.8	-1.4	-0.3	3.79	0.11	3	3.3	-1.8	-1.3	3.63	0.11	3
6.0	-4.0	-2.0	14-156	3.9	-1.5	0.2	3.94	0.10	3	3.8	-0.8	-0.8	4.15	0.24	3
6.0	-4.0	2.0	14-143	9.8	4.0	-4.0	10.68	0.72	6	6.8	1.3	0.3	5.58	NEL	4
6.0	-4.0	2.0	14-150	5.7	-1.6	1.5	2.43	0.23	2	5.8	-2.3	1.8	1.79	0.11	2
6.0	-4.0	2.0	14-155	3.9	-1.3	2.7	3.50	0.12	3	4.8	0.3	1.3	4.49	NEL	3
6.0	-4.0	6.0	14-142	5.9	-2.4	5.7	1.64	0.13	2	5.8	-2.8	5.8	1.30	0.06	2
6.0	-4.0	6.0	14-148	5.0	-2.6	6.3	1.78	0.10	2	5.8	-2.3	5.3	1.92	0.15	2
6.0	-4.0	6.0	14-154	5.0	-2.6	6.3	1.74	0.09	2	5.8	-2.3	5.3	1.92	0.14	2
10.0	-4.0	-10.0	11-30	96.0	4.0	-12.0	86.39	>10.00	6	18.8	-3.8	-11.3	8.84	NEL	5
10.0	-4.0	-10.0	12-72	96.0	-4.0	-12.0	86.02	>10.00	6	9.8	-1.8	-9.8	2.28	0.09	2
10.0	-4.0	-10.0	12-73	12.2	1.5	-7.2	6.52	0.19	4	10.3	-1.3	-11.3	3.03	0.13	3
10.0	-4.0	-10.0	13-41	12.0	2.7	-9.4	7.04	0.24	4	10.3	0.3	-11.8	4.60	0.28	3
10.0	-4.0	-6.0	13-42	11.8	1.1	-8.7	6.05	0.17	4	10.3	-0.3	-6.3	3.77	0.40	3
10.0	-4.0	-6.0	14-167	7.6	2.7	-7.9	7.37	0.15	4	9.3	0.8	-7.8	5.12	0.08	4
10.0	-4.0	-2.0	14-161	8.5	-1.9	-2.9	2.73	0.28	3	8.8	0.3	-2.8	4.49	0.53	3
10.0	-4.0	-2.0	14-164	10.5	2.0	-4.5	6.51	0.14	4	10.3	-1.8	-5.3	3.96	0.23	3
10.0	-4.0	2.0	13-43	14.1	-0.2	3.6	5.81	0.30	4	10.3	-2.3	3.3	2.17	0.08	2
10.0	-4.0	2.0	14-160	10.7	0.9	1.1	5.08	0.11	4	10.8	-2.3	2.8	2.05	NEL	2
10.0	-4.0	2.0	14-163	10.8	0.7	1.1	4.81	0.14	3	11.3	-1.8	0.8	2.86	0.12	3
10.0	-4.0	2.0	14-166	11.0	0.4	1.0	4.60	0.15	3	11.3	-1.8	0.8	2.86	0.07	3
10.0	-4.0	6.0	14-159	12.9	-2.1	6.0	3.49	0.09	3	12.3	-1.8	6.8	3.27	0.11	3
10.0	-4.0	6.0	14-162	11.4	-2.2	5.7	2.33	0.10	2	11.3	-2.3	5.8	2.17	0.19	2
10.0	-4.0	6.0	14-165	11.6	-1.2	6.5	3.27	0.11	3	11.3	-1.3	6.8	3.11	0.12	3
14.0	-4.0	-10.0	10-20	16.2	-4.0	-12.0	3.01	0.44	3	11.8	-3.8	-11.8	2.86	0.24	3
14.0	-4.0	-10.0	10-21	14.1	-1.7	-5.7	4.92	NaN	3	13.3	-1.8	-5.8	4.87	0.05	3
14.0	-4.0	-10.0	10-24	14.1	-1.7	-6.4	4.28	NaN	3	13.8	-1.8	-6.3	4.38	0.05	3
14.0	-4.0	-6.0	10-23	-24.0	-4.0	-12.0	38.43	8.14	6	18.8	-3.8	-9.8	6.06	NEL	4
14.0	-4.0	-2.0	10-22	-5.8	-4.0	-12.0	22.21	5.13	6	10.3	-2.3	-10.3	9.23	NEL	5
14.0	-4.0	-2.0	11-32	2.7	0.7	-12.0	15.79	NaN	6	10.3	-1.3	-7.3	7.01	NEL	4
14.0	-4.0	-2.0	11-33	18.5	-2.7	-1.2	4.76	0.25	3	10.3	-2.3	-9.8	8.79	NEL	5
14.0	-4.0	2.0	13-45	15.2	-1.9	2.0	2.39	0.13	2	12.8	-2.8	1.8	1.79	0.09	2
14.0	-4.0	2.0	13-47	17.6	-1.9	3.8	4.57	0.17	3	12.8	-1.8	1.3	2.68	NEL	3
14.0	-4.0	2.0	13-49	14.3	-1.0	0.6	3.33	0.14	3	14.3	-1.8	1.3	2.38	0.37	2
14.0	-4.0	6.0	13-44	14.3	-2.4	5.9	1.64	0.09	2	13.8	-2.3	6.3	1.79	0.11	2
14.0	-4.0	6.0	13-46	16.1	-1.5	7.6	3.70	0.17	3	13.8	-2.3	6.3	1.79	0.07	2
14.0	-4.0	6.0	13-48	14.2	-2.2	6.0	1.79	0.09	2	13.8	-2.3	6.3	1.79	0.09	2
14.0	-4.0	6.0	13-50	17.8	-2.3	6.0	4.21	0.10	3	17.8	-2.3	6.3	4.15	0.13	3
18.0	-4.0	-10.0	9-20	17.1	-1.7	-8.5	2.95	0.64	3	16.8	0.8	-11.3	5.07	NEL	4
18.0	-4.0	-6.0	10-27	-13.1	-4.0	-12.0	31.63	9.84	6	15.3	0.3	-9.3	6.02	NEL	4
18.0	-4.0	-6.0	10-28	7.9	-2.9	2.4	13.14	NaN	6	20.3	-3.8	-1.8	4.82	NEL	3
18.0	-4.0	-6.0	10-31	7.6	-4.0	5.2	15.25	NaN	6	13.3	-3.3	-11.8	7.50	NEL	4
18.0	-4.0	-2.0	10-26	23.4	-2.7	-1.1	5.58	0.45	4	11.8	-0.3	-11.8	12.17	NEL	6
18.0	-4.0	-2.0	10-30	86.7	-0.8	2.1	68.94	4.26	6	19.8	-2.3	-2.3	2.49	1.00	2
18.0	-4.0	2.0	12-74	17.4	-1.9	1.4	2.25	0.11	2	17.3	-2.8	1.8	1.48	0.20	2
18.0	-4.0	2.0	12-76	17.5	-2.2	1.3	2.02	0.12	2	17.3	-3.3	1.8	1.09	0.23	2
18.0	-4.0	2.0	12-77	17.2	-1.8	1.5	2.36	0.11	2	17.3	-2.8	1.8	1.48	0.22	2
18.0	-4.0	6.0	12-75	22.3	-1.4	7.8	5.38	0.31	4	17.8	-2.8	5.8	1.30	0.07	2

Tab. B.43: SW I PLB b - "Front" - Crack, part 3: Coordinates of the pencil-lead breaks and estimated source locations determined using Geiger's method and *FastWay*. Estimated source locations excluded during the verification process (see Section 7.3.4) are shown in gray.

PLB			Set	Geiger's method						*FastWay*					
x [in]	y [in]	z [in]	#	x [in]	y [in]	z [in]	d [in]	eei [-]	ac [-]	x [in]	y [in]	z [in]	d [in]	eei [-]	ac [-]
18.0	-4.0	6.0	13-51	17.7	-2.2	6.0	1.81	0.09	2	17.3	-2.3	6.3	1.92	0.14	2
22.0	-4.0	-10.0	8-7	96.0	4.0	-12.0	74.46	NaN	6	23.8	3.8	-11.8	8.14	0.53	5
22.0	-4.0	-10.0	9-23	27.8	-0.2	-12.0	7.20	3.19	4	23.8	-0.3	-11.3	4.32	0.65	3
22.0	-4.0	-10.0	10-35	96.0	12.0	-12.0	75.74	NaN	6	20.3	0.8	-11.8	5.36	0.33	4
22.0	-4.0	-10.0	10-38	17.2	-1.5	0.4	11.72	NaN	6	23.8	-0.3	-11.3	4.32	0.45	3
22.0	-4.0	-10.0	10-50	29.5	-0.5	-2.2	11.40	1.84	6	23.8	-0.3	-10.8	4.21	0.48	3
22.0	-4.0	-6.0	10-45	22.9	-0.8	-11.9	6.72	5.15	4	23.8	-0.8	-10.3	5.63	0.49	4
22.0	-4.0	-6.0	10-49	92.1	-1.5	12.0	72.40	6.26	6	20.8	-2.3	-2.3	4.32	NEL	3
22.0	-4.0	-2.0	10-34	18.9	-0.8	-2.0	4.46	0.12	3	18.8	-1.3	-1.3	4.32	0.10	3
22.0	-4.0	-2.0	10-40	20.0	-0.6	-2.0	3.90	0.23	3	23.8	-3.8	-2.8	1.92	0.21	2
22.0	-4.0	2.0	9-24	96.0	4.0	-12.0	75.74	NaN	6	22.3	-0.8	-7.8	10.28	NEL	6
22.0	-4.0	2.0	10-36	20.9	-1.7	1.4	2.60	0.12	3	21.3	-2.3	1.8	1.92	0.20	2
22.0	-4.0	2.0	10-39	1.0	-0.5	2.9	21.33	NaN	6	14.8	3.8	-3.8	12.07	NEL	6
22.0	-4.0	2.0	10-48	20.7	-1.9	1.7	2.51	0.12	3	20.8	-2.3	2.3	2.17	0.21	2
22.0	-4.0	6.0	9-22	25.7	-2.0	-2.6	9.57	NaN	5	23.8	-0.8	-10.8	17.15	0.67	6
22.0	-4.0	6.0	10-41	22.0	-2.0	6.1	2.01	0.10	2	21.8	-2.3	5.8	1.79	0.09	2
22.0	-4.0	6.0	10-43	19.6	-1.7	2.3	4.97	NaN	3	19.8	-2.3	2.3	4.71	0.07	3
22.0	-4.0	6.0	10-46	50.1	2.3	12.0	29.41	1.54	6	23.8	-0.8	8.3	4.32	NEL	3
22.0	-4.0	6.0	11-37	22.4	-1.9	6.5	2.17	0.10	2	22.3	-2.3	6.3	1.79	0.11	2
22.0	-4.0	6.0	11-38	22.4	-1.9	6.5	2.19	0.10	2	22.3	-2.3	6.3	1.79	0.10	2
22.0	-4.0	6.0	12-78	22.0	-2.0	6.5	2.05	0.10	2	21.8	-2.3	6.3	1.79	0.13	2

Tab. B.44: SW I PLB b - "Front" - Crack, part 4: Coordinates of the pencil-lead breaks and estimated source locations determined using Geiger's method and *FastWay*. Estimated source locations excluded during the verification process (see Section 7.3.4) are shown in gray.

B.4.4 Back

PLB			Set	Geiger's method						*FastWay*					
x [in]	y [in]	z [in]	#	x [in]	y [in]	z [in]	d [in]	eei [-]	ac [-]	x [in]	y [in]	z [in]	d [in]	eei [-]	ac [-]
-22.0	4.0	-10.0	8-10	-56.9	3.5	3.0	37.18	NaN	6	-18.8	0.8	-11.3	4.76	0.95	3
-22.0	4.0	-6.0	10-67	-21.4	3.5	-4.6	1.63	NaN	2	-23.3	3.8	-4.8	1.79	0.10	2
-22.0	4.0	-6.0	10-69	-17.9	2.3	-5.0	4.56	NaN	3	-20.3	2.8	-4.8	2.49	NEL	2
-22.0	4.0	-2.0	11-63	-16.5	2.3	-2.7	5.78	NaN	4	-17.8	2.8	-2.3	4.44	0.05	3
-22.0	4.0	-2.0	11-65	96.0	-4.0	-12.0	118.69	NaN	6	-23.8	2.3	1.3	4.09	0.97	3
-22.0	4.0	-2.0	11-67	-96.0	-4.0	-12.0	75.10	>10.00	6	-3.8	-1.3	-7.8	19.84	NEL	6
-22.0	4.0	2.0	11-62	-23.8	2.1	0.8	2.83	0.20	3	-20.3	2.8	1.3	2.28	0.18	2
-22.0	4.0	2.0	11-66	-17.8	2.8	1.3	4.39	0.09	3	-20.3	2.8	1.8	2.17	0.20	2
-22.0	4.0	2.0	12-117	-23.7	2.1	1.0	2.79	0.20	3	-23.8	0.8	0.3	4.09	0.31	3
-22.0	4.0	6.0	11-61	-21.1	2.7	5.9	1.58	0.11	2	-21.8	2.8	5.8	1.30	0.15	2
-22.0	4.0	6.0	11-64	-21.6	2.6	5.7	1.45	0.09	2	-21.8	2.3	5.8	1.79	0.21	2
-22.0	4.0	6.0	12-118	-21.5	2.5	6.0	1.62	0.10	2	-21.8	2.3	5.8	1.79	0.13	2
-18.0	4.0	-10.0	10-71	-29.9	-4.0	-12.0	14.47	4.06	6	-20.8	-0.8	-11.8	5.76	NEL	4
-18.0	4.0	-6.0	9-26	-96.0	-4.0	-12.0	78.64	>10.00	6	-14.3	-3.3	-8.3	8.47	NEL	5
-18.0	4.0	-6.0	9-29	14.1	3.3	-12.0	32.67	NaN	6	-19.3	0.3	-11.8	6.98	0.26	4
-18.0	4.0	-2.0	11-68	-9.0	-4.0	-12.0	15.65	1.40	6	-23.8	3.3	-4.3	6.22	0.43	4
-18.0	4.0	-2.0	11-70	-24.0	-0.9	-7.5	9.51	0.75	5	-13.3	-1.3	-8.8	9.78	0.16	5
-18.0	4.0	2.0	12-120	-19.9	2.2	1.1	2.77	0.17	3	-17.3	2.8	1.3	1.64	0.12	2
-18.0	4.0	2.0	12-122	-21.1	2.0	1.6	3.68	0.17	3	-23.8	3.3	1.3	5.85	0.14	4
-18.0	4.0	2.0	12-123	-15.3	2.8	1.3	2.99	0.19	3	-17.3	2.3	1.8	1.92	0.14	2
-18.0	4.0	6.0	12-119	-18.5	2.5	6.2	1.63	0.11	2	-17.8	2.8	5.8	1.30	0.10	2
-18.0	4.0	6.0	12-121	-18.1	2.8	6.3	1.23	0.10	2	-18.3	2.3	6.3	1.79	0.19	2
-14.0	4.0	-10.0	11-71	-7.4	-4.0	-12.0	10.56	5.09	6	-17.3	-1.8	-11.3	6.72	NEL	4
-14.0	4.0	-10.0	11-72	-18.1	1.7	-5.9	6.27	0.48	4	-13.8	-1.8	-11.8	6.02	0.34	4
-14.0	4.0	-10.0	11-74	-96.0	-4.0	-12.0	82.41	>10.00	6	-19.3	-3.3	-6.3	9.71	0.59	5
-14.0	4.0	-6.0	12-124	-17.3	0.8	-3.6	5.16	0.29	4	-13.8	-2.3	-8.8	6.83	0.28	4
-14.0	4.0	-6.0	12-126	-18.1	1.3	-5.2	4.99	0.46	3	-13.8	-2.3	-10.8	7.85	0.60	5
-14.0	4.0	-2.0	12-125	-14.0	1.8	-2.2	2.16	0.21	2	-10.3	-2.3	-7.3	8.98	NEL	5
-14.0	4.0	-2.0	12-127	-10.3	-0.6	-5.6	6.92	0.45	4	-14.8	-2.8	-7.3	8.58	NEL	5
-14.0	4.0	-2.0	13-81	96.0	-4.0	-12.0	110.74	NaN	6	-10.3	-2.3	-7.3	8.98	NEL	5
-14.0	4.0	2.0	14-225	-18.2	2.2	3.0	4.67	0.22	3	-12.8	1.8	2.3	2.59	0.04	3
-14.0	4.0	2.0	14-227	-14.9	2.0	2.8	2.33	0.17	2	-11.8	2.3	1.8	2.86	0.05	3
-14.0	4.0	2.0	14-229	-13.8	1.7	2.9	2.47	0.12	2	-13.3	1.3	2.8	2.95	0.12	3
-14.0	4.0	6.0	13-80	-96.0	-12.0	-12.0	85.46	NaN	6	-13.8	4.8	8.3	2.38	NEL	2
-14.0	4.0	6.0	14-224	-14.2	2.5	6.9	1.75	0.10	2	-14.3	2.3	6.8	1.92	0.07	2
-14.0	4.0	6.0	14-226	-14.0	2.1	4.7	2.37	0.10	2	-13.8	1.8	4.3	2.86	0.09	3
-14.0	4.0	6.0	14-228	-14.2	2.2	6.7	1.93	0.09	2	-14.3	1.8	6.8	2.38	0.18	2
-10.0	4.0	-10.0	13-83	-96.0	-4.0	-12.0	86.39	>10.00	6	-14.8	-3.3	-11.8	8.84	NEL	5
-10.0	4.0	-6.0	13-82	-10.1	0.5	-5.7	3.47	0.25	3	-10.8	3.8	-5.3	1.09	0.35	2
-10.0	4.0	-6.0	13-84	-10.1	-4.0	-4.5	8.13	0.18	5	-10.8	-3.3	-6.8	7.33	0.45	4
-10.0	4.0	-6.0	13-85	-3.3	4.0	-3.5	7.19	0.17	4	-5.8	3.8	-5.3	4.32	0.68	3
-10.0	4.0	-6.0	13-87	-12.8	-1.0	-5.5	5.72	0.51	4	-10.3	3.3	-4.8	1.48	0.08	2
-10.0	4.0	-2.0	14-232	-12.8	-3.4	-1.1	7.98	0.32	5	-23.8	-3.3	-5.8	15.99	NEL	6
-10.0	4.0	-2.0	14-235	-10.6	-2.5	-0.8	6.63	0.15	4	-13.8	3.8	-5.8	5.31	NEL	4
-10.0	4.0	-2.0	14-238	-8.6	-1.3	-1.2	5.55	0.21	4	-23.8	1.8	6.8	16.45	NEL	6
-10.0	4.0	2.0	14-234	-11.7	-0.0	4.1	4.81	0.20	3	-13.3	-0.8	4.8	6.38	0.18	4
-10.0	4.0	2.0	14-237	-12.5	1.1	4.0	4.36	0.14	3	-12.3	1.3	3.3	3.77	0.25	3

Tab. B.45: SW I PLB b - "Back" - Crack, part 1: Coordinates of the pencil-lead breaks and estimated source locations determined using Geiger's method and *FastWay*. Estimated source locations excluded during the verification process (see Section 7.3.4) are shown in gray.

PLB			Set	Geiger's method						*FastWay*					
x [in]	y [in]	z [in]	#	x [in]	y [in]	z [in]	d [in]	eei [-]	ac [-]	x [in]	y [in]	z [in]	d [in]	eei [-]	ac [-]
-10.0	4.0	6.0	13-86	15.9	12.0	12.0	27.73	NaN	6	-4.8	8.3	11.8	8.87	NEL	5
-10.0	4.0	6.0	14-230	-9.8	2.0	7.1	2.26	0.10	2	-10.3	2.3	6.8	1.92	0.11	2
-10.0	4.0	6.0	14-231	-12.2	0.6	4.9	4.24	0.14	3	-14.3	3.3	5.3	4.38	0.45	3
-10.0	4.0	6.0	14-233	-9.4	2.0	6.5	2.18	0.10	2	-9.3	2.3	6.3	1.92	0.17	2
-10.0	4.0	6.0	14-236	-11.5	2.8	7.5	2.47	0.12	2	-11.8	2.8	7.3	2.49	0.14	2
-6.0	4.0	-10.0	12-129	96.0	12.0	-12.0	102.33	NaN	6	9.3	3.3	-5.8	15.85	NEL	6
-6.0	4.0	-10.0	12-131	3.3	-3.4	2.6	17.34	NaN	6	-4.8	-2.8	-8.3	7.08	NEL	4
-6.0	4.0	-6.0	14-243	-6.7	-4.0	-3.3	8.46	0.27	5	-4.3	-3.3	-3.3	7.95	NEL	5
-6.0	4.0	-6.0	14-248	96.0	-4.0	-12.0	102.49	>10.00	6	-10.3	-2.3	-7.3	7.66	NEL	5
-6.0	4.0	-6.0	14-252	-10.1	-0.2	-3.4	6.43	0.52	4	-18.3	-3.3	-6.8	14.25	NEL	6
-6.0	4.0	-2.0	14-242	-5.2	-3.5	0.5	7.93	0.14	5	-3.3	-2.8	0.3	7.63	0.02	5
-6.0	4.0	-2.0	14-247	-7.3	-0.1	-1.8	4.34	0.24	3	-13.3	3.3	-6.3	8.44	0.44	5
-6.0	4.0	-2.0	14-251	-6.3	0.6	2.6	5.74	0.11	4	-7.3	0.8	2.3	5.49	0.09	4
-6.0	4.0	-2.0	14-253	-5.0	-4.0	-2.0	8.06	0.19	5	-5.8	-3.8	-5.8	8.61	0.37	5
-6.0	4.0	2.0	14-241	-5.8	-0.1	3.2	4.31	0.11	3	-7.3	0.3	2.3	3.96	0.09	3
-6.0	4.0	2.0	14-246	-0.6	-3.7	6.6	10.46	0.21	6	-7.3	0.3	2.8	4.02	0.06	3
-6.0	4.0	2.0	14-250	-6.7	-0.4	2.8	4.51	0.11	3	-7.3	0.3	2.8	4.02	0.07	3
-6.0	4.0	6.0	14-239	-6.4	1.8	6.1	2.19	0.10	2	-6.8	2.3	5.8	1.92	0.15	2
-6.0	4.0	6.0	14-240	-96.0	12.0	12.0	90.55	NaN	6	-4.8	5.8	8.3	3.11	0.17	3
-6.0	4.0	6.0	14-244	-6.9	1.9	5.7	2.33	0.14	2	-7.3	1.8	5.8	2.59	NEL	3
-6.0	4.0	6.0	14-249	-7.5	2.0	5.4	2.52	0.11	3	-7.8	2.3	5.3	2.59	0.08	3
-2.0	4.0	-10.0	14-263	-3.6	0.3	-6.1	5.62	1.14	4	-11.8	-2.3	-8.8	11.65	NEL	6
-2.0	4.0	-6.0	14-257	-8.8	0.8	-6.6	7.54	0.37	5	-21.3	3.3	-7.3	19.31	NEL	6
-2.0	4.0	-6.0	14-262	-4.6	-3.0	-5.5	7.48	0.48	4	-0.3	-0.3	-8.3	5.12	NEL	4
-2.0	4.0	-6.0	14-267	-3.4	-2.3	-6.0	6.44	0.29	4	-23.3	2.3	-9.3	21.57	NEL	6
-2.0	4.0	-2.0	14-256	2.4	-0.7	-2.8	6.50	0.36	4	4.8	3.8	-5.3	7.50	NEL	4
-2.0	4.0	-2.0	14-261	-5.0	-4.0	6.2	11.81	0.89	6	-6.3	-1.8	1.8	8.07	NEL	5
-2.0	4.0	-2.0	14-266	-4.6	3.3	-0.6	3.02	0.31	3	-3.3	1.8	-1.3	2.68	0.77	3
-2.0	4.0	2.0	14-255	-0.1	0.8	2.3	3.72	0.35	3	-1.3	2.3	1.8	1.92	0.05	2
-2.0	4.0	2.0	14-260	-4.0	4.0	3.2	2.38	0.24	2	-10.8	3.8	7.3	10.21	NEL	6
-2.0	4.0	2.0	14-265	-9.8	1.7	6.1	9.11	2.34	5	-0.3	2.8	1.3	2.28	0.03	2
-2.0	4.0	6.0	14-254	-2.1	2.9	6.4	1.20	0.10	2	-2.8	3.3	6.3	1.09	0.21	2
-2.0	4.0	6.0	14-259	-1.4	2.5	6.2	1.64	0.10	2	-1.8	1.8	5.8	2.28	0.10	2
-2.0	4.0	6.0	14-264	-2.3	3.5	6.3	0.63	0.10	1	-2.8	3.8	6.8	1.09	0.36	2
2.0	4.0	-10.0	12-132	-0.3	-4.0	-1.3	12.04	0.59	6	-6.8	3.3	-8.8	8.87	NEL	5
2.0	4.0	-10.0	13-89	-1.5	-0.7	-6.5	6.87	0.43	4	6.8	-2.3	-9.8	7.85	NEL	5
2.0	4.0	-6.0	13-90	0.0	-3.5	-7.3	7.82	0.41	5	-0.3	-3.8	-6.8	8.10	NEL	5
2.0	4.0	-6.0	14-276	2.0	-1.8	-3.5	6.26	0.26	4	0.8	-0.3	-3.8	4.97	0.05	3
2.0	4.0	-6.0	14-282	1.5	-3.0	-6.1	7.04	0.44	4	-0.3	-1.3	-6.8	5.76	NEL	4
2.0	4.0	-2.0	14-271	2.0	0.6	-1.0	3.52	0.50	3	1.3	1.8	-1.3	2.49	0.05	2
2.0	4.0	-2.0	14-272	-2.6	-1.0	-2.6	6.81	0.23	4	-1.8	3.8	-5.3	4.97	0.08	3
2.0	4.0	-2.0	14-275	1.0	2.5	-1.2	2.00	0.10	2	0.8	1.3	-0.8	3.27	0.07	3
2.0	4.0	-2.0	14-281	1.1	-0.6	-0.5	4.91	0.54	3	3.3	3.8	-3.3	1.79	0.23	2
2.0	4.0	2.0	14-270	1.7	1.9	2.9	2.32	0.22	2	1.8	1.8	2.8	2.38	0.05	2
2.0	4.0	2.0	14-274	1.7	2.1	2.3	1.95	0.13	2	1.8	1.8	2.3	2.28	0.05	2
2.0	4.0	2.0	14-279	2.1	2.9	2.3	1.11	0.14	2	1.8	2.3	2.3	1.79	0.07	2
2.0	4.0	6.0	14-269	1.9	2.4	6.0	1.64	0.12	2	1.8	2.3	5.8	1.79	0.16	2
2.0	4.0	6.0	14-273	1.4	1.7	6.5	2.44	0.09	2	0.8	1.3	6.3	3.03	0.08	3
2.0	4.0	6.0	14-277	1.7	2.1	6.3	1.89	0.09	2	1.8	1.8	5.8	2.28	0.10	2

Tab. B.46: SW I PLB b - "Back" - Crack, part 2: Coordinates of the pencil-lead breaks and estimated source locations determined using Geiger's method and *FastWay*. Estimated source locations excluded during the verification process (see Section 7.3.4) are shown in gray.

PLB			Set	Geiger's method						*FastWay*					
x [in]	y [in]	z [in]	#	x [in]	y [in]	z [in]	d [in]	eei [-]	ac [-]	x [in]	y [in]	z [in]	d [in]	eei [-]	ac [-]
6.0	4.0	-10.0	13-93	1.2	2.7	-9.0	5.08	0.57	4	-14.8	3.8	-4.8	21.41	NEL	6
6.0	4.0	-10.0	13-94	4.3	-4.0	-9.6	8.20	0.52	5	4.3	-3.8	-8.8	8.04	0.90	5
6.0	4.0	-10.0	13-95	3.8	-3.0	-9.7	7.40	0.47	4	-14.3	1.8	-5.3	20.92	NEL	6
6.0	4.0	-6.0	13-92	-1.4	4.0	-12.0	9.52	2.10	5	5.8	2.8	-6.8	1.48	0.21	2
6.0	4.0	-2.0	14-291	1.7	-2.4	0.6	8.14	0.29	5	-1.3	3.8	-2.3	7.26	0.41	4
6.0	4.0	-2.0	14-293	2.5	-4.0	-1.9	8.75	0.18	5	2.3	-3.8	-2.3	8.61	0.66	5
6.0	4.0	-2.0	14-297	3.7	-3.6	0.5	8.28	0.22	5	4.3	-0.8	-0.3	5.36	0.05	4
6.0	4.0	-2.0	14-299	3.6	-0.8	-2.6	5.43	0.19	4	3.8	-2.8	-2.3	7.12	0.24	4
6.0	4.0	2.0	14-285	5.5	2.6	2.2	1.49	0.09	2	5.3	1.8	2.3	2.38	0.10	2
6.0	4.0	2.0	14-286	3.5	1.3	-1.2	4.87	0.12	3	2.8	-0.8	-0.3	6.18	0.12	4
6.0	4.0	2.0	14-289	4.1	-0.4	2.4	4.79	0.13	3	-2.3	-3.3	7.8	12.40	NEL	6
6.0	4.0	2.0	14-296	4.4	0.8	2.5	3.63	0.15	3	5.3	1.8	1.8	2.38	0.20	2
6.0	4.0	6.0	14-283	4.6	1.1	7.2	3.40	0.13	3	5.3	1.3	6.3	2.86	0.20	3
6.0	4.0	6.0	14-284	5.5	5.2	9.1	3.41	0.12	3	5.3	5.3	8.3	2.68	0.17	3
6.0	4.0	6.0	14-287	5.5	2.4	7.0	1.96	0.13	2	5.3	2.3	6.3	1.92	0.14	2
6.0	4.0	6.0	14-288	35.5	12.0	12.0	31.12	5.83	6	11.8	5.8	11.8	8.32	NEL	5
6.0	4.0	6.0	14-294	4.8	1.8	6.8	2.68	0.09	3	5.8	2.8	5.3	1.48	0.09	2
10.0	4.0	-10.0	13-96	10.0	4.0	-12.0	2.00	0.73	2	10.3	0.8	-11.8	3.70	0.40	3
10.0	4.0	-10.0	13-98	10.4	-4.0	-3.6	10.25	0.48	6	10.3	-1.8	-8.3	6.02	0.56	4
10.0	4.0	-10.0	14-311	9.3	-4.0	-4.2	9.89	0.48	5	10.3	0.8	-11.8	3.70	0.41	3
10.0	4.0	-6.0	12-136	13.0	-4.0	-12.0	10.45	0.78	6	10.3	3.8	-8.8	2.77	0.25	3
10.0	4.0	-6.0	14-303	8.9	-4.0	-0.4	9.84	0.49	5	9.3	2.3	-8.3	2.95	NEL	3
10.0	4.0	-6.0	14-307	96.0	-4.0	-12.0	86.58	>10.00	6	15.8	-0.3	-3.3	7.66	0.04	5
10.0	4.0	-2.0	14-302	9.9	4.0	-4.1	2.06	0.11	2	9.3	3.3	-1.8	1.09	0.51	2
10.0	4.0	-2.0	14-306	9.8	3.1	-2.2	0.97	0.12	1	9.3	1.8	-1.3	2.49	0.21	2
10.0	4.0	-2.0	14-310	7.2	-3.0	-1.9	7.53	0.22	5	8.3	-3.8	-1.3	7.98	NEL	5
10.0	4.0	2.0	14-301	9.6	1.0	1.0	3.22	0.17	3	9.3	3.3	1.3	1.30	0.12	2
10.0	4.0	2.0	14-305	9.5	1.4	-0.3	3.52	0.13	3	8.8	2.8	0.3	2.49	0.13	2
10.0	4.0	2.0	14-309	9.1	2.5	1.5	1.82	0.11	2	8.3	2.3	1.8	2.49	0.12	2
10.0	4.0	6.0	13-97	6.5	2.8	6.0	3.73	NaN	3	12.3	3.8	11.8	6.18	NEL	4
10.0	4.0	6.0	14-300	9.9	1.6	3.7	3.39	0.14	3	10.3	1.8	3.8	3.19	0.31	3
10.0	4.0	6.0	14-304	9.8	2.3	6.0	1.69	0.10	2	9.3	1.8	5.8	2.38	0.04	2
10.0	4.0	6.0	14-308	9.4	1.7	6.0	2.39	0.13	2	9.3	1.8	6.3	2.38	0.15	2
14.0	4.0	-10.0	10-77	-96.0	-4.0	-12.0	110.31	>10.00	6	11.3	-3.3	-11.8	7.95	0.46	5
14.0	4.0	-6.0	10-76	9.0	4.0	-12.0	7.78	NaN	5	16.8	3.8	-9.8	4.66	NEL	3
14.0	4.0	-6.0	12-140	21.7	-1.2	-6.4	9.34	0.16	5	20.8	-1.3	-4.3	8.73	0.16	5
14.0	4.0	-2.0	10-78	16.5	0.7	-1.0	4.30	0.18	3	14.3	1.8	-0.8	2.59	0.03	3
14.0	4.0	-2.0	10-80	14.6	3.0	-1.9	1.21	0.16	2	14.3	1.8	-0.8	2.59	0.04	3
14.0	4.0	-2.0	11-77	17.5	-0.2	-0.9	5.59	0.25	4	14.3	1.8	-0.8	2.59	0.03	3
14.0	4.0	2.0	12-138	15.9	0.0	2.0	4.41	0.19	3	14.3	1.8	2.3	2.28	0.02	2
14.0	4.0	2.0	12-139	15.1	1.9	2.1	2.38	0.13	2	14.3	2.3	2.3	1.79	0.08	2
14.0	4.0	2.0	12-142	15.8	1.1	2.3	3.47	0.14	3	14.8	2.3	2.8	2.05	0.11	2
14.0	4.0	6.0	12-137	19.7	6.1	10.3	7.41	1.21	4	14.3	4.8	8.8	2.86	0.06	3
14.0	4.0	6.0	12-141	14.1	2.3	5.8	1.70	0.11	2	13.8	2.3	5.8	1.79	0.19	2
14.0	4.0	6.0	13-99	14.3	1.9	6.2	2.11	0.11	2	12.3	2.8	4.8	2.49	NEL	2
14.0	4.0	6.0	13-100	14.2	2.3	5.8	1.75	0.10	2	13.8	2.3	5.8	1.79	0.20	2
18.0	4.0	-10.0	9-33	26.0	-4.0	-8.2	11.44	1.35	6	23.8	-2.3	-7.3	8.93	NEL	5
18.0	4.0	-10.0	9-34	-39.5	-4.0	-12.0	58.13	9.04	6	23.8	-0.8	-10.3	7.46	0.43	4
18.0	4.0	-6.0	9-32	21.1	-1.0	-5.1	6.00	0.45	4	18.3	1.3	-3.8	3.56	0.10	3

Tab. B.47: SW I PLB b - "Back" - Crack, part 3: Coordinates of the pencil-lead breaks and estimated source locations determined using Geiger's method and *FastWay*. Estimated source locations excluded during the verification process (see Section 7.3.4) are shown in gray.

PLB			Set	Geiger's method						*FastWay*					
x [in]	y [in]	z [in]	#	x [in]	y [in]	z [in]	d [in]	eei [-]	ac [-]	x [in]	y [in]	z [in]	d [in]	eei [-]	ac [-]
18.0	4.0	-6.0	9-36	13.3	-0.0	-0.3	8.46	NaN	5	23.8	-2.3	-7.8	8.67	NEL	5
18.0	4.0	-6.0	10-85	24.4	-1.3	-3.7	8.58	0.41	5	23.8	-0.3	-6.8	7.19	NEL	4
18.0	4.0	-2.0	9-35	28.2	-2.6	-1.2	12.17	1.27	6	21.3	-0.3	-3.8	5.63	NEL	4
18.0	4.0	-2.0	10-84	21.4	0.4	-2.2	4.95	0.59	3	18.8	1.8	-1.3	2.49	0.06	2
18.0	4.0	-2.0	10-87	21.5	0.4	-2.4	5.05	0.52	4	19.8	1.3	-1.3	3.34	NEL	3
18.0	4.0	2.0	10-82	20.4	1.1	-1.8	5.30	0.31	4	17.8	2.3	-1.3	3.70	0.07	3
18.0	4.0	2.0	11-82	19.4	1.4	1.5	3.01	0.17	3	17.8	2.8	2.3	1.30	0.06	2
18.0	4.0	2.0	11-84	18.2	2.8	2.2	1.24	0.11	2	17.8	2.8	2.3	1.30	0.09	2
18.0	4.0	2.0	11-87	27.2	4.0	5.2	9.73	0.48	5	18.3	2.3	2.3	1.79	0.07	2
18.0	4.0	6.0	12-143	18.2	2.7	6.2	1.36	0.10	2	18.3	2.8	6.3	1.30	0.16	2
18.0	4.0	6.0	12-144	18.0	2.6	5.9	1.38	0.09	2	17.8	2.8	5.8	1.30	0.14	2
18.0	4.0	6.0	12-145	18.3	2.5	6.4	1.57	0.09	2	18.3	2.8	6.3	1.30	0.17	2
22.0	4.0	-10.0	8-13	96.0	4.0	-12.0	74.03	NaN	6	23.8	0.3	-8.3	4.49	0.14	3
22.0	4.0	-10.0	9-38	13.6	1.0	0.0	13.47	NaN	6	23.8	-0.3	-8.3	4.92	0.46	3
22.0	4.0	-6.0	10-90	45.8	-4.0	-10.5	25.56	1.82	6	23.8	3.8	-8.3	2.86	0.55	3
22.0	4.0	-6.0	10-96	23.8	-2.0	-8.7	6.78	0.70	4	23.8	-0.3	-8.3	5.12	NEL	4
22.0	4.0	-2.0	9-37	20.3	-2.0	1.1	6.98	NaN	4	23.8	3.3	-7.3	5.58	0.57	4
22.0	4.0	-2.0	10-89	96.0	4.0	-12.0	74.67	>10.00	6	23.8	3.3	-2.8	2.05	0.06	2
22.0	4.0	-2.0	10-95	33.4	-2.8	-8.6	14.79	1.21	6	23.8	1.3	-5.3	4.60	NEL	3
22.0	4.0	2.0	10-88	65.3	4.0	-3.4	43.63	2.44	6	22.8	3.3	2.8	1.30	0.05	2
22.0	4.0	2.0	10-92	96.0	4.0	-12.0	75.31	>10.00	6	21.8	2.3	-1.3	3.70	0.04	3
22.0	4.0	2.0	10-94	96.0	4.0	-12.0	75.31	>10.00	6	23.8	3.3	-2.3	4.66	0.06	3
22.0	4.0	6.0	10-91	39.5	4.0	6.6	17.55	1.18	6	21.8	2.8	2.3	3.96	0.08	3
22.0	4.0	6.0	10-93	23.8	3.2	2.1	4.38	0.11	3	22.3	2.8	2.3	3.96	0.14	3
22.0	4.0	6.0	11-89	25.6	3.3	6.9	3.80	0.22	3	21.8	3.3	6.8	1.09	0.14	2
22.0	4.0	6.0	12-146	26.5	2.2	5.0	4.96	0.22	3	22.3	0.8	4.8	3.49	NEL	3
22.0	4.0	6.0	12-147	21.5	3.2	6.6	1.16	0.08	2	22.3	3.8	7.3	1.30	0.11	2

Tab. B.48: SW I PLB b - "Back" - Crack, part 4: Coordinates of the pencil-lead breaks and estimated source locations determined using Geiger's method and *FastWay*. Estimated source locations excluded during the verification process (see Section 7.3.4) are shown in gray.

Appendix C

Large T-shaped concrete beam SW II

C.1 Pencil-lead breaks SW IIa

C.1.1 Top

PLB			Set	Geiger's method						*FastWay*					
x [in]	y [in]	z [in]	#	x [in]	y [in]	z [in]	d [in]	eei [-]	ac [-]	x [in]	y [in]	z [in]	d [in]	eei [-]	ac [-]
26.0	-10.0	12.0	9-3	19.2	-8.0	10.8	7.21	1.27	4	25.8	-11.8	9.3	3.27	NEL	3
26.0	-10.0	12.0	9-5	24.8	-8.4	11.7	2.04	0.48	2	25.8	-11.8	9.3	3.27	NEL	3
26.0	-10.0	12.0	11-4	-96.0	-4.0	-12.0	124.48	>10.00	6	25.8	-11.8	9.3	3.27	0.18	3
26.0	-6.0	12.0	9-4	-96.0	-4.0	-12.0	124.35	>10.00	6	25.8	-6.8	10.8	1.48	NEL	2
26.0	-6.0	12.0	10-1	-96.0	-4.0	-12.0	124.35	>10.00	6	25.3	-6.8	10.8	1.64	NEL	2
26.0	-6.0	12.0	11-11	16.7	-6.4	10.5	9.45	1.05	5	24.3	-7.3	9.8	3.11	0.25	3
26.0	-2.0	12.0	9-1	-96.0	-4.0	-12.0	124.35	>10.00	6	24.3	-4.8	10.3	3.70	0.24	3
26.0	-2.0	12.0	9-2	-96.0	-4.0	-12.0	124.35	>10.00	6	28.8	-1.3	10.3	3.34	NEL	3
26.0	-2.0	12.0	10-8	-96.0	-4.0	-12.0	124.35	>10.00	6	27.3	-1.8	10.3	2.17	NEL	2
30.0	-10.0	12.0	10-10	-96.0	-4.0	-12.0	128.41	>10.00	6	30.8	-9.8	10.3	1.92	NEL	2
30.0	-10.0	12.0	11-5	-96.0	-4.0	-12.0	128.41	>10.00	6	28.8	-11.8	11.8	2.17	NEL	2
30.0	-10.0	12.0	11-13	29.3	-7.5	11.4	2.71	0.41	3	28.8	-11.8	11.8	2.17	NEL	2
30.0	-6.0	12.0	10-2	-96.0	-4.0	-12.0	128.28	>10.00	6	31.8	-4.8	11.3	2.28	0.04	2
30.0	-6.0	12.0	10-5	26.0	-6.4	12.0	4.02	0.99	3	25.3	-11.8	9.3	7.95	NEL	5
30.0	-6.0	12.0	10-9	26.2	-6.5	12.0	3.85	0.91	3	25.3	-11.8	8.8	8.14	NEL	5
30.0	-2.0	12.0	11-1	-96.0	-4.0	-12.0	128.28	>10.00	6	24.3	-5.8	11.8	6.87	0.18	4
30.0	-2.0	12.0	11-8	-96.0	-4.0	-12.0	128.28	>10.00	6	25.3	-5.3	11.8	5.76	0.11	4
30.0	-2.0	12.0	11-15	3.0	-5.0	12.0	27.19	1.57	6	24.3	-5.8	11.8	6.87	0.25	4
34.0	-10.0	12.0	11-6	-96.0	-4.0	-12.0	132.33	>10.00	6	30.3	-11.8	11.8	4.15	NEL	3
34.0	-10.0	12.0	11-14	-96.0	-4.0	-12.0	132.33	>10.00	6	42.8	0.8	11.8	13.86	NEL	6
34.0	-10.0	12.0	12-11	-96.0	-4.0	-12.0	132.33	>10.00	6	43.3	1.3	11.8	14.57	NEL	6
34.0	-10.0	12.0	13-20	-96.0	-4.0	-12.0	132.33	>10.00	6	34.8	-9.8	9.3	2.86	0.05	3
34.0	-6.0	12.0	12-1	-96.0	-4.0	-12.0	132.21	>10.00	6	29.8	-11.8	9.8	7.50	NEL	4
34.0	-6.0	12.0	12-7	-96.0	-4.0	-12.0	132.21	>10.00	6	32.8	-7.8	10.3	2.77	NEL	3
34.0	-6.0	12.0	13-28	29.5	-5.2	11.2	4.68	0.49	3	28.8	-11.8	9.3	8.26	NEL	5
34.0	-2.0	12.0	12-5	-96.0	4.0	-12.0	132.33	>10.00	6	29.8	-4.3	11.8	4.82	NEL	3
34.0	-2.0	12.0	12-10	-96.0	4.0	-12.0	132.33	>10.00	6	33.8	-2.8	10.8	1.48	0.24	2
34.0	-2.0	12.0	13-1	-96.0	4.0	-12.0	132.33	>10.00	6	33.3	-2.8	11.3	1.30	0.11	2
38.0	-10.0	12.0	13-7	23.7	-10.3	12.0	14.30	1.98	6	35.8	-11.8	10.3	3.34	0.09	3
38.0	-10.0	12.0	13-19	-96.0	-4.0	-12.0	136.26	>10.00	6	34.3	-10.8	9.8	4.44	0.23	3
38.0	-10.0	12.0	13-32	36.4	-7.0	10.4	3.73	0.64	3	34.3	-10.8	9.8	4.44	NEL	3
38.0	-6.0	12.0	13-5	-96.0	-4.0	-12.0	136.15	>10.00	6	39.8	-6.8	11.8	1.92	0.10	2
38.0	-6.0	12.0	13-16	-96.0	-4.0	-12.0	136.15	>10.00	6	39.3	-6.8	11.8	1.48	0.15	2
38.0	-6.0	12.0	13-29	-96.0	4.0	-12.0	136.50	>10.00	6	38.8	-6.3	11.8	0.83	0.12	1
38.0	-2.0	12.0	12-6	-96.0	-4.0	-12.0	136.15	NaN	6	37.3	-6.3	11.3	4.38	0.03	3
38.0	-2.0	12.0	13-2	-96.0	-4.0	-12.0	136.15	>10.00	6	38.8	-2.3	11.3	1.09	0.11	2
38.0	-2.0	12.0	13-13	-96.0	4.0	-12.0	136.26	>10.00	6	37.8	-2.3	9.3	2.77	0.21	3
38.0	-2.0	12.0	13-25	-96.0	-4.0	-12.0	136.15	>10.00	6	38.8	-2.3	11.3	1.09	0.07	2
42.0	-10.0	12.0	13-8	-96.0	-4.0	-12.0	140.20	>10.00	6	37.3	-8.8	10.3	5.21	0.05	4
42.0	-10.0	12.0	13-33	-96.0	-4.0	-12.0	140.20	>10.00	6	37.3	-8.8	9.8	5.40	0.04	4
46.0	-10.0	12.0	13-9	46.6	-10.0	8.6	3.51	0.13	3	46.3	-9.3	8.3	3.83	0.10	3
46.0	-10.0	12.0	13-21	44.8	-12.0	12.0	2.33	0.59	2	46.3	-10.3	8.3	3.77	0.22	3
46.0	-10.0	12.0	13-34	45.8	-12.0	11.9	2.02	0.39	2	46.3	-11.8	9.3	3.27	0.37	3

Tab. C.1: SW II PLB a - "Top", part 1: Coordinates of the pencil-lead breaks and estimated source locations determined using Geiger's method and *FastWay*. Estimated source locations excluded during the verification process (see Section 7.3.4) are shown in gray.

PLB			Set	Geiger's method						*FastWay*					
x [in]	y [in]	z [in]	#	x [in]	y [in]	z [in]	d [in]	eei [-]	ac [-]	x [in]	y [in]	z [in]	d [in]	eei [-]	ac [-]
50.0	-10.0	12.0	13-10	50.2	-4.0	7.8	7.34	0.30	4	49.8	-11.8	8.3	4.15	0.34	3
50.0	-10.0	12.0	13-22	-96.0	4.0	-12.0	148.62	>10.00	6	49.8	-11.8	8.3	4.15	0.38	3
50.0	-10.0	12.0	13-35	48.5	-11.9	8.6	4.16	0.17	3	48.3	-11.8	8.3	4.49	0.38	3
54.0	-10.0	12.0	13-11	55.9	-7.1	10.1	3.95	0.17	3	56.8	-8.8	9.8	3.77	0.08	3
54.0	-10.0	12.0	13-23	53.1	-10.5	11.9	1.03	0.17	2	53.3	-10.3	8.3	3.83	0.09	3
54.0	-10.0	12.0	13-36	-96.0	4.0	-12.0	152.55	>10.00	6	53.8	-9.3	8.3	3.83	0.25	3
58.0	-10.0	12.0	13-12	59.3	-10.6	11.7	1.47	0.22	2	60.8	-10.3	10.3	3.27	0.21	3
58.0	-10.0	12.0	13-24	59.2	-12.0	9.1	3.72	0.44	3	59.8	-11.3	10.8	2.49	0.16	2
58.0	-10.0	12.0	13-37	57.5	-9.7	12.0	0.58	0.12	1	58.8	-9.3	10.3	2.05	0.08	2
58.0	-6.0	12.0	13-6	60.3	-5.0	10.9	2.74	0.14	3	59.3	-5.3	8.3	4.02	0.11	3
58.0	-6.0	12.0	13-17	59.3	-5.7	11.9	1.31	0.16	2	61.3	-4.3	8.3	5.26	NEL	4
58.0	-6.0	12.0	13-30	57.7	-5.5	12.0	0.60	0.09	1	58.3	-5.8	11.8	0.43	0.24	1
58.0	-2.0	12.0	13-3	59.9	-1.1	9.9	2.97	0.11	3	61.3	-1.3	11.8	3.34	0.29	3
58.0	-2.0	12.0	13-4	62.2	-1.6	10.8	4.36	0.09	3	62.3	-1.3	10.3	4.66	0.16	3
58.0	-2.0	12.0	13-14	58.8	-1.2	9.9	2.41	0.11	2	60.3	-1.8	11.8	2.28	0.29	2
58.0	-2.0	12.0	13-26	58.3	-1.7	10.5	1.56	0.09	2	58.8	-2.3	11.3	1.09	0.23	2
62.0	-10.0	12.0	12-4	63.0	-8.2	10.7	2.43	0.17	2	64.8	-10.3	8.3	4.66	0.61	3
62.0	-10.0	12.0	12-8	64.4	-11.0	12.0	2.60	0.38	3	63.8	-11.8	8.3	4.49	0.65	3
62.0	-10.0	12.0	12-12	62.8	-8.4	10.8	2.16	0.18	2	62.8	-8.8	8.3	4.02	NEL	3
62.0	-6.0	12.0	12-2	66.1	-5.7	8.6	5.36	0.33	4	66.8	-3.8	11.3	5.31	NEL	4
62.0	-6.0	12.0	13-18	64.8	-10.4	8.7	6.14	0.11	4	66.3	-10.3	8.3	7.08	NEL	4
62.0	-6.0	12.0	13-31	63.3	-4.8	10.6	2.23	0.16	2	64.8	-3.3	7.8	5.76	NEL	4
62.0	-2.0	12.0	13-15	61.7	-1.6	10.4	1.65	0.10	2	61.3	-1.8	10.8	1.48	0.18	2
62.0	-2.0	12.0	13-27	62.2	-1.5	10.8	1.31	0.09	2	62.3	-1.3	10.3	1.92	0.17	2
66.0	-10.0	12.0	11-7	68.2	-3.8	11.0	6.68	0.81	4	55.8	-7.8	11.3	10.52	NEL	6
66.0	-10.0	12.0	12-9	65.9	-9.1	12.0	0.88	0.42	1	66.8	-10.8	8.3	3.90	0.04	3
66.0	-10.0	12.0	12-13	67.3	-8.5	10.8	2.34	0.21	2	67.3	-11.8	8.3	4.32	NEL	3
66.0	-6.0	12.0	10-3	87.2	-10.4	12.0	21.62	0.57	6	77.8	-7.8	11.3	11.90	NEL	6
66.0	-6.0	12.0	11-12	96.0	-4.0	-12.0	38.47	>10.00	6	65.3	-6.3	11.3	1.09	0.08	2
66.0	-6.0	12.0	11-18	96.0	-4.0	-12.0	38.47	>10.00	6	65.3	-6.3	10.8	1.48	0.04	2
66.0	-6.0	12.0	12-3	96.0	-4.0	-12.0	38.47	>10.00	6	74.8	-4.3	10.8	9.01	NEL	5
66.0	-2.0	12.0	11-2	65.5	-1.8	10.7	1.39	0.09	2	65.3	-2.3	11.3	1.09	0.14	2
66.0	-2.0	12.0	11-9	65.6	-1.9	10.9	1.23	0.09	2	65.3	-2.3	11.3	1.09	0.16	2
66.0	-2.0	12.0	11-16	65.4	-2.0	11.0	1.13	0.09	2	65.3	-2.3	11.3	1.09	0.17	2
70.0	-10.0	12.0	10-4	53.5	-12.0	12.0	16.63	3.82	6	70.3	-11.8	11.3	1.92	0.61	2
70.0	-10.0	12.0	10-7	72.9	-11.6	12.0	3.34	0.63	3	70.8	-11.8	11.8	1.92	0.76	2
70.0	-10.0	12.0	10-11	75.2	-10.5	12.0	5.23	1.01	4	70.8	-11.8	11.3	2.05	0.31	2
70.0	-6.0	12.0	10-6	58.9	-6.8	12.0	11.16	1.27	6	55.3	-11.8	11.3	15.85	NEL	6
70.0	-6.0	12.0	11-19	64.6	-2.1	12.0	6.68	0.70	4	72.8	7.8	11.8	14.02	NEL	6
70.0	-2.0	12.0	11-3	67.0	-0.9	12.0	3.23	0.17	3	69.3	1.3	11.8	3.34	0.29	3
70.0	-2.0	12.0	11-10	63.6	-1.2	8.5	7.37	0.24	4	69.3	1.3	11.8	3.34	0.27	3
70.0	-2.0	12.0	11-17	68.6	-1.6	12.0	1.48	0.09	2	68.3	-2.3	11.8	1.79	0.06	2

Tab. C.2: SW II PLB a - "Top", part 2: Coordinates of the pencil-lead breaks and estimated source locations determined using Geiger's method and *FastWay*. Estimated source locations excluded during the verification process (see Section 7.3.4) are shown in gray.

C.1.2 Top-Front

PLB			Set	Geiger's method						*FastWay*					
x [in]	y [in]	z [in]	#	x [in]	y [in]	z [in]	d [in]	eei [-]	ac [-]	x [in]	y [in]	z [in]	d [in]	eei [-]	ac [-]
26.0	-12.0	10.0	9-1	25.4	-8.4	11.5	3.97	0.51	3	27.8	-11.8	8.8	2.17	1.01	2
26.0	-12.0	10.0	9-2	25.6	-7.8	11.5	4.48	0.61	3	33.8	-4.8	11.8	10.76	NEL	6
26.0	-12.0	10.0	9-3	27.4	-7.0	11.7	5.44	0.60	4	27.8	-11.8	8.8	2.17	1.02	2
30.0	-12.0	10.0	10-1	35.4	-5.9	11.9	8.37	NaN	5	31.3	-9.8	9.8	2.59	NEL	3
30.0	-12.0	10.0	10-2	37.5	-6.1	12.0	9.75	NaN	5	34.8	-6.3	11.8	7.66	NEL	5
30.0	-12.0	10.0	11-3	-96.0	-4.0	-12.0	128.16	>10.00	6	30.3	-11.8	9.8	0.43	0.44	1
34.0	-12.0	10.0	11-4	-96.0	-4.0	-12.0	132.09	>10.00	6	35.8	-11.8	10.8	1.92	0.17	2
34.0	-12.0	10.0	12-1	32.7	-7.3	12.0	5.27	0.59	4	35.8	-11.8	10.8	1.92	0.15	2
34.0	-12.0	10.0	12-5	32.8	-7.3	12.0	5.27	0.59	4	32.3	-11.3	9.8	1.92	0.87	2
38.0	-12.0	10.0	13-1	34.3	-6.3	12.0	7.06	0.47	4	33.8	-9.8	9.3	4.87	0.63	3
38.0	-12.0	10.0	13-7	35.5	-9.0	12.0	4.41	0.46	3	31.8	-11.8	9.8	6.26	0.52	4
38.0	-12.0	10.0	13-13	34.9	-7.6	12.0	5.78	0.43	4	32.8	-10.8	9.8	5.40	0.69	4
42.0	-12.0	10.0	13-2	39.9	-9.1	11.2	3.75	0.17	3	37.8	-6.8	11.8	6.98	0.32	4
42.0	-12.0	10.0	13-8	35.6	-10.2	12.0	6.97	0.36	4	33.8	-10.8	9.8	8.35	0.23	5
42.0	-12.0	10.0	13-14	-96.0	-4.0	-12.0	139.97	>10.00	6	40.3	-11.8	9.3	1.92	NEL	2
42.0	-12.0	10.0	13-15	96.0	12.0	-12.0	63.06	>10.00	6	40.3	-11.8	9.3	1.92	0.09	2
46.0	-12.0	10.0	13-3	45.0	-8.2	9.4	3.95	NaN	3	43.3	-5.8	8.3	7.05	NEL	4
46.0	-12.0	10.0	13-9	38.7	4.0	4.0	18.58	NaN	6	39.8	3.8	2.8	18.43	NEL	6
50.0	-12.0	10.0	13-4	49.7	-11.1	10.8	1.26	0.12	2	49.3	-11.8	8.3	1.92	0.21	2
50.0	-12.0	10.0	13-10	50.4	-10.1	10.6	2.01	0.13	2	50.3	-11.8	8.3	1.79	0.32	2
50.0	-12.0	10.0	13-16	50.7	-10.2	10.4	1.99	0.20	2	49.3	-11.8	8.3	1.92	0.42	2
54.0	-12.0	10.0	13-5	55.0	-9.7	12.0	3.17	0.13	3	55.3	-11.8	8.3	2.17	0.10	2
54.0	-12.0	10.0	13-11	54.6	-9.8	9.3	2.42	NaN	2	54.8	-11.8	8.3	1.92	0.08	2
54.0	-12.0	10.0	13-17	54.5	-11.7	12.0	2.08	0.20	2	53.8	-11.8	8.3	1.79	0.24	2
58.0	-12.0	10.0	13-6	-96.0	-4.0	-12.0	155.77	>10.00	6	59.3	-11.3	10.3	1.48	0.04	2
58.0	-12.0	10.0	13-12	59.9	-8.4	12.0	4.50	0.55	3	60.3	-7.3	11.8	5.54	NEL	4
58.0	-12.0	10.0	13-18	60.0	-10.1	12.0	3.40	0.37	3	59.3	-11.8	9.8	1.30	0.61	2
58.0	-12.0	10.0	13-19	61.1	-8.7	9.8	4.53	0.34	3	61.3	-8.8	8.3	4.92	0.83	3
62.0	-12.0	10.0	12-2	54.0	-4.0	2.3	13.69	0.49	6	61.8	-11.8	10.3	0.43	0.08	1
62.0	-12.0	10.0	12-3	61.8	-9.9	11.3	2.49	0.14	2	62.3	-11.3	9.8	0.83	0.09	1
62.0	-12.0	10.0	12-6	63.1	-9.2	10.1	3.05	0.24	3	62.8	-10.8	8.3	2.28	0.76	2
66.0	-12.0	10.0	11-1	63.8	-12.0	12.0	2.98	NaN	3	64.8	-11.3	11.3	1.92	0.04	2
66.0	-12.0	10.0	11-6	66.4	-9.0	11.6	3.45	0.26	3	66.3	-11.8	8.3	1.79	0.76	2
66.0	-12.0	10.0	12-4	66.9	-8.9	12.0	3.78	0.31	3	65.8	-10.8	8.8	1.79	0.83	2
70.0	-12.0	10.0	11-2	71.8	-9.7	12.0	3.51	0.43	3	69.3	-11.8	9.8	0.83	0.21	1
70.0	-12.0	10.0	11-5	77.4	-9.7	10.9	7.82	0.85	5	69.3	-11.8	8.8	1.48	0.19	2
70.0	-12.0	10.0	11-7	66.8	-9.1	12.0	4.76	0.60	3	69.3	-11.8	9.8	0.83	0.22	1

Tab. C.3: SW II PLB a - "Top-Front", part 1: Coordinates of the pencil-lead breaks and estimated source locations determined using Geiger's method and *FastWay*. Estimated source locations excluded during the verification process (see Section 7.3.4) are shown in gray.

C.1.3 Front

PLB			Set	Geiger's method						*FastWay*					
x	y	z	#	x	y	z	d	eei	ac	x	y	z	d	eei	ac
[in]	[in]	[in]		[in]	[in]	[in]	[in]	[-]	[-]	[in]	[in]	[in]	[in]	[-]	[-]
26.0	-4.0	-10.0	8-2	23.5	0.8	3.4	14.49	NaN	6	24.3	-0.8	7.8	18.13	NEL	6
26.0	-4.0	-6.0	10-3	3.7	-4.0	-3.7	22.42	1.33	6	24.3	0.3	-4.3	4.92	NEL	3
26.0	-4.0	-6.0	10-7	24.4	-1.5	3.7	10.09	0.61	6	26.3	-2.3	5.3	11.39	0.45	6
26.0	-4.0	-6.0	10-10	-69.1	3.9	-1.4	95.50	>10.00	6	24.3	1.3	6.8	13.90	NEL	6
26.0	-4.0	-2.0	9-1	17.1	-4.4	10.6	15.44	2.08	6	24.3	-3.8	9.8	11.88	NEL	6
26.0	-4.0	-2.0	10-5	19.4	-5.0	9.4	13.23	1.22	6	24.8	-3.3	-0.3	2.28	NEL	2
26.0	-4.0	-2.0	10-6	-96.0	-4.0	-12.0	122.41	>10.00	6	24.3	-1.3	-1.3	3.34	NEL	3
26.0	-4.0	2.0	9-3	18.5	-6.3	10.1	11.26	2.01	6	28.3	-4.3	9.8	8.07	0.09	5
26.0	-4.0	2.0	10-2	15.5	-3.0	2.6	10.53	2.43	6	24.8	-1.8	-0.8	3.77	NEL	3
26.0	-4.0	2.0	10-9	7.0	-4.0	-2.2	19.44	3.47	6	28.3	-3.8	3.8	2.86	NEL	3
26.0	-4.0	6.0	10-1	-96.0	-4.0	-12.0	123.32	>10.00	6	25.3	-3.8	5.3	1.09	0.17	2
26.0	-4.0	6.0	10-4	15.5	-6.6	12.0	12.33	1.28	6	24.3	-4.8	9.8	4.21	NEL	3
26.0	-4.0	6.0	10-8	19.1	-5.4	9.8	7.99	1.46	5	26.3	-2.8	5.8	1.30	0.03	2
30.0	-4.0	-10.0	10-15	-44.3	-4.0	-12.0	74.31	5.38	6	25.3	-3.8	3.8	14.55	NEL	6
30.0	-4.0	-6.0	9-9	96.0	-12.0	12.0	68.88	NaN	6	24.3	-1.3	-1.3	7.95	NEL	5
30.0	-4.0	-2.0	9-5	96.0	-12.0	12.0	67.94	NaN	6	24.8	-3.8	-5.8	6.46	NEL	4
30.0	-4.0	-2.0	9-8	-7.2	-4.0	6.1	38.08	NaN	6	28.3	-3.8	3.8	6.02	NEL	4
30.0	-4.0	2.0	10-12	26.9	-5.4	9.1	7.86	1.37	5	29.8	-3.8	5.3	3.27	NEL	3
30.0	-4.0	2.0	10-14	30.3	0.4	2.7	4.50	0.50	3	25.8	-3.8	-3.3	6.76	NEL	4
30.0	-4.0	2.0	10-17	27.9	-5.3	9.0	7.43	0.69	4	32.3	-3.8	6.3	4.82	0.71	3
30.0	-4.0	6.0	10-11	20.3	-5.7	12.0	11.50	1.18	6	24.3	-6.8	10.8	7.95	NEL	5
30.0	-4.0	6.0	10-13	22.2	-6.1	11.1	9.55	2.08	5	29.3	-3.3	5.8	1.09	0.08	2
30.0	-4.0	6.0	10-16	20.4	-7.0	11.4	11.40	2.33	6	28.8	-3.8	6.3	1.30	0.07	2
34.0	-4.0	-10.0	11-3	-96.0	4.0	-12.0	130.26	>10.00	6	24.3	1.3	-0.8	14.43	NEL	6
34.0	-4.0	-6.0	12-2	31.9	1.0	0.5	8.46	0.23	5	30.3	-0.3	-11.3	7.46	NEL	4
34.0	-4.0	-2.0	11-8	29.7	0.7	2.0	7.51	0.33	5	31.3	-0.3	-6.8	6.65	NEL	4
34.0	-4.0	-2.0	11-1	-96.0	4.0	-12.0	130.63	>10.00	6	27.8	-2.8	-9.3	9.65	NEL	5
34.0	-4.0	-2.0	12-5	-96.0	4.0	-12.0	130.63	NaN	6	29.3	-3.8	5.8	9.09	0.05	5
34.0	-4.0	2.0	12-3	-96.0	4.0	-12.0	131.00	>10.00	6	33.3	-1.3	2.8	2.95	0.08	3
34.0	-4.0	6.0	11-4	34.0	-2.0	7.0	2.26	0.14	2	33.8	-1.8	6.8	2.38	0.18	2
34.0	-4.0	6.0	12-1	-96.0	4.0	-12.0	131.48	>10.00	6	33.8	-2.3	5.8	1.79	0.11	2
34.0	-4.0	6.0	12-4	30.6	-1.5	6.4	4.25	0.41	3	31.3	-3.8	7.3	3.03	0.19	3
38.0	-4.0	-10.0	12-8	-14.5	4.0	-12.0	53.11	9.68	6	32.8	3.8	-11.3	9.44	0.37	5
38.0	-4.0	-10.0	12-10	-96.0	4.0	-12.0	134.25	>10.00	6	24.3	-0.8	-9.8	14.13	NEL	6
38.0	-4.0	-6.0	12-13	26.7	-2.3	-11.7	12.80	0.83	6	32.3	3.8	-4.8	9.73	0.17	5
38.0	-4.0	-6.0	13-3	-96.0	4.0	-12.0	134.37	>10.00	6	35.3	2.8	-7.8	7.50	0.41	4
38.0	-4.0	-2.0	12-9	34.7	3.2	0.6	8.36	0.25	5	36.3	0.3	3.8	7.36	NEL	4
38.0	-4.0	2.0	12-11	38.1	-0.6	0.8	3.57	0.11	3	37.3	-0.3	1.8	3.83	NEL	3
38.0	-4.0	2.0	13-2	37.0	1.0	-0.3	5.56	0.15	4	36.8	-0.3	1.8	3.96	NEL	3
38.0	-4.0	2.0	13-5	36.7	1.4	-0.4	6.01	0.11	4	37.3	-0.3	2.8	3.90	NEL	3
38.0	-4.0	6.0	13-1	36.9	-0.6	7.4	3.85	0.15	3	29.8	2.8	4.8	10.73	NEL	6
38.0	-4.0	6.0	13-4	37.3	-1.1	10.6	5.51	0.30	4	37.3	-3.8	4.3	1.92	NEL	2
38.0	-4.0	6.0	13-6	-96.0	4.0	-12.0	135.44	>10.00	6	37.8	-1.3	7.8	3.27	0.03	3
42.0	-4.0	-10.0	12-16	34.3	4.0	-12.0	11.31	1.20	6	38.3	3.8	-11.8	8.79	0.16	5
42.0	-4.0	-10.0	13-11	29.8	4.0	-12.0	14.69	3.07	6	38.8	0.8	-11.8	6.02	0.27	4

Tab. C.4: SW II PLB a - "Front", part 1: Coordinates of the pencil-lead breaks and estimated source locations determined using Geiger's method and *FastWay*. Estimated source locations excluded during the verification process (see Section 7.3.4) are shown in gray.

PLB			Set	Geiger's method						*FastWay*					
x [in]	y [in]	z [in]	#	x [in]	y [in]	z [in]	d [in]	eei [-]	ac [-]	x [in]	y [in]	z [in]	d [in]	eei [-]	ac [-]
42.0	-4.0	-10.0	13-17	-96.0	4.0	-12.0	138.25	>10.00	6	39.3	3.8	-10.8	8.26	NEL	5
42.0	-4.0	-6.0	12-15	41.0	4.0	-7.8	8.27	0.34	5	41.8	-0.3	-5.8	3.77	0.03	3
42.0	-4.0	-6.0	13-10	43.3	0.1	-6.7	4.31	0.48	3	47.8	5.8	8.8	18.59	NEL	6
42.0	-4.0	-6.0	13-16	-96.0	4.0	-12.0	138.36	>10.00	6	49.8	2.3	-0.8	11.26	NEL	6
42.0	-4.0	-2.0	13-15	38.7	4.0	-4.7	9.07	0.20	5	39.3	3.8	-4.8	8.67	0.19	5
42.0	-4.0	-2.0	13-20	-96.0	12.0	-12.0	139.28	NaN	6	40.3	2.8	-1.8	6.98	NEL	4
42.0	-4.0	2.0	13-8	43.3	-1.6	0.7	2.97	0.11	3	42.3	-1.8	1.8	2.28	0.19	2
42.0	-4.0	2.0	13-9	42.9	3.7	-3.7	9.65	0.16	5	43.3	1.3	-3.3	7.53	0.17	5
42.0	-4.0	2.0	13-14	42.8	-1.3	1.8	2.83	0.11	3	41.3	-1.8	1.3	2.49	0.05	2
42.0	-4.0	2.0	13-19	40.7	1.8	-0.9	6.66	0.10	4	41.8	-1.8	2.3	2.28	0.24	2
42.0	-4.0	6.0	13-7	-96.0	4.0	-12.0	139.40	>10.00	6	42.3	-3.3	5.3	1.09	NEL	2
42.0	-4.0	6.0	13-12	-96.0	12.0	-12.0	140.09	NaN	6	41.3	-0.8	9.3	4.66	NEL	3
42.0	-4.0	6.0	13-18	42.8	-2.1	7.6	2.65	0.09	3	42.8	-2.8	6.8	1.64	NEL	2
46.0	-4.0	-10.0	13-26	49.6	0.4	-10.0	5.70	0.35	4	43.8	-3.8	-11.8	2.86	0.45	3
46.0	-4.0	-10.0	13-31	45.1	0.8	-12.0	5.26	0.73	4	55.8	2.3	-3.8	13.16	NEL	6
46.0	-4.0	-10.0	13-35	44.9	2.0	-6.8	6.86	0.19	4	44.3	0.3	-7.3	5.36	NEL	4
46.0	-4.0	-6.0	13-24	45.7	0.5	-4.4	4.79	0.22	3	50.8	1.8	0.8	10.06	NEL	6
46.0	-4.0	-6.0	13-25	41.2	3.7	-9.8	9.85	0.36	5	41.8	1.8	-9.8	8.07	0.18	5
46.0	-4.0	-6.0	13-30	44.5	0.5	-6.0	4.79	0.12	3	44.8	-0.3	-5.8	3.96	NEL	3
46.0	-4.0	-6.0	13-34	48.0	1.5	-1.9	7.13	0.19	4	46.8	-0.3	-2.3	5.36	0.09	4
46.0	-4.0	-2.0	13-29	47.4	0.8	-2.2	5.06	0.16	4	46.3	0.3	-2.8	4.32	0.18	3
46.0	-4.0	-2.0	13-33	46.6	-1.0	1.6	4.74	0.10	3	45.8	-1.3	1.8	4.66	0.16	3
46.0	-4.0	2.0	13-22	-96.0	4.0	-12.0	142.91	>10.00	6	46.3	-1.3	1.8	2.77	0.18	3
46.0	-4.0	2.0	13-28	-96.0	4.0	-12.0	142.91	>10.00	6	46.3	-1.8	2.3	2.28	0.20	2
46.0	-4.0	6.0	13-21	46.5	-2.4	6.4	1.71	0.09	2	46.3	-2.8	6.3	1.30	0.06	2
46.0	-4.0	6.0	13-27	46.5	-2.4	6.1	1.66	0.09	2	46.3	-2.8	6.3	1.30	0.04	2
46.0	-4.0	6.0	13-32	46.2	-1.7	5.8	2.28	0.10	2	45.8	-2.3	5.8	1.79	0.15	2
50.0	-4.0	-10.0	12-18	39.3	4.0	-12.0	13.55	4.57	6	51.3	-1.3	-9.8	3.03	0.22	3
50.0	-4.0	-10.0	12-19	33.0	-1.0	-12.0	17.41	2.92	6	49.3	-3.8	-11.3	1.48	NEL	2
50.0	-4.0	-10.0	13-49	23.3	-4.0	-12.0	26.77	5.77	6	47.3	-3.8	-11.8	3.27	NEL	3
50.0	-4.0	-6.0	13-39	49.8	-3.4	-7.1	1.21	0.13	2	49.8	-3.3	-7.3	1.48	0.19	2
50.0	-4.0	-6.0	13-43	50.2	-4.0	-0.7	5.32	0.13	4	50.3	-2.3	-2.3	4.15	0.03	3
50.0	-4.0	-6.0	13-44	-96.0	-4.0	-12.0	146.12	NaN	6	48.3	-3.8	-8.8	3.27	0.09	3
50.0	-4.0	-6.0	13-48	53.6	-0.5	-5.4	5.10	0.26	4	49.8	-2.8	-6.3	1.30	0.02	2
50.0	-4.0	-2.0	13-38	49.4	-3.4	-2.9	1.21	0.14	2	49.8	-2.3	-2.8	1.92	0.11	2
50.0	-4.0	-2.0	13-42	50.3	-0.9	1.2	4.46	0.09	3	49.8	-1.8	1.8	4.38	0.12	3
50.0	-4.0	-2.0	13-47	50.7	-2.4	-3.0	1.98	0.15	2	52.3	-1.8	-3.3	3.42	0.04	3
50.0	-4.0	2.0	13-37	51.3	0.1	1.2	4.38	0.12	3	50.8	-1.3	1.3	2.95	0.17	3
50.0	-4.0	2.0	13-41	53.8	-2.5	2.0	4.05	0.09	3	53.3	-2.8	1.8	3.49	0.09	3
50.0	-4.0	2.0	13-46	50.5	-1.4	1.7	2.64	0.09	3	50.8	-0.8	1.3	3.42	0.16	3
50.0	-4.0	6.0	13-36	50.4	-2.0	6.4	2.10	0.13	2	50.3	-2.3	6.3	1.79	0.21	2
50.0	-4.0	6.0	13-40	50.3	-2.1	5.6	1.98	0.10	2	49.8	-3.3	5.8	0.83	0.08	1
50.0	-4.0	6.0	13-45	50.6	-2.6	5.6	1.59	0.09	2	50.3	-3.8	5.8	0.43	0.17	1
54.0	-4.0	-10.0	13-55	53.9	-2.5	6.2	16.27	0.10	6	53.8	-2.8	7.3	17.30	0.11	6
54.0	-4.0	-10.0	11-15	23.9	4.0	-12.0	31.19	6.35	6	58.3	0.3	-11.3	6.14	NEL	4
54.0	-4.0	-10.0	12-20	92.9	4.0	-12.0	39.79	>10.00	6	58.3	0.3	-10.8	6.06	NEL	4
54.0	-4.0	-10.0	12-23	59.8	0.9	-11.3	7.71	0.88	5	52.3	-3.8	-10.8	1.92	NEL	2

Tab. C.5: SW II PLB a - "Front", part 2: Coordinates of the pencil-lead breaks and estimated source locations determined using Geiger's method and *FastWay*. Estimated source locations excluded during the verification process (see Section 7.3.4) are shown in gray.

PLB			Set	Geiger's method						*FastWay*					
x [in]	y [in]	z [in]	#	x [in]	y [in]	z [in]	d [in]	eei [-]	ac [-]	x [in]	y [in]	z [in]	d [in]	eei [-]	ac [-]
54.0	-4.0	-6.0	13-58	52.9	-3.8	-2.4	3.75	0.17	3	53.8	-2.3	-2.8	3.70	NEL	3
54.0	-4.0	-6.0	11-13	30.3	-4.0	-12.0	24.45	6.40	6	49.8	-3.8	-11.8	7.15	NEL	4
54.0	-4.0	-6.0	11-14	26.7	-4.0	-12.0	27.94	5.84	6	32.3	-3.3	-11.8	22.51	NEL	6
54.0	-4.0	-6.0	12-22	-96.0	-4.0	-12.0	150.12	>10.00	6	52.3	-3.3	-9.8	4.21	0.01	3
54.0	-4.0	-2.0	13-52	53.6	-2.4	-2.3	1.72	0.09	2	53.3	-2.3	-2.8	2.05	0.11	2
54.0	-4.0	-2.0	13-57	-96.0	-12.0	12.0	150.86	>10.00	6	53.8	-3.8	1.8	3.77	0.15	3
54.0	-4.0	-2.0	12-21	51.4	-4.0	-2.0	2.57	0.22	3	53.3	-2.8	-2.3	1.48	0.07	2
54.0	-4.0	2.0	13-51	53.7	-2.9	1.8	1.15	0.09	2	53.3	-3.8	1.8	0.83	0.14	1
54.0	-4.0	2.0	13-54	53.8	-3.3	2.4	0.82	0.09	1	53.3	-3.8	2.3	0.83	0.16	1
54.0	-4.0	6.0	13-50	53.9	-1.3	6.0	2.70	0.10	3	52.8	-5.3	8.3	2.86	NEL	3
54.0	-4.0	6.0	13-53	54.5	-1.4	5.4	2.68	0.10	3	55.8	-0.3	4.3	4.49	0.07	3
54.0	-4.0	6.0	13-56	54.0	-1.8	5.3	2.26	0.10	2	53.8	-3.8	5.8	0.43	0.19	1
58.0	-4.0	-10.0	12-25	62.6	-1.6	-11.3	5.34	0.92	4	58.8	-3.8	-10.8	1.09	0.42	2
58.0	-4.0	-10.0	12-26	54.5	-3.7	-12.0	4.04	0.44	3	54.8	-1.3	-7.8	4.82	NEL	3
58.0	-4.0	-10.0	12-28	44.5	-4.0	-12.0	13.63	2.15	6	43.8	-3.8	4.8	20.51	NEL	6
58.0	-4.0	-6.0	11-16	58.8	-4.0	-12.0	6.06	0.63	4	58.8	-3.8	-9.8	3.83	NEL	3
58.0	-4.0	-6.0	11-17	57.9	-4.0	-8.8	2.76	0.27	3	58.8	-3.8	-8.8	2.86	0.26	3
58.0	-4.0	-6.0	12-24	49.0	-4.0	2.9	12.63	NaN	6	58.8	-3.3	-7.3	1.64	NEL	2
58.0	-4.0	-2.0	13-61	65.1	3.9	-11.2	14.07	0.35	6	57.3	-3.3	-1.8	1.09	0.10	2
58.0	-4.0	-2.0	13-64	59.6	-1.5	-4.2	3.67	0.16	3	59.3	-0.8	-3.3	3.70	0.23	3
58.0	-4.0	-2.0	13-66	60.2	-2.1	-4.1	3.64	0.10	3	58.8	-2.8	-3.3	1.92	0.13	2
58.0	-4.0	2.0	13-60	57.7	-2.8	1.6	1.30	0.09	2	58.3	-1.8	1.3	2.38	0.23	2
58.0	-4.0	2.0	13-63	57.7	-3.2	2.5	1.02	0.09	2	57.8	-3.3	2.3	0.83	0.17	1
58.0	-4.0	2.0	13-65	65.3	2.5	-4.7	11.89	0.21	6	58.3	-3.3	1.8	0.83	0.10	1
58.0	-4.0	6.0	13-59	58.4	-1.3	4.6	3.12	0.10	3	58.3	-2.3	5.3	1.92	0.11	2
58.0	-4.0	6.0	13-62	58.3	-1.6	4.6	2.78	0.10	3	58.3	-2.8	5.3	1.48	0.09	2
58.0	-4.0	6.0	12-27	58.8	-1.5	5.1	2.76	0.11	3	58.8	-2.3	5.3	2.05	0.21	2
62.0	-4.0	-10.0	12-32	61.6	-4.0	-9.3	0.79	0.37	1	62.3	-2.8	-8.3	2.17	NEL	2
62.0	-4.0	-10.0	12-37	77.7	2.6	-12.0	17.20	2.97	6	44.8	-6.3	10.3	26.70	NEL	6
62.0	-4.0	-10.0	12-41	56.0	2.0	5.2	17.44	NaN	6	61.3	-3.8	-9.8	0.83	NEL	1
62.0	-4.0	-6.0	11-18	49.0	-5.5	11.0	21.45	NaN	6	62.8	-2.3	-6.8	2.05	NEL	2
62.0	-4.0	-6.0	11-21	82.4	4.0	-12.0	22.71	2.74	6	66.8	0.3	-11.8	8.58	NEL	5
62.0	-4.0	-6.0	12-35	70.9	1.0	-10.9	11.30	0.33	6	71.8	0.8	-11.8	12.28	NEL	6
62.0	-4.0	-6.0	12-36	61.2	-4.0	-5.7	0.87	0.17	1	62.3	-3.3	-6.8	1.09	0.09	2
62.0	-4.0	-6.0	12-40	63.9	-2.0	-4.2	3.35	0.09	3	65.3	-0.8	-6.3	4.60	NEL	3
62.0	-4.0	-2.0	12-31	61.7	-3.7	-2.2	0.47	0.12	1	62.3	-3.3	-2.8	1.09	0.10	2
62.0	-4.0	-2.0	12-34	66.1	0.4	-3.9	6.30	0.20	4	65.3	0.3	-3.3	5.49	0.03	4
62.0	-4.0	-2.0	12-39	65.9	-0.0	-2.3	5.60	0.20	4	65.3	-0.3	-2.3	4.97	NEL	3
62.0	-4.0	2.0	12-30	65.8	-0.1	-3.5	7.77	0.19	5	64.8	0.3	-2.3	6.61	0.19	4
62.0	-4.0	6.0	12-29	62.2	-2.2	5.2	1.98	0.09	2	62.3	-2.8	6.3	1.30	0.04	2
62.0	-4.0	6.0	12-33	62.4	-2.5	5.8	1.58	0.09	2	62.3	-2.8	6.3	1.30	0.10	2
62.0	-4.0	6.0	12-38	62.4	-2.4	6.0	1.65	0.09	2	62.3	-2.8	6.3	1.30	0.16	2
66.0	-4.0	-10.0	11-24	60.1	-12.0	8.0	20.55	NaN	6	73.3	3.8	-9.8	10.62	NEL	6
66.0	-4.0	-10.0	11-29	96.0	4.0	-12.0	31.11	>10.00	6	66.8	0.3	-11.8	4.66	NEL	3
66.0	-4.0	-6.0	12-43	-96.0	-12.0	12.0	163.19	NaN	6	71.3	0.8	-11.3	8.81	NEL	5
66.0	-4.0	-6.0	12-45	70.6	-3.7	-7.9	4.98	0.95	3	67.3	-3.8	-11.8	5.89	0.40	4
66.0	-4.0	-6.0	12-47	74.2	1.7	-12.0	11.63	1.52	6	67.3	0.8	-11.8	7.56	NEL	5

Tab. C.6: SW II PLB a - "Front", part 3: Coordinates of the pencil-lead breaks and estimated source locations determined using Geiger's method and *FastWay*. Estimated source locations excluded during the verification process (see Section 7.3.4) are shown in gray.

PLB			Set	Geiger's method						*FastWay*					
x [in]	y [in]	z [in]	#	x [in]	y [in]	z [in]	d [in]	eei [-]	ac [-]	x [in]	y [in]	z [in]	d [in]	eei [-]	ac [-]
66.0	-4.0	-2.0	12-42	65.1	-3.7	-2.1	0.97	0.13	1	64.8	-3.8	-1.8	1.30	NEL	2
66.0	-4.0	-2.0	12-44	69.1	0.4	-7.6	7.76	0.39	5	76.3	-2.3	-9.3	12.68	NEL	6
66.0	-4.0	-2.0	12-46	79.4	4.0	-12.0	18.55	1.07	6	75.3	2.8	-10.3	14.11	NEL	6
66.0	-4.0	2.0	11-22	66.3	-10.8	9.9	10.40	0.21	6	66.3	-8.3	8.3	7.56	0.75	5
66.0	-4.0	2.0	11-23	68.7	-2.5	-0.6	4.03	0.13	3	65.8	-2.8	1.8	1.30	0.13	2
66.0	-4.0	2.0	11-26	65.5	-3.2	2.2	1.00	0.12	1	65.3	-3.3	2.3	1.09	0.10	2
66.0	-4.0	2.0	11-28	65.7	-2.6	1.9	1.40	0.11	2	65.8	-2.8	1.8	1.30	0.15	2
66.0	-4.0	6.0	9-16	66.9	-2.2	5.8	1.99	0.10	2	66.3	-2.8	5.8	1.30	0.10	2
66.0	-4.0	6.0	10-21	67.5	-1.7	5.2	2.86	0.11	3	66.8	-1.8	5.3	2.49	0.16	2
66.0	-4.0	6.0	11-25	67.1	-2.2	5.8	2.12	0.10	2	66.3	-2.8	5.8	1.30	0.15	2
70.0	-4.0	-10.0	10-26	96.0	4.0	-12.0	27.28	>10.00	6	70.3	3.3	-11.8	7.46	NEL	4
70.0	-4.0	-10.0	10-33	96.0	12.0	8.0	35.44	NaN	6	67.3	0.3	-11.8	5.36	NEL	4
70.0	-4.0	-6.0	9-20	91.2	4.0	-12.0	23.46	3.40	6	73.3	-2.8	-11.8	6.72	NEL	4
70.0	-4.0	-6.0	10-25	85.4	3.6	-12.0	18.17	2.64	6	67.3	0.8	-11.8	7.95	NEL	5
70.0	-4.0	-2.0	10-24	68.5	-2.8	-1.9	1.92	0.15	2	70.8	-3.3	-3.8	2.05	NEL	2
70.0	-4.0	2.0	9-19	48.4	-4.0	-12.0	25.73	NaN	6	70.8	-3.8	-1.8	3.83	NEL	3
70.0	-4.0	2.0	10-23	67.1	-3.1	2.8	3.13	0.09	3	69.8	-2.8	1.8	1.30	0.09	2
70.0	-4.0	2.0	10-28	67.2	-3.0	2.9	3.06	0.09	3	69.3	-2.3	2.3	1.92	0.10	2
70.0	-4.0	2.0	10-29	66.6	-3.4	-0.5	4.25	0.12	3	70.8	-2.8	-3.3	5.45	NEL	4
70.0	-4.0	6.0	9-18	70.9	-0.7	-4.5	11.07	0.90	6	73.3	-3.8	-1.8	8.41	NEL	5
70.0	-4.0	6.0	10-22	70.5	-2.4	5.6	1.70	0.09	2	69.8	-2.8	5.8	1.30	0.06	2
70.0	-4.0	6.0	10-27	69.9	-2.6	5.8	1.44	0.09	2	69.3	-2.8	6.3	1.48	0.08	2
70.0	-4.0	6.0	10-31	70.8	-2.3	5.1	2.04	0.10	2	70.3	-2.8	5.3	1.48	0.10	2

Tab. C.7: SW II PLB a - "Front", part 4: Coordinates of the pencil-lead breaks and estimated source locations determined using Geiger's method and *FastWay*. Estimated source locations excluded during the verification process (see Section 7.3.4) are shown in gray.

C.2 Shear Test - SW II

C.2.1 Localized events

Event	Geiger's method					*FastWay*				
#	x [in]	y [in]	z [in]	t_s [hh:mm:ss]	*eei* [-]	x [in]	y [in]	z [in]	t_s [hh:mm:ss]	*eei* [-]
9	51.3	-0.7	-3.2	10:42:56.108436	NaN	50.8	-0.8	-3.5	10:42:56.108438	0.03
77	49.1	2.2	-3.0	10:52:08.494677	0.27	53.3	2.3	0.0	10:52:08.494663	NEL
95	36.5	3.5	-1.6	10:52:12.029115	0.36	37.3	3.3	-1.0	10:52:12.029109	0.38
102	47.3	2.9	-5.2	10:52:14.697180	0.38	50.3	2.3	-3.0	10:52:14.697183	0.28
103	50.1	0.1	0.5	10:52:14.856182	0.43	49.3	3.8	-0.5	10:52:14.856187	0.16
113	38.1	4.0	-12.0	10:52:16.606252	6.32	47.3	3.8	-11.5	10:52:16.606332	0.33
122	-96.0	4.0	-12.0	10:52:18.315567	NaN	39.8	3.8	-7.5	10:52:18.335811	0.36
123	49.3	0.8	-5.8	10:52:18.533461	0.75	56.8	3.8	4.0	10:52:18.533400	NEL
140	56.0	4.0	-12.0	10:52:21.845747	NaN	56.3	3.8	-11.5	10:52:21.845773	0.27
151	45.6	4.0	-2.7	10:52:26.399727	0.50	45.3	-2.8	-7.5	10:52:26.399713	NEL
154	53.0	-9.1	10.7	10:52:29.225427	NaN	53.3	-7.3	8.5	10:52:29.225441	0.19
263	44.5	2.7	-1.4	10:58:48.502788	0.26	25.8	-3.8	-6.5	10:58:48.502678	NEL
264	58.0	-1.1	-12.0	10:58:48.544359	0.72	57.3	1.3	-9.0	10:58:48.544381	0.13
268	44.2	2.2	-12.0	10:58:48.673736	1.67	46.3	0.8	-11.5	10:58:48.673764	0.14
292	-96.0	4.0	-12.0	10:58:50.288632	>10.00	45.8	2.8	-11.5	10:58:50.388625	0.52
296	-5.1	4.0	-12.0	10:58:51.287467	>10.00	38.8	3.8	-11.5	10:58:51.287738	0.42
332	49.8	4.0	-0.9	10:58:54.935929	NaN	48.3	3.8	-2.0	10:58:54.935929	0.13
336	49.4	-1.3	-0.7	10:58:55.167784	0.22	48.3	-1.8	-1.5	10:58:55.167789	0.24
339	67.0	-3.6	-12.0	10:58:55.361976	2.12	62.3	-1.3	-11.5	10:58:55.361980	0.16
361	-96.0	4.0	-12.0	10:58:57.660213	>10.00	44.3	2.8	-11.0	10:58:57.718102	0.20
375	49.2	4.0	-12.0	10:58:58.688467	>10.00	61.3	-3.8	-11.5	10:58:58.688590	0.37
380	-96.0	-4.0	-12.0	10:58:58.790895	NaN	64.3	3.8	-8.0	10:58:58.811281	0.42
386	-96.0	4.0	-12.0	10:58:58.945435	>10.00	46.8	-3.8	8.0	10:58:58.996504	0.49
397	61.5	4.0	-12.0	10:58:59.492632	1.61	61.3	-2.8	-8.0	10:58:59.492666	0.10
423	27.2	-2.6	4.2	10:59:00.398500	1.07	32.8	0.3	11.5	10:59:00.398528	0.11
462	53.2	4.0	-4.2	10:59:01.771436	0.61	51.8	2.8	-4.5	10:59:01.771446	NEL
467	60.2	-2.8	-10.9	10:59:02.142690	0.05	60.3	-3.3	-10.0	10:59:02.142692	0.06
470	63.2	2.9	-12.0	10:59:02.357359	2.13	60.3	-2.3	-10.5	10:59:02.357368	0.01
479	47.6	2.4	-5.5	10:59:02.885577	0.57	49.3	3.8	-4.5	10:59:02.885580	NEL
499	37.6	-4.0	-12.0	10:59:03.641523	>10.00	62.3	-3.8	-11.5	10:59:03.641670	0.86
523	50.4	4.0	-3.2	10:59:04.514601	NaN	46.3	3.8	-11.5	10:59:04.514113	0.80
529	62.9	-3.3	-7.8	10:59:04.801800	0.42	62.8	-3.8	-6.0	10:59:04.801786	0.80
556	92.2	-4.0	-12.0	10:59:05.832544	>10.00	62.8	-3.8	-10.5	10:59:05.832774	0.40
570	-96.0	12.0	-12.0	10:59:05.915820	NaN	59.8	-3.8	-11.5	10:59:06.303120	0.94
618	61.3	-2.4	-8.0	10:59:10.589583	NaN	60.8	-2.3	-8.0	10:59:10.589589	0.06
657	59.5	-0.9	-5.1	10:59:20.999888	0.43	59.3	-0.3	-5.5	10:59:20.999900	0.36
777	42.9	4.0	-12.0	11:05:15.200707	>10.00	54.3	2.3	-10.0	11:05:15.200833	0.24
781	62.1	-0.7	-10.5	11:05:16.621931	0.25	62.3	-1.8	-9.0	11:05:16.621935	0.23
783	64.7	4.0	-12.0	11:05:17.397690	2.62	61.3	-3.3	-7.5	11:05:17.397727	0.28
833	54.1	-1.7	-12.0	11:05:30.932833	0.89	50.3	-3.8	-11.0	11:05:30.932815	0.42

Tab. C.8: SW II - localized events, part 1: Coordinates of the estimated source locations determined using Geiger's method and *FastWay*. Estimated source locations excluded during the verification process (see Section 7.3.4) are shown in gray.

Event	Geiger's method					*FastWay*				
#	x [in]	y [in]	z [in]	t_s [hh:mm:ss]	*eei* [-]	x [in]	y [in]	z [in]	t_s [hh:mm:ss]	*eei* [-]
860	-96.0	-4.0	-12.0	11:05:33.714338	NaN	50.8	-0.8	-11.5	11:05:33.747200	0.81
876	50.2	4.0	-3.2	11:05:34.809907	0.90	25.3	-1.3	-9.5	11:05:34.809785	NEL
902	41.6	-0.1	-2.2	11:05:36.016234	0.85	27.3	-3.3	-4.0	11:05:36.016167	NEL
907	96.0	4.0	-12.0	11:05:36.250897	>10.00	56.8	0.8	-11.5	11:05:36.251340	0.72
969	62.2	4.0	-12.0	11:05:39.225521	4.45	62.3	-2.8	-11.5	11:05:39.225580	0.78
979	51.1	0.2	1.5	11:05:39.756459	NaN	51.3	0.8	1.5	11:05:39.756458	0.04
1000	-27.8	-12.0	12.0	11:05:40.580792	NaN	52.8	-3.8	3.0	11:05:40.581367	0.77
1015	60.0	4.0	6.9	11:05:41.002585	NaN	64.8	3.8	-11.0	11:05:41.002609	0.25
1042	26.2	12.0	12.0	11:05:42.021987	>10.00	43.3	1.3	-3.0	11:05:42.022250	0.12
1050	-96.0	12.0	12.0	11:05:42.221018	>10.00	61.3	-1.3	-8.5	11:05:42.288808	0.02
1051	48.9	2.9	-10.7	11:05:42.320277	0.29	58.8	-3.8	-9.5	11:05:42.320239	NEL
1054	35.8	4.0	-1.4	11:05:42.363512	2.16	45.8	2.3	4.5	11:05:42.363562	0.56
1090	48.3	-0.4	1.2	11:05:43.338569	0.11	47.3	-0.8	1.0	11:05:43.338573	0.06
1091	-96.0	4.0	-12.0	11:05:43.351684	NaN	49.8	-1.8	1.0	11:05:43.353208	0.02
1094	61.3	-2.3	-6.5	11:05:43.447631	0.39	60.8	-2.3	-6.0	11:05:43.447635	0.21
1096	67.1	-4.0	-12.0	11:05:43.534308	1.48	64.3	-3.8	-11.5	11:05:43.534330	0.84
1100	63.4	-4.0	-12.0	11:05:43.669370	0.41	62.3	-2.8	-11.5	11:05:43.669378	0.35
1127	49.9	0.0	-9.9	11:05:44.652025	0.85	64.3	1.8	-3.0	11:05:44.651969	NEL
1186	96.0	-4.0	-12.0	11:05:46.519569	>10.00	57.8	1.3	-11.5	11:05:46.521138	0.91
1214	-96.0	-4.0	-12.0	11:05:47.165603	>10.00	38.8	3.8	-11.5	11:05:47.267337	0.20
1218	58.8	0.2	-1.1	11:05:47.331749	0.58	62.3	-0.3	-1.0	11:05:47.331728	NEL
1223	56.8	-3.3	0.7	11:05:47.422829	0.41	60.8	-2.8	-6.5	11:05:47.422832	0.06
1224	63.8	4.0	-12.0	11:05:47.445716	2.03	59.3	1.3	-5.5	11:05:47.445718	0.01
1243	45.2	2.4	-6.2	11:05:47.945794	0.36	45.8	-0.8	-1.0	11:05:47.945814	NEL
1275	46.4	2.0	2.2	11:05:48.909462	0.20	24.3	0.3	3.0	11:05:48.909362	NEL
1280	49.1	1.7	-0.8	11:05:49.122266	0.04	48.8	1.3	-0.5	11:05:49.122267	0.11
1284	-96.0	4.0	-12.0	11:05:49.200052	>10.00	47.3	-1.8	4.0	11:05:49.204823	0.09
1311	42.7	4.0	-10.7	11:05:49.915104	1.11	45.8	3.8	-6.5	11:05:49.915127	0.11
1319	96.0	4.0	-12.0	11:05:50.286244	>10.00	61.3	-3.8	-10.0	11:05:50.290699	0.46
1331	50.4	1.9	-1.8	11:05:50.830921	0.19	48.3	1.8	-3.0	11:05:50.830922	0.06
1341	-96.0	4.0	-12.0	11:05:51.308194	>10.00	44.3	2.3	7.5	11:05:51.371335	0.03
1358	-96.0	4.0	-12.0	11:05:51.828608	>10.00	63.8	3.8	-10.5	11:05:51.893331	0.26
1363	62.0	-1.2	-6.1	11:05:52.173132	0.10	61.8	-1.8	-6.5	11:05:52.173129	0.26
1392	60.1	4.0	-0.6	11:05:53.087746	1.00	58.3	3.8	-3.0	11:05:53.087761	0.78
1408	60.2	-0.6	-4.6	11:05:53.523752	NaN	60.3	-0.3	-5.0	11:05:53.523754	0.04
1411	-96.0	12.0	-12.0	11:05:53.196135	NaN	54.8	-11.8	8.5	11:05:53.602660	0.93
1413	59.4	0.5	-12.0	11:05:53.615434	1.02	55.3	-3.8	-11.5	11:05:53.615424	0.48
1518	57.0	-4.0	-5.0	11:05:56.650978	0.95	52.3	-3.8	-4.5	11:05:56.650990	0.48
1519	45.7	4.0	-3.0	11:05:56.668203	0.29	46.3	3.8	-2.5	11:05:56.668215	0.29
1525	8.5	4.0	-12.0	11:05:56.891976	NaN	50.8	3.8	-8.5	11:05:56.892321	0.96
1528	56.9	-0.8	-2.4	11:05:56.941647	0.22	58.8	-3.8	-1.0	11:05:56.941624	NEL
1532	45.4	1.1	-2.1	11:05:57.011709	0.25	38.8	-3.8	-4.5	11:05:57.011661	NEL
1550	96.0	-4.0	-12.0	11:05:57.722415	>10.00	61.8	-3.8	-6.5	11:05:57.727989	0.41
1552	60.8	2.1	-4.4	11:05:57.746273	0.34	60.8	2.3	-6.0	11:05:57.746258	0.45
1573	-96.0	4.0	-12.0	11:05:58.247524	>10.00	45.8	3.8	-11.5	11:05:58.272067	0.26
1577	61.6	4.0	-6.3	11:05:58.336402	0.79	58.8	-0.8	0.0	11:05:58.336396	0.42

Tab. C.9: SW II - localized events, part 2: Coordinates of the estimated source locations determined using Geiger's method and *FastWay*. Estimated source locations excluded during the verification process (see Section 7.3.4) are shown in gray.

Event	Geiger's method					*FastWay*				
#	x [in]	y [in]	z [in]	t_s [hh:mm:ss]	*eei* [-]	x [in]	y [in]	z [in]	t_s [hh:mm:ss]	*eei* [-]
1585	65.8	4.0	-7.4	11:05:58.464979	0.81	61.8	0.8	-6.0	11:05:58.464970	0.15
1637	7.0	4.0	-12.0	11:05:59.412193	>10.00	44.3	-0.8	-11.5	11:05:59.412476	0.72
1673	56.2	-4.0	2.4	11:06:00.267560	NaN	57.8	-3.8	1.0	11:06:00.267563	0.16
1755	47.8	0.4	0.9	11:06:02.603431	0.54	45.8	1.3	5.0	11:06:02.603436	0.07
1773	63.7	-4.0	-12.0	11:06:03.382208	2.16	60.8	-1.8	-11.5	11:06:03.382261	0.41
1821	64.3	-4.0	-12.0	11:06:05.725270	NaN	62.3	-3.8	-11.0	11:06:05.725291	0.59
1826	48.7	3.0	-2.6	11:06:05.890284	0.54	49.8	1.8	1.5	11:06:05.890284	0.63
1853	59.3	2.6	-12.0	11:06:06.959935	1.34	61.3	-3.8	-7.5	11:06:06.959982	0.16
1857	60.8	-0.2	-7.7	11:06:07.117586	0.90	62.8	-3.8	-11.5	11:06:07.117584	0.48
1892	-96.0	-4.0	-12.0	11:06:09.148339	NaN	46.8	1.3	-11.5	11:06:09.163358	0.11
1910	55.8	-0.2	-5.8	11:06:10.347109	0.13	56.3	-0.3	-6.5	11:06:10.347110	NEL
1932	56.1	2.1	-3.1	11:06:12.232001	0.38	49.8	3.8	6.5	11:06:12.231946	NEL
1944	61.1	-2.6	-7.8	11:06:13.041814	0.56	63.3	2.8	-5.5	11:06:13.041829	0.46
1947	58.6	-1.0	-2.6	11:06:13.365169	0.76	59.8	-0.3	-4.0	11:06:13.365158	NEL
1957	61.6	-3.7	-5.6	11:06:14.283957	0.24	58.3	-3.8	-2.0	11:06:14.283964	NEL
1959	59.6	0.7	-4.4	11:06:14.857802	NaN	59.8	0.8	-5.0	11:06:14.857810	0.05
1980	8.2	-12.0	12.0	11:06:16.793045	>10.00	60.3	-3.8	-8.5	11:06:16.793478	0.29
1988	61.9	-2.0	-9.8	11:06:17.807640	0.60	61.3	1.3	-6.0	11:06:17.807651	0.08
2002	61.2	-0.4	-7.9	11:06:19.669080	NaN	60.8	-0.3	-8.0	11:06:19.669085	0.08
2007	59.6	-1.4	-3.2	11:06:20.380902	NaN	59.8	-1.3	-4.0	11:06:20.380902	0.02
2026	58.3	-0.4	-0.1	11:06:23.550788	0.42	56.3	-1.8	5.5	11:06:23.550762	NEL
2030	48.7	3.3	-7.4	11:06:24.655514	0.69	54.3	2.3	-2.5	11:06:24.655502	NEL
2034	61.2	-1.0	-6.8	11:06:25.370909	NaN	61.3	-0.8	-7.5	11:06:25.370906	0.07
2054	60.3	-1.6	-3.5	11:06:29.115897	0.58	60.3	-0.3	-4.5	11:06:29.115884	0.69
2061	67.0	4.0	-12.0	11:06:31.120838	1.11	67.3	1.3	-8.5	11:06:31.120852	0.06
2089	56.9	-1.2	2.4	11:06:43.244642	NaN	58.3	0.3	1.0	11:06:43.244595	0.54
2129	-96.0	4.0	-12.0	11:07:08.761233	>10.00	51.8	3.3	-9.5	11:07:08.777634	0.42
2132	62.1	-1.9	-6.3	11:07:10.221304	0.04	61.8	-1.8	-6.5	11:07:10.221303	0.09
2143	61.5	-2.3	-5.9	11:07:26.141557	0.29	60.8	-0.3	-8.5	11:07:26.141546	0.03
2196	39.0	4.0	-12.0	11:10:07.070247	9.38	48.8	-1.3	-8.5	11:10:07.070336	0.07
2233	32.7	3.5	-12.0	11:10:12.288689	2.90	38.8	3.8	-5.5	11:10:12.288721	0.71
2257	57.7	2.9	0.2	11:10:15.383306	NaN	41.3	-0.3	-11.5	11:10:15.382453	0.55
2311	57.4	-1.3	-0.9	11:12:20.616666	0.23	55.8	-1.8	1.5	11:12:20.616658	0.52
2321	57.9	1.6	-3.6	11:12:23.583156	0.51	49.3	-0.3	9.5	11:12:23.583099	NEL
2333	52.1	4.0	-2.8	11:12:27.582588	0.41	53.8	3.8	-1.0	11:12:27.582575	NEL
2334	51.6	4.0	-9.7	11:12:27.824564	3.52	49.3	3.8	-4.5	11:12:27.824586	0.88
2351	86.3	-4.0	-12.0	11:12:30.037663	NaN	63.8	-3.8	-11.0	11:12:30.037828	0.62
2375	40.4	-0.3	-9.5	11:12:33.135668	0.56	40.3	-2.8	-7.5	11:12:33.135661	NEL
2397	66.6	1.0	-12.0	11:12:34.793678	0.38	66.8	0.8	-11.5	11:12:34.793689	0.03
2438	92.5	4.0	-12.0	11:12:37.815217	NaN	66.8	3.3	-11.5	11:12:37.815402	0.51
2447	58.7	-0.3	-5.4	11:12:38.500455	0.04	58.8	-0.3	-6.0	11:12:38.500455	0.11
2449	60.2	4.0	-0.6	11:12:38.568333	0.87	59.3	3.8	-4.0	11:12:38.568375	NEL
2455	54.6	-4.0	-4.0	11:12:38.967315	0.75	56.8	-3.8	-5.5	11:12:38.967341	0.86
2461	84.4	1.9	-12.0	11:12:39.476262	>10.00	63.8	-3.8	-11.0	11:12:39.476412	0.43
2475	62.8	-4.0	-2.5	11:12:40.274283	0.66	62.3	-2.8	-6.0	11:12:40.274288	NEL

Tab. C.10: SW II - localized events, part 3: Coordinates of the estimated source locations determined using Geiger's method and *FastWay*. Estimated source locations excluded during the verification process (see Section 7.3.4) are shown in gray.

Event	Geiger's method					*FastWay*				
#	x [in]	y [in]	z [in]	t_s [hh:mm:ss]	*eei* [-]	x [in]	y [in]	z [in]	t_s [hh:mm:ss]	*eei* [-]
2476	48.7	0.2	-0.2	11:12:40.311682	0.07	47.3	-0.3	-0.5	11:12:40.311684	0.12
2481	59.4	-2.4	-9.4	11:12:40.501137	3.49	53.8	-3.8	-6.0	11:12:40.501123	0.47
2482	62.3	-4.0	-10.9	11:12:40.576656	1.53	60.3	-2.8	-3.0	11:12:40.576696	0.98
2505	-17.5	-4.0	-12.0	11:12:41.363569	>10.00	70.8	-3.3	1.5	11:12:41.364184	0.05
2534	38.5	-4.0	-12.0	11:12:42.048395	>10.00	49.8	-3.8	-8.5	11:12:42.048488	0.20
2536	60.9	0.6	-8.0	11:12:42.088361	0.46	59.8	-0.3	-6.0	11:12:42.088366	NEL
2559	44.6	-1.3	3.0	11:12:42.599448	NaN	57.8	-0.3	2.0	11:12:42.599265	0.77
2567	66.3	2.9	-10.9	11:12:42.725191	2.45	60.8	0.3	-11.5	11:12:42.725168	0.58
2569	60.7	4.0	-7.0	11:12:42.751200	0.19	49.8	3.8	6.5	11:12:42.751170	NEL
2578	47.8	1.6	-8.8	11:12:43.000645	0.52	50.3	1.8	-6.5	11:12:43.000648	0.36
2597	61.6	-2.1	-7.3	11:12:43.592427	0.11	61.8	-3.3	-7.5	11:12:43.592421	0.14
2616	58.7	4.0	-12.0	11:12:44.150775	1.13	60.3	-0.3	-5.5	11:12:44.150804	0.02
2624	-96.0	4.0	-12.0	11:12:44.350191	>10.00	45.3	0.3	5.0	11:12:44.357687	0.10
2632	67.0	-4.0	-12.0	11:12:44.698389	3.16	63.3	-3.8	-11.0	11:12:44.698441	0.48
2637	62.5	-4.0	-4.7	11:12:44.750903	0.84	58.8	-3.8	-1.0	11:12:44.750892	0.63
2661	62.8	-1.0	-6.6	11:12:45.303849	NaN	62.3	-0.8	-7.0	11:12:45.303851	0.10
2674	-96.0	-4.0	-12.0	11:12:45.544814	NaN	54.3	-0.3	-5.0	11:12:45.576281	0.04
2696	56.4	-0.3	1.5	11:12:45.883289	0.12	56.8	-0.3	2.0	11:12:45.883286	0.30
2738	43.2	-4.0	-12.0	11:12:46.444823	>10.00	59.8	-3.8	-11.5	11:12:46.444903	0.60
2749	-96.0	-4.0	-12.0	11:12:46.555627	>10.00	60.3	0.3	-3.5	11:12:46.607143	0.71
2773	48.6	3.5	-5.0	11:12:47.045661	0.22	49.3	1.3	-0.5	11:12:47.045665	0.33
2785	60.5	-3.0	-3.9	11:12:47.242689	0.19	56.3	-2.8	2.0	11:12:47.242683	0.31
2830	62.3	-4.0	-11.9	11:12:48.171469	0.63	62.8	-1.8	-7.5	11:12:48.171495	0.10
2872	62.8	-1.5	-7.1	11:12:48.869389	0.38	63.3	-3.8	-10.5	11:12:48.869371	0.26
2908	56.6	-2.7	-0.1	11:12:49.457466	0.28	56.3	-3.8	1.5	11:12:49.457458	0.45
3028	76.8	-4.0	-12.0	11:12:51.331002	9.55	64.8	-2.3	-11.5	11:12:51.331075	0.86
3043	57.1	-0.3	3.1	11:12:51.572768	0.04	56.8	-0.3	3.5	11:12:51.572767	0.19
3062	69.3	1.8	-12.0	11:12:51.907551	1.59	65.8	3.8	-11.0	11:12:51.907568	0.89
3066	64.6	-4.0	-12.0	11:12:51.945254	NaN	61.8	-3.8	-6.0	11:12:51.945281	0.43
3079	60.3	-2.3	-3.3	11:12:52.199695	0.42	59.8	0.8	-3.5	11:12:52.199685	0.46
3138	53.6	-4.0	-0.3	11:12:53.246947	0.76	61.8	-3.8	-8.0	11:12:53.246937	0.46
3167	68.3	-0.3	-12.0	11:12:53.690734	5.75	63.8	0.3	-11.5	11:12:53.690782	0.30
3174	59.7	-1.8	-2.9	11:12:53.755008	0.16	59.3	-0.8	-2.0	11:12:53.755008	0.19
3192	64.9	-0.4	6.8	11:12:54.038835	NaN	65.8	0.3	7.5	11:12:54.038836	0.03
3318	59.6	0.3	-7.0	11:12:56.112823	NaN	63.8	3.8	1.0	11:12:56.112859	0.03
3329	60.5	3.5	-1.6	11:12:56.350481	0.55	61.8	3.8	-1.0	11:12:56.350462	0.59
3332	96.0	-4.0	-12.0	11:12:56.396558	>10.00	55.8	0.3	-11.5	11:12:56.397220	0.87
3341	96.0	-12.0	-12.0	11:12:56.609931	NaN	59.3	3.8	-10.5	11:12:56.610593	0.52
3345	52.4	7.9	9.3	11:12:56.741058	0.24	52.8	5.8	9.0	11:12:56.741043	0.78
3346	53.5	-2.6	5.0	11:12:56.758209	0.40	55.3	0.3	4.0	11:12:56.758220	0.21
3353	89.8	4.0	-12.0	11:12:57.044318	>10.00	66.8	0.3	-11.5	11:12:57.044480	0.56
3384	96.0	-4.0	-12.0	11:12:57.654130	NaN	62.3	-3.8	-6.0	11:12:57.655777	0.35
3395	96.0	12.0	9.2	11:12:57.817150	>10.00	75.3	2.3	6.5	11:12:57.817338	0.66
3466	60.6	-2.2	-5.3	11:12:58.899475	0.42	60.3	-2.8	-4.5	11:12:58.899472	0.38

Tab. C.11: SW II - localized events, part 4: Coordinates of the estimated source locations determined using Geiger's method and *FastWay*. Estimated source locations excluded during the verification process (see Section 7.3.4) are shown in gray.

Event	Geiger's method					*FastWay*				
#	x [in]	y [in]	z [in]	t_s [hh:mm:ss]	*eei* [-]	x [in]	y [in]	z [in]	t_s [hh:mm:ss]	*eei* [-]
3475	63.4	-2.7	-2.6	11:12:59.018916	0.12	76.8	-7.8	8.5	11:12:59.018887	NEL
3478	55.0	1.5	-9.0	11:12:59.059344	0.85	56.3	3.3	-11.5	11:12:59.059343	NEL
3503	77.2	4.0	-12.0	11:12:59.378706	>10.00	57.3	-0.8	-9.0	11:12:59.378901	0.25
3528	56.6	1.0	-12.0	11:12:59.739257	0.54	55.8	0.8	0.5	11:12:59.739302	0.19
3533	-96.0	4.0	-12.0	11:12:59.712989	NaN	38.8	3.8	-11.0	11:12:59.804845	0.50
3582	49.2	-12.0	9.5	11:13:00.768215	3.13	60.3	-3.3	-4.0	11:13:00.768327	0.17
3597	-4.8	4.0	-12.0	11:13:01.069985	>10.00	46.8	-1.3	1.5	11:13:01.070269	0.05
3612	65.0	1.7	-1.5	11:13:01.369690	NaN	64.8	2.3	-1.5	11:13:01.369693	0.04
3635	67.9	-4.0	4.0	11:13:02.039410	NaN	67.8	-3.8	4.0	11:13:02.039384	0.96
3657	-96.0	4.0	-12.0	11:13:02.471969	>10.00	35.3	3.8	4.0	11:13:02.510299	0.12
3663	48.6	2.3	1.5	11:13:02.608096	0.58	48.3	3.8	-4.5	11:13:02.608065	NEL
3674	-96.0	4.0	-12.0	11:13:02.851504	>10.00	58.8	3.8	0.5	11:13:02.866779	0.63
3675	57.5	1.7	2.4	11:13:02.881057	0.21	58.3	3.8	5.0	11:13:02.881059	0.42
3679	-96.0	-12.0	8.0	11:13:02.777992	NaN	37.8	-11.8	12.0	11:13:02.950286	0.71
3733	74.6	-4.0	-8.5	11:13:04.394500	2.31	69.3	-3.8	-4.5	11:13:04.394532	0.13
3747	59.8	-4.0	0.3	11:13:04.690195	0.48	57.3	1.3	-4.5	11:13:04.690208	0.55
3764	55.2	-0.3	2.1	11:13:04.993866	0.10	52.3	-3.8	3.5	11:13:04.993843	0.28
3770	-96.0	12.0	-12.0	11:13:04.734563	NaN	53.8	11.8	8.5	11:13:05.086130	0.98
3805	48.4	-0.7	-3.0	11:13:05.975319	NaN	50.3	-2.8	-0.5	11:13:05.975323	0.05
3819	22.2	4.0	-12.0	11:13:06.182396	>10.00	63.3	-3.8	-11.0	11:13:06.182689	0.69
3828	61.6	-3.8	12.0	11:13:06.429624	0.05	65.3	-3.8	12.0	11:13:06.429612	NEL
3840	68.0	-2.8	0.5	11:13:06.664737	0.71	70.8	-0.8	6.0	11:13:06.664754	NEL
3887	65.9	0.9	-8.4	11:13:07.966346	0.74	62.8	-1.3	-11.5	11:13:07.966314	0.66
3890	29.7	-1.6	4.8	11:13:08.053217	0.34	30.3	-2.8	5.0	11:13:08.053230	NEL
3893	58.6	3.2	5.0	11:13:08.142305	0.11	58.8	3.8	5.5	11:13:08.142305	0.11
3899	-96.0	12.0	-12.0	11:13:07.989032	>10.00	50.3	0.3	0.0	11:13:08.260399	0.02
3921	65.1	-2.8	-12.0	11:13:09.036712	2.22	60.8	-3.8	-11.5	11:13:09.036715	0.40
3925	54.2	-4.0	-6.1	11:13:09.159798	2.21	53.8	-3.8	-6.0	11:13:09.159761	0.87
3947	-96.0	-4.0	-12.0	11:13:09.660052	>10.00	45.3	-3.8	5.0	11:13:09.674699	0.11
3959	52.3	4.0	-4.1	11:13:10.049358	0.55	54.8	3.8	0.0	11:13:10.049366	NEL
4004	-96.0	-4.0	-12.0	11:13:11.269107	>10.00	55.8	1.8	1.5	11:13:11.326590	0.13
4012	60.1	-4.0	-3.8	11:13:11.526002	0.14	59.8	-1.3	-3.5	11:13:11.526004	0.05
4039	59.6	0.2	-0.4	11:13:13.206434	0.36	60.8	-3.8	-2.5	11:13:13.206428	0.32
4052	55.2	1.2	4.3	11:13:14.039410	0.21	55.3	0.8	4.5	11:13:14.039416	0.11
4055	64.2	-3.7	-10.6	11:13:14.219631	2.09	61.8	-3.8	-4.5	11:13:14.219634	0.52
4068	-96.0	-4.0	-12.0	11:13:14.859106	>10.00	57.3	0.8	-11.0	11:13:14.871471	0.98
4074	45.6	-0.9	-3.4	11:13:15.165576	NaN	45.8	-0.8	-3.0	11:13:15.165578	0.03
4079	37.9	4.0	-9.0	11:13:15.557654	0.37	38.8	3.8	-7.0	11:13:15.557663	0.13
4097	59.8	1.6	-1.8	11:13:17.145669	0.26	57.3	-1.8	5.5	11:13:17.145629	NEL
4106	57.3	-0.4	-2.2	11:13:18.093450	0.23	55.8	-3.3	1.0	11:13:18.093458	0.45
4113	48.4	0.1	4.0	11:13:19.622313	0.04	48.3	-0.8	4.5	11:13:19.622311	0.16
4127	65.8	-3.1	-5.3	11:13:21.840279	NaN	65.8	-2.8	-6.0	11:13:21.840293	0.06
4133	49.9	-4.0	6.1	11:13:24.220951	0.51	51.3	-1.8	12.0	11:13:24.220965	1.10
4135	58.8	-0.6	-2.1	11:13:24.857908	0.34	57.3	-1.8	0.5	11:13:24.857914	0.13
4168	60.0	2.6	-12.0	11:13:37.066358	1.22	58.8	3.8	-11.0	11:13:37.066338	0.94

Tab. C.12: SW II - localized events, part 5: Coordinates of the estimated source locations determined using Geiger's method and *FastWay*. Estimated source locations excluded during the verification process (see Section 7.3.4) are shown in gray.

Event	Geiger's method					*FastWay*				
#	x [in]	y [in]	z [in]	t_s [hh:mm:ss]	*eei* [-]	x [in]	y [in]	z [in]	t_s [hh:mm:ss]	*eei* [-]
4170	42.1	-1.5	-1.0	11:13:37.660559	0.53	38.8	3.8	-0.5	11:13:37.660551	0.61
4171	56.5	1.6	3.5	11:13:38.247878	NaN	56.3	0.3	4.5	11:13:38.247885	0.06
4176	61.6	-1.6	-3.9	11:13:42.568850	0.51	59.8	2.3	-5.5	11:13:42.568851	0.36
4193	67.2	4.0	-0.2	11:13:54.055927	0.65	64.3	3.8	-10.5	11:13:54.055891	0.30
4506	33.2	-4.0	-10.6	11:18:19.983461	>10.00	59.8	3.8	-11.5	11:18:19.983559	0.81
4525	57.8	2.4	0.4	11:18:48.394783	0.31	58.8	2.8	0.5	11:18:48.394777	0.78
4578	62.2	-4.0	5.7	11:19:01.333681	1.60	61.3	-3.8	3.5	11:19:01.333685	0.79
4582	48.8	4.0	-2.3	11:19:01.537428	1.04	49.8	3.8	-2.5	11:19:01.537427	0.61
4626	-96.0	4.0	-12.0	11:19:05.864596	NaN	59.3	3.8	-10.0	11:19:05.884690	0.29
4628	75.1	-4.0	-12.0	11:19:06.070388	>10.00	65.8	3.8	-11.0	11:19:06.070478	0.70
4642	49.4	12.0	8.0	11:19:07.381959	NaN	55.8	3.8	-4.0	11:19:07.381958	0.37
4685	59.6	-0.2	-2.2	11:19:09.326456	0.60	62.3	1.8	-6.5	11:19:09.326426	0.63
4693	44.4	1.0	-2.5	11:19:09.784832	0.74	46.3	-3.3	-3.5	11:19:09.784841	0.02
4704	59.6	0.2	-9.0	11:19:10.986824	1.48	60.3	-0.3	-6.0	11:19:10.986830	0.26
4707	74.0	4.0	-0.6	11:19:11.115289	0.82	73.8	3.8	-2.0	11:19:11.115298	0.20
4758	46.8	12.0	12.0	11:19:13.295357	NaN	61.3	-4.3	12.0	11:19:13.295544	0.63
4780	-96.0	4.0	-12.0	11:19:14.521861	>10.00	53.3	-3.8	-6.5	11:19:14.543474	0.57
4793	96.0	4.0	-12.0	11:19:14.957066	>10.00	61.8	2.3	-7.5	11:19:14.958336	0.36
4795	55.5	-4.0	3.7	11:19:14.977689	0.52	56.3	0.3	5.5	11:19:14.977677	0.44
4799	74.9	2.2	-12.0	11:19:15.210511	6.30	66.8	0.8	-11.5	11:19:15.210580	0.33
4803	-96.0	4.0	-12.0	11:19:15.283935	>10.00	58.8	0.3	-4.0	11:19:15.309298	0.46
4830	62.6	4.0	-12.0	11:19:16.226042	>10.00	64.3	3.8	-10.5	11:19:16.226101	0.61
4913	48.3	1.7	0.4	11:19:18.879351	0.34	43.3	-3.8	0.0	11:19:18.879336	0.06
4958	62.5	-4.0	-8.0	11:19:20.078715	NaN	66.8	-2.8	-9.0	11:19:20.078719	0.07
4963	46.6	0.3	-7.8	11:19:20.167295	0.29	24.3	-0.8	-9.5	11:19:20.167182	NEL
4986	57.7	4.0	-6.9	11:19:20.611397	NaN	51.8	3.8	-8.0	11:19:20.611263	0.82
5089	56.2	-1.1	4.0	11:19:22.772123	0.26	52.8	0.3	3.5	11:19:22.772108	NEL
5097	-96.0	-4.0	-12.0	11:19:22.933457	NaN	51.8	3.8	2.5	11:19:22.962958	0.27
5106	67.7	-0.1	-9.6	11:19:23.235978	NaN	62.3	-2.8	-2.5	11:19:23.236013	0.05
5168	55.6	-3.4	-12.0	11:19:24.219399	>10.00	58.8	-3.8	-11.5	11:19:24.219451	0.73
5178	-96.0	-4.0	-12.0	11:19:24.360208	>10.00	65.3	-0.3	-11.5	11:19:24.398211	0.04
5220	66.8	3.1	2.4	11:19:25.058935	NaN	66.8	3.8	3.0	11:19:25.058936	0.06
5249	54.3	4.0	-5.4	11:19:25.485380	0.46	60.3	3.8	-8.0	11:19:25.485345	NEL
5256	62.0	-4.0	-2.5	11:19:25.578204	0.24	66.3	-3.8	-4.5	11:19:25.578176	NEL
5268	63.0	-2.5	-9.3	11:19:25.773688	1.59	61.3	0.3	-10.5	11:19:25.773672	0.47
5357	54.4	-4.0	-0.4	11:19:27.277876	NaN	57.3	-3.8	-2.0	11:19:27.277910	0.79
5408	57.0	0.8	1.2	11:19:28.075717	0.16	55.8	-1.3	3.0	11:19:28.075722	0.07
5449	48.4	3.0	-1.5	11:19:28.773591	0.10	48.8	1.8	-0.5	11:19:28.773589	0.15
5531	96.0	-12.0	-12.0	11:19:30.188392	NaN	74.8	3.8	-2.5	11:19:30.205566	0.80
5661	47.9	-5.2	12.0	11:19:32.709435	0.77	44.8	-4.3	12.0	11:19:32.709453	0.28
5699	55.4	1.5	5.2	11:19:33.187585	0.19	56.3	3.8	6.0	11:19:33.187578	0.16
5739	61.5	12.0	12.0	11:19:33.798689	NaN	58.3	9.8	9.5	11:19:33.798713	0.35
5745	-96.0	12.0	-12.0	11:19:33.467423	>10.00	52.8	3.8	10.5	11:19:33.849155	0.49
5796	57.4	-1.6	0.7	11:19:34.907798	0.26	57.3	-2.3	0.0	11:19:34.907800	0.08

Tab. C.13: SW II - localized events, part 6: Coordinates of the estimated source locations determined using Geiger's method and *FastWay*. Estimated source locations excluded during the verification process (see Section 7.3.4) are shown in gray.

Event	Geiger's method					*FastWay*				
#	x [in]	y [in]	z [in]	t_s [hh:mm:ss]	*eei* [-]	x [in]	y [in]	z [in]	t_s [hh:mm:ss]	*eei* [-]
5822	58.9	1.5	4.3	11:19:35.626184	0.24	54.8	-1.3	7.0	11:19:35.626189	0.07
5857	63.1	4.0	1.6	11:19:36.353442	NaN	62.8	3.8	0.0	11:19:36.353445	0.54
5868	-96.0	4.0	-12.0	11:19:36.515727	>10.00	58.8	-3.8	2.0	11:19:36.556997	0.17
5874	59.0	-4.0	-5.8	11:19:36.665639	2.22	62.8	-3.8	-11.0	11:19:36.665611	0.56
5940	45.4	-3.2	-4.1	11:19:37.885682	0.65	49.8	-2.8	2.5	11:19:37.885662	NEL
6039	79.6	4.0	-3.4	11:19:39.651465	3.99	67.8	1.3	-0.5	11:19:39.651506	0.38
6234	72.1	1.2	-2.1	11:19:43.891721	3.83	65.3	3.8	-8.5	11:19:43.891675	0.35
6276	48.3	0.5	2.6	11:19:46.850890	0.18	49.8	2.3	5.0	11:19:46.850878	0.38
6279	65.1	-4.0	0.6	11:19:46.954974	NaN	77.8	-3.8	-7.0	11:19:46.954907	0.32
6410	67.7	-1.0	-10.7	11:20:25.209674	1.29	57.8	-1.3	-4.0	11:20:25.209710	0.79
6420	59.0	-4.0	-2.6	11:20:31.206651	0.55	62.8	-2.8	-6.5	11:20:31.206623	NEL
6440	66.1	4.0	-5.1	11:20:54.098759	0.58	64.8	3.3	-6.5	11:20:54.098754	NEL
6450	56.2	-8.9	12.0	11:21:03.800318	0.34	57.8	-7.3	8.5	11:21:03.800336	0.10
6456	52.4	4.0	2.0	11:21:19.048476	1.02	46.3	6.3	8.5	11:21:19.048474	0.08
6459	57.9	2.6	2.4	11:21:31.768710	0.12	58.8	1.8	3.0	11:21:31.768712	0.18
6461	71.2	-4.0	-12.0	11:26:01.843103	>10.00	55.8	0.3	-11.5	11:26:01.843237	0.26
6474	58.7	2.3	-6.5	11:26:06.844952	1.25	56.8	-0.3	-5.0	11:26:06.844989	0.07
6887	61.0	2.6	-0.6	11:26:52.492708	NaN	47.8	-1.8	-11.5	11:26:52.492160	0.89
6895	58.0	1.2	-6.7	11:27:55.504655	3.57	58.3	3.8	-3.0	11:27:55.504652	0.79
6927	60.1	2.3	-0.5	11:28:35.420726	0.56	59.3	3.3	1.0	11:28:35.420712	0.78
6987	61.3	2.2	-0.2	11:29:06.841551	NaN	58.8	2.3	-2.0	11:29:06.841531	0.17
6990	55.8	4.0	-7.1	11:29:07.164407	3.50	55.8	3.8	-4.0	11:29:07.164397	0.96
7065	58.8	4.0	0.7	11:29:15.465137	0.91	45.8	-3.8	-1.5	11:29:15.465178	NEL
7084	54.2	-4.0	6.3	11:29:16.771104	0.67	54.8	-3.8	10.5	11:29:16.771092	NEL
7141	38.8	1.8	3.4	11:29:20.637328	NaN	27.3	3.8	-10.5	11:29:20.605676	0.80
7149	54.6	4.0	3.4	11:29:20.786818	0.33	53.3	3.8	-10.5	11:29:20.786771	0.38
7270	44.8	-4.1	12.0	11:29:27.718168	1.57	48.8	-2.3	9.0	11:29:27.718197	0.03
7279	42.6	1.9	-9.6	11:29:27.980377	NaN	46.3	3.8	1.5	11:29:27.980294	0.84
7315	66.2	3.6	-2.7	11:29:28.870137	0.41	65.8	3.8	0.0	11:29:28.870143	0.16
7330	43.4	-0.4	-9.4	11:29:29.231126	2.93	48.8	-0.3	-11.5	11:29:29.231122	0.13
7406	96.0	4.0	-12.0	11:29:31.298990	>10.00	57.3	1.8	3.0	11:29:31.300264	0.16
7478	55.6	2.2	0.6	11:29:32.987849	0.19	54.8	0.3	2.0	11:29:32.987836	0.36
7495	-96.0	-4.0	-12.0	11:29:33.317295	NaN	33.3	-2.8	6.5	11:29:33.435912	0.23
7502	85.3	-4.0	-5.5	11:29:33.102776	NaN	65.8	3.8	-6.0	11:29:33.586158	0.81
7536	-96.0	4.0	-12.0	11:29:34.518969	>10.00	36.3	-0.3	6.0	11:29:34.535362	0.05
7541	64.5	2.0	0.6	11:29:34.736148	2.26	56.3	-3.8	5.5	11:29:34.736182	0.38
7573	51.9	4.0	-8.0	11:29:35.904820	1.64	51.8	3.8	-8.0	11:29:35.904775	0.89
7747	51.7	3.9	-2.4	11:29:40.512812	0.26	52.8	-3.8	-4.5	11:29:40.512794	0.10
7854	66.9	0.3	1.3	11:29:43.191326	0.13	66.3	0.8	2.5	11:29:43.191325	0.05
7982	73.7	-0.5	1.1	11:29:45.943328	1.11	76.8	-3.8	0.5	11:29:45.943309	0.66
7988	72.4	-12.0	12.0	11:29:46.187121	>10.00	59.8	-11.8	12.0	11:29:46.187297	0.83
7989	54.5	1.1	-1.4	11:29:46.272923	0.40	54.8	3.8	-3.5	11:29:46.272917	NEL
8007	59.4	0.2	-4.2	11:29:46.915859	0.33	59.8	2.8	-10.0	11:29:46.915820	0.19
8029	96.0	-4.0	-12.0	11:29:47.375993	>10.00	70.3	-2.3	-11.5	11:29:47.376336	0.73
8063	58.1	1.6	4.2	11:29:48.137327	0.23	60.3	2.8	3.0	11:29:48.137325	0.57

Tab. C.14: SW II - localized events, part 7: Coordinates of the estimated source locations determined using Geiger's method and *FastWay*. Estimated source locations excluded during the verification process (see Section 7.3.4) are shown in gray.

Event	Geiger's method					*FastWay*				
#	x [in]	y [in]	z [in]	t_s [hh:mm:ss]	*eei* [-]	x [in]	y [in]	z [in]	t_s [hh:mm:ss]	*eei* [-]
8158	-96.0	-4.0	-12.0	11:29:49.949447	>10.00	54.3	-3.8	1.5	11:29:49.997599	0.07
8176	55.8	0.5	2.9	11:29:50.529822	0.33	70.8	-1.3	2.0	11:29:50.529768	NEL
8181	64.9	-0.4	2.9	11:29:50.620191	NaN	69.8	-3.8	0.5	11:29:50.620032	0.32
8334	48.0	4.0	-12.0	11:29:55.818688	>10.00	53.8	-3.8	-6.0	11:29:55.819001	0.60
8472	59.7	-2.6	1.1	11:30:02.340867	0.35	60.8	3.3	2.5	11:30:02.340884	0.27
8473	-96.0	-4.0	-12.0	11:30:02.295821	NaN	54.8	1.8	2.0	11:30:02.445336	0.03
8478	-96.0	-4.0	-12.0	11:30:03.027211	>10.00	66.3	-3.8	5.5	11:30:03.123243	0.61
8492	29.9	-9.0	12.0	11:30:04.909201	3.78	35.8	-2.8	7.5	11:30:04.909224	0.03
8551	-96.0	-4.0	-12.0	11:30:14.194388	>10.00	68.8	-1.8	6.0	11:30:14.249620	0.13
8569	96.0	-4.0	-12.0	11:30:20.689646	>10.00	74.8	-0.3	0.5	11:30:20.690008	0.51
8607	60.7	-3.2	-12.0	11:31:07.464305	7.93	62.8	-3.8	-6.0	11:31:07.464336	0.81
8635	-96.0	-4.0	-12.0	11:33:07.386811	NaN	70.8	3.8	-11.0	11:33:07.434697	0.73
8731	-96.0	-4.0	-12.0	11:33:14.000569	>10.00	71.8	-1.3	-11.5	11:33:14.045895	0.22
9063	-96.0	-12.0	12.0	11:33:28.813074	NaN	71.8	-11.8	12.0	11:33:28.846736	0.65
9139	58.6	0.6	-3.1	11:33:31.382591	0.17	62.3	-1.8	-3.0	11:33:31.382574	NEL
9224	55.2	4.0	2.8	11:33:35.030757	0.30	55.3	1.3	6.0	11:33:35.030748	0.05
9230	56.7	-0.4	-7.6	11:33:41.738375	0.90	54.8	-3.8	-2.5	11:33:41.738340	NEL
9231	44.0	4.0	-12.0	11:33:41.772887	1.53	47.8	3.8	1.5	11:33:41.772967	0.24
9340	60.4	-4.0	-4.7	11:35:46.541803	NaN	58.3	-3.8	-6.0	11:35:46.541783	0.47
9379	-96.0	-4.0	-12.0	11:35:52.937407	>10.00	60.8	0.8	4.5	11:35:53.030446	0.29
9394	96.0	12.0	-12.0	11:35:53.951137	NaN	57.8	3.3	-6.0	11:35:53.952060	0.33
9404	-96.0	4.0	-12.0	11:35:55.861287	NaN	51.8	-0.8	1.5	11:35:55.877633	0.04
9428	68.0	-4.0	4.0	11:35:58.922360	0.67	63.3	3.3	8.5	11:35:58.922357	NEL
9475	54.4	4.0	2.3	11:36:02.835366	0.19	55.3	3.8	3.5	11:36:02.835359	0.23
9487	-96.0	-4.0	-12.0	11:36:03.472155	>10.00	49.8	-3.8	-10.0	11:36:03.512061	0.64
9496	59.5	-2.1	-1.9	11:36:03.973464	0.12	56.3	-2.8	1.5	11:36:03.973459	0.09
9517	41.7	4.0	-0.3	11:36:04.628423	0.51	39.8	3.8	2.0	11:36:04.628424	NEL
9521	-96.0	12.0	-12.0	11:36:04.710796	NaN	61.3	0.8	5.0	11:36:04.956364	0.03
9663	60.0	3.9	-0.2	11:36:11.675576	0.53	59.8	3.8	0.0	11:36:11.675573	NEL
9719	96.0	-12.0	12.0	11:36:13.238036	NaN	61.8	2.3	12.0	11:36:13.238388	0.64
9861	-96.0	-4.0	-12.0	11:36:16.925400	NaN	63.8	-2.3	5.0	11:36:17.008234	0.04
9888	62.4	0.8	5.0	11:36:18.031822	0.21	63.8	0.3	4.0	11:36:18.031823	0.10
10028	62.8	2.1	3.9	11:36:21.656791	0.48	55.8	4.3	12.0	11:36:21.656765	0.26
10031	-96.0	-4.0	-12.0	11:36:21.708314	>10.00	55.3	1.8	5.0	11:36:21.715786	0.44
10095	-96.0	-12.0	8.0	11:36:23.232550	NaN	61.8	-2.3	-3.0	11:36:23.257075	0.65
10109	-96.0	-4.0	-12.0	11:36:23.575265	>10.00	63.8	-3.8	-4.0	11:36:23.584783	0.36
10140	65.8	2.8	12.0	11:36:24.312747	0.61	62.8	0.8	12.0	11:36:24.312741	0.48
10145	69.7	-2.0	2.5	11:36:24.487859	NaN	68.3	-2.3	4.0	11:36:24.487851	0.14
10150	66.3	-4.0	-7.3	11:36:24.575110	0.98	66.8	-3.8	3.0	11:36:24.575152	NEL
10198	44.0	1.2	3.6	11:36:26.220910	0.79	47.3	3.8	5.5	11:36:26.220868	0.58
10304	50.5	-4.0	2.2	11:36:29.068954	0.60	46.3	2.3	-1.5	11:36:29.068968	0.23
10321	-96.0	4.0	-12.0	11:36:29.645053	>10.00	50.8	-3.3	-11.5	11:36:29.776396	0.22
10396	-96.0	-4.0	-12.0	11:36:31.245366	NaN	52.8	3.8	-10.5	11:36:31.290914	0.33
10436	96.0	-9.9	12.0	11:36:32.288275	>10.00	77.3	-6.3	10.5	11:36:32.288413	0.85
10486	-96.0	-4.0	-12.0	11:36:33.747271	>10.00	46.3	-3.8	-6.0	11:36:33.777654	0.37

Tab. C.15: SW II - localized events, part 8: Coordinates of the estimated source locations determined using Geiger's method and *FastWay*. Estimated source locations excluded during the verification process (see Section 7.3.4) are shown in gray.

Event	Geiger's method					*FastWay*				
#	x [in]	y [in]	z [in]	t_s [hh:mm:ss]	*eei* [-]	x [in]	y [in]	z [in]	t_s [hh:mm:ss]	*eei* [-]
10597	70.2	-0.3	-3.8	11:36:36.365570	0.48	70.8	3.8	0.0	11:36:36.365584	0.29
10712	-96.0	-4.0	-12.0	11:36:44.360458	NaN	71.3	3.8	-10.5	11:36:44.426460	0.39
10746	-96.0	-4.0	-12.0	11:36:49.549627	>10.00	64.8	-3.8	2.5	11:36:49.668634	0.99
10747	-96.0	4.0	-12.0	11:36:49.765139	>10.00	65.3	3.8	-10.5	11:36:49.795805	0.56
10792	63.9	3.8	4.5	11:37:03.455262	0.24	64.8	2.8	7.0	11:37:03.455252	0.37
10797	-96.0	-4.0	-12.0	11:37:08.079991	NaN	27.3	-0.8	5.0	11:37:08.085917	0.03
10798	51.0	8.1	12.0	11:37:09.986499	0.63	52.8	11.8	11.5	11:37:09.986474	0.60
10818	36.2	3.9	-4.0	11:37:27.355621	5.04	42.8	3.8	-3.0	11:37:27.355623	0.43
10862	-96.0	-12.0	-12.0	11:38:31.999819	NaN	43.8	3.8	4.0	11:38:32.279919	0.70
10942	32.8	-1.6	12.0	11:46:00.807995	0.61	34.8	1.8	12.0	11:46:00.807972	0.52
10945	-96.0	-4.0	-12.0	11:46:05.921789	>10.00	34.8	-3.3	11.5	11:46:05.929232	0.03
10948	40.5	-5.4	12.0	11:46:12.300269	1.83	56.3	-1.8	9.0	11:46:12.300341	0.20
10951	58.7	-0.2	2.9	11:46:15.772894	0.45	59.3	-1.3	10.0	11:46:15.772903	0.42
10955	-96.0	-4.0	-12.0	11:46:25.088006	>10.00	75.3	3.8	12.0	11:46:25.153834	0.53
10957	-30.0	-12.0	12.0	11:46:52.023771	>10.00	24.3	-7.8	10.5	11:46:52.024174	0.72
10963	59.8	-10.8	12.0	11:47:17.710481	1.91	56.8	-7.3	8.5	11:47:17.710513	0.34
10974	96.0	-12.0	12.0	11:47:44.462644	NaN	35.3	-9.8	12.0	11:47:44.488463	0.85
10978	36.3	-5.3	9.1	11:48:01.812598	1.46	45.8	-11.8	8.5	11:48:01.812542	0.84
10983	-96.0	-4.0	-12.0	11:48:29.781861	>10.00	58.3	-10.8	11.5	11:48:29.809161	0.80
10992	-96.0	4.0	-12.0	11:48:51.388586	NaN	41.8	1.3	9.5	11:48:51.516611	0.06
10994	-1.8	0.0	12.0	11:49:05.853646	>10.00	24.3	-7.8	12.0	11:49:05.853827	0.62
11005	-20.2	-4.0	-3.2	11:49:44.131265	>10.00	26.3	-11.8	12.0	11:49:44.131544	0.26
11008	37.9	-5.6	12.0	11:50:02.049884	0.93	33.3	-7.8	10.0	11:50:02.049898	NEL
11010	55.5	-5.8	9.1	11:50:09.463091	0.15	55.8	-4.8	8.5	11:50:09.463098	0.22
11015	-96.0	-4.0	-12.0	11:50:18.743505	>10.00	64.8	-8.8	8.5	11:50:18.773475	0.19
11038	-96.0	4.0	-12.0	11:51:34.851063	NaN	32.3	-0.8	7.5	11:51:34.885281	0.04
11041	-96.0	-12.0	12.0	11:52:01.924587	>10.00	57.8	-2.3	10.5	11:52:01.932131	0.18
11043	-96.0	-4.0	-12.0	11:52:05.838220	>10.00	61.3	-0.8	10.0	11:52:05.901471	0.07
11065	10.5	-12.0	12.0	11:53:15.540936	NaN	31.3	-11.8	8.5	11:53:15.541117	0.43
11068	22.7	-6.6	12.0	11:53:25.558250	>10.00	31.8	-11.8	8.5	11:53:25.558293	0.79
11070	36.5	-3.1	12.0	11:53:30.207945	1.29	45.3	-11.8	9.5	11:53:30.207927	0.36
11071	-96.0	-4.0	-12.0	11:53:34.528947	>10.00	41.8	-11.8	12.0	11:53:34.629069	0.32
11073	46.7	-12.0	12.0	11:53:41.734721	2.68	47.8	-11.8	9.0	11:53:41.734711	0.95
11074	-96.0	-4.0	-12.0	11:53:46.702623	>10.00	52.8	-10.8	8.5	11:53:46.730045	0.58
11096	95.5	-4.5	12.0	11:56:58.532776	>10.00	67.8	-7.3	12.0	11:56:58.532963	0.82
11103	55.0	-9.7	10.2	11:57:44.423147	4.85	59.8	-10.3	8.5	11:57:44.423179	0.82
11112	-96.0	-4.0	-12.0	11:58:37.948553	>10.00	24.3	1.8	-7.5	11:58:37.957452	0.14
11118	73.1	-1.5	11.8	11:59:14.152215	1.88	73.8	-5.8	12.0	11:59:14.152310	0.88
11120	96.0	-12.0	12.0	11:59:24.228903	>10.00	68.3	-11.8	12.0	11:59:24.230834	0.22
11123	-13.0	-11.9	12.0	11:59:57.735163	NaN	24.3	-5.3	10.0	11:59:57.686937	0.95
11127	19.1	-10.7	12.0	12:00:19.131230	>10.00	25.3	-11.8	12.0	12:00:19.131225	0.92
11145	-96.0	-4.0	-12.0	12:01:24.030952	NaN	24.3	-8.8	9.0	12:01:24.058303	0.59
11233	-49.3	4.0	-12.0	12:08:22.457477	>10.00	24.3	0.3	-9.5	12:08:22.458047	0.82
11260	50.3	3.8	-5.7	12:12:22.797342	1.69	53.8	0.8	-10.0	12:12:22.797379	0.87
11269	-96.0	-4.0	-12.0	12:12:42.480089	>10.00	44.3	-3.8	-11.5	12:12:42.493948	0.43

Tab. C.16: SW II - localized events, part 9: Coordinates of the estimated source locations determined using Geiger's method and *FastWay*. Estimated source locations excluded during the verification process (see Section 7.3.4) are shown in gray.

Event	Geiger's method					*FastWay*				
#	x	y	z	t_s	*eei*	x	y	z	t_s	*eei*
	[in]	[in]	[in]	[hh:mm:ss]	[-]	[in]	[in]	[in]	[hh:mm:ss]	[-]
11270	13.9	4.0	-12.0	12:12:44.968414	NaN	44.3	3.8	-11.5	12:12:44.968693	0.44
11271	51.7	-1.9	-10.4	12:12:49.482100	3.31	51.3	-3.8	-9.5	12:12:49.482077	0.67
11280	47.4	1.8	-2.1	12:13:24.206229	0.39	51.3	1.3	1.0	12:13:24.206227	0.34
11284	55.0	-0.7	-9.6	12:13:31.285455	2.38	55.3	-2.3	-10.0	12:13:31.285500	0.94
11287	58.0	4.0	-3.5	12:13:41.885522	0.85	60.3	3.8	-4.5	12:13:41.885573	NEL
11293	-96.0	-12.0	12.0	12:14:12.951772	>10.00	55.3	-2.8	8.5	12:14:12.966238	0.28
11299	-96.0	-4.0	-12.0	12:14:34.009119	>10.00	57.8	-0.8	8.0	12:14:34.068131	0.21
11305	-96.0	-4.0	-12.0	12:14:56.451743	>10.00	57.3	-1.8	7.5	12:14:56.524750	0.47
11310	59.4	-3.3	6.4	12:15:17.078227	0.51	59.8	-3.8	8.0	12:15:17.078219	0.80
11312	96.0	4.0	-12.0	12:15:20.890225	NaN	77.8	8.8	8.5	12:15:20.895722	0.72
11315	53.8	3.4	-3.1	12:15:23.919050	0.46	56.8	-3.3	-3.5	12:15:23.919013	0.75
11318	96.0	4.0	-8.3	12:15:37.735673	>10.00	63.8	1.3	6.5	12:15:37.735996	0.95
11332	96.0	4.0	-10.8	12:16:16.684127	>10.00	64.8	0.8	9.5	12:16:16.684715	0.44
11341	67.6	2.1	5.4	12:16:44.110817	0.75	55.3	-3.8	-5.0	12:16:44.110758	NEL
11345	96.0	4.0	-9.2	12:16:58.327014	>10.00	67.8	-1.3	6.5	12:16:58.327471	0.39
11347	68.3	-4.0	1.3	12:16:59.931214	1.43	67.3	-3.8	3.0	12:16:59.931211	0.91
11357	58.9	0.0	5.3	12:17:44.602372	0.11	57.8	0.8	6.5	12:17:44.602373	NEL
11362	60.0	0.6	7.3	12:17:59.012844	0.20	59.8	0.3	7.5	12:17:59.012847	0.08
11364	-96.0	-4.0	-12.0	12:18:00.424251	>10.00	69.8	2.8	6.0	12:18:00.471263	0.12
11368	35.0	-4.0	-12.0	12:18:13.896319	NaN	69.3	-2.8	7.0	12:18:13.896531	0.09
11371	96.0	4.0	-2.1	12:18:19.097848	>10.00	70.3	0.3	5.0	12:18:19.099003	0.07
11703	73.3	4.0	-1.5	12:19:02.430487	NaN	77.3	3.8	1.5	12:19:02.430461	0.26
11970	-96.0	-12.0	-12.0	12:19:13.423629	>10.00	73.3	-3.8	0.5	12:19:13.765412	0.61
12113	-0.3	-4.0	-12.0	12:19:20.792121	NaN	61.8	0.3	-11.0	12:19:20.792633	0.89

Tab. C.17: SW II - localized events, part 10: Coordinates of the estimated source locations determined using Geiger's method and *FastWay*. Estimated source locations excluded during the verification process (see Section 7.3.4) are shown in gray.

C.3 Pencil-lead breaks SW II b

C.3.1 Top

PLB			Set	Geiger's method						*FastWay*					
x	y	z	#	x	y	z	d	eei	ac	x	y	z	d	eei	ac
[in]	[in]	[in]		[in]	[in]	[in]	[in]	[-]	[-]	[in]	[in]	[in]	[in]	[-]	[-]
26.0	-10.0	12.0	11-13	96.0	-12.0	12.0	70.03	>10.00	6	25.3	-11.8	11.8	1.92	NEL	2
26.0	-6.0	12.0	11-11	-96.0	-12.0	12.0	122.15	>10.00	6	56.3	9.8	8.3	34.31	NEL	6
26.0	-2.0	12.0	11-8	38.4	-0.7	11.6	12.51	>10.00	6	51.3	1.3	8.3	25.73	NEL	6
30.0	-10.0	12.0	14-5	-96.0	4.0	-12.0	129.03	>10.00	6	37.8	-11.8	11.8	7.95	0.11	5
30.0	-6.0	12.0	11-12	-96.0	12.0	8.0	127.34	>10.00	6	26.8	-4.3	10.8	3.90	0.46	3
30.0	-6.0	12.0	13-8	-96.0	4.0	6.3	126.53	>10.00	6	30.3	-5.8	11.8	0.43	NEL	1
30.0	-2.0	12.0	11-6	-96.0	12.0	8.0	126.84	>10.00	6	46.8	3.8	1.3	20.72	NEL	6
30.0	-2.0	12.0	11-9	8.7	-7.1	9.5	22.07	>10.00	6	46.8	3.8	1.3	20.72	NEL	6
34.0	-10.0	12.0	13-12	-96.0	-12.0	12.0	130.02	>10.00	6	33.3	-8.8	11.8	1.48	NEL	2
34.0	-10.0	12.0	13-22	-96.0	-4.0	-12.0	132.33	>10.00	6	30.3	-11.8	8.3	5.58	NEL	4
34.0	-10.0	12.0	14-6	-96.0	4.0	-12.0	132.94	>10.00	6	43.3	-11.3	9.8	9.60	1.01	5
34.0	-6.0	12.0	11-2	-96.0	12.0	8.0	131.30	>10.00	6	26.8	-4.3	10.8	7.56	0.54	5
34.0	-2.0	12.0	13-17	-96.0	4.0	-10.1	132.00	>10.00	6	26.8	-1.3	6.3	9.28	NEL	5
38.0	-10.0	12.0	13-13	-96.0	-4.0	-12.0	136.26	>10.00	6	30.3	-11.8	8.3	8.79	NEL	5
38.0	-10.0	12.0	14-7	-96.0	12.0	-12.0	137.90	>10.00	6	44.8	-5.3	8.3	9.07	NEL	5
38.0	-10.0	12.0	14-22	-96.0	4.0	-12.0	136.85	>10.00	6	40.3	-11.8	9.8	3.63	0.14	3
38.0	-6.0	12.0	11-3	23.0	-1.7	12.0	15.61	4.36	6	36.3	-0.3	11.8	6.02	0.80	4
38.0	-6.0	12.0	13-9	42.3	-0.6	12.0	6.89	1.96	4	26.3	-8.8	8.3	12.64	NEL	6
38.0	-6.0	12.0	13-20	26.6	-9.0	11.2	11.80	2.31	6	33.8	-7.8	8.3	5.93	NEL	4
38.0	-2.0	12.0	13-18	-96.0	4.0	-12.0	136.26	>10.00	6	30.8	-5.3	8.3	8.79	NEL	5
42.0	-10.0	12.0	14-8	-96.0	4.0	-12.0	140.77	>10.00	6	50.3	-11.8	9.3	8.87	0.12	5
42.0	-10.0	12.0	14-23	-96.0	12.0	-12.0	141.79	>10.00	6	43.8	-4.3	8.3	7.08	NEL	4
42.0	-6.0	12.0	13-1	-96.0	-4.0	-12.0	140.09	>10.00	6	30.3	-11.8	8.3	13.61	NEL	6
42.0	-6.0	12.0	13-10	26.1	-8.8	11.4	16.13	2.58	6	33.8	-7.3	8.3	9.15	NEL	5
42.0	-2.0	12.0	14-1	-96.0	4.0	-12.0	140.20	>10.00	6	37.8	-0.3	7.8	6.26	0.18	4
42.0	-2.0	12.0	14-12	-96.0	4.0	-12.0	140.20	>10.00	6	37.8	-0.3	7.8	6.26	0.24	4
42.0	-2.0	12.0	14-19	61.9	0.3	9.4	20.21	0.12	6	59.8	0.8	11.3	17.98	0.05	6
46.0	-10.0	12.0	13-14	29.9	-12.0	12.0	16.24	3.95	6	34.8	-9.3	8.3	11.88	NEL	6
46.0	-10.0	12.0	14-9	-96.0	-4.0	-12.0	144.14	>10.00	6	52.8	-11.8	8.3	7.92	0.24	5
46.0	-10.0	12.0	14-24	49.5	-9.0	10.2	4.09	0.12	3	49.3	-8.3	8.3	5.26	0.21	4
46.0	-6.0	12.0	14-4	-96.0	-4.0	-12.0	144.03	>10.00	6	55.8	-6.3	8.3	10.45	0.23	6
46.0	-2.0	12.0	14-2	60.9	0.0	8.9	15.35	0.17	6	58.8	0.3	9.3	13.24	0.03	6
46.0	-2.0	12.0	14-13	60.5	-0.4	8.9	14.94	0.11	6	60.3	-0.8	8.8	14.67	0.22	6
46.0	-2.0	12.0	14-20	63.5	-0.1	12.0	17.63	0.14	6	62.8	2.3	8.8	17.58	0.09	6
50.0	-10.0	12.0	14-10	-96.0	-4.0	-12.0	148.08	>10.00	6	58.3	-7.8	8.3	9.34	0.61	5
50.0	-10.0	12.0	14-15	47.0	-4.0	1.8	12.25	0.29	6	44.3	-5.8	8.3	8.07	0.20	5
50.0	-10.0	12.0	14-25	54.0	-8.2	8.9	5.36	0.13	4	53.3	-10.3	8.3	4.97	0.08	3
50.0	-6.0	12.0	14-14	-96.0	-4.0	-12.0	147.97	>10.00	6	56.8	-5.3	8.3	7.76	0.31	5
50.0	-2.0	12.0	13-6	96.0	-12.0	12.0	47.07	>10.00	6	77.8	-5.8	11.8	28.00	NEL	6
54.0	-10.0	12.0	13-4	-96.0	-4.0	-12.0	152.03	>10.00	6	38.3	-7.8	10.3	16.01	NEL	6
54.0	-10.0	12.0	13-23	-96.0	-12.0	12.0	150.01	>10.00	6	64.3	-11.8	8.3	11.05	NEL	6
54.0	-10.0	12.0	14-16	-96.0	4.0	-12.0	152.55	>10.00	6	48.8	-11.8	8.3	6.68	0.10	4
54.0	-6.0	12.0	13-2	-96.0	-12.0	12.0	150.12	>10.00	6	46.3	-11.8	8.8	10.18	NEL	6

Tab. C.18: SW II PLB b - "Top", part 1: Coordinates of the pencil-lead breaks and estimated source locations determined using Geiger's method and *FastWay*. Estimated source locations excluded during the verification process (see Section 7.3.4) are shown in gray.

PLB			Set	Geiger's method						*FastWay*					
x [in]	y [in]	z [in]	#	x [in]	y [in]	z [in]	d [in]	eei [-]	ac [-]	x [in]	y [in]	z [in]	d [in]	eei [-]	ac [-]
54.0	-6.0	12.0	14-21	-96.0	-4.0	-12.0	151.92	>10.00	6	55.3	-6.3	8.3	3.96	0.24	3
54.0	-2.0	12.0	13-7	96.0	12.0	12.0	44.27	>10.00	6	72.8	-3.8	6.3	19.69	NEL	6
54.0	-2.0	12.0	14-3	62.5	0.2	12.0	8.79	0.14	5	60.3	0.8	11.8	6.83	0.22	4
58.0	-10.0	12.0	13-5	-96.0	-12.0	12.0	154.01	>10.00	6	64.3	-11.8	8.3	7.50	NEL	4
58.0	-10.0	12.0	14-17	53.2	-9.6	12.0	4.80	0.14	3	53.3	-10.3	8.8	5.76	0.18	4
58.0	-6.0	12.0	13-11	-96.0	-12.0	12.0	154.12	>10.00	6	67.3	-11.8	8.3	11.52	NEL	6
58.0	-6.0	12.0	13-21	96.0	-12.0	12.0	38.47	>10.00	6	67.3	-11.8	8.3	11.52	NEL	6
58.0	-2.0	12.0	11-10	96.0	-4.0	-6.8	42.44	>10.00	6	61.3	-1.8	11.8	3.27	0.80	3
62.0	-10.0	12.0	14-18	56.3	-9.9	11.6	5.77	0.15	4	57.3	-7.8	9.3	5.93	0.16	4
62.0	-6.0	12.0	13-3	-96.0	-12.0	12.0	158.11	>10.00	6	63.3	-8.3	8.3	4.55	NEL	3
62.0	-2.0	12.0	11-7	96.0	-4.0	-6.7	38.88	>10.00	6	61.3	-1.8	11.8	0.83	0.77	1
62.0	-2.0	12.0	13-19	96.0	12.0	12.0	36.77	>10.00	6	77.3	7.8	8.3	18.48	NEL	6
66.0	-10.0	12.0	11-5	96.0	-4.0	2.0	32.20	>10.00	6	71.3	-6.3	11.8	6.46	0.16	4
66.0	-10.0	12.0	13-15	-96.0	-12.0	12.0	162.01	>10.00	6	63.8	-11.8	8.3	4.71	NEL	3
66.0	-2.0	12.0	11-1	96.0	-4.0	-6.7	35.41	>10.00	6	61.3	-1.3	11.8	4.82	0.91	3
70.0	-10.0	12.0	13-16	-96.0	-12.0	12.0	166.01	>10.00	6	69.3	-11.8	8.3	4.21	NEL	3
70.0	-10.0	12.0	14-11	-96.0	-4.0	-12.0	167.83	>10.00	6	36.8	-5.8	8.8	33.68	NEL	6
70.0	-6.0	12.0	11-4	96.0	-12.0	12.0	26.68	>10.00	6	77.8	-7.8	9.8	8.26	1.32	5

Tab. C.19: SW II PLB b - "Top", part 2: Coordinates of the pencil-lead breaks and estimated source locations determined using Geiger's method and *FastWay*. Estimated source locations excluded during the verification process (see Section 7.3.4) are shown in gray.

C.3.2 Top-Front

PLB			Set	Geiger's method						*FastWay*					
x	y	z	#	x	y	z	d	eei	ac	x	y	z	d	eei	ac
[in]	[in]	[in]		[in]	[in]	[in]	[in]	[-]	[-]	[in]	[in]	[in]	[in]	[-]	[-]
30.0	-12.0	10.0	13-24	30.5	-9.5	11.2	2.86	2.09	3	33.8	-8.3	11.8	5.58	NEL	4
34.0	-12.0	10.0	13-25	-96.0	-12.0	12.0	130.02	>10.00	6	27.8	-11.8	8.3	6.50	NEL	4
34.0	-12.0	10.0	13-28	28.7	-10.2	11.3	5.73	6.00	4	30.3	-11.8	11.8	4.15	NEL	3
38.0	-12.0	10.0	13-29	30.0	-12.0	12.0	8.28	2.28	5	27.8	-11.8	8.3	10.40	NEL	6
38.0	-12.0	10.0	13-34	14.2	-4.0	6.5	25.35	4.05	6	31.8	-9.8	8.3	6.87	NEL	4
38.0	-12.0	10.0	14-26	-96.0	4.0	-12.0	136.73	>10.00	6	40.3	-6.8	11.8	5.97	0.38	4
42.0	-12.0	10.0	13-30	-96.0	-4.0	-12.0	139.97	>10.00	6	35.8	-7.8	8.3	7.76	NEL	5
42.0	-12.0	10.0	14-27	46.2	-4.0	7.6	9.34	0.31	5	46.3	-11.8	8.3	4.60	0.24	3
42.0	-12.0	10.0	14-34	-96.0	4.0	-12.0	140.66	>10.00	6	42.8	-7.8	11.3	4.49	1.02	3
46.0	-12.0	10.0	14-28	49.1	-4.0	1.8	11.87	0.40	6	48.8	-11.8	8.3	3.27	0.77	3
46.0	-12.0	10.0	14-31	46.3	-8.6	8.7	3.62	0.14	3	47.3	-8.8	8.3	3.90	0.25	3
46.0	-12.0	10.0	14-35	45.7	-4.0	7.3	8.46	0.29	5	45.3	-10.3	8.3	2.59	0.21	3
50.0	-12.0	10.0	14-29	53.6	-5.0	8.0	8.11	0.26	5	54.3	-11.8	8.3	4.60	0.48	3
50.0	-12.0	10.0	14-32	48.4	-4.0	6.5	8.88	0.26	5	47.8	-11.8	8.3	2.86	0.44	3
50.0	-12.0	10.0	14-36	49.5	-4.0	0.2	12.68	0.30	6	49.8	-11.8	8.3	1.79	0.43	2
54.0	-12.0	10.0	14-30	-96.0	-4.0	-12.0	151.82	>10.00	6	61.3	-8.3	8.3	8.35	NEL	5
54.0	-12.0	10.0	14-33	53.2	-9.0	10.4	3.14	0.20	3	54.3	-10.3	8.3	2.49	0.24	2
54.0	-12.0	10.0	14-37	52.2	-4.0	1.8	11.56	0.33	6	53.3	-11.8	8.3	1.92	0.63	2
58.0	-12.0	10.0	11-14	63.4	-12.0	12.0	5.80	5.54	4	59.8	-10.3	8.3	3.03	1.07	3
58.0	-12.0	10.0	13-31	-96.0	-12.0	12.0	154.01	>10.00	6	60.3	-11.3	8.8	2.68	NEL	3
58.0	-12.0	10.0	14-38	-96.0	-4.0	-12.0	155.77	>10.00	6	55.3	-10.3	8.3	3.70	0.22	3
62.0	-12.0	10.0	13-26	96.0	-12.0	12.0	34.06	>10.00	6	71.8	-11.8	8.3	9.91	NEL	5
62.0	-12.0	10.0	13-32	-96.0	-12.0	12.0	158.01	>10.00	6	65.3	-11.8	8.3	3.70	NEL	3
62.0	-12.0	10.0	13-35	-96.0	-12.0	12.0	158.01	>10.00	6	67.3	-11.8	8.3	5.54	NEL	4
66.0	-12.0	10.0	13-27	-96.0	-12.0	12.0	162.01	>10.00	6	69.8	-11.8	8.3	4.15	NEL	3
66.0	-12.0	10.0	13-33	-96.0	-12.0	12.0	162.01	>10.00	6	70.3	-11.8	8.3	4.60	NEL	3
66.0	-12.0	10.0	13-36	96.0	-12.0	12.0	30.07	>10.00	6	70.3	-11.8	8.3	4.60	NEL	3

Tab. C.20: SW II PLB b - "Top-Front", part 1: Coordinates of the pencil-lead breaks and estimated source locations determined using Geiger's method and *FastWay*. Estimated source locations excluded during the verification process (see Section 7.3.4) are shown in gray.

C.3.3 Front

PLB			Set	Geiger's method						*FastWay*					
x [in]	y [in]	z [in]	#	x [in]	y [in]	z [in]	d [in]	eei [-]	ac [-]	x [in]	y [in]	z [in]	d [in]	eei [-]	ac [-]
34.0	-4.0	-10.0	13-37	-2.2	-12.0	12.0	43.14	>10.00	6	32.3	-9.3	8.3	19.07	NEL	6
34.0	-4.0	-2.0	11-15	96.0	12.0	8.0	64.81	>10.00	6	24.3	-3.8	6.8	13.10	1.10	6
38.0	-4.0	-10.0	11-16	-6.8	-4.0	-12.0	44.84	>10.00	6	38.3	3.8	-4.3	9.65	0.39	5
38.0	-4.0	-6.0	13-39	-40.4	1.7	-12.0	78.86	>10.00	6	39.3	-0.8	-9.8	5.12	NEL	4
38.0	-4.0	-6.0	13-41	-96.0	12.0	12.0	136.15	>10.00	6	36.8	3.8	-9.8	8.70	NEL	5
38.0	-4.0	-2.0	13-40	-46.5	4.0	2.7	85.05	>10.00	6	24.3	1.8	-0.3	15.01	NEL	6
38.0	-4.0	-2.0	13-42	-20.8	4.0	0.9	59.42	6.01	6	24.3	1.8	-0.3	15.01	NEL	6
38.0	-4.0	2.0	11-17	-11.5	-6.5	12.0	50.51	>10.00	6	44.8	-11.8	8.3	12.03	NEL	6
38.0	-4.0	2.0	13-38	-1.0	0.3	-9.0	40.78	5.93	6	24.3	1.8	-0.3	15.07	NEL	6
38.0	-4.0	2.0	14-41	-96.0	12.0	-12.0	135.68	>10.00	6	41.3	-11.8	9.3	11.10	0.20	6
38.0	-4.0	6.0	14-39	36.6	1.6	6.0	5.76	0.27	4	34.8	3.8	4.8	8.50	NEL	5
38.0	-4.0	6.0	14-40	-96.0	4.0	-12.0	135.44	>10.00	6	43.3	-0.8	-11.8	18.79	NEL	6
38.0	-4.0	6.0	14-42	-96.0	4.0	-12.0	135.44	>10.00	6	44.8	1.8	-10.3	18.51	NEL	6
42.0	-4.0	-10.0	11-23	-9.4	-4.0	-12.0	51.48	>10.00	6	35.3	3.3	-9.3	9.93	0.13	5
42.0	-4.0	-6.0	13-49	-27.7	4.0	-12.0	70.43	>10.00	6	43.3	3.8	3.3	12.13	NEL	6
42.0	-4.0	-6.0	13-54	-96.0	12.0	12.0	140.09	>10.00	6	27.8	3.8	-11.3	17.05	NEL	6
42.0	-4.0	-2.0	13-48	33.5	2.2	-3.6	10.67	1.65	6	40.8	3.8	1.3	8.50	NEL	5
42.0	-4.0	-2.0	13-51	29.0	2.4	-6.3	15.11	2.16	6	25.3	3.8	-11.3	20.64	NEL	6
42.0	-4.0	-2.0	13-52	31.6	3.9	0.5	13.34	1.25	6	37.3	3.8	3.3	10.50	NEL	6
42.0	-4.0	-2.0	13-53	28.7	2.4	-6.3	15.38	2.17	6	25.3	3.8	-10.8	20.43	NEL	6
42.0	-4.0	2.0	13-46	41.6	-4.0	4.2	2.20	1.44	2	36.3	-5.8	8.3	8.67	NEL	5
42.0	-4.0	2.0	13-47	-21.9	4.0	0.8	64.38	6.12	6	24.3	1.8	-0.3	18.79	NEL	6
42.0	-4.0	2.0	13-50	11.1	2.2	-5.3	32.34	7.63	6	24.3	1.8	-0.3	18.79	NEL	6
42.0	-4.0	2.0	14-53	-96.0	4.0	-12.0	138.94	>10.00	6	44.3	-11.8	8.3	10.21	0.67	6
42.0	-4.0	6.0	14-50	41.3	-3.8	4.0	2.16	0.39	2	44.3	-1.8	5.8	3.19	NEL	3
42.0	-4.0	6.0	14-51	41.2	-3.6	3.9	2.23	0.40	2	44.3	-1.8	5.8	3.19	NEL	3
42.0	-4.0	6.0	14-52	-96.0	4.0	-12.0	139.40	>10.00	6	41.8	-1.8	3.3	3.56	NEL	3
46.0	-4.0	-10.0	11-18	19.6	-4.0	-12.0	26.44	9.60	6	51.3	2.3	-0.3	12.72	NEL	6
46.0	-4.0	-10.0	11-20	8.3	-4.0	-12.0	37.76	>10.00	6	49.8	3.8	-3.3	10.94	NEL	6
46.0	-4.0	-10.0	11-22	37.6	-3.7	-0.1	13.02	>10.00	6	42.3	-0.8	-3.3	8.38	NEL	5
46.0	-4.0	-6.0	11-19	15.8	-4.0	-12.0	30.81	>10.00	6	53.8	3.3	3.3	14.08	NEL	6
46.0	-4.0	-6.0	11-21	23.7	-4.6	12.0	28.65	4.93	6	44.3	-11.8	8.3	16.32	0.17	6
46.0	-4.0	-6.0	13-44	-96.0	12.0	12.0	144.03	>10.00	6	36.8	3.8	-9.8	12.64	NEL	6
46.0	-4.0	-2.0	14-49	-96.0	4.0	-12.0	142.58	>10.00	6	48.8	3.8	7.3	12.38	NEL	6
46.0	-4.0	2.0	13-43	41.9	-4.0	3.8	4.45	1.09	3	36.3	-7.3	8.3	12.03	NEL	6
46.0	-4.0	2.0	13-45	43.3	-4.0	3.5	3.07	1.45	3	57.8	-9.3	8.3	14.31	NEL	6
46.0	-4.0	2.0	14-44	-96.0	4.0	-12.0	142.91	>10.00	6	44.8	-5.8	11.8	9.98	0.39	5
46.0	-4.0	2.0	14-45	-96.0	4.0	-12.0	142.91	>10.00	6	48.8	0.3	7.8	7.66	NEL	5
46.0	-4.0	2.0	14-47	-96.0	4.0	-12.0	142.91	>10.00	6	47.3	3.8	5.3	8.50	0.06	5
46.0	-4.0	6.0	14-43	44.6	-1.0	5.9	3.33	0.10	3	44.8	-1.3	6.3	3.03	0.12	3
46.0	-4.0	6.0	14-46	37.4	4.0	3.4	12.01	0.24	6	44.8	-1.3	6.8	3.11	0.10	3
46.0	-4.0	6.0	14-48	35.7	4.0	2.8	13.39	0.36	6	45.8	-1.3	7.3	3.03	0.16	3
50.0	-4.0	-10.0	11-24	-3.6	-4.0	-12.0	53.60	>10.00	6	48.8	-0.3	-11.8	4.32	1.38	3
50.0	-4.0	-10.0	11-25	-6.5	-4.0	-12.0	56.51	>10.00	6	45.8	-0.8	-11.8	5.63	NEL	4
50.0	-4.0	-6.0	13-56	-96.0	-4.0	-12.0	146.12	>10.00	6	50.8	-3.8	-7.8	1.92	NEL	2
50.0	-4.0	-2.0	13-55	56.4	-0.5	-10.4	11.14	2.47	6	58.8	-3.8	-11.3	12.74	NEL	6

Tab. C.21: SW II PLB b - "Front", part 1: Coordinates of the pencil-lead breaks and estimated source locations determined using Geiger's method and *FastWay*. Estimated source locations excluded during the verification process (see Section 7.3.4) are shown in gray.

PLB			Set	Geiger's method						*FastWay*					
x [in]	y [in]	z [in]	#	x [in]	y [in]	z [in]	d [in]	eei [-]	ac [-]	x [in]	y [in]	z [in]	d [in]	eei [-]	ac [-]
50.0	-4.0	-2.0	14-57	47.8	1.1	-2.1	5.53	0.10	4	48.8	-2.8	1.3	3.70	0.05	3
50.0	-4.0	-2.0	14-61	-96.0	-4.0	-12.0	146.34	>10.00	6	32.8	-2.3	-9.8	18.99	NEL	6
50.0	-4.0	2.0	14-55	-96.0	4.0	-12.0	146.89	>10.00	6	49.3	-2.3	4.3	2.95	NEL	3
50.0	-4.0	2.0	14-59	46.0	-4.0	4.9	4.96	0.42	3	48.3	-11.8	8.3	10.11	0.62	6
50.0	-4.0	2.0	14-60	-96.0	-4.0	-12.0	146.67	>10.00	6	47.8	-2.8	4.3	3.42	0.05	3
50.0	-4.0	6.0	14-54	-96.0	-12.0	12.0	146.34	>10.00	6	54.8	1.3	4.3	7.29	0.09	4
50.0	-4.0	6.0	14-56	48.9	-3.9	3.8	2.47	0.17	2	49.3	-3.8	7.3	1.48	0.22	2
50.0	-4.0	6.0	14-58	50.1	-1.1	6.3	2.89	0.19	3	48.3	-1.8	11.8	6.42	0.13	4
54.0	-4.0	-10.0	11-26	78.8	4.0	-12.0	26.13	>10.00	6	52.3	-3.8	-9.8	1.79	1.32	2
54.0	-4.0	-10.0	11-27	79.1	4.0	-12.0	26.41	>10.00	6	52.8	-3.8	-9.8	1.30	1.37	2
54.0	-4.0	-10.0	13-58	-78.1	-4.0	-12.0	132.11	>10.00	6	48.8	-3.8	-7.8	5.72	NEL	4
54.0	-4.0	-6.0	14-64	48.7	-3.5	12.0	18.77	0.41	6	49.8	-11.8	8.3	16.77	0.99	6
54.0	-4.0	-2.0	13-60	-45.1	-4.0	-12.0	99.58	>10.00	6	47.8	0.8	-11.8	12.52	NEL	6
54.0	-4.0	-2.0	14-63	51.7	0.9	-1.1	5.44	0.14	4	49.8	-1.8	-0.8	4.97	0.08	3
54.0	-4.0	2.0	13-57	-80.3	-12.0	12.0	134.94	>10.00	6	46.3	-11.8	8.3	12.62	NEL	6
54.0	-4.0	2.0	13-59	-96.0	-4.0	-12.0	150.65	>10.00	6	51.8	-3.8	-5.8	8.07	NEL	5
54.0	-4.0	2.0	14-67	50.7	1.5	-2.2	7.65	0.10	5	50.8	0.3	-0.8	6.02	0.18	4
54.0	-4.0	6.0	14-62	-96.0	-12.0	12.0	150.33	>10.00	6	49.3	-0.3	6.3	6.06	0.07	4
54.0	-4.0	6.0	14-65	-96.0	-12.0	12.0	150.33	>10.00	6	49.8	-0.8	5.8	5.36	0.22	4
54.0	-4.0	6.0	14-66	53.5	-4.0	5.8	0.54	0.23	1	53.3	-11.8	8.3	8.10	0.17	5
54.0	-4.0	6.0	14-68	-96.0	-4.0	-12.0	151.08	>10.00	6	45.3	-3.8	6.8	8.79	0.03	5
58.0	-4.0	-6.0	13-63	-16.2	-4.0	-12.0	74.47	>10.00	6	57.8	0.3	-10.8	6.38	NEL	4
58.0	-4.0	-6.0	13-67	53.9	-3.7	-6.2	4.14	1.30	3	59.8	0.3	-10.8	6.61	NEL	4
58.0	-4.0	-6.0	13-72	-96.0	4.0	-12.0	154.32	>10.00	6	71.8	0.8	-11.8	15.64	NEL	6
58.0	-4.0	-6.0	13-73	54.0	-3.8	-6.1	4.03	1.32	3	59.8	0.3	-10.8	6.61	NEL	4
58.0	-4.0	-2.0	13-62	57.4	1.5	-7.8	8.05	1.48	5	70.3	0.8	-11.3	16.07	NEL	6
58.0	-4.0	-2.0	13-66	-96.0	4.0	-12.0	154.53	>10.00	6	70.3	0.8	-11.3	16.07	NEL	6
58.0	-4.0	-2.0	13-71	56.4	-10.6	11.8	15.37	1.88	6	53.8	-11.8	8.3	13.53	NEL	6
58.0	-4.0	2.0	13-61	96.0	4.0	-12.0	41.28	>10.00	6	65.8	3.8	2.8	10.99	NEL	6
58.0	-4.0	2.0	13-65	96.0	4.0	-12.0	41.28	>10.00	6	64.3	3.8	-4.8	12.03	NEL	6
58.0	-4.0	2.0	13-70	96.0	4.0	-12.0	41.28	>10.00	6	67.8	3.8	3.8	12.58	NEL	6
58.0	-4.0	6.0	13-64	-96.0	4.0	-12.0	155.25	>10.00	6	71.3	1.8	6.3	14.45	NEL	6
58.0	-4.0	6.0	13-68	74.2	-1.2	-1.1	17.91	1.00	6	69.3	1.8	6.3	12.64	NEL	6
58.0	-4.0	6.0	13-69	-96.0	12.0	12.0	154.95	>10.00	6	61.3	-9.8	8.3	6.98	NEL	4
58.0	-4.0	6.0	14-69	-96.0	-4.0	-12.0	155.05	>10.00	6	57.8	-0.8	7.8	3.70	0.21	3
62.0	-4.0	-10.0	11-29	61.9	4.0	-12.0	8.25	3.00	5	31.8	-3.3	11.3	36.98	NEL	6
62.0	-4.0	-6.0	11-28	96.0	4.0	-12.0	35.44	>10.00	6	58.3	3.3	0.3	10.28	0.04	6
62.0	-4.0	-6.0	11-30	96.0	4.0	-12.0	35.44	>10.00	6	57.8	3.8	5.3	14.31	NEL	6
62.0	-4.0	-6.0	13-80	64.4	3.3	-4.3	7.87	1.99	5	61.8	3.8	-4.3	7.95	NEL	5
62.0	-4.0	-2.0	13-76	-96.0	4.0	-12.0	158.52	>10.00	6	71.3	3.8	5.3	14.08	NEL	6
62.0	-4.0	-2.0	13-79	-96.0	4.0	-12.0	158.52	>10.00	6	67.8	3.8	3.8	11.23	NEL	6
62.0	-4.0	-2.0	13-83	-96.0	4.0	-12.0	158.52	>10.00	6	76.3	3.8	4.3	17.38	NEL	6
62.0	-4.0	2.0	13-75	96.0	4.0	-12.0	37.63	>10.00	6	67.8	3.8	3.8	9.81	NEL	5
62.0	-4.0	2.0	13-78	96.0	4.0	-12.0	37.63	>10.00	6	71.3	3.8	5.3	12.50	NEL	6
62.0	-4.0	2.0	13-82	-82.2	4.0	-12.0	145.09	>10.00	6	65.8	3.8	2.8	8.64	NEL	5
62.0	-4.0	6.0	13-74	-96.0	4.0	-12.0	159.22	>10.00	6	74.3	2.8	3.8	14.17	NEL	6
62.0	-4.0	6.0	13-77	-96.0	4.0	-12.0	159.22	>10.00	6	72.8	2.3	6.3	12.44	NEL	6
62.0	-4.0	6.0	13-81	-96.0	4.0	-12.0	159.22	>10.00	6	77.8	3.3	6.3	17.34	NEL	6
66.0	-4.0	-10.0	11-37	96.0	4.0	-12.0	31.11	>10.00	6	59.8	3.8	-2.3	12.62	0.14	6

Tab. C.22: SW II PLB b - "Front", part 2: Coordinates of the pencil-lead breaks and estimated source locations determined using Geiger's method and *FastWay*. Estimated source locations excluded during the verification process (see Section 7.3.4) are shown in gray.

PLB			Set	Geiger's method						*FastWay*					
x [in]	y [in]	z [in]	#	x [in]	y [in]	z [in]	d [in]	eei [-]	ac [-]	x [in]	y [in]	z [in]	d [in]	eei [-]	ac [-]
66.0	-4.0	-6.0	11-32	96.0	4.0	-12.0	31.62	>10.00	6	64.3	3.8	-4.3	8.14	0.29	5
66.0	-4.0	-6.0	11-36	72.8	4.0	-8.7	10.86	3.61	6	63.3	3.8	-2.8	8.84	0.04	5
66.0	-4.0	-6.0	11-39	96.0	4.0	-12.0	31.62	>10.00	6	64.3	3.8	-4.3	8.14	0.29	5
66.0	-4.0	-2.0	11-35	96.0	4.0	-12.0	32.62	>10.00	6	69.8	6.8	11.8	17.85	NEL	6
66.0	-4.0	2.0	11-31	95.3	-0.6	12.0	31.15	>10.00	6	72.3	-2.8	3.8	6.61	0.06	4
66.0	-4.0	2.0	11-34	84.4	-1.5	12.0	21.05	8.85	6	62.8	-3.8	4.3	3.96	0.10	3
66.0	-4.0	2.0	11-38	69.0	0.9	3.5	5.92	1.66	4	71.8	-3.8	1.8	5.76	0.10	4
66.0	-4.0	6.0	11-33	96.0	-4.0	-5.6	32.15	>10.00	6	67.3	-8.8	8.3	5.40	NEL	4
70.0	-4.0	-6.0	11-41	96.0	4.0	-12.0	27.86	>10.00	6	72.3	3.8	8.3	16.38	NEL	6
70.0	-4.0	-6.0	11-42	96.0	4.0	-12.0	27.86	>10.00	6	68.3	5.3	10.8	19.21	NEL	6
70.0	-4.0	-2.0	11-40	92.4	-0.7	12.0	26.65	>10.00	6	69.3	-2.3	0.3	2.95	0.24	3
70.0	-4.0	-2.0	11-43	81.6	-0.7	3.1	13.15	8.90	6	70.3	0.3	4.8	7.98	0.07	5

Tab. C.23: SW II PLB b - "Front", part 3: Coordinates of the pencil-lead breaks and estimated source locations determined using Geiger's method and *FastWay*. Estimated source locations excluded during the verification process (see Section 7.3.4) are shown in gray.

Nomenclature

Abbreviations and technical terms

2D	two-dimensional
3D	three-dimensional
AE	Acoustic Emission
AIC	Akaike Information Criterion
CT	Computer Tomography
DIC	Digital Image Correlation
EEP	Effective Elastic Properties
EFIT	Elastodynamic Finite-Integration Technique
FD	Finite Differences
LVDT	Linear Variable Differential Transformer
NaN	Not a Number
NCM	Numerical Concrete Model
NEL	No Exact Localization
nodes	point located in the center of a voxel
NRCM	Numerical Reinforced Concrete Model
NRM	Numerical Reinforcement Model
NVM	Numerical Velocity Model
OS	Ortho Slice
p-wave	compression or primary wave; elastic body wave with the highest velocity
PLB	Pencil-Lead Breaks
s-wave	shear or secondary wave; elastic body wave
sh-wave	s-wave with horizontally polarized particles

sv-wave	s-wave with vertically polarized particles
TRM	Time Reverse Modeling
vicinity	area containing all nodes which can be connected with the center node n_c
voxel	volumetric pixel

Symbols

Roman upper-case letters

A_{AE}	maximum amplitude of the recorded AE	[-]
A_i	amplitude of signal i	[-]
$\mathbf{A}_t$	arrival time matrix	[s]
$\mathbf{A}_{\text{tot}}$	arrival time matrix with values for each node for one source location	[s]
A_w	maximum amplitude of white noise	[-]
C'	4×4 covariance matrix	
C	3×3 covariance matrix	
$\mathbf{C}_{mo}$	wave velocity matrix	[m/s]
E	Young's modulus	[kg / (m×s^2)]
$\mathbf{E}_{\text{source}}$	normalized error matrix	[-]
F	force	[N]
J	all-ones matrix	[-]
K	kink point along a wave travel path	
$K_{r(E)}$	reflection coefficient with regard to energy	[-]
$K_{r(P)}$	reflection coefficient with regard to the sound pressure	[-]
$K_{t(E)}$	transmission coefficient with regard to energy	[-]
$K_{t(P)}$	transmission coefficient with regard to the sound pressure	[-]
M	binary control matrix	[-]
O	center of bending radius	
P_0	incident p-wave	
P_1	reflected or refracted p-wave	
R	rotation matrix	
R_i	relaxation parameter for i	[-]

R	bending radius	[m]
EP	End Point	
$\mathbf{S}_{\text{pot}}$	potential source time matrix	[s]
SP	Start Point	
SV_0	incident p-wave	
SV_1	reflected or refracted p-wave	
X_i	random number	[-]
Z	impedance coefficient	[kg × s/m^2]
$Z(c_p)$	impedance coefficient based on the p−wave velocity c_p	[kg × s/m^2]

Roman lower-case letters

$a_{\text{tot};xyz}$	entry in $\mathbf{A}_{\text{tot}}$ for a single node	[s]
ac	accuracy class	
$\mathbf{a}_e$	translation vector for an ellipsoid	[m]
$\mathbf{a}_s$	translation vector for a sphere	[m]
c	wave velocity	[m/s]
c_p	p-wave velocity	[m/s]
c_s	s-wave velocity	[m/s]
$c_{material}$	wave travel velocity of *material* as implemented in *FastWay*	[m/s]
$\bar{c}_{p\_het,se}$	average wave velocity	[m/s]
$c_{p,material}$	p-wave velocity of *material*	[m/s]
d	deviation	[m]
$d_{a,b}$	wave propagation duration time from a to b	[s]
$d_{i;j}$	distance between sensors i and j	[m]
d_i	distance from sensors i to the vertex of $s_p(i,j)$	[m]
dim	number of dimensions	[-]
$\bar{d_i}, j, k$	identical wave travel duration for $\bar{p}_i, j, k$	[s]
$e_{\text{source;AE}}$	entry in $\mathbf{E}_{\text{source}}$ for the node representing the estimated source location	[-]
$e_{\text{source};xyz}$	entry in $\mathbf{E}_{\text{source}}$ for a single node	[-]
eei_{FW}	error estimation index for *FastWay*	[-]

eei_G	error estimation index for the Geiger's method	[-]
ela	estimated localization error	
err_s	systematic error	[m]
f_{FW}	scale factor for eei_{FW}	[-]
f_G	scale factor for eei_G	[-]
f_v	velocity factor	[-]
gp	grid point; edge length of pixels or voxels	[m]
k	number of voxels which the wave propagation path passes through	[-]
l_{bd}	actual wave travel path between source and sensor	[m]
l_d	straight distance between source and sensor	[m]
l_p	length of a wave propagation path	[m]
l_{pk}	length of the wave travel path within voxel or pixel k	
l_x	length of the numerical model or specimen in x direction	[m],[gp]
l_y	length of the numerical model or specimen in y direction	[m],[gp]
l_z	length of the numerical model or specimen in z direction	[m],[gp]
l_{α_t}	wave travel path with regards to α_t	[m]
n	number of nodes	[-]
n_c	center node (see section 3.4.1)	
n_e	end node; end point of a wave propagation path	
n_i	node i	
n_s	start node; start point of a wave propagation path	
n_{tot}	total number of nodes in the model	[-]
p_i	wave travel path i	[m]
$\bar{p}_i, j, k$	identical wave travel path for i, j, and k	[m]
r	radius	[m]
r_a	length of the longest half axis of an ellipsoid	[m]
r_b	length of an ellipsoid half axis perpendicular to r_a, r_c	[m]
r_c	length of an ellipsoid half axis perpendicular to r_a, r_b	[m]
$r_{r_i:r_j}$	radius of a circle consisting of possible source locations	[m]
r_{se}	radius around sensor se	[m]

s	source	
s	residual	
s'	substitution of the variance	
$s_p(i,j)$	hyperbolic curve (2D) or surface (3D) consisting of possible source locations	[m]
$s_{\text{pot};xyz}$	entry in $\mathbf{S}_{\text{pot}}$ for a single node	[s]
se	sensor	
t	time	[s]
t_a	arrival time	[s]
$\mathbf{t}_a$	arrival time vector	[s]
$t_a(se)$	arrival time of the wave at sensor se	[s]
$t_{a;AIC}$	arrival time picked with an AIC-picker	[s]
$t_{a;FT}$	arrival time picked with a fixed threshold	[s]
t_{a_o}	observed (picked) arrival time	[s]
t_{a_t}	theoretical arrival time	[s]
t_c	arrival time of the wave at center node n_c	[s]
t_e	calculated arrival time at end node n_e	[s]
t_i	calculated arrival time of a wave at node n_i	[s]
t_{norm}	normalized wave travel duration	[s]
t_s	source time	[s]
t_{se}	arrival time of the wave at sensor se	[s]
$t_{a,se}$	arrival time of the wave at sensor se	[s]
t_{ct}	constant threshold	
t_{dyn}	dynamic threshold	
$t_{i,rev}$	reverse calculated arrival time at i	[s]
t_{min}	earliest calculated arrival time	[s]
v	velocity	[m/s]
v_{lev}	vicinity level (see section 3.4.1)	
v_{tot}	total number of voxels in the model	[-]
w_{eff}	effective deflection	[m]
$\mathbf{w}_i$	Eigenvalues	

$\tilde{x}$	x-axis of a coordinate system identical to the main axes of an ellipsoids	
x_s	x-coordinate of the source	[m],[gp]
x_{se}	x-coordinate of sensor se	[m],[gp]
$x_{s_{pot}}$	x-coordinate of the potential source	[m],[gp]
$\tilde{y}$	y-axis of a coordinate system identical to the main axes of an ellipsoids	
y_s	y-coordinate of the source	[m],[gp]
y_{se}	y-coordinate of sensor se	[m],[gp]
$y_{s_{pot}}$	y-coordinate of the potential source	[m],[gp]
$\tilde{z}$	z-axis of a coordinate system identical to the main axes of an ellipsoids	
z_s	z-coordinate of the source	[m],[gp]
z_{se}	z-coordinate of sensor se	[m],[gp]
$z_{s_{pot}}$	z-coordinate of the potential source	[m],[gp]

Greek upper-case letters

$\mathbf{\Delta cor}$	correction array	
Δi	correction value for i	
$\Delta_{r_{se1;se2}}$	difference between the radii around sensor $se1$ and $se2$	[m]
$\Delta t_{a,se}$	difference between $t_{a_o,se}$ and $t_{a_t,se}$ for sensor se	[s]
Θ_0	angle of incidence	[rad]
Θ_K	critical angle of incidence	[rad]
Θ_P	angle of reflected or refracted p-wave	[rad]
Θ_S	angle of reflected or refracted s-wave	[rad]
Θ_{SV}	angle of reflected or refracted sv-wave	[rad]
Λ	wavelength	[m]

Greek lower-case letters

α	angle between reinforcement bar and straight connection of s and se	[rad]
α_B	bending angle	[rad]
$\alpha_{ij,ik}$	angle between $s_p(i,j)$ and $s_p(i,k)$	[rad]
α_t	angle between reinforcement bar and wave travel path	[rad]

$\alpha_{t;\min(t_{\text{norm}})}$	α_t leading to the shortest normalized wave travel duration	[rad]
ζ	third vector of $\mathbf{R}$	
η	second vector of $\mathbf{R}$	
ϑ	angle of nutation	[rad]
ν_0	dynamic Poisson's ratio	[-]
ξ	first vector of $\mathbf{R}$	
ρ	density	[kg/m^3]
φ	angle of precision	[rad]
ψ	angle of intrinsic rotation	[rad]
ω	angle between two possible wave travel paths	[rad]

Bibliography

[1] J. D. Achenbach. *Wave Propagation in Elastic Solids (Applied Mathematics and Mechanics)*. North Holland Publishing Company, Amsterdam, 1987.

[2] K. Aki and P. G. Richards. *Quantitative seismology - theory and methods*, volume 1. W. H. Freeman and Company, San Francisco, 1980.

[3] H. Chai, D. Aggelis, S. Momoki, and T. Shiotani. Single-side access tomography for evaluating interior defect of concrete. *Construction and Building Materials*, 24:2411–24187, 2010.

[4] H. Chai, S. Momoki, Y. Kobayashi, D. Aggelis, and T. Shiotani. Tomographic reconstruction for concrete using attenuation of ultrasound. *NDT&E International*, 44:206–215, 2011.

[5] L. de Wreede. *Willbrord Senellius (1581-1626): A Humanist reshaping the Mathematical Siences*. PhD thesis, Universiteit Utrecht, 2007.

[6] E. W. Dijkstra. A Note on Two Problems in Connexion with Graphs. *Numerische Mathematik 1*, pages 269–271, 1959.

[7] P. Fellinger, R. Marklein, K. J. Langenberg, and S. Klaholz. Numerical modeling of elastic wave propagation and scattering with EFIT - elastodynamic finite integration technique. *Wave Motion*, 21:47–66, 1995.

[8] M. Fink. Time reverse acoustics. *Physics today*, 50(3):34–40, 1997.

[9] S. Fricker and T. Vogel. Acoustic monitoring of post-tensioned bridges. In *Structural Faults & Repair 2006, Edinburgh*, pages 48 and CD–ROM file OBRI–FRI.pdf: pp1–8, June 13-15 2006.

[10] S. Fricker and T. Vogel. Feldversuche mit dem akustischen Überwachungssystem SoundPrint. Bericht 609, Eidgenössisches Department für Umwelt, Verkehr, Energie und Kommunikation (UVEK), Bundesamt für Strassen, ASTRA BERN, Februar 2007.

[11] S. Fricker and T. Vogel. Site installation and testing of continous acoustic monitoring. *Construction and Building Materials*, 21(3):501–510, 2007.

[12] M. Ge. Analysis of source location algorithms, Part I: Overview and non-iterative methodes. *Journal of Acoustic Emission*, 21:14–28, 2003.

[13] M. Ge. Analysis of source location algorithms, Part II: Iterative methodes. *Journal of Acoustic Emission*, 21:29–51, 2003.

[14] L. Geiger. Herdbestimmung bei Erdbeben aus der Ankunftszeit. *Nachrichten von der Königlichen Gesellschaft der Wissenschaften zu Göttingen, Math.-phys. Klasse*, 4:331–349, 1910.

[15] J. M. Gere and S. P. Timoshenko. *Mechanics of Materials*. Pws Pub Co, 1997.

[16] S. Gollob, G. K. Kocur, T. Schumacher, L. Mhamdi, and T. Vogel. A novel multi-segment path analysis based on a heterogeneous velocity model for the localization of acoustic emission sources in complex propagation media. *Ultrasonics*, 74:48–61, 2017.

[17] S. Gollob, G. K. Kocur, and T. Vogel. Localization of Acoustic Emissions in a numerically simulated T-shaped Concrete Beam. In *Proceedings - WCAE-2015*, 2015.

[18] S. Gollob, L. Mhamdi, G. K. Kocur, T. Schumacher, and T. Vogel. A Novel Multi-Segmented Path Analysis-Based Technoque for Acoustic Emission Source Localization in Complex Solid Media. In *FraMCoS-9 - 9th International Conference on Fracture Mechanics of Concrete and Concrete Structures*, 2016.

[19] S. Gollob and T. Vogel. Localisation of Acoustic Emission in Reinforced Concrete Using Heterogeneous Velocity Models. In *Proceedings - 31st Conference of the European Working Group on Acoustic Emission (EWGAE)*, 2014.

[20] S. Gollob and T. Vogel. Localisation of acoustic emission sources in reinforced concrete using heterogeneous and orthotropic velocity models. In *Proceedings - 10th fib International PhD Symposium in Civil Engineering - Quebec*, 2014.

[21] S. Gollob and T. Vogel. Localization of Acoustic Emission in Reinforced Concrete using a Heterogeneous Velocity Model and Multilinear Wave Propagation Paths. In *Proceedings - Fib Symposium 2015 - Copenhagen*, 2015.

[22] K. F. Graff. *Wave Motion in Elastic Solids*. Dover Books on Physics, 1975.

[23] C. U. Grosse and M. Ohtsu, editors. *Acoustic Emission Testing, Basics for Research - Applications in Civil Engineering*. Springer-Verlag Berlin Heidelberg, 2008.

[24] Y. Guéguen and V. Palciauskas. *Introduction to the Physics of Rocks*. Princeton University Press, 1994.

[25] H. . R. Hardy. *Acoustic Emission/Microseismic Activity Volume 1: Principles, Techniques and Geotechnical Applications*. Taylor & Francis, 2003.

[26] J. Kaiser. *A study of acoustic phenomena in tensile tests*. PhD thesis, Technical University of Munich, 1950.

[27] G. K. Kocur. *Time reverse modeling of acoustic emission in structural concrete*. PhD thesis, ETH Zürich, 2012.

[28] G. K. Kocur, E. H. Saenger, C. U. Grosse, and T. Vogel. Time reverse modeling of acoustic emissions in a reinforced concrete beam. *Ultrasonics*, 65:96 – 104, 2016.

[29] G. K. Kocur, E. H. Saenger, and T. Vogel. Elastic wave propagation in a segmented X-ray computed tomography model of a concrete specimen. *Construction and Building Materials*, 24:2393–2400, 2010.

[30] G. K. Kocur, E. H. Saenger, and T. Vogel. *RILEM Bookseries, Vol. 6*, chapter Time Reverse Modeling versus Automatic Onset Detection: A Study on Localization of Acoustic Emission in Reinforced Concrete, pages 45–55. Nondestructive Testing of Materials und Structures, 2013.

[31] G. K. Kocur, T. Vogel, and E. H. Saenger. Crack localization in a double-punched concrete cuboid with time reverse modeling of acoustic emissions. *International Journal of Fracture*, 171:1–10, 2011.

[32] G. Korn and T. Korn. *Mathematical Handbook for Scientists and Engineers*. Dover Pubns, 2000.

[33] V. Kose and S. Wagner, editors. *F. Kohlrausch Praktische Physik; Kapitel 2: Akustik*. B. G. Teubner Stuttgart, 1996.

[34] S. Köppel and T. Vogel. Localisation and idendification of cracking mechanisms in reinforced concrete using acoustic emission analysis. In M. J. Ryall, editor, *Bridge Managment 4*, 2000.

[35] J. H. Kurz, C. U. Grosse, and H.-W. Reinhardt. Strategies for reliable automatic onset time picking of acoustic emission and of ultrasound signals in concrete. *Ultrasonics*, 43(7):538–546, 2005.

[36] E. N. Landis and S. P. Shah. Recovery of microcrack parameters in mortar using quantitative acoustic emission. *Journal of Nondestructive Evaluation*, 12(4):219–232, 1993.

[37] J. Li and G. Qi. Improving Source Location Accuracy of Acoustic Emission in Complicated Structures. *Journal of Nondestructive Evaluation*, 28(1):1–8, 2009.

[38] L. Lui and T. Guo. Seismic non-destructive testing on a reinforced concrete bridge column using tomographic imaging techniques. *Journal of geophysics and engineering*, 2:23–31, 2005.

[39] G. C. McLaskey, S. D. Glaser, and C. U. Grosse. Beamforming array techniques for acoustic emission monitoring of large concrete structures. *Journal of Sound and Vibration*, 329(12):2384 – 2394, 2010. Structural Health Monitoring Theory Meets Practice.

[40] M. Ohtsu. The history and development of acoustic emission in concrete engineering. *Magazine of Concrete Research*, 48(177):321–330, 1996.

[41] M. Ohtsu, editor. *Acoustic Emission and Related Non-destructive Evaluation Techniques in the Fracture Mechanics of Concrete*. Woodhead Publishing, 2015.

[42] G. M. Parton, A. A. Shariatmadari, and R. G. Hansom. Efficency in aggregate mix design: a 'least squares' method. *The International Journal of Concrete Composites and Lightweight Concrete*, 11:167–174, 1989.

[43] C. Prada, K. Estelle, D. Cassereau, and M. Fink. Time reversal techniques in ultrasonic nondestructive testing of scattering media. *Reports on Progress in Physics*, pages 1761–1773, December 2000.

[44] E. H. Saenger, N. Gold, and S. A. Shapiro. Modeling the propagation of elastic waves using a modified finite-difference grid. *Wave Motion*, 31(1):77–92, 2000.

[45] E. H. Saenger, O. S. Krüger, and S. A. Shapiro. Effective elastic properties of randomly fractured soils: 3-D numerical experiments. *Geophysical Prospecting*, 52:183–195, 2004.

[46] B. Schechinger. *Schallemissionsanalyse zur Überwachung der Schädigung von Stahlbeton.* PhD thesis, ETH Zürich, 2006.

[47] B. Schechinger and T. Vogel. Acoustic emission for monitoring a reinforced concrete beam subject to four-point-bending. *Construction and Building Materials*, 21(3):483–490, 2007.

[48] F. Schubert. *Ausbreitungsverhalten von Ultraschallpulsen in Beton und Schlussfolgerungen für die zerstörungsfreie Prüfung.* PhD thesis, Technical University of Dresden, 1999.

[49] F. Schubert. Basic principles of acoustic emission tomography. *J. Acoustic Emission*, 22:147–157, 2004.

[50] P. M. Shearer. *Introduction to Seismology - second edition.* Cambridge University Press, 2009.

[51] T. Shiotani, S. Osawa, Y. Kobayashi, and S. Momoki. Application of 3d ae tomography for triaxial tests of rocky specimens. In *31st Conference of the European Working Group on Acoustic Emission (EWGAE)*, 2014.

[52] T. Shiotani, S. Osawa, S. Momoki, and H. Ohtsu. *Advances in Acoustic Emission Technology*, chapter Visualization of Damage in RC Bridge Deck for Bullet Trains with AE Tomography, pages 357–368. Springer, 2013.

[53] G. E. Stavroulakis. Auxetic behaviour: appearance and engineering applications. *physica status solidi (b)*, 3:710–720, 2005.

[54] S. Stein and M. Wysession. *An Introduction to Seismology, Earthquakes, and Earth Structure.* Malden, MA, Blackwell Publishing Ltd., 2003.

[55] V. A. Sulitov. *Physik des Ultraschalls.* Springer-Verlag Wien NewYork, 1984.

[56] A. Tarantola and B. Valette. Inverse problems = quest of information. *Journal of Geophysics*, 50:159–170, 1982.

[57] J. Virieux. SH wave propagation in heterogeneous media: Velocity-stress finite-difference method. *Geophysics*, 49(11):1933–1957, 1984.

[58] J. Virieux. P-SV wave propagation in heterogeneous media: Velocity stress finite-difference method. *Geophysics*, 51(4):889–901, 1986.

[59] J. Vollmann and J. Dual. *Wave Propagation in Elastic Solids.* Institute of Mechanical Systems, ETH Zurich, Swiss Federal Institute of Technology, 2012.